On the transport of angular momentum in stellar radiative zones in 2D

Louis Manchon

université
PARIS-SACLAY

On the transport of angular momentum in stellar radiative zones in 2D

Thèse de doctorat de l'université Paris-Saclay

École doctorale n° 127, Astronomie et Astrophysique d'Ile de France (AAIF)
Spécialité de doctorat: Astronomie et Astrophysique
Unité de recherche: Université Paris-Saclay, CNRS, Institut d'astrophysique spatiale, 91405, Orsay, France
Référent: Faculté des Sciences d'Orsay

Thèse présentée et soutenue à Orsay, le 19 janvier 2021, par

Louis MANCHON

Composition du jury:

Mathieu LANGER Professeur, IAS, Université Paris-Saclay, France	Président
Juan Carlos SUÁREZ Professeur, Dept. Física Teórica y del Cosmos. Universidad de Granada, España	Rapporteur & Examinateur
Marc-Antoine DUPRET Professeur, AGO, Université de Liège, Belgique	Rapporteur & Examinateur
Ana PALACIOS Astronome, LUPM, Université de Montpellier, France	Examinatrice
Daniel REESE Astronome-adjoint, LESIA, Observatoire de Paris, France	Examinateur
Frédéric BAUDIN Astronome, IAS, CNRS/Université Paris-Saclay, France	Directeur de thèse
João Pedro Cadilhe MARQUES Maître de conférence, IAS, Université Paris-Saclay, France	Co-encadrant

Thèse de doctorat

NNT: 2021UPASP006

Remerciements

Je voudrais d'abord à remercier mes directeurs de thèse, Frédéric Baudin et João P. C. Marques, qui m'ont accompagné pendant ces trois années. Je voudrais les remercier de m'avoir fait confiance pour travailler sur ce sujet, pour les nombreuses discussions, scientifiques ou autres, que nous avons eu, et pour leur amitié.

Je voudrais ensuite remercier Mathieu Langer, Marc-Antoine Dupret, Juan Carlos Suárez, Ana Palacios et Daniel Reese d'avoir accepté de composer mon jury de thèse. Je souhaiterais aussi mentionner le nom d'Yveline Lebreton qui avait initialement accepté d'en faire parti et dont j'ai du malheureusement la retirer pour que la composition du jury corresponde aux règles de l'Université. Qu'elle en soit ici remerciée. Je remercie aussi John Leibacher pour sa relecture de ma thèse. Cette deuxième version lui doit beaucoup.

Je remercie tous les membres de l'équipe de physique solaire et stellaire de l'IAS qui m'ont accueilli pendant ces trois ans et qui m'ont fait me sentir comme chez moi. J'ai partagé avec eux de nombreux moments, pauses café, repas, construction d'installations artistiques en tout genre. Une pensée particulière pour tous les thésards et postdocs qui s'y sont succédés. Parmi eux: Frédéric, Charly, Florian, Gabriel, Barbara et enfin, et non pas des moindre, Natalia, avec qui j'ai partagé un magnifique bureau sans vis-à-vis pendant toute la thèse.

Je tiens aussi à remercier les membres du pôle étoile du LESIA, en particulier Rhita pour son aide et son temps passé à répondre à mes questions à propos d'ACOR, et Kevin et Reza pour notre travail sur les effets de surface. Ma compréhension de l'astérosismologie vous doit beaucoup.

Merci aussi à l'équipe enseignante de l'IUT de Cachan: D. Pénard, J.-O. Klein et G. Raynaud, qui m'ont fait découvrir leur pédagogie et m'ont beaucoup aidé dans mes enseignements.

Je voudrais remercier mes parents, mon frère et ma soeur pour m'avoir toujours soutenu. Enfin, je voudrais remercier Lova pour tout son amour depuis toutes ces années. Sans toi je n'y serai pas arrivé.

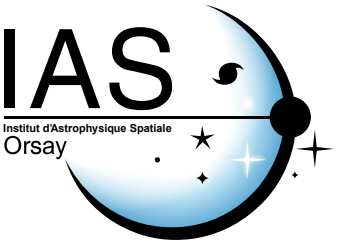

Abstract

Rotation has important consequences for stellar internal structure and evolution. The centrifugal acceleration deforms the star and balances the gravitational one, mimicking a lower mass star. Most importantly, meridional circulations and rotation-induced turbulence mix chemical elements, extending the life of the star and affecting stellar age determinations, one of the most important problems in astrophysics. Lastly, the interaction between rotation and convection generates magnetic fields, maintaining a dynamo. The associated activity has a determining influence on the survival of stellar atmospheres.

Asteroseismic observations from the space missions CoRoT and *Kepler* have clearly shown that current 1D models of angular momentum transport in stellar radiative zones (turbulent viscosity and meridional circulation) are not satisfactory. Other mechanisms must be in action, such as internal gravity waves, magnetic fields and mixed modes. All models proposed for these mechanisms are incomplete. In particular, their description must account for 2D effects.

The 1D description of rotation is usually justified by the fact that horizontal turbulence is much stronger than the vertical in stellar radiative zones, and it suppresses all the latitudinal gradients. Rotation should then be uniform in latitude. This is surely not the case in a convection zone which has differential rotation in latitude. Because internal gravity waves are generated at the base of convective envelopes, the Doppler shift experienced by these waves when they enter the radiation zone should depend on latitude. These waves are further filtered in the transition zone between the convection and radiation zones (the so-called tachocline), a zone that has a strong differential rotation.

This PhD thesis is devoted to the implementation of a simplified treatment of transport of angular momentum in a stellar evolution code in which the structure is still partly treated in 1D. This treatment is based on a deformation method that enables the computation of the 2D structure of the star, as well as the induced perturbation of the various fields (density, effective gravity, etc.). The transport of angular momentum is then treated in 2D, and will allow the further study of additional mechanisms of transport.

Résumé

La rotation a des conséquences importantes sur la structure interne et l'évolution stellaire. La force centrifuge déforme l'étoile et équilibre en partie la gravité, imitant une étoile de masse inférieure. Plus important encore, la circulation méridienne et la turbulences induites par la rotation mélangent les éléments chimiques, prolongeant la vie de l'étoile et affectant la détermination de l'âge stellaire, l'un des problèmes les plus importants en astrophysique. Enfin, l'interaction entre la rotation et la convection génère des champs magnétiques. L'activité associée a une influence déterminante sur la survie des atmosphères stellaires.

Les observations astérosismiques des missions spatiales CoRoT et *Kepler* ont clairement montré que les modèles 1D actuels de transport du moment cinétique dans les zones radiatives stellaires (viscosité turbulente et circulation méridienne) ne sont pas satisfaisants. D'autres mécanismes entrent certainement en jeu, tels que les ondes de gravité interne, les champs magnétiques ou les modes mixtes. Tous les modèles proposés pour ces mécanismes sont, pour l'instant, incomplets. En particulier, leur description doit tenir compte des effets en 2D.

La description 1D de la rotation est généralement justifiée par le fait que la turbulence horizontale est beaucoup plus forte que la verticale dans les zones radiatives stellaires, et supprime tous les gradients latitudinaux. La rotation doit donc être uniforme en latitude. Ce n'est cependant pas le cas dans une zone de convection qui présente une rotation différentielle en latitude. Comme les ondes de gravité internes sont générées à la base des enveloppes convectives, le décalage Doppler subi par ces ondes lorsqu'elles entrent dans la zone radiative devrait dépendre de la latitude. Ces ondes sont ensuite filtrées dans la zone de transition entre les zones de convection et de rayonnement (appelée tachocline), une zone qui présente une forte rotation différentielle.

Ce doctorat est consacré à la mise en œuvre d'un traitement simplifié du transport du moment cinétique dans un code d'évolution stellaire dans lequel la structure est toujours traitée en 1D. Ce traitement est basé sur une méthode de déformation qui permet de calculer la structure 2D de l'étoile, ainsi que la perturbation induite des différents champs (densité, gravité effective, etc.). Le transport du moment angulaire est ensuite traité en 2D, et permettra d'étudier plus en détail d'autres mécanismes de transport.

À Pierre

Contents

List of Figures

List of Tables

Acronyms

ABCD Axisymmetric BaroClinic Diffusive instability.

ACOR Adiabatic Code of Oscillation including Rotation.

AGB Asymptotic Giant Branch.

AM Angular Momentum.

BC Boundary condition.

BRITE Bright-star Target Explorer.

CESAM2K Code d'Évolution Stellaire Adaptatif et Modulaire 2000.

CESAM Code d'Évolution Stellaire Adaptatif et Modulaire.

CESTAM2D Code d'Évolution Stellaire en 2D, avec Transport, Adaptatif et Modulaire.

CESTAM Code d'Évolution Stellaire, avec Transport, Adaptatif et Modulaire.

CME Coronal Mass Ejection.

CTTS Classical T Tauri Stars.

CZ Convective zone.

CoRoT Convection Rotation and Transits.

ESTER Evolution STEllaire en Rotation.

ES Eddington-Sweet.

EOS Equation of State.

FST Full Spectrum of Turbulence.

GGM Gas Γ_1 Model.

GSF Goldreich-Schubert-Fricke.

HSE Hydrostatic equilibrium.

IGW Internal Gravity Waves.

JWKB Jeffreys-Wentzel-Kramers-Brillouin.

LHS Left Hand Side.

MHD Magneto-HydroDynamics.

MLT Mixing-Length Theory.

MRI Magneto-Rotational Instability.

MS Main Sequence.

PLATO PLAnetary Transits and Oscillations of stars.

PMS Pre-Main Sequence.

PM Patched Model.

RGB Red Giant Branch.

RGM Reduced Γ_1 Model.

RHS Right Hand Side.

RZ Radiative Zone.

R-MHD Radiative-Magneto-HydroDynamics.

SEM Standard Envelope Model.

SLO Shear Layer Oscillation.

SoHO Solar and Heliospheric Observatory.

TAMS Terminal-Age Main Sequence.

TAR Traditional Approximation of Rotation.

TESS Transiting Exoplanet Survey Satellite.

TOP Two-dimensional Oscillation Program.

UPM Unpatched Model.

ZAMS Zero-Age Main Sequence.

Introduction: Context and objectives

> On clear winter nights, I have stood on mountains just to be closer to the stars. Some say that these shimmering lights are the souls of warriors who have died in battle; some say that at the beginning of time, Arwe himself cast an infinite number of diamonds into the sky to shine forever and defeat the darkness of night. But I believe the stars are other suns like our own.
>
> *The Lightstone, Part One: The Ninth Kingdom, Ea Cycle*, David Zindell

On the transport of angular momentum in stellar radiative zones

Stars are some of the most opaque objects in the Universe. The only photons we can gather from them are emitted in their atmosphere. Thus we cannot obtain direct and precise information on their interior. Photons emitted from the atmosphere carry global information on the surface such as luminosity, effective temperature, surface chemical composition or information on characteristics of the upper fluid motions. Therefore, for a long time, the only way to glean knowledge on stellar interiors was through analytical and numerical modelling. The theoretical efforts to understand the stellar internal structure started during the second half of the 19th century with the progress made in thermodynamics in the 1st and 2nd industrial revolutions. Simple models of stellar-structure had been established using polytropic relations[1] (e.g. Lane, 1870; Emden, 1902). But the origin of stellar energy remained an enigma. This question is deeper than it may seem because, asking the question of the mechanism of energy generation brings to mind that stars may not be eternal objects and are evolving. The industrial revolutions supported the development of thermodynamics and statistical physics. Classical mechanics had also been well developed before and physicists had *almost* all the necessary knowledge to understand the physics of stars. W. Thomson (Lord Kelvin) and H. Helmholtz suggested that the Sun got its energy from gravitational contraction and derived an age for the Sun of $\sim$ 20 Myr (Thomson 1862; see Stacey 2000 for a review). This was in disagreement with the oldest fossils known at the time (Darwin, 1859; Lyell, 1863) and was ruled out at the dawn of the 20th century when much older fossils and sediments were studied.

At the turn of the century, Becquerel (1896) discovered natural radioactivity and soon after Einstein (1905) understood that matter contained a formidable amount of energy. Eddington

[1] A polytropic relation expresses the pressure as a power law of the density. See further details in this manuscript. It conveniently does not require a computer to obtain a pressure, temperature and density profile inside stars.

(1926) was among the first to propose that energy was dominantly produced by thermonuclear reactions inside stars (Eddington, 1926). Since then, stellar models have experienced important developments. Henyey et al. (1955, 1959a,b, 1964) were the first to compute stellar models using computers and these models were extended by Iben (1965a,b, 1966a,b). These works lead to the standard model of stellar physics (for general texts, see Chandrasekhar, 1957; Cox & Giuli, 1968; Kippenhahn et al., 2012). Star are considered as plasma spheres in hydrostatic and local thermal equilibrium. The energy produced by nuclear fusion reactions, or lost by neutrinos inside stars can be radiated away or converted into thermal energy. All other phenomena that could complicate the physics of stars had, for a long time, been neglected. Among them, one could cite turbulence, magnetic fields, diffusion processes, tidal forces, rotation, etc. With these hypotheses, a physical system as complex as a star can be simplified to a one dimensional system, *i.e.* all the quantities depend only on the radial coordinate. Despite its simplicity, this modelling is extremely powerful. One of its greatest achievements was the correct prediction of the solar neutrino flux, that forced particle physicists to revise their models. Indeed, three flavours of neutrinos were known: ν, ν_τ and ν_μ; but they were thought to be massless. The resolution of the neutrino problem came by understanding that neutrinos could oscillate from one flavour to the other, implying that they had a mass (Haxton, 1995). However, many other models needed direct measurements to be tested which were lacking because of the impossibility to observe the stellar interiors.

Fortunately, a new way of making direct observations of the stellar interior appeared more than half a century ago with the advent of asteroseismology. Asteroseismology is the study of stellar oscillations. The properties of these waves are affected by the characteristics of the medium in which they propagate and, therefore, carry information about it. Helioseismology, the seismology of the Sun, started with the observation of the five-minute oscillation on its surface (Leighton, 1960; Leighton et al., 1962; Evans & Michard, 1962). After these detections, theoretical works started to study their physical nature, and to relate them to physical phenomena taking place inside stars. Ulrich (1970) and Leibacher & Stein (1971) showed that the waves observed at the surface of the Sun are standing acoustic waves. The development of physical theories together with the development of mathematical methods quickly allowed direct tests of models of stellar-structure. For instance the study of long time series of the Sun's photometry or velocity made possible the measurement of the sound speed profiles which provides constraints on the pressure and on the density. Accounting for the impact of the rotation on the mode frequencies also lead to the inversion of the internal solar rotation profile (Brown & Morrow, 1987).

In parallel, theoretical models were being developed to include a description of the evolution of the rotation profile in the standard model in which it was supposed to be neglected (von Zeipel, 1924; Sweet, 1950; Mestel, 1953; Zahn, 1974; Endal & Sofia, 1976, 1978, 1979; Busse, 1981, 1982). modelling the rotation profile and its evolution is needed for several reasons. Rotation is intimately linked to stellar magnetic activity through its interaction with convection. An enhanced magnetic activity induces an increased emission of UV and X-rays, which, in turn, impacts the atmosphere of planets and may hinder the development of life on them. The Sun is thought to have known such an intense-activity phase, soon after its formation. It is one of the reasons for suggesting that on Earth, life started to develop in seas or in pools, water being opaque to UV (Miller, 1953; Rosing et al., 2006; Gallet et al., 2017). The second main reason to study rotation is related to the age estimation of stars. Stars are very often used as proxies for estimating the age of their host and hosted structures (clusters, galaxies, exoplanets, etc.). The alteration of the estimation of the age by rotation is mainly attributable to two phenomena. First, in stars with a central convective zone, hydrogen-rich material from the radiative zone (RZ) can be injected by rotation-induced turbulent diffusion into the central

regions in which thermonuclear reactions take place. Since there is more hydrogen to burn, the stellar life-time is extended. Secondly, the surface chemical composition can also be altered by rotation and change during its evolution. This is, in particular, the case of Lithium, which is observed to be depleted in stars in a very specific mass range ($1.3M_\odot < M < 1.5M_\odot$). However, the temperature in the convective zone of these stars is not high enough to consume Li. The only way to explain the Li depletion is to call on a rotation-induced mechanism transporting Li-poor material inside the convective envelope. Rotation also induces large scale flows (meridional circulation), in the convective zone and RZ[2]. The induced chemical mixing modifies the surface chemical abundances and if this mixing is not properly modelled, the age is misestimated.

Until the end of the 1980s, most stellar rotation models assumed stars to be *barotropic*, *i.e.*, they assumed that isobars coincide with isopycnals[3]. Such a hypothesis is valid only under if the angular velocity is constant on cylinders. The measurement of the solar internal rotation profile obtained by Brown & Morrow (1987) made apparent that the barotropic approximation was not verified and revealed other disagreements. Indeed, in the convection zone, the angular velocity varies with radius and latitude but is not constant on cylinders. In the RZ although, it seems to be nearly constant in the upper part and still unknown elsewhere. The transition region between these two zones (coined the *tachocline*) is very thin, suggesting that here, shear is very strong. Soon, Spiegel & Zahn (1992) and Zahn (1992) proposed a model to explain the shape of the rotation profile in the RZ and its evolution. This model relies on three main ideas. First, in the RZ, angular momentum is advected by the meridional circulation. During the star's evolution, small readjustments of pressure and density gradients creates a baroclinic torque that must be compensated by a meridional circulation so that the star is in baroclinic equilibrium. Second, the angular velocity gradients create shears, prone to instabilities. Thus, the angular velocity is diffused by shear-induced turbulence. They argued that the shear-induced turbulence would be much stronger horizontally than radially, because of the stable stratification. This results in the so-called *shellular rotation* approximation, which is the third assumption of the model. This approximation amounts to assuming that the rotation profile is constant in latitude. Within this assumption, the rotating stellar-structure equations maintain a one dimensional form, while describing a non-spherical star. The quantities do not depend on the radius any more but on the pressure. This model predicts a width of the tachocline that agrees with the observed one.

The development of asteroseismology for stars other than the Sun and especially the high-quality data made available by the space-borne missions CoRoT (Catala et al., 1995; Baglin et al., 2006; Michel et al., 2008), *Kepler* (Borucki et al., 2010) and TESS (Ricker et al., 2014) made apparent disparities between models' predictions and reality. Despite a predicted tachocline width in agreement with the observed one, Zahn (1992)'s model and its later refinements (Maeder, 1995; Meynet & Maeder, 1997; Talon et al., 1997; Maeder, 2003) still predict a radial differential rotation in the solar RZ, in contradiction with the nearly constant rotation profile. Furthermore, the core rotation rate of red giants stars has been found to be around two orders of magnitude lower than that predicted by models (Beck et al., 2012; Deheuvels et al., 2012; Marques et al., 2013). These observations made clear that additional mechanisms of transport of angular momentum need to be included in the modelling of stellar rotation evolution. Many of them have been suggested: hydrodynamic instabilities, magneto-hydrodynamic (MHD) instabilities, transport by mixed modes, internal gravity waves (IGW), etc. Currently, none of these mechanisms are properly and self-consistently modelled. Indeed, MHD instabilities would require that the magnetic field is accounted for in stellar models, which is not the case. As of today, there exists

[2]Although in these zones motion velocities are order of magnitude apart.

[3]Isopycnals are surfaces of constant density.

no complete model of IGW excitation. In addition, IGW are known to induce on small scales very sharp gradients of angular velocity , the sign of which oscillates on very small time scales. This phenomenon, still poorly modelled, is known as a shear layer oscillation (SLO) and filters out IGW in certain ranges of frequencies. In order to allow for a proper modelling of these additional mechanisms of transport of angular momentum, some changes must be made to the standard model of stellar physics.

I choose to relax the hypothesis of spherical symmetry. Different arguments may be put forward to motivate this change in the modelling. First of all, we have seen that in the convective zone, the angular velocity depends on latitude. Therefore, at the transition between the convective and RZ, the boundary condition varies in latitude, not only in radius. Another reason is that the centrifugal acceleration breaks the spherical symmetry. We have seen that the assumption of a shellular profile, underpinned by the fact that turbulence is thought to be much stronger horizontally than radially, allows physicists to keep a 1D description. The turbulent viscosity coefficients are proportional to the gradient of rotation velocity with respect to the distance to the rotation axis. Near the poles, the rotation velocity vanishes and so does its derivative. Therefore the shear becomes negligible, turbulence disappears, and nothing can prevent latitudinal gradients from existing. In this case, the shellular rotation approximation would break down and a 2D description would be needed. Finally, a 2D description is fundamental for a proper modelling of the additional transport mechanisms. For the case of instabilities, many instability criteria depend on the latitude. As a consequence, several instabilities may occur only above or below a certain latitude. This aspect would certainly be missed by a one dimensional description. In the case of waves, and especially internal gravity waves, their properties and the amount of angular momentum that they carry depend on their region of excitation. Internal gravity waves are excited in the convective zone, the angular velocity of which depends on latitude and must be described in two dimensions.

In the early 2000s, models were developed to incorporate two-dimensional effects in stellar modelling. Roxburgh (2004, 2006) developed a method that allows us to deform a 1D model, rotating with a possibly non-uniform angular velocity. This method is able to provide the fluctuations of density, of gravitational potential and of effective gravity over isobars. It also enables the computation of various quantities averaged over isobars that are needed in the modified stellar-structure equations. Mathis & Zahn (2004, 2005) further extended Zahn (1992)'s formalism to go beyond the shellular approximation. I implemented those models in an originally one dimensional stellar evolution code CESTAM (Morel, 1997; Morel & Lebreton, 2008; Marques et al., 2013), which is now able to study stellar evolution with a modelling of the 2D effect of rotation on the interior structure. These developments are primarily intended for testing the transport of angular momentum by internal gravity waves (Kumar et al., 1999; Pinçon et al., 2016).

In this work I restricted ourselves to modelling the transport of angular momentum in the RZ. I set aside the description of rotating convective zones which would require dedicated models. The convective motions have been primarily studied as a mechanism of transport of thermal energy and atomic species but they also transport angular momentum with Reynolds stresses and meridional circulation. Rotation, through the action of the Coriolis force, modifies the trajectories of the convective fluid parcels. The best approach available at the moment is to impose a boundary condition between a radiative and convective zone derived from observations or from 3D simulations. This transition region requires some care because, at this location, exchanges of angular momentum and atomic species can occur. The stars I focused on are low- and intermediate-mass stars, but nothing prevents CESTAM from modelling higher-mass stars (except the domain of validity of the equation of state and opacity tables). The only physical restriction on the stellar mass is the lower limit of $\sim 0.3 M_\odot$ because below that mass,

stars are completely convective. For stars with mass higher than $1.4 M_{\odot}$, other mechanisms should be included in the standard model of stellar physics, such as radiative acceleration and mass loss. These phenomena are studied in parallel by other teams using CESTAM (e.g. Deal et al., 2020). The mass range studied in this PhD is quite representative of the majority of stars in the *Kepler* sample (e.g. Yu et al., 2018).

On the problem of surface effects on adiabatic oscillations

At the beginning of my PhD, I continued the work started during my Masters thesis on the study of the significant disparities between observed and modelled frequencies of modes probing mainly the surface regions of stars. Such systematic discrepancies have now been observed for around three decades (Dziembowski et al., 1988). They are called the surface effects because they are attributed to the deficient modelling of the upper layers of stars with a convective envelope and to the neglect of energy exchanges between modes and convection in this region. One dimensional stellar models oversimplify the physics of these layers, which are subject to highly turbulent flows as well as a complex transition between a convective to a radiative-dominated region (e.g. Kupka & Muthsam, 2017). The effects have been thoroughly studied in the solar case (Rosenthal et al., 1995; Christensen-Dalsgaard & Thompson, 1997; Rosenthal et al., 1999).

Individual frequencies are used to constrain models and the shift of the mode frequencies prevent a direct comparison between observations and models. To overcome this issue, frequency combinations are often used. These combinations are less sensitive to the surface modelling (e.g. Roxburgh & Vorontsov, 2003). Yet, an accurate determination of frequencies is necessary to unlock the full potential of asteroseismology. To that end, several empirical correction laws, relying on adjustable parameters, have been proposed to correct the modelled frequencies (Kjeldsen et al., 2008; Ball & Gizon, 2014; Sonoi et al., 2015). These corrections have proven to be very effective in reproducing the target frequencies and are now widely used in the community (e.g. Lebreton & Goupil, 2014; Silva Aguirre et al., 2017). Nonetheless, the correction laws have at least two caveats. First, the values of their adjustable parameters are not physically grounded. Therefore, different models could be corrected to fit the same observations. It poses a problem of uniqueness of the solution. Secondly, these empirical correction laws do not teach us anything about the physical causes of the problem of surface effect.

Consequently, the physical nature of the surface effect has been the focus of intense work. The effects of the poor modelling of the uppermost convective layers on oscillation frequencies are classified into two categories (e.g. Houdek et al., 2017). The first category, called the structural effects, results from neglecting the turbulent pressure in the stellar-structure. It translates into a smaller resonant cavity and increases the frequencies of its modes of oscillation. The second category, called the modal effects, encompasses the effects coming from oversimplifications of oscillation equations. These simplifications come from the adiabatic hypothesis which is not perfectly valid in the uppermost layers of stars (Balmforth, 1992; Houdek et al., 2017), and from the neglect of the perturbation of the turbulent pressure by the oscillations (Sonoi et al., 2017). Other mechanisms have been suggested to have an impact on the mode frequencies such as convective back-warming (Trampedach et al., 2017) or magnetic activity (Piau et al., 2014; Magic & Weiss, 2016). Still, the dominant source of surface effects is due to the neglect of turbulent pressure, as shown by the pioneering work of Rosenthal et al. (1999) who used more realistic 3D simulation of the Sun's uppermost layers and estimated the elevation of the surface when turbulent pressure was added to hydrostatic equilibrium. They found a relation

depending on the surface elevation that matches very well the frequency differences.

The method of coupling 1D stellar models to 3D models of stellar atmospheres has been used to study the variations of the surface effects across the $T_{\rm eff} - \log g$ plane (Kiel diagram) (Sonoi et al., 2015; Ball et al., 2016; Trampedach et al., 2017). Sonoi et al. (2015) also proposed a physically motivated scaling relation (Samadi et al., 2013) depending on effective temperature and on surface gravity, that prescribes the value of the adjustable parameters of the correction laws. In all previously mentioned works, the chemical composition was assumed to be the same as in the Sun. However, the distribution of metallicity observed in solar-like pulsators spans quite a large range (e.g. Pinsonneault et al., 2014). Our goal in this work is then to study what influences can the metallicity have on the surface effects.

Structure of the manuscript

- Chapter 1: I start by deriving the stellar-structure equations without rotation and I provide a description of the main physical ingredients that must be added to the modelling in addition to the structural quantities. I then show how the structure equations are modified when rotation is included. I explain why these equations must now be solved on isobars and not on spheres if one wants to keep a 1D modelling.

- Chapter 2: The main aspects of the transport of angular momentum are reviewed. I start with the mechanisms that transfer angular momentum out of the system. Then I show that rotating stars cannot locally be in a radiative equilibrium. This is Von Zeipel's theorem, and it results in a misalignment of isobars and isopycnals, which in turn induces a meridional circulation advecting angular momentum. Then, prescriptions for the shear-induced turbulence that diffuses angular velocity are exposed. The formalisms for the computation of the effective gravity, the velocity of the meridional circulation and of the transport of angular momentum are derived.

- Chapter 3: The problem of the surface effects is discussed. I start by writing the oscillation equation in the case of no rotation and by giving some general concepts used in asteroseismology. Then I detail my work on the problem of surface effects, which led to an article Manchon et al. (2018). This Chapter also prepares the groundwork for the seismology of a rotating star, needed in the rest of this PhD thesis.

- Chapter 4: I summarize the observational constraints that we have on the rotation profiles of stars across the Hertzsprung-Russell diagram. The agreement between observed and model rotation profiles is discussed.

- Chapter 5: The additional transport mechanisms that have been proposed to the present are described. It also advocates for the inclusion of a 2D description in stellar evolution modelling.

- Chapter 6: I present all the numerical methods and the algorithm that I implemented into CESTAM. It starts with a brief description of how CESTAM works without the new 2D modules. Then I describe the numerical methods used to deform the models and to compute the velocity of the meridional circulation and to solve the equation of transport of angular momentum. I emphasize some points that are usually left aside in the literature but that are trickier than it seems.

- Chapter 7 I devoted this chapter to the testing and the validation of my work. Each aspect of the algorithms is thoroughly inspected. The testing is performed partly with the help of ACOR, a 2D, non-perturbative oscillation code (Ouazzani et al., 2012).
- Chapter 8: I conclude this work and present what remains to be done and what studies are made possible with this new version of CESTAM. I also describe the on-going collaborations that have been started.

Part I

Basic concepts of stellar evolution and rotation

Chapter 1

Stellar interior modelling

Nous imitons, horreur ! la toupie et la boule
Dans leur valse et leurs bonds; même dans nos sommeils
La Curiosité nous tourmente et nous roule,
Comme un Ange cruel qui fouette des soleils

C. Baudelaire, *Le voyage*, Les Fleurs du Mal

Contents

After the star's formation, its evolution begins with a phase of contraction. During this phase, the effective temperature stays almost constant while the total luminosity decreases because the star is shrinking. This is the *Hayashi track* (Hayashi, 1961). The core temperature increases by $1-2$ order of magnitudes and the opacity decreases. After a short time (~ 1 Myr, depending on the stellar mass), the opacity becomes small enough so that a radiative core appears. The luminosity and the effective temperature then start to increase slowly. From the moment where they start increasing, we enter a stage called the Henyey line (Henyey et al., 1955). In the core, temperature and density increase, resulting in the ignition of the nuclear

reactions. The Hayashi track and the Henyey line form the *Pre-Main Sequence* (PMS) stage. PMS stars radiate energy coming mainly from the potential gravitational energy released during the contraction. The star leaves the PMS to enter the *Main Sequence* (MS) phase. This moment is called the Zero Age Main Sequence (ZAMS) and it is usually defined as the moment where the luminosity is dominated at least at 99% by nuclear reactions. A star spends most of its life in the MS where it is subject to very slow transformations. In low mass stars ($\lesssim 1.25M_\odot$) the principal nuclear reactions are the fusion of hydrogen nuclei to form ^{4}He through the PP chains. Above $1.25M_\odot$, fusion of H into ^{4}He proceeds dominantly through the CNO cycles. Eventually, at some point all the core hydrogen is exhausted. It marks the end of the MS and the star becomes a subgiant star. The core contracts with temperature increasing while the envelope slowly decouples and expands. Hydrogen continues to burn in a shell around a helium core. Then, the star enters the *Red Giant Branch* (RGB). Its radius can increase by more than two orders of magnitude. The core temperature keeps increasing until reaching $\sim 10^8$ K and the degenerate ^{4}He core ignites. In stars with $M \lesssim 2.3M_\odot$, this ignition produces the so-called helium flash, a phenomenon that is extremely violent. In a few hours, the region of helium fusion extends and eventually settles burning He in non-degenerate conditions, releasing an energy of order 10^{41} J. After He is exhausted in the core, it continues in a shell for around 100 Myr (depending on the mass) and the star reaches the Asymptotic Giant Branch (AGB). Stars with initial mass below $\sim 8M_\odot$ end up becoming white dwarfs, above that they become neutron stars or even black holes.

The following chapter is divided as follows. The first section presents the standard stellar-structure equations in the case where rotation is neglected. Then I derive those equations assuming shellular rotation in a baroclinic star. Finally, I give a bit of an overview of the way I computed the equilibrium quantities on isobars. The notations defined in these sections will be used in all the manuscript.

1.1 One dimensional stellar modelling in a nutshell

I start by deriving the structure equations and the physical ingredients used in the standard, one dimensional, model of stellar physics, so that the reader has all the necessary basics.

1.1.1 Derivation of the structure equations in 1D

A star is a static sphere of plasma. Its dynamics can be described by the Navier-Stokes equations. Let us write the equation of motion in which we neglected the viscous stress:

$$\rho \frac{\mathrm{d}\mathbf{v}}{\mathrm{d}t} = \rho \mathbf{g} - \boldsymbol{\nabla} p, \tag{1.1}$$

where ρ is the density field, $\mathbf{v}$ is the velocity, $\mathbf{g} = g\mathbf{e}_r$ is the gravitational acceleration, p the pressure, and $\mathbf{e}_r$ the unit vector in the radial direction. On a sphere of radius r inside the star, the gravitational acceleration is given by:

$$g = -\frac{\mathcal{G}m}{r^2}, \tag{1.2}$$

where $\mathcal{G}$ is the universal gravitational constant[1] and m is the mass inside the sphere of radius r. The star being spherical, the gradient operator reduces to the radial partial derivative and

[1]Values of main universal constants are given in App. A..

Eq. (1.1) becomes:

$$\frac{\mathrm{d}^2 r}{\mathrm{d}t^2} = -\frac{\mathcal{G}m}{r^2} - \frac{1}{\rho}\frac{\partial p}{\partial r}. \tag{1.3}$$

What is the typical value of the acceleration (left hand side of Eq. (1.3))? Let us imagine that the gravitational force is much stronger than the pressure gradient. In this case, the system evolves with a characteristic time-scale called the dynamical time-scale, defined as

$$\tau_{\mathrm{dyn}} = \sqrt{\frac{R_\star^3}{\mathcal{G}M_\star}}. \tag{1.4}$$

Using solar values (see App. A.), $\tau_{\mathrm{dyn}} \simeq 1.6 \times 10^3$ s $\simeq 30$ min. It is evident that such rapid transformations of the Sun are not observed, which means that stars are in hydrostatic equilibrium:

$$\frac{1}{\rho}\frac{\partial p}{\partial r} = -\frac{\mathcal{G}m}{r^2}. \tag{1.5}$$

This equation provides us with a first equation for the stellar-structure. However, we shall see that using the radius as our coordinate of reference is not the best choice we can do. The current description is called a *Eulerian description*. In stellar evolution modelling we actually prefer a *Lagrangian description*, with the mass as our reference coordinate, for several reasons. While the radius can vary by several orders of magnitude (because of contraction during the PMS and dilation of the envelope after MS), the total mass experiences usually very small changes. These changes can either be due to the mass being converted to energy by nuclear reactions, mass lost through stellar winds or gained by accretion. However, the cumulated mass gain/loss is very small (at least during the main sequence). From its birth to the present day, the Sun's mass loss adds up to $\sim 10^{-5} M_\odot$ [2] (Kippenhahn et al., 2012). More importantly, even if the mass change is large, it can be computed before the calculation of the new structure. Therefore the upper mass limit is fixed during the computation, while the total radius is the result of computation of the stellar-structure and cannot be known *a priori*. Furthermore, since Lagrangian description amounts to following a mass element, the substantial or material derivative $\mathrm{d}/\mathrm{d}t$ equals the partial time derivative $\partial/\partial t|_m$. In this framework, all the conservation laws can be written much more simply than if we were using the Eulerian time derivative $\partial/\partial t|_r$.

In order to switch from the Eulerian description used in (1.5) to the Lagrangian description, one needs to express the derivative $\partial r/\partial m$. With $m(r,t)$ the mass contained inside a sphere of radius r, one can write its infinitesimal change as:

$$\mathrm{d}m(r,t) = 4\pi\rho r^2 \mathrm{d}r - 4\pi\rho r^2 v \mathrm{d}t. \tag{1.6}$$

The first term in the right hand side is the change of mass due to a change in radius $\mathrm{d}r$ and the second term is the change of mass due to the displacement of fluid with velocity v during a time $\mathrm{d}t$. From this equation, one obtains that the time derivative of the mass at constant radius is:

$$\left.\frac{\partial m}{\partial t}\right|_r = -4\pi r^2 \rho v. \tag{1.7}$$

[2] In this PhD, we focused on stars with $M \lesssim 10 M_\odot$. In these stars accretion is negligible, even during the PMS. However for more massive stars, accretion can be added to the modelling. Haemmerlé et al. (2019) have computed grid of stellar models up to $120 M_\odot$. For stars with $M > 20 M_\odot$, the accretion phase overlaps with the MS and for $M > 70 M_\odot$, hydrogen is already significantly depleted at the centre when accretion stops.

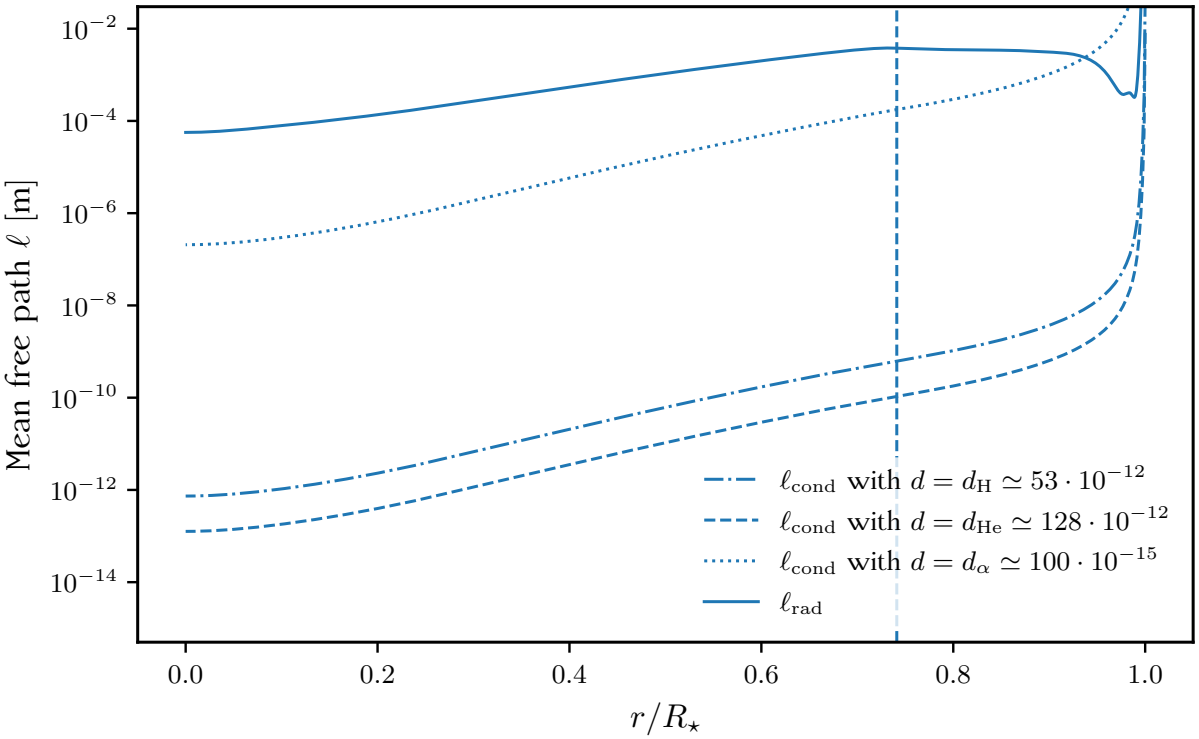

Figure 1.1: Mean free paths against radius normalized to total radius, in a $1 M_\odot$ model at $\simeq 4700$ Myr. The radiative mean free path $\ell_{\rm rad}$ is represented as solid lines and estimates for the conductive one, $\ell_{\rm cond} = k_{\rm B}T/(\sqrt{2}\pi d^2 p)$ are represented as dotted-dashed lines (for $d_{\rm H} \simeq 53$ pm), dashed lines (for $d_{\rm He} \simeq 128$ pm) and dotted lines (for $d_\alpha \simeq 100$ fm). The radius of the convection zone is represented as vertical dashed line.

Since we considered that the star is static, the above derivative is zero. Therefore, in the Lagrangian description

$$\textit{mass conservation:} \qquad \frac{\partial r}{\partial m} = \frac{1}{4\pi\rho r^2}. \tag{1.8}$$

This equation is nothing more than the expression of the density or, more pompously, it is also called the *continuity equation*.

Now that this derivative is known, we can rewrite the hydrostatic equilibrium in its Lagrangian form:

$$\textit{hydrostatic equilibrium:} \qquad \frac{\partial p}{\partial m} = -\frac{\mathcal{G}m}{4\pi r^4}. \tag{1.9}$$

Equations (1.8) and (1.9) describe the mechanical equilibrium of the star. Eqs. (1.8) involves the density which, generally, depends on pressure and temperature (among others). We already have an equation describing pressure variations, we need one for temperature.

Energy is generated and transported inside stars and we will start with the latter. Using the chain rule,

$$\textit{energy transport:} \qquad \frac{\partial T}{\partial m} = \frac{\partial p}{\partial m}\frac{\mathrm{d}T}{\mathrm{d}p} = -\frac{\mathcal{G}m}{4\pi r^4}\frac{T}{p}\nabla, \tag{1.10}$$

where we have defined the *actual* temperature gradient $\nabla = \frac{\mathrm{d}\ln T}{\mathrm{d}\ln p} = \frac{p}{T}\frac{\mathrm{d}T}{\mathrm{d}p}$.

The temperature gradient depends on the energy transport mechanism. There are three of them: conduction, convection and radiation. An easy way to compare the efficiency of radiation with respect to conduction is to compare their mean free path, *i.e.* the mean distance a photon travels before interacting with a particle (in case of radiation) and the mean distance a particle carrying thermal energy can travel before interacting with another one (in case of conduction). The mean free path of a photon is of the order of 10^{-2} m on average in a main-sequence star and 10^{-4} m in the core, while that of conduction is 10^{-5} m on average and 10^{-9} m in the core. Furthermore, the velocity of photons is much higher than the thermal velocity of particles in the plasma. Therefore, radiation is, everywhere in a star, a much more efficient transport process than conduction (Kippenhahn et al., 2012). In Fig. 1.1 are represented the mean free paths of radiation and estimates for the one of conduction. The mean free path of radiation is computed using the relation $\ell = (\kappa\rho)^{-1}$. The one of conduction is more difficult to estimate. The kinetic theory of gas gives the following relation for a gas of molecules:

$$\ell = \frac{k_{\mathrm{B}}T}{\sqrt{2}\pi d^2 p}, \tag{1.11}$$

where p is the pressure and T the temperature, k_{B} is the Boltzmann constant and πd^2 is the collisional cross-section of the molecules. It is rather complicated to find a good estimate for the cross-section because stars are composed of plasma with complex chemical compositions. I computed three estimates for the Bohr radius of Hydrogen: $d_{\mathrm{H}} \simeq 53$ pm (nucleus and electron in first orbit); for the equivalent of the Bohr radius for Helium: $d_{\mathrm{He}} \simeq 128$ pm; and finally for the radius of alpha particles (ionized helium) estimated by scattering 5 MeV alpha particle on gold nuclei: $d_\alpha \simeq 100$ fm. This last radius represents an extreme value. In any case, the mean free path of radiation is much higher than the one of conduction.

Stellar radiative media are optically thick because the radiative mean free path is very small compared to the characteristic scale of the radiative zone (RZ). Thus, these zones are in radiative equilibrium. In such a case, the radiative flux $\mathbf{F}_{\mathrm{r}} = F \cdot \mathbf{u}_r$ can be written as follows:

$$\mathbf{F}_{\mathrm{r}} = -D\nabla U = -\frac{c}{3\kappa\rho}\nabla U, \tag{1.12}$$

where $D = \frac{c}{3\kappa\rho}$ is a diffusion coefficient, c the speed of light, κ the Rosseland opacity and U the radiation energy density (Kippenhahn et al., 2012). Because the medium is in radiative equilibrium, the radiation energy density is linked to the temperature by the Stephan's law: $U = aT^4$, with $a = 7.565 \times 10^{16}$ J m^{-3} K^{-4}. Furthermore, the luminosity l is the flux integrated over a sphere of radius r: $l = 4\pi r^2 F$. Putting everything together leads to

$$F = \frac{l}{4\pi r^2} = -\frac{c}{3\kappa\rho}\frac{\partial U}{\partial r} = -\frac{4ac}{3\kappa\rho}T^3\frac{\partial T}{\partial r}. \tag{1.13}$$

Using the continuity equation (1.8) and then the definition of the temperature gradient of Eq. (1.10), we obtain:

$$l = -\frac{64\pi^2 r^4 ac}{3\kappa}T^3\frac{\partial T}{\partial m} = \frac{16\pi ac\mathcal{G}}{3}\frac{mT^4}{\kappa p}\nabla. \tag{1.14}$$

This equation allows us to define the *radiative gradient*:

$$\nabla_{\mathrm{rad}} = \frac{3}{16\pi ac\mathcal{G}}\frac{\kappa l p}{mT^4}. \tag{1.15}$$

And in the radiative zone, $\nabla = \nabla_{\mathrm{rad}}$, therefore the temperature gradients reads

$$\frac{\partial T}{\partial m} = -\frac{\mathcal{G}m}{4\pi r^4}\frac{T}{p}\nabla_{\mathrm{rad}}. \tag{1.16}$$

In this expression, $l/m = \bar{\varepsilon}$ corresponds to the averaged energy generation rate in a sphere or radius r. If the actual gradient is too high, the medium becomes convectively unstable.

The medium can become convectively unstable for two reasons: κ or $\bar{\varepsilon}$ become too high. In most of the star, opacity is either dominated by free-free (ff) interactions (regions with $T \gtrsim 10^4$ K), or by bound-free (bf) interactions (regions with $T \lesssim 10^4$ K). In these cases, the opacities can be approximated by the Kramers law, which have the same form for both interactions: $\kappa \propto \rho T^{-3.5}$. Despite having the same form, the bf interactions leads to much higher opacities that the ff ones. In stars with masses $\gtrsim 1.4 M_\odot$, the temperature is so high that ff interactions dominate in almost the whole star apart from the uppermost layers. For stars with masses $\simeq 1 M_\odot$, the temperature is sufficiently low so that the opacity is dominated by bf interactions in a significantly large envelope. In this region, κ is high enough for convection to take place (in the Sun, the radial extent of the convection zone is around $0.3 R_\odot$). This mechanism is responsible for the formation of an *envelope* convective zone. On the main sequence, stars with mass above $\sim 1.25 M_\odot$ have a core temperature so high that the CNO cycle[3] dominates the nuclear production of energy. The nuclear reaction rate of the CNO cycle is proportional to T^{16}, while for the PP chain[4] it is only proportional to T^4. The consequence is that, with CNO cycles becoming dominant, the nuclear energy generation rate $\bar{\varepsilon}$ become so high that it is responsible for the formation of a core convective zone. In stars with $1.25 \lesssim M \lesssim 2.5 M_\odot$) the extent of the core convection zone is $\simeq 10\%$ of the total radius. A special case is found for stars with $M \lesssim 0.5 M_\odot$ which are fully convective because of a high opacity. In a convective medium, the temperature gradient takes a different form from a radiative one.

Let us consider a small parcel of fluid rising to a small height. If it does not exchange heat with its surroundings, it expands and cools adiabatically because the pressure of the environment is lower. But if the temperature gradient in the surroundings is more negative than in the parcel, the parcel of gas remains hotter than the environment and buoyancy accelerates its rise. This configuration is encountered when, during the expansion of the parcel of gas, adiabatic change of temperature with respect to pressure is smaller than the change of temperature with respect to pressure in the surrounding (Schwarzschild & Härm, 1958; Ledoux, 1947). This rule can be formalized as follows. A medium is convective if:

$$\left.\frac{\partial T}{\partial m}\right|_{\text{surrounding}} \leq \left.\frac{\partial T}{\partial m}\right|_{\text{parcel}} \leq \left.\frac{\partial T}{\partial m}\right|_{\text{adiabatic}}, \tag{1.17}$$

or in terms of pressure derivatives (note the change of the inequality due to $\partial m/\partial p < 0$):

$$\left.\frac{\partial \ln T}{\partial \ln p}\right|_{\text{ad}} \leq \left.\frac{\partial \ln T}{\partial \ln p}\right|_{\text{surrounding}}. \tag{1.18}$$

In a radiative medium, $\left.\frac{\partial \ln T}{\partial \ln p}\right|_{\text{sur.}} = \nabla_{\text{rad}}$ and by denoting $\left.\frac{\partial \ln T}{\partial \ln p}\right|_{\text{ad.}} = \nabla_{\text{ad}}$, one can write the Schwarzschild criterion for convection instability:

$$\nabla_{\text{ad}} < \nabla_{\text{rad}}. \tag{1.19}$$

Using a more rigorous formalism, the above reasoning can be written as an equation of motion for the fluid parcel at radius r:

$$\rho_{\text{p}} \frac{\mathrm{d}^2 r}{\mathrm{d}t^2} = -g\rho_{\text{p}} - \frac{\mathrm{d}p}{\mathrm{d}r}, \tag{1.20}$$

[3]The CNO cycle can actually take the form of 4 cycles. The most probable one goes through the following steps: ${}^{12}_{6}\mathrm{C} \rightarrow {}^{13}_{7}\mathrm{N} \rightarrow {}^{13}_{6}\mathrm{C} \rightarrow {}^{14}_{7}\mathrm{N} \rightarrow {}^{15}_{8}\mathrm{O} \rightarrow {}^{15}_{7}\mathrm{N} \rightarrow {}^{12}_{6}\mathrm{C}$, generating 26.73 MeV. Noteworthy, ${}^{15}_{8}\mathrm{O}$ is a radioactive isotope of oxygen, but the other CNO cycles can produce stable isotopes.

[4]The PP chain is the sequence of nuclear reactions leading to the production of ${}^4\mathrm{He}$ from four protons. Three different chains are possible and they are called PP1, PP2 and PP3. I give only PP1 but the other two can be found easily. PP1 is written ${}^1\mathrm{H}(p, e^+\nu_e){}^2\mathrm{H}(p,\gamma){}^3\mathrm{He}({}^3\mathrm{He}, 2p){}^4\mathrm{He}$ (in the stellar core, ${}^1\mathrm{H}$ are actually protons).

where $\rho_{\rm p}$ is the density in the parcel and g the gravity. The pressure gradient felt by the parcel is $\mathrm{d}p/\mathrm{d}r = -\rho_{\rm s} g$, where $\rho_{\rm s}$ is the density of the surrounding. Thus, the above equation reduces to

$$\rho_{\rm p} \frac{\mathrm{d}^2 r}{\mathrm{d}t^2} + g(\rho_{\rm p} - \rho_{\rm s}) = 0, \tag{1.21}$$

Assuming that the parcel is displaced from an equilibrium location $r_0 \simeq r$ with equilibrium density $\rho_0 = \rho_{\rm p}(r_0) = \rho_{\rm s}(r_0)$, the above equation can be developed to first order as

$$\frac{\mathrm{d}^2 r}{\mathrm{d}t^2} + \frac{g}{\rho}\left(\left.\frac{\mathrm{d}\rho_{\rm p}}{\mathrm{d}r}\right|_{r_0} - \left.\frac{\mathrm{d}\rho_{\rm s}}{\mathrm{d}r}\right|_{r_0} \right)(r - r_0) = 0. \tag{1.22}$$

The properties of this equation depend on the quantity

$$N^2 = \frac{g}{\rho}\left(\left.\frac{\mathrm{d}\rho_{\rm p}}{\mathrm{d}r}\right|_{r_0} - \left.\frac{\mathrm{d}\rho_{\rm s}}{\mathrm{d}r}\right|_{r_0} \right). \tag{1.23}$$

If N^2, called the square of the *Brunt-Väisälä frequency*, is positive, Eq. (1.22) is the differential equation of a harmonic oscillator. Its solutions are oscillating and we are in a radiative zone. In this case, N corresponds to the frequency at which a small displaced parcel would oscillate. The resulting waves are called *gravity waves*. If on the contrary N^2 is negative, the amplitude of the solution diverges exponentially and we are in a convectively unstable medium.

We have expressed the Brunt-Väisälä frequency with density gradients but we are looking to obtain an expression with temperature gradients. In a general way, the radial derivative $\mathrm{d}\ln\rho/\mathrm{d}r$ can be rewritten

$$\frac{\mathrm{d}\ln\rho}{\mathrm{d}r} = \left.\frac{\partial \ln\rho}{\partial \ln p}\right|_{T,\mu} \frac{\mathrm{d}\ln p}{\mathrm{d}r} + \left.\frac{\partial \ln\rho}{\partial \ln T}\right|_{p,\mu} \frac{\mathrm{d}\ln T}{\mathrm{d}r} + \left.\frac{\partial \ln\rho}{\partial \ln \mu}\right|_{p,T} \frac{\mathrm{d}\ln \mu}{\mathrm{d}r} = \alpha \underbrace{\frac{\mathrm{d}\ln p}{\mathrm{d}r}}_{(i)} - \delta \underbrace{\frac{\mathrm{d}\ln T}{\mathrm{d}r}}_{(ii)} + \varphi \underbrace{\frac{\mathrm{d}\ln \mu}{\mathrm{d}r}}_{(iii)}, \tag{1.24}$$

with μ the mean molecular weight. The parcel and the surrounding are supposed to be in pressure equilibrium therefore the term (i) is the same in the parcel and in the environment. The second term (ii) is equal to the adiabatic gradient in the parcel and to the actual gradient in the surrounding. Finally, the composition of the parcel is unchanged during its rise, therefore, term (iii) is 0 inside it. This term is, however, not necessarily 0 in the environment. In a region with constant chemical composition, the Brunt-Väisälä frequency reads

$$N^2 = \frac{g\delta}{H_{\rm p}}\left(\nabla_{\rm ad} - \nabla\right) \quad \text{with} \quad \frac{1}{H_{\rm p}} = -\frac{\mathrm{d}\ln p}{\mathrm{d}r}, \tag{1.25}$$

where all the terms vanished, except the temperature gradients. The quantity $H_{\rm p}$ is called the pressure scale height. We recognize the term between parenthesis to be the Schwarzschild criterion, and this term decides the sign of N^2. The term (iii) of Eq. (1.24) in the surrounding can be non-zero when the composition varies with the radius. In this case, the Schwarzschild criterion can be modified to include it and becomes the Ledoux criterion (Ledoux, 1947):

$$N^2 = \frac{g\delta}{H_{\rm p}}\left(\nabla_{\rm ad} - \nabla\right) + \frac{g\varphi}{H_{\rm p}}\nabla_\mu = N_T^2 + N_\mu^2, \tag{1.26}$$

where $\nabla_\mu = \mathrm{d}\ln\mu/\mathrm{d}\ln p$ is the mean molecular weight gradient. The terms N_T^2 and N_μ^2 are the thermal and composition parts of the Brunt-Väisälä frequency. Because nuclear reactions

increase the mass of nuclei in the core, the mean molecular weight is usually a decreasing function of the radius. Therefore, N_μ^2 is in general positive and acts as a stabilizing effect because it increases the value of N^2. Brunt-Väisälä frequency allows us to rewrite the convective instability criterion:

$$\textit{Schwarzschild criterion:} \qquad N_T^2 < 0, \tag{I.27}$$

$$\textit{Ledoux criterion:} \qquad N_T^2 + N_\mu^2 < 0. \tag{I.28}$$

We have drawn the main ideas allowing us to understand the physics of convection but we still do not have an expression for ∇ in the convective zones. Such an expression is established by *ad hoc* models, as we will see later. For the moment, we need one last equation that would express the variations of the luminosity that appeared in the formulation of the radiative gradient, in Eq. (I.15). The equations for the conservation of energy will provide this last missing piece. The flux of energy going outward a spherical shell is the energy produced within it minus the one converted into heat. The energy production encompasses the energy gained by nuclear reaction or lost by neutrinos. The energy flux simply writes

$$\textit{energy conservation:} \qquad \frac{\partial l}{\partial m} = \varepsilon_{\rm nuc} + \varepsilon_{\rm grav} - \varepsilon_\nu, \tag{I.29}$$

where $\varepsilon_{\rm nuc}$ (resp. $\varepsilon_{\rm grav}$ and ε_ν) is the energy production rates by nuclear reactions (resp. heat gained and neutrinos) per unit mass . The energy conservation can be seen other way. The energy flowing outside a sphere $\mathcal{S}$ of radius r and mass m during a certain interval of time is the energy produced in the sphere minus the heat gained/lost by the fluid:

$$\oint_{\mathcal{S}} \mathbf{F}\cdot\mathbf{d}\boldsymbol{\sigma} = \int_0^m \varepsilon \mathrm{d}m - \int_0^m \frac{\mathrm{d}q}{\mathrm{d}t}\mathrm{d}m. \tag{I.30}$$

Here, $\mathbf{F}$ is the energy flux, $\boldsymbol{\sigma}$ the surface element, q the specific heat gained by the fluid per unit time and $\varepsilon = \varepsilon_{\rm nuc} - \varepsilon_\nu$ the specific energy produced in the fluid per unit time. This heat gained/lost may have been converted to internal energy or into work to change the volume:

$$\mathrm{d}q = \mathrm{d}u + p\mathrm{d}v \tag{I.31}$$

with u the specific internal energy and $\mathrm{d}v$ the change of specific volume. Using Ostrogradsky theorem in Eq. (I.30), the left hand side can be written as the volume integral of the divergence of the flux and therefore, by integrating over the volume of the sphere, it leads to

$$\boldsymbol{\nabla}\cdot\mathbf{F} = \rho\varepsilon - \rho\frac{\mathrm{d}q}{\mathrm{d}t}. \tag{I.32}$$

By definition of l, $\boldsymbol{\nabla}\cdot\mathbf{F} = \rho\partial l/\partial m$ and we obtain

$$\frac{\partial l}{\partial m} - \varepsilon = -\frac{\mathrm{d}q}{\mathrm{d}t} = -T\frac{\partial s}{\partial t}, \tag{I.33}$$

where s is the specif entropy. The last term correspond to the term $\varepsilon_{\rm grav}$ in Eq. (I.29).

Finally, equations (I.8), (I.9), (I.29), (I.10) form a set of the four standard structure equations:

$$\begin{cases} \dfrac{\partial r}{\partial m} &= \dfrac{1}{4\pi\rho r^2}, \\ \dfrac{\partial p}{\partial m} &= -\dfrac{\mathcal{G}m}{4\pi r^4}, \\ \dfrac{\partial T}{\partial m} &= \dfrac{\partial p}{\partial m}\dfrac{T}{p}\nabla, \\ \dfrac{\partial l}{\partial m} &= \varepsilon_{\rm nuc} + \varepsilon_{\rm grav} - \varepsilon_\nu = \varepsilon_{\rm nuc} - \varepsilon_\nu - T\dfrac{\partial s}{\partial t}, \end{cases} \tag{I.34}$$

with $\nabla = \nabla_{\rm rad}$ in the RZ, and prescribed by a convection model in convective zones.

1.1.2 Physical ingredients

To solve system (1.34), we need the quantities $\rho = \rho(p, T, \mu)$, $\kappa = \kappa(p, T, \mu)$, $\varepsilon = \varepsilon(p, T, \mu)$, $u = u(p, T, \mu)$, $\nabla_{\rm ad}$, etc. These quantities are specific to the material and they can be provided by laboratory experiments, computations or prescribed by models and observations. The chemical composition needs also to be provided and is either measured in stars using spectroscopic observations or assumed. Since some of the following points are discussed in much more detail in upcoming chapters, I will only present the general picture.

Equation of state (EOS) and opacity tables

$\rho(p, T, \mu)$ and $\kappa(p, T, \mu)$ are provided by Equation of State EOS and opacity tables. An EOS can refer to two different concepts. The first one, more limited, is called the thermal equation of state and provides ρ as a function of p, T and μ. The second, more general, provides the thermodynamic potential that allows us to recover all other thermodynamic quantities. The EOS could simply be derived assuming a monoatomic or a perfect gas but such an approach would neglect many complex phenomena such as radiation pressure, Coulomb interactions, etc. Modern stellar evolution codes use EOS provided in tables ready for interpolation. These tables have been calculated by groups specialized in atomic computations who often also compute opacity tables providing κ. The most popular of them are the OPAL opacity table (Rogers & Iglesias, 1992; Iglesias & Rogers, 1996; Rogers & Nayfonov, 2002) and OP from the Opacity Project (Seaton et al., 1994; Badnell et al., 2005; Seaton, 2005, 2007) which are more precise than OPAL but cover a smaller parameter space. EOS is also provided by OPAL or by MHD (Hummer & Mihalas, 1988) associated with OP. These tables are supplemented at low temperatures by the Wichita opacity tables (Ferguson et al., 2005).

Concerning the adiabatic gradient, it is usually an entry of the EOS. If it is not, it can be expressed through another quantity given in them: the 2$^{\rm nd}$ adiabatic index Γ_2 (Chandrasekhar, 1957)

$$\nabla_{\rm ad} = \frac{\Gamma_2 - 1}{\Gamma_2} \quad \text{with} \quad \frac{{\rm d}p}{p} + \frac{\Gamma_2}{1 - \Gamma_2}\frac{{\rm d}T}{T} = 0. \tag{1.35}$$

Nuclear reaction rates

An imprecision on the nuclear reaction rates actually does not change much the longevity of a star because the energy production rate adapts to the luminosity. However, they do have an impact on the structure. Furthermore, nuclear reaction rates are a combination of experimental data and theory-based extrapolations from high to low energy regime because laboratory conditions in which those data are measured are very far from the conditions of density, pressure or temperature in the centre of stars. Finally, for national security reasons, high precision nuclear reaction data are classified. Popular nuclear reaction tables are NACRE (Aikawa et al., 2006) and its update NACREII (Xu et al., 2013) and the LUNA collaboration (Broggini et al., 2018).

Chemical composition

Elements are separated into three categories: Hydrogen (X), Helium (Y) and metals (Z) which includes all other elements. Quite precise abundances can be measured for the Sun and it has been the object of many publications through the years with lower and lower uncertainties affecting abundances (Grevesse & Noels, 1993; Grevesse & Sauval, 1998; Asplund et al., 2005, 2009). The abundances of certain non-volatile elements (Ne, Mg, Si, S, Fe) have also been

refined using meteorites (Scott et al., 2015b,a; Grevesse et al., 2015). See Serenelli (2016) for a review.

The initial chemical composition[5] is a problem in stellar modelling because, apart from the Sun, we only have access to approximate chemical abundances in the stellar atmosphere of other stars. Since elements are usually not depleted by nuclear reactions in the convective envelope (stars with mass $\lesssim 0.5 M_\odot$ are completely convective, therefore, nuclear reactions do occur in the cz), the changes between the current and the initial chemical composition are only due to mixing processes: diffusion or advection. If the modelling does not include these processes, we can assume that the abundances measured in atmosphere are unchanged since the formation of the star. This is actually not a very good approximation, first because diffusion can have a major impact (for instance, see Sect. 2.5), second because at the frontier between radiative and convective zones, mixing does occur (see Sect. 1.1.2, convection). It can have an important impact on the evolution of the star. For instance, the hydrogen rich material injected from convective to a radiative region and vice versa, can increase the lifetime of the star. Mixing is also the cause of a nagging problem in stellar physics: the well mixed convective envelope of a large fraction of stars seem to lack lithium, although, lithium burning temperature is not reached in it. This lithium depletion pleads for complex mixing processes involving convection and rotation (see 4.3.2, lithium depletion problem).

In order to find a prescription for the initial chemical composition of other stars, it is often assumed to scale as the one of the Sun. We usually define ratios of elements to hydrogen, for instance metals to hydrogen: Z/X; or Iron to hydrogen: $[\mathrm{Fe/H}]$. If a star is measured to be 10% less metallic than the Sun, its initial composition of metal is taken to be 10% less than the one of the Sun and X and Y are modified accordingly.

Convection

Convection is a thorny issue in stellar physics. Convection is a purely 3D phenomenon. Moreover, convective motions are highly turbulent in stars (Reynolds number going up to 10^{14}), very sensitive to boundary conditions, and of primary importance in stellar evolution. For a one dimensional treatment, however, *ad hoc* theories of convection have been developed. The goal of such theories is to provide an expression for the actual gradient ∇ of Eq. (1.10). The Mixing Length Theory (MLT; Böhm-Vitense, 1958) is the most used. MLT assumes that all the convective flux is carried by the largest turbulent eddy. In other words, it approximates the turbulence spectrum by a Dirac distribution. MLT supposes that a blob of fluid, hotter and less dense than its surrounding medium rises to a height of ℓ_{MLT}, so-called mixing length, before mixing and releasing its energy. The convective flux, *i.e.* energy carried by convection, can be written as (Hubeny & Mihalas, 2014):

$$F_{\mathrm{conv}} = \left(\frac{gQH_p}{32}\right)^{1/2} \rho c_p T (\nabla - \nabla_{\mathrm{parcel}})^{3/2} \left(\frac{\ell_{\mathrm{MLT}}}{H_{\mathrm{p}}}\right)^2, \tag{1.36}$$

where g is the gravity, $Q = 1 - \partial \ln \mu / \partial \ln T|_p$ with μ the mean molecular weight and c_p the specific heat at constant pressure. MLT makes the assumption that the mixing length is proportional to the pressure scale height: $\ell_{\mathrm{MLT}} = \alpha_{\mathrm{MLT}} H_{\mathrm{p}}$, with α_{MLT} called the MLT parameter. The coefficient α_{MLT} is a free parameter adjusted to retrieve some observables of a particular star. In case of the Sun, $\alpha_{\mathrm{MLT}} \simeq 1.65$. In the deep interior, convection is adiabatic which means that rising gas parcel exchange very little energy with the surrounding medium and $\nabla_{\mathrm{parcel}} \simeq \nabla_{\mathrm{ad}} \simeq \nabla$ (Böhm-Vitense, 1992). In the MLT framework, this is confirmed by a quick

[5] In this context, "initial" means "at the formation of the star", not "at the formation of the Universe".

calculation. In the Sun, the bottom boundary of the convective zone starts at $r \simeq 0.70 R_\odot$ and $m \simeq 0.98 M_\odot$. Here, $F_{\rm conv} \simeq 1.29 \times 10^{11}$ erg cm^{-2} s^{-1}, $g \simeq 5.47 \times 10^4$ cm s^{-2}, $T \simeq 2.2 \times 10^6$ K, $\rho \simeq 1.8 \times 10^{-1}$ g cm^{-3}, $c_p \simeq 3.5 \times 10^8$ erg K^{-1}, $\ell_{\rm MLT} = \alpha_{\rm MLT} H_{\rm p}$ with $\alpha_{\rm MLT} = 1.65$ and $H_{\rm p} = 0.08 R_\odot$, and finally $Q = 1$. With these values, the difference of the thermal gradients are

$$-H_{\rm p} T (\nabla - \nabla_{\rm parcel}) = \left(\left. \frac{{\rm d}T}{{\rm d}r} \right|_{\rm parcel} - \frac{{\rm d}T}{{\rm d}r} \right) \simeq 4.9 \times 10^{-11} {\rm K\,cm^{-1}}, \tag{1.37}$$

and average along a distance of $\ell_{\rm MLT}/2$ it gives

$$\left(\left. \frac{{\rm d}T}{{\rm d}r} \right|_{\rm parcel} - \frac{{\rm d}T}{{\rm d}r} \right) \frac{\ell_{\rm MLT}}{2} \simeq 2.2 \times 10^{-1} {\rm K}. \tag{1.38}$$

It means that only a difference of order 10^{-1}K between the convective parcels and the surrounding medium is able to carry all the necessary flux up to the surface. Near the surface, convection becomes inefficient and the convective parcels exchange large amounts of energy with the medium. Such zone is called superadiabatic because $\nabla > \nabla_{\rm parcel} > \nabla_{\rm ad}$ and the MLT provide an expression for ∇ and $\nabla_{\rm parcel}$.

MLT is one model among a myriad of convection models. We can cite the Full Spectrum of Turbulence (FST) models (Canuto & Mazzitelli, 1991, 1992; Canuto et al., 1996) which provide a more detailed spectrum for the turbulence, or models that propose to introduce new structure equations, some of them describing the geometry of the convection. This has been done for core convection where most of the flux is carried by plumes (Gabriel & Belkacem, 2018). All those models make use of adjustable parameters. The FST models introduce a quantity $\Lambda = z$ where z is the distance to the nearest cz limit. The quantity Λ is thought of as a mixing length and FST models assume that Λ is the same whatever the star is, in other words, FST models do not introduce adjustable parameters. Ludwig et al. (1999) tried to verify this assumption by writing $\Lambda = \alpha_{\rm CM} z$ with $\alpha_{\rm CM}$ a parameter adjusted to match observable parameter of various stars. If FST models were to be right in their assumption that they do not contain any adjustable parameter, $\alpha_{\rm CM}$ would be constant from one star to the other. Ludwig et al. (1999) actually showed that $\alpha_{\rm CM}$ vary as much as $\alpha_{\rm MLT}$ (although their value is not identical). The core convection model of Gabriel & Belkacem (2018) introduce even more free parameters. The energy is carried by N ascending plumes and $N_{\rm D}$ descending ones, N and $N_{\rm D}$ being free parameters. Furthermore, the energy flux is divided into three parts: the radiation flux, the flux of kinetic energy dissipated by plumes (to which is affected an equivalent of the free parameter $\alpha_{\rm MLT}$) and a convective flux (to which is affected another free parameter α_2). Taking into account the kinetic energy flux makes the overshoot possible (which in the MLT formalism should be added afterwards). The convective flux is the flux of energy associated with the plumes and has different sign for ascending and descending ones.

Atmosphere

The structure equations derived above need boundary conditions. While they are simple to derive at the centre of the star, the cases of the top boundary conditions are more complicated. To tackle this issue, an *ad hoc* modelling of the first layers of the atmosphere is added and the idea is to connect the solutions of the structure equations to the solution in the atmosphere. Many atmosphere models can be found, from stratification extracted from complex and specific 1D, 2D or 3D models patched at the surface of the star (see Sect. 3.3) to simple analytical models. The atmosphere can be modelled as a single layer or reconstructed on a grid, if more precision is needed. The atmosphere's structure is described with a modified version

of the structure equations and with the optical depth τ as the independent variable. The temperature is directly given as a function of the optical depth, the so-called $T(\tau)$ relations. With $\mathrm{d}\tau = -\kappa\rho\mathrm{d}r$, the structure equations read

$$\frac{\mathrm{d}m}{\mathrm{d}\tau} = -\frac{4\pi r^2}{\kappa}, \tag{1.39}$$

$$\frac{\mathrm{d}p}{\mathrm{d}\tau} = \frac{\mathcal{G}m}{\kappa r^2}, \tag{1.40}$$

$$\frac{\mathrm{d}T}{\mathrm{d}\tau} = \frac{T}{p}\frac{\mathrm{d}p}{\mathrm{d}\tau}\nabla, \tag{1.41}$$

$$\frac{\mathrm{d}r}{\mathrm{d}\tau} = -\frac{1}{\kappa\rho}. \tag{1.42}$$

The luminosity is assumed constant in the atmosphere and taken as the one at the surface of the star. The surface, and therefore the beginning of the photosphere, is defined as the location where the optical depth reaches a certain value τ_{ph}. In the Eddington approximation[6], $\tau_{\mathrm{ph}} = 2/3$.

1.2 The Modified structure equations in the case of shellular rotation

The above equations have been derived assuming no rotation. But stars do rotate. We would want to incorporate the effects of rotation into the stellar-structure equations in a way that does not change much their shape. It would allow us to keep the same numerical scheme for the structure equations with and without rotation. If we want to properly take rotation into account, the structure equations need to be adapted to the new geometry. Fortunately, we will see that by suitably describing the geometry of the star, structure equations can still be written in one dimension provided some quantities are computed in two dimensions and then averaged over a well chosen surface.

1.2.1 Shellular rotation

In the following, we assume that the angular velocity is constant in spherical or spheroidal shells. The structure equations can then be written in a very convenient way. Such a rota-

[6] In the gray atmosphere model, we make the approximation that the opacity of the medium does not depend on the wavelength (Hubeny & Mihalas, 2014). Using the plane-parallel approximation, one can write the transfer equation of specific intensity $I_{\mu\nu}$ (integrated over frequency) in a direction with angle $\mu = \cos\theta$:

$$\mu\frac{\partial I_\mu}{\partial\tau} = I_\mu - S = I_\mu - J,$$

where S is the source function and J is the mean intensity averaged over solid angles. The functions S and J are integrated over frequencies and $S \equiv J$ because of the hypothesis of radiative equilibrium. Further assuming *local thermodynamic equilibrium*, J as a function of the optical depth is given by the Stephan-Boltzmann law:

$$J(\tau) = \frac{\sigma}{\pi}T(\tau)^4.$$

Furthermore, in the diffusion limit ($\tau \to \infty$),

$$J(\tau) = \frac{3}{2}\int_{-1}^{1} I_\nu\left[\tau + q(\tau)\right]\mu\mathrm{d}\mu = 3H\left[\tau + q(\tau)\right] = \frac{3}{4\pi}\sigma T_{\mathrm{eff}}^4\left[\tau + q(\tau)\right],$$

where H is called the 1$^{\mathrm{st}}$ angular moment of I, and the $q(\tau)$ is called the Hopf function. The provision of $q(\tau)$ allows us to define a $T(\tau)$ relation. The Eddington approximation amounts to approximating the Hopf function as a constant. Its value can be found to be $2/3$.

tion profile is called a *shellular rotation profile* (Zahn, 1992). This approximation is justified if turbulent viscosity is much higher horizontally than vertically:

$$\nu_{\rm h} \gg \frac{l_{\rm h}^2}{l_{\rm v}^2}\nu_{\rm v}, \tag{1.43}$$

where $\nu_{\rm h}$ (resp. $\nu_{\rm v}$) is the horizontal (resp. vertical) turbulent viscosity and $l_{\rm h}$ (resp. $l_{\rm v}$) is the horizontal (resp. vertical) distance over which the transported quantity significantly varies (see Sect. 2.3). This quantity can be the angular momentum but it can also be the chemical abundances. If criterion (1.43) is respected, any small horizontal gradient of Ω would be immediately flattened by turbulent viscosity. A shellular rotation profile is formalized as follow:

$$\Omega(r,\theta) = \overline{\Omega}(r) + \widehat{\Omega}(r,\theta) \quad \text{with} \quad \overline{\Omega}(r) = \frac{\int \Omega \sin^3\theta {\rm d}\theta}{\int \sin^3\theta {\rm d}\theta}, \tag{1.44}$$

and with $\widehat{\Omega} \ll \overline{\Omega}$, Ω is almost constant in a spherical shell. The quantity θ denotes the co-latitude, *i.e* the angle is taken from the pole (see Fig. 1.2). The fluctuation $\widehat{\Omega}$ can be decomposed over functions of θ. Zahn (1992) first proposed to decompose them into Legendre polynomials P_ℓ (see definition in App. B.), and Mathis & Zahn (2004) slightly modified the decomposition of the 2$^{\rm nd}$ order term, this leading to simplifications in the equation for horizontal transport of angular momentum (see Sect. 2.7 for an explanation). This decomposition reads:

$$\widehat{\Omega}(r,\theta) = \sum_{k=1} \Omega_{2k} Q_{2k}(\cos\theta), \tag{1.45}$$

where

$$Q_\ell(\cos\theta) = P_\ell(\cos\theta) - I_\ell \quad \text{with} \quad I_\ell = \frac{\int P_\ell(\cos\theta)\sin^3\theta {\rm d}\theta}{\int \sin^3\theta {\rm d}\theta} = \delta_{\ell,0} - \frac{1}{5}\delta_{\ell,2}, \tag{1.46}$$

with $\delta_{i,j}$ being the Kronecker symbol. For the origin of the factor $1/5$, see the definition of the scalar product of two Legendre polynomials in Eq. (B.12). Then, $Q_2(\cos\theta) = P_2(\cos\theta) + \frac{1}{5}$ and higher degrees reduce to P_ℓ.

In the following, any quantity X can be decomposed as a linear combination of Legendre polynomials on spherical surfaces

$$X(r,\theta) = \sum_{k=0} \widehat{X}_{2k}(r) P_{2k}(\cos\theta) = X_0(r) + \sum_{k=1} \widehat{X}_{2k}(r) P_{2k}(\cos\theta), \tag{1.47}$$

or as a linear combination of Legendre polynomials on isobars:

$$X(p,\theta) = \sum_{k=0} \widetilde{X}_{2k}(p) P_{2k}(\cos\theta) = \overline{X}(p) + \sum_{k=1} \widetilde{X}_{2k}(p) P_{2k}(\cos\theta), \tag{1.48}$$

with $\widetilde{X}_{2k} \neq \hat{X}_{2k}$ and the 0$^{\rm th}$ order term X_0 is defined as

$$X_0(r) = \overline{X}(p) = \frac{\int_0^\pi X(r,\theta)\sin\theta {\rm d}\theta}{\int_0^\pi \sin\theta {\rm d}\theta}. \tag{1.49}$$

If we limit the expansion to P_2, the angle at which $X(p,\theta) = \overline{X}(p)$ is a critical angle $\theta_{\rm m} = \arccos(1/\sqrt{3})$. At this particular angle, only the 0$^{\rm th}$-order (θ-independent) component plays a role (see Fig. 1.2).

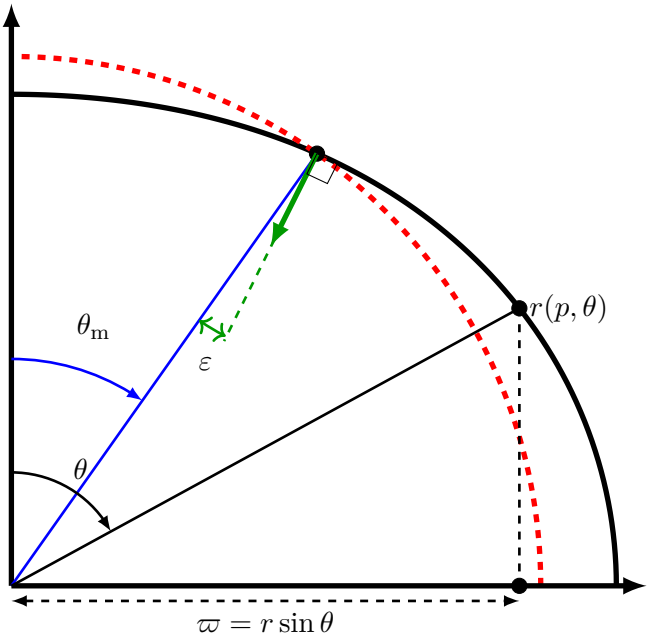

Figure 1.2: Spheroidal polar coordinate system. The radius $r(p,\theta)$ of an isobar p is represented in black. A spherical surface intersecting the isobar at an angle $\theta_{\rm m}$ is represented in red dashes. ε is the angle between the vector normal to a sphere and normal to an isobar. Of course, ε varies over isobar.

1.2.2 Force balance

When rotation is taken into account, one cannot rigorously speak of hydrostatic equilibrium because another force enters the equation: the centrifugal force. Nonetheless, for simplicity, I will keep using the expression "hydrostatic equilibrium" instead of the more general expression "force balance". Let us write the Navier-Stokes equation for a rotating fluid:

$$\frac{\mathrm{D}\mathbf{u}}{\mathrm{D}t} = -\boldsymbol{\nabla}\phi - \frac{1}{\rho}\boldsymbol{\nabla}p - \boldsymbol{\Omega}\times(\boldsymbol{\Omega}\times\mathbf{r}) - 2\boldsymbol{\Omega}\times\mathbf{u}, \tag{1.50}$$

where $\mathbf{u}$ is the velocity field, p the pressure, ρ the density, ϕ the gravitational potential, $\boldsymbol{\Omega}(r,\theta) = \Omega(r,\theta)\mathbf{e}_z = \Omega(r,\theta)\cos\theta\mathbf{e}_r - \Omega(r,\theta)\sin\theta\mathbf{e}_\theta$ the angular velocity and $\mathbf{r} = r\mathbf{e}_r$ is the position vector. We neglected the viscous term. In a static system, $\mathbf{u} = \mathbf{0}$, and the Coriolis acceleration can also be neglected. The star being static, the left hand side vanishes and one can write:

$$\frac{1}{\rho}\boldsymbol{\nabla}p = -\boldsymbol{\nabla}\phi + \Omega^2\boldsymbol{\varpi} = \mathbf{g}_{\rm eff}, \tag{1.51}$$

where $\boldsymbol{\varpi} = \varpi\mathbf{e}_\perp = \varpi\sin\theta\mathbf{e}_r + \varpi\cos\theta\mathbf{e}_\theta$ with $\varpi = r\sin\theta$ and we defined the effective gravity or gravito-centrifugal acceleration $\mathbf{g}_{\rm eff}$, whose radial and colatitudinal components are:

$$g_{{\rm eff},r} = -\frac{\partial\phi}{\partial r} + \Omega^2 r\sin^2\theta = \frac{1}{\rho}\frac{\partial p}{\partial r}, \tag{1.52}$$

$$g_{{\rm eff},\theta} = -\frac{1}{r}\frac{\partial\phi}{\partial\theta} + \Omega^2 r\sin\theta\cos\theta = \frac{1}{\rho r}\frac{\partial p}{\partial\theta}. \tag{1.53}$$

Fig. 1.3, left panel, represents the relative difference between $|\mathbf{g}_{\rm eff}|$ at different latitudes and its value averaged over an isobar (see definition in Eq. (1.69). It clearly shows that the effective gravity is stronger near the pole than near the equator.

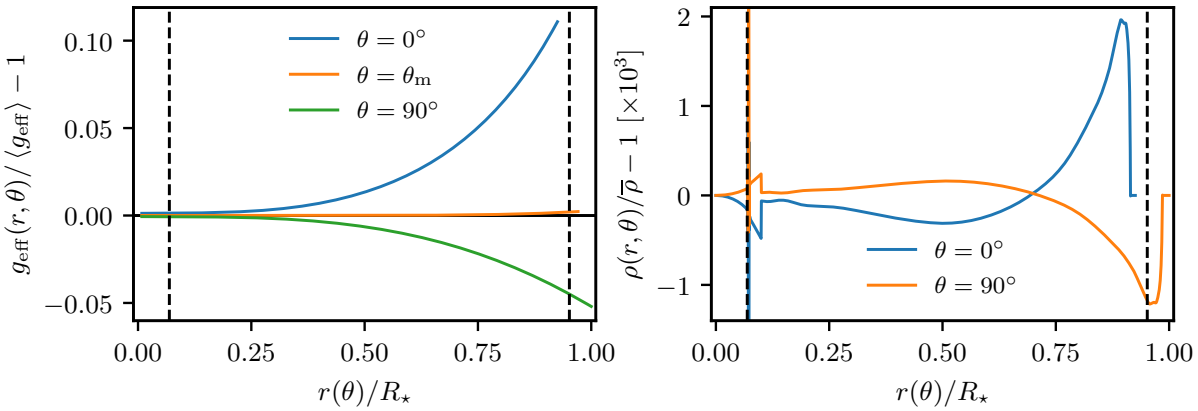

Figure 1.3: Model of mass $1.5M_\odot$ and an age of 1000 Myr with an initial disk lifetime of $\tau_{\rm disk} = 5$ Myr and period of the disk $P_{\rm disk} = 3$ Myr. The angular velocity is around 42% of $\Omega_{\rm K,surf}$ ($\sim 44\%$ in the core and $\sim 40\%$ at the surface). The dashed vertical black lines represent the location of the top limit (resp. the bottom limit) of the core (resp. envelope) convective zone. *Left:* Relative differences between the effective gravity at a colatitude θ and the average effective gravity $\langle g_{\rm eff}\rangle$ as a function of radius. The ordinate 0 is represented as a solid black line and makes it apparent that $\langle g_{\rm eff}\rangle(r) \neq g_{\rm eff}(r,\theta_{\rm m})$. The quantity $g_{\rm eff}(r,\theta_{\rm m})$ is represented as the orange line. *Right:* Relative difference between the density at θ and the density at $\theta_{\rm m}$ as a function of radius.

One interesting thing is that Eq. (1.52) provides a criterion to establish if the star rotates too fast and has reached the break-up velocity. This criterion is

$$\frac{\partial \phi}{\partial r} - \Omega^2 r \sin^2\theta < 0, \tag{1.54}$$

and it amounts to saying that the centrifugal acceleration in the vertical direction is stronger than the gravity in the vertical direction. If this condition is met, the star starts loosing material because it is sent into orbit. By writing, near the equator $\partial\phi/\partial r = \mathcal{G}M/R^2$, we define the surface *Keplerian break-up velocity* $\Omega_{\rm K}$:

$$\Omega_{\rm K,surf} = \sqrt{\frac{\mathcal{G}M}{R^3}}. \tag{1.55}$$

In the remainder of the manuscript, the rotation rate Ω will often be expressed in units of the surface Keplerian break-up velocity, which provides a rapid estimate of the importance of the centrifugal acceleration in the star. It must be noted that $\Omega(r,\theta)$ can reach values higher that $\Omega_{\rm K,surf}$ because, $\Omega_{\rm K}$ is not constant in the interior. Since the radial gradient of angular velocity remains quite unimportant and since the centrifugal force decreases as we get closer to the centre, higher rotation rates are possible in the deep interior.

By taking the curl of the force balance expressed in Eq. (1.51) we obtain the equation for the baroclinic equilibrium:

$$\frac{\boldsymbol{\nabla}\rho \times \boldsymbol{\nabla} p}{\rho^2} = \frac{\boldsymbol{\nabla}\rho \times \mathbf{g}_{\rm eff}}{\rho} = -\frac{1}{2}\boldsymbol{\nabla}\left(\Omega^2\right) \times \boldsymbol{\nabla}\left(r^2\sin^2\theta\right). \tag{1.56}$$

The right hand side is actually the cylindrical derivative of Ω^2: $-r\sin\theta\partial\Omega^2/\partial z \mathbf{e}_\varphi$, with z being the vertical coordinate, parallel to the rotation axis. Therefore the baroclinic equilibrium reduces to

$$\frac{\boldsymbol{\nabla}\rho \times \boldsymbol{\nabla} p}{\rho^2} = -r\sin\theta\frac{\partial\Omega^2}{\partial z}\mathbf{e}_\varphi. \tag{1.57}$$

And this relation is of fundamental importance. The torque on the left hand side is called the *baroclinic torque*, created by a misalignment between isobars and isopycnals, which balances the torque of the centrifugal force on the right hand side. If isobars coincide with isopycnals, $\boldsymbol{\nabla}\rho \parallel \boldsymbol{\nabla}p$ and therefore the baroclinic torque is null and $\partial\Omega/\partial z$ must also be zero. However, any small misalignment of $\boldsymbol{\nabla}\rho$ or $\boldsymbol{\nabla}p$ results in the apparition of a gradient of Ω in the z-direction. And the reverse is true. The implications of this relation will be studied in more detail in Chapter 2.

Going back to Eq. (1.51), one can define the quantity ψ (Meynet & Maeder, 1997) such that:

$$\textit{gravito-centrifugal quasi-potential:} \qquad \psi = \phi - \frac{1}{2}\Omega^2\varpi^2. \tag{1.58}$$

In the case where Ω is constant, ψ is indeed a true potential, constant over non-spherical surfaces and the gravity and centrifugal accelerations are derived from it:

$$\frac{1}{\rho}\boldsymbol{\nabla}p = -\boldsymbol{\nabla}\psi \quad \text{and} \quad \boldsymbol{\nabla}\psi = \boldsymbol{\nabla}\phi + \Omega^2\boldsymbol{\varpi}. \tag{1.59}$$

Here, equipotentials and isobars coincide (as well as isopycnals[7]). Such stars are said to be *barotropic*. This is also the case of stars with Ω constant in cylinders, although the gravito-centrifugal potential is not given in general by Eq. (1.58).

In any other case, ψ *cannot* be considered as a potential in the sense that $\mathbf{g}_{\rm eff} \neq -\boldsymbol{\nabla}\psi$ does not hold. From Eq. (1.51), we have

$$\frac{1}{\rho}\boldsymbol{\nabla}p = -\boldsymbol{\nabla}\psi - \varpi^2\Omega\boldsymbol{\nabla}\Omega = \mathbf{g}_{\rm eff}. \tag{1.60}$$

As we will see shortly, iso-ψ are not equipotential any more but are isobars. Isobars cross isopycnals (as well as isotherms, isentropics etc.) and the star is said to be *baroclinic*. With any rotation profile but a shellular, isobars cross iso-ψ.

As we will see, averaging the structure equations (1.34) over isobars provide a very convenient way to keep a one dimensional description. In the following, we add a subscript p to denote quantities over an isobar. We would want to use m_p, the mass inside the volume enclosed by the isobar located by p, as the independent variable. We have to find an expression for $\mathrm{d}\psi/\mathrm{d}m_p$. Let $\mathrm{d}n$ be the distance between two infinitely close isobars, at a given latitude.

$$g_{\rm eff} = \frac{\mathrm{d}\psi}{\mathrm{d}n} + \varpi^2\Omega\frac{\mathrm{d}\Omega}{\mathrm{d}n} = \frac{\mathrm{d}\psi}{\mathrm{d}n} + \varpi^2\Omega\frac{\mathrm{d}\Omega}{\mathrm{d}\psi}\frac{\mathrm{d}\psi}{\mathrm{d}n}, \tag{1.61}$$

with $g_{\rm eff} = |\mathbf{g}_{\rm eff}|$. All the terms in this equation depend on the colatitude but we did not write it for simplicity. Since we assumed shellular rotation, Ω is constant over isobars, therefore, $\boldsymbol{\nabla}\Omega \parallel \boldsymbol{\nabla}\psi$ and one can write $\boldsymbol{\nabla}\Omega = -\alpha\boldsymbol{\nabla}\psi$, with $\alpha = |\mathrm{d}\Omega/\mathrm{d}\psi|$. Thus, Eq. (1.61) reads

$$g_{\rm eff} = (1 - \varpi^2\Omega\alpha)\frac{\mathrm{d}\psi}{\mathrm{d}n}. \tag{1.62}$$

Hence,

$$\frac{\mathrm{d}p}{\mathrm{d}n} = -\rho(1 - \varpi^2\Omega\alpha)\frac{\mathrm{d}\psi}{\mathrm{d}n}, \tag{1.63}$$

$$\frac{\mathrm{d}p}{\mathrm{d}\psi} = -\rho(1 - \varpi^2\Omega\alpha), \tag{1.64}$$

[7] If in addition there is no fluctuations of mean molecular weight over isobars, isobars also coincide with isotherms

$$\text{and } \frac{\mathrm{d}\psi}{\mathrm{d}n} = \frac{g_{\text{eff}}}{1-\varpi^2\Omega\alpha}. \tag{I.65}$$

We deduce that $\rho(1-\varpi^2\Omega\alpha)$ is constant over isobars since isobars are iso-ψ. Then, by denoting ψ_p the iso-ψ identified by the pressure coordinate, we shall write the mass enclosed between two infinitely close isobars

$$\mathrm{d}m_p = \int_{\psi_p} \rho \mathrm{d}n \mathrm{d}\sigma = \int_{\psi_p} \rho \mathrm{d}\psi \frac{\mathrm{d}n}{\mathrm{d}\psi} \mathrm{d}\sigma = \mathrm{d}\psi \int_{\psi_p} \rho \frac{1-\varpi^2\Omega\alpha}{g_{\text{eff}}} \mathrm{d}\sigma, \tag{I.66}$$

with $\mathrm{d}\sigma$ an isobar surface element defined by

$$\mathrm{d}\sigma = \frac{r^2 \sin\theta \mathrm{d}\varphi \mathrm{d}\theta}{\cos\varepsilon} \quad \text{with} \quad \cos\varepsilon = -\frac{\mathbf{g}_{\text{eff}} \cdot \mathbf{r}}{|\mathbf{g}_{\text{eff}}| \cdot |\mathbf{r}|} = \frac{1}{\sqrt{1+\frac{1}{r^2}\left(\frac{\mathrm{d}r}{\mathrm{d}\theta}\right)^2}}, \tag{I.67}$$

where $r = r(p,\theta)$ is the radius of an isobar (for simplicity we have omitted the θ-dependence), and ε is the angle between the effective gravity and the vector $\mathbf{n}$ perpendicular to an isobar. Since $\rho(1-\varpi^2\Omega\alpha)$ is constant over an isobar, it simply follows that

$$\frac{\mathrm{d}\psi}{\mathrm{d}m_p} = \frac{1}{\rho(1-\varpi^2\Omega\alpha)} \frac{1}{S_p \left\langle g_{\text{eff}}^{-1} \right\rangle}, \tag{I.68}$$

where S_p is the surface of the isobar and we have define the average $\langle\cdot\rangle$ of a quantity f over an isobar as

$$\langle f \rangle = \frac{1}{S_p} \int_{\psi_p} f \mathrm{d}\sigma. \tag{I.69}$$

Coming back to the hydrostatic equilibrium, using Eqs. (I.64) and (I.68), it now reads

$$\textit{hydrostatic equilibrium:} \quad \frac{\partial p}{\partial m_p} = \frac{\mathrm{d}p}{\mathrm{d}\psi} \frac{\partial \psi}{\partial m_p} = -\frac{1}{S_p \left\langle g_{\text{eff}}^{-1} \right\rangle} = -\frac{\mathcal{G} m_p}{4\pi r_p^4} f_p, \tag{I.70}$$

where we have introduce a two new quantities: r_p and f_p. The first is defined as the radius of a sphere such that its volume equals the volume V_p enclosed in an isobar:

$$V_p = \frac{4\pi}{3} r_p^3. \tag{I.71}$$

The second quantity is

$$f_p = \frac{4\pi r_p^4}{\mathcal{G} m_p} \frac{1}{S_p \left\langle g_{\text{eff}}^{-1} \right\rangle}. \tag{I.72}$$

The new expression of the hydrostatic equilibrium is almost identical to the non-rotating case. The gradient $\partial p/\partial m_p$ and the mass m_p do not depend on θ, therefore the right hand side must only depend on one coordinate: the radius. The computation of f_p needs the knowledge of g_{eff} and r_p in two dimensions in order to compute the averages but f_p needs to be evaluated at only one colatitude. Fig. I.4, left panel, represents the value of f_p computed in a $1.5 M_\odot$ model rotating at around 41% of the surface Keplerian break-up velocity. The value of f_p is very close to unity but reaches 0.89 at the surface, which marks an important deviation from the 1D solution. This is also coherent with the value of the relative difference between the surface of a sphere of radius r_p and the surface of the isobar S_p, represented in the right panel. The closer we are to the surface, the larger the relative differences are.

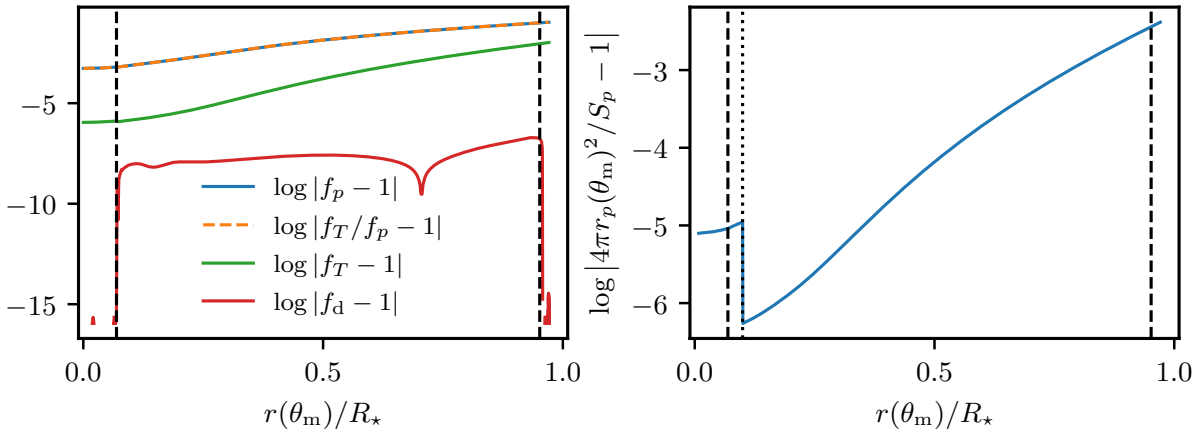

Figure 1.4: Model of mass $1.5M_\odot$ and an age of 1000 Myr with an initial disk lifetime of $\tau_\mathrm{disk} = 5$ Myr and period of the disk $P_\mathrm{disk} = 3$ Myr. The angular velocity is around 42% of $\Omega_\mathrm{K,surf}$ ($\sim 44\%$ in the core and $\sim 40\%$ at the surface). The dashed vertical black lines represent the location of the top limit (resp. the bottom limit) of the core (resp. envelope) convective zone. *Left:* value of $f_p - 1$, $f_T/f_p - 1$, $f_T - 1$ and $f_\mathrm{d} - 1$ as a function of the radius along θ_m. The first two almost superimpose, therefore $f_T/f_p - 1$ is plotted as a dashed line in order to distinguish it from $f_p - 1$. *Right:* Relative difference between the surface of a sphere of radius $r(\theta_\mathrm{m})$ and the surface of the isobar located by p as a function of the radius. The quantity $4\pi r(\theta_\mathrm{m})^2/S_p - 1$ changes sign at the location indicated by the dotted vertical black line. Here, we plotted the log of its absolute value, which explains the sharp glitch at this location.

1.2.3 Conservation of mass

Let $\mathrm{d}V_p$ be the element of volume comprised between two isobars (Meynet & Maeder, 1997; Palacios, 2013):

$$\mathrm{d}V_p = \int_{\psi_p} \mathrm{d}n\mathrm{d}\sigma = \mathrm{d}\psi \int_{\psi_p} \frac{\mathrm{d}n}{\mathrm{d}\psi}\mathrm{d}\sigma = \mathrm{d}\psi \int_{\psi_p} \frac{1-\varpi^2\Omega\alpha}{g_\mathrm{eff}}\mathrm{d}\sigma = \mathrm{d}\psi S_p \left[\left\langle g_\mathrm{eff}^{-1}\right\rangle - \left\langle g_\mathrm{eff}^{-1}\varpi^2\right\rangle \Omega\alpha\right]. \quad (1.73)$$

Using Eq. (1.68), we obtain

$$\textit{mass conservation:} \qquad \frac{\partial r_p}{\partial m_p} = \frac{1}{4\pi r_p^2 \breve{\rho}}. \quad (1.74)$$

Doing so, we have defined $\breve{\rho}$, the mean density in the volume between two infinitely close isobars. This quantity is not equal to average quantity over an isobar $\bar{\rho}$ defined in Eq. (1.49). In a spherical star, the density found in the mass conservation equation, for instance in Eq. (1.8) is also this mean density between two infinitely close spherical surfaces. However, in this particular case, it is also the average density over a spherical surface, because of the spherical symmetry. In our case, since the star is deformed by the centrifugal acceleration, two isobars are closer near the pole than near the equator. Therefore, $\breve{\rho} \neq \bar{\rho}$. Following Eq. (1.73), $\breve{\rho}$ is formally defined as

$$\breve{\rho} = \frac{\rho\left(1-\varpi^2\Omega\alpha\right)\left\langle g_\mathrm{eff}^{-1}\right\rangle}{\left\langle g_\mathrm{eff}^{-1}\right\rangle - \left\langle g_\mathrm{eff}^{-1}\varpi^2\right\rangle \Omega\alpha} = \rho f_\mathrm{d} \quad \text{with} \quad f_\mathrm{d} = \frac{\left(1-\varpi^2\Omega\alpha\right)\left\langle g_\mathrm{eff}^{-1}\right\rangle}{\left\langle g_\mathrm{eff}^{-1}\right\rangle - \left\langle g_\mathrm{eff}^{-1}\varpi^2\right\rangle \Omega\alpha}. \quad (1.75)$$

It shall be noted that $\breve{\rho}$ is also not equal to $\bar{\rho}$ defined by the Legendre decomposition of Eq. (1.48). The value of f_d for a $1.5M_\odot$ model is represented in Fig. 1.4, left panel. Among the quantities plotted in this panel, this is the one that is the closest to one.

In our model, we assume that the convective zones either have a uniform angular velocity (see Eq. (2.122)) or have a uniform specific angular momentum distribution (see Sect. 2.7.3). These assumptions are not correct. As we will see in Chapter 4, the convective zone of the Sun is differentially rotating in latitude and radius. However, we assume these profiles for the sake of simplicity because these distributions satisfy the conditions for a shellular rotation. The model used in Fig. 1.4 was computed with a uniformly rotating convection zone. Therefore, in those regions, $f_{\rm d} = 1$. Indeed, $f_{\rm d}$ depends on the gradient of angular velocity through $\alpha = |{\rm d}\Omega/{\rm d}\psi|$, which is zero in the convection zones. The only discrepancies between $f_{\rm d}$ and unity are purely numerical.

1.2.4 Conservation of energy

The net energy flowing from a volume comprised between two infinitely close isobars is:

$$ {\rm d}L_p = \int_{\psi_p} \varepsilon\rho {\rm d}n {\rm d}\sigma = {\rm d}\psi \int_{\psi_p} \varepsilon\rho \frac{{\rm d}n}{{\rm d}\psi} {\rm d}\sigma, \tag{1.76} $$

where we introduced $\varepsilon = \varepsilon_{\rm nucl} + \varepsilon_{\rm grav} - \varepsilon_\nu$ the net energy production rate in the shell defined in Eq. (1.29). Making use of Eq. (1.65), it follows

$$ {\rm d}L_p = {\rm d}\psi \left\langle \frac{\varepsilon}{g_{\rm eff}} \right\rangle S_p \rho (1 - \varpi^2 \Omega \alpha), \tag{1.77} $$

and using again Eq. (1.68),

$$ \textit{energy conservation:} \qquad \frac{\partial L_p}{\partial m_p} = \frac{\left\langle (\varepsilon_{\rm nucl} + \varepsilon_{\rm grav} - \varepsilon_\nu) g_{\rm eff}^{-1} \right\rangle}{\left\langle g_{\rm eff}^{-1} \right\rangle}. \tag{1.78} $$

We do not have a simple way of calculating the average of the energy generation rates over an isobar. Meynet & Maeder (1997) proposed to use the $0^{\rm th}$-order term in the Legendre decomposition of T and ρ and approximate $\langle \varepsilon_i \rangle$ by $\varepsilon_i(\overline{\rho}, \overline{T})$. However, energy generation rates have been defined by integrating over a small volume. Therefore, it would be more appropriate to use mean density $\breve{\rho}$ and temperature $\breve{T}$ in the volume between two infinitely close isobars. As we do not have a simple expression for $\breve{T}$ we will use

$$ \frac{\left\langle (\varepsilon_{\rm nucl} + \varepsilon_{\rm grav} - \varepsilon_\nu) g_{\rm eff}^{-1} \right\rangle}{\left\langle g_{\rm eff}^{-1} \right\rangle} \simeq \varepsilon_{\rm nucl}(\breve{\rho}, \overline{T}) + \varepsilon_{\rm grav}(\breve{\rho}, \overline{T}) - \varepsilon_\nu(\breve{\rho}, \overline{T}). \tag{1.79} $$

This leads to:

$$ \textit{simplified energy conservation:} \qquad \frac{\partial L_p}{\partial m_p} = \varepsilon_{\rm nucl}(\breve{\rho}, \overline{T}) + \varepsilon_{\rm grav}(\breve{\rho}, \overline{T}) - \varepsilon_\nu(\breve{\rho}, \overline{T}). \tag{1.80} $$

1.2.5 Energy transport

As in Sect. 1.1.1, the temperature gradient can be written in a general way

$$ \frac{{\rm d}T}{{\rm d}m_p} = \frac{\partial p}{\partial m_p} \frac{{\rm d}T}{{\rm d}p}. \tag{1.81} $$

Using the ∇ notation and injecting Eq. (1.70) in Eq. (1.81) we obtain:

$$ \frac{{\rm d}T}{{\rm d}m_p} = -\frac{\mathcal{G} m_p}{4\pi r_p^4} f_p \frac{T}{p} \nabla, \tag{1.82} $$

where once again the only difference with Eq. (1.10) is the factor f_p. The next step is to find an expression for ∇. The reasoning follows the same steps as for the standard energy transport equation but this time with averaging over isobars.

In a radiative medium

Eq. (1.12) expressed with Eq. (1.65) and (1.68) yields

$$F = -\frac{4acT^3}{3\kappa\rho}\frac{\mathrm{d}T}{\mathrm{d}n} = -\frac{4acT^3}{3\kappa}\frac{\mathrm{d}T}{\mathrm{d}m_p}\left\langle g_{\rm eff}^{-1}\right\rangle S_p g_{\rm eff}. \tag{1.83}$$

We may think that we implicitly supposed that $\boldsymbol{\nabla} T \parallel \mathbf{g}_{\rm eff}$. However, this is not true: $\mathrm{d}T/\mathrm{d}n$ depends on $\mathrm{d}T/\mathrm{d}m_p$. If we had $\boldsymbol{\nabla} T \parallel \mathbf{g}_{\rm eff}$, then $\mathrm{d}T/\mathrm{d}m_p$ would depend only on the pressure, not on latitude. But this is not true because, in general, isotherms cross isobars, thus cross iso-$g_{\rm eff}$. And by integrating this flux over an isobar, one retrieves an expression for the luminosity

$$L_p = -\frac{4ac}{3}\left\langle g_{\rm eff}^{-1}\right\rangle S_p^2 \left\langle \frac{T^3 g_{\rm eff}}{\kappa}\frac{\mathrm{d}T}{\mathrm{d}m_p}\right\rangle, \tag{1.84}$$

leading to a modified expression of the radiative gradient:

$$\nabla_{{\rm rad},p} = \frac{3\kappa}{16\pi ac\mathcal{G}}\frac{p}{T^4}\frac{L_p}{m_p}\frac{f_T}{f_p} = \nabla_{\rm rad}\frac{f_T}{f_p} \quad \text{with} \quad f_T = \left(\frac{4\pi r_p^2}{S_p}\right)^2 \frac{1}{\langle g_{\rm eff}\rangle\left\langle g_{\rm eff}^{-1}\right\rangle}. \tag{1.85}$$

The values differences between f_T or f_T/f_p and unity are represented in Fig. 1.4. The quantity $f_T - 1$ is almost 2-3 orders of magnitude below $f_p - 1$, which explains that $|f_T/f_p - 1| \simeq |f_p - 1|$.

In a convective medium

In a convection zone, one has locally

$$\frac{\mathrm{d}\ln T}{\mathrm{d}\ln p} = \nabla_{\rm conv}, \tag{1.86}$$

where $\nabla_{\rm conv}$ is obtained from a model of convection. Averaging over an isobar,

$$\left\langle \frac{\mathrm{d}\ln T}{\mathrm{d}\ln p}\right\rangle = \langle \nabla_{\rm conv}\rangle\,. \tag{1.87}$$

In convective zones, the chemical composition is the same everywhere because of the very efficient mixing and we can write the following approximations:

$$\left\langle \frac{T^3 g_{\rm eff}}{\kappa}\frac{\mathrm{d}T}{\mathrm{d}m_p}\right\rangle \simeq \frac{\overline{T}^3\langle g_{\rm eff}\rangle}{\kappa(\breve{\rho},\overline{T})}\frac{\mathrm{d}\overline{T}}{\mathrm{d}m_p}, \tag{1.88}$$

$$\left\langle \frac{\mathrm{d}\ln T}{\mathrm{d}\ln p}\right\rangle \simeq \frac{\mathrm{d}\ln \overline{T}}{\mathrm{d}\ln p}, \tag{1.89}$$

$$\langle \nabla_{\rm conv}\rangle \simeq \nabla_{\rm conv}(\breve{\rho},\overline{T}). \tag{1.90}$$

Finally,

$$\textit{energy transport:} \qquad \frac{\partial T}{\partial m_p} = -\frac{\mathcal{G}m_p}{4\pi r_p^4} f_p \min\left[\nabla_{\rm conv}, \nabla_{\rm rad}\frac{f_T}{f_p}\right]. \tag{1.91}$$

In this equation, the $\min(\cdot,\cdot)$ operator plays the role of the Schwarzschild criterion. This expression states the radiative equilibrium *on average over an isobar*, whereas Eq. (1.83) shows that the local radiative flux depends on latitude through $g_{\rm eff}(p,\theta)$ and therefore its direction varies over an isobar.

It is also interesting to go back on the equation of motion (1.21) derived for a displaced parcel of material in a stellar interior. In the case of rotating star, an additional term must be added to the equation related to the additional rotation motion experienced by the parcel. Eq. (1.21) becomes

$$\frac{\mathrm{d}^2 r}{\mathrm{d}t^2} + \frac{g}{\rho_\mathrm{p}}(\rho_\mathrm{p} - \rho_\mathrm{s}) - \varpi\left(\Omega_\mathrm{p}^2 - \Omega_\mathrm{s}^2\right) = 0. \tag{1.92}$$

Hence, the linearised equation of motion (1.22) now reads

$$\frac{\mathrm{d}^2 r}{\mathrm{d}t^2} + \left[\frac{g}{\rho}\left(\left.\frac{\mathrm{d}\rho_\mathrm{p}}{\mathrm{d}r}\right|_{r_0} - \left.\frac{\mathrm{d}\rho_\mathrm{s}}{\mathrm{d}r}\right|_{r_0}\right) + \frac{1}{\varpi^3}\frac{\mathrm{d}\varpi^4\Omega^2}{\mathrm{d}\varpi}\sin\theta\right](r - r_0) = 0, \tag{1.93}$$

where we used $(\varpi^4\Omega_\mathrm{p}^2 - \varpi^4\Omega_\mathrm{s}^2)/\varpi^3 \simeq \frac{1}{\varpi^3}\left(\mathrm{d}\varpi^4\Omega^2/\mathrm{d}\varpi\right)(\varpi - \varpi_0)$. The term in square brackets defines a new expression for the Brunt-Väisälä frequency that incorporates the effect of the angular momentum distribution (Wasiutynski 1946)

$$N^2 = \frac{g\delta}{H_\mathrm{p}}\left(\nabla_\mathrm{ad} - \nabla\right) + \frac{g\varphi}{H_\mathrm{p}}\nabla_\mu + \frac{1}{\varpi^3}\frac{\mathrm{d}\varpi^4\Omega^2}{\mathrm{d}\varpi}\sin\theta = N_T^2 + N_\mu^2 + N_\Omega^2\sin\theta, \tag{1.94}$$

and allows us to write:

$$\textit{Solberg-Høiland criterion:} \qquad N_T^2 + N_\mu^2 + N_\Omega^2\sin\theta < 0, \tag{1.95}$$

where N_Ω^2 is called the Rayleigh-Taylor frequency or the epicyclic frequency. The angular momentum has a stabilizing effect when $\mathrm{d}\varpi^4\Omega^2/\mathrm{d}\varpi > 0$ (or, equivalently, $N_\Omega^2 > 0$), which is the case in general. When $N_\Omega^2 < 0$, the angular momentum distribution can destabilize the medium if it overcomes the effects of N_T^2 and N_μ^2. If so, it gives rise to the Rayleigh-Taylor instability, described in 5.1.1.

Eqs. (1.70), (1.74), (1.80) and (1.91) form the new structure equations system in case of shellular rotation:

$$\begin{cases} \dfrac{\partial r_p}{\partial m_p} &= \dfrac{1}{4\pi r_p^2 \breve{\rho}}, \\ \dfrac{\mathrm{d}p}{\mathrm{d}m_p} &= \dfrac{\mathcal{G}m_p}{4\pi r_p^4} f_p, \\ \dfrac{\partial T}{\partial m_p} &= \dfrac{\mathcal{G}m_p}{4\pi r_p^4} f_p \min\left[\nabla_\mathrm{conv}, \nabla_\mathrm{rad}\dfrac{f_T}{f_p}\right], \\ \dfrac{\partial L_p}{\partial m_p} &= \dfrac{\left\langle(\varepsilon_\mathrm{nucl} + \varepsilon_\mathrm{grav} - \varepsilon_\nu) g_\mathrm{eff}^{-1}\right\rangle}{\left\langle g_\mathrm{eff}^{-1}\right\rangle}, \end{cases} \tag{1.96}$$

where ∇_conv stands for the gradient in the convective zone, which should be prescribed by a convection theory.

Finding a way to keep a one dimensional form for the baroclinic structure equations without the shellular approximation is a task that remains to be done, and may not even be possible.

Chapter 2

Transport of angular momentum in radiative zones

> Il faut beaucoup de chaos en soi pour faire surgir une étoile qui danse.
>
> Nietzsche

Contents

A star is not strictly speaking isolated because, after its formation, it can exchange angular momentum (AM in the following) with a residual accretion disk or loose some through stellar winds. Such processes extract AM from the upper regions of the star and need to be taken into account into the modelling because they determine the angular velocity at the surface. In the rest of the stellar interior, AM can be transported by various processes. It has been said in the introduction that one of the major problems of rotation is that it induces a transport of chemicals and it perturbs our estimation of stellar ages. The issue is less important in convective zones because here, chemicals are very well mixed by convective motions. In such regions, the rotation profile can be prescribed, either from observations or from models. In the radiative zone, one of these mechanisms is the advection of AM by a large scale stream, called the *meridional circulation*. If the transport of AM leads to sharp gradients of angular velocity, the shear can become sufficiently strong to overcome the stabilizing effect of the stratification and creates instabilities. The shear-induced turbulence results in the diffusion of angular velocity.

The mechanisms of transport of AM mentioned above are going to be discussed in this Chapter. They are now implemented in a many 1D stellar evolution codes, with the simplifying assumption that the star is spherical. However, while the meridional circulation *advects* AM, it is often modelled as a purely diffusive process (e.g. Paxton et al., 2019). During this PhD, I implemented the model described in this Chapter by relaxing the hypothesis of sphericity and by effectively modelling the action of the meridional circulation as an advection.

2.1 Losses of angular momentum

2.1.1 Disk magnetic braking

The path from a molecular cloud to a rotating star is not a simple process. Any molecular cloud has a non zero AM. If the material would collapse straight onto the protostar, by conservation of AM, the angular velocity would become extremely high and the centrifugal acceleration would overcome gravity by several orders of magnitude. The same can be said for the magnetic field. The collapse would concentrate the magnetic field and increase the magnetic pressure which would also overcome gravity. However, stars do form. There must therefore exist mechanisms that prevent AM and magnetic fields to concentrate into the collapsing cloud. In reality, the gas does not fall directly to the centre but forms an accretion disk. At the beginning of the accretion, the disk is optically thick and is called a Class 0, Young Accreting Protostar.[1]

Once the disk becomes sufficiently thin, the accretion rate decreases and becomes negligible. This is the beginning of the PMS and such a star is called a Classical T Tauri Star (CTTS). Despite all the angular momentum and magnetic fields extracted during the accretion process, CTTS are fast rotators with intense magnetic fields. The strong magnetic field is sustained by a dynamo effect caused by the interaction between rotation and convection. Bouvier et al. (1997) have proposed the model of disk locking, suggesting that due to Alfvén's frozen-in theorem, the magnetic field lines that spread across the outer convective zone and the disk force them to co-rotate as a solid body. During this phase, the CTTS is still contracting but the disk locking

[1]We are not even on the pre-main-sequence. André (2002). As long as the rotation velocity of the inner layers increases, they transfer part of their AM (and magnetic field) to the outer layers due to the turbulent viscosity of the disk. With the AM being slowly transported from the central layers to the outer ones, the gas slowly spiral and accrete to form a star.

allows the star to transfer a large amount of angular momentum to the disk. The remaining disk dissipates itself by forming planets and the star unlocks from the disk.

Typical disk lifetimes $\tau_{\rm disk}$ can be estimated from observational data (e.g. Czekala et al., 2019) to be between 0.1 Myr to 10 Myr, with a median of 3 Myr, and a Keplerian rotation period $P_{\rm disk}$ of 1 to 10 d. It seems coherent with observations that are starting to be possible using radio interferometry. Czekala et al. (2019) studied the disks around binary systems with $P_{\rm disk} \in [1; 10^3]$ d but fast rotating disks ($P_{\rm disk} < 50$ d) are less than 0.2 a.u. from their host star, while slowly rotating disks ($P_{\rm disk} > 50$ d) were above 1 a.u. and up to 100 a.u., suggesting that slow and far disks may be magnetically decoupled from the host star. Apart from a few outliers, all the systems considered in their sample were less than 10 Myr old.

2.1.2 Stellar winds

After the decoupling between star and disk, a magnetic field remains. The magnetic field maintains a hot corona and the hotter material is blown away into the interplanetary medium to form the so-called stellar winds. Solar winds have first been theorized by Eugene Parker in 1958 (Parker, 1958) and then predicted in CTTS (Kuhi, 1964, 1966). In order to understand the behaviour of the stellar wind and the associated AM transport, it is interesting to introduce a quantity called the *Alfvén radius* $r_{\rm A}$. The Alfvén radius is defined as the location where the magnetic pressure equals the kinetic energy density of the wind. Between the corona and $r_{\rm A}$, the dynamics are dominated by the magnetic field and the wind follows the magnetic field lines. Above $r_{\rm A}$, it is the magnetic field lines that are carried by the wind. This wind also carries an amount of AM associated to a lever arm equal to the Alfvén radius (Weber & Davis, 1967). In order to provide a law for the amount of AM lost by a star as a function of relevant parameters, we shall see how magnetism and rotation are linked.

An important stellar magnetic activity induces a higher ratio of X-ray luminosity to the bolometric (total) luminosity. Therefore the ratio $R_{\rm X} = L_{\rm X}/L_{\rm bol}$ can be used as a proxy of stellar activity. On the other hand, the efficiency of the dynamo effect can be estimated through a dimensionless number called the *Rossby number* ${\rm Ro} = P_{\rm rot}/\tau$, with $P_{\rm rot}$ the surface rotation period of the star and τ the convective turnover time, *i.e.* the time it takes for a parcel of material to rise from the bottom of the outer convective zone to reach the surface and then go back to the bottom. This number measures the interaction between rotation and convection. A high Rossby number is associated to a slow rotator. Measurements and comparisons of $R_{\rm X}$ and Ro have been performed by many authors in field stars or open cluster[2] stars (e.g. Wright et al., 2011; Núñez et al., 2015). They have shown that for Ro greater than a certain threshold ${\rm Ro}_{\rm sat}$, $R_{\rm X} \propto {\rm Ro}^{\beta}$, with $\beta < 0$. Below this threshold, $R_{\rm X}$ remains constant equal to $R_{\rm X,sat}$. It means that, for a reason yet to be understood, above a certain angular velocity of saturation $\Omega_{\rm sat}$, the dynamo effect saturates. Many authors have proposed laws based on this saturation feature. The first of them, and the simplest was proposed by Kawaler (1988). The AM $\mathrm{d}\mathcal{J}/\mathrm{d}t$ lost by a wind that co-rotates with the star up to a radius $r_{\rm A}$ is, for $\Omega < \Omega_{\rm sat}$,

$$\frac{\mathrm{d}\mathcal{J}}{\mathrm{d}t} = -K_{\rm W}\Omega^3 \left(\frac{R}{R_\odot}\right)^{1/2} \left(\frac{M}{M_\odot}\right)^{-1/2}, \tag{2.1}$$

and for $\Omega > \Omega_{\rm sat}$,

$$\frac{\mathrm{d}\mathcal{J}}{\mathrm{d}t} = -K_{\rm W}\Omega\Omega_{\rm sat}^2 \left(\frac{R}{R_\odot}\right)^{1/2} \left(\frac{M}{M_\odot}\right)^{-1/2}, \tag{2.2}$$

[2] An open cluster is a cluster of young stars that are loosely linked by gravity. The interesting point for stellar physicists is that these stars are formed from the same molecular cloud and, therefore, they have the same chemical composition and the same age.

where $K_{\mathrm{W}} \simeq 6.5 \cdot 10^{47}$ g cm^{-2} is a free parameter, adjusted to observations, M and R the mass and radius of the star. The value of Ω_{sat} is not precisely prescribed and is often taken to be $8\Omega_{\odot}$

To summarize, at the beginning of its formation, the star is magnetically coupled with its disk and its outer convective zone is forced to co-rotate with the disk, with a constant angular velocity during the disk lifetime. After a few million years, the disk becomes sparse enough so that the star decouples. Since it is still contracting, the angular velocity increases and possibly exceeds the saturation velocity. The faster the star rotates, the more efficient magnetic breaking is. With the combined action of magnetic braking and of the end of the contraction phase, the star starts to slow down. In order to see how surface rotation evolves during Main Sequence (MS), one can write Eq. (2.1) assuming that there is no contraction or dilation. In this case the moment of inertia $\mathcal{I}$, the total radius R and total mass M are constant and the AM variation rate reads

$$\frac{\mathrm{d}\mathcal{J}}{\mathrm{d}t} = \frac{\mathrm{d}\mathcal{I}\Omega}{\mathrm{d}t} = \mathcal{I}\frac{\mathrm{d}\Omega}{\mathrm{d}t} = -K_{\mathrm{W}}\Omega^3 \left(\frac{R}{R_{\odot}}\right)^{1/2} \left(\frac{M}{M_{\odot}}\right)^{-1/2} = -k\Omega^3. \tag{2.3}$$

By setting Ω_0 the initial angular velocity, the solution as a function of time of this equation immediately follows:

$$\Omega(t) = \sqrt{\frac{1}{2\frac{k}{\mathcal{I}}t + \Omega_0^{-2}}} \propto t^{-1/2}. \tag{2.4}$$

The decrease of angular velocity as an inverse square root of time is called the Skumanich's law (Skumanich, 1972). It shall be noted that as t increases, $\Omega(t)$ becomes less and less impacted by the initial condition. This means that after around 1 Gyr, all stars have their surface rotating with the same velocity, regardless of the initial angular disk period and lifetime. As the star leaves the main sequence and its upper layers start dilating, surface angular velocity drops dramatically. Indeed, Fig. 2.1 shows models with the same disk lifetime but with different initial disk periods. These models have extremely different surface angular velocity during the PMS but quickly reach a value close to the one predicted by the Skumanich law. More complex models have been obtained by fitting power law similar to Eqs. (2.1) and (2.2) on loss of AM computed using 3D MHD simulations which account for non-ideal (not open or dipolar field) magnetic field geometry (Matt et al., 2015). They lead to very similar results, except in fast rotating phase after the disappearance of the disk. However, at the moment, observations are not precise enough to constraint the different models.

2.1.3 Coronal mass ejections

Another candidate has recently been brought up as a mechanism of loss of AM. While stars lose AM through stellar winds in a continuous way, at least some of them also experience highly energetic eruptions called coronal mass ejections (CME) that expel material (and therefore AM) into interplanetary space in a very short time. As for now, AM loss by CME has only been studied through order of magnitude considerations. In particular, the efficiency of CME AM-loss is studied by comparing the characteristic spin-down time of stellar wind and CME with the characteristic time of angular velocity evolution caused by contraction or dilation of the star. Those studies have estimated mass-loss and AM-loss using *Kepler*'s measurements of flares (sudden increase of luminosity) emission frequencies and CME-flare association distributions (Aarnio et al., 2012, 2013). These authors found that in case of the Sun, CME AM-loss could represent 10% of the AM lost by solar wind. For CTTS, they estimate the CME mass-loss to be

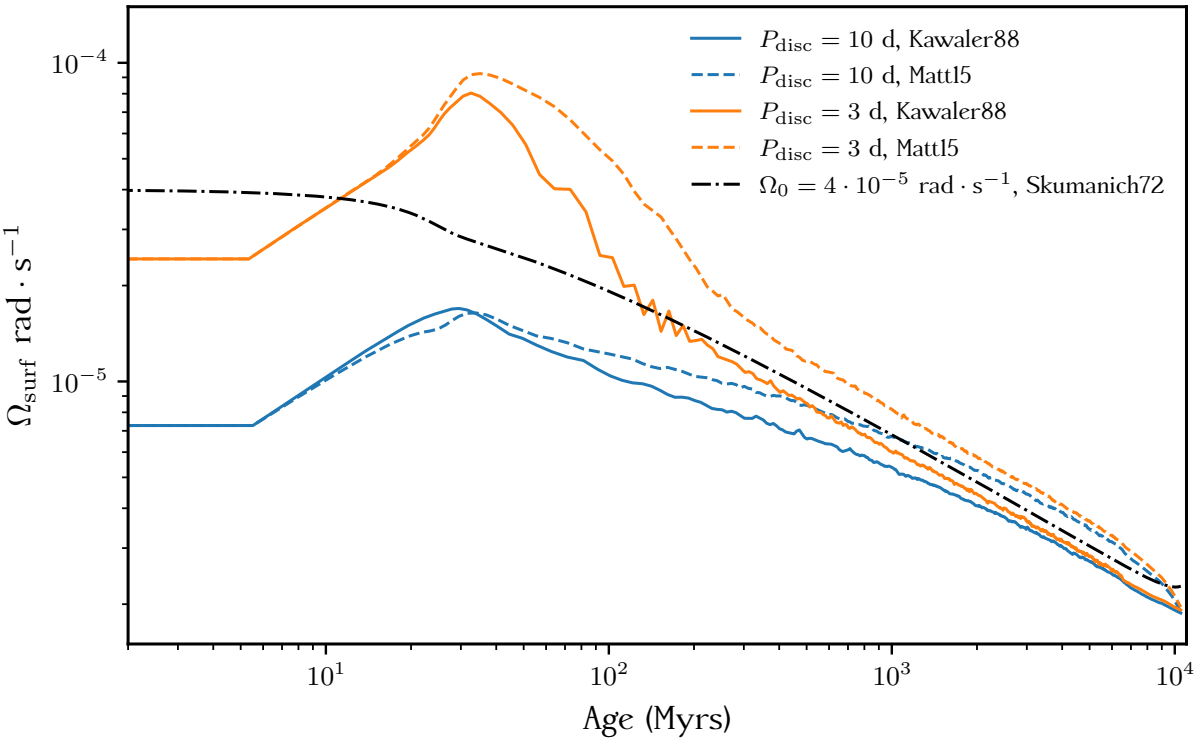

Figure 2.1: Surface angular velocity as a function of stellar age. Models are computed with a disk lifetime of 5 Myr and a period of the disk of 3 days (orange) and 10 days (blue). The AM loss is computed for 2 models: Kawaler (1988) (solid lines) and Matt et al. (2015) (dashed lines). The angular velocity predicted by the Skumanich law with initial angular velocity of 4×10^{-5} rad s^{-1} is represented as a black dotted-dashed line.

around 4% of the wind mass-loss. However, due to their very strong magnetic field, their Alfvén radius is much farther, so the amount of AM-loss could be much higher. These estimates are to be taken with caution because part of the data used are obtained from extrapolated data of the Sun. Furthermore, strong biases tarnish the measurement of the distribution of CME frequency as a function of their energy because low-energy CMEs are not seen but are numerous. In stars other than the Sun, the occurrence of CMEs is inferred by the detection of flares. But not all flares are associated with CME and the knowledge of the flare-CME association probability still suffers from many uncertainties (Odert et al., 2017; Odert et al., 2020). Eventually, in the case of the Sun, CME are much more frequent during the high activity phase of the solar cycle. However, not all stars display an activity cycle pattern (Brandenburg, 2020), therefore it would be interesting to know if CME AM-loss would have an impact on those stars.

2.2 From the Von-Zeipel theorem to the meridional circulation

Let us write again the baroclinic equilibrium equation. We take the curl of Eq. (1.50) and the new equation states the conservation of vorticity $\boldsymbol{\omega} = \boldsymbol{\nabla} \times \mathbf{v}$:

$$\frac{\partial \boldsymbol{\omega}}{\partial t} + (\mathbf{u} \cdot \boldsymbol{\nabla})\, \boldsymbol{\omega} = [(\boldsymbol{\omega} \cdot \boldsymbol{\nabla})\, \mathbf{u} - \boldsymbol{\omega} \cdot (\boldsymbol{\nabla} \cdot \mathbf{u})] + \frac{\boldsymbol{\nabla} p \times \boldsymbol{\nabla} \rho}{\rho^2} + \frac{1}{2} \boldsymbol{\nabla} \Omega^2 \times \boldsymbol{\nabla} \left(r \sin \theta\right)^2 . \tag{2.5}$$

We recognize, from left to right, the time variation of vorticity, the advection of vorticity, the stretching of vorticity by shear, the stretching of vorticity due to fluid compressibility

and then the so-called *baroclinic torque* and the curl of the centrifugal acceleration (Ouazzani, 2011). By assuming that in the radiative zone, $\mathbf{u}$ and $\boldsymbol{\omega}$ are small, the terms $(\mathbf{u}\cdot\boldsymbol{\nabla})\,\boldsymbol{\omega}$ and $[(\boldsymbol{\omega}\cdot\boldsymbol{\nabla})\,\boldsymbol{\omega}-\boldsymbol{\omega}\cdot(\boldsymbol{\nabla}\cdot\mathbf{u})]$ are 2^{nd}-order terms and can be neglected. Doing so, one obtains a simplified equation for the time variation of vorticity:

$$\frac{\partial\boldsymbol{\omega}}{\partial t}=\frac{\boldsymbol{\nabla}p\times\boldsymbol{\nabla}\rho}{\rho^2}+\frac{1}{2}\boldsymbol{\nabla}\Omega^2\times\boldsymbol{\nabla}\left(r\sin\theta\right)^2. \tag{2.6}$$

Since we consider only steady state solutions, $\partial_t\boldsymbol{\omega}=\mathbf{0}$. Furthermore, recalling that the last term of the right hand side is the cylindrical derivative of Ω^2: $r\sin\theta\partial\Omega^2/\partial z\mathbf{e}_\varphi$, with z the coordinate along the rotation axis, we obtain the crucial baroclinic equilibrium

$$\frac{\boldsymbol{\nabla}p\times\boldsymbol{\nabla}\rho}{\rho^2}=r\sin\theta\frac{\partial\Omega^2}{\partial z}\mathbf{e}_\varphi. \tag{2.7}$$

Any change in the density or pressure profile automatically translates into a change of the z-gradient of Ω. Any change in the z-gradient of Ω automatically translates into a change of the pressure and density profiles.

In the radiative zone of a non-rotating star, we have seen with Eq. (1.12) that the radiative flux is proportional to $\mathrm{d}T/\mathrm{d}r$. It means that the radiative flux is constant over spherical surface and therefore is perpendicular to it. Let us now consider the radiative zone of a star in solid-body rotation (therefore barotropic). We have shown that the radiative flux has a slightly different form and in particular is not constant any more over a spherical surfaces or isobars. This is seen if we express $\boldsymbol{\nabla}U$ in (1.12) with respect to the gravito-centrifugal quasi-potential ψ:

$$\mathbf{F}_{\text{r}}=-\chi\frac{\mathrm{d}T}{\mathrm{d}\psi}\boldsymbol{\nabla}\psi\quad\text{with}\quad\chi=\frac{4acT^3}{3\kappa\rho}, \tag{2.8}$$

where χ is the thermal diffusivity. In this case, $\mathbf{F}_{\text{r}}$ is parallel and proportional to $\boldsymbol{\nabla}\psi$ since $\chi\mathrm{d}T/\mathrm{d}\psi$ is constant over an isobar. Consequently, a change in T or any other quantity enclosed in χ will only change the *averaged* value of $\mathbf{F}_{\text{r}}$, not its direction. The radiative flux can simply be expressed in terms of the effective gravity $\mathbf{g}_{\text{eff}}$:

$$\mathbf{F}_{\text{r}}=\chi\frac{\mathrm{d}T}{\mathrm{d}\psi}\mathbf{g}_{\text{eff}}. \tag{2.9}$$

This expression was first derived by von Zeipel (1924) for barotropic stars. At the poles, the iso-ψ are closer to one another, in other words, the effective gravity and the radiative flux are larger. This effect is called the *gravity darkening*. To go further, let us write the divergence of the radiative flux in a layer, which expresses the local energy conservation:

$$\boldsymbol{\nabla}\cdot\mathbf{F}_{\text{r}}=-\underbrace{\frac{\mathrm{d}}{\mathrm{d}\psi}\left(\frac{4acT^3}{3\kappa\rho}\frac{\mathrm{d}T}{\mathrm{d}\psi}\right)}_{(i)}\underbrace{(\nabla\psi)^2}_{(ii)}-\underbrace{\left(\frac{4acT^3}{3\kappa\rho}\frac{\mathrm{d}T}{\mathrm{d}\psi}\right)}_{(iii)}\underbrace{\nabla^2\psi}_{(iv)}=\underbrace{\rho\varepsilon(\rho,T)}_{(v)}. \tag{2.10}$$

The divergence of the radiative flux equals the production of energy $\rho\varepsilon$ in the layer. In solid-body rotating stars, isobars coincide with isopycnals and iso-ψ. In this case, terms *(i)*, *(iii)* are constant on isobars because $\boldsymbol{\nabla}T\parallel\boldsymbol{\nabla}\psi$. Term *(iv)* is constant in case of barotropicity *and* uniform rotation (see Eq. (1.58) and the Poisson equation). In the right hand side, ε depends on density and on the temperature, therefore is also constant on isobars. We are left with term *(ii)* which is not constant, even for a cylindrical rotation profile, because the direction and

the value of $\boldsymbol{\nabla}\psi$ varies over an isobar. To summarize, we have a not constant left hand side equaling a constant right hand side ! This is the so-called *Von Zeipel paradox*.

In order to overcome this paradox, von Zeipel (1924) suggested that there should be heating and cooling at different regions on the same isobars. This means that equation for energy conservation is satisfied on average over an isobar (*i.e.* $\langle \boldsymbol{\nabla} \cdot \mathbf{F}_{\rm r} \rangle = \langle \rho\varepsilon \rangle$, where $\langle \cdot \rangle$ stands for the isobar averaging), but not locally. In the case of cylindrical rotation, it results into polar regions becoming hotter than the equatorial region[3]. The gravity darkening can be used to test Von Zeipel theorem and more generally model predictions (Ohishi et al., 2004; Domiciano de Souza et al., 2005; Bouchaud et al., 2020). The original Von Zeipel theorem was derived assuming a constant angular velocity. This assumption was found to overestimate the variation of effective temperature with latitude (Lovekin et al., 2006; McAlister et al., 2005; Zhao et al., 2009). Von Zeipel-like laws accounting for baroclinicity lead to a much better agreement between observation and theory (Espinosa Lara & Rieutord, 2011). It shall be stressed that the previous reasoning only holds in the *radiative* region of a star. In a convective zone, as we have seen in Chapter 1, the thermal flux takes a different form and therefore, the formulation of the Von Zeipel theorem is not identical to the one in the radiative zone (Lucy, 1967).

The implications of Von Zeipel theorem are of crucial importance in stellar physics. Soon after Von Zeipel published his paper, Eddington (1925) and independently Vogt (1925) proposed the following picture. Let us imagine a star in radiative equilibrium, isotherms equal isobars. Then suddenly, rotation is enforced and Von Zeipel's theorem applies. What happens? We have seen that different locations on the same isobar are heated or cooled differentially. Temperature, density and pressure being linked through an equation of state, the heating and cooling modifies the direction of $\boldsymbol{\nabla} p$ and $\boldsymbol{\nabla}\rho$ which creates a baroclinic torque and therefore creates a gradient of Ω in the z direction, breaking barotropicity. In other words, barotropicity, even if assumed as initial state, cannot be sustained and baroclinicity settles. To easily see that, one may imagine the caricatural situation where isopycnals are not only inclined to isobars but perpendicular (see Fig. 2.2). In this case, on the same isobar, the fluid goes from heavier to lighter as we move to the right in Fig. 2.2. As on a weighing scale, the fluid leans to the left, creating vorticity.

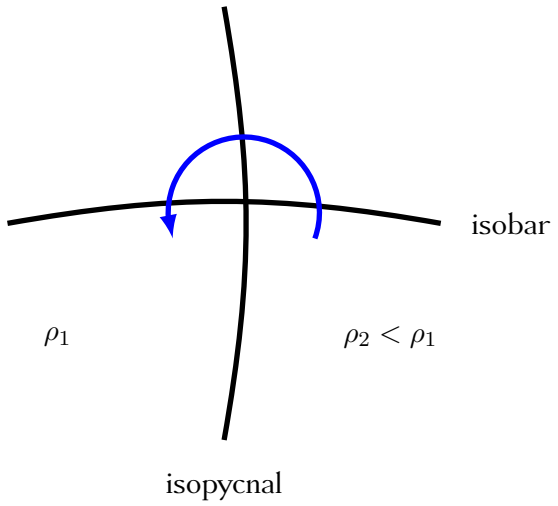

Figure 2.2: Extreme case of isobar perpendicular to isopycnals. Density decreases from left to right.

The later work of Sweet (1950) gave a more formal description assuming a steady circulation

[3]Although, inside the star, it may not be the case.

in an inviscid fluid, with no magnetic fields, which allowed him to estimate a characteristic time-scale over which equilibrium is restored. They are called Eddington-Sweet (hereafter ES) circulation and time-scale. A simple expression for the velocity U of this circulation is derived by Sweet (1950) as

$$U \propto \frac{1}{\nabla_{\rm ad} - \nabla + \frac{\phi}{\delta}\nabla_\mu} \frac{LR^5\Omega^2}{\mathcal{G}^2M^3} \propto \frac{LR^5\Omega^2}{\mathcal{G}^2M^3}, \tag{2.11}$$

and the ES time-scale is defined as the time needed for this circulation to cover a distance of a stellar radius:

$$t_{\rm ES} = \frac{R}{U} \simeq \frac{\mathcal{G}^2M^3}{LR^4\Omega^2} \simeq t_{\rm KH}\frac{\mathcal{G}M}{\Omega^2R^3}, \tag{2.12}$$

with $t_{\rm KH} = \frac{\mathcal{G}M^2}{RL}$ the Kelvin-Helmholtz time-scale corresponding to the time needed for a star to radiate with a luminosity L all its gravitational energy (it is for instance the characteristic time-scale of the PMS phase). The time-scale $t_{\rm ES}$ is the time needed to reach a steady state after a contraction or dilation of the star. For slow rotators, $t_{\rm ES} \gg t_{\rm KH}$ and therefore, the ES is too slow to adapt to a change in the structure. However, for rapid rotators, $t_{\rm ES} \simeq t_{\rm KH}$ meaning that a steady state is reached on a Kelvin-Helmholtz time-scale. Few years after Sweet (1950), Mestel (1953) showed the stabilizing effect of μ-gradient to the ES circulation. Its effect can be seen in Eq. (2.11) where an increase in ∇_μ decreases U and therefore increases $t_{\rm ES}$.

However, Sweet's solution of meridional circulation has some caveats that have been pointed out by Busse (1981) (and later Busse 1982) in a paper asking the question *Do Eddington-Sweet circulations exist?*. Eddington-Sweet circulation advects angular momentum but if $t_{\rm ES}$ is larger (or comparable) to the stellar lifetime, it can be considered that the amount of angular momentum advected is so small that the ES circulation corresponds to a steady state. It has already been said that this is not verified for rapid rotators, but Busse (1981) actually showed that the solution of the ES circulation breaks down on a much shorter time scale, incompatible with the assumption of a steady state. Assuming an inviscid star with an ES circulation as initial state, he showed that, owing to the little deviation in angular velocity due to the non-local conservation of AM, an extra centrifugal force develops, rapidly overcoming the pressure and slowing down the ES circulation in a time of order the rotation period: $\sim (2\Omega)^{-1}$. To completely understand meridional circulation, Busse's idea was that the AM advected by the circulation should be balanced by the angular velocity diffused by any force (magnetic forces or shear-induces viscous stresses).

This idea was exploited first by Zahn (1992) who proposed that, due to the stable stratification of the radiative zone, horizontal diffusion caused by the shear turbulence would be much stronger than the vertical one. In his formalism, quantities were decomposed in Legendre series, only up to the 2$^{\rm nd}$ order Legendre polynomial (in the same way as in Eqs. (1.47) and (1.48)), with a simplified equation of state and neglecting the μ-gradients. Zahn (1992) couples the baroclinic equation to provide an expression for the fluctuations of density and gravity on isobars, the equation of transport of AM to ensure its conservation and the equation of transport of energy. These hypotheses (except the order of the development) were relaxed by Maeder & Zahn (1998). Mathis & Zahn (2004) later developed the equations to provide solutions for the meridional circulation and the transport of angular momentum for any order in the decomposition in Legendre polynomials. Soon after, Mathis & Zahn (2005) introduced the effect of an axisymmetric magnetic fields balancing the AM advected by meridional circulation. This work is motivated by observations that tend to show that magnetic fields can be found in a large variety of main-sequence stars (see Donati & Landstreet, 2009, for a review).

CESTAM does not support modelling of magnetic fields, therefore I have only implemented the formalism of Mathis & Zahn (2004) for any degree ℓ, described in Sect. 2.6. The equations for the transport of AM are described in Sect. 2.7. But first, I will describe the modelling of shear-induced turbulence.

2.3 Shear-induced turbulence

Stellar radiative zones are prone to many magneto-hydrodynamic (MHD) instabilities. Those instabilities do not occur on the same characteristic time-scales and will be detailed in Sect. 5.2. However, one of them acts on a shorter time-scale and is much more efficient. In radiative zones, the settlement of meridional circulation increases the shear between successive layers. If the stabilizing effect of stable stratification is overcome, the shear can induce the well known Kelvin-Helmholtz instability (see, for instance, Davidson, 2013). The criterion setting the threshold for the Kelvin-Helmholtz is known as the Richardson criterion for instability which compares buoyancy to shear. Let us imagine a small parcel of material rising from a layer of depth z and velocity U to another layer of depth $z + \delta z$ and velocity $U + \delta U$. At this new location, the parcel has a difference of density $\Delta\rho$ with its surrounding. If the difference of velocity ΔU were to be 0, we have seen that the parcel oscillates around an equilibrium position and the the motion is stable (we are in a radiative zone). The gradient of density $\mathrm{d}\Delta\rho/\mathrm{d}z$ can be seen as a potential barrier. However, if the the velocity difference is sufficiently high, it can overcome the potential barrier and instead of oscillating, the parcel diverges, leading to an instability. In 1920, under these conditions, Lewis Richardson proposed a criterion for instability of the form

$$\mathrm{Ri} \equiv \frac{g}{\rho}\frac{\mathrm{d}\Delta\rho/\mathrm{d}z}{\left(\mathrm{d}U/\mathrm{d}z\right)^2} < \frac{1}{4}, \tag{2.13}$$

and Ri being the *Richardson number*. This criterion is known as the *Richardson criterion*. The threshold $1/4$ was derived by Taylor (1931), although the value of the critical Richardson number $\mathrm{Ri}_{\mathrm{crit}}$ is subject to question since numerical simulations have shown that instabilities may occur with $\mathrm{Ri} \simeq 1.0$ (Brüggen & Hillebrandt, 2001). Indeed, a solid estimation of $\mathrm{Ri}_{\mathrm{crit}}$ requires a theory of turbulence which is lacking (Maeder, 1995; Canuto, 2002). In any case, this criterion is almost never met because in general $\mathrm{d}\Delta\rho/\mathrm{d}z \gg \mathrm{d}U/\mathrm{d}z$. We also recognize in the expression (2.13) the thermal component of the Brunt-Väisälä frequency $N_T^2 \equiv (g/\rho)\mathrm{d}\Delta\rho/\mathrm{d}z$, defined in Eq. (1.23). Furthermore, other stabilizing or destabilizing effects such as the energy lost through radiation by the turbulent flow (Townsend, 1958) could also be taken into account in the expression of Ri. Zahn (1992) derived a new criterion:

$$\frac{N_T^2}{\left(\mathrm{d}U/\mathrm{d}z\right)^2}\frac{vl}{K} < Ri_{\mathrm{crit}}, \tag{2.14}$$

where v and l are the velocity and the size of an eddy in the turbulent flow behaving adiabatically, and K is the thermal diffusivity. Let us expand the reasoning we made above with the small displaced parcel of material, this time accounting for the thermal diffusivity. The term vl could be seen as the kinetic energy per unit time and mass advected by the small parcel and K corresponds to the ability of the material of losing energy by radiation. If $K \ll vl$, the small parcel loses very little energy through diffusion, the sum of kinetic and potential energy is conserved along its path and the parcel is pushed back to its equilibrium position. On the contrary, $K \gg vl$ amounts to saying that the transformation of the small parcel is not adiabatic any more, which reduces the stabilizing effect of the stable stratification. The quantity

$\mathrm{Pe} \equiv vl/K$ defines the Péclet number which measure the importance of the energy carried by advection compared to the energy lost by radiation. This number is related to the shear viscosity[4]. Rieutord (2015) gives $\nu = \beta v \ell$ with $\beta = \mathcal{O}(1)$, v is a characteristic velocity in the direction of the shear and ℓ is the mean free path of particles in the fluid. In stellar radiative interiors, taking criterion (2.14) leads to predicting much more turbulent regions than what would have been obtained with (2.13). With a little more work it is also possible to include the effect of the μ-gradients (Maeder, 1995).

The study of shear instabilities and especially its impact through turbulent viscosities and diffusion coefficients is of crucial importance. Indeed, shellular rotation is based on the assumption that the horizontal diffusion coefficient ν_{h} is large compare to the vertical one (ν_{v}). With this assumption, any horizontal fluctuation of the angular velocity would immediately be flattened up by horizontal shear and enforce shellular rotation (Zahn, 1992). This assumption is supported by the fact that, in the rotating turbulent flow, the vertical motions of the largest eddies will be attenuated by the stable stratification. Moreover, shear instabilities also contribute to the transport of chemicals inside the star, strongly influencing its evolution path.

A lot of prescriptions have been proposed for the diffusion and viscosity coefficients. It is often complicated to determine which one is the more physically correct. Some are based on laboratory experiments with the risk of oversimplifying the processes operating in a star. Some are supported by numerical simulations that can only reproduce turbulent flows with a Reynolds number very far from what can be reached in stars (see Kupka & Muthsam, 2017, for a review). Sorting through all the different prescriptions by comparing-models to observations can be very tricky as we will see in Chapter 4, because the effects of a different modelling of turbulence is buried under layers of somewhat dubious modelling of rotation-related phenomenon. As a side remark, if we wanted to be particularly rigorous, we should use viscosity coefficients ν_i in the angular momentum transport equation and diffusion coefficients D_i in the chemical transport equations and we will keep these notations in this text. However, many authors consider that $\nu_i \simeq D_i$ (e.g. Talon & Zahn, 1997; Mathis et al., 2004, 2018).

2.3.1 A first approach (Zahn, 1992)

Zahn (1992) gave an estimate of ν_{h}, neglecting the μ-gradients and for small Péclet numbers, *i.e.* for turbulent eddies with important radiation losses. Based on Eq. (2.14), Zahn (1992) provides the following expression for the vertical turbulent viscosity created by the vertical shear, averaged over an isobar:

$$\nu_{\mathrm{v,v}} = \frac{vl}{3} = \frac{8\mathrm{Ri}_{\mathrm{crit}}}{45} K \left(\frac{r}{N_T} \frac{\mathrm{d}\Omega}{\mathrm{d}r} \right)^2 , \tag{2.15}$$

where r is the radius of an isobar and $r\mathrm{d}\Omega/\mathrm{d}r$ is the shear, equivalent to the term $\mathrm{d}U/\mathrm{d}z$ of Eqs. (2.13) and (2.14). This shear was averaged over the colatitude θ to give expression (2.15). Zahn (1992) also gives an expression for vertical turbulent viscosity created by the horizontal shear. To reach such an expression, he first writes the rate of energy ε_{t} injected locally by the

[4]In the fluid dynamics literature, this quantity is often called the kinematic viscosity (for instance, see Feireisl et al., 2016). For a flow of velocity $\mathbf{u} = [u_i(t, \mathbf{x})]$ and velocity gradient $\nabla_{\mathbf{x}}\mathbf{u} = \{\partial_{x_j} u_i\}_{i,j,=1}^{N}$, one can define the stress tensor $\mathbb{S}$ of this flow by

$$\mathbb{S} = \mu \left(\nabla_{\mathbf{x}}\mathbf{u} + \nabla_{\mathbf{x}}^T\mathbf{u} - \frac{2}{3}\boldsymbol{\nabla} \cdot \mathbf{u}\mathbb{I} \right) + \eta \boldsymbol{\nabla} \cdot \mathbf{u}\mathbb{I}.$$

In this case, μ is termed the shear or dynamic viscosity and η the bulk viscosity, while the kinematic viscosity $\nu = \frac{\mu}{\rho} \propto v\ell$ is what is called "shear viscosity" in stellar physics.

shear into the turbulent motions:

$$\varepsilon_{\rm t}(r,\theta) = \nu_{\rm h}\left(\sin\theta\frac{\partial\Omega_2}{\partial\theta}\right)^2, \tag{2.16}$$

where Ω_2 is the 2$^{\rm nd}$-order term of the angular velocity in the Legendre decomposition, and $\nu_{\rm h}$ is the horizontal turbulent viscosity created by the horizontal shear. Assuming that turbulence follows a Kolmogorov's law (e.g. Davidson, 2013), one can write $v^3/l \propto \varepsilon_{\rm t}$. Furthermore, Townsend (1958) proposed to write, in the case of a stratified region destabilized by radiation $v/l^3 \simeq \frac{N_T^2}{K}$. Therefore, the local vertical turbulent viscosity created by the horizontal shear $\nu^\dagger_{\rm v,h}$ is

$$\nu^\dagger_{\rm v,h} \simeq \frac{vl}{3} \simeq \frac{\sqrt{\varepsilon_{\rm t}K}}{3N} = \frac{\sqrt{\nu_{\rm h}K}}{3N}\left|\sin\theta\frac{\partial\Omega_2}{\partial\theta}\right|. \tag{2.17}$$

To include this effect in a 1D stellar evolution code, one need to average it over isobars:

$$\nu_{\rm v,h} \simeq \frac{1}{10}\frac{\Omega}{N_T}\left(\frac{K}{\nu_{\rm h}}\right)^{1/2} r|2V_2 - \alpha U_2| \quad \text{with} \quad \alpha = \frac{1}{2}\frac{{\rm d}\ln r^2\overline{\Omega}}{{\rm d}\ln r}. \tag{2.18}$$

To be more rigorous, we must say that this formulation hides a multiplicative term, factor of the whole expression. This constant is estimated to be of order unity by laboratory experiments and this is why we did not write it. In Eq. (2.18), U_2 (resp. V_2) is the radial (resp. latitudinal) component of the meridional circulation. The change from $\partial\Omega_2/\partial\theta$ to a combination of U_2 and V_2 comes from the equation for the horizontal transport of angular momentum detailed in section 2.7. We now only need to find an expression for $\nu_{\rm h}$. Despite the fact that it cannot be derived from first principles, Zahn (1992) shows that the only way for the shellular rotation approximation to be verified is to consider that

$$\nu_{\rm h} = \frac{1}{c_{\rm h}} r|2V_2 - \alpha U_2| \quad \text{with} \quad c_{\rm h} = \frac{5\Omega_2}{\overline{\Omega}}. \tag{2.19}$$

This relation follows from the equation giving the 2$^{\rm nd}$-order term Ω_2 of the angular velocity (see Eq. (2.120)). Zahn (1992)'s modelling relies on the assumption that all the kinetic energy of the turbulence is dissipated into heat through viscous stresses. One could argue, however, that part of the energy is injected into gravito-inertial waves, or is lost through radiation because of the small Péclet number hypothesis. But, Maeder (2003) have stressed many issues in this formulation. First, Ω_2 does not depends on $\nu_{\rm h}$, which is expected to be the case. Then, the ratio $\frac{\Omega_2}{\overline{\Omega}}$ is also independent of $\overline{\Omega}$, meaning that the fluctuations of angular velocity are always the same, for low and fast rotators. Finally, Maeder (2003) showed that, for stars with low metallicity, $\nu_{\rm h}$ becomes of the same order as $\nu_{\rm v}$ which would break the necessary conditions for shellular rotation to exist. This last point is justified in Sect. 2.6.

It is worth noting that Zahn (1992) adopts a local point of view on vertical diffusion in the sense that the vertical coefficients depend on local gradient or local Richardson number. It means that the vertical shear in Zahn (1992)'s theory does not depend on properties of the turbulence far from the region studied. This is only true if the shear-induced turbulence acts on a small enough scale. If the characteristic scale of turbulent eddies becomes too important, the diffusion properties in one point do not depend on the local properties of the medium only, but mixes effects from a broader region.

2.3.2 Inclusion of Coriolis effects (Maeder, 2003)

The next decade has seen many refinements of the Richardson criterion, with the attempt of many authors to include the effects of μ-gradients (Maeder, 1995), to better estimate ${\rm Ri_c}$

(Brüggen & Hillebrandt, 2001; Canuto, 2002) and with the implementation of Zahn (1992)'s theory of transport of angular momentum in stellar evolution codes (Meynet & Maeder, 1997; Maeder & Zahn, 1998). In order to palliate the above shortcomings of Zahn's theory, Maeder (2003) proposed to focus on the characteristic time-scale τ on which a little excess of kinetic energy is flattened by turbulence. Turbulence can be impacted by differential rotation, by the radial or the latitudinal component of the meridional circulation, or by the Coriolis force. If the last three are dominant, then $\tau \simeq \sqrt{\frac{r}{\Omega_2 V_2}}$ and

$$\nu_{\rm h} = A\sqrt{r^3\Omega_2 V_2} = Ar\left(r\overline{\Omega}V_2\left(2V_2 - \alpha U_2\right)\right)^{1/3}, \tag{2.20}$$

where A is a constant estimated to be less than 0.1. To obtain the last side of this equation, Ω_2 was replaced by the simplified expression (2.121).

The vertical diffusion coefficient incorporates the effects of μ-gradients (Meynet & Maeder, 1997) and of horizontal shear (Talon & Zahn, 1997):

$$\nu_{\rm v} = \frac{2{\rm Ri_c}}{\frac{N_T^2}{K+\nu_{\rm h}} + \frac{N_\mu^2}{\nu_{\rm h}}}\left(r\frac{{\rm d}\Omega}{{\rm d}r}\right)^2, \tag{2.21}$$

where N_T^2 and N_μ^2 have been defined in Eq. (1.26). This expression has been widely used with slight changes to the factor 2: Palacios et al. (2003) use $\frac{8}{5}$, Mathis et al. (2004) use 1, etc.

2.3.3 Prescription derived from laboratory experiments (Mathis et al., 2004)

The kind of flow encountered in rotating radiative zones can be approached in a laboratory with a Taylor-Couette flow (Taylor, 1923). A Taylor-Couette apparatus is composed of two coaxial cylinders separated by a gap with a viscous fluid filling it. The two cylinders have a radius r_1 and r_2 and can rotate at different rotation rates Ω_1 and Ω_2 (for instance, see Davidson, 2013; Regev et al., 2016). Let us imagine that we start to rotate the inner cylinder with a small angular velocity. Angular momentum is transferred to the fluid and rapidly, all the fluid simply rotates differentially between the two cylinders. The angular momentum is $r_1^2\Omega_1$ at the inner cylinder and 0 at the other. Such a flow where angular momentum is decreasing with increasing radius (contrary to what is expected in stars) is subject to instabilities. Indeed, Rayleigh criterion states that an axisymmetric rotating inviscid fluid is stable to turbulence if

$$\frac{1}{r^3}\frac{{\rm d}r^2\Omega}{{\rm d}r} \geq 0. \tag{2.22}$$

This criterion amounts to saying that the epicyclic frequency defined in Eq. (1.95) is positive. It emerges from the linearised equation of motion written in Eq. (1.93), in the case of a unstratified fluid. In our case, since the fluid is not inviscid, for slow enough rotation, the flow is stable. However, above a certain threshold in Ω, turbulence starts to develop. The turbulent flow takes the form of axisymmetric steady poloidal vortices called *Taylor's vortices* or *Taylor cells* (see Fig. 2.3, picture a.). The total motion is a composition of the primary rotational motion and of the poloidal vortices. Therefore, particles follow helicoidal trajectories. If Ω_1 keeps increasing, a new regime is reached where the Taylor vortices are composed to a wavy motion. These are called wavy Taylor vortices (pictures b. and c.). Finally, after a third threshold, the flow becomes unsteady and turbulent but still resembles Taylor vortices when time-averaged (pictures d. and e.).

Richard & Zahn (1999) made the assumption that in radiative zones, shear-induced turbulence follow the same turbulent regime as in the Taylor-Couette flow. In this case where

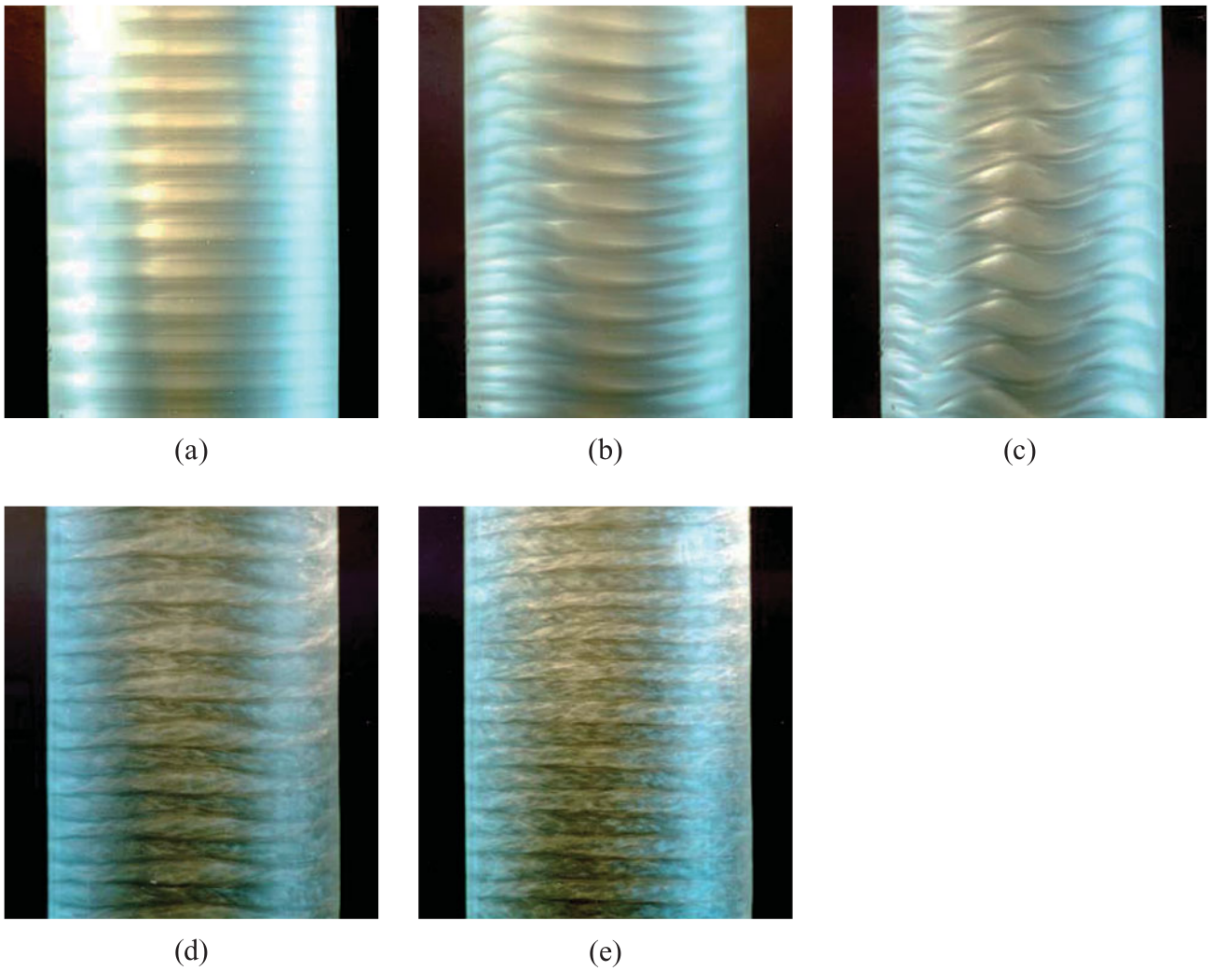

Figure 2.3: Flow in a Taylor-Couette apparatus. The rotation rate of the inner cylinder increases from (a) to (e). See the text for a description of the flow. Credits: Davidson (2013).

the turbulence is purely dominated by differential rotation, they measured that the turbulent viscosity ν_t follows from:

$$\nu_\mathrm{t} = \beta \varpi^3 \left| \frac{\mathrm{d}\Omega}{\mathrm{d}\varpi} \right|, \tag{2.23}$$

with $\beta = 1.5 \pm 0.5 \cdot 10^{-5}$ and $\varpi = r \sin\theta$ is the distance to rotation axis defined in Eq. (1.51). Using the Legendre decomposition, Mathis et al. (2004) proposed to write this viscosity

$$\nu_\mathrm{t} = \beta r^3 |\Omega_2| \sin^3\theta \left| \frac{\mathrm{d}P_2}{\mathrm{d}\theta} \right| \quad \xrightarrow{\text{horiz. av.}} \quad \nu_\mathrm{h} = \frac{1}{2}\beta r^2 |\Omega_2| = \sqrt{\frac{\beta}{10} r^2 \overline{\Omega} r |2V_2 - \alpha U_2|}. \tag{2.24}$$

As for the vertical shear coefficient, Mathis et al. (2004) use Eq. (2.21) with a factor 1 instead of 2 and $\mathrm{Ri_c} = \frac{1}{6}$. Maeder (2003) and Mathis et al. (2004) reach rather similar results, although the first one gives a little more weight to the effect of meridional circulation velocity in the diffusion by shear.

2.3.4 Effects of rotation and stratification (Mathis et al., 2018)

The most recent prescription of diffusion coefficients was proposed by Mathis et al. (2018) who tried to relate ν_h and ν_v to the characteristic dynamical time-scale of turbulence τ, *i.e* the time

needed for turbulence to be damped. This approach somewhat resembles Maeder (2003)'s who also tried to estimate the characteristic turbulent time-scale. In a general way, $\nu_{\rm v}$ (and the same for $\nu_{\rm h}$) can be written

$$\nu_{\rm v} \propto u_{\rm v}\ell_{\rm v} = u_{\rm v}^2\tau = \frac{\ell_{\rm v}^2}{\tau}, \tag{2.25}$$

where $u_{\rm v}$ and $\ell_{\rm v}$ are the characteristic velocity and distance in the vertical direction. Mathis et al. (2018) follow a spectral method developed by Kitchatinov & Brandenburg (2012) in order to express the ratio $\nu_{\rm v}/\nu_{\rm h}$. Their method allows us to express the velocity field $\mathbf{u} = [u_r, u_\theta, u_\varphi]$ of turbulence generated in a rotating stably stratified medium by assuming that the velocity field $\mathbf{u}^0$ of turbulence in a non rotating stratified fluid is known. Skipping the details, they derived an expression for the statistically average squared component of the velocity field:

$$\begin{aligned} &\left\langle u_\theta^2 \right\rangle \simeq \left\langle u_\varphi^2 \right\rangle \simeq \frac{\left\langle (\mathbf{u}^0)^2 \right\rangle}{2} \quad \text{and} \quad \left\langle u_r^2 \right\rangle \simeq \left\langle (\mathbf{u}^0)^2 \right\rangle \frac{2\Omega^2}{\tau^2 N_T^4}, \\ &\text{with} \quad u_\perp^2 = \left\langle u_\theta^2 \right\rangle + \left\langle u_\varphi^2 \right\rangle \quad \text{and} \quad u_\parallel^2 = \left\langle u_r^2 \right\rangle. \end{aligned} \tag{2.26}$$

Using these expression yields

$$\frac{\nu_{\rm v}}{\nu_{\rm h}} = \frac{u_\parallel^2}{u_\perp^2} = 2\left(\frac{2\Omega}{N_T^2\tau}\right)^2. \tag{2.27}$$

Contrary to previous prescriptions, this result is deduced from first principles, and does not incorporate results of laboratory experiments. Moreover, these expressions treat simultaneously the effect of stable stratification and Coriolis force. There only remains to find an expression for either $\nu_{\rm v}$ or $\nu_{\rm h}$ and τ.

The studies of turbulence in radiative zones using 3D numerical simulations (Prat & Lignières, 2013; Prat et al., 2016; Garaud & Kulenthirarajah, 2016) have corroborated the prescription for the vertical shear diffusion coefficients suggested by Zahn (1992) (Eq. (2.15)). The approach synthesized in Maeder (2003) is not found to appropriately reproduce $\nu_{\rm v}$, Prat & Lignières (2014) found. However, more recent papers (Garaud et al., 2017; Gagnier & Garaud, 2018; Kulenthirarajah & Garaud, 2018) have shown that Zahn (1992)'s model only works when the hypothesis of locality is valid. Indeed, they showed that as $\mathrm{Ri}\frac{\mathrm{Pe}}{\mathrm{Re}}$ ($\mathrm{Re} \equiv vl/\nu$ is the Reynolds number which characterize the susceptibility of the fluid to be turbulent[5]) decreases, the vertical size of turbulent eddies increases until reaching a size that is comparable to the size of the radiative region, which breaks locality.

Nonetheless, we will assume with Mathis et al. (2018) that $\nu_{\rm v} = \nu_{\rm v,v}$ is given by

$$\nu_{\rm v} = \frac{\mathrm{Ri_c}}{3} K \left(\frac{r\sin\theta\partial_r\Omega}{N_T}\right)^2, \tag{2.28}$$

which is the un-horizontally-averaged version of Eq. (2.15). We finally need an expression for τ. Mathis et al. (2018) identifies three possible expressions for τ.

- If the turbulence is dominated by radial shears $S = r\sin\theta\partial_r\Omega$, then $\tau = 1/S$. With this expression of τ together with expression (2.28) for $\nu_{\rm v}$ in the equation (2.27) relating $\nu_{\rm h}$ and $\nu_{\rm v}$, we obtain:

$$\nu_{\rm h} = \frac{2\mathrm{Ri_c}}{3} K \left(\frac{N_T}{2\Omega}\right)^2. \tag{2.29}$$

[5] I use the word "susceptibility" because there exists no fixed threshold for the Reynolds number below which the flow is laminar and turbulent above. For instance, in an infinite plumbing pipe, first small eddies appear for $\mathrm{Re} \gtrsim 5$. The fuselage of some air-planes is designed to push the transition at $\mathrm{Re} \gtrsim 10^5 - 10^6$.

- When the rotation become non-negligible, the Coriolis acceleration starts to act in addition to the shear and $\tau = 1/(2\Omega + S)$. We notice that for $\Omega \to 0$, we recover the above time-scale. Injected in Eq. (2.27) yields $\nu_{\rm h}$ average over θ:

$$\nu_{\rm h} = \frac{2{\rm Ri_c}}{3} K \left(\frac{N_T}{2\Omega}\right)^2 \left\langle \frac{\sin^2\theta}{\left[\frac{r}{2\Omega}\partial_r\Omega\right]^{-1} + \sin^2\theta} \right\rangle_\theta \quad \text{with} \quad \langle f \rangle_\theta = \frac{\int_0^\pi f \sin\theta {\rm d}\theta}{\int_0^\pi \sin\theta {\rm d}\theta}. \tag{2.30}$$

- One final characteristic time-scale proposed by Mathis et al. (2018) is to use the epicyclic frequency defined in Eq. (1.95) which characterizes the stability of rotating differentially rotating flows. With this choice, $\tau = \frac{1}{N_\Omega} = (2\Omega(2\Omega + S\sin\theta))^{-1/2}$. If this alternative were to be chosen, caution should be used to ensure that N_Ω^2 does not become negative because the flow would become prone to Rayleigh-Taylor instability, needing its own modelling of turbulence (see Chapter 5). In addition, it should be noted that this definition of τ is not compatible with the two previous choices because in the case where $S \gg 2\Omega$, $\tau \simeq \sqrt{2\Omega S \sin\theta} \neq \frac{1}{S}$. Yet, with this value of τ, $\nu_{\rm h}$ reads

$$\nu_{\rm h} = \frac{2{\rm Ri_c}}{3} K \left(\frac{N_T}{2\Omega}\right)^2 \left\langle \frac{\frac{r}{2\Omega}\partial_r\Omega \sin^2\theta}{\left[\frac{r}{2\Omega}\partial_r\Omega\right]^{-1} + \sin^2\theta} \right\rangle_\theta . \tag{2.31}$$

Mathis et al. (2018) argue that it will be possible to test those choices when 3D numerical simulations of radiative zones will be able to reach stellar turbulent regimes. Moreover, the dependence on the $N_T/(2\Omega)$ ratio is the same for any choice of characteristic time-scale which can be seen as a sign of consistency in this model of shear-induced turbulence.

2.4 Fluctuations over isobars

We have seen the main mechanism involved in the loss and in the transport of angular momentum. The goal of the upcoming sections is to built the mathematical formalism necessary to include those physical processes into the modelling. As we said in Chapter 1, structure equations will be expressed on isobars instead of spheres. Therefore, the first thing we need to do is provide a way to compute the locations of these isobars, and then to express the fluctuations of density, gravitational potential and effective gravity over isobars. To my knowledge, there exists two methods that have been developed to compute these fluctuations in *baroclinic* stars. Both of them decompose any field X in the same way as the one written in Eqs. (1.47) and (1.48). Describing the angular variations of X with Legendre polynomials is particularly suitable for the resolution of the Poisson equation, as we will see shortly. The first method has been developed by Mathis & Zahn (2004) and relies on the hydrostatic equilibrium equation (1.51) and on the baroclinic equilibrium equation (1.56) to express the terms $\widetilde{\rho}_\ell$, $\widetilde{\phi}_\ell$ and $\widetilde{g}_\ell$ of the Legendre decomposition of density, gravitational potential and effective gravity respectively, for any degree ℓ. They are expressed as functions of the different terms $\widetilde{\Omega}_\ell$ of the angular velocity. The expressions of these functions quickly become cumbersome as the degree ℓ increases.

Thus, we turned to the second method, developed by Roxburgh (2004, 2006). While the first paper treats the case of uniformly rotating (therefore barotropic) stars, the second applies to baroclinic stars, with any rotation profile. The idea of Roxburgh is to start from the structure of a 1D model and deform it. In particular, for any quantity X decomposed in Legendre polynomials on a given isobar located by p, there always exists at least one characteristic latitude $\theta_{\rm c}$ such that

$$\sum_{\ell=0} \widetilde{X}_\ell(p) P_\ell(\cos\theta_{\rm c}) = X^{\rm 1D}(p). \tag{2.32}$$

I will only derive the equations and the way I solve them is described in Sect. 6.2. It seemed important to me that the reader have some idea on how fluctuations can be computed, since they will be extensively used in the mathematics developed in the current Chapter.

With Roxburgh (2006), we consider an axisymmetric rotating star. The equations to be solved are the hydrostatic equilibrium equation in its complete form of Eq. (1.51) and the Poisson equation (Roxburgh, 2004, 2006):

$$\frac{1}{\rho}\boldsymbol{\nabla} p = -\boldsymbol{\nabla}\phi + \Omega^2\boldsymbol{\varpi} = \mathbf{g}_{\rm eff}, \tag{2.33}$$

$$\boldsymbol{\nabla}^2\phi = 4\pi\mathcal{G}\rho. \tag{2.34}$$

Roxburgh (2006)'s method works by determining iteratively the solution of the fluctuations of the gravitational potential and of the density over isobars. In other words, the computation of these fluctuations needs to repeated until convergence. We compute ϕ knowing ρ and then ρ knowing ϕ.

2.4.1 Computation of ϕ knowing ρ

We decompose ϕ and ρ on a Legendre polynomial[6] basis on the spherical mesh:

$$\phi(r,\theta) = \sum_{\ell=0}^{N_\ell} \widetilde{\phi}_\ell(r) P_\ell(\cos\theta) = \bar{\phi}(r) + \sum_{\ell=1}^{N_\ell} \widetilde{\phi}_\ell(r) P_\ell(\cos\theta), \tag{2.35}$$

$$\rho(r,\theta) = \sum_{\ell=0}^{N_\ell} \widetilde{\rho}_\ell(r) P_\ell(\cos\theta) = \bar{\rho}(r) + \sum_{\ell=1}^{N_\ell} \widetilde{\rho}_\ell(r) P_\ell(\cos\theta). \tag{2.36}$$

All odd degrees ℓ are null because otherwise, the solutions would not be symmetrical with respect to the equatorial plane. Injecting Eqs. (2.35) and (2.36) in Eq. (2.34) leads to:

$$\begin{aligned} \frac{1}{r^2}\frac{\mathrm{d}}{\mathrm{d}r}\left[r^2\frac{\mathrm{d}\widetilde{\phi}_\ell}{\mathrm{d}r}\right] P_\ell(\cos\theta) + \frac{1}{r^2\sin\theta}\frac{\mathrm{d}}{\mathrm{d}\theta}\left[\sin\theta\frac{\mathrm{d}P_\ell(\cos\theta)}{\mathrm{d}\theta}\right]\widetilde{\phi}_\ell &= 4\pi\mathcal{G}\widetilde{\rho}_\ell P_\ell(\cos\theta), \\ \frac{1}{r^2}\frac{\mathrm{d}}{\mathrm{d}r}\left[r^2\frac{\mathrm{d}\widetilde{\phi}_\ell}{\mathrm{d}r}\right] - \frac{\ell(\ell+1)}{r^2}\widetilde{\phi}_\ell &= 4\pi\mathcal{G}\widetilde{\rho}_\ell, \end{aligned} \tag{2.37}$$

where the last line was obtained by projecting on $P_\ell(\cos\theta)$. Eq. (2.37) obeys the boundary condition $\widetilde{\phi}_\ell(0) = 0, \ell \neq 0$ and outside the star, $\widetilde{\rho}_\ell = 0$ and therefore admits an analytical solution of the form $\widetilde{\phi}_\ell = Ar^a$, where A and a are constants. Plugging this solution into Eq. (2.37), leads to $a = \ell$ or $a = -(\ell+1)$. The first solution is unphysical because $\widetilde{\rho}_\ell$ would diverge with increasing r. Therefore, keeping the second solution allows us to provide a limit condition, outside the star:

$$(\ell+1)\widetilde{\phi}_\ell + r\frac{\mathrm{d}\widetilde{\phi}_\ell}{\mathrm{d}r} = 0. \tag{2.38}$$

With $\widetilde{\rho}_\ell$ being provided, $\widetilde{\phi}_\ell$ are found computing an integral form of the solution of Eq. (2.37) together with (2.38) (Roxburgh, 2006):

$$\widetilde{\phi}_\ell(r) = r^\ell \int_{R_{\rm max}}^{r} \frac{4\pi\mathcal{G}}{r^{2\ell+2}}\left[\int_0^r \widetilde{\rho}_\ell(r) r^{\ell+2}\mathrm{d}r\right]\mathrm{d}r - \lambda_\ell r^\ell, \tag{2.39}$$

[6] If the reader wants to refresh hir memory concerning Legendre polynomials, Appendix B. is devoted to them.

where

$$\lambda_\ell = \frac{4\pi\mathcal{G}}{(2\ell+1)R_{\max}^{2\ell+1}} \int_0^{R_{\max}} \widetilde{\rho}_\ell(r) r^{\ell+2} \mathrm{d}r, \tag{2.40}$$

and $R_{\max}$ is a distance outside the star.

2.4.2 Computation of ρ knowing ϕ

Following Roxburgh (2006), we take the curl of Eq. (1.51) which leads to a new differential equation:

$$\boldsymbol{\nabla} \times \left(\rho \left[\boldsymbol{\nabla}\phi - \Omega^2 \boldsymbol{\varpi} \right] \right) = \mathbf{0}. \tag{2.41}$$

We define

$$\mathbf{F} = \boldsymbol{\nabla}\phi - \Omega^2 \boldsymbol{\varpi} = F_r \mathbf{e}_r + F_\theta \mathbf{e}_\theta, \tag{2.42}$$

and we shall compute $\boldsymbol{\nabla} \times (\rho \mathbf{F})$

$$\begin{aligned} \frac{1}{r}\left(\frac{\partial r \rho F_\theta}{\partial r} - \frac{\partial \rho F_r}{\partial \theta} \right) &= 0, \\ \left(F_\theta \frac{\partial \rho}{\partial r} - \frac{1}{r} F_r \frac{\partial \rho}{\partial \theta} \right) \mathbf{e}_\varphi &= \frac{1}{r}\rho \left(\frac{\partial F_r}{\partial \theta} - F_\theta - r \frac{\partial F_\theta}{\partial r} \right) \mathbf{e}_\varphi = \rho \boldsymbol{\nabla} \times \mathbf{F} = \rho \boldsymbol{\nabla} \times (\Omega^2 \boldsymbol{\varpi}), \\ \frac{\partial \rho}{\partial \theta} - r \frac{F_\theta}{F_r} \frac{\partial \rho}{\partial r} &= -\frac{r}{F_r} \rho \boldsymbol{\nabla} \times (\Omega^2 \boldsymbol{\varpi}) \cdot \mathbf{e}_\varphi. \end{aligned} \tag{2.43}$$

The last line is a partial differential equation (PDE). In order to reduce it to a system of ordinary differential equations (ODEs), we shall use the method of characteristics.

We define a surface $\mathcal{S} \equiv [r; \theta; \rho(r,\theta)]$. The vector $[\partial\rho/\partial r; \partial\rho/\partial\theta; -1]$ is normal to the surface while a tangent vector could be defined by $[a(r,\theta); b(r,\theta); c(r,\theta)] = [rF_\theta/F_r; -1; (r/F_r)\rho \boldsymbol{\nabla} \times (\Omega^2 \boldsymbol{\varpi}) \cdot \mathbf{e}_\varphi]$. We look for a curve $\mathcal{C}$ parametrized by s lying in $\mathcal{S}$ such that $[a(r(s),\theta(s)); b(r(s),\theta(s)); c(r(s),\theta(s))]$ is tangent to $\mathcal{C}$. Therefore, $\mathcal{C}$ should satisfy the three following ODEs:

$$\frac{\mathrm{d}r}{\mathrm{d}s} = a(r(s),\theta(s)) = -r\frac{F_\theta}{F_r}, \tag{2.44}$$

$$\frac{\mathrm{d}\theta}{\mathrm{d}s} = b(r(s),\theta(s)) = 1, \tag{2.45}$$

$$\frac{\mathrm{d}\rho}{\mathrm{d}s} = c(r(s),\theta(s)) = -\frac{r}{F_r}\rho \boldsymbol{\nabla} \times (\Omega^2 \boldsymbol{\varpi}) \cdot \mathbf{e}_\varphi. \tag{2.46}$$

Eq. (2.45) implies $\mathrm{d}\theta = \mathrm{d}s$ and we can choose $s = \theta$. The characteristic curves $r(\theta)$ actually define the radius of an isobars p and $\rho(\theta)$ is the density over such an isobar. The function $r(\theta)$ satisfies (2.44):

$$\frac{\mathrm{d}r}{\mathrm{d}\theta} = -\frac{\frac{\partial\phi}{\partial\theta} - \Omega^2 r^2 \sin\theta\cos\theta}{\frac{\partial\phi}{\partial r} - \Omega^2 r \sin^2\theta}, \tag{2.47}$$

and density over isobars satisfies

$$\frac{\mathrm{d}\rho}{\mathrm{d}\theta} = -r\rho \frac{\boldsymbol{\nabla} \times (\Omega^2 \boldsymbol{\varpi}) \cdot \mathbf{e}_\varphi}{\frac{\partial\phi}{\partial r} - \Omega^2 r \sin^2\theta} = -\rho \frac{\frac{\partial}{\partial r}\left(\Omega^2 r^2 \sin\theta\cos\theta\right) - \frac{\partial}{\partial\theta}\left(\Omega^2 r \sin^2\theta\right)}{\frac{\partial\phi}{\partial r} - \Omega^2 r \sin^2\theta}. \tag{2.48}$$

Once the radius of the characteristics, the gravitational potential and the density over isobars are known, it is easy to compute the effective gravity using Eqs. (1.52) and (1.53).

One could think that with Roxburgh's method, local radiative equilibrium is not ensured because the equation for energy transport is not solved together with hydrostatic equilibrium and Poisson equations. However, this is not a problem because rotating stars *cannot* be in local radiative equilibrium as shown in Sect. 2.2 together with von Zeipel (1924).

2.5 Transport of chemical elements

Before exposing the modern formalism used to model the meridional circulation and the associated transport of angular momentum, I make a little detour via the transport of chemical elements as it will facilitate the understanding of the effect of μ-gradients on the meridional circulation.

2.5.1 Fluctuations of chemical abundances over isobars

Shear-induced turbulence has a direct effect on latitudinal μ-gradients because if chemical inhomogeneities starts building-up, turbulence immediately erases them and strongly attenuates abundance fluctuations over isobars. For a chemical abundance per unit mass c_i of a chemical species i, the equation of transport of chemicals reads (Mathis & Zahn, 2004):

$$\rho\frac{\partial c_i}{\partial t}+\rho\boldsymbol{\mathcal{U}}\cdot\boldsymbol{\nabla}c_i=\frac{1}{r^2}\frac{\partial}{\partial r}\left(r^2\rho D_{\rm v}\frac{\partial c_i}{\partial r}\right)+\frac{1}{r\sin\theta}\frac{\partial}{\partial\theta}\left(\sin\theta\rho D_{\rm h}\frac{\partial c_i}{\partial\theta}\right), \tag{2.49}$$

where the velocity field $\boldsymbol{\mathcal{U}}$ is a combination of contraction/dilation of the star, meridional circulation velocities and microscopic diffusion velocity $U_i^{\rm diff}$ of elements:

$$\boldsymbol{\mathcal{U}}=\dot{r}\mathbf{e}_r+\boldsymbol{\mathcal{U}}_{\rm M}+U_i^{\rm diff}\mathbf{e}_r=\dot{r}\mathbf{e}_r+\sum_{\ell>0}U_\ell P_\ell(\cos\theta)\mathbf{e}_r+V_\ell\frac{{\rm d}P_\ell(\cos\theta)}{{\rm d}\theta}\mathbf{e}_\theta+U_i^{\rm diff}\mathbf{e}_r. \tag{2.50}$$

By combining the terms $\rho\partial c_i/\partial t$ and $\rho\left(\dot{r}\mathbf{e}_r\right)\cdot\boldsymbol{\nabla}c_i$, we obtain the material derivative (time derivative at constant mass) ${\rm d}c_i/{\rm d}t$.

Microscopic diffusion, or atomic diffusion, directly stems from the different response of chemical species (for instance due to their different masses or different cross-section) to the forces at stake in stars (gravity, radiative acceleration, etc.). $U_i^{\rm diff}$ gathers the diffusion velocities due to the various microscopic diffusion processes such as the diffusion due to a gradient of concentration, the gravitational settling, the radiative accelerations, the thermal diffusion, etc. The question of their importance in the transport of chemicals is discussed at the end of this section. Macroscopic diffusion is induced by large scale flows such as meridional circulation and instabilities. The abundance c_i can be decomposed according to Eq. (1.48):

$$c_i=\overline{c_i}+\sum_{\ell>0}\widetilde{c}_{i,\ell}P_\ell(\cos\theta)=\overline{c_i}+c_i'. \tag{2.51}$$

We inject this expression in Eq. (2.49) and average the result in latitude (with the same averaging as defined in Eq. (2.30)) and with the usual approximation that $D_{\rm h}\gg D_{\rm v}$,

$$\rho\frac{{\rm d}\overline{c_i}}{{\rm d}t}+\frac{1}{r^2}\frac{\partial}{\partial r}\left[r^2\rho\left\langle c_i'\sum_{\ell>0}U_\ell P_\ell(\cos\theta)\right\rangle\right]+\frac{1}{r^2}\frac{\partial}{\partial r}\left(r^2\rho\overline{c_i}U_i^{\rm diff}\right)=\frac{1}{r^2}\frac{\partial}{\partial r}\left(r^2\rho D_{\rm v}\frac{\partial\overline{c_i}}{\partial r}\right), \tag{2.52}$$

where the anelastic approximation $\boldsymbol{\nabla}\cdot(\rho\boldsymbol{\mathcal{U}}_{\rm M})=0$ was used. We shall also write the equation for the transport of fluctuations

$$\begin{aligned}&\rho\frac{{\rm d}c_i'}{{\rm d}t}+\rho\sum_{\ell>0}U_\ell P_\ell(\cos\theta)\frac{\partial\overline{c_i}}{\partial r}+\rho\boldsymbol{\mathcal{U}}_{\rm M}\cdot\boldsymbol{\nabla}c_i'-\frac{1}{r^2}\frac{\partial}{\partial r}\left[r^2\rho\left\langle c_i'\sum_{\ell>0}U_\ell P_\ell(\cos\theta)\right\rangle\right]\\ =\;&\frac{1}{r^2}\frac{\partial}{\partial r}\left(r^2\rho D_{\rm v}\frac{\partial c_i'}{\partial r}\right)+\frac{1}{r\sin\theta}\frac{\partial}{\partial\theta}\left(\sin\theta\rho D_{\rm h}\frac{\partial c_i'}{\partial\theta}\right).\end{aligned}\tag{2.53}$$

Finally, by assuming $|\boldsymbol{\nabla}c_i'|\ll\partial_r\overline{c_i}$, one obtains

$$\frac{{\rm d}\widetilde{c}_{i\ell}}{{\rm d}t}+U_\ell\frac{\partial\overline{c}_i}{\partial r}=-\frac{\ell(\ell+1)}{r^2}D_{\rm h}\widetilde{c}_{i\ell}.\tag{2.54}$$

Further assuming that the time of evolution ${\rm d}t$ is much longer than the characteristic time of horizontal diffusion $r^2/D_{\rm h}$ (which is valid on the main sequence), the above equation reduces to

$$\widetilde{c}_{i\ell}=-\frac{r^2U_\ell}{\ell(\ell+1)D_{\rm h}}\frac{\partial\overline{c}_i}{\partial r}\tag{2.55}$$

and

$$\rho\frac{{\rm d}\overline{c_i}}{{\rm d}t}+\frac{1}{r^2}\frac{\partial}{\partial r}\left(r^2\rho\overline{c_i}U_i^{\rm diff}\right)=\frac{1}{r^2}\frac{\partial}{\partial r}\left[r^2\rho(D_{\rm v}+D_{\rm eff})\frac{\partial\overline{c_i}}{\partial r}\right],\tag{2.56}$$

where

$$D_{\rm eff}=\sum_{\ell>0}\frac{r^2U_\ell^2}{\ell(\ell+1)(2\ell+1))D_{\rm h}},\tag{2.57}$$

The development in Legendre polynomials is often stopped at $\ell=2$ and we usually find $D_{\rm eff}=(rU_2)^2/\left(30D_{\rm h}\right)$ (Zahn, 1992; Maeder & Zahn, 1998; Mathis & Zahn, 2004).

2.5.2 Microscopic diffusion

For a long time, the study of microscopic diffusion has been considered beyond the scope of standard stellar modelling, which lead to neglecting the term of advection by $U_i^{\rm diff}$. Nonetheless, the inclusion of its effect is now quite common. Taking it into account has revealed that microscopic diffusion can have an important impact on the interior structure of stars. Microscopic diffusion can have many origins. Let us take the equation of motion verified by an element i of mass m_i, with a small abundance such that it does not modify the total density (test element approximation[7]). Each particle of element i has a velocity $\mathbf{U}_i=\overline{\mathbf{U}}+\mathbf{V}_i$ where $\overline{\mathbf{U}}$ is the mean flow velocity (for instance, the meridional circulation) and $\mathbf{V}_i$ is the peculiar velocity of this particle, in other word, a discrepancy with respect to the mean flow velocity. One can also define the average velocity of all particle of the same element i. It is defined as the average in the phase space $\mathfrak{P}$ (Maeder, 2009):

$$\langle\mathbf{U}_i\rangle=\frac{1}{n_i}\int_{\mathfrak{P}}f_i\mathbf{U}_i{\rm d}\tau_{\mathfrak{P}}\quad\text{with}\quad\int_{\mathfrak{P}}f_i{\rm d}\tau_{\mathfrak{P}}=n_i,\tag{2.58}$$

[7]The test element approximation is valid only for element with $n_im_i\ll\rho$. In particular it is not verified for H and He, the expression of the diffusion velocity of which should be modified.

where we used $f_i(\mathbf{x}, \mathbf{v}, t)$ the probability distribution to find particle of an element i at position $\mathbf{x}$, velocity $\mathbf{U}_i$ and time t in the phase space. Therefore, the mean flow velocity is the average of the velocities $\langle U_i \rangle$ for all elements:

$$\overline{\mathbf{U}} = \frac{\sum_i m_i n_i \langle \mathbf{U}_i \rangle}{\sum_i m_i n_i}, \tag{2.59}$$

where n_i is chemical abundance per mole (contrary to c_i which is the chemical abundance per unit mass). The mean peculiar velocity, or diffusion velocity, of element i is written as:

$$\mathbf{U}_i^{\rm diff} = \langle \mathbf{V}_i \rangle = \frac{1}{n_i} \int_{\mathfrak{P}} f_i \mathbf{V}_i \mathrm{d}\tau_{\mathfrak{P}}. \tag{2.60}$$

From (2.59), we see that the diffusion velocity must satisfy the condition

$$\sum_i m_i n_i \mathbf{U}_i^{\rm diff} = 0, \tag{2.61}$$

ensuring that on average, a diffusive process does not have momentum (it is actually a necessary condition for a process to be considered diffusive).

Let us start with a simple case. We suppose that pressure, density and temperature are constant and the abundance of element i varies along r only. We define the mass flux of the element i (projected along direction $\mathbf{e}_{\rm r}$) $J = \rho c_i U_i^{\rm diff}$. This flux a little above or below can be written

$$J(r \pm \delta r) = \frac{1}{6} \rho \left(c_i(r) \pm \frac{\partial c_i}{\partial r} \delta r \right) U_i^{\rm diff}. \tag{2.62}$$

The origin of factor $1/6$ is two fold. First a factor $1/3$ comes from the fact that we projected the flux along one of the three degree of freedom. Second, a factor $1/2$ comes from the fact that we look only along $\mathbf{e}_r$ or $-\mathbf{e}_r$. The net flux is

$$J = J(r + \delta r) - J(r - \delta r) = \rho c_i U_i^{\rm diff} = \frac{1}{3} \rho U_i^{\rm diff} \frac{\partial c_i}{\partial r} \delta r. \tag{2.63}$$

As we have seen in Sect. 2.3, for instance in Eq. (2.15), diffusion coefficients are defined as $D = vl/3$. Identifying vl with $U_i^{\rm diff} \delta r$, we obtain for the diffusion velocity caused by an abundance gradient the following expression:

$$U_i^{\rm diff} = -D \frac{\partial \ln c_i}{\partial r}. \tag{2.64}$$

An element i can be further subjected to a net force $F_i = m_i a_i$, with a_i the acceleration. The equilibrium is reached when:

$$\frac{\partial p_i}{\partial r} - \rho c_i a_i = 0, \tag{2.65}$$

with p_i the partial pressure associated with element i and ρc_i the fraction per unit volume of element i. Assuming that it is a perfect gas, $p_i = \rho c_i k_{\rm B} T / m_i$, and Eq. (2.65) reads

$$\frac{\partial \ln c_i}{\partial r} - \frac{F_i}{k_{\rm B} T} = 0. \tag{2.66}$$

Using this expression, one can define the expression for the diffusion velocity when other forces are accounted for:

$$U_i^{\rm diff} = -D_i \left(\frac{\partial \ln c_i}{\partial r} - \frac{F_i}{k_{\rm B} T} \right). \tag{2.67}$$

We see that when $U_i^{\rm diff} = 0$, the equilibrium state is reached. One could account for gravity effects with $F_i = -m_i g$ and for the screening effect due to the separation of ions an electron in the form:

$$U_i^{\rm diff} = -D_i \left(\frac{\partial \ln c_i}{\partial r} - k_p \frac{\partial \ln p}{\partial r} \right), \tag{2.68}$$

where k_p is a coefficient that we do not reproduce here but that gather the effects of the gravitational and electric field (Chapman & Cowling, 1970). This effect is called the *gravitational settling*. Despite acting on long time-scales, it leads to the concentration of massive elements in the inner region of stars if no other transport processes come against it.

Likewise, atoms can be diffused by thermal gradients. At a microscopic level, a higher temperature translates into a thermal agitation with higher velocities. Imagine that at a location r, atoms are agitated with a mean velocity $v_T(r)$. On average, some of them move to a hotter region $r + {\rm d}r$, where particles are agitated with a mean velocity $v_{T+{\rm d}T}(r + {\rm d}r)$. By successive shocks, the original mean velocity v_T will increase. This process further depends on the cross-section of the considered element which is related to the probability that two particles interact. The cross-section of neutral elements do not vary with temperature while the one of ionized ones are proportional to T^{-2}. Obviously, neutral elements are found in the coolest region of the stars and differential effects of thermal diffusion on neutral and ionized elements usually have no impact in most of the radiative zone. In addition, at a given temperature T, particles with different masses do not move with same velocity. Indeed, the average kinetic energy of element i is given by $3 n_i k_B T/2$, independently of the mass. We see immediately that heavier particles will move slower than lighter one. Hence, light element will diffuse faster. It must be noted that this effect exists also when no temperature gradient is present. Using a thermal diffusivity k_T, Chapman & Cowling (1970) propose to include the effect of thermal diffusion in (2.68) as

$$U_i^{\rm diff} = -D_i \left(\frac{\partial \ln c_i}{\partial r} - k_p \frac{\partial \ln p}{\partial r} - k_T \frac{\partial \ln T}{\partial r} \right). \tag{2.69}$$

Finally, a very interesting mechanism of diffusion is the *radiative* acceleration induced by the interaction between photon and ions. Radiative acceleration pushes high opacity particles towards the surface. Its effect is added through the force F_i, in Eq. (2.66), that is replaced by $-m_i g_{{\rm rad},i}$:

$$U_i^{\rm diff} = -D_i \left(\frac{\partial \ln c_i}{\partial r} - k_p \frac{\partial \ln p}{\partial r} - k_T \frac{\partial \ln T}{\partial r} + \frac{m_i g_{{\rm rad},i}}{k_{\rm B} T} \right), \tag{2.70}$$

where $g_{{\rm rad},i}$ is the acceleration resulting from the interaction between photons and ions. It is proportional to the frequency integral of the product of the energy flux and the cross-section of a given absorption (this integral is slightly modified in case the absorption leads to another ionization). Radiative acceleration is important in massive stars where the energy flux is high. With increasing mass, this process can rapidly compete with gravitational settling. This competition can produce an accumulation of certain elements in small regions of the star. In some cases, it can create the so-called thermohaline or double-diffusive convection (Théado et al., 2009). Indeed, if locally $\nabla_\mu > 0$ (μ increases upward), ∇_μ can overcome the stabilizing effect of the density stratification and the medium becomes unstable (if the Ledoux criterion (1.28) is satisfied). If this accumulation occurs in a region where this element contributes to increase opacity, the convective zone deepens and the star is able to maintain a stronger dynamo effect. As shown in Sect. 2.1, it increases the amount of AM blown in the interplanetary medium. In turn, rotational mixing is increased and the importance of microscopic diffusion is

lowered (Deal et al., 2020). We have seen in Sect. 2.2, that the AM advected by meridional circulation may rapidly yield a region with strong diffusion of angular velocity by shear-induced turbulence. Therefore, meridional circulation, shear-induced turbulence and stellar wind form a highly coupled system. The shear-induced diffusion coefficients depend not only on the circulation velocities but indirectly on the AM lost by winds. Deal et al. (2020) have studied the interaction between rotation, atomic diffusion with/without radiative acceleration, and AM loss by winds. They have shown that, for stars with mass around and below $1.3M_{\odot}$, there is no accumulation of chemical species anywhere in the star, which suggests that rotational mixing annihilates microscopic diffusion. Above $1.44M_{\odot}$, stars show large accumulation of iron at their surface when they are modelled accounting for radiative acceleration, suggesting that in this case, microscopic diffusion overcome rotational mixing. However, Deal et al. (2020) stress that this accumulation is not observed in *Kepler* data, suggesting that a mechanism(s) of transport of chemicals remains to be found.

2.6 Modern formalism of meridional circulation

The modern formalism for computing the velocity of meridional circulation has been developed by Mathis & Zahn (2004). In this section we will make profitable use of the Legendre polynomial decomposition, then it shall be recalled that we assume that any quantity can be written following Eq. (1.48). We start our derivation from the time dependent equation for the conservation of thermal energy:

$$\rho T\left[\frac{\partial s}{\partial t}+\boldsymbol{\mathcal{U}}\cdot\boldsymbol{\nabla}s\right]=\boldsymbol{\nabla}\cdot(\chi\boldsymbol{\nabla}T)+\rho\varepsilon-\boldsymbol{\nabla}\cdot\mathbf{F}_{\rm h}, \tag{2.71}$$

where s is the specific entropy, $\boldsymbol{\mathcal{U}}$ is the combination of the contraction/dilation term and of the meridional flow, χ is the thermal conductivity, ε is the nuclear energy generation rate per unit mass and $\mathbf{F}_{\rm h}$ if the energy flux carried by horizontal turbulence. The flux carried by vertical turbulence has been neglected because of the hypothesis of shellular rotation relying on the assumption that the horizontal turbulence diffusion coefficient $D_{\rm h}$ is much higher than its vertical counterpart. We will tackle the terms one by one.

2.6.1 Entropy's material derivative

We project the left hand side term on the Legendre polynomial basis and it reads:

$$\rho T\left[\frac{\partial s}{\partial t}+\boldsymbol{\mathcal{U}}\cdot\boldsymbol{\nabla}s\right]=\overline{\rho}\,\overline{T}\left[\frac{\mathrm{d}\overline{s}}{\mathrm{d}t}+\sum_{\ell>0}\left(\frac{\mathrm{d}\widetilde{s}_{\ell}}{\mathrm{d}t}+U_{\ell}\frac{\partial\overline{s}}{\partial r}\right)P_{\ell}(\cos\theta)\right], \tag{2.72}$$

where $\overline{\rho}\,\overline{T}\mathrm{d}\overline{s}/\mathrm{d}t=-\overline{\rho}\overline{\varepsilon}_{\rm g}$. The velocity field $\boldsymbol{\mathcal{U}}$ is expressed by

$$\boldsymbol{\mathcal{U}}=\dot{r}\mathbf{e}_r+\sum_{\ell>0}\left[U_{\ell}(r)P_{\ell}(\cos\theta)\mathbf{e}_r+V_{\ell}(r)\frac{\mathrm{d}P_{\ell}(\cos\theta)}{\mathrm{d}\theta}\mathbf{e}_{\theta}\right]=\dot{r}\mathbf{e}_r+\boldsymbol{\mathcal{U}}_{\rm M}. \tag{2.73}$$

The term $\dot{r}\mathbf{e}_r$ is the contraction/dilation term. The next ones are the vertical component U_{ℓ} and the horizontal component V_{ℓ} of the meridional circulation. The $0^{\rm th}$-order terms U_0 and V_0 are zeros because otherwise, a flow would constantly ascend or descend in the star. It would not be possible to consider it as a perturbation. In this section and the following we make the anelastic approximation: $\boldsymbol{\nabla}\cdot(\rho\boldsymbol{\mathcal{U}}_{\rm M})=0$. The anelastic approximation amounts to saying that

any acoustic wave is filtered out. In this case, using relation (B.7), a simple relation between U_ℓ and V_ℓ can be obtained:

$$V_\ell(r) = \frac{1}{\ell(\ell+1)\rho r}\frac{\mathrm{d}}{\mathrm{d}r}\left(\rho r^2 U_\ell\right). \tag{2.74}$$

For a variable chemical composition, the change of entropy can be expressed as (Maeder & Zahn, 1998):

$$\mathrm{d}s = c_p\left(\frac{\mathrm{d}T}{T} - \nabla_{\mathrm{ad}}\frac{\mathrm{d}p}{p} + \Phi(p,T,\mu)\frac{\mathrm{d}\mu}{\mu}\right), \tag{2.75}$$

where $\Phi = \mathrm{d}s/\mathrm{d}\ln\mu$ depends on the mean molecular weight and on the abundances of the different elements. An expression for Φ is provided in App. C.1.

By multiplying Eq. (2.75) by $1/\mathrm{d}\ln p$ and keeping only the 0^{th}-order term, we derive the expression for $\partial_r\overline{s}$:

$$\partial_r\overline{s} = \frac{c_p}{H_{\mathrm{p}}}\left(\nabla_{\mathrm{ad}} - \nabla - \Phi\nabla_\mu\right), \tag{2.76}$$

where H_{p} is the previously defined pressure scale height (see Eq. (1.25)) and $\nabla_\mu = \mathrm{d}\ln\mu/\mathrm{d}\ln p$ is the μ-gradient.

In order to give an expression for the terms $\widetilde{s}_\ell$, one needs first to define several quantities. Instead of using $\widetilde{\rho}_\ell$, $\widetilde{T}_\ell$ and $\widetilde{\mu}_\ell$ we will often use their ratio to the 0^{th} order term:

$$\Theta_\ell = \frac{\widetilde{\rho}_\ell}{\overline{\rho}} \qquad \Psi_\ell = \frac{\widetilde{T}_\ell}{\overline{T}} \qquad \Lambda_\ell = \frac{\widetilde{\mu}_\ell}{\overline{\mu}}. \tag{2.77}$$

A relation between the three is found from a general equation of state (Kippenhahn et al., 2012):

$$\frac{\mathrm{d}\rho}{\rho} = \left.\frac{\partial\ln\rho}{\partial\ln p}\right|_{T,\mu}\frac{\mathrm{d}p}{p} + \left.\frac{\partial\ln\rho}{\partial\ln T}\right|_{p,\mu}\frac{\mathrm{d}T}{T} + \left.\frac{\partial\ln\rho}{\partial\ln\mu}\right|_{p,T}\frac{\mathrm{d}\mu}{\mu}, \tag{2.78}$$

which, when written on an isobar, gives, by setting $\delta = -\left.\partial\ln\rho/\partial\ln T\right|_{p,\mu}$ and $\varphi = \left.\partial\ln\rho/\partial\ln\mu\right|_{p,T}$

$$\Theta_\ell = \varphi\Lambda_\ell - \delta\Psi_\ell, \tag{2.79}$$

thus providing a link between Θ_ℓ, Ψ_ℓ and Λ_ℓ. Then, using these notations, it is easy to keep only the ℓ^{th}-order component of equation (2.75) and write

$$\widetilde{s}_\ell = c_p\left(\Psi_\ell + \Phi\Lambda_\ell\right). \tag{2.80}$$

Then, from Eqs. (2.76) and (2.80), we can write

$$\overline{T}\left(\frac{\mathrm{d}\widetilde{s}_\ell}{\mathrm{d}t} + U_\ell\frac{\partial\overline{s}_\ell}{\partial r}\right) = c_p\overline{T}\left(\frac{\mathrm{d}\Psi_\ell}{\mathrm{d}t} + \Phi\frac{\mathrm{d}\Lambda_\ell}{\mathrm{d}t} + \frac{U_\ell}{H_{\mathrm{p}}}\left(\nabla_{\mathrm{ad}} - \nabla - \Phi\nabla_\mu\right)\right). \tag{2.81}$$

2.6.2 Time variation of mean molecular weight fluctuations

Eq. (2.81) includes two time derivatives, coupled by Eq. (2.79). We need another expression for one of them. Eq. (2.54) gave an expression for the transport of the fluctuations of chemicals. The mean molecular weight is defined as

$$\frac{1}{\mu} = \sum_i \frac{1+Z_i}{A_i}c_i, \tag{2.82}$$

where Z_i is the number of electrons and A_i the number of nucleons. Then from Eq. (2.54) we write the equation for time variation of mean molecular weight fluctuations:

$$\frac{\mathrm{d}\Lambda_\ell}{\mathrm{d}t} = \frac{U_\ell}{H_\mathrm{p}}\nabla_\mu + \frac{\mathrm{d}\ln\overline{\mu}}{\mathrm{d}t}\Lambda_\ell - \frac{\ell(\ell+1)}{r^2}D_\mathrm{h}\Lambda_\ell. \tag{2.83}$$

Finally we go back to Eq. (2.81) and by injecting Eq. (2.83) in it we obtain

$$\begin{aligned}
&\overline{\rho}\overline{T}\left(\frac{\mathrm{d}\widetilde{s}_\ell}{\mathrm{d}t} + U_\ell\frac{\partial\overline{s}}{\partial r}\right)\\
&= c_p\overline{\rho}\overline{T}\left[\frac{\mathrm{d}\Psi_\ell}{\mathrm{d}t} + \Phi\left(\frac{U_\ell}{H_\mathrm{p}}\nabla_\mu + \frac{\mathrm{d}\ln\overline{\mu}}{\mathrm{d}t}\Lambda_\ell - \frac{\ell(\ell+1)}{r^2}D_\mathrm{h}\Lambda_\ell\right) + \frac{U_\ell}{H_\mathrm{p}}\left(\nabla_\mathrm{ad} - \nabla - \Phi\nabla_\mu\right)\right]\\
&= c_p\overline{\rho}\overline{T}\left[\frac{\mathrm{d}\Psi_\ell}{\mathrm{d}t} + \Phi\frac{\mathrm{d}\ln\overline{\mu}}{\mathrm{d}t}\Lambda_\ell - \frac{\ell(\ell+1)}{r^2}\Phi D_\mathrm{h}\Lambda_\ell + \frac{U_\ell}{H_\mathrm{p}}\left(\nabla_\mathrm{ad} - \nabla\right)\right].
\end{aligned} \tag{2.84}$$

We have the left hand side of (2.71).

2.6.3 Horizontal turbulent energy flux

Let us turn to the last term of Eq. (2.71). Only the horizontal part of the turbulent energy flux has been retained because turbulent diffusion is much stronger horizontally. Maeder & Zahn (1998) approximate the horizontal turbulent energy $\mathbf{F}_\mathrm{h}$ by $-D_\mathrm{h}\rho T\boldsymbol{\nabla}S$ and

$$\begin{aligned}
\boldsymbol{\nabla}\cdot\mathbf{F}_\mathrm{h} &= -\frac{1}{r^2\sin\theta}\frac{\partial}{\partial\theta}\left[\sin\theta D_\mathrm{h}\rho T\frac{\partial s(r,\theta)}{\partial\theta}\right] = \sum_{\ell>0}\frac{\ell(\ell+1)}{r^2}\overline{\rho T}D_\mathrm{h}\widetilde{s}(r,\theta)P_\ell(\cos\theta)\\
&= \sum_{\ell>0}\frac{\ell(\ell+1)}{r^2}\overline{\rho T}D_\mathrm{h}c_p\left(\Psi_\ell + \Phi\Lambda_\ell\right)P_\ell(\cos\theta).
\end{aligned} \tag{2.85}$$

2.6.4 Radiative transport

The temperature, as any other variable, is decomposed on the Legendre basis on an isobar:

$$T(p,\theta) = \overline{T}(p) + \sum_{\ell>0}^{\infty}\widetilde{T}_\ell(p)P_\ell(\cos\theta). \tag{2.86}$$

Its gradient is

$$\begin{aligned}
\boldsymbol{\nabla}T &= \frac{\mathrm{d}\overline{T}}{\mathrm{d}p}\frac{\mathrm{d}p}{\mathrm{d}r}\mathbf{e}_r + \sum_{\ell>0}^{\infty}\frac{\partial\widetilde{T}_\ell}{\partial p}\frac{\partial p}{\partial r}P_\ell(\cos\theta)\mathbf{e}_r + \frac{1}{r}\sum_{\ell>0}^{\infty}\frac{\partial\widetilde{T}_\ell}{\partial p}\frac{\partial p}{\partial\theta}P_\ell(\cos\theta)\mathbf{e}_\theta + \frac{1}{r}\sum_{\ell>0}^{\infty}\widetilde{T}_\ell\frac{\partial P_\ell}{\partial\theta}(\cos\theta)\mathbf{e}_\theta\\
&= \rho\left[\frac{\mathrm{d}\overline{T}}{\mathrm{d}p} + \sum_{\ell>0}^{\infty}\frac{\partial\widetilde{T}_\ell}{\partial p}P_\ell(\cos\theta)\right]\frac{\boldsymbol{\nabla}p}{\rho} + \sum_{\ell>0}^{\infty}\widetilde{T}_\ell\boldsymbol{\nabla}P_\ell(\cos\theta).
\end{aligned} \tag{2.87}$$

Latitudinal derivatives of pressure disappeared because we are on an isobar. The term for thermal diffusion reads

$$\begin{aligned}
\boldsymbol{\nabla}\left(\chi\boldsymbol{\nabla}T\right) &= \rho\chi\left(\frac{\mathrm{d}\overline{T}}{\mathrm{d}p} + \sum_{\ell>0}^{\infty}\frac{\partial\widetilde{T}_\ell}{\partial p}P_\ell(\cos\theta)\right)\boldsymbol{\nabla}\cdot\left(\frac{\boldsymbol{\nabla}p}{\rho}\right) + \boldsymbol{\nabla}\left[\rho\chi\left(\frac{\mathrm{d}\overline{T}}{\mathrm{d}p} + \sum_{\ell>0}^{\infty}\frac{\partial\widetilde{T}_\ell}{\partial p}P_\ell(\cos\theta)\right)\right]\cdot\frac{\boldsymbol{\nabla}p}{\rho}\\
&+ \sum_{\ell>0}^{\infty}\boldsymbol{\nabla}(\chi\widetilde{T}_\ell)\cdot\boldsymbol{\nabla}P_\ell(\cos\theta) + \sum_{\ell>0}^{\infty}\chi\widetilde{T}_\ell\boldsymbol{\nabla}^2P_\ell(\cos\theta).
\end{aligned} \tag{2.88}$$

We need to find an expression for each of these terms. First, the equation for hydrostatic equilibrium is easily recognized:

$$\frac{\boldsymbol{\nabla} p}{\rho} = \mathbf{g} = -\boldsymbol{\nabla}\varphi + \mathfrak{F}_{\mathrm{C}}, \quad \text{with} \begin{cases} |\mathbf{g}| &= \overline{g}(p) + \sum_{\ell>0} \widetilde{g}_\ell(p) P_\ell(\cos\theta) \\ \mathfrak{F}_{\mathrm{C}} &= \frac{1}{2}\Omega^2 \boldsymbol{\nabla}(r\sin^2\theta) \end{cases} . \tag{2.89}$$

Here, $\mathbf{g}$ denotes the effective gravity and $\mathfrak{F}_{\mathrm{C}}$ is the centrifugal force. This decomposition will be useful for the expression of the divergence of the hydrostatic equation. Indeed,

$$\boldsymbol{\nabla}\cdot\left(\frac{\boldsymbol{\nabla} p}{\rho}\right) = -\boldsymbol{\nabla}^2\varphi + \boldsymbol{\nabla}\cdot\mathfrak{F}_{\mathrm{C}}. \tag{2.90}$$

First term is obviously given by the Poisson equation:

$$\nabla^2\varphi = 4\pi\mathcal{G}\overline{\rho} + 4\pi\mathcal{G}\sum_{\ell>0}\widetilde{\rho}_\ell P_\ell(\cos\theta), \tag{2.91}$$

and the divergence of $\mathfrak{F}_{\mathrm{C}}$ is expanded on Legendre polynomials:

$$\boldsymbol{\nabla}\cdot\mathfrak{F}_{\mathrm{C}} = \overline{f}_{\mathrm{C}} + \sum_{\ell>0}\widetilde{f}_{\mathrm{C},\ell} P_\ell(\cos\theta). \tag{2.92}$$

Mathis & Zahn (2004) provide an analytical expression for the components of this divergence, at any degree ℓ. However, we will see in Chapter 6 that we can obtain it numerically in a way that is more consistent with the rest of our approach. Finally, the product $\rho\chi$ is also decomposed on Legendre polynomials:

$$\rho\chi = \overline{\rho\chi} + \sum_{\ell>0}\widetilde{\rho\chi}_\ell P_\ell(\cos\theta). \tag{2.93}$$

2.6.5 Right hand side

It is now time to put everything back together. We recall that from Eq. (2.71), the right hand side reads

$$\boldsymbol{\nabla}\cdot(\chi\boldsymbol{\nabla}T) + \rho\varepsilon + \overline{\rho\varepsilon}_{\mathrm{g}} - \boldsymbol{\nabla}\cdot\mathbf{F}_{\mathrm{h}} = \mathrm{RHS}, \tag{2.94}$$

where $\overline{\rho\varepsilon}_{\mathrm{g}}$ comes from the other side. The details of the following calculation are described in App. C.2. The right hand side can be written in the form:

$$\begin{aligned} \mathrm{RHS} \;=& \left\langle \overline{\rho\chi}\frac{\mathrm{d}\overline{T}}{\mathrm{d}p}\left(\overline{f}_{\mathrm{C}} - 4\pi\mathcal{G}\overline{\rho}\right) + \overline{\rho}\frac{\mathrm{d}}{\mathrm{d}p}\left(\overline{\rho\chi}\frac{\mathrm{d}\overline{T}}{\mathrm{d}p}\right)\overline{g}^2 + \overline{\rho}(\overline{\varepsilon}+\overline{\varepsilon}_{\mathrm{g}})\right\rangle \\ &+ \sum_{\ell>0}^{\infty}\Bigg\{ \left(\overline{\rho\chi}\frac{\mathrm{d}\widetilde{T}_\ell}{\mathrm{d}p} + \widetilde{\rho\chi}_\ell\frac{\mathrm{d}\overline{T}}{\mathrm{d}p}\right)\left(\overline{f}_{\mathrm{C}} - 4\pi\mathcal{G}\overline{\rho}\right) + \overline{\rho\chi}\frac{\mathrm{d}\overline{T}}{\mathrm{d}p}\left(\widetilde{f}_{\mathrm{C},\ell} - 4\pi\mathcal{G}\widetilde{\rho}_\ell\right) \\ &+ 2\overline{\rho}\frac{\mathrm{d}}{\mathrm{d}p}\left(\overline{\rho\chi}\frac{\mathrm{d}\overline{T}}{\mathrm{d}p}\right)\overline{g}\widetilde{g}_\ell + \widetilde{\rho}\frac{\mathrm{d}}{\mathrm{d}p}\left(\overline{\rho\chi}\frac{\mathrm{d}\overline{T}}{\mathrm{d}p}\right)\overline{g}^2 + \overline{\rho}\frac{\mathrm{d}}{\mathrm{d}p}\left(\overline{\rho\chi}\frac{\mathrm{d}\widetilde{T}_\ell}{\mathrm{d}p}\right)\overline{g}^2 + \overline{\rho}\frac{\mathrm{d}}{\mathrm{d}p}\left(\widetilde{\rho\chi}_\ell\frac{\mathrm{d}\overline{T}}{\mathrm{d}p}\right)\overline{g}^2 \\ &- \frac{\ell(\ell+1)}{r^2}\left(\overline{\chi}\widetilde{T}_\ell + \overline{\rho}\overline{T}D_{\mathrm{h}}c_p\left(\Psi_\ell + \Phi\Lambda_\ell\right)\right) + \widetilde{\rho\varepsilon}_\ell\Bigg\} P_\ell(\cos\theta). \end{aligned} \tag{2.95}$$

The term between angular brackets is zero because it states the global radiative equilibrium (equilibrium *over* an isobar, *not locally*). This term vanishes but it shall be kept in mind because it will provide a useful relation to simplify the right hand side.

Remember that this large expression is equal to the left hand side stated in Eq. (2.84). All the quantities with a tilde are fluctuations over isobars. Let us imagine that the star is barotropic, steady and that there are no latitudinal gradients of mean-molecular weight. Then, isobars and isopycnals coincide, hence, $\Theta_\ell = 0$. In addition, with $\Lambda_\ell = 0$, Ψ_ℓ is also 0. With the steadiness hypothesis, $\mathrm{d}\Psi_\ell/\mathrm{d}t = 0$. Then on the left hand side (Eq. (2.84)), only the term in factor of U_ℓ remains. On the right hand side (Eq. (2.95)), all terms are 0. If the star is barotropic, if $\Lambda_\ell = 0$ *and* if the star is steady, then U_ℓ is necessarily 0. However, is this situation even possible ? We have seen with the Von Zeipel theorem that rotating stars (even barotropic) experience differential heating and cooling over a given isobar. Therefore, even if we assume an initial state with no fluctuation of temperature over an isobar ($\Psi_\ell = 0$), such fluctuations will necessarily appear and $\mathrm{d}\Psi_\ell/\mathrm{d}t \neq 0$. The hypothesis of a steady description of meridional circulation is unphysical. The only way to satisfy above equation with $\Theta_\ell = 0$, $\Lambda_\ell = 0$, $\Psi_\ell = 0$ and $\mathrm{d}\Psi_\ell/\mathrm{d}t \neq 0$ is to have $U_\ell \neq 0$. The non-vanishing meridional circulation will advect angular momentum (see next section), and the initially assumed barotropicity will break.

After some manipulations described in App. C.3, the right hand side simplifies to:

$$\begin{aligned}\text{RHS} \;&= -\overline{\rho}\left(\frac{\mathrm{d}\widetilde{T}_\ell}{\mathrm{d}\overline{T}} + \frac{\widetilde{\rho\chi}_\ell}{\overline{\rho\chi}}\right)(\overline{\varepsilon} + \overline{\varepsilon}_\mathrm{g}) + \frac{L}{4\pi\mathcal{G}M}\left(\widetilde{f}_{\mathrm{C},\ell} - 4\pi\mathcal{G}\widetilde{\rho}_\ell\right) \\ &+ \frac{L\overline{\rho}}{M}\left\{\left(1 - \frac{\overline{f}_\mathrm{C}}{4\pi\mathcal{G}\overline{\rho}} - \frac{M}{L}(\overline{\varepsilon} + \overline{\varepsilon}_\mathrm{g})\right)\left(2\frac{\widetilde{g}_\ell}{\overline{g}} + \Theta_\ell\right) - \frac{\overline{g}}{4\pi\mathcal{G}\overline{\rho}}\frac{\mathrm{d}}{\mathrm{d}r}\left(\frac{\mathrm{d}\widetilde{T}_\ell}{\mathrm{d}\overline{T}} + \frac{\widetilde{\rho\chi}_\ell}{\overline{\rho\chi}}\right)\right\} \\ &- \frac{\ell(\ell+1)}{r^2}\left(\overline{\chi}\widetilde{T}_\ell + \overline{\rho}\overline{T}D_\mathrm{h}c_p\left(\Psi_\ell + \Phi\Lambda_\ell\right)\right) + \widetilde{\rho\varepsilon}_\ell. \end{aligned} \tag{2.96}$$

We can now bring back the left (Eq. (2.84)) and right (Eq. (2.96)) hand sides together:

$$\begin{aligned}&c_p\overline{\rho}\overline{T}\left[\frac{\mathrm{d}\Psi_\ell}{\mathrm{d}t} + \Phi\frac{\mathrm{d}\ln\overline{\mu}}{\mathrm{d}t}\Lambda_\ell - \frac{\ell(\ell+1)}{r^2}\Phi D_\mathrm{h}\Lambda_\ell + \frac{U_\ell}{H_\mathrm{p}}\left(\nabla_\mathrm{ad} - \nabla\right)\right] \\ &= -\overline{\rho}\left(\frac{\mathrm{d}\widetilde{T}_\ell}{\mathrm{d}\overline{T}} + \frac{\widetilde{\rho\chi}_\ell}{\overline{\rho\chi}}\right)(\overline{\varepsilon} + \overline{\varepsilon}_\mathrm{g}) + \frac{L}{4\pi\mathcal{G}M}\left(\widetilde{f}_{\mathrm{C},\ell} - 4\pi\mathcal{G}\widetilde{\rho}_\ell\right) \\ &+ \frac{L\overline{\rho}}{M}\left\{\left(1 - \frac{\overline{f}_\mathrm{C}}{4\pi\mathcal{G}\overline{\rho}} - \frac{M}{L}(\overline{\varepsilon} + \overline{\varepsilon}_\mathrm{g})\right)\left(2\frac{\widetilde{g}_\ell}{\overline{g}} + \Theta_\ell\right) - \frac{\overline{g}}{4\pi\mathcal{G}\overline{\rho}}\frac{\mathrm{d}}{\mathrm{d}r}\left(\frac{\mathrm{d}\widetilde{T}_\ell}{\mathrm{d}\overline{T}} + \frac{\widetilde{\rho\chi}_\ell}{\overline{\rho\chi}}\right)\right\} \\ &- \frac{\ell(\ell+1)}{r^2}\left(\overline{\chi}\widetilde{T}_\ell + \overline{\rho}\overline{T}D_\mathrm{h}c_p\left(\Psi_\ell + \Phi\Lambda_\ell\right)\right) + \widetilde{\rho\varepsilon}_\ell. \end{aligned} \tag{2.97}$$

The terms of diffusion of fluctuations of mean molecular weight cancel from both sides. Moreover, we divide everything by $\overline{\rho}$:

$$\begin{aligned}&c_p\overline{T}\left[\frac{\mathrm{d}\Psi_\ell}{\mathrm{d}t} + \Phi\frac{\mathrm{d}\ln\overline{\mu}}{\mathrm{d}t}\Lambda_\ell + \frac{U_\ell}{H_\mathrm{p}}\left(\nabla_\mathrm{ad} - \nabla\right)\right] \\ &= \frac{L}{M}\left\{2\left(1 - \frac{\overline{f}_\mathrm{C}}{4\pi\mathcal{G}\overline{\rho}} - \frac{M}{L}(\overline{\varepsilon} + \overline{\varepsilon}_\mathrm{g})\right)\frac{\widetilde{g}_\ell}{\overline{g}} + \frac{\widetilde{f}_{\mathrm{C},\ell}}{4\pi\mathcal{G}\overline{\rho}} - \left(\frac{\overline{f}_\mathrm{C}}{4\pi\mathcal{G}\overline{\rho}} + \frac{M}{L}(\overline{\varepsilon} + \overline{\varepsilon}_\mathrm{g})\right)\Theta_\ell\right. \\ &- \left(\frac{\mathrm{d}\widetilde{T}_\ell}{\mathrm{d}\overline{T}} + \frac{\widetilde{\rho\chi}_\ell}{\overline{\rho\chi}}\right)\frac{M}{L}(\overline{\varepsilon} + \overline{\varepsilon}_\mathrm{g}) + \frac{M\overline{\varepsilon}}{L}\frac{\widetilde{\rho\varepsilon}_\ell}{\overline{\rho\varepsilon}} - \frac{\overline{g}}{4\pi\mathcal{G}\overline{\rho}}\frac{\mathrm{d}}{\mathrm{d}r}\left(\frac{\mathrm{d}\widetilde{T}_\ell}{\mathrm{d}\overline{T}} + \frac{\widetilde{\rho\chi}_\ell}{\overline{\rho\chi}}\right) \\ &\left.- \frac{\ell(\ell+1)}{r^2}c_p\overline{T}\frac{M}{L}\left(\frac{\overline{\chi}}{c_p\overline{\rho}} + D_\mathrm{h}\right)\Psi_\ell\right\}. \end{aligned} \tag{2.98}$$

We shall introduce several quantities in order to simplify above equation. First, one can write

$$\frac{\mathrm{d}\widetilde{T}_\ell}{\mathrm{d}\overline{T}} = \Psi_\ell - H_\mathrm{T}\frac{\partial\Psi_\ell}{\partial r} \quad \text{with} \quad H_\mathrm{T} = -\overline{T}\frac{\mathrm{d}r}{\mathrm{d}\overline{T}}, \tag{2.99}$$

where $H_{\rm T}$ is called the temperature scale height. Furthermore, a simplifying expression for $\widetilde{\chi}_\ell/\overline{\chi}$ and $\widetilde{\varepsilon}_\ell/\overline{\varepsilon}$ can be provided.

$$\frac{\widetilde{\chi}_\ell}{\overline{\chi}} = \left.\frac{\partial \ln \chi}{\partial \ln T}\right|_{p,\mu} \Psi_\ell + \left.\frac{\partial \ln \chi}{\partial \ln \mu}\right|_{p,T} \Lambda_\ell = \chi_T \Psi_\ell + \chi_\mu \Lambda_\ell, \tag{2.100}$$

and

$$\frac{\widetilde{\varepsilon}_\ell}{\overline{\varepsilon}} = \left.\frac{\partial \ln \varepsilon}{\partial \ln T}\right|_{p,\mu} \Psi_\ell + \left.\frac{\partial \ln \varepsilon}{\partial \ln \mu}\right|_{p,T} \Lambda_\ell = \varepsilon_T \Psi_\ell + \varepsilon_\mu \Lambda_\ell. \tag{2.101}$$

From these, one can express $\widetilde{\rho\varepsilon}/\overline{\rho\varepsilon}$ and $\widetilde{\rho\chi}/\overline{\rho\chi}$:

$$\frac{\widetilde{\rho\chi}}{\overline{\rho\chi}} = \frac{\partial \ln \rho\chi}{\partial \ln T}\Psi_\ell + \frac{\partial \ln \rho\chi}{\partial \ln \mu}\Lambda_\ell = (\chi_T - \delta)\,\Psi_\ell + (\varphi + \chi_\mu)\,\Lambda_\ell, \tag{2.102}$$

and

$$\frac{\widetilde{\rho\varepsilon}}{\overline{\rho\varepsilon}} = \frac{\partial \ln \rho\varepsilon}{\partial \ln T}\Psi_\ell + \frac{\partial \ln \rho\varepsilon}{\partial \ln \mu}\Lambda_\ell = (\varepsilon_T - \delta)\,\Psi_\ell + (\varphi + \varepsilon_\mu)\,\Lambda_\ell, \tag{2.103}$$

Then, we can define some shorthand notations proposed by Mathis & Zahn (2004) as

$$\varepsilon_{\rm m} = \frac{L(r)}{M(r)} \qquad K = \frac{\overline{\chi}}{\overline{\rho} c_p} \qquad f_\varepsilon = \frac{\overline{\varepsilon}}{\overline{\varepsilon} + \overline{\varepsilon}_{\rm g}} \qquad \rho_{\rm m} = \frac{m(r)}{\frac{4}{3}\pi r^3}. \tag{2.104}$$

Eventually, after some steps described in App. C.4 and using the above new notations, Eq. (2.98) simplifies and the term of degree ℓ of the meridional circulation is

$$\overline{T} c_p \left[\frac{{\rm d}\Psi_\ell}{{\rm d}t} + \Phi \frac{{\rm d}\ln \overline{\mu}}{{\rm d}t}\Lambda_\ell + \frac{U_\ell}{H_{\rm p}}\left(\nabla_{\rm ad} - \nabla\right)\right] = \frac{L_p}{M_p}\mathcal{T}_\ell, \tag{2.105}$$

where we defined $\mathcal{T}_\ell$ in the same way as Mathis & Zahn (2004):

$$\begin{aligned}
\mathcal{T}_\ell &= 2\left(1 - \frac{\overline{f}_{\rm C}}{4\pi\mathcal{G}\overline{\rho}} - \frac{\overline{\varepsilon} + \overline{\varepsilon}_{\rm g}}{\varepsilon_{\rm m}}\right)\frac{\widetilde{g}_\ell}{\overline{g}} + \frac{\widetilde{f}_{{\rm C},\ell}}{4\pi\mathcal{G}\overline{\rho}} - \frac{\overline{f}_{\rm C}}{4\pi\mathcal{G}\overline{\rho}}\Theta_\ell \\
&+ \frac{\rho_{\rm m}}{\overline{\rho}}\left[\frac{r}{3}\frac{\rm d}{{\rm d}r}\left(H_{\rm T}\frac{\partial\Psi_\ell}{\partial r} - (1 - \delta + \chi_T)\,\Psi_\ell - (\varphi + \chi_\mu)\,\Lambda_\ell\right) - \frac{\ell(\ell+1)H_{\rm T}}{3r}\left(1 + \frac{D_{\rm h}}{K}\right)\Psi_\ell\right] \\
&+ \frac{\overline{\varepsilon} + \overline{\varepsilon}_{\rm g}}{\varepsilon_{\rm m}}\left[\left(H_{\rm T}\frac{\partial\Psi_\ell}{\partial r} - (1 - \delta + \chi_T)\,\Psi_\ell - (\varphi + \chi_\mu)\,\Lambda_\ell\right) + (f_\varepsilon\varepsilon_T - f_\varepsilon\delta + \delta)\,\Psi_\ell\right. \\
&+ \left.(f_\varepsilon\varepsilon_\mu + f_\varepsilon\varphi - \varphi)\,\Lambda_\ell\right].
\end{aligned} \tag{2.106}$$

Because it will simplify its resolution we stress that by defining a new quantity Υ_ℓ :

$$\Upsilon_\ell = H_{\rm T}\frac{\partial\Psi_\ell}{\partial r} - (1 - \delta + \chi_T)\,\Psi_\ell - (\varphi + \chi_\mu)\,\Lambda_\ell. \tag{2.107}$$

The term $\mathcal{T}_\ell$ becomes a first order partial differential equation.

The resolution of this equation requires the provision of a boundary condition. Since the meridional circulation depends on Ω, boundary conditions for both the meridional circulation and the angular velocity will be provided after the derivation of the equation for the transport of angular momentum, at the end of this Chapter (Sect. 2.7.3)

In Sect. 2.3, we said that the prescription for the horizontal turbulent viscosity $\nu_{\rm h}$ proposed by Zahn (1992) suffered from some problem, in particular that in low metallic stars, $\nu_{\rm h} \sim \nu_{\rm v}$ at the surface. Zahn (1992) gives $\nu_{\rm h} = \frac{1}{c_{\rm h}} r|2V_2 - \alpha U_2| \simeq r|U_2|$. If we are close to the surface, the energy generation rates $\overline{\varepsilon} + \overline{\varepsilon}_{\rm g}$ are small. In addition, if the mean molecular weight gradients are negligible, $\mathcal{T}_\ell$ is dominated by the first term:

$$\mathcal{T}_\ell \simeq 2\left(1 - \frac{\overline{f}_{\rm C}}{4\pi\mathcal{G}\overline{\rho}}\right)\frac{\widetilde{g}_\ell}{\overline{g}}. \tag{2.108}$$

The term $\overline{f}_{\rm C}/4\pi\mathcal{G}\overline{\rho} \simeq \overline{\Omega}^2/4\pi\mathcal{G}\overline{\rho}$ is called the Gratton-Öpik term (Gratton, 1945; Öpik, 1951). Near the surface, the density becomes very small, so that $\mathcal{T}_\ell$ changes sign and the meridional velocity changes direction in the uppermost layers. The surface-meridional-circulation cell, rotating in the opposite direction of the inner cell, is called the *Gratton-Öpik cell*. In this cell, due to the very low density, U_2 can become very large so that $\nu_{\rm h} \gg \nu_{\rm v}$ and the shellular rotation approximation stays valid. However, in very sub-metallic stars ($Z = 10^{-5}$ in Meynet & Maeder 2002, while $Z_\odot \simeq 0.02$) the velocity of the meridional circulation near the surface stays small. Near the surface, the opacity is mainly due to negative hydrogen and is given by (Hansen & Kawaler, 1994):

$$\kappa_{\rm H^-} \propto \rho^{1/2} T^9 Z. \tag{2.109}$$

In our case, the metallicity is small, and so is the opacity. Therefore, the luminosity is higher, the stellar radius smaller and the density is higher (the star is more compact than a highly metallic star with the same mass). The density being important, $\mathcal{T}_\ell$ is significantly reduced, and the velocity in the Gratton-Öpik cell especially so. In this special case, one can have $\nu_{\rm h} \simeq \nu_{\rm v}$.

2.7 Equations for the transport of angular momentum

The infinitesimal amount of AM contained in a small element of volume at a distance r of the centre and colatitude θ, with density ρ and angular velocity Ω is

$$\mathrm{d}\mathcal{J} = \rho r^4 \sin^3\theta \Omega \mathrm{d}r\mathrm{d}\theta\mathrm{d}\varphi, \tag{2.110}$$

where the mass of this small element is $\rho r^2 \sin\theta \mathrm{d}r\mathrm{d}\theta\mathrm{d}\varphi$ and the angular momentum is $r^2\sin^2\theta\Omega$. Following (Maeder, 2009), the time derivative of AM at a constant mass coordinate m is

$$\rho\,\frac{\mathrm{d}}{\mathrm{d}t}\left(r^2\sin^2\theta\Omega\right)\Big|_m = \frac{\partial}{\partial t}\left(\rho r^2\sin^2\theta\Omega\right)\Big|_r + \boldsymbol{\mathcal{U}}\cdot\boldsymbol{\nabla}\left(\rho r^2\sin^2\theta\Omega\right) - r^2\sin^2\theta\Omega\,\frac{\mathrm{d}\rho}{\mathrm{d}t}\Big|_m, \tag{2.111}$$

where $\boldsymbol{\mathcal{U}}$ is the velocity of the flow, in this case, the meridional circulation and the contraction/dilation. The differentials $\mathrm{d}r\mathrm{d}\theta\mathrm{d}\varphi$ have been simplified on both sides. Again, we express the time derivative of ρ as

$$\frac{\mathrm{d}\rho}{\mathrm{d}t}\Big|_m = \frac{\partial\rho}{\partial t}\Big|_r + \boldsymbol{\mathcal{U}}\cdot\boldsymbol{\nabla}\rho = -\rho\boldsymbol{\nabla}\cdot\boldsymbol{\mathcal{U}}, \tag{2.112}$$

where the continuity equation has been used. Injecting this expression into Eq. (2.111) leads to

$$\rho\,\frac{\mathrm{d}}{\mathrm{d}t}\left(r^2\sin^2\theta\Omega\right)\Big|_m = \frac{\partial}{\partial t}\left(\rho r^2\sin^2\theta\Omega\right)\Big|_r + \boldsymbol{\nabla}\cdot\left(\boldsymbol{\mathcal{U}}\rho r^2\sin^2\theta\Omega\right). \tag{2.113}$$

Furthermore, the time variation of AM is of course equal to the torque of the (viscous) forces applied to the element of volume. Those forces are produced by the shear and follow

the direction of the velocity gradient. We separate them in a vertical force f_v per unit surface and a horizontal force f_h per unit surface:

$$f_\mathrm{v} = \rho\nu_\mathrm{v} r\sin\theta\frac{\partial\Omega}{\partial r} \quad \text{and} \quad f_\mathrm{h} = \rho\nu_\mathrm{h}\sin\theta\frac{\partial r\Omega}{\partial\theta}, \tag{2.114}$$

f_v applies on a small *horizontal* surface element $r^2\sin\theta\mathrm{d}\theta\mathrm{d}\varphi$ and f_h applies on a small *vertical* surface element $r\sin\theta\mathrm{d}r\mathrm{d}\varphi$. These forces apply with a lever arm of $r\sin\theta$, therefore the associated torque M_v (resp. M_h) gained by a small element of volume submitted to f_v (resp. f_h) are

$$M_\mathrm{v} = \frac{\partial}{\partial r}\left(\rho\nu_\mathrm{v} r^4\sin^3\theta\mathrm{d}\theta\mathrm{d}\varphi\frac{\partial\Omega}{\partial r}\right)\mathrm{d}r \quad \text{and} \quad M_\mathrm{h} = \frac{1}{r}\frac{\partial}{\partial\theta}\left(\rho\nu_\mathrm{h} r^2\sin^3\theta\mathrm{d}r\mathrm{d}\varphi\frac{\partial\Omega}{\partial\theta}\right)r\mathrm{d}\theta. \tag{2.115}$$

Then, the time variation of angular momentum at fixed mass coordinate reads (we simplified the differentials $\mathrm{d}r\mathrm{d}\theta\mathrm{d}\varphi$):

$$\rho r^2\sin\theta\left.\frac{\partial}{\partial t}\left(\rho r^2\sin^2\theta\Omega\right)\right|_m = \frac{\partial}{\partial r}\left(\rho\nu_\mathrm{v} r^4\sin^3\theta\frac{\partial\Omega}{\partial r}\right) + \frac{\partial}{\partial\theta}\left(\rho\nu_\mathrm{h} r^2\sin^3\theta\frac{\partial\Omega}{\partial\theta}\right). \tag{2.116}$$

And finally one can use it to express the left hand side of Eq. (2.113) and reorganize it to obtain the general equation for the transport of angular momentum:

$$\frac{\partial}{\partial t}\left(\rho r^2\sin^2\theta\Omega\right) + \boldsymbol{\nabla}\cdot\left(\rho r^2\sin^2\theta\Omega\boldsymbol{\mathcal{U}}\right) = \frac{\sin^2\theta}{r^2}\frac{\partial}{\partial r}\left(\rho\nu_\mathrm{v} r^4\frac{\partial\Omega}{\partial r}\right) + \frac{1}{\sin\theta}\frac{\partial}{\partial\theta}\left(\rho\nu_\mathrm{h}\sin^3\theta\frac{\partial\Omega}{\partial\theta}\right). \tag{2.117}$$

2.7.1 Vertical transport of angular momentum

The details necessary to go from Eq. (2.117) to the equation for the vertical transport of angular momentum are exposed in App. D.1. This equation can be written in the form

$$\rho\frac{\mathrm{d}r^2\overline{\Omega}}{\mathrm{d}t} = \frac{1}{5r^2}\frac{\partial}{\partial r}\left(\rho r^4\overline{\Omega}U_2\right) + \frac{1}{r^2}\frac{\partial}{\partial r}\left(\rho\nu_\mathrm{v} r^4\frac{\partial\overline{\Omega}}{\partial r}\right), \tag{2.118}$$

where $\overline{\Omega}$ is defined as

$$\overline{\Omega}(r) = \frac{\int_0^\pi\Omega(r,\theta)\sin^3\theta\mathrm{d}\theta}{\int_0^\pi\sin^3\theta\mathrm{d}\theta}. \tag{2.119}$$

2.7.2 Horizontal transport of angular momentum

In the following we limit ourself to the 2$^\mathrm{nd}$-order term in the Legendre decomposition, but adding higher orders would follow quite simply (but painfully). Again, the details are gathered in App. D.2. The final form of the equation for the horizontal transport of angular momentum is:

$$\rho\frac{\mathrm{d}}{\mathrm{d}t}\left(r^2\Omega_2\right) + \frac{1}{r^2}\frac{\partial}{\partial r}\left(\rho r^4\bar{\Omega}U_2\right) - \frac{10}{6}\frac{\mathrm{d}\rho r^2U_2}{\mathrm{d}r}\bar{\Omega} = \frac{1}{r^2}\frac{\partial}{\partial r}\left[\rho\nu_\mathrm{v} r^4\frac{\partial\Omega_2}{\partial r}\right] - 10\rho\nu_\mathrm{h}\Omega_2. \tag{2.120}$$

During the main sequence, $\frac{\mathrm{d}}{\mathrm{d}t}\left(r^2\Omega_2\right) \simeq 0$ and assuming $\nu_\mathrm{v} \ll \nu_\mathrm{h}$ one can neglect the first term of right hand side. In this case, Eq. (2.120) reads

$$\nu_\mathrm{h}\Omega_2 = \frac{1}{5}r\left[2V_2 - \alpha U_2\right]\overline{\Omega}, \tag{2.121}$$

where α as defined in Eq. (2.18).

2.7.3 Boundary conditions

Equation (2.105) needs to be supplemented by boundary conditions (BC) that link the radiative zone to an eventual convective zone. The expression of the BC depends on the way angular momentum (AM) conservation is treated in the convection zone: either *solid body rotation* (uniform Ω) or *local conservation of* AM (uniform specific angular momentum). It must be noted that neither of these models reproduce well the rotation profile observed in stars, especially the latitudinal variations (see Chapter 4).

Properly defined BC should obviously conserve AM in the stars. The amount of AM in the convective zone can vary in two ways: either AM is lost through stellar wind or AM is extracted/injected from/in CZ by meridional circulation or any other process connecting the radiative and convective zone such as mixed modes, internal gravity waves, etc (see Chapter 5).

- Uniform angular velocity: The convective zones are assumed to be in uniform rotation. Denoting $m_{\rm b}$ and $m_{\rm t}$ the bottom and top mass limits of the radiative zone, one can write the first BC on Ω. The radial gradient of angular velocity at each boundary of the radiative zone is supposed to vanish:

$$\left.\frac{\partial\overline{\Omega}}{\partial r}\right|_{m_{\rm b,t}} = 0. \tag{2.122}$$

  Then, the conservation of AM can be written:

$$\frac{\rm d}{{\rm d}t}\left(\int_0^{M_\star} r^2\Omega{\rm d}m\right) = \frac{\rm d}{{\rm d}t}\left(\int_0^{m_{\rm b}} r^2\Omega{\rm d}m\right) + \frac{\rm d}{{\rm d}t}\left(\int_{m_{\rm b}}^{m_{\rm t}} r^2\Omega{\rm d}m\right) + \frac{\rm d}{{\rm d}t}\left(\int_{m_{\rm t}}^{M_\star} r^2\Omega{\rm d}m\right) = 0. \tag{2.123}$$

  The 2$^{\rm nd}$ term of the right hand side is given by Eq. (2.118).

$$\frac{1}{4\pi}\frac{\rm d}{{\rm d}t}\left(\int_{m_{\rm b}}^{m_{\rm t}} r^2\Omega{\rm d}m\right) = \int_{r_{\rm b}}^{r_{\rm t}} r^2\rho\frac{{\rm d}r^2\Omega}{{\rm d}t}{\rm d}r = \left[\frac{1}{5}\rho r^4\overline{\Omega}U_2\right]_{m_{\rm b}}^{m_{\rm t}}, \tag{2.124}$$

  where we used Eq. (2.122). Then, a BC can be derived for U_2 at bottom and at the top. At the bottom

$$\int_0^{m_{\rm b}}\frac{{\rm d}r^2\Omega}{{\rm d}t}{\rm d}m = \left.\frac{1}{5}\rho r^4\overline{\Omega}U_2\right|_{m_{\rm b}}. \tag{2.125}$$

  And at the top

$$\frac{\rm d}{{\rm d}t}\left(\int_0^{m_{\rm t}}\Omega r^2{\rm d}m\right) = \left.\frac{1}{5}\rho r^4\overline{\Omega}U_2\right|_{m_{\rm t}} - \frac{{\rm d}\mathcal{J}_{\rm wind}}{{\rm d}t} - \int_0^{m_{\rm b}}\frac{{\rm d}\mathcal{J}_{\rm extra}}{{\rm d}t}\frac{{\rm d}m}{\rho}. \tag{2.126}$$

  Here we have introduced two other quantities. The rate ${\rm d}\mathcal{J}_{\rm wind}/{\rm d}t$ corresponds to the amount of AM lost by winds. It can be provided by Eqs. (2.1)-(2.3) or any other model. The quantity ${\rm d}\mathcal{J}_{\rm extra}/{\rm d}t$ encapsulates the angular momentum per unit mass extracted by any other mechanism of transport of angular momentum.

- Uniform specific angular momentum: In this case, the angular velocity profiles in the convective zones are assumed to follow $\Omega(r) = \Omega(r_{\rm b,t})r_{\rm b,t}^2/r^2$, where $r_{\rm b,t}$ is either the radius of the bottom limit or of the top limit of the radiative zone. The factor $\Omega(r_{\rm b,t})$ is the angular velocity at these limits. Then, the reasoning is the same as above but with this particular profile.

Chapter 3

The problem of the surface effects

> Au bord du lac il y a un écho. On s'y tient avec un livre ouvert dont les passages préférés sont redits de l'autre côté par la voix qui s'éloigne et répète. Au double écho, Lucie Maure crie la phrase de Phénarète, je dis que ce qui est, est. Je dis que ce qui n'est pas, est également. Quand elle reprend plusieurs fois la phrase, la voix dédoublée, puis triple, superpose sans cesse ce qui est et ce qui n'est pas. Les ombres couchées sur le lac bougent et se mettent à trembler à cause des vibrations de la voix.
>
> Monique Wittig, *Les guérillères*

Contents

Asteroseismology is the study of the propagation of waves and resulting modes inside stars. The wave frequencies depend on the physical characteristics of the medium in which the waves propagate, and therefore carry information on the stellar interior. To fully exploit the potential of asteroseismology, we need to know by which mechanisms waves are excited and damped in a star, and what are their resulting characteristics (frequency, amplitude, ...). This chapter is

organized as follows. In the first section I derive the system of equations that describe stellar oscillations. In this section we make no particular assumption on the rotation profile of the star. The next section is devoted to solving the oscillation equations when the star is not rotating. The last section presents the work I performed on the surface effects on the frequencies of stellar oscillations.

3.1 Non-radial oscillations equation

The equations we will use to describe oscillations are the time dependent versions of Eqs. (1.50), (1.6) and (2.71) and for a general flow $\mathbf{u}$ (Unno et al., 1989). Those equations read:

$$\frac{\partial \rho}{\partial t} + \boldsymbol{\nabla} \cdot (\rho \mathbf{u}) = 0, \tag{3.1}$$

$$\rho \left(\frac{\partial}{\partial t} + \mathbf{u} \cdot \boldsymbol{\nabla} \right) \mathbf{u} = \rho \mathbf{f} - \boldsymbol{\nabla} p - \rho \boldsymbol{\nabla} \phi + \boldsymbol{\nabla} \cdot \boldsymbol{\tau}, \tag{3.2}$$

$$\rho T \left(\frac{\partial}{\partial t} + \mathbf{u} \cdot \boldsymbol{\nabla} \right) s = \rho \left(\varepsilon_{\mathrm{nuc}} + \varepsilon_{\mathrm{visc}} \right) - \boldsymbol{\nabla} \cdot \mathbf{F}, \tag{3.3}$$

$$\boldsymbol{\nabla}^2 \phi = 4\pi \mathcal{G} \rho, \tag{3.4}$$

where ρ is the density, t the time, p the pressure, ϕ the gravitational potential, T the temperature, s the entropy, $\varepsilon_{\mathrm{nuc}}$ the nuclear energy production rate, $\mathbf{f}$ the external forces (electromagnetic or others) felt by the flow, $\boldsymbol{\tau}$ the viscous stress tensor, $\varepsilon_{\mathrm{visc}}$ the viscous heat generation rate and $\mathbf{F}$ the radiative flux. The convective flux is already included in the left hand side because the convection velocity is part of the velocity $\mathbf{u}$. The external forces are usually neglected, as well as the viscous heat generation. In stellar convective zones, convection flows certainly have an impact on wave propagation and conversely. However, treating both phenomena at the same time is a difficult problem in stellar physics (see e.g. Gough, 1977; Grigahcène et al., 2005; Xiong et al., 2015). The dynamics of convection and oscillations are usually modelled independently. Because the dynamical time-scale of evolution of the waves is much shorter than the thermal time-scale, oscillations are often assumed to be adiabatic. In the remaining of this Chapter, I will make this assumption, unless mentioned otherwise.

3.1.1 Equilibrium solutions

The equilibrium solutions to these equations are given in Chapter 1. In the following, the equilibrium quantities will be denoted with a 0. For the sake of clarity, I recall the differential equations satisfied by equilibrium quantities:

$$\boldsymbol{\nabla} \cdot (\rho_0 \mathbf{u}_0) = 0, \tag{3.5}$$

$$(\mathbf{u}_0 \cdot \boldsymbol{\nabla}) \mathbf{u}_0 = -\frac{1}{\rho_0} \boldsymbol{\nabla} p_0 - \boldsymbol{\nabla} \phi_0, \tag{3.6}$$

$$\rho_0 T_0 (\mathbf{u}_0 \cdot \boldsymbol{\nabla}) s_0 = \rho_0 \left(\varepsilon_{\mathrm{nuc},0} + \varepsilon_{\mathrm{visc},0} \right), \tag{3.7}$$

$$\boldsymbol{\nabla}^2 \phi_0 = 4\pi \mathcal{G} \rho_0. \tag{3.8}$$

The equilibrium state is supposed steady ($\partial / \partial t = 0$). Since convection is treated separately, the equilibrium flow is supposed to be solely composed of the axisymmetrical rotation: $\mathbf{u}_0 = \boldsymbol{\Omega} \times \mathbf{r}$. Using these notations, one can define the linear Eulerian perturbation X' of a quantity X around the equilibrium value X_0:

$$X(\mathbf{r}, t) = X_0(\mathbf{r}, t) + X'(\mathbf{r}, t), \tag{3.9}$$

with $X' \ll X_0$. From the Lagrangian point of view, the small displacement from an equilibrium point $\mathbf{r}_0$ to a location $\mathbf{r} = \mathbf{r}_0 + \boldsymbol{\delta} r$ results, for the quantity X, in a small change:

$$\delta X = X(\mathbf{r}, t) - X_0(\mathbf{r}_0, t). \tag{3.10}$$

The small displacement is often noted with a $\boldsymbol{\xi} = (\xi_r, \xi_\theta, \xi_\varphi)$ (Aerts et al., 2010), which allows us to express the Lagrangian perturbation as a function of the Eulerian one:

$$\delta X = X' + \boldsymbol{\xi} \cdot \boldsymbol{\nabla} X_0, \tag{3.11}$$

where, $\boldsymbol{\xi}$ is also linked to the Eulerian perturbation of the velocity of the flow:

$$\mathbf{u}' = \frac{\partial \boldsymbol{\xi}}{\partial t} + (\mathbf{u}_0 \cdot \boldsymbol{\nabla})\boldsymbol{\xi} - (\boldsymbol{\xi} \cdot \boldsymbol{\nabla})\mathbf{u}_0. \tag{3.12}$$

3.1.2 linearised equations with rotation

The perturbed equations in the adiabatic approximation are (e.g. Ouazzani et al., 2010)

$$\left(\frac{\partial}{\partial t} + \mathbf{u}_0 \cdot \boldsymbol{\nabla}\right) \rho' + \boldsymbol{\nabla} \cdot (\rho_0 \mathbf{u}') = 0, \tag{3.13}$$

$$\left(\frac{\partial}{\partial t} + \mathbf{u}_0 \cdot \boldsymbol{\nabla}\right) \mathbf{u}' + 2\boldsymbol{\Omega} \times \mathbf{u}' + [\mathbf{u}' \cdot \boldsymbol{\nabla}\Omega]\, r \sin\theta \mathbf{e}_\varphi = \frac{\rho'}{\rho_0^2}\boldsymbol{\nabla} p_0 - \frac{1}{\rho_0}\boldsymbol{\nabla} p' - \boldsymbol{\nabla}\phi', \tag{3.14}$$

$$\begin{aligned} \left(\frac{\partial}{\partial t} + \mathbf{u}_0 \cdot \boldsymbol{\nabla}\right)\left(\frac{\rho'}{\rho_0} - \frac{1}{\Gamma_1}\frac{p'}{p_0}\right) + \mathbf{u}'\left(\frac{\boldsymbol{\nabla}\rho_0}{\rho_0} - \frac{1}{\Gamma_1}\frac{\boldsymbol{\nabla} p_0}{p_0}\right) &= [\rho\,(\varepsilon_{\rm nuc} + \varepsilon_{\rm visc})]' - \boldsymbol{\nabla} \cdot \mathbf{F}', \\ &= 0 \end{aligned} \tag{3.15}$$

$$\nabla^2 \phi' = 4\pi \mathcal{G} \rho', \tag{3.16}$$

where Γ_1 is the 1st adiabatic index defined by $\Gamma_1 = \partial \ln p / \partial \ln \rho|_{\rm ad}$ or by the relation $\mathrm{d}p/p + \Gamma_1 \mathrm{d}V/V = 0$ (Chandrasekhar, 1957). The right hand side of Eq. (3.15) vanishes because of the hypothesis of adiabaticity. Eqs. (3.13)-(3.16) form a set of equations for four variables $\mathbf{u}'$ (in the literature, one also find those equations written with $\boldsymbol{\xi}$ as independent variable), p', ρ' and ϕ'. We will further simplify this system.

Eq. (3.15), reduces to the adiabatic relation

$$\frac{\delta\rho}{\rho_0} = \frac{1}{\Gamma_1}\frac{\delta p}{p_0}, \tag{3.17}$$

thanks to the adiabatic approximation: $\delta s = 0$. Replacing the Lagrangian perturbations by the Eulerian ones, leads to:

$$\frac{\rho'}{\rho_0} - \frac{1}{\Gamma_1}\frac{p'}{p_0} + \boldsymbol{\xi} \cdot \mathbf{A} = 0 \quad \text{with} \quad \mathbf{A} = \boldsymbol{\nabla} \ln \rho - \frac{1}{\Gamma_1}\boldsymbol{\nabla} \ln p, \tag{3.18}$$

where, $\mathbf{A}$ is the Schwarzschild discriminant. With $\mathbf{g}_{\rm eff} = -\boldsymbol{\nabla} p/\rho$, the square of the Brunt-Väisälä frequency can be rewritten in term of the Schwarzschild discriminant:

$$N^2 = \mathbf{g}_{\rm eff} \cdot \mathbf{A} \tag{3.19}$$

We recall that the Brunt-Väisälä frequency is the frequency at which a small displaced parcel oscillates in a stably stratified zone. By using Eq. (3.12) in Eq. (3.13) the linearised continuity equation can be written:

$$\rho' + \boldsymbol{\nabla}\,(\rho_0 \boldsymbol{\xi}) = 0. \tag{3.20}$$

Equations in system (3.13) to (3.15) are linear 1st order differential equations in time t and azimuth φ. Furthermore, the coefficients of these differential equations are independent of time and azimuth because they are only combinations of equilibrium quantities. Therefore, the temporal and azimuthal dependencies in the perturbed quantities, are of the form $\exp(i(\omega t + m\varphi))$. The term ω is the temporal angular frequency and the integer m is the so called *azimuthal number* and it enforces the 2π periodicity in φ. Therefore, the advection of any scalar X or vector $\mathbf{V}$ by $\mathbf{u}_0$ simplifies to

$$\mathbf{u}_0 \cdot \boldsymbol{\nabla} X = \Omega \frac{\partial X}{\partial \varphi} = im\Omega X, \tag{3.21}$$

and

$$\mathbf{u}_0 \cdot \boldsymbol{\nabla} \mathbf{V} = im\Omega \mathbf{V} + \boldsymbol{\Omega} \times \mathbf{V}. \tag{3.22}$$

Therefore, the Lagrangian time derivatives ($\mathrm{D}/\mathrm{D}t = \partial/\partial t + \mathbf{u}_0 \cdot \boldsymbol{\nabla}$) at the beginnings of Eqs. (3.13)-(3.15) are replaced by

$$\left(\frac{\partial}{\partial t} + (\mathbf{u}_0 \cdot \boldsymbol{\nabla})\right) = i\omega + im\Omega = i\hat{\omega}, \tag{3.23}$$

where $\hat{\omega}$ is the oscillation intrinsic angular frequency[1] of the wave in the co-rotating (with the star or with a given layer) frame of reference. Using this relation, the perturbed part of the velocity, Eq. (3.12) becomes:

$$\mathbf{u}' = i\hat{\omega}\boldsymbol{\xi} - (\boldsymbol{\xi} \cdot \boldsymbol{\nabla}\Omega) r \sin\theta \mathbf{e}_\varphi. \tag{3.24}$$

Hence, the momentum conservation equation (3.14) reads:

$$-\hat{\omega}^2\boldsymbol{\xi} + 2i\hat{\omega}\boldsymbol{\Omega} \times \boldsymbol{\xi} - (\boldsymbol{\xi} \cdot \boldsymbol{\nabla}\Omega^2) r \sin\theta \mathbf{e}_\perp = \frac{\rho'}{\rho_0^2}\boldsymbol{\nabla} p_0 - \frac{1}{\rho_0}\boldsymbol{\nabla} p' - \boldsymbol{\nabla}\phi', \tag{3.25}$$

where $\mathbf{e}_\perp = \sin\theta \mathbf{e}_r + \cos\theta \mathbf{e}_\theta$, already defined in (1.51), corresponds to the vector in the direction perpendicular to the rotation axis. Eqs. (3.20), (3.25), (3.18) and (3.16) form a system equivalent to the system (3.13)-(3.16) but expressed with the displacement instead of velocity fluctuations.

We will be looking for particular solutions of the perturbed quantities, developed on spherical harmonics. Because of the non-spherical symmetry, the solutions are non-separable into a radial part and angular part, as is the case when rotation is neglected. However, one can express any vector $\mathbf{V}$ or scalar X, solution of system (3.13)-(3.16), in the following general form (Rieutord, 1987):

$$\begin{aligned} \mathbf{V}(r,\theta,\varphi,t) &= e^{i\omega t} \sum_{\ell,m} u_m^\ell(r_p) Y_\ell^m(\theta,\varphi)\mathbf{e}_r + v_m^\ell(r_p)\boldsymbol{\nabla} Y_\ell^m(\theta,\varphi) + w_m^\ell(r_p)\boldsymbol{\nabla} \times (Y_\ell^m(\theta,\varphi)\mathbf{e}_r) \\ &= e^{i\omega t} \sum_{\ell,m} u_m^\ell(r_p)\mathbf{R}_\ell^m(\theta,\varphi) + v_m^\ell(r_p)\mathbf{S}_\ell^m(\theta,\varphi) + w_m^\ell(r_p)\mathbf{T}_\ell^m(\theta,\varphi), \end{aligned} \tag{3.26}$$

and

$$X(r,\theta,\varphi,t) = e^{i\omega t} \sum_{\ell,m} x_m^\ell(r_p) Y_\ell^m(\theta,\varphi), \tag{3.27}$$

[1]Several frequencies can be defined. The intrinsic frequency $\hat{\omega}$ is the frequency in the reference frame, actually in $\mathrm{rad\,s^{-1}}$. It is related to the cyclic frequency $\hat{\nu}$, in $\mathrm{s^{-1}}$ by the relation: $\hat{\omega} = 2\pi\hat{\nu}$. The same relation exists for the temporal frequency ω.

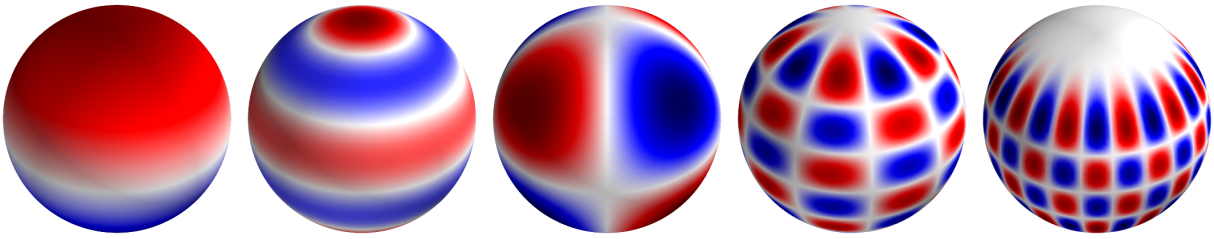

Figure 3.1: Real part of the radial component of $(l, m) = \{(1, 0), (5, 0), (3, 2), (10, 5), (15, 12)\}$ modes. The red and the blue surfaces can be viewed respectively as an elevation and a depression of the surface, due to stellar oscillation.

where u_m^ℓ, v_m^ℓ and w_m^ℓ are the projections of $\mathbf{V}$ on $\mathbf{R}_\ell^m$, $\mathbf{S}_\ell^m$ and $\mathbf{T}_\ell^m$. The radius r_p is the radius of an isobar as defined in Eq. (2.47). It can be any other suitable parametrization, the important point being that this coordinate must depends on the radius *and* on the latitude. Finally, $Y_\ell^m(\theta, \varphi)$ are the spherical harmonics (see Fig. 3.1) defined by

$$Y_\ell^m(\theta, \varphi) = (-1)^m c_{\ell,m} P_\ell^m(\cos\theta) e^{im\varphi} \quad \text{with} \quad c_{\ell,m} = \sqrt{\frac{2\ell+1}{4\pi}\frac{(\ell-m)!}{(\ell+m)!}}, \tag{3.28}$$

where $c_{\ell,m}$ is a normalization constant allowing the integral of $|Y_\ell^m|^2$ over a unit sphere to equal unity, and P_ℓ^m is the associated Legendre polynomial (see Eq. (B.9)).

- $n \in \mathbb{Z}$ is called the radial order. It is the number of radial nodes of an eigenfunction along the stellar radius (although this is not true for mixed modes which have two more nodes; Scuflaire 1974);
- $\ell \in [\![0; n]\!]$ is called the degree of the mode. It corresponds to the total number of nodal lines on the sphere, parallel to the latitudes or to the longitudes (see Fig. 3.1). The surfaces formed by the "latitudinal" nodal lines are conical surfaces, while the one formed by "longitudinal" nodal lines are planes;
- $m \in [\![\ell; \ell]\!]$ is the azimuthal order. It is the number of the nodal planes parallel to the longitudes. Consequently, the integer $\ell - m$ is the number of plane parallel to the latitudes.

As said in the introduction, my goal in this Chapter is not to provide a full resolution of the system (3.13)-(3.16), especially since this system is not completely solved yet. Oscillation codes such as TOP (two-dimensional Oscillation Program; Reese et al. 2006) or ACOR (Adiabatic Code of Oscillation including Rotation; Ouazzani et al. 2012) can however provide 2D non-perturbative solutions to oscillation equations (including rotation). They also provide a framework to test various methods developed to approximate oscillation spectra of rotating stars. I will quickly describe some of these approximations, starting from no rotation at all, then slow and finally fast rotation.

3.2 Non-rotating asteroseismology

3.2.1 Oscillation equations

A large fraction of stars are slow rotators. A very good description of their frequency spectrum can be reached by assuming no rotation in the system (3.13)-(3.16). We decompose the displacement vector $\boldsymbol{\delta r} = \boldsymbol{\xi}$ into a radial component ξ_r and horizontal component $\boldsymbol{\xi}_\mathrm{h} = (0, \xi_\theta, \xi_\varphi)$

and $\boldsymbol{\delta}r = \xi_{\rm r}\mathbf{e}_r + \boldsymbol{\xi}_{\rm h}$. With $\boldsymbol{\Omega} = \mathbf{0}$, Eq. (3.25) projected on the radial and horizontal direction becomes (Aerts et al., 2010):

$$\frac{\partial^2 \xi_r}{\partial t^2} = -\omega^2 \xi_r = -\frac{1}{\rho_0}\frac{\partial p'}{\partial r} - \frac{\rho'}{\rho_0} g_0 - \frac{\partial \phi'}{\partial r}, \tag{3.29}$$

$$\text{and} \quad \frac{\partial^2 \boldsymbol{\xi}_{\rm h}}{\partial t^2} = -\omega^2 \boldsymbol{\xi}_{\rm h} = -\boldsymbol{\nabla}_{\rm h}\left(\frac{p'}{\rho_0} + \phi'\right), \tag{3.30}$$

where $\boldsymbol{\nabla}_{\rm h} = (0, \frac{1}{r}\frac{\partial}{\partial\theta}, \frac{1}{r\sin\theta}\frac{\partial}{\partial\varphi})$ is the horizontal spherical gradient. We need three more equations for p' ρ' and ϕ'. We inject Eqs. (3.29) and (3.30) into Eq. (3.20) and we further develop the Poisson equation to separate the radial and horizontal part:

$$\rho' + \xi_r \frac{\partial \rho_0}{\partial r} + \frac{\rho_0}{r^2}\frac{\partial r^2 \xi_r}{\partial r} + \frac{\rho_0}{\omega^2}\nabla_{\rm h}^2\left(\frac{p'}{\rho_0} + \phi'\right) = 0 \tag{3.31}$$

$$\frac{1}{r^2}\frac{\partial}{\partial r}\left(r^2 \frac{\partial \phi'}{\partial r}\right) + \nabla_{\rm h}^2 \phi' = 4\pi \mathcal{G}\rho'. \tag{3.32}$$

Finally, in the case of no rotation, Eq. (3.18) only depends on ξ_r because of the spherical symmetry:

$$\frac{\rho'}{\rho_0} - \frac{1}{\Gamma_1}\frac{p'}{p_0} + \xi_r A_r = 0 \quad \text{with} \quad A_r = \frac{\partial \ln \rho}{\partial r} - \frac{1}{\Gamma_1}\frac{\partial \ln p}{\partial r}. \tag{3.33}$$

Therefore, Eqs. (3.29), (3.31), (3.32) and (3.33) form a system with ξ_r, p', ρ' and ϕ' as unknowns.

Because of the spherical symmetry, the solution for the components of the displacement are, this time, separable into a radial and an angular part. The displacement (eigenfunctions) of an eigenmode is identified by the quantum numbers (n, ℓ, m) in the (r, θ, φ) directions:

$$\xi_r(r,\theta,\varphi,t) = \xi_{r,n\ell}(r) Y_\ell^m(\theta,\varphi)\exp(-2i\pi\nu_{n\ell m}t), \tag{3.34}$$

$$\xi_\theta(r,\theta,\varphi,t) = \xi_{{\rm h},n\ell}(r)\frac{\partial Y_\ell^m}{\partial\theta}(\theta,\varphi)\exp(-2i\pi\nu_{n\ell m}t), \tag{3.35}$$

$$\xi_\varphi(r,\theta,\varphi,t) = \frac{\xi_{{\rm h},n\ell}(r)}{\sin\theta}\frac{\partial Y_\ell^m}{\partial\varphi}(\theta,\varphi)\exp(-2i\pi\nu_{n\ell m}t), \tag{3.36}$$

where $\nu_{n\ell m} = \omega_{n\ell m}/2\pi$ is the cyclic frequency. Moreover, any scalar can be written in the same way as in Eq. (3.27) with the amplitudes depending on $r_p = r$. We note that the horizontal Laplacian of a spherical harmonics is:

$$\nabla_{\rm h}^2 Y_\ell^m(\theta,\varphi) = -\frac{\ell(\ell+1)}{r^2} Y_\ell^m(\theta,\varphi). \tag{3.37}$$

We also introduce the so-called *Lamb frequency* (Lamb, 1881):

$$S_\ell^2 = \frac{\ell(\ell+1)}{r^2}c_{\rm s}^2 \quad \text{with} \quad c_{\rm s}^2 = \sqrt{\frac{\Gamma_1 p_0}{\rho_0}}, \tag{3.38}$$

where $c_{\rm s}^2$ is the sound speed. The quantity $k_{\rm h}^2 \equiv \ell(\ell+1)/r^2$ is the horizontal wave number. The Lamb frequency is thus the inverse of the time needed for a wave to cross a distance $2\pi/k_{\rm h}$ at speed $c_{\rm s}$. Now, from Eq. (3.18) we derive:

$$\rho' = \frac{p'}{c_{\rm s}^2} + \xi_r \frac{\rho_0 N^2}{g_0} \quad \text{and} \quad \frac{\partial \rho_0}{\partial r} = -\rho_0\left(\frac{g_0}{c_{\rm s}^2} + \frac{N^2}{g_0}\right). \tag{3.39}$$

Then using relations (3.39) successively into Eq (3.29), (3.31) and (3.32), gives for Eq (3.29)

$$\begin{aligned} -\omega^2\xi_r &= -\frac{1}{\rho_0}\frac{\partial p'}{\partial r} - \left(\frac{p'}{\rho_0 c_{\rm s}^2} + \xi_r\frac{N^2}{g_0}\right) g_0 - \frac{\partial \phi'}{\partial r} \\ \frac{\partial p'}{\partial r} + \frac{g_0}{c_{\rm s}^2}p' &= \rho_0\left(\omega^2 - N^2\right)\xi_r - \rho_0\frac{\partial \phi'}{\partial r}, \end{aligned} \tag{3.40}$$

for Eq. (3.31):

$$\begin{aligned} \frac{p'}{c_{\rm s}^2} + \xi_r\frac{\rho_0 N^2}{g_0} + \rho_0\left(\frac{2}{r}\xi_r + \frac{\partial \xi_r}{\partial r}\right) &= \rho_0\xi_r\left(\frac{g_0}{c_{\rm s}^2} + \frac{N^2}{g_0}\right) + \frac{\ell(\ell+1)}{r^2\omega^2}\left(p' + \rho_0\phi'\right), \\ \frac{\partial \xi_r}{\partial r} + \xi_r\left(\frac{2}{r} - \frac{g_0}{c_{\rm s}^2}\right) &= \frac{\ell(\ell+1)}{r^2\omega^2}\phi' + \frac{p'}{\rho_0 c_{\rm s}^2}\left(\frac{S_\ell^2}{\omega^2} - 1\right), \end{aligned} \tag{3.41}$$

and for Eq. (3.32):

$$\frac{1}{r^2}\frac{\partial}{\partial r}\left(r^2\frac{\partial \phi'}{\partial r}\right) - \frac{\ell(\ell+1)}{r^2}\phi' = 4\pi\mathcal{G}\left(\frac{p'}{c_{\rm s}^2} + \xi_r\frac{\rho_0 N^2}{g_0}\right). \tag{3.42}$$

The solution of the radial parts of the perturbed gravitational potential ϕ' can be expressed as (Aerts et al., 2010)

$$\phi'(r) = -\frac{4\pi\mathcal{G}}{2\ell+1}\left[\frac{1}{r^{\ell+1}}\int_0^r \rho'(r_2) r_2^{\ell+2}{\rm d}r_2 + r^\ell\int_r^R \frac{\rho'(r_2)}{r_2^{\ell-1}}{\rm d}r_2\right]. \tag{3.43}$$

When ℓ is large, the ratios $r_2^{\ell+2}/r^{\ell+1}$ and $r^\ell/r_2^{\ell-1}$ in both integral are small because in the first one $r_2/r_1 < 1$ and in the second one, $r_1/r_2 < 1$. There is also the factor $1/(2\ell+1)$ that reduces further the value of ϕ'. When n is large, the perturbation of the density is fast-varying and the integrals are small. Therefore, for large n and large ℓ, ϕ' goes to 0. It justifies the so-called *Cowling approximation* (Cowling, 1941) which amounts to assuming that the fluctuations of the gravitational potential vanish. This approximation is justified for waves propagating in regions of low density, *i.e.* the envelope of the star. With this approximation, our system simplifies to only two equations:

$$\frac{\partial p'}{\partial r} + \frac{g_0}{c_{\rm s}^2}p' = \rho_0\left(\omega^2 - N^2\right)\xi_r, \tag{3.44}$$

$$\frac{\partial \xi_r}{\partial r} + \xi_r\left(\frac{2}{r} - \frac{g_0}{c_{\rm s}^2}\right) = \frac{p'}{\rho_0 c_{\rm s}^2}\left(\frac{S_\ell^2}{\omega^2} - 1\right). \tag{3.45}$$

The term $g_0/c_{\rm s}^2$ is of the order of the inverse of the pressure scale height[2]. Eigenfunctions of oscillations with large n vary on spatial scales much shorter than the equilibrium structure of the star (which vary on characteristic scales of order $H_{\rm p}$). Therefore, one can make the hypothesis that $g_0/c_{\rm s}^2$ is small compared to $\partial\xi_r/\partial r$. Moreover, the term $2/r$, near the surface goes to 0 and is also small compared to $\partial\xi_r/\partial r$. The second term of the left hand side of Eq. (3.45) can then be neglected[3]. Hence, the above system becomes

$$\frac{\partial p'}{\partial r} = \rho_0\left(\omega^2 - N^2\right)\xi_r, \tag{3.46}$$

[2]I recall that the pressure scale height is defined as

$$\frac{1}{H_{\rm p}} = -\frac{{\rm d}\ln p}{{\rm d}r}.$$

[3]These approximations are questionable. Indeed the pressure scale height goes to 0 near the surface, therefore the neglect of $g_0/c_{\rm s}^2$ is not valid at the surface. On the other side, $2/r$ becomes high near the centre and cannot be neglected either.

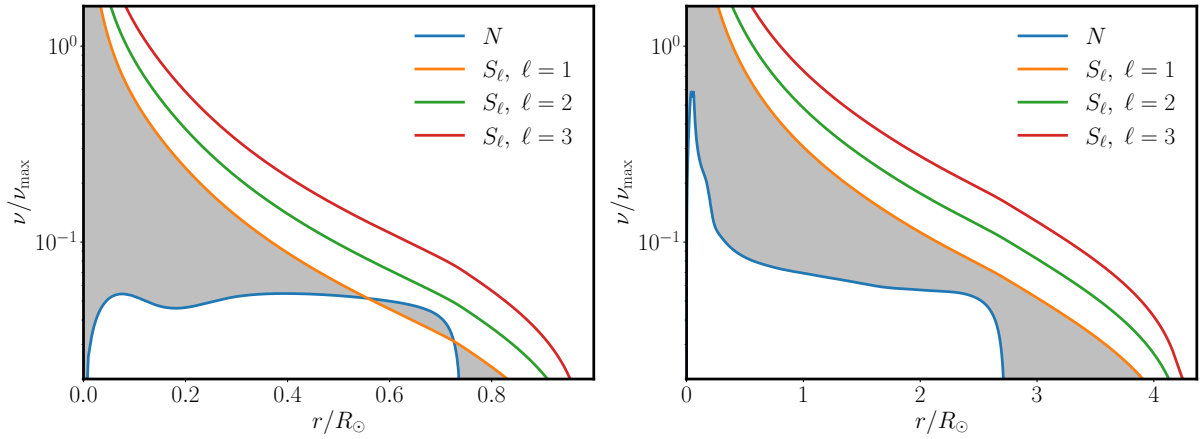

Figure 3.2: Propagation diagram for two stellar models. Mode with frequency (normalized by $\nu_{\max}$). Shaded areas represent the zones where degree $l = 1$ modes vanish. *left*: Sun model with $\nu_{\max} = 3090$ µHz and an age of 4570 Myr (main-sequence star). *right*: Model with $M = 2.21\ M_\odot$, $R = 4.37\ R_\odot$, $\nu_{\max} = 347$ µHz and an age of 1016 Myr (sub-giant star).

$$\frac{\partial \xi_r}{\partial r} = \frac{p'}{\rho_0 c_s^2}\left(\frac{S_\ell^2}{\omega^2} - 1\right). \tag{3.47}$$

And finally we obtain a wave equation for ξ_r (or p'):

$$\frac{\partial^2 \xi_r}{\partial r^2} = \frac{\omega^2}{c_s^2}\left(1 - \frac{N^2}{\omega^2}\right)\left(\frac{S_\ell^2}{\omega^2} - 1\right)\xi_r = -\omega^2 k^2(r)\xi_r, \tag{3.48}$$

$$\frac{\partial^2 \xi_r}{\partial r^2} - k^2(r)\frac{\partial^2 \xi_r}{\partial t^2} = 0 \tag{3.49}$$

Figure 3.2 represents the profile of the Brunt-Väisälä frequency N and of the Lamb frequency S_ℓ for three values of ℓ. The frequency N is positive inside the radiative region. The behaviour of ξ_r is determined by the sign of $k^2(r) = \frac{1}{c^2}\left(1 - \frac{N^2}{\omega^2}\right)\left(1 - \frac{S_\ell^2}{\omega^2}\right)$, the local wave number.

- If $k^2(r) > 0$: the solution is a propagating wave. This happens when
  - *(i):* $\omega^2 > N^2$ and $\omega^2 > S_\ell^2$;
  - *(ii):* $\omega^2 < N^2$ and $\omega^2 < S_\ell^2$;
- If $k^2(r) < 0$: the solution is an exponentially increasing or decreasing wave. This happens when
  - *(iii):* $S_\ell^2 < \omega^2 < N^2$;
  - *(iv):* $N^2 < \omega^2 < S_\ell^2$.

The regions where conditions *(iii)* or *(iv)* are satisfied are represented as grey shaded areas in figure 3.2. Waves existing in such regions are called evanescent waves. In propagating regions, in case some conditions on the excitation and damping rates are met (see Sect 3.2.4), the wave reflections form standing waves. Those regions are often called trapping regions and are separated from each other by evanescent regions. Therefore, standing waves are confined in the trapping region. One can identify two types of modes:

- modes satisfying condition (i) (high-frequency): they are called *p-modes* because their restoring force is the pressure gradient and they are confined to the surface layers;
- modes satisfying condition (ii) (low-frequency): they are called *g-modes* because their restoring force is the gravity and they are confined to the radiative zones.

Consequently, a single mode displays different behaviours according to the region we are looking at. It is oscillating everywhere, however its amplitude exponentially decreases while propagating in evanescent regions. Let us imagine that a star has two distinct regions, and that a mode can propagate in the central regions and is evanescent in the outer one. If the exponentially decreasing amplitude has not vanished at the surface, this mode could be observable. This is for instance not the case in the Sun in which *g*-modes are not measurable at the surface because they are confined in the deep interior of the star, and their residual amplitude at the surface is almost 0. Modes in a particular range of frequencies, can display both *g*-mode and *p*-mode behaviour because the corresponding cavities are so close to one another and a mode can propagate into both cavities and be measured at the surface. Those modes are called *mixed-modes* and they provide a powerful opportunity to collect data from the stellar core structure (e.g. Mosser et al., 2014).

3.2.2 Asymptotic relations

The study of the oscillation equations and of seismic observations have revealed the presence of regular patterns in the frequency spectra. Indeed, it can be shown that the frequencies of modes with large n (asymptotic modes) follow very simple relations, called *asymptotic relations* (Shibahashi, 1979; Tassoul, 1980, 1990; Vorontsov, 1991). These relations are powerful tools because they allow astronomers to easily identify the different modes (*i.e.* identify the quantum numbers associated with a particular mode), which enables them to use them as constraints for the modelling of a specific star. For *p*-modes, the frequency $\nu_{n\ell}$ of a mode for n large can be approximated by a 2$^{\text{nd}}$ order asymptotic approximation (even a 4$^{\text{th}}$-order approximation has been proposed; Roxburgh & Vorontsov 1994):

$$\nu_{n\ell} \simeq \left(n + \frac{\ell}{2} + \frac{1}{4} + \alpha(\nu_{n\ell})\right)\Delta\nu - \frac{1}{\nu_{n\ell}}\left(A\ell(\ell+1) - 2\Phi\right)\Delta\nu^2. \tag{3.50}$$

Here, α contains the residual of the neglected higher orders and the so-called *surface effect*, that will be discussed in more detail in Sect 3.3. The term α depends on the stellar-structure and on the frequency. The term $\alpha\Delta\nu$ and the 2$^{\text{nd}}$-order term (factor of $\Delta\nu^2$) are very small compared with the remaining 1$^{\text{st}}$-order one. Therefore, one sees that, if α was not here, the mode $\nu_{n+1,\ell}$ would have the same frequency as $\nu_{n,\ell+2}$. This degeneracy is lifted by α. The factor $\Delta\nu$ is called the *large separation*. In a 1$^{\text{st}}$-order approximation, one can consider that $\Delta\nu$ is constant over the whole spectrum:

$$\forall n \in \mathbb{N}, \ell \in [\![0; n]\!], \quad \Delta\nu \simeq \Delta\nu_{n,\ell} = \nu_{n+1,\ell} - \nu_{n,\ell}. \tag{3.51}$$

The *p*-modes are therefore said to be evenly spaced in frequency. Asymptotically, the large separation is proportional to the inverse of the stellar acoustic diameter, *i.e.* the time a sound wave takes to travel across a stellar diameter:

$$\Delta\nu = \left(2\int_0^{R_\star} \frac{\mathrm{d}r}{c}\right)^{-1}. \tag{3.52}$$

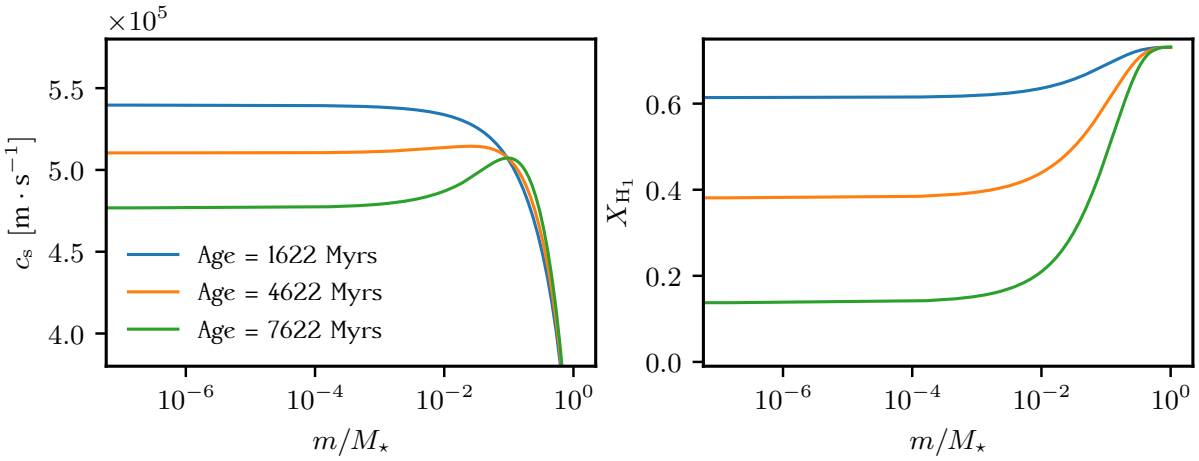

Figure 3.3: *left*: Sound speed profile as a function of mass at different stages in the main-sequence phase of a $1M_\odot$ stellar model. *right*: H_1 mass fraction profile as a function of mass at different stages in the main-sequence phase of a $1M_\odot$ stellar model.

This particular frequency is of extreme importance in asteroseismology because it is very easy to measure (with only a few measured frequencies) and it is linked to the mean density of the star (Ulrich, 1986):

$$\Delta\nu \propto \sqrt{\frac{M}{R^3}} \propto \sqrt{\langle\rho\rangle}. \tag{3.53}$$

The term in factor of $\Delta\nu^2$ includes a quantity A:

$$A = \frac{1}{4\pi^2\Delta\nu}\left(\frac{c_\mathrm{s}(R_\star)}{R_\star} - \int_0^{R_\star}\frac{\mathrm{d}c_\mathrm{s}}{\mathrm{d}r}\frac{\mathrm{d}r}{r}\right). \tag{3.54}$$

This quantity is linked to another regularity in the frequency pattern called the *small separation*:

$$\delta\nu_{n\ell} = \nu_{n\ell} - \nu_{n-1,\ell+2} \simeq -(4\ell+6)\frac{\Delta\nu}{4\pi^2\nu_{n\ell}}\int_0^{R_\star}\frac{\mathrm{d}c_\mathrm{s}}{\mathrm{d}r}\frac{\mathrm{d}r}{r}. \tag{3.55}$$

This expression neglects the influence of the gravitational potential perturbation. A more detailed discussion can be found in Gabriel (1989). The small separation $\delta\nu$ depends on the sound-speed gradient which is much higher in the stellar core. As shown in Fig. 3.3, the sound speed is a marker of the composition at the centre and it decreases during the evolution due to the increasing of the mean molecular weight in the core. Therefore $\delta\nu$ provides a proxy for stellar evolution.

The final term needing a definition is the quantity Φ in Eq. (3.50). A very complex expression for Φ is given in Vorontsov (1991), I do not reproduce it here but it depends mostly on quantities such as the gravity, the gravitational potential, the sound speed, the Brunt-Väisälä frequency and the radius.

In the case of g-modes, the asymptotic relation is different. Indeed, g-modes are not evenly spaced in frequency but in period. Therefore we will not talk about the large frequency separation but about the *period spacing*. This asymptotic relation is given as an integral

relation:

$$\int_{r_1}^{r_2} \left(\frac{N^2}{\nu_{n\ell}^2} - 1 \right)^{1/2} \frac{\mathrm{d}r}{r} = \frac{\pi(n + \ell/2 + \alpha_\mathrm{g})}{\ell(\ell+1)}. \tag{3.56}$$

First of all, the radii r_1 and r_2 are the limit (called turning points) of the trapping cavity in which the considered *g*-mode propagates. The term $\alpha_\mathrm{g} \simeq 1$ plays a similar role as α in Eq. (3.50) but its value depends on the nature of the interface on which the *g*-mode is reflected. By assuming, $\nu_{n\ell} \ll N$, one can write for the period $P_{n\ell}$:

$$P_{n\ell} \simeq \Delta\Pi_\ell (n + \ell/2 + \alpha_\mathrm{g}) \quad \text{with} \quad \Delta\Pi_\ell = \frac{2\pi^2}{\ell(\ell+1)} \int_{r_1}^{r_2} N \frac{\mathrm{d}r}{r}, \tag{3.57}$$

with $\Delta\Pi_\ell$ being the period spacing.

An asymptotic relation for mixed-modes, that behave as *g*-modes in the g cavity and as *p*-modes in the p cavity, can also be defined. It has been the subject of many works since the advent of CoRoT and *Kepler* because mixed modes carry a wealth of information on stellar cores. This asymptotic relation depends on the coupling between the two cavities (Shibahashi, 1979; Unno et al., 1989; Mosser et al., 2012, 2014, 2015; Vrard et al., 2016; Mosser et al., 2017, 2018; Pinçon et al., 2020).

3.2.3 Ensemble asteroseismology

As shown with Eq. (3.53), characteristic oscillation frequencies can provide important information on stellar global parameters. Since, for instance, $\Delta\nu$ is proportional to the mean stellar density, dividing Eq. (3.53) by solar values gives access to a very precise measurement of the mean density of any star for which $\Delta\nu$ is measured:

$$\frac{\Delta\nu}{\Delta\nu_\odot} \simeq \sqrt{\frac{M}{R^3}\frac{R_\odot^3}{M_\odot}} \simeq \sqrt{\frac{\langle\rho\rangle}{\langle\rho\rangle_\odot}} \quad \text{with} \quad \Delta\nu_\odot = 134.9\ \mu\mathrm{Hz} \text{ and } \langle\rho\rangle_\odot = 1408\ \mathrm{kg\,m^{-3}}. \tag{3.58}$$

This method is called *ensemble asteroseismology*. Since the resolution on the measurement of the frequency spectrum is much better than the determination of mass and radius for isolated stars by other means, the parameters estimated through asteroseismology are of much higher quality. Nonetheless, this relation is not quite exact, as it should account for effects from a varying effective temperature or metallicity (White et al., 2011).

Other interesting frequencies are the *acoustic cut-off frequency* ν_ac and *frequency of the maximum power* ν_max (see Fig. (3.4)) which share a close link. Stellar oscillation spectra have a Gaussian-shaped envelop. This Gaussian peaks at the frequency ν_max. This frequency is directly linked to the acoustic cut-off frequency:

$$\nu_\mathrm{ac} = \frac{c_\mathrm{s}}{4\pi H_\mathrm{p}} \quad \text{and} \quad \nu_\mathrm{max} \propto \nu_\mathrm{ac}, \tag{3.59}$$

where c_s is the sound speed. Above this frequency there is no total reflection at the stellar surface any more. Furthermore,

$$\frac{1}{H_\mathrm{p}} = -\frac{1}{p}\frac{\partial p}{\partial r} = \frac{1}{p}\rho g \propto \frac{g}{T} \underset{\text{surface}}{\propto} \frac{g}{T_\mathrm{eff}}. \tag{3.60}$$

Then, since $c_\mathrm{s}^2 \propto \sqrt{p/\rho}$, we finally have

$$\nu_\mathrm{max} \propto \nu_\mathrm{ac} \propto \frac{g}{\sqrt{T_\mathrm{eff}}} \propto \frac{M}{R^2\sqrt{T_\mathrm{eff}}}. \tag{3.61}$$

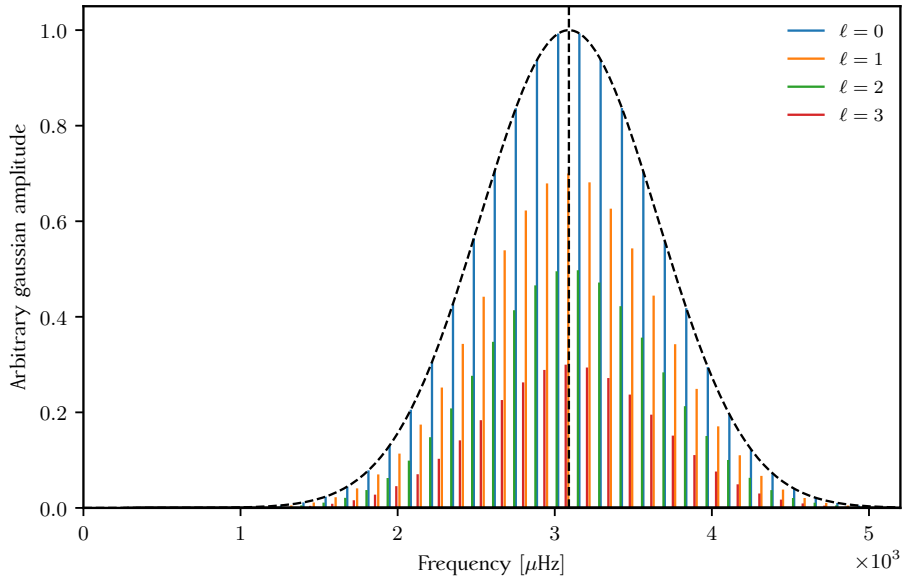

Figure 3.4: modelled solar spectrum showing Gaussian-shaped arbitrary amplitude as a function of frequencies of eigenmodes. Because of the adiabatic hypothesis, the amplitudes do not come from physical computation but are assumed to have a Gaussian shaped centreed on $\nu_{\max} = 3090$ µHz (vertical dashed line). The Gaussian-shaped enveloped of the $\ell = 0$ modes is represented by the black dashed curve.

This scaling relation is remarkably well verified by observation and Belkacem et al. (2011) provided a theoretical explanation for it.

Finally, one can use $\nu_{\max}$ and $\Delta\nu$ jointly by writing:

$$\frac{\Delta\nu}{\Delta\nu_\odot} \propto \left(\frac{M}{M_\odot}\right)^{-1/4} \left(\frac{T_{\rm eff}}{T_{\rm eff,\odot}}\right)^{3/8} \left(\frac{\nu_{\max}}{\nu_{\max,\odot}}\right)^{3/4}, \tag{3.62}$$

which provides a link between $\Delta\nu$ and the effective temperature. We will see in Sect. 3.3 that it is possible to derive many more scaling relations.

3.2.4 Mode excitation and damping

As we will see shortly, the adiabatic approximation is valid in a large portion of the star. However, it is the energy exchanges between the wave and the medium that excite and damp the waves and control their amplitudes. Therefore, the adiabatic approximation has ruled out the possibility of predicting oscillation amplitudes, which would be especially helpful for identifying modes and for searching and defining new classes of pulsators.

When variations of entropy are not neglected, *i.e.* the non-adiabatic case, the thermodynamic identity defined in Eq. (3.17) reads

$$\frac{\delta\rho}{\rho_0} = \frac{1}{\Gamma_1}\frac{\delta p}{p_0} - \frac{\rho_0}{p_0}\frac{(\Gamma_3 - 1)}{\Gamma_1} T\delta s \quad \text{with} \quad \Gamma_3 - 1 = \left(\frac{\partial \ln T}{\partial \ln \rho}\right)_{\rm ad}. \tag{3.63}$$

If one takes the time derivative of this equation (bearing in mind that the time derivative of equilibrium quantities is zero), one obtains

$$\frac{1}{\rho_0}\frac{\partial\delta\rho}{\partial t} = \frac{1}{\Gamma_1 p_0}\frac{\partial\delta p}{\partial t} - \frac{\rho_0}{p_0}\frac{(\Gamma_3 - 1)}{\Gamma_1} T\frac{\partial\delta s}{\partial t}. \tag{3.64}$$

From Eq. (1.33), we shall also derive

$$T\frac{\partial \delta s}{\partial t} = \delta\left(\varepsilon - \frac{\partial l}{\partial m}\right), \tag{3.65}$$

with $l(m)$ the luminosity. For simplicity, we assume oscillating solutions for $\delta\rho$, δp and δs. We see that, if these quantities do not reach their maximums at the same time, one can have for instance when $\partial\delta p/\partial t = 0$,

$$\frac{\partial \delta\rho}{\partial t} = \frac{\rho_0^2}{p_0}\frac{(\Gamma_3 - 1)}{\Gamma_1} T\frac{\partial \delta s}{\partial t} \neq 0. \tag{3.66}$$

The phase-lag between δp and $\delta\rho$ translates into the wave gaining or losing energy. With Eq. (3.63) taken into account and with appropriate boundary conditions, the eigenmode solution of the system look like (Samadi et al., 2015)

$$\boldsymbol{\xi}(r,t) = \boldsymbol{\xi}(r)e^{-i\omega t}e^{\gamma t} = \boldsymbol{\xi}(r)e^{-i\omega^\dagger t} \quad \text{with} \quad \omega^\dagger = \omega - i\gamma, \tag{3.67}$$

where γ is called the *growth/damping rate*. In order to decide whether a mode is stable or not, one should study the cumulated gain/loss of energy over a wave cycle. To do so, we have to study γ defined as

$$\gamma = \frac{\left\langle \frac{\mathrm{d}W}{\mathrm{d}t} \right\rangle_{\mathrm{cycle}}}{\langle E_{\mathrm{osc}} \rangle_{\mathrm{cycle}}}. \tag{3.68}$$

The quantity $\mathrm{d}W/\mathrm{d}t$ is the positive or negative work received by the mode from the medium per unit time and E_{osc} is the total energy of the mode. The operator $\langle\cdot\rangle_{\mathrm{cycle}}$ denotes the average over a pulsation cycle.

- If $\gamma > 0$, the mode is growing and unstable. The eigenmode will obey the linear system of equations we derived above until the linear approximation breaks down. At that point, other mechanisms come into play. For instance it is the case of modes observed in δ Scuti stars (see Sect. 4.3.2, γ Dor and δ Sct), excited by the κ mechanism in H and He ionization regions. Where H or He become ionized, the opacity suddenly increases due to the increased concentration of electrons (Thomson[4] and Compton[5] scattering; e.g. Kippenhahn et al. 2012). The enhanced opacity acts as a pot lid and blocks radiation. Temperature increases and the star expands. This is the beginning of an unstable growing-mode. Non-linear effects appear when due to dilation, density and opacity decrease which leads to the star contraction.

- If $\gamma < 0$, the mode is stable and its amplitude will progressively decrease. This is the case of solar-like pulsators where pressure modes are mainly excited by stochastic convective turbulence (Samadi & Goupil, 2001) and by convective plumes (Belkacem et al., 2006a,b).

In order to find the region where the adiabatic relation is a good approximation or not, one introduces two characteristic time-scales. First, the dynamical time-scale τ_{dyn} is of the same order as the modal period Π. If one takes as an example the oscillation at maximum power of the Sun, its frequency is $\nu_{\max} = 3090$ µHz and its period is $\Pi_{\max} = 324$ s $= 5$ min 24 s. The second characteristic time-scale is the thermal time-scale τ_{th} which gives the approximate

[4]When an electromagnetic wave encounters an electron, it starts oscillating and radiates part of the energy in other directions. This phenomenon is called Thomson scattering.

[5]Same as Thomson scattering but with relativistic corrections (needed when $T \gtrsim 10^8$ K).

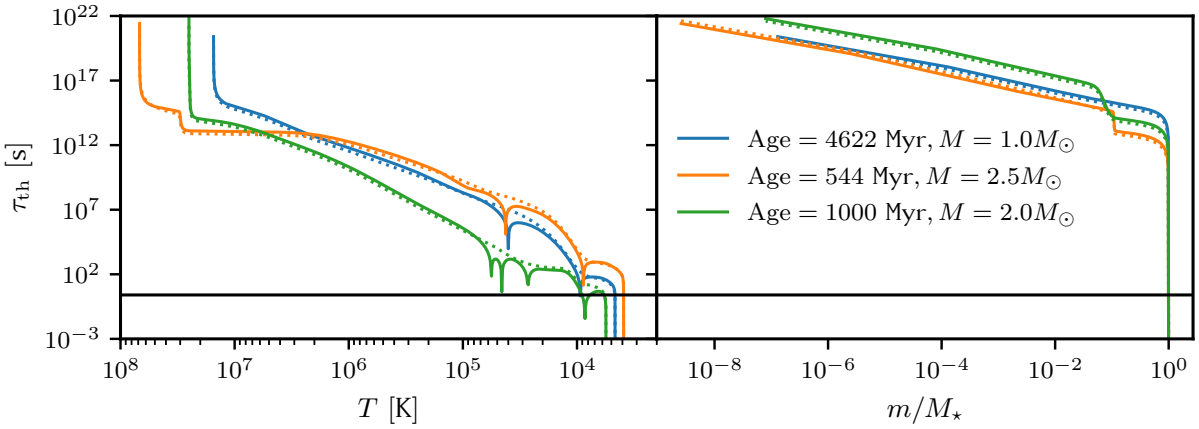

Figure 3.5: Thermal time-scale profiles for models of $1M_\odot$, $2M_\odot$, $2.5M_\odot$ as a function of *left*: $\log T$ and *right*: $\log(m/M_\star)$. The specific heat capacity at constant volume $c_{\rm v}$ is computed in two ways: either $c_{\rm v} = c_{\rm p} - \frac{\delta^2 p}{\rho T \alpha}$ (solid lines) or $c_{\rm v} = \frac{c_{\rm p}}{\Gamma_1}$ (dashed lines). The solid black line corresponds to a modal period Π of 5.39 min, *i.e.* the period of $\nu_{\rm max,\odot} = 3090$ µHz.

amount of time needed for a small parcel of warm (cold) material to lose (gain) energy. In a region where nuclear reactions do not occur, $\tau_{\rm th}$ at radius r is the ratio of the thermal energy contained into the material divided by the energy loss rate, *i.e.* the luminosity:

$$\tau_{\rm th} \simeq \frac{\langle c_{\rm v} T \rangle \, \Delta m}{L} \quad \text{with} \quad \langle c_{\rm v} T \rangle = \frac{\int_r^{R_\star} c_{\rm v} T \mathrm{d}m}{\int_r^{R_\star} \mathrm{d}m}, \tag{3.69}$$

where Δm is the mass enclosed between the surface and the sphere of radius r, *i.e.* the mass above r, $c_{\rm v}$ is the specific heat capacity at constant volume. The Fig. 3.5 represents the thermal time-scale profile for three models of mass $1M_\odot$, $2M_\odot$, $2.5M_\odot$. We see that a thermal time-scale of the same order of the modal period $\Pi_{\rm max}$ is reached very close to the surface ($m/M_\star \simeq 1$). In regions where $\tau_{\rm th} \gg \Pi$ holds, the time-scale on which a wave exchanges energy with the propagative medium is much longer than the oscillation period. Therefore, energy exchanges can be neglected and adiabatic approximation holds. However, this is not the case in non-adiabatic regions where $\tau_{\rm th} \lesssim \Pi$. In this region, waves can be excited if the medium gives energy to the wave and conversely, the wave is damped if it gives energy to the medium. For a given mode, one can find damping dominated regions and excitation dominated regions. In the model with $2M_\odot$, the region where $\tau_{\rm th} < \Pi$ has a significantly larger extent than for the other two models.

3.3 The problem of near-surface effects on oscillation frequencies

This section presents and provides further information on an article (Manchon et al. 2018; also attached to the present manuscript at page 88[6]).

3.3.1 Context

Turbulent convection has an influence on p-modes eigenfrequencies. Indeed, an inhomogeneous velocity, temperature and density field affects the phase of the oscillation and its propagation,

[6]Reproduced with permission © ESO.

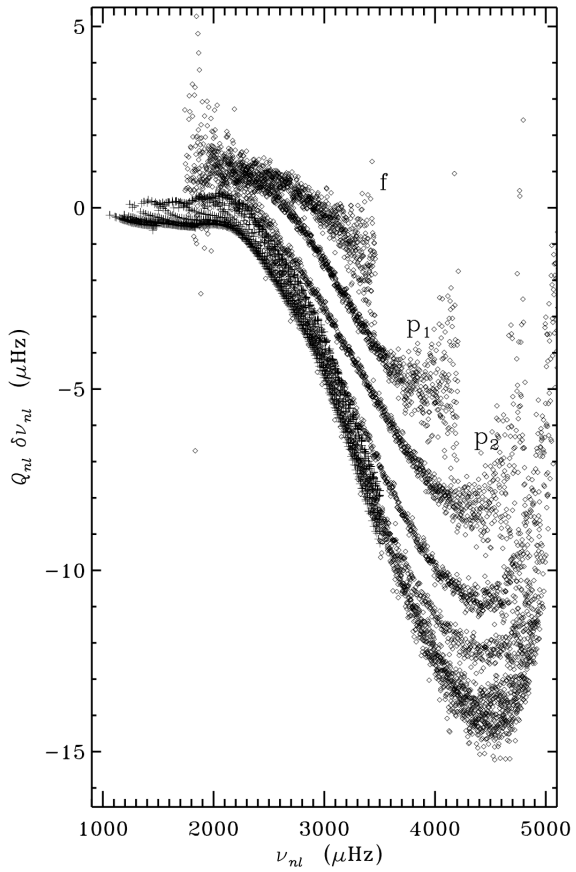

Figure 3.6: Scaled frequency differences between observed (Tomczyk et al., 1995; Bachmann et al., 1995) and modelled (Christensen-Dalsgaard et al., 1996) frequencies. Credits: Rosenthal et al. (1999).

in general slowing it down and decreasing the frequency (Brown, 1984). However, 1D stellar models implement simplified models of convection (such as the mixing-length theory; MLT) that completely remove turbulence from the problem. Dziembowski et al. (1988) was the first to observe the effect of the neglecting of the turbulent convection on eigenfrequencies, pointing out systematic discrepancies at high frequency between observed and calculated p-modes and called theoreticians for an in-depth study of what causes those dissonances. Those have been studied in more detail by Rosenthal et al. (1995); Christensen-Dalsgaard & Thompson (1997); Rosenthal et al. (1999). Figure 3.6 shows scaled frequency differences between observed and computed solar frequencies: $\delta\nu_{n\ell} \equiv \nu_{n\ell}^{\rm obs} - \nu_{n\ell}^{\rm mod}$. The observations gather data from the instrument LOWL deployed at HAO's observing station on Mauna Loa, Hawaii (Tomczyk et al., 1995) for low-degree oscillations and from High-L Helioseismometer (HLH) installed on Kitt Peak telescope (Bachmann et al., 1995), for high-degree oscillations. Modelled frequencies are computed using the Model S of the Sun (Christensen-Dalsgaard et al., 1996) that was the state-of-the-art solar model at that time. In Fig. 3.6, we distinguish several groups of frequencies that follows similar trends. Each of those groups correspond to modes with the same degree ℓ. Because the high-degree modes propagate less deeply, in a less dense medium than low-degree modes, their mode inertia is smaller and therefore they are more affected by perturbations in the shallowest layers of the star (Christensen-Dalsgaard & Thompson, 1997). In order to suppress this effect, Rosenthal et al. (1999) use a scale factor $Q_{n\ell}$ defined as being the ratio at

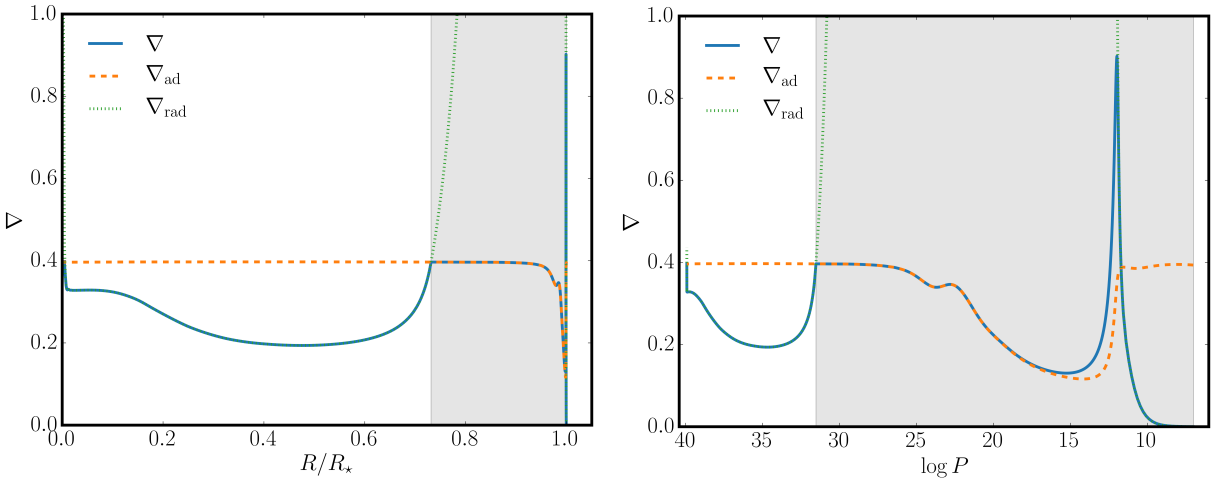

Figure 3.7: Actual temperature gradient (solid blue line), adiabatic gradient (dashed orange line) and radiative gradient (dotted green line) as a function of the radius (left) and of the pressure (right), for a $1M_\odot$ model with solar chemical composition and an age of 4613 Myr. Convective zone is represented by shaded area.

frequency $\omega_{n\ell}$ of the mode inertia $I_{n\ell}$ of modes of degrees $n\ell$ and $n0$:

$$Q_{n\ell} = \frac{I_{n\ell}}{I_{n0}(\omega_{n\ell})}. \tag{3.70}$$

This is those scaled frequency differences that are represented in figure 3.6. Although the scaling factor $Q_{n\ell}$ does not mask completely the degree dependency to surface effects.

From the theoretical analysis of the causes of surface effects, it emerged that two main consequences of the convection on the propagation of oscillations can be found (Houdek et al., 2017).

- The first effects are due to modification of the mean stellar-structure due to the neglect of the turbulent pressure term, therefore, they are called *structural effects*. The turbulent pressure term adds support against the gravity in the hydrostatic equilibrium equilibrium. It extends the cavity and increases the frequency of its modes of oscillation.

- The second source of surface effects comes from simplifications of the oscillation equations. First of all, these equations are derived within the adiabatic approximation. In reality, non-adiabatic effects become less negligible near the limit of the propagation cavity (especially at the surface). Non-adiabatic terms appear in the perturbed energy conservation equation (3.63) and modify the wave propagation. Secondly, as we will see shortly, it is quite uncertain how the turbulent pressure should be included in the oscillation equation. More precisely, the effect of a mode on the Lagrangian perturbation of the turbulent pressure is still undecided (Sonoi et al., 2017). They are called *modal effects* (Balmforth, 1992).

The caveats of mixing-length theory (MLT)

Figure 3.7 shows the values for the actual gradient ∇, the adiabatic gradient ∇_{ad} and the radiative gradient ∇_{rad} inside a 1 $M_\odot$ MS star. The convective envelope starts where ∇_{ad} becomes smaller than ∇_{rad}. In the deep convective zone, we see that, as we said in Sect.

1.1.2, $\nabla \simeq \nabla_{\rm ad}$. In this region, the entropy is constant and a convection theory is actually not needed because the value of the actual gradient is given by the adiabatic one. Near the surface, for $\log p \in [12-17]$, $\nabla > \nabla_{\rm ad}$, and even $\nabla \gg \nabla_{\rm ad}$ very close to the surface. In this region, convection becomes inefficient, due to the sudden decrease in mass density. Becoming inefficient means that the velocity of the convective flow has to increase dramatically in order to maintain the required energy flux. This zone is called the *superadiabatic zone* because $\nabla > \nabla_{\rm ad}$. This difference between ∇ and $\nabla_{\rm ad}$ means that there is an entropy jump between the beginning of the superadiabatic zone and the surface. The MLT is actually designed to reproduce, through the adjustment of $\alpha_{\rm MLT}$, the desired entropy jump.

The MLT may seem too simple, even simplistic, but works surprisingly very well. However, it has some deficiencies that hinder the modelling of stellar upper layers (see Trampedach, 2010, for a review):

- The MLT is based on the Boussinesq approximation that justifies neglecting the compressibility of the convective flow if $\ell_{\rm MLT} \ll H_{\rm p}$, *i.e.* $\alpha_{\rm MLT} \ll 1$. In practice, this condition is never met and is actually very far from being met. In the solar model used to produce Fig. 3.7, $\alpha_{\rm MLT} \simeq 1.65$;
- There exists no theoretical formulation that gives the mixing length $\ell_{\rm MLT}$, therefore it must be calibrated[7] (Trampedach & Stein, 2011; Serenelli, 2016). Very often, the data and/or the time is lacking for a proper calibration of the $\alpha_{\rm MLT}$ and the solar $\alpha_{\rm MLT}$ is assumed, whatever the characteristics of the star. This is obviously not satisfying from a physical point of view;
- Furthermore, $\alpha_{\rm MLT}$ is assumed to be constant inside the star and for all its convection zones and does not change along stellar evolution, despite the dimension of the surface convective zone varying over several orders of magnitude (Kippenhahn et al., 2012);
- In the MLT framework, the kinetic energy spectrum $E(k)$ is treated as if there were only one large eddy, and one forgets about all other turbulent motions (Canuto & Mazzitelli, 1991). In MLT, $E(k)$ is approximated by a Dirac distribution;
- MLT cannot describe overshooting. Overshoot is the fluid motion outside the convective zone due to the velocity gained during convective motion. Overshoot of the core convective zone[8] is a very important process in stellar evolution because it connects the hydrogen-rich radiative zone to core convective zone where nuclear reactions take place. Overshoot thus injects a hydrogen-rich material into this zone, which extends the lifetime of the star and perturbs our estimation of the age.

Some other models have been introduced in order to overcome those limitations, including the Full Spectrum Turbulent (FST) convective model which proposes to replace the Dirac distribution approximation of the turbulence spectrum by a Kolmogorov one (Canuto & Mazzitelli, 1991, 1992; Canuto et al., 1996). Whilst the turbulent velocity spectrum is much better described than with MLT, this theory still has a free parameter: a mixing length that also corresponds to the size of the largest eddy, which is found smaller than with MLT, because of the energy distributed within a larger spectrum. However, FST model assumes a homogeneous turbulence for up and down flows, which is not confirmed by realistic 3D simulations of surface convection that predicts a laminar up-flow and a turbulent down-flow.

[7] The value of $\alpha_{\rm MLT}$ is calculated by adjusting it so that the modelled stars display the same values for some global parameters. For instance, if one wants to model a star with a specific luminosity and a specific radius, it is usual to adjust the initial helium abundance and $\alpha_{\rm MLT}$ to do so.

[8] A core convective zone is present in stars with $M > 1.2\ M_\odot$.

A method to study theoretically surface effects

Surface effects appear when comparing observed frequencies with frequencies computed in a 1D model. In order to study theoretically surface effects, we need a way to artificially replace observed frequencies. For a proper computation of the fluid motions at the surface of the star, we can make use of 3D stellar convection codes. Those numerical codes compute convective motions directly from first principles, *i.e.* directly from magnetohydrodynamics (MHD) equations: no assumption is made about the turbulence spectrum. They are called Direct Numerical Simulation (DNS) codes. They are three-dimensional, time-dependent and the radiative transfer is also treated in three dimensions. Last but not least, they make no use of tunable parameters. 3D codes produces more physically realistic simulations than 1D stellar codes.

Ideal MHD relies on the following assumptions (Spruit, 2013):

- The fluid approximation: the plasma is a fluid where the thermodynamic quantities are meaningful and the variations of these quantities are slow compare to the characteristic time scales of the microscopic processes taking place in the plasma;
- The relation between the electric field and the current density (The Ohm's law) is assumed instantaneous;
- The plasma is globally neutral.

The MHD equations combine the Navier-Stokes equations for a plasma (*i.e.* taking into account the extra electromagnetic terms), the Maxwell-Ampère equation and the Ohm's law.

Codes solving these equations are often coupled to a radiative transfer solver, especially for spectroscopic usages. They are called R-MHD codes. Notable R-MHD codes used to perform surface convection simulations are the STAGGER-code (Nordlund & Galsgaard, 1995), the MURAM code (Vögler, 2003) and the one used in this work: CO^{5}BOLD (Freytag et al., 2002, 2012). R-MHD codes can be considered as solvers of R-MHD equations. One just has to specify some boundary conditions in order to model the physical phenomenon needed. The same code can, therefore, simulate radiative transfer in the interstellar medium, dynamics of plasma jets, sunspots, or convection. No extra *ad hoc* theory is needed.

But using a R-MHD code to compute the complete stellar-structure is completely out of reach (Kupka & Muthsam, 2017). And actually, we do not really need that to obtain a more realistic model, we just need a 3D model of the superadiabatic region and a 1D model for the rest of the star. This is the idea behind *patched models* (PM). A PM is build by connecting a 1D stellar model to a horizontally-averaged 3D model. The matching point is the location where the pressure and the temperature of both models are equal (see Fig. 3.8). After this operation, we obtain two models. The PM (more realistic) is the combination of the 1D model and the 1D stratification obtained from a 3D model. The unpatched model (UPM) is the original 1D model with no amendment. In order to perform our theoretical work, we will compare two sets of frequencies. The one obtained from the PM which are the closest to the observations, and the one issued from the UPM that are surface-affected. This method gives $\nu_{n\ell}^{\mathrm{PM}} - \nu_{n\ell}^{\mathrm{UPM}} \simeq \nu_{n\ell}^{\mathrm{obs}} - \nu_{n\ell}^{\mathrm{mod}} \equiv \delta\nu_{n\ell}$.

3.3.2 Adiabatic oscillation including turbulent pressure

We have seen that the two main causes of the surface effects are the adiabatic approximation, which acts through the modal effects, and the turbulent pressure which acts through the structural *and* modal ones. The impacts of the turbulent pressure and of the adiabatic approximation are hard to disentangle, therefore, we must find a way to focus on the first one,

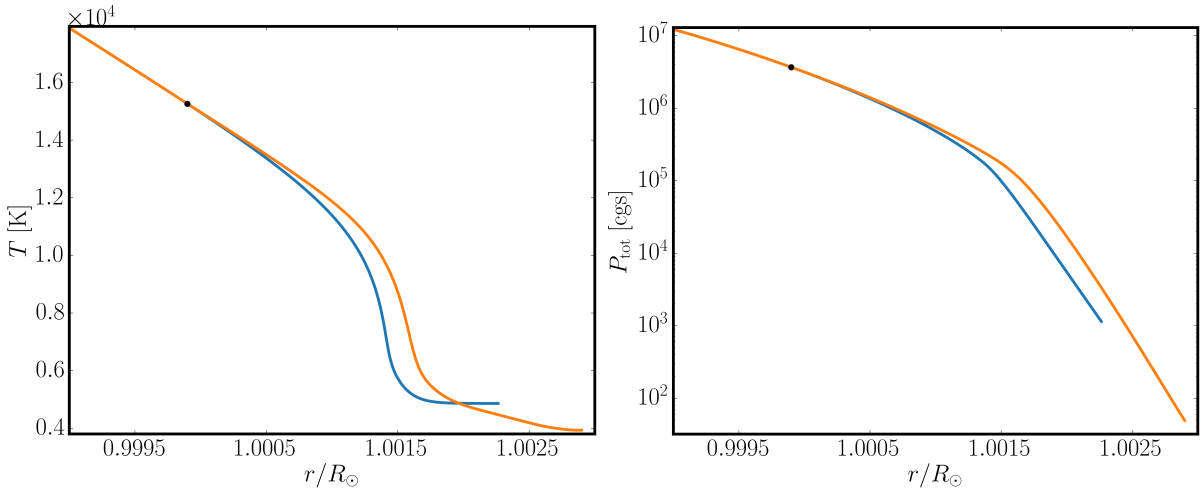

Figure 3.8: Temperature and total pressure stratifications for a patched (orange line) and unpatched (blue line) model of the Sun. The matching point is represented by the black point.

while keeping an adiabatic treatment. To that end, we follow the reasoning established by Rosenthal et al. (1999).

First of all, we place ourselves in a plane-parallel description of the stellar atmosphere. This approximation is justified because the atmosphere is thin, therefore the curvature is negligible. In this case, the coordinates are $(x, y, z; t)$, the usual Cartesian coordinates. Let f be any field. We introduce a first decomposition of f of the form:

$$f = \overline{f} + f', \tag{3.71}$$

where $\overline{\cdot}$ denotes the horizontal average operator. The quantity $\overline{f}$ contains both the mean value[9] of f and the p-mode oscillation part. Here it is important to stress that $\overline{\cdot}$ does not average over time, therefore saying that $\overline{f}$ contains the oscillation part is meaningful: at a given altitude, $\overline{f}$ oscillates in time but not horizontally. This is no problem for a radial mode ($\ell = 0$) because p-mode amplitudes are constant over a sphere (at least in non-rotating stars). This is not true if we are considering a non-radial mode. In this case, the horizontal average operator removes part or all the information on the mode. The primed quantity f' is the convective fluctuation and we have, by definition, $\overline{f'} = 0$. In addition, the Eulerian perturbation of the average quantity $\overline{f}(z, t)$ can be written as (Rosenthal et al., 1999)

$$\overline{f}(z, t) = f_0(z) + \varepsilon f_1(z, t), \tag{3.72}$$

where $f_0(z)$ is the time averaged value of $\overline{f}(z, t)$, ε is a very small non-dimensional number and $f_1(z, t)$ is a time-dependent perturbation. The only special case is for the velocity field. For instance, the z-component is defined by: $\hat{u}_z = \overline{\rho u_z}/\overline{\rho}$. This expression has two advantages: *(i):* it will simplify the future calculation and *(ii):* $\overline{\rho u_z}$ corresponds to the mean mass flux, which vanishes when averaged over time because of the conservation of mass in the star, therefore this expression makes the oscillations more visible. The perturbed form of u_z slightly changes because, due to the density weighted average, its average is not zero:

$$u_z = \hat{u}_z + u_z' \quad \Rightarrow \quad \rho u_z = \rho \frac{\overline{\rho u_z}}{\overline{\rho}} + \rho u_z' \quad \Rightarrow \quad \overline{\rho u_z} = \overline{\rho u_z} + \overline{\rho u_z'} \quad \Rightarrow \quad \overline{\rho u_z'} = 0 \ . \tag{3.73}$$

[9]Here, the expression *mean value* stands for the value of the *mean flow* or of the *mean stellar-structure*. It is the one given by 1D stellar code.

As for the Eulerian perturbation of u_z, we assume that $u_{z,0} = 0$, which amounts to saying that u_z is at rest except for the perturbation due to the p-mode $\hat{u}_z$ and for the vertical velocity of the convective flow u'_z. The total pressure will be separated into its two sources: the gas pressure p_g and the turbulent pressure p_t due to the fluctuations of the velocity field. Its expression will be given later.

With those notations, the continuity equation (3.1) reads

$$\frac{\partial}{\partial t}(\overline{\rho} + \rho') + \boldsymbol{\nabla} \cdot [(\overline{\rho} + \rho')(\hat{\mathbf{u}} + \mathbf{u}')] = 0. \tag{3.74}$$

By keeping only 1st-order term and averaging horizontally, it becomes

$$\frac{\partial \overline{\rho}}{\partial t} + \frac{\partial}{\partial z}\left(\overline{\rho u_z}\right) = 0. \tag{3.75}$$

The momentum conservation equation (3.2) needs a little more work. This equation can be written in a slightly more suitable way for us:

$$\frac{\partial \rho \mathbf{u}}{\partial t} + \boldsymbol{\nabla} \cdot (\rho \mathbf{u}\mathbf{u}) = -\boldsymbol{\nabla} p_\mathrm{g} + \rho g. \tag{3.76}$$

After injecting perturbed quantities, developing, projecting on z and averaging horizontally we obtain the following equation:

$$\frac{\partial}{\partial t}\left[\overline{\rho(\hat{u}_z + u'_z)}\right] + \boldsymbol{\nabla} \cdot \left(\overline{\rho(\hat{u_z}^2 + 2\hat{u}_z u'_z + u'^2_z)}\right) = -\boldsymbol{\nabla}(p_\mathrm{g} + p_\mathrm{t}) + \overline{\rho(\overline{g} + g')}. \tag{3.77}$$

Let us tackle the terms one by one

- 1st term:

$$\overline{\rho(\hat{u}_z + u'_z)} = \overline{\rho \hat{u}_z} = \overline{\rho}\hat{u}_z \tag{3.78}$$

- 2nd term:

$$\overline{\rho\left(\hat{u}_z^2 + 2u'_z\hat{u}_z + u'^2_z\right)} = \overline{\rho\hat{u}_z^2} + 2\underbrace{\overline{\rho u'_z}}_{=0}\hat{u}_z + \overline{\rho u'^2_z} = \overline{\rho u_z^2} + \overline{\rho}\overline{u'^2_z}. \tag{3.79}$$

- 3rd term:

$$\frac{\partial}{\partial z}\overline{\overline{p_\mathrm{g}} + p'_\mathrm{g}} = \frac{\partial \overline{p_\mathrm{g}}}{\partial z}. \tag{3.80}$$

- 4th term: the plane-parallel approximation amounts to making the Cowling approximation, *i.e.* the perturbation g' of the gravitational field can be neglected. This approximation is also applied in 3D simulations. Therefore, $\overline{\overline{g} + g'} = g$ and thus,

$$\overline{(\overline{\rho} + \rho')g} = \overline{\rho} g. \tag{3.81}$$

Finally, Eq. (3.76) reads:

$$\frac{\partial \overline{\rho}\hat{u}_z}{\partial t} = -\frac{\partial}{\partial z}\left(\overline{\rho u_z^2} + \overline{\rho}\overline{u'^2_z}\right) - \frac{\partial \overline{p_\mathrm{g}}}{\partial z} + \overline{\rho} g. \tag{3.82}$$

With $p = p_\mathrm{g} + p_\mathrm{t}$, p_t the turbulent pressure, an expression for the turbulent pressure can be extracted from the above equation:

$$\frac{\partial \overline{\rho}\hat{u}_z}{\partial t} = -\frac{\partial \overline{\rho}\hat{u}_z^2}{\partial z} - \frac{\partial p}{\partial z} + \overline{\rho} g \quad \text{with} \quad p_\mathrm{t} \equiv \overline{\rho u_z'^2}. \tag{3.83}$$

Contrarily to $\overline{\rho u_z'}$, p_t does not vanish.

Eventually, we apply the same recipe on Eq. (3.63):

$$\frac{\partial p_\mathrm{g}}{\partial t} + u_z \frac{\partial p_\mathrm{g}}{\partial z} + \frac{p_\mathrm{g}\Gamma_1}{\rho}\left(\rho \frac{\partial u_z}{\partial z}\right) = -(\Gamma_3 - 1)\boldsymbol{\nabla}\cdot\mathbf{F}_\mathrm{rad} \tag{3.84}$$

$$\frac{\partial p_\mathrm{g}}{\partial t} + \hat{u}_z \frac{\partial p_\mathrm{g}}{\partial z} + u_z' \frac{\partial p_\mathrm{g}}{\partial z} + p_\mathrm{g}\Gamma_1\left(\frac{\partial \hat{u}_z}{\partial z} + \frac{\partial u_z'}{\partial z}\right) = -(\Gamma_3 - 1)\boldsymbol{\nabla}\cdot\mathbf{F}_\mathrm{rad}$$

$$\frac{\partial \overline{p_\mathrm{g}}}{\partial t} + \hat{u}_z \frac{\partial \overline{p_\mathrm{g}}}{\partial z} + \overline{\frac{\partial p_\mathrm{g} u_z'}{\partial z} - p_\mathrm{g}\frac{\partial u_z'}{\partial z}} + \overline{p_\mathrm{g}\Gamma_1}\left(\frac{\partial \hat{u}_z}{\partial z} + \frac{\partial u_z'}{\partial z}\right) = -\overline{(\Gamma_3 - 1)\boldsymbol{\nabla}\cdot\mathbf{F}_\mathrm{rad}}. \quad \text{(horizontal average)}$$

After tidying up, we obtain

$$\frac{\partial \overline{p_\mathrm{g}}}{\partial t} + \hat{u}_z \frac{\partial \overline{p_\mathrm{g}}}{\partial z} + \overline{p_\mathrm{g}\Gamma_1}\frac{\partial \hat{u}_z}{\partial z} = -\overline{p_\mathrm{g}(\Gamma_1 - 1)\frac{\partial u_z'}{\partial z}} - \frac{\partial \overline{p_\mathrm{g} u_z'}}{\partial z} - \overline{(\Gamma_3 - 1)\boldsymbol{\nabla}\cdot\mathbf{F}_\mathrm{rad}}. \tag{3.85}$$

On the right hand side, the first term is the compressible work and the second and third terms are respectively the divergence of the convective flux and of the radiative flux, both multiplied by $\Gamma_3 - 1$.

We now introduce the Eulerian perturbation defined in Eq. (3.72). The linearised Eqs. (3.75) and (3.83) now read:

$$\frac{\partial \overline{\rho}}{\partial t} + \frac{\partial \rho_0 u_{z,1}}{\partial z} = 0 \quad \text{and} \quad \rho_0 \frac{\partial u_{z,1}}{\partial t} = \frac{\partial p_1}{\partial z} + \rho_1 g. \tag{3.86}$$

The equation for the conservation of energy requires some attention. Stein & Nordlund (1991) argued that the first term in the RHS of Eq. (3.85) almost vanishes. Moreover, they showed that the divergence fluxes (2nd and 3rd terms of RHS of Eq. (3.85)) have opposite signs and nearly cancel each other. Assuming that there are no departures from the perfect gas law, their sum is proportional to the total flux divergence (Rosenthal et al., 1999). Rosenthal et al. (1999) considered that their perturbation could be neglected, meaning that the heating/cooling terms are zero. This affirmation follows from the adiabatic equation. In reality, simulations show that the non-adiabatic effects are small but non-negligible. This can be seen from the residual frequency after correction in Fig. 3.9. Part of the remaining surface effect is due to the non-adiabaticity. Therefore, the whole perturbation of the RHS of Eq. (3.85) can be neglected. Furthermore, in order to stick to the adiabatic treatment, (Rosenthal et al., 1999) suggested that either one of the following approximations could be made:

- *Reduced* Γ_1 *approximation* (RGM):
  The Lagrangian perturbation of the turbulent pressure is neglected, leading to

  $$\frac{\delta p}{p} = \frac{\delta p_\mathrm{g}}{p_\mathrm{g}} \Longleftrightarrow \frac{\delta p_\mathrm{t}}{p_\mathrm{t}} = 0, \tag{3.87}$$

  where δ is the Lagrangian perturbation. Therefore,

  $$\overline{\frac{\partial p}{\partial z}} = \overline{\frac{\partial p_\mathrm{g}}{\partial z}} \quad \text{and} \quad \overline{\frac{\partial p}{\partial t}} = \overline{\frac{\partial p_\mathrm{g}}{\partial t}}, \tag{3.88}$$

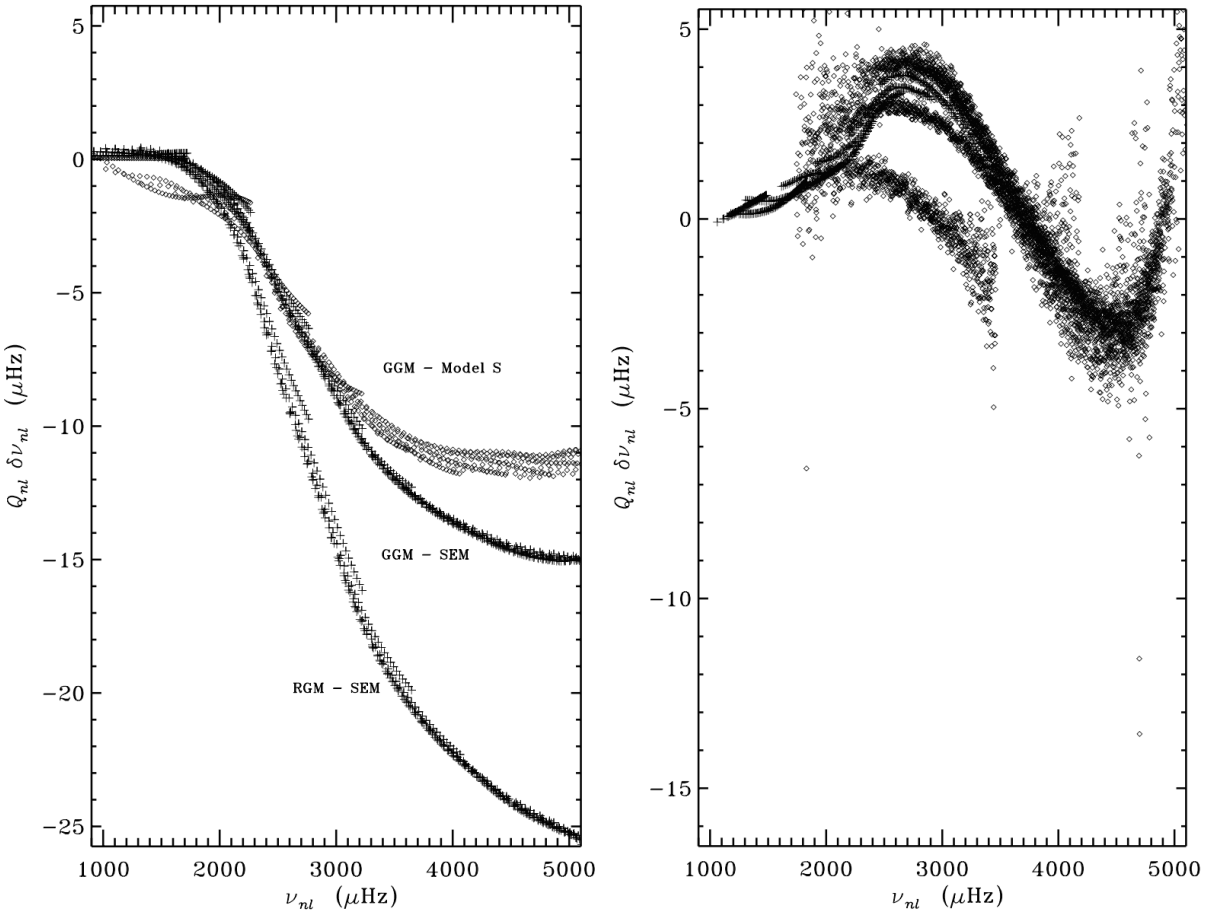

Figure 3.9: *left*: Comparison between scaled frequency differences between patched model and pure 1D models. *right*: Scaled frequency differences between real observations and GGM. Observations are described in detail in Chapter 2, Section 3. (Credits: Rosenthal et al. (1999)).

With this approximation, the linearised Eq. (3.85) reads:

$$\frac{\partial p_1}{\partial t} + u_{z,1}\frac{\partial p_0}{\partial z} + \Gamma_1^{\rm r}\frac{\partial u_{z,1}}{\partial z} = 0 \quad \text{with} \quad \Gamma_1^{\rm r} \equiv \frac{\overline{p_{\rm g}\Gamma_1}}{p_0}, \tag{3.89}$$

where we introduced the reduced $\Gamma_1^{\rm r}$.

- *Gas* Γ_1 *approximation* (GGM):
  The Lagrangian perturbation of the turbulent pressure is assumed to be equal to the perturbation of the gas pressure (Houdek et al., 2017):

$$\frac{\delta p_{\rm t}}{p_{\rm t}} \simeq \frac{\delta p_{\rm g}}{p_{\rm g}} = \Gamma_1\frac{\delta\rho}{\rho}. \tag{3.90}$$

  Thus, the linearised Eq. (3.85) reads:

$$\frac{\partial \rho_1}{\partial t} + u_{z,1}\frac{\partial \rho_0}{\partial z} + \overline{p_{\rm g}\Gamma_1}\frac{\partial u_{z,1}}{\partial z} = 0. \tag{3.91}$$

Which approximation must we use ? Rosenthal et al. (1999) have compared the frequency differences that these approximations generate when the frequency spectrum is computed with

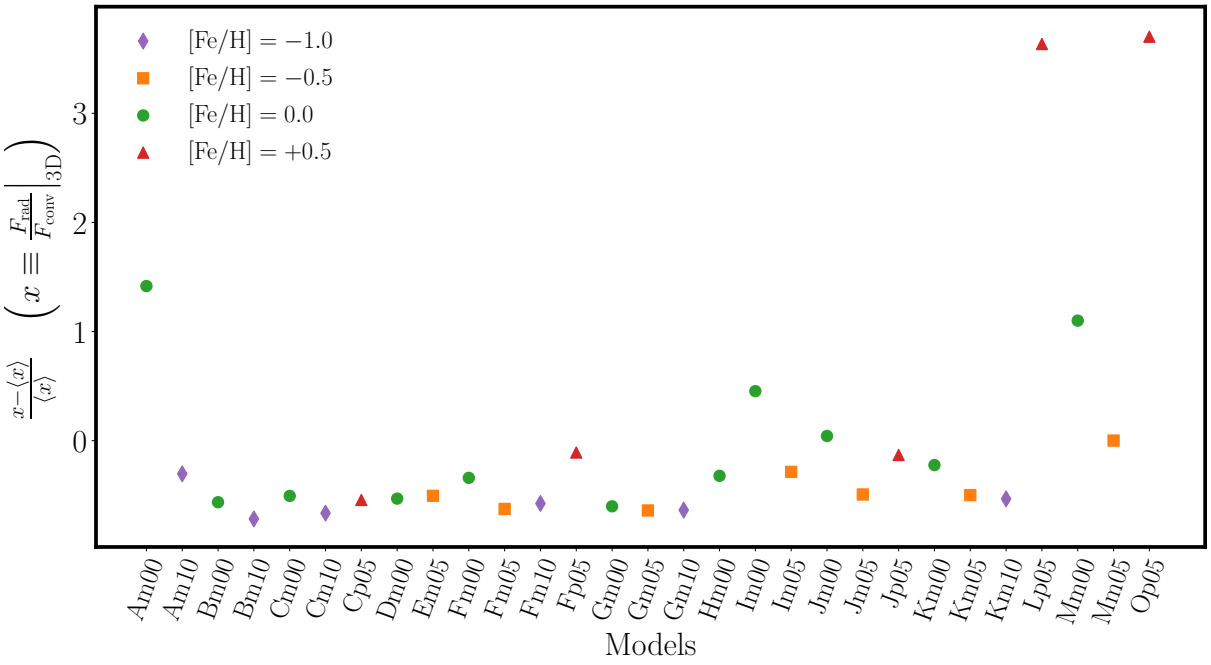

Figure 3.10: Relative difference between $F_{\rm rad}/F_{\rm conv}$ and the mean value of $F_{\rm rad}/F_{\rm conv}$ of all the models in our grid. Values are computed at the altitude in the atmosphere where $T = T_{\rm eff}$.

a patched and an unpatched model. The unpatched model has its turbulent pressure set to zero, therefore neither the GGM or the RGM changes anything in the frequencies. On the contrary, the patched model has non-zero turbulent pressure computed using 3D R-MHD code. Therefore frequencies are affected in a different way by the GGM or the RGM. Rosenthal et al. (1999) computed the 1D part of their models with two different prescriptions. In the first case, they used the Model S (Christensen-Dalsgaard et al., 1996) (which at that time was considered as the state-of-the-art solar model) and a model called SEM (Standard Envelope Model), where the mixing-length parameter was adjusted so that its adiabatic convective zone and the one of the 3D model have the same entropy. Since the entropy is related to the extent of the convective zone, this manipulation amounts to having the same convection zone depth as in the 3D model. The aim of the second model is to isolate the effect of convection from other possible effects. The differences between SEM and Model S, according to Rosenthal et al. (1999), come mainly from a different treatment of the atmosphere which results in a change in the temperature and density stratifications. Those changes are located in the very near-surface layers, and explain the divergence for high frequency (> 3000 µHz) while the divergence started around 2000 µHz between patched and 1D models (see Fig 3.9).

It appears from figure 3.9, on the left, that the frequency differences between RGM and SEM are almost twice as high as the differences between GGM and SEM. Furthermore, the right panel of figure 3.9 shows quite a good agreement between observations and GGM. Consequently, we conclude that the most accurate approximation in order to include the effects of turbulent pressure while keeping an adiabatic treatment of the oscillations is the Gas Γ_1 approximation. This has been confirmed later by Sonoi et al. (2017) with modern 3D simulations. In Manchon et al. (2018), the computation of adiabatic oscillations are made in the framework of the Gas Γ_1 approximation.

3.3.3 more detail on the approximation $F_{\rm rad}/F_{\rm conv} \simeq {\rm cnst}$

In Manchon et al. (2018), just after equation (9), we make the hypothesis that the ratio $F_{\rm rad}/F_{\rm conv}$ of the radiative flux to the convective flux at the surface is nearly constant from one star to an other. This is a strong hypothesis and the question whether it is justified or not has been raised by the referee. Our answer satisfied the referee but was not reproduced in the published article. I provide here further justification.

First of all, this assumption is only made at the surface of the star. The surface is defined, in our case, by the location where the horizontally averaged temperature equals the effective temperature. Below this point, energy is dominantly carried by convection, we have $F_{\rm conv} \gg F_{\rm rad}$. Above this point, we enter the atmosphere and the medium becomes radiative again because the opacity suddenly drops, and we have $F_{\rm rad} \gg F_{\rm conv}$. In the transition region, $F_{\rm rad}$ should be roughly of the same order as $F_{\rm conv}$. In order to test this approximation, we compared the relative difference between $F_{\rm rad}/F_{\rm conv}$ obtained at the location where $T(r) = T_{\rm eff}$, and the mean value of $F_{\rm rad}/F_{\rm conv}$ of all the models of our grid. The main characteristics of this grid as well as the labels of each model are defined in the Table 1. of Manchon et al. (2018). Despite a few outliers, for all models $F_{\rm rad}$ and $F_{\rm conv}$ approximately have the same order of magnitude. This approximation may seem harsh and would certainly need refinement. However, it allows us to understand physically some aspects of the problem at stake (here the influence of the chemical composition on the surface effects).

3.3.4 Recent developments

Since the publication of Manchon et al. (2018), the study of surface effects has known some evolutions. First of all, concerning the method of model patching and its use to correct the surface effects. Normally, patched models are only used for theoretical studies. Indeed, computing a 3D stellar atmosphere model is time consuming. We usually have a grid of 3D models ready to use and the goal is to find a matching 1D model. It is much easier to compute, but painful. Indeed, the good 1D model is found using a Levenberg-Marquardt algorithm (Press et al., 1992) which sometimes necessitates to compute dozens of 1D stellar models in order to be close enough to the desired matching point. Being able to compute a patched model for any star would provide a very precise correction of the surface effects. However, due to the computational cost, astronomers use empirical correction laws calibrated on small grid of patched models. The idea developed by Jørgensen et al. (2018); Mosumgaard et al. (2019) is to couple 1D model to 3D atmospheres *on-the-fly* along evolution. They computed once and for all a large and tight grid of 3D stellar atmosphere models spanning a populated part of the HR diagram. From this grid is extracted a grid of horizontally averaged 1D stratifications. When a 1D stellar evolution is computed, the upper layers are not computed using MLT and with a simple atmospheric model such as Eddington atmosphere (see Sect. 1.1.2, atmospheres), but the upper stratification is directly interpolated in the grid of 3D stratifications. The matching point between the 3D model atmosphere and the 1D stellar model is limited by the maximum depth of the 3D model. However, Jørgensen et al. (2018) did not found that their 1D models were sensitive on the location of this matching point, owing to the fact that their 3D simulations are all sufficiently deep. They found limitations on the size of their 3D grid, but this is not a problem of the method. They later used their *on-the-fly* method to investigate its impact of the surface effects (Jørgensen & Weiss, 2019). By comparing the observed frequencies of the Sun with the one calculated on a present-day model the Sun, whose evolution has been computed using the *on-the-fly* method. They found that it suppresses the structural effects and only leaves the modal one. This conclusion is rather expected but is a good validation of their method. Their grid has been recently extended to include non-solar metallicities models

(Jørgensen et al., 2019).

A&A 620, A107 (2018)
https://doi.org/10.1051/0004-6361/201833783

Astronomy & Astrophysics

Influence of metallicity on the near-surface effect on oscillation frequencies

L. Manchon[1,2⋆], K. Belkacem[2], R. Samadi[2], T. Sonoi[2,3], J. P. C. Marques[1], H.-G. Ludwig[4,5], and E. Caffau[5]

[1] Institut d'Astrophysique Spatiale, Université Paris-Sud, Orsay, France
e-mail: louis.manchon@ias.u-psud.fr
[2] LESIA, Observatoire de Paris, PSL Research University, CNRS, Université Pierre et Marie Curie, Université Denis Diderot, 92195 Meudon, France
[3] Astronomical Institute, Tohoku University, 6-3 Aramaki Aza-Aoba, Aoba-ku, Sendai 980-8578, Japan
[4] Zentrum für Astronomie der Universität Heidelberg, Landessternwarte, Königstuhl 12, 69117 Heidelberg, Germany
[5] GEPI, Observatoire de Paris, PSL University, CNRS, 5 Place Jules Janssen, 92190 Meudon, France

Received 6 July 2018 / Accepted 18 September 2018

ABSTRACT

Context. The CoRoT and *Kepler* missions have provided high-quality measurements of the frequency spectra of solar-like pulsators, enabling us to probe stellar interiors with a very high degree of accuracy by comparing the observed and modelled frequencies. However, the frequencies computed with 1D models suffer from systematic errors related to the poor modelling of the uppermost layers of stars. These biases are what is commonly named the near-surface effect. The dominant effect is thought to be related to the turbulent pressure that modifies the hydrostatic equilibrium and thus the frequencies. This has already been investigated using grids of 3D hydrodynamical simulations, which also were used to constrain the parameters of the empirical correction models. However, the effect of metallicity has not been considered so far.
Aims. We aim to study the impact of metallicity on the surface effect, investigating its influence across the Hertzsprung-Russell diagram, and providing a method for accounting for it when using the empirical correction models.
Methods. We computed a grid of patched 1D stellar models with the stellar evolution code CESTAM in which poorly modelled surface layers have been replaced by averaged stratification computed with the 3D hydrodynamical code CO^{5}BOLD. It allowed us to investigate the dependence of both the surface effect and the empirical correction functions on the metallicity.
Results. We found that metallicity has a strong impact on the surface effect: keeping $T_{\rm eff}$ and $\log g$ constant, the frequency residuals can vary by up to a factor of two (for instance from [Fe/H] = +0.0 to [Fe/H] = +0.5). Therefore, the influence of metallicity cannot be neglected. We found that the correct way of accounting for it is to consider the surface Rosseland mean opacity. It allowed us to give a physically grounded justification as well as a scaling relation for the frequency differences at $\nu_{\rm max}$ as a function of $T_{\rm eff}$, $\log g$ and κ. Finally, we provide prescriptions for the fitting parameters of the most commonly used correction functions.
Conclusions. We show that the impact of metallicity through the Rosseland mean opacity must be taken into account when studying and correcting the surface effect.

Key words. asteroseismology – convection – stars: low-mass – stars: oscillations – stars: solar-type

1. Introduction

The space-borne missions CoRoT (Baglin et al. 2006; Michel et al. 2008; Auvergne et al. 2009) and *Kepler* (Borucki et al. 2010) have provided a rich harvest of high-quality seismic data for solar-like pulsators. This has allowed a leap forward in our understanding and modelling of low-mass stars (see the reviews by Chaplin & Miglio 2013; Hekker & Christensen-Dalsgaard 2017). However, for the last three decades (e.g. Dziembowski et al. 1988) it has been known that the comparison between modelled and observed acoustic-mode frequencies suffer from systematic discrepancies. This bias is called the surface effect and has been widely studied in the solar case (Rosenthal et al. 1995; Christensen-Dalsgaard & Thompson 1997; Rosenthal & Christensen-Dalsgaard 1999). They are attributed to our deficient modelling of the uppermost layers of stars with a convective envelope. Indeed, 1D stellar models hardly take into account the complexity of these layers that are subject to highly turbulent flows as well as a complex transition between a convective to a radiative-dominated energy flux transport (e.g. Kupka & Muthsam 2017).

More generally, these frequency residuals prevent a direct comparison between modelled and observed frequencies. Frequency combinations are commonly used to circumvent this problem (e.g. Roxburgh & Vorontsov 2003), but still, an accurate determination of frequencies is highly desirable to take advantage of the full potential of asteroseismology. To reach this goal, a handful of empirical prescriptions with adjustable free parameters have been proposed (Kjeldsen et al. 2008; Ball & Gizon 2014, 2017; Sonoi et al. 2015) and allow one to apply a posteriori corrections to the modelled frequencies. Such an approach is now widely used (e.g. Lebreton & Goupil 2014; Silva Aguirre et al. 2017) and has proven to be quite efficient in inferring a stellar model that fits the observed frequencies. However, it suffers from some fundamental drawbacks. The choice of the parameters is not physically motivated. Consequently, there is no guarantee that this optimal model is unique and accurate (i.e. that it properly reproduces the real physical structure of the observed star).

⋆ Present address: Institut d'Astrophysique Spatiale, Université Paris Sud, Orsay, France

Another complementary approach then consists of investigating the physical nature of the surface effect. This motivated a number of studies to unveil and constrain the physical ingredients responsible for these biases. More precisely, surface effect has been shown to be the result of two distinct effects (e.g. Houdek et al. 2017): *structural* effects coming mainly from turbulent pressure in the hydrostatic equation which is usually absent in 1D stellar evolution codes, and *modal* effects gathering modifications of the eigenmodes, mostly due to non-adiabaticity (e.g. Balmforth 1992; Houdek et al. 2017) as well as the perturbation of turbulent pressure induced by the oscillations (Sonoi et al. 2017). Other related processes were also invoked, such as convective backwarming (Trampedach et al. 2017) or magnetic activity (Piau et al. 2014; Magic & Weiss 2016). Nonetheless, as demonstrated by the early work by Rosenthal & Christensen-Dalsgaard (1999) on the Sun using a 3D hydrodynamical simulation, the dominant physical ingredient is thought to be the turbulent pressure that modifies the hydrostatic equilibrium and subsequently introduces an elevation of the star surface. Then, the acoustic cavity is modified and therefore the frequencies are as well.

Based on a grid of 3D numerical simulations, this method was used by Sonoi et al. (2015), Ball et al. (2016), Trampedach et al. (2017) who investigated the surface effect variations across the Hertzsprung-Russell diagram. These works clearly demonstrated that surface effects sharply depend on effective temperature and surface gravity of star. In addition, Sonoi et al. (2015) presented a way to provide parameters for the empirical surface corrections by fitting them against a physically motivated scaling relation derived by Samadi et al. (2013). However, all these works considered solar metallicity models while the distribution of metallicity for observed solar-like pulsators is quite large (see e.g. Pinsonneault et al. 2014). Our goal is thus to study the influence of metallicity on the surface effects and propose a method to account for it.

The article is organized as follows: in Sect. 2 we describe the method of model patching, which is constructed by replacing the upper layers of a 1D model by horizontally averaged stratification of a 3D model atmosphere, and our set of models. Then in Sect. 3 we show that metallicity has a strong impact on the frequency residuals and therefore its influence cannot be ignored. We also study the variation of the frequency differences with effective temperature, surface gravity and opacity and give a theoretical justification. Finally, in Sect. 4 we provide constraints on the various parameters usually used in the empirical surface effect function across the $T_{\rm eff} - \log g - \log \kappa$ space.

2. Model-patching method

In this section we explain the method we used to patch our models and describe our final set of models.

2.1. Grid of 3D models

We used a grid of 3D hydrodynamical models from the CIFIST grid of stellar atmosphere including the superadiabatic region to the shallowest layers of the photosphere, computed using the CO^{5}BOLD code (see Ludwig et al. 2009; Freytag et al. 2012 for details). The chemical mixture is based on the solar abundances of Grevesse & Sauval (1998) apart from the CNO elements which follow Asplund et al. (2005). We considered 29 models with effective temperature ($T_{\rm eff}$) ranging from 4500 K to 6800 K, a surface gravity ($\log g$) ranging from 3.5 to 4.5, and a metallicity [Fe/H] $= -1.0, -0.5, +0.0, +0.5$. We note that

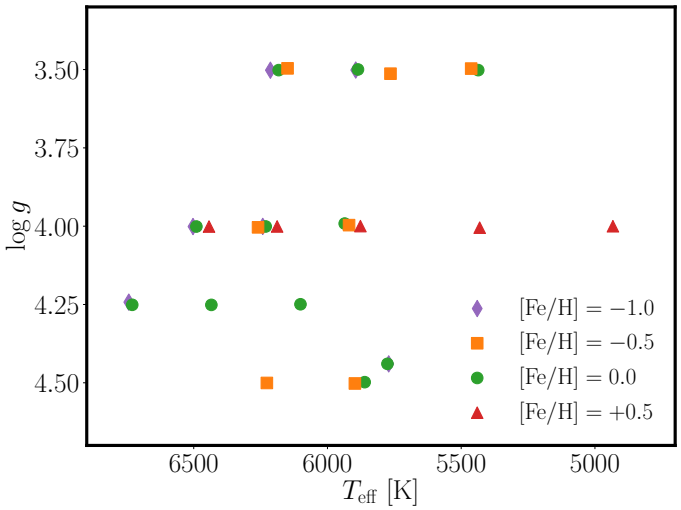

Fig. 1. Patched models represented in Kiel diagram (see Sect. 2.1). The metallicities are shape- and colour-coded and are [Fe/H] $= \{-1.0, -0.5, +0.0, +0.5\}$.

[Fe/H] refers to the logarithmic iron abundance, which in our simulations is different from the logarithmic metallicity abundance [M/H]. Thus, models with same [Fe/H] do not necessarily have the same [M/H].

Table 1 summarizes the global parameters of the 3D models. The range of metallicities we considered corresponds to the metallicities of observed solar-like pulsators (Anders et al. 2017; Serenelli et al. 2017). Table 1 exhibits small groups of models (labelled with same first letter) with very similar $T_{\rm eff}$ and $\log g$. Those groups for instance in Fig. 1 at $\log g = 4.0$, help us to investigate the influence of metallicity on the surface effect by keeping other global parameters fixed. However, we pointed out that, whereas within a group the dispersion in $\log g$ is rather small (of the order of 0.1%), the dispersion in $T_{\rm eff}$ is much higher (of the order of 1%). Indeed, surface gravity is an input parameter of the hydrodynamical simulations while effective temperature is controlled by adjusting the entropy at the bottom of 3D models. It is therefore difficult to match an accurate effective temperature.

2.2. Computation of patched models

For each 3D model, both a patched (hereafter PM) and an unpatched model (hereafter UPM) have been constructed. A patched model is a model computed using a 1D stellar evolutionary code in which we replaced the surface layers with the stratification obtained by horizontally averaging a 3D model computed with a R-MHD code. The fully 1D model is called an unpatched model. The construction of PM and UPM has been widely described in Trampedach (1997), Samadi et al. (2007, 2008), Sonoi et al. (2015), Jørgensen et al. (2017). The 1D counterparts of 3D hydrodynamical models have been obtained using the 1D stellar evolutionary code CESTAM (Morel 1997; Marques et al. 2013) by tuning the age (or the central temperature for advanced stages), the total stellar mass M, and the mixing length parameter $\alpha_{\rm MLT}$ in order to match the effective temperature, the surface gravity and the temperature at the bottom of the 3D model, located just below the superadiabatic region. We chose to remove the first four bottom layers and the last top layer of the 3D hydrodynamical model to be sure to remove any numerically induced errors and that the patching point is deeply inside the

Table 1. Characteristics of the 3D hydrodynamical models and of the UPM and PM.

Model	$T_{\rm eff}$ K	$\log g$	$T_{\rm b}$ ($\times 10^4$) K	$\nu_{\rm max}$ μHz	M ($M_\odot$)	Age (Myr)	$Y_{\rm init}$ %	$Z_{\rm init}$ %	$\alpha_{\rm MLT}$	$R_{\rm PM}$ ($R_\odot$)	$\Delta r/R_{\rm PM}$ ($\times 10^{-3}$)	Stage
Cp05	6443	4	3.20	1057	1.91	1341	24.2	4.14	1.61	2.29	1.3	MS
Fp05	6188	4	2.71	1078	1.81	1820	24.2	4.14	1.68	2.23	0.89	MS
Jp05	5877	4	2.17	1103	1.53	4129	24.2	4.16	1.74	2.05	0.67	SG
Lp05	5431	4	2.03	1161	1.32	8361	24.2	4.14	1.74	1.89	0.45	SG
Op05	4933	4	1.98	1205	2.12	3.808	24.2	4.14	1.75	2.41	0.16	PMS
Am00	5776	4.44	1.55	3063	1.02	4628	24.9	1.35	1.65	1.01	0.21	MS
Bm00	6730	4.25	7.89	1839	1.38	1306	24.9	1.35	1.68	1.46	1.4	MS
Cm00	6490	4	2.79	1053	1.48	2397	24.9	1.35	1.65	2.01	1.3	MS
Dm00	6434	4.25	2.76	1881	1.27	2562	24.9	1.35	1.67	1.4	0.77	MS
Fm00	6231	4	2.30	1074	1.28	4352	24.9	1.35	1.69	1.87	0.96	SG
Gm00	6182	3.5	3.63	341.7	1.93	1158	24.9	1.35	1.7	4.09	2.4	SG
Hm00	6101	4.25	2.51	1923	1.13	5413	24.9	1.35	1.67	1.32	0.53	SG
Im00	5861	4.5	2.31	3479	1.09	34.8	24.9	1.35	1.66	0.976	0.2	PMS
Jm00	5936	3.99	2.18	1077	1.16	6753	24.9	1.35	1.74	1.8	0.51	SG
Km00	5886	3.5	2.18	348.5	1.88	1249	24.9	1.35	1.68	4.05	1.5	SG
Mm00	5436	3.5	2.03	364.4	2.21	1017	24.9	1.35	1.71	4.37	0.83	SG
Em05	6227	4.5	2.22	3395	1.02	644.2	25.1	0.597	1.74	0.938	0.24	MS
Fm05	6260	4	2.26	1079	1.06	6520	25.1	0.597	1.79	1.7	0.85	SG
Gm05	6149	3.5	3.27	338.2	1.66	1389	25.1	0.597	1.76	3.82	2	SG
Im05	5897	4.5	2.25	3502	0.902	4290	25.1	0.597	1.62	0.882	0.17	MS
Jm05	5919	4	2.19	1091	0.949	10 130	25.1	0.597	1.76	1.62	0.52	SG
Km05	5764	3.51	2.13	363.2	1.59	1623	25.1	0.597	1.74	3.66	1.5	SG
Mm05	5463	3.5	2.01	359.4	1.63	1483	25.1	0.597	1.74	3.78	0.7	SG
Bm10	6743	4.24	7.60	1801	0.776	12 030	25.3	0.0205	1.84	1.1	1.2	SG
Am10	5771	4.44	1.53	3065	0.768	13.47	25.3	0.0205	1.26	0.875	0.32	PMS
Cm10	6503	4	2.63	1052	0.765	13 770	25.3	0.0205	1.75	1.45	1.4	SG
Fm10	6242	4	2.25	1073	1.17	3.639	25.3	0.0205	1.67	1.79	0.8	PMS
Gm10	6213	3.5	3.14	341	1.03	5093	25.3	0.0275	1.7	2.99	3	SG
Km10	5894	3.5	2.15	349.7	0.906	7858	25.3	0.0205	1.62	2.8	1.9	SG

Notes. The final three letters of the model labels correspond to [Fe/H]: (m00, m05, m10, p05) refer to [Fe/H] = $(0.0, -0.5, -1.0, +0.5)$, respectively. $T_{\rm b}$ is the mean temperature at the bottom of the 3D model and $\nu_{\rm max}$ is the frequency with the largest amplitude in the oscillation power spectrum ($\nu_{\rm max} = 3050.0(M/M_\odot)(R_\odot^2/R^2)(5777/T_{\rm eff})^{1/2}$, Kjeldsen & Bedding 1995) and M is the mass of the PM which differs by a fraction $\lesssim 10^{-7}$ from the one of UPM. The initial helium and metal abundances are close to the ones at the surface. We recall that the metal abundance is different from the iron abundance [Fe/H] imposed in our models. The evolutionary stages PMS, MS, and SG stand for pre-main-sequence, main-sequence and sub-giant.

adiabatic region, which has been shown to be a condition for a obtaining reliable PM (Jørgensen et al. 2017).

The 1D models use the equation of state, and opacities given by OPAL2005 (Rogers & Nayfonov 2002; Iglesias & Rogers 1996) and implement standard mixing-length theory (Böhm-Vitense 1958) with no overshoot. We ignore diffusion processes, rotation and turbulent pressure. The atmosphere is computed using the Eddington approximation. The helium abundance in 1D models is set to the one used in 3D models.

Finally, we note that for some 3D models one can find a degenerate solution for the corresponding 1D model: we could patch either a PMS or a sub-giant model. We opted for evolved models since they corresponds to stars in which solar-like oscillations are observed so far. However, when the evolved models are too old (older than the age of the Universe) we kept the PMS model, except if lying on the Hayashi track.

Table 1 also summarizes the stellar parameters of both UPM and PM together with relative radius differences $R_{\rm PM}/R_{\rm UPM} - 1$. Our set of models covers a wide portion of the Hertzsprung-Russel Diagram for intermediate mass stars. We note that our patched models with metallicity [Fe/H] = +0.5 only have $\log g = 4.0$. Indeed, 3D models from the CIFIST grid with [Fe/H] = +0.5 were only available for $\log g \geq 4.0$. In addition, 3D models with $\log g \gtrsim 4.5$ are located below the main sequence diagonal, and therefore it is impossible to find a 1D model matching their characteristics (with the physical ingredients we used). Thus, a large portion of our initial [Fe/H] = +0.5 3D hydrodynamical models were not suitable for our purposes.

2.3. Computation of oscillation frequencies

In this work, we consider only structural effects and an adiabatic treatment of the oscillations. The frequencies are computed using the ADIPLS code (Christensen-Dalsgaard 2011) for both UPM and PM by assuming the gas Γ_1 approximation, which assumes that the relative Lagrangian perturbations of gas pressure and turbulent pressure are equal (Rosenthal & Christensen-Dalsgaard 1999; Sonoi et al. 2017). Besides this distinction in the treatment of Γ_1 entering the calculation of the model frequencies, we emphasize that the frequency differences studied in this work are only emerging

from structural effects. Therefore, it should be emphasized that the frequency differences studied in this work concern only purely structural effects. We have checked that we recovered the previous results of Sonoi et al. (2015) for the solar metallicity. For the sake of simplicity, we mainly focussed on the surface effect affecting radial modes: non-radial modes exhibit a mixed behaviour that would make our analysis more complex (however, see Sect. 4.2.2 for a discussion).

3. Influence of metallicity

Until now, surface effects have always been studied assuming a solar metallicity. Corrections depend only on $T_{\rm eff}$ and $\log g$ such as the power law proposed by Kjeldsen et al. (2008), cubic and combined inverse-cubic laws (Ball & Gizon 2014), or a modified Lorentzian (Sonoi et al. 2015). This section is intended to motivate the investigation of the dependence of the surface effect on metallicity.

3.1. Qualitative influence of metallicity on frequency differences

We begin this section by quickly describing the effects of a change of metallicity on the frequency residuals. Frequency differences are induced by the surface elevation between PM and UPM due to turbulent pressure, which extends the size of the resonant cavities and therefore decreases the mode frequencies for PM, leading to negative frequency differences $\delta\nu = \nu_{\rm PM} - \nu_{\rm UPM}$.

Up to now, only the influence of effective temperature and surface gravity on surface effects have been studied. However, the abundance of heavy elements has a strong impact on opacity and hence on the convective flux imposed by a change in the radiative flux. In turn, a change in the convective flux leads to a change of convective velocity and therefore a change of turbulent pressure and finally it changes the location of the surface. We mention here that metallicity also has an effect on gas pressure, through the mean molecular weight μ, which varies in the opposite direction of the turbulent pressure and therefore counteracts its effect. Finally, while mechanisms by which a change of metallicity can act on the surface effect are known, those mechanisms are too intricate to identify the resulting effect on the variations of surface term without a deeper analysis as will be demonstrated in the following (see Sect. 4).

Figure 2 shows the (purely structural) frequency differences for three groups of models that have approximately the same effective temperature and surface gravity. The discrepancies in $\nu_{n\ell}$ between two models appear at relatively low frequencies and generally increase towards high frequencies. As for finding a general trend of the evolution of the surface effect against the metallicity, it seems from Fig. 2 no such trend exists: in the top panel, frequency differences, at $\nu_{\rm max}$ for instance, slightly decrease from [Fe/H] = −0.5 to 0.0 and then are much higher for the [Fe/H] = +0.5 model. In the middle panel, the frequency residual at $\nu_{\rm max}$ significantly increases from [Fe/H] = −0.5 to 0.0. Finally, in the bottom panel, very little variations at $\nu_{\rm max}$ can be noticed from one composition to an other. However, the variation of the frequency differences seems to follow closely the variations of the elevation of the stellar surface between UPM and PM:

$$\Delta r \equiv R_{\rm PM} - R_{\rm UPM}. \quad (1)$$

The slight disagreement between [Fe/H] = 0.0 and −0.5 in the top panel may be explained by the large dispersion in effective temperature.

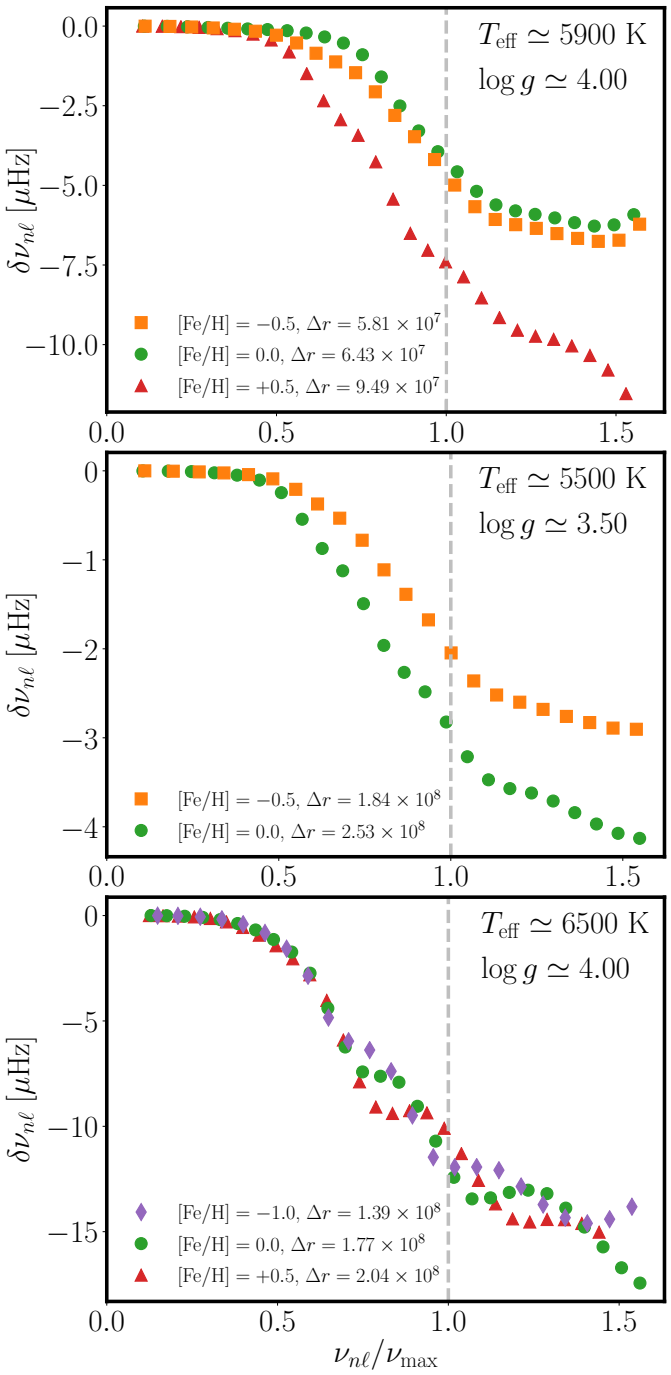

Fig. 2. Frequency differences of PM vs. UPM for radial modes with frequencies less than the acoustic cut-off frequency $\nu_{\rm ac} = c/(4\pi H_p)$. Frequencies on the abscissa are normalized by the $\nu_{\rm max}$ of each models. *Top panel*: models J*: $T_{\rm eff} \simeq 5900$ K and $\log g = 4.0$. *Middle panel*: models M*: $T_{\rm eff} \simeq 5500$ K and $\log g = 3.5$. *Bottom panel*: models C*: $T_{\rm eff} \simeq 6500$ K and $\log g = 4.0$.

3.2. Effect of the elevation on the frequency differences

To gain some insight into the influence of metallicity on surface effect, we tried to scale the normalized frequency differences at $\nu_{\rm max}$ for our set of models. This is a necessary step to allow an estimate of the surface effect correction parameters (see Sect. 4). Thus, let us start with the perturbative approach as adopted by (Christensen-Dalsgaard & Thompson 1997; see also Goldreich et al. 1991; Balmforth et al. 1996). The authors show

that the frequency difference can be well approximated by

$$\frac{\delta\nu}{\nu} = \int_0^R \left[\tilde{K}^{n\ell}_{c^2,v} \frac{\delta_m c^2}{c^2} + \tilde{K}^{n\ell}_{v,c^2} \frac{\delta_m v}{v} \right] \mathrm{d}r \tag{2}$$

$$\simeq \int_0^R \tilde{K}^{n\ell}_{v,c^2} \frac{\delta_m v}{v} \mathrm{d}r\,, \tag{3}$$

where c is the adiabatic sound speed, the variable v is defined by $v = \Gamma_1/c$, $\tilde{K}^{n\ell}_{c^2,v}$ and $\tilde{K}^{n\ell}_{v,c^2}$ are the kernels that can be determined from eigenfunctions, $\delta_m c^2$ and $\delta_m v$ are the Lagrangian differences of c^2 and v, respectively, at fixed mass.

Rosenthal & Christensen-Dalsgaard (1999) further approximated the frequency differences for radial modes, based on the expression of $\tilde{K}^{n\ell}_{v,c^2}$ and using a first-order asymptotic expansion for the eigen-function, by

$$\frac{\delta\nu}{\nu} \simeq \frac{\Delta\nu \Delta r}{c_{\rm ph}}, \tag{4}$$

where $\Delta\nu$ is the asymptotic large frequency separation, Δr is the previously defined elevation, and $c_{\rm ph}$ the photospheric sound speed (see Appendix A for a demonstration of this relation).

This relation has been previously tested by Sonoi et al. (2015) at solar metallicity using surface effect derived from a grid of 3D numerical simulations. It turns out that Eq. (4) reproduces the overall scale of the surface effect (such as in Fig. 3 were the surface effect is considered at $\nu_{\rm max}$) for a set of models. It is thus necessary to determine whether this relation holds for models with a non-solar metallicity. To this end, we have compared frequency residuals at $\nu = \nu_{\rm max}$ given by Eq. (4) as shown in Fig. 3 (top panel). There is still a good agreement between the frequency differences and the approximated expression given by Eq. (4). Moreover, it appears that the frequency differences are dominated by the surface elevation Δr. To understand the link to metallicity, it is thus necessary to go a step further and to investigate the relation between surface elevation and metallicity.

3.3. Scaling law for the frequency differences

In this section, we aim to determine a relation between frequency differences at $\nu_{\rm max}$ and global parameters of the models. First, as shown in the previous section, there is no clear trend between the surface term and metallicity. Indeed, at constant metallicity and considering our rather large range of effective temperatures and surface gravities, the dominant opacity mechanisms are not the same from a model to an other for instance, the opacity at the surface is dominated by the negative hydrogen ions for $T_{\rm eff} \lesssim 5000$ K. Therefore, the relation between $\delta\nu/\nu$ and Z is non-trivial. To overcome this problem, we directly consider the Rosseland mean opacity at the photosphere instead of the metallicity as a global parameter in addition to the effective temperature and to the surface gravity (in the following, the photosphere is defined as the radius at which $T = T_{\rm eff}$).

Let us begin by considering the elevation in Eq. (1) which must be expressed as a function of these global parameters. Using the hydrostatic equilibrium equation, it reads

$$\Delta r = \int_0^{R_{\rm PM}} H_p^{\rm PM} \frac{\mathrm{d}p_{\rm tot}}{p_{\rm tot}} - \int_0^{R_{\rm UPM}} H_p^{\rm UPM} \frac{\mathrm{d}p_{\rm g}}{p_{\rm g}}, \tag{5}$$

where $H_p^{\rm PM}$ and $H_p^{\rm UPM}$ are the pressure scale heights at the photosphere associated with the patched and unpatched models, $p_{\rm tot}$ is the total pressure such as $p_{\rm tot} = p_{\rm turb} + p_{\rm g}$ with $p_{\rm turb}$ and $p_{\rm g}$ the turbulent and gas pressure, respectively. Further assuming that

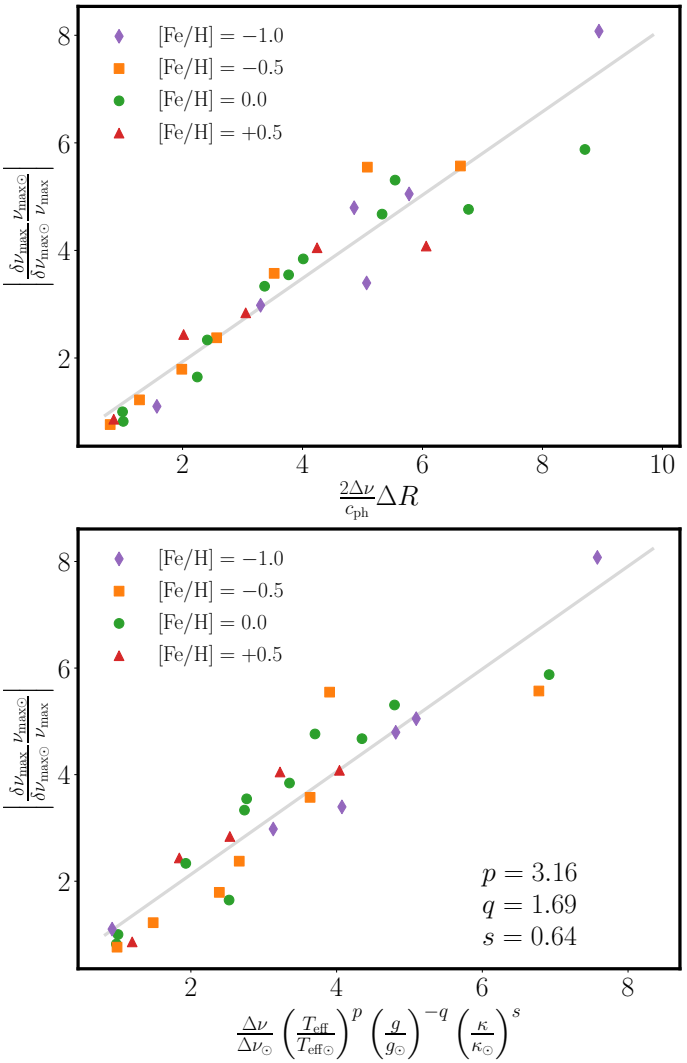

Fig. 3. Frequency differences scaled by the frequency, taken at $\nu_{\rm max}$ against a scaling relation given by Rosenthal & Christensen-Dalsgaard (1999) (*top panel*; with $\sigma = 0.89$) and a scaling relation given by Eq. (13) where powers are left free (*bottom panel*; with $\sigma_\kappa = 0.63$).

$H_p^{\rm PM} \simeq H_p^{\rm UPM}$ and $p_{\rm turb}/p_{\rm tot} \ll 1$ one can approximate Eq. (5) by

$$\Delta r \simeq H_p^{\rm PM} \frac{p_{\rm turb}}{p_{\rm tot}}. \tag{6}$$

Finally, since the pressure scale-height scales as $T_{\rm eff}/g$, the elevation scales as $\Delta r \propto (T_{\rm eff} p_{\rm turb})/(g p_{\rm g})$.

To go further, we need to find an expression for $p_{\rm turb}/p_{\rm g}$. Near the photosphere, the turbulent pressure can be written as

$$p_{\rm turb} = \rho v_{\rm conv}^2, \tag{7}$$

where $v_{\rm conv}$ is the vertical component of the convective velocity. We now need an expression for this velocity and for the density. Assuming a standard Eddington grey atmosphere, the optical depth is approximated by $\tau = H_p \rho \kappa$, and in the Eddington approximation, we have $\tau = 2/3$ at the bottom of the photosphere. Then, and accordingly:

$$\rho \propto \frac{g}{T_{\rm eff}\kappa}. \tag{8}$$

As for finding an expression for $v_{\rm conv}$, we note that $F_{\rm tot} = F_{\rm rad} + F_{\rm conv}$, with $F_{\rm rad}$ and $F_{\rm conv}$ the radiative and convective component of the total energy flux respectively. The convective flux

is proportional to the kinetic energy flux (as shown for instance within the MLT framework). Then,

$$\rho v_{\rm conv}^3 \propto T_{\rm eff}^4 \left(1 + \frac{F_{\rm rad}}{F_{\rm conv}}\right)^{-1}. \quad (9)$$

The ratio $F_{\rm rad}/F_{\rm conv}$ is assumed to remain nearly constant from one model to an other. Therefore, $v_{\rm conv}$ finally reads,

$$v_{\rm conv}^2 \propto \frac{T_{\rm eff}^{8/3}}{\rho^{2/3}}. \quad (10)$$

Inserting the expressions of Eqs. (8) and (10) into Eq. (7) leads to:

$$p_{\rm turb} \propto \left(\frac{T_{\rm eff}}{T_{\rm eff\odot}}\right)^{7/3} \left(\frac{g}{g_\odot}\right)^{1/3} \left(\frac{\kappa}{\kappa_\odot}\right)^{-1/3}, \quad (11)$$

where $\kappa_\odot = 0.415\,{\rm cm^2\,g^{-1}}$. From the perfect gas law for, $p_{\rm g} \propto \rho T_{\rm eff}$ and using Eq. (8), we can rewrite Δr as

$$\Delta r \propto \left(\frac{T_{\rm eff}}{T_{\rm eff\odot}}\right)^{10/3} \left(\frac{g}{g_\odot}\right)^{-5/3} \left(\frac{\kappa}{\kappa_\odot}\right)^{2/3}. \quad (12)$$

Replacing Δr into Eq. (4) one finally obtains the following estimate:

$$\frac{\delta\nu}{\nu} \propto \frac{\Delta\nu}{\Delta\nu_\odot} \left(\frac{T_{\rm eff}}{T_{\rm eff\odot}}\right)^{17/6} \left(\frac{g}{g_\odot}\right)^{-5/3} \left(\frac{\kappa}{\kappa_\odot}\right)^{2/3} \equiv z_1. \quad (13)$$

This expression provides us with a simple relation between the frequency differences and the global parameters. The dependence on the metallicity is embedded into the Rosseland mean opacity. We note that it is possible to go further and to explicitly introduce the metallicity. For instance, in the vicinity of the solar effective temperature and gravity, the opacity is dominated by the H^- so that $\kappa \propto \rho^{-1/2} T_{\rm eff}^9 Z$. However, given the wide range of effective temperatures and surface gravities of our grid of models, it is more relevant to keep the Rosseland mean opacity at $T = T_{\rm eff}$ (surface opacity) as a global parameter. Indeed, the Rosseland mean opacity is a quantity available in any 1D stellar evolutionary code.

Then, using Eq. (13) as a guideline, we performed a fit where the powers of the temperature (p), gravity (q), and opacity (s) have been adjusted at $\nu = \nu_{\rm max}$ for each model. Figure 3, bottom panel, displays the result. This figure shows a very good agreement between exponents derived in Eq. (13) and the one actually obtained using our simulations. Consequently this scaling can be used to provide a physically-grounded values for the parameters of the empirical correction function of the surface effect. Finally, we note that using the opacity instead of the metallicity allows us to take a detailed mixture into account.

In addition to our crude approximations, a possible source of discrepancies between values predicted by Eq. (13) and the one calculated can be that we did not fix the helium abundance from one model to the other when varying the metallicity. The changing helium abundances have an impact both on the evolution of the model and on its opacity at the surface. However, the helium abundances [He/H] range between -5.8×10^{-3} and $+1.2 \times 10^{-2}$ and should be a negligible source of uncertainty. A final source of error comes from the method we used to average the 3D stratifications. Indeed, since the Rosseland opacity is involved Eq. (13), it would be more precise to patch the models using a stratification averaged against the Rosseland optical depth instead of the actual geometrically averaged stratification, but this is beyond the scope of this paper and will be investigated in a forthcoming work.

4. Surface-effect corrections

A handful of empirical functions have been suggested to perform a posteriori corrections on the modelled frequencies. After having given a theoretical background that explains variations of $\delta\nu/\nu$, we considered the most commonly used correction models to study the evolution of the related free parameters as a function of effective temperature, surface gravity, and surface opacity. This is intended to provide constraints on those parameters and thus to provide physically-grounded values for use on seismic observations.

4.1. Empirical functions for correcting modelled frequencies

4.1.1. Kjeldsen et al. (2008) power law

Kjeldsen et al. (2008) proposed a power law which was found to match the frequency differences obtained between the observed and modelled solar frequencies:

$$\frac{\delta\nu}{\nu_{\rm max}} = a \left[\frac{\nu_{\rm PM}(n)}{\nu_{\rm max}}\right]^b, \quad (14)$$

where a and b are the parameter to be adjusted. They found $a = -4.73$ and $b = 4.9$ for their model of the Sun by matching a subset of nine radial modes centred on $\nu_{\rm max}$.

Kjeldsen et al. (2008) provided a method to correct the frequency for a star similar to the Sun without having to calibrate b. Let us assume we want to model a star with near solar global parameters and we want to constrain our model using the individual frequencies. The radial mode frequencies spectrum of our best model which include a surface term are denoted $\nu_{i,\rm best}$ and the frequencies of solar radial modes for the same order are denoted $\nu_{i,\rm ref}$. Then, Kjeldsen et al. (2008) proposed that the frequencies can be linked, to a good approximation, by $\nu_{i,\rm best} \simeq r\nu_{i,\rm ref}$, using the proportionality factor r between mean densities of both models: $\bar{\rho}_{\rm best} = r^2\bar{\rho}_{\rm ref}$. Using this relation and the large separations of both models, they provided a way to obtain a and b. Further assuming b constant (the value of which depends of the physical ingredients used in the model), they derived a value for a for a set of theoretical models close to the Sun.

This power law has been widely used since and many authors (e.g. Metcalfe et al. 2009; Bedding et al. 2010) have used a constant value for b (not necessarily 4.90 though) derived from solar frequency measurements. Keeping b constant is often necessary in the case for which observations do not provide enough constraints to adjust it. However, using the solar value leads to a bad correction if the modelled star is too different from the Sun (e.g. Kallinger et al. 2010). Furthermore, $b_\odot$ depends on the input physics. Otherwise, b can be considered as a variable parameter in the modelling and therefore significantly improve the correction. Different models of the star HD 52265 have been compared by Lebreton & Goupil (2014) using various input physics and found approximatively the same predicted age models when either frequency ratios (Roxburgh & Vorontsov 2003) or individual corrected frequencies were used as constraints. The age dispersion was slightly higher with models constrained by individual corrected frequencies ($\sim\pm9.5\%$) and using uncorrected individual frequencies lead to ages 40% larger (Lebreton et al. 2014).

In the following, we have studied two versions of this parametric function. The first, adjusted on the whole radial mode frequency spectrum for frequency less than the acoustic cut-off frequency, will be referred to as K08. The second, adjusted on

a reduced frequency interval $0 < \nu/\nu_{\rm max} < 1.05$ is refered to as K08r (see Fig. 6 and Appendixes B and C).

4.1.2. Ball & Gizon (2014) cubic and combined inverse-cubic laws

Ball & Gizon (2014) suggested a new function to correct frequency differences. It is partially based on the early work by Gough (1990; for the cubic part). They accounted for two leading effects introducing systematic errors in the theoretical computation of the frequency spectrum: the modification of the sound speed caused by a magnetic field concentrated into a filament by convective motions, causing a frequency shift scaling as ν^3/E (Libbrecht & Woodard 1990), E being the normalized mode inertia; and the modification of the pressure scale height caused by a poor description of convection, inducing a frequency shift scaling as ν^{-1}/E. This correction funtional has the advantages of being independent of a solar calibration and including a dependence on the normalized mode inertia which allows us to correct non-radial modes, without the need of re-scaling their frequency differences. Because of this, they suggested a cubic correction taking only into account the dominant effect and a combined inverse-cubic correction including the perturbation.

The cubic correction (in the following BG1) is defined by

$$\frac{\delta\nu}{\nu_{\rm max}} = \frac{a_{3,\rm BG1}}{E}\left(\frac{\nu}{\nu_{\rm max}}\right)^3, \tag{15}$$

and the combined inverse-cubic correction (in the following BG2) is

$$\frac{\delta\nu}{\nu_{\rm max}} = \frac{1}{E}\left[a_{-1,\rm BG2}\left(\frac{\nu}{\nu_{\rm max}}\right)^{-1} + a_{3,\rm BG2}\left(\frac{\nu}{\nu_{\rm max}}\right)^3\right], \tag{16}$$

where E is the normalized mode mass:

$$E = \frac{4\pi\int_0^R \left[|\xi_{\rm r}(r)|^2 + \ell(\ell+1)|\xi_{\rm h}(r)|^2\right]\rho r^2 {\rm d}r}{M\left[|\xi_{\rm r}(R)|^2 + \ell(\ell+1)|\xi_{\rm h}(R)|^2\right]}, \tag{17}$$

where R, M, and ρ are respectively the photospheric radius, mass and density of the star, and $\xi_{\rm r}$ and $\xi_{\rm h}$ are the radial and the horizontal component of the displacement of an eigenmode of degree ℓ. $a_{3,\rm BG1}$, $a_{-1,\rm BG2}$, and $a_{3,\rm BG2}$ are the parameters to be adjusted. They used the acoustic cut-off frequency $\nu_{\rm c}$ instead of $\nu_{\rm max}$ in order to normalize their fitting parameters: it only results in a modification of a_{-1} and a_3 and does not change the law itself.

4.1.3. Sonoi et al. (2015) modified Lorentzian

The final function to be introduced was a modified Lorentzian (Sonoi et al. 2015) that was found to better correct the surface effect derived from the 3D simulations at high frequency. It reads

$$\frac{\delta\nu}{\nu_{\rm max}} = \alpha\left[1 - \frac{1}{1+\left(\frac{\nu_{\rm PM}}{\nu_{\rm max}}\right)^\beta}\right], \tag{18}$$

where α and β parameters are to be determined. When $\nu_{\rm PM}/\nu_{\rm max} \ll 1$ we get back to Kjeldsen et al. (2008) law. When $\nu_{\rm PM} = \nu_{\rm max}$, $\delta\nu/\nu_{\rm max} = \alpha/2$. Therefore, a and α are directly linked to $\delta\nu/\nu$ given by Eq. (13), which gives physical justification for its variations. In the following, we will refer to this correction law as S15.

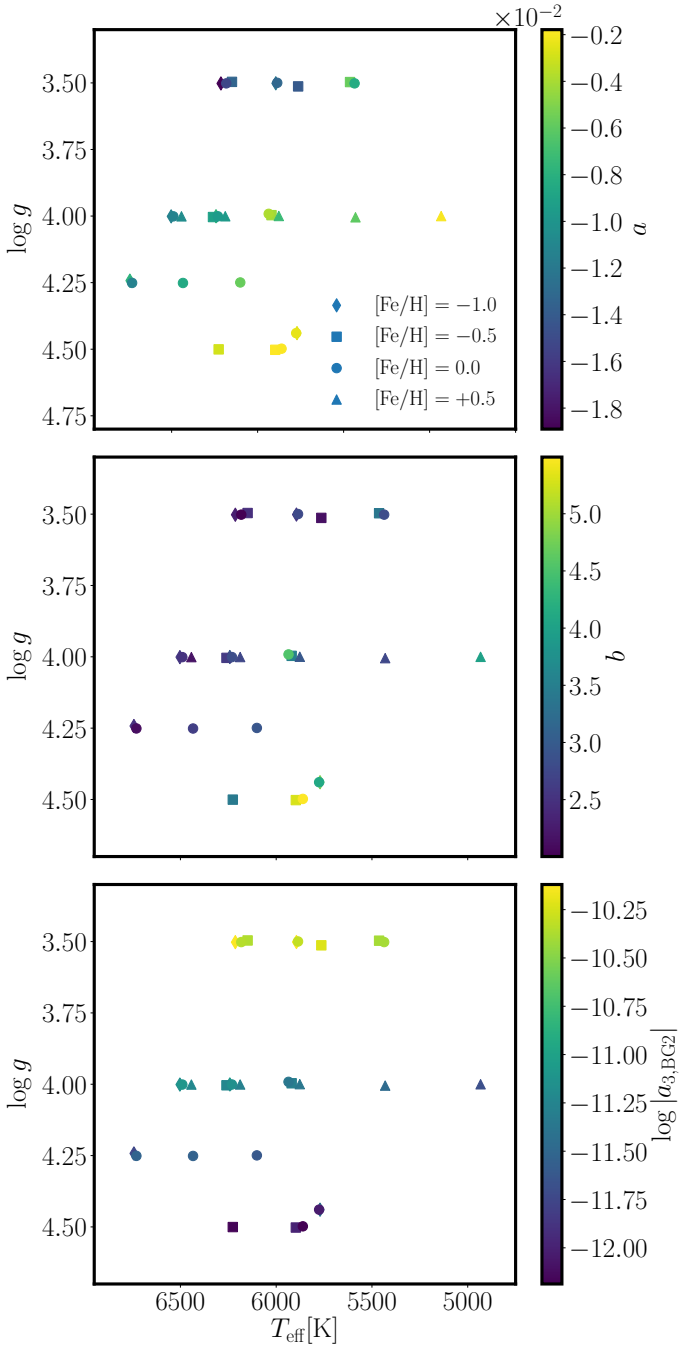

Fig. 4. Parameters a (*top panel*), b (*middle panel*) and $a_{3,\rm BG2}$ (*bottom panel*) across the Kiel diagram from K08 and BG2. The symbols refer to [Fe/H] = −1.0 (diamond), [Fe/H] = −0.5 (square), [Fe/H] = +0.0 (circle) and [Fe/H] = +0.5 (triangle).

A recent comparison of the above correction laws has been performed by Ball & Gizon (2017) on six sub- and red giants from the *Kepler* Input Catalog. We note that since these are evolved stars, they display mixed-modes which have their frequency residuals off the general trend of radial p-modes frequency residuals. This should have consequences on the quality of the correction. They computed stellar models matching their six stars constrained by the effective temperature, the metallicity and the individual frequencies. They tested five correction relations: BG1, BG2, S15, and K08 with power $b = 5.0$ calibrated with a solar model computed with their own input physics and K08 with power b left free.

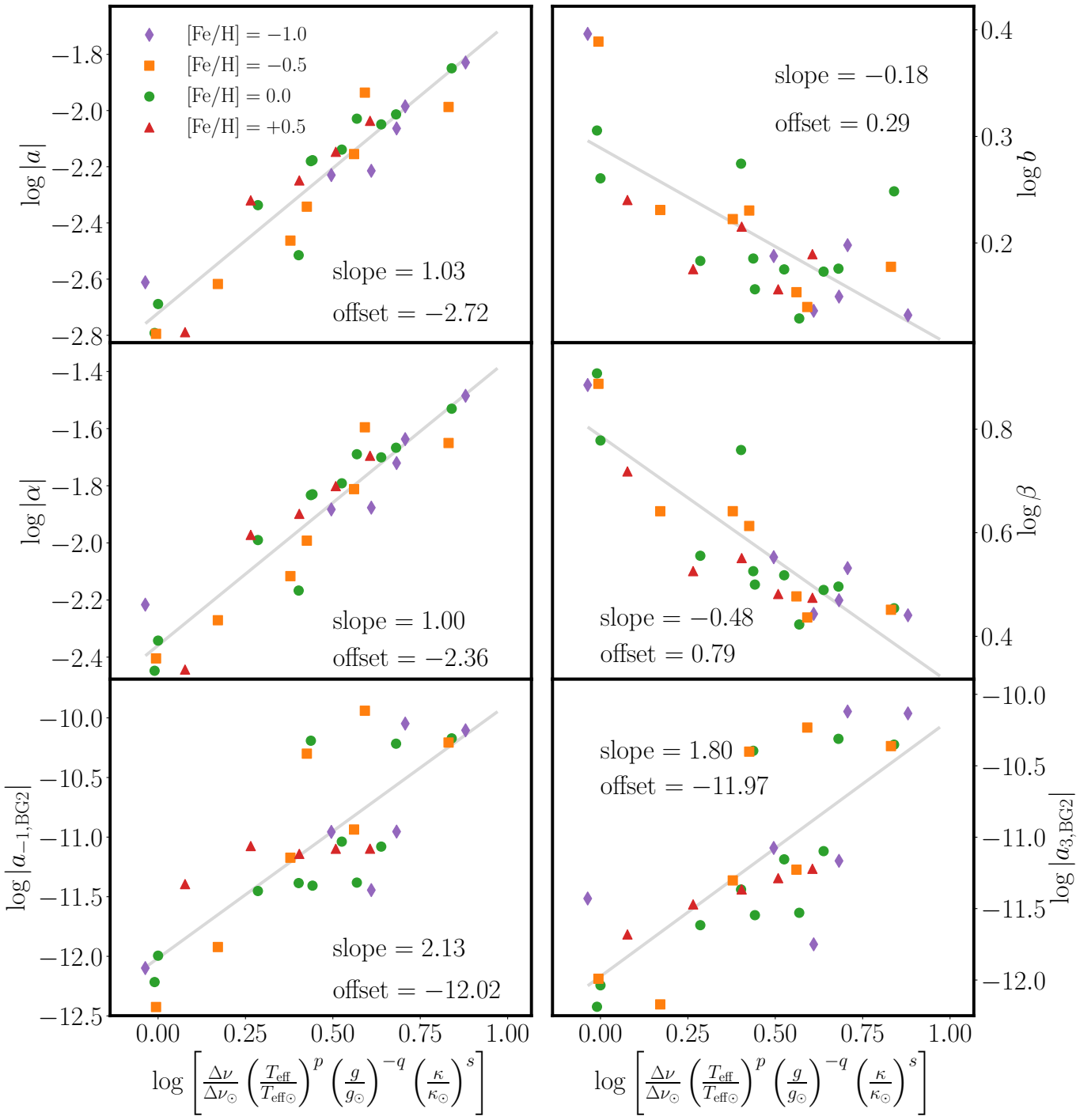

Fig. 5. Logarithms of K08 (first row), S15 (second row) and BG2 (third row; $\log|a_{3,\mathrm{BG1}}|$ behaves almost identically to $\log|a_{3,\mathrm{BG2}}|$) fitting coefficients as a function of $\log z_1$ (Eq. 13): $\log f$ = slope × $\log z_1$ + offset. Purple dots (resp. yellow, green and red) corresponds to [Fe/H] = −1.0 (resp. −0.5, 0.0 and +0.5).

Ball & Gizon (2017) found no correction to be clearly superior than the others for all stars. However BG2 and then BG1 performed slightly better than the others, followed by the free power law, S15 and finally K08. S15 was shown to poorly correct high frequencies and the K08 with $b = 5.0$ correction gave worse results than no correction for their of their stars. We present very similar conclusions in the following.

4.2. Variation of the coefficients in the $\Delta\nu - T_{\mathrm{eff}} - \log g - \kappa$ space

4.2.1. Prescriptions for radial modes

In order to fit the parameters of the correction functions and to determine the fitting parameters, we used a least square minimization algorithm implementing a Levenberg-Marquardt

method which minimizes the squared deviation defined as

$$\mathcal{D} = \sum_{i=1}^{N} \left[\frac{\nu_{\mathrm{PM},i} - \nu_{\mathrm{UPM},i} - \delta\nu_i}{\nu_{\max}} \right]^2, \tag{19}$$

where i corresponds to the eigenmode index, N to the total number of radial modes and $\delta\nu$ the correction computed from the considered correction relation. Tables B.1 and C.1 summarize the coefficients and their squared deviations from our computations. We also define $\sqrt{\mathcal{D}/N}$ as the root-mean frequency differences after correction.

Coefficients a and b involved in Eq. (14) and $a_{3,\mathrm{BG2}}$ from Eq. (16) are presented in $T_{\mathrm{eff}} - \log g$ plane in Fig. 4. Furthermore, all coefficients are represented as a function of $\log z_1$ in Fig. 5. a, α and $a_{3,\mathrm{BG2}}$ (and therefore $a_{3,\mathrm{BG1}}$) show similar trends. Indeed, they are related to the amplitude of the surface effect at $\nu_{\max}$ and Eq. (13) allows one to understand their variations. However, this theoretical justification for the variations of a, α, $a_{3,\mathrm{BG1}}$ and $a_{3,\mathrm{BG2}}$ does not provide a way to favour one correction law over an other. Coefficient $a_{-1,\mathrm{BG2}}$ exhibits the same behaviour as above. However, we cannot offer the same explanation for its trend because the inverse term in BG2 is a second correction to the cubic term and is not related to the amplitude of the surface effect at $\nu_{\max}$.

The trends followed by b and β are related to the slope of the frequency differences. As shown in Sonoi et al. (2015) and in Fig. 4, the coefficients b (whatever the metallicity) increase significantly towards cooler stars, which again contradicts the assumption of a constant b. Regarding the relevance of giving a prescription for $\log b$ and $\log\beta$ thanks to the linear relationship with $\log z_1$, we can see in Fig. 5 that $\log b$ and $\log\beta$ are affected by a high dispersion compared to the grey line. This could mean either that we omitted a physical dependency in Eq. (13) that only affects the agreement with $\log b$ and $\log\beta$, or a prescription based on same other physical basis should be investigated.

Table 2 shows the prescriptions for the variations in the $T_{\mathrm{eff}} - \log g - \kappa$ space of all coefficients c_0 studied in this article in the form

$$\log c_0 = c_1 \log \Delta\nu/\Delta\nu_\odot + c_2 \log T_{\mathrm{eff}}/T_{\mathrm{eff}\odot} + c_3 \log g/g_\odot + c_4 \log \kappa/\kappa_\odot + c_5. \tag{20}$$

We note that the opacity has a strong impact on each of the coefficients and must, therefore be taken into account when correcting the surface effect.

The top panel of Fig. 6, top panel also shows the value of the root-mean frequency differences after correction for each model and each correction law. From this, we see that BG1 is the worst performer followed by K08. Those laws provide a correction that leaves frequency residuals comprised between 1 and 10 μHz which are still higher than the frequency resolution provided by CoRoT and *Kepler*. The better performance of K08 over BG1 can be explained by the fact that K08 have two degrees of freedom whereas BG1 has only one. For radial modes, the inclusion of the normalized mode mass $E_{n\ell}$ in BG1 does not compensate the loss of a degree of freedom.

Then, the remaining laws K08r, S15 and BG2 provide correction almost as good as the resolution of CoRoT and *Kepler*. K08r and BG2 are slightly better than S15, yet K08r is applied only on the frequency range $0 < \nu/\nu_{\max} < 1.05$.

4.2.2. Mixed-modes case

We also performed the same test as in Ball & Gizon (2017) on evolved models that present mixed-modes in their frequency spectrum. In Sect. 4.1.2 we see that, thanks to the dependence in the normalized mode inertia, BG1 and BG2 can be applied to non-radial modes without any change of the law. However, in order to be able to compare all empirical corrections on non-radial modes, one had to rescale the frequency differences on which K08, K08r and S15 by mean of the inertia ratio $Q_{n\ell}$ for a mode of frequency $\nu_{n\ell}$ defined as the ratio of the inertia of this mode by the inertia of a radial mode interpolated at the frequency $\nu_{n\ell}$: $Q_{n\ell} = E_{n\ell}/E_{n0}(\nu_{n\ell})$ (e.g. Rosenthal & Christensen-Dalsgaard 1999). Furthermore, we added one last empirical relation by modifying the expression given for S15 in Eq. (18) similarly to BG1 and BG2 in which we replaced α by α/E where E is defined in Eq. (17) (the new function is denoted S15E). This allows S15E to be applied directly on non-radial modes frequency differences.

The empirical relations K08, K08r and S15 were then adjusted on $Q_{n\ell}\delta\nu_{n\ell}$, with $0 \leq \ell \leq 2$ and S15E, BG1 and BG2 were adjusted directly on $\delta\nu_{n\ell}$, with $0 \leq \ell \leq 2$. For 9 of the 16 evolved models considered, the least-square algorithm converge to a solution of K08, K08r or S15 very remote from the general trend of frequency differences, whereas for the second group of relations (S15E, BG1 and BG2), the residual root-mean frequency differences after correction are greatly improved to a value between 0.1 and 1 μHz.

As a third test, we performed the same fits excluding the quadrupolar modes (i.e. we fit modes with $0 \leq \ell \leq 1$). This time, corrections laws accuracies are similar to the one presented in Sect. 4.2.1. As for the newly introduced S15E, it performs slightly worse than S15 but still better than K08. This third test suggests that the failure of K08, K08r and S15 in fitting $Q_{n\ell}\delta\nu_{n\ell}$, with $0 \leq \ell \leq 2$ is due to quadripolar modes. There are two reasons for it.

First, the p and g cavity are less coupled for $\ell = 2$ than for $\ell = 1$ mixed-modes which induces more important changes on the behaviour of a mode when the surface layers are changed between UPM and PM. Indeed, modifying the surface layers changes the frequency of pure p modes that couple with different g modes for PM and UPM (Ball & Gizon 2017). As a consequence, when computing $Q_{n,2}\delta\nu_{n,2}$, it so happens that we deal with mixed-modes from PM and UPM that have different properties. Second, due to the presence of mixed-modes, $Q_{n,2}$ sometimes becomes higher than ten, while it is normally of the order of unity (see example of Cm10 in Fig. 7). It over-scales the corresponding quadrupolar mixed-modes and gives much weight

Table 2. Prescriptions for the fitting coefficients involve in the empirical relations K08, K08r, S15, BG1, BG2.

Law	$\log c_0$	c_1	c_2	c_3	c_4	c_5
K08	$\log \lvert a\rvert$	1.03	3.26	−1.75	0.655	−2.72
	$\log b$	−0.185	−0.584	0.313	−0.117	0.289
K08r	$\log \lvert a\rvert$	1.08	3.39	−1.82	0.683	−2.65
	$\log b$	−0.387	−1.22	0.655	−0.246	0.647
S15	$\log \lvert\alpha\rvert$	0.999	3.15	−1.69	0.635	−2.36
	$\log\beta$	−0.477	−1.51	0.808	−0.303	0.787
BG1	$\log \lvert a_3\rvert$	1.93	6.09	−3.26	1.22	−11.9
BG2	$\log \lvert a_{-1}\rvert$	2.13	6.72	−3.6	1.35	−12
	$\log \lvert a_3\rvert$	1.8	5.67	−3.04	1.14	−12

Notes. The prescriptions are written: $\log c_0 = c_1 \log \Delta\nu/\Delta\nu_\odot + c_2 \log T_{\mathrm{eff}}/T_{\mathrm{eff}\odot} + c_3 \log g/g_\odot + c_4 \log \kappa/\kappa_\odot + c_5$. Our solar values are computed from model Am00. $\Delta\nu_\odot = 137$ [μHz], $T_{\mathrm{eff}\odot} = 5776$ [K], $g_\odot = 27511$ [cm s^{-2}], and $\kappa_\odot = 0.415$ [cm^2 g^{-1}].

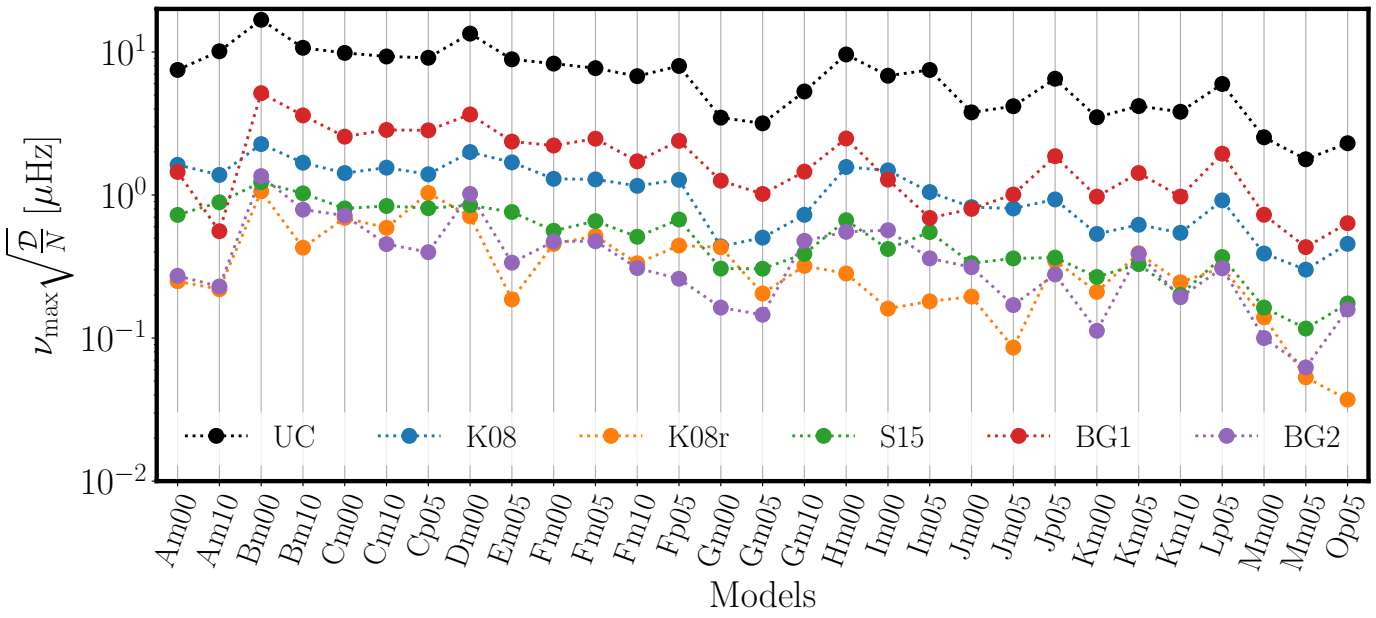

Fig. 6. Root-mean frequency differences $\nu_{\max}\sqrt{\mathcal{D}/N}$ of radial modes after correction for each empirical law and for each model. It shall be noticed that the deviation for K08r is computed only on the range $0 < \nu/\nu_{\max} < 1.05$. Black dots corresponds to uncorrected frequencies (UC), that is root mean frequency differences between PM and UPM frequencies.

to those modes, which in turns has strong impact on the quality of the fit. The peaks in the value of $Q_{n,2}$ arise for mixed-modes having most of their amplitude in the g mode cavity, contrary to dipolar mixed-modes which have their $Q_{n,1}$ staying close to unity. On the other hand, fitting directly $\delta\nu_{n\ell}$ with S15E, BG1 and BG2 does not amplify the frequency differences affecting mixed-modes, providing a much better correction.

For all these reasons, we recommend the use of BG2 or S15E when correcting sets of radial and non-radial modes and we recommend either S15 or BG2 when correcting only radial modes (K08r can be used for frequencies $\lesssim\nu_{\max}$). The remaining advantages of S15 over BG2 is that the coefficients α and β are better described as a function of Eq. (13) than coefficients of BG2 which present a bigger dispersion on Fig. 5. This being said, many of the correction laws considered in this paper gives a root-mean frequency difference of the order of 0.1 μHz (at least for few models), similar to the frequency uncertainties of CoRoT and *Kepler*. Furthermore, the search for the best a posteriori correction law should not set aside the need of a theoretical understanding of the surface effect.

5. Conclusion

We have computed a grid of 29 couples of one dimensional models using the method of patched models consisting in replacing poorly modelled surface layers of a 1D model by the stratification, averaged over the geometrical depth and time, computed from 3D hydrodynamical models. The grid includes models with effective temperature ranging from $T_{\rm eff}$ = 5000 K to 6800 K, surface gravity ranging from $\log g$ = 3.5 to 4.5 and iron abundance ranging from [Fe/H] = −1.0 to +0.5.

Our aim was to estimate and understand the impact of varying metallicities on the surface effect. Our main result is that, in the considered range of metallicities (i.e. [Fe/H] = −1.0 to +0.5) the amplitude of the surface effect computed at $\nu_{\max}$, and for models with same effective temperature and same surface gravity, can be up to a factor of three between the model with the lowest amplitude and the model with the highest one. However, it appears that studying the amplitude as a function of the metallicity does not lead to a clear trend, whereas the Rosseland mean opacity κ turned out to be the adapted quantity for understanding the variation of the surface effect. Based on relatively simple physical arguments, consolidated using the grid of 3D models, we found a scaling relation between the amplitude of the surface effect and the global parameters $T_{\rm eff}$, $\log g$ and the opacity κ computed at the photosphere.

We also tested the accuracy of existing surface effect empirical corrections of radial modes frequency differences on each model of our grid in order to obtain a prescription for the

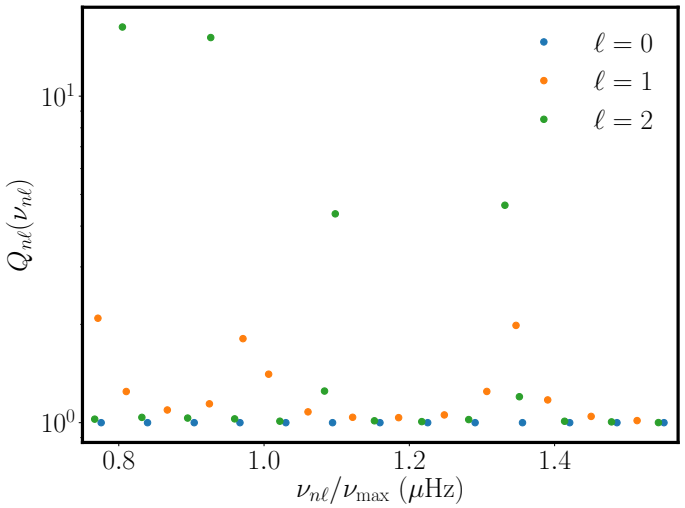

Fig. 7. Ratio $Q_{n\ell}$ of a mode of degree $n\ell$ against frequency of the same mode normalized by $\nu_{\max}$ (only $\nu_{n\ell}/\nu_{\max} > 0.75$ for clarity), for the subgiant model Cm10 with $T_{\rm eff}$ = 6503 K, $\log g$ = 4.0 and [Fe/H] = −1.0. Each colour corresponds to a degree ℓ. Yellow (resp. green) dots breaking from the general trend correspond to dipolar (resp. quadrupolar) mixed modes.

coefficients. Then, we tested those laws on radial and non-radial modes for evolved models exhibiting mixed-modes, in order to test how the empirical corrections perform when mixed-modes are involved. Overall, the combined correction law proposed by Ball & Gizon (2014) is found to give the best performer, closely followed by the law proposed by Sonoi et al. (2015). These two laws leave frequency differences that are less than 1 μHz on average, even reaching 0.1 μHz for the coolest stars of our set of model, which is of the order the frequency resolution provided by CoRoT and *Kepler*. We note that, on a low frequency range ($0 < \nu/\nu_{\rm max} < 1.05$), the Kjeldsen et al. (2008) power law (calibrated on this reduced range) gives equivalent results. Then the Kjeldsen et al. (2008) power law calibrated on the whole range of frequency and the purely cubic correction proposed by Ball & Gizon (2014) are the worst performer with remaining mean frequency differences of the order of few μHz. When applying those corrections on frequency spectra including mixed-modes, only the empirical corrections BG1 and BG2 proposed by Ball & Gizon (2014) and the modified S15E where we added a factor of $1/E$ improve the mean frequency dispersion. Only S15E and BG2 leave a satisfying root-mean dispersion of the order of the CoRoT and *Kepler* frequency resolution.

Therefore, we derived prescriptions for the fitting parameters of those radial modes correction empirical models as functions of $\log \Delta\nu$, $\log T_{\rm eff}$, $\log g$ and $\log \kappa$ which are quantities easily computed by 1D stellar evolution model. The next step will be to test our prescriptions against observed frequency spectrum in order to determine their degree of accuracy. We will focus on this in a furture work.

Finally, we only considered in this article the issue of structural effects. However, other effects such as non-adiabaticity effects may also play a non-negligible role in the propagation of acoustic waves in the surface layers. This will be studied in a forthcoming paper.

Acknowledgements. L.M. thanks Dr C. Pinçon for many interesting discussions. H.G.L. acknowledges financial support by the Sonderforschungsbereich SFB 881 "The Milky Way System" (sub-projects A4) of the German Research Foundation (DFG).

References

Anders, F., Chiappini, C., Rodrigues, T. S., et al. 2017, A&A, 597, A30
Asplund, M., Grevesse, N., & Sauval, A. J. 2005, in Cosmic Abundances as Records of Stellar Evolution and Nucleosynthesis, eds. T. R. Barnes, III, & F. N. Bash, ASP Conf. Ser., 336, 25
Auvergne, M., Bodin, P., Boisnard, L., et al. 2009, A&A, 506, 411
Baglin, A., Auvergne, M., Barge, P., et al. 2006, in The CoRoT Mission Pre-Launch Status – Stellar Seismology and Planet Finding, eds. M. Fridlund, A. Baglin, J. Lochard, & L. Conroy, ESA SP, 1306, 33
Ball, W. H., & Gizon, L. 2014, A&A, 568, A123
Ball, W. H., & Gizon, L. 2017, A&A, 600, A128
Ball, W. H., Beeck, B., Cameron, R. H., & Gizon, L. 2016, A&A, 592, A159
Balmforth, N. J. 1992, MNRAS, 255, 603
Balmforth, N. J., Gough, D. O., & Merryfield, W. J. 1996, MNRAS, 278, 437
Bedding, T. R., Kjeldsen, H., Campante, T. L., et al. 2010, ApJ, 713, 935
Böhm-Vitense, E. 1958, Z. Astrophys., 46, 108
Borucki, W. J., Koch, D., Basri, G., et al. 2010, Science, 327, 977
Chaplin, W. J., & Miglio, A. 2013, ARA&A, 51, 353
Christensen-Dalsgaard, J. 2011, Adiabatic Oscillation Package (ADIPACK), Astrophysics Source Code Library
Christensen-Dalsgaard, J., & Thompson, M. J. 1997, MNRAS, 284, 527
Dziembowski, W. A., Paterno, L., & Ventura, R. 1988, A&A, 200, 213
Freytag, B., Steffen, M., Ludwig, H.-G., et al. 2012, J. Comput. Phys., 231, 919
Goldreich, P., Murray, N., Willette, G., & Kumar, P. 1991, ApJ, 370, 752
Gough, D. O. 1990, in Progress of Seismology of the Sun and Stars, eds. Y. Osaki, & H. Shibahashi (Berlin: Springer Verlag), Lect. Notes Phys., 367, 283
Grevesse, N., & Sauval, A. J. 1998, Space Sci. Rev., 85, 161
Hekker, S., & Christensen-Dalsgaard, J. 2017, A&ARv, 25, 1
Houdek, G., Trampedach, R., Aarslev, M. J., et al. 2017, MNRAS, 464, L124
Iglesias, C. A., & Rogers, F. J. 1996, ApJ, 464, 943
Jørgensen, A. C. S., Weiss, A., Mosumgaard, J. R., Silva-Aguirre, V., & Sahlholdt, C. L. 2017, MNRAS, 472, 3264
Kallinger, T., Gruberbauer, M., Guenther, D. B., Fossati, L., & Weiss, W. W. 2010, A&A, 510, A106
Kjeldsen, H., & Bedding, T. R. 1995, A&A, 293, 87
Kjeldsen, H., Bedding, T. R., & Christensen-Dalsgaard, J. 2008, ApJ, 683, L175
Kupka, F., & Muthsam, H. J. 2017, Living Rev. Comput. Astrophys., 3, 1
Lebreton, Y., & Goupil, M. J. 2014, A&A, 569, A21
Lebreton, Y., Goupil, M. J., & Montalbán, J. 2014, EAS Pub. Ser., 65, 177
Libbrecht, K. G., & Woodard, M. F. 1990, in Observations of Solar Cycle Variations in Solar *p*-mode Frequencies and Splittings (Berlin, Heidelberg: Springer), Lect. Notes Phys., 145
Ludwig, H.-G., Caffau, E., Steffen, M., et al. 2009, Mem. Soc. Astron. It., 80, 711
Magic, Z., & Weiss, A. 2016, A&A, 592, A24
Marques, J. P., Goupil, M. J., Lebreton, Y., et al. 2013, A&A, 549, A74
Metcalfe, T. S., Creevey, O. L., & Christensen-Dalsgaard, J. 2009, ApJ, 699, 373
Michel, E., Baglin, A., Auvergne, M., et al. 2008, Science, 322, 558
Morel, P. 1997, A&AS, 124, 597
Piau, L., Collet, R., Stein, R. F., et al. 2014, MNRAS, 437, 164
Pinsonneault, M. H., Elsworth, Y., Epstein, C., et al. 2014, ApJS, 215, 19
Rogers, F. J., & Nayfonov, A. 2002, ApJ, 576, 1064
Rosenthal, C. S., Christensen-Dalsgaard, J., Houdek, G., et al. 1995, Helioseismology, 376, 459
Rosenthal, C. S., Christensen-Dalsgaard, J., et al. 1999, A&A, 351, 689
Roxburgh, I. W., & Vorontsov, S. V. 2003, A&A, 411, 215
Samadi, R., Georgobiani, D., Trampedach, R., et al. 2007, A&A, 463, 297
Samadi, R., Belkacem, K., Goupil, M. J., et al. 2008, A&A, 489, 291
Samadi, R., Belkacem, K., Ludwig, H.-G., et al. 2013, A&A, 559, A40
Serenelli, A., Johnson, J., Huber, D., et al. 2017, ApJS, 233, 23
Silva-Aguirre, V., Lund, M. N., Antia, H. M., et al. 2017, ApJ, 835, 173
Sonoi, T., Samadi, R., Belkacem, K., et al. 2015, A&A, 583, A112
Sonoi, T., Belkacem, K., Dupret, M.-A., et al. 2017, A&A, 600, A31
Trampedach, R. 1997, Master's Thesis, Aarhus University
Trampedach, R., Aarslev, M. J., Houdek, G., et al. 2017, MNRAS, 466, L43
Unno, W., Osaki, Y., Ando, H., Saio, H., & Shibahashi, H. 1989, Nonradial Oscillations of Stars (University of Tokyo Press)

Appendix A: Derivation of the scaling relation Eq. (4)

We start from Eq. (3). After Christensen-Dalsgaard & Thompson (1997), we have

$$\begin{aligned}\tilde{K}^{n\ell}_{c^2,v} &\simeq 0\\ \tilde{K}^{n\ell}_{v,c^2} &= \omega^{-2}\left(\int_0^M \xi_{\rm r}^2 {\rm d}m\right)^{-1}\left(\frac{{\rm d}\xi_{\rm r}}{{\rm d}r}\right)^2 4\pi r^2\rho c_{\rm s}^2,\end{aligned} \tag{A.1}$$

where $\omega = 2\pi\nu$ and $\xi_{\rm r}$ are respectively the angular frequency and the radial displacement of the mode, $c_{\rm s}$ is the sound speed and M and R are respectively the total mass and the total radius of the star.

The first term in parentheses in the expression of $\tilde{K}^{n\ell}_{v,c^2}$ is the inertia of a mode:

$$\mathcal{I} \simeq \int_0^M \xi_{\rm r}^2 {\rm d}m = \int_0^R \xi_{\rm r^2} 4\pi r^2\rho {\rm d}r. \tag{A.2}$$

Using a first-order expansion, we can write the radial displacement as (e.g. Unno et al. 1989):

$$\xi_{\rm r}(r) \simeq A\rho^{-1/2}c_{\rm s}^{-1/2}r^{-1}\cos\left(\omega\int_0^r \frac{{\rm d}r'}{c_{\rm s}} - \zeta\right), \tag{A.3}$$

where A is a constant and ζ is a phase factor. Further inserting Eq. (A.3) into Eq. (A.2) leads to

$$\mathcal{I} = \int_0^R 4\pi A^2\cos^2\left(\omega\int_0^{\rm R}\frac{{\rm d}r'}{c_{\rm s}} - \zeta\right)\frac{{\rm d}r}{c_{\rm s}}. \tag{A.4}$$

Averaging the cosine term gives $1/2$ and then simply

$$\mathcal{I} = 2\pi A^2\int_0^R \frac{{\rm d}r}{c_{\rm s}} = \frac{\pi A^2}{\Delta\nu}, \tag{A.5}$$

with $\Delta\nu$ defined by $\Delta\nu = \left(2\int_0^R {\rm d}r/c_{\rm s}\right)^{-1}$. Then, $\tilde{K}^{nl}_{v,c^2}$ reads

$$\tilde{K}^{n\ell}_{v,c^2} = \frac{\omega^{-2}\Delta\nu}{\pi A^2}\left(\frac{{\rm d}\xi_{\rm r}}{{\rm d}r}\right)^2 4\pi r^2\rho c_{\rm s}^2. \tag{A.6}$$

Yet, $({\rm d}\xi_{\rm r}/{\rm d}r)^2 \simeq k_{\rm r}^2\xi_{\rm r}^2 = \omega^2\xi_{\rm r}^2/c_{\rm s}^2$. Then,

$$\begin{aligned}\tilde{K}^{n\ell}_{v,c^2} &= \frac{\omega^{-2}\Delta\nu}{\pi A^2}\frac{\omega^2}{c_{\rm s}^2}4\pi r^2\rho c_{\rm s}^2\xi_{\rm r}^2\\ &= \frac{4\Delta\nu}{A^2}r^2\rho A^2\rho^{-1}c_{\rm s}^{-1}r^{-2}\cos^2\left(\omega\int_0^{\rm r}\frac{{\rm d}r'}{c_{\rm s}} - \zeta\right),\end{aligned} \tag{A.7}$$

where the last line was obtained by replacing ξ_r^2 by its expression. Finally, by simplifying this expression we obtain:

$$\tilde{K}^{n\ell}_{v,c^2} \simeq \frac{2\Delta\nu}{c_{\rm s}}\cos^2\left(\omega\int_0^{\rm r}\frac{{\rm d}r'}{c_{\rm s}} - \zeta\right). \tag{A.8}$$

Eventually, inserting Eq. (A.8) into Eq. (3), approximating the cosine by $1/2$ as in (A.5) and using Eq. (19) from Rosenthal & Christensen-Dalsgaard (1999):

$$\int_0^R \frac{\delta_m v}{v}\frac{{\rm d}r}{c_{\rm s}} \simeq \frac{\Delta r}{2c_{\rm s,ph}}, \tag{A.9}$$

with $c_{\rm s,ph}$ the sound speed at the photosphere, we obtain the expression of the amplitude of the surface effect proposed in Rosenthal & Christensen-Dalsgaard (1999)

$$\frac{\delta\nu}{\nu} \simeq \frac{\Delta\nu\Delta r}{c_{\rm s,ph}}. \tag{A.10}$$

Appendix B: Fitting coefficients

In Table B.1 we gather the values of the fitting parameters introduced in Eqs. (14), (15), (16), and (18) used in order to perform the fits shown in Fig. 5 and toderive the coefficients for the prescriptions given in Table 2.

Table B.1. Fitting parameters of K08, K08r, S15, BG1, and BG2.

	K08		K08r		S15		BG1	BG2	
Model	$\lvert a\rvert$	b	$\lvert a\rvert$	b	$\lvert\alpha/2\rvert$	β	$\lvert a_{3,\mathrm{BG1}}\rvert$	$\lvert a_{-1,\mathrm{BG2}}\rvert$	$\lvert a_{3,\mathrm{BG2}}\rvert$
Cp05	9.19×10^{-3}	1.55	1.06×10^{-2}	2.17	1.01×10^{-2}	2.98	-9.66×10^{-12}	-7.99×10^{-12}	-6.01×10^{-12}
Fp05	7.13×10^{-3}	1.43	9.66×10^{-3}	2.74	7.90×10^{-3}	3.03	-8.03×10^{-12}	-7.98×10^{-12}	-5.17×10^{-12}
Jp05	5.64×10^{-3}	1.64	7.30×10^{-3}	2.95	6.32×10^{-3}	3.56	-6.94×10^{-12}	-7.23×10^{-12}	-4.31×10^{-12}
Lp05	4.79×10^{-3}	1.5	6.03×10^{-3}	2.75	5.33×10^{-3}	3.36	-6.03×10^{-12}	-8.41×10^{-12}	-3.38×10^{-12}
Op05	1.63×10^{-3}	1.74	1.98×10^{-3}	4	1.80×10^{-3}	5.23	-3.30×10^{-12}	-4.03×10^{-12}	-2.08×10^{-12}
Am00	2.05×10^{-3}	1.82	2.39×10^{-3}	4.1	2.27×10^{-3}	6	-1.24×10^{-12}	-1.01×10^{-12}	-9.19×10^{-13}
Bm00	9.36×10^{-3}	1.35	1.14×10^{-2}	2.12	1.02×10^{-2}	2.65	-4.66×10^{-12}	-4.15×10^{-12}	-2.96×10^{-12}
Cm00	8.93×10^{-3}	1.49	1.12×10^{-2}	2.51	9.96×10^{-3}	3.09	-1.12×10^{-11}	-8.32×10^{-12}	-7.99×10^{-12}
Dm00	6.66×10^{-3}	1.43	8.58×10^{-3}	2.65	7.40×10^{-3}	3.16	-4.19×10^{-12}	-3.92×10^{-12}	-2.84×10^{-12}
Fm00	7.26×10^{-3}	1.5	9.54×10^{-3}	2.82	8.08×10^{-3}	3.29	-1.03×10^{-11}	-9.16×10^{-12}	-7.00×10^{-12}
Gm00	1.41×10^{-2}	1.77	1.53×10^{-2}	2	1.47×10^{-2}	2.85	-9.66×10^{-11}	-6.73×10^{-11}	-4.44×10^{-11}
Hm00	4.61×10^{-3}	1.52	5.76×10^{-3}	2.93	5.11×10^{-3}	3.59	-3.63×10^{-12}	-3.53×10^{-12}	-2.42×10^{-12}
Im00	1.62×10^{-3}	2.02	1.90×10^{-3}	5.5	1.78×10^{-3}	8.09	-8.51×10^{-13}	-6.08×10^{-13}	-6.50×10^{-13}
Jm00	3.06×10^{-3}	1.88	3.88×10^{-3}	4.54	3.40×10^{-3}	5.75	-5.79×10^{-12}	-4.12×10^{-12}	-4.30×10^{-12}
Km00	9.69×10^{-3}	1.5	1.32×10^{-2}	2.79	1.08×10^{-2}	3.13	-7.23×10^{-11}	-6.07×10^{-11}	-4.88×10^{-11}
Mm00	6.61×10^{-3}	1.53	8.45×10^{-3}	2.8	7.35×10^{-3}	3.36	-6.35×10^{-11}	-6.43×10^{-11}	-4.03×10^{-11}
Em05	2.41×10^{-3}	1.7	2.92×10^{-3}	3.43	2.68×10^{-3}	4.38	-1.09×10^{-12}	-1.20×10^{-12}	-6.75×10^{-13}
Fm05	7.00×10^{-3}	1.42	9.11×10^{-3}	2.59	7.71×10^{-3}	3	-1.02×10^{-11}	-1.16×10^{-11}	-5.92×10^{-12}
Gm05	1.03×10^{-2}	1.51	1.34×10^{-2}	2.47	1.12×10^{-2}	2.83	-7.51×10^{-11}	-6.21×10^{-11}	-4.34×10^{-11}
Im05	1.60×10^{-3}	2.45	1.79×10^{-3}	5.29	1.97×10^{-3}	7.72	-1.15×10^{-12}	-3.76×10^{-13}	-1.02×10^{-12}
Jm05	3.44×10^{-3}	1.67	4.25×10^{-3}	3.52	3.82×10^{-3}	4.38	-7.33×10^{-12}	-6.72×10^{-12}	-4.98×10^{-12}
Km05	1.16×10^{-2}	1.38	1.41×10^{-2}	2.15	1.27×10^{-2}	2.73	-1.03×10^{-10}	-1.15×10^{-10}	-5.85×10^{-11}
Mm05	4.55×10^{-3}	1.7	5.76×10^{-3}	3.38	5.09×10^{-3}	4.1	-5.81×10^{-11}	-5.01×10^{-11}	-3.97×10^{-11}
Bm10	6.10×10^{-3}	1.37	7.93×10^{-3}	2.48	6.64×10^{-3}	2.77	-3.21×10^{-12}	-3.59×10^{-12}	-1.78×10^{-12}
Am10	2.45×10^{-3}	2.49	2.56×10^{-3}	4.79	3.04×10^{-3}	7.68	-4.00×10^{-12}	-7.97×10^{-13}	-3.72×10^{-12}
Cm10	8.64×10^{-3}	1.41	1.13×10^{-2}	2.57	9.51×10^{-3}	2.95	-1.11×10^{-11}	-1.11×10^{-11}	-6.83×10^{-12}
Fm10	5.89×10^{-3}	1.54	7.47×10^{-3}	2.96	6.55×10^{-3}	3.57	-1.24×10^{-11}	-1.11×10^{-11}	-8.41×10^{-12}
Gm10	1.48×10^{-2}	1.36	1.89×10^{-2}	2.3	1.64×10^{-2}	2.76	-1.04×10^{-10}	-7.87×10^{-11}	-7.35×10^{-11}
Km10	1.04×10^{-2}	1.58	1.23×10^{-2}	2.54	1.15×10^{-2}	3.4	-1.11×10^{-10}	-8.96×10^{-11}	-7.59×10^{-11}

Notes. Coefficients a, α, $a_{3,\mathrm{BG1}}$, $a_{-1,\mathrm{BG2}}$ and $a_{3,\mathrm{BG2}}$ are all negative.

Appendix C: Root-mean frequency differences after correction

In Table C.1 we gather the values of the root-mean frequency differences $\nu_{\max}\sqrt{\mathcal{D}/N}$ of radial modes after correction for each empirical law shown in Fig. 6.

Table C.1. Root-mean frequency differences $\nu_{\max}\sqrt{\mathcal{D}/N}$ [μHz] of radial modes after correction for each empirical law K08, K08r, S15, BG1, and BG2 and for each model.

	UC	K08	K08r	S15	BG1	BG2
Cp05	9.11	1.4	1.03	0.808	2.83	0.398
Fp05	7.99	1.28	0.443	0.675	2.39	0.26
Jp05	6.5	0.931	0.347	0.365	1.87	0.279
Lp05	5.98	0.917	0.311	0.369	1.95	0.308
Op05	2.3	0.456	0.0371	0.175	0.635	0.158
Am00	7.49	1.63	0.249	0.726	1.45	0.272
Bm00	16.8	2.27	1.06	1.23	5.15	1.36
Cm00	9.85	1.42	0.692	0.806	2.56	0.719
Dm00	13.4	2	0.709	0.848	3.66	1.02
Fm00	8.29	1.3	0.455	0.562	2.22	0.474
Gm00	3.47	0.437	0.432	0.306	1.26	0.163
Hm00	9.6	1.57	0.283	0.667	2.48	0.553
Im00	6.82	1.49	0.161	0.419	1.28	0.567
Jm00	3.78	0.822	0.195	0.334	0.8	0.313
Km00	3.5	0.534	0.21	0.267	0.974	0.112
Mm00	2.53	0.39	0.14	0.163	0.728	0.1
Em05	8.88	1.69	0.186	0.761	2.36	0.337
Fm05	7.7	1.29	0.517	0.657	2.48	0.475
Gm05	3.17	0.504	0.205	0.305	1.02	0.146
Im05	7.48	1.05	0.181	0.551	0.691	0.361
Jm05	4.18	0.805	0.0858	0.36	1.01	0.17
Km05	4.19	0.62	0.392	0.329	1.42	0.388
Mm05	1.78	0.301	0.0532	0.117	0.432	0.0624
Bm10	10.7	1.68	0.428	1.03	3.6	0.791
Am10	10.1	1.38	0.219	0.89	0.558	0.229
Cm10	9.3	1.55	0.59	0.838	2.85	0.454
Fm10	6.77	1.16	0.333	0.511	1.72	0.308
Gm10	5.29	0.727	0.32	0.388	1.46	0.478
Km10	3.82	0.544	0.245	0.2	0.975	0.193

Notes. UC denotes $\nu_{\max}\sqrt{\mathcal{D}/N}$ for uncorrected frequencies.

Chapter 4

Observational constraints on rotation

Mes nuits blanches ne sont pas blanches
À peine clairsemées d'étoiles
Petits trous dans la toile étanche
Tristes Strass sur le voile

Pomme, *Ceux qui rêvent*

Contents

In the three previous chapters, I have presented the standard modelling of stellar-structure and angular momentum transport as well as the key concepts of rotating asteroseismology. I expose in this chapter the main observations that plead for a complete reappraisal of the modelling of rotation. My PhD work focuses on the modelling and theoretical aspect of the angular momentum transport problem. However, theory should never lose sight of experimental and observational facts. I introduce this Chapter with the main methods and instruments that are used today to infer direct or indirect constraints on stellar rotation. Then I show the principal results on the rotation of the Sun and for other stars with different evolutionary status.

4.1 Methods and instruments

4.1.1 Methods

For the majority of stars, the only information we know about their rotation is their surface rotation velocity. In their pioneering work, Struve & Elvey (1931) proposed to use the Doppler broadening induced by rotation on the many absorption lines produced by elements at the stellar atmosphere to measure surface rotation. On the side of the star coming toward the observer, lines are blue-shifted and on the side moving away, lines are red-shifted. The measured Doppler broadening is the result of the projected equatorial velocity onto the line of sight: $v \sin i$, with the angle i between the rotation axis and the line of sight. For instance, a star seen pole-on will not have its absorption lines Doppler-shifted and no rotation measurement can be made. The $v \sin i$ have been measured for a large number of stars, assuming a uniform distribution of the orientation of rotation axis. Doing so allows astronomers to retrieve a distribution of the absolute surface velocities, not only the projected one (e.g. Hill, 1995; Royer et al., 2002; Zorec et al., 2017; Houdebine et al., 2016).

The $v \sin i$ measurement, for an unresolved star, gathers the signal emitted by the whole surface and does not allow physicists to measure differential rotation. However, the presence of an inhomogeneity can locally change the emission properties of the surface. Such an inhomogeneity can be caused by the passage of a spot or a change in chemical abundances, which enhances or reduces local stellar emission. If this local enhancement or reduction is strong enough, it produces visible variations of the total signal emitted by the star. The distortion depends on the intrinsic characteristic of the inhomogeneity and on its location on the surface. This location cannot be determined by only one observation. Yet, the star being in rotation, the signal perturbation will move from the blue-side of the Doppler broadening to the red side. Therefore, by studying the signal time-series, one can extract the stellar rotation velocity at the very location of the inhomogeneity. For a large number of inhomogeneities located at different latitudes, the latitudinal rotation profile can be determined (Kochukhov, 2016).

If, in addition, the star is able to maintain a (strong) magnetic field, the light emitted by a star is polarized. Its polarization state can be decomposed into four Stokes coefficients, each coefficient carrying specific information about the magnetic field characteristics (modulus, magnetic field vectors projected on the line of sight, etc.). Magnetization of the emission zone causes the so-called Zeeman effect, *i.e.* line splitting or broadening. The Zeeman effect preferably produces circular rather than a linear polarization (about 10 times more). The former is the one providing information on the magnetic fields vectors. Zeeman-Doppler imaging allows the observer to reconstruct the magnetic field morphology, even tiny details such as spots, and the modulation of the circular polarization reveals the effect rotation (Babcock, 1947; Semel, 1989; Kochukhov, 2016).

We have described the information that can be gleaned from spectroscopy and spectropolarimetry on the surface rotation of the stars. In order to learn about their interior rotation profile we shall turn to asteroseismology. We have seen in Chapter 3, that the general oscillation equations in a non-rotating star. Here, we assume the star is slowly rotating, the effect of the deformation due to the centrifugal acceleration is small compared to the effect of the Coriolis acceleration. Therefore, in Eq. (3.25), the term $-(\boldsymbol{\xi} \cdot \boldsymbol{\nabla}\Omega^2) r \sin\theta \mathbf{e}_\mathrm{s}$ is neglected and the momentum conservation equation reads

$$-\rho\hat{\omega}^2\boldsymbol{\xi} + 2i\rho\hat{\omega}\boldsymbol{\Omega}\times\boldsymbol{\xi} = \frac{\rho'}{\rho}\boldsymbol{\nabla}p - \boldsymbol{\nabla}p' - \rho\boldsymbol{\nabla}\phi'. \tag{4.1}$$

In order to avoid confusions in the forthcoming developments, I have dropped the 0 subscripts for equilibrium quantities. I recall that here, $\hat{\omega} = \omega + m\Omega$. However, ω is not the same

frequency as in the non-rotating case because ω verifies a different system of equations. In order to clarify, I note $\omega_0 = \omega_{n\ell}$ the angular frequency in case of no rotation and $\omega_m = \omega_{n\ell m}$ the angular frequency in the corotating frame of a star. Therefore, we will now use $\hat{\omega}_m = \omega_m + m\Omega$ instead of $\hat{\omega}$.

We follow the derivation of Goupil (2011). First, we introduce the notation $\omega_m = \omega_0 + \omega_{1,m}$ ($n\ell$ are omitted) with $\omega_{1,m} \ll \omega_m, \omega_0$, and $\boldsymbol{\xi} = \boldsymbol{\xi}_0 + \boldsymbol{\xi}_1$ with $\boldsymbol{\xi}_1 \ll \boldsymbol{\xi}, \boldsymbol{\xi}_0$. Eigenfunctions $\boldsymbol{\xi}_0$ and $\boldsymbol{\xi}_1$ can be decomposed in spherical harmonics. Therefore, abbreviating $n\ell$ by k, $\boldsymbol{\xi}_{1,k}$ can be written as a linear combination of other 0-th order solution $\boldsymbol{\xi}_{0,i\neq k}$ (Ouazzani, 2011):

$$\boldsymbol{\xi}_{1,k} = \sum_{i\neq k} a_k^i \boldsymbol{\xi}_{0,i}. \tag{4.2}$$

In addition, since the fluctuations of density, pressure and gravitational potential can also be perturbed in the same way, we denote with $\mathcal{L}_0(Y_\ell^m) = \mathcal{L}(\boldsymbol{\xi}_0)$ the right hand side of (4.1):

$$\mathcal{L}_0(Y_\ell^m) = \mathcal{L}(\boldsymbol{\xi}_0) = \frac{\rho'}{\rho_0}\boldsymbol{\nabla} p_0 - \boldsymbol{\nabla} p' - \rho_0 \boldsymbol{\nabla}\phi' \quad \text{and} \quad \mathcal{L}(\boldsymbol{\xi}_0) = -\rho\hat{\omega}_0^2 \boldsymbol{\xi}_0, \tag{4.3}$$

and now, $\mathcal{L} = \mathcal{L}_0 + \mathcal{L}_1$.

Injecting all these quantities into Eq. (4.1) and keeping only the 1st-order terms in Ω yields:

$$-\rho\left[2\omega_0(\omega_{1,m} + m\Omega)\boldsymbol{\xi}_0 + \omega_0^2\boldsymbol{\xi}_1\right] = \mathcal{L}(\boldsymbol{\xi}_1) - 2i\rho\omega_0\boldsymbol{\Omega}\times\boldsymbol{\xi}_0, \tag{4.4}$$

where we used the second equation in Eq. (4.3). We now project onto $\boldsymbol{\xi}_0$. To that end, we define the scalar product:

$$\langle \mathbf{a}|\mathbf{b}\rangle = \int_{\mathcal{V}} \mathbf{a}^* \cdot \mathbf{b}\,\mathrm{d}^3 r. \tag{4.5}$$

with $\mathcal{V}$ the volume of the star and $\cdot^*$ being the complex conjugate. It can be shown that $\langle\boldsymbol{\xi}_0|\boldsymbol{\xi}_1\rangle = 0$, therefore

$$-\left\langle \boldsymbol{\xi}_0 | \rho\left[2\omega_0(\omega_{1,m} + m\Omega)\boldsymbol{\xi}_0 + \omega_0^2\boldsymbol{\xi}_1\right]\right\rangle = \langle\boldsymbol{\xi}_0|\mathcal{L}(\boldsymbol{\xi}_1) - 2i\rho\omega_0\boldsymbol{\Omega}\times\boldsymbol{\xi}_0\rangle\,. \tag{4.6}$$

It follows that,

$$\omega_{1,m}\int_{\mathcal{V}} \rho\boldsymbol{\xi}_0^*\boldsymbol{\xi}_0\mathrm{d}^3 r = \int_{\mathcal{V}} \rho\boldsymbol{\xi}_0^*\left(i\boldsymbol{\Omega}\times\boldsymbol{\xi}_0 - m\Omega\boldsymbol{\xi}_0\right)\mathrm{d}^3 r. \tag{4.7}$$

In above equation, we define two quantities I_0 and R as

$$I_0 = \int_{\mathcal{V}} \rho\boldsymbol{\xi}_0^*\boldsymbol{\xi}_0\mathrm{d}^3 r \quad \text{and} \quad R = \int_{\mathcal{V}} \rho\boldsymbol{\xi}_0^*\left(i\boldsymbol{\Omega}\times\boldsymbol{\xi}_0 - m\Omega\boldsymbol{\xi}_0\right)\mathrm{d}^3 r, \tag{4.8}$$

where I_0 is called the *mode inertia*[1]. Developing R gives (Aerts et al., 2010)

$$R = i\int_{\mathcal{V}} \rho\Omega\boldsymbol{\xi}_0^*\left[-\xi_\mathrm{h}\frac{\partial Y_\ell^m}{\partial\varphi}\mathbf{e}_r - \xi_\mathrm{h}\frac{\cos\theta}{\sin\theta}\frac{\partial Y_\ell^m}{\partial\varphi}\mathbf{e}_\theta + \left(\xi_r\sin\theta Y_\ell^m + \xi_\mathrm{h}\cos\theta\frac{\partial Y_\ell^m}{\partial\theta}\right)\mathbf{e}_\varphi\right]\mathrm{d}^3 r$$

[1]This term is also often referred to as the mode *moment of inertia*. This denomination seems quite improper because the moment of inertia is defined as the product of the mass with the square of the distance to the pivot point or to the rotation axis. In the definition of I_0, $\boldsymbol{\xi}_0$ is only the displacement from an equilibrium location, induced by the passage of an oscillation (in the case of no rotation). Nor can it be called the perturbed moment of inertia of the mode because if an element of fluid is displaced from $\mathbf{r}$ to $\mathbf{r} + \boldsymbol{\xi}_0$ by an oscillation, the perturbation of its moment of inertia with respect to its equilibrium moment of inertia is, at first order, $2\rho\mathbf{r}^*\boldsymbol{\xi}_0$.

$$
\begin{aligned}
& -m\int_{\mathcal{V}}\rho\Omega|\boldsymbol{\xi}_0|^2\mathrm{d}^3r \\
= \; & i\int_{\mathcal{V}}\rho\Omega\Bigg[-\xi_r^*\,Y_\ell^m|^*\,\xi_\mathrm{h}\frac{\partial Y_\ell^m}{\partial\varphi}-|\xi_\mathrm{h}|^2\frac{\cos\theta}{\sin\theta}\,\frac{\partial Y_\ell^m}{\partial\theta}\Big|^*\,\frac{\partial Y_\ell^m}{\partial\varphi}+\xi_\mathrm{h}^*\xi_r\,\frac{\partial Y_\ell^m}{\partial\varphi}\Big|^*\,Y_\ell^m \\
& +|\xi_\mathrm{h}|^2\frac{\cos\theta}{\sin\theta}\,\frac{\partial Y_\ell^m}{\partial\varphi}\Big|^*\,\frac{\partial Y_\ell^m}{\partial\theta}\Bigg]\mathrm{d}^3r-m\int_{\mathcal{V}}\rho\Omega|\boldsymbol{\xi}_0|^2\mathrm{d}^3r. \qquad (4.9)
\end{aligned}
$$

Useful relations concerning spherical harmonics are defined in (B.15). In particular, the φ-derivatives of the spherical harmonics are, $\partial Y_\ell^m/\partial\varphi = imY_\ell^m$ and $\partial\, Y_\ell^m|^*/\partial\varphi = -imY_\ell^m$. Thus, above expression of R becomes

$$
\begin{aligned}
R \;=\; & mc_{\ell m}^2\int_{\mathcal{V}}\rho\Omega\Bigg[|\xi_r|^2P_\ell^m(\cos\theta)^2+|\xi_\mathrm{h}|^2\left[\left(\frac{\mathrm{d}P_\ell^m}{\mathrm{d}\theta}\right)^2+\frac{m^2}{\sin^2\theta}P_\ell^m(\cos\theta)^2\right] \\
& -P_\ell^m(\cos\theta)^2\left[\xi_r^*\xi_\mathrm{h}+\xi_r\xi_\mathrm{h}^*\right]-2|\xi_\mathrm{h}|^2\frac{\cos\theta}{\sin\theta}P_\ell^m(\cos\theta)\frac{\mathrm{d}P_\ell^m}{\mathrm{d}\theta}\Bigg]\mathrm{d}^3r, \qquad (4.10)
\end{aligned}
$$

and the mode inertia is

$$
\begin{aligned}
I_0 \;=\; & \int_{\mathcal{V}}\rho\boldsymbol{\xi}_0^*\boldsymbol{\xi}_0\mathrm{d}^3r \\
= \; & c_{\ell m}^2\int_{\mathcal{V}}\rho\left\{|\xi_r|^2P_\ell^m(\cos\theta)^2+|\xi_\mathrm{h}|^2\left[\left(\frac{\mathrm{d}P_\ell^m}{\mathrm{d}\theta}\right)^2+\frac{m^2}{\sin^2\theta}P_\ell^m(\cos\theta)^2\right]\right\}\mathrm{d}^3r \qquad (4.11) \\
& . \qquad (4.12)
\end{aligned}
$$

Since we neglected centrifugal acceleration, the star is spherical. Therefore $\int_{\mathcal{V}}\mathrm{d}^3r = \int_0^\pi\int_0^{R_\star}\sin\theta r^2\mathrm{d}\theta\mathrm{d}r$ and I_0 further reduces to:

$$
\begin{aligned}
I_0 \;=\; & c_{\ell m}^2\int_0^\pi\int_0^{R_\star}\rho P_\ell^m(\cos\theta)^2\left(|\xi_r|^2+\ell(\ell+1)|\xi_\mathrm{h}|^2\right)r^2\sin\theta\mathrm{d}\theta\mathrm{d}r \\
= \; & c_{\ell m}^2\frac{2(\ell+|m|)!}{(2\ell+1)(\ell-|m|)!}\int_0^{R_\star}\rho\left(|\xi_r|^2+\ell(\ell+1)|\xi_\mathrm{h}|^2\right)r^2\mathrm{d}r, \qquad (4.13)
\end{aligned}
$$

where Eqs. (B.11) and (B.12) have been used. Until now, we have made no assumption on the angular velocity profile, except that Ω is small. From now on, we also assume a shellular rotation profile, which allows us to write

$$
\begin{aligned}
R =& mc_{\ell m}^2\int_0^\pi\int_0^{R_\star}\left[|\xi_r|^2+\ell(\ell+1)|\xi_\mathrm{h}|^2-(\xi_r^*\xi_\mathrm{h}+\xi_r\xi_\mathrm{h}^*)-|\xi_\mathrm{h}|^2\right]\rho\Omega P_\ell^m(\cos\theta)^2r^2\sin\theta\mathrm{d}\theta\mathrm{d}r \\
=& c_{\ell m}^2\frac{2(\ell+|m|)!}{(2\ell+1)(\ell-|m|)!}\int_0^{R_\star}\left[|\xi_r|^2+\ell(\ell+1)|\xi_\mathrm{h}|^2-(\xi_r^*\xi_\mathrm{h}+\xi_r\xi_\mathrm{h}^*)-|\xi_\mathrm{h}|^2\right]\rho\Omega r^2\mathrm{d}r. \qquad (4.14)
\end{aligned}
$$

Finally, the small change of frequency induced by a small rotation rate can be written

$$
\begin{aligned}
\omega_{1,m} \;=\; & \frac{R}{I_0}=m\frac{\displaystyle\int_0^{R_\star}\left[|\xi_r|^2+(\ell(\ell+1)-1)|\xi_\mathrm{h}|^2-(\xi_r^*\xi_\mathrm{h}+\xi_r\xi_\mathrm{h}^*)\right]\rho\Omega r^2\mathrm{d}r}{\displaystyle\int_0^{R_\star}\rho\left(|\xi_r|^2+\ell(\ell+1)|\xi_\mathrm{h}|^2\right)r^2\mathrm{d}r} \\
= \; & m\frac{R_{n\ell m}}{I_{n\ell m}}, \qquad (4.15)
\end{aligned}
$$

where $R_{n\ell m}$ and $I_{n\ell m}$ have been defined to follow standard notation (e.g. Aerts et al., 2010).

It is common to define the generalised rotational splitting $\delta\nu_{n\ell m}$ (or sometimes noted S_m; Goupil 2011) as

$$\delta\nu_{n\ell m} = \frac{\omega_{1,m} - \omega_{1,-m}}{2m} = \int_0^{R_\star} K_{n\ell m}(r)\Omega(r)\mathrm{d}r, \tag{4.16}$$

where $K_{n\ell m}$ is the rotational kernel:

$$K_{n\ell m}(r) = \frac{\left[|\xi_r|^2 + (\ell(\ell+1)-1)|\xi_\mathrm{h}|^2 - (\xi_r^*\xi_\mathrm{h} + \xi_r\xi_\mathrm{h}^*)\right]\rho r^2}{I_{n\ell m}}. \tag{4.17}$$

Obtaining the rotation profile from rotational splittings is done through so-called *inversion techniques*. We gave the expression of the rotational splitting for an angular velocity depending only on r. Let us move a step forward and assume that it has the same functional form in 2D:

$$\delta\nu_{n\ell m} = \int_0^R \int_0^\pi K_{n\ell m}(r,\theta)\Omega(r,\theta) r\mathrm{d}r\mathrm{d}\theta + \varepsilon_{n\ell m}, \tag{4.18}$$

where $\varepsilon_{n\ell m}$ is the measurement error on the rotational splitting and $K_{n\ell m}(r,\theta)$ is the rotational kernel of Eq. (4.17) in two dimensions. 2D inversion methods, such as the one developed by Schou et al. (1994), amounts to finding $\Omega(r,\theta)$ such that in Eq. (4.18), LHS equals RHS. More precisely, Schou et al. (1994) proposed to use a regularized least square method which enforces smoothness on the second derivatives of Ω. The quantity to minimize is:

$$\begin{aligned}\chi^2 \;=\; & \sum_{n\ell m} \frac{\left[\delta\nu_{n\ell m} - \int_0^R\int_0^\pi K_{n\ell m}(r,\theta)\Omega(r,\theta) r\mathrm{d}r\mathrm{d}\theta\right]^2}{\sigma^2_{n\ell m}} + \mu_r^2 \int_0^R\int_0^\pi f_r(r,\theta)\left(\frac{\mathrm{d}^2\Omega}{\mathrm{d}r^2}\right)^2 \mathrm{d}r\mathrm{d}\theta \\ & + \mu_\theta^2 \int_0^R\int_0^\pi f_\theta(r,\theta)\left(\frac{\mathrm{d}^2\Omega}{\mathrm{d}\theta^2}\right)^2 \mathrm{d}r\mathrm{d}\theta,\end{aligned} \tag{4.19}$$

where $\sigma_{n\ell m}$ is the standard deviation of the error affecting $\delta\nu_{n\ell m}$, μ_r and μ_θ are so-called *trade-off* parameters and are meant to control the accepted variation of the solution. Finally, f_r and f_θ are non-negative functions attributing a weight to different points. This quantity can easily be minimized using a least squares method to find Ω from rotation splittings.

4.1.2 Ground-based observations

The spectroscopic and spectropolarimetric observations are mainly realized with 4 spectropolarimeters. ESPADONS (Echelle SpectroPolarimetric Device for the Observation of Stars; Donati et al. 2006) and SPIROU (SpectroPolarimetre Infra Rouge; Artigau et al. 2014) installed at the 3.6m Canada-France-Hawaii Telescope (CFHT). NARVAL (Aurière, 2003) on the Bernard Lyot Telescope (TBL) at the Pic du Midi Observatory is a twin of ESPADONS and is designed to take over ESPADONS's nights of observations. Finally, HARPS (High Accuracy Radial Velocity Planet Searcher; Pepe et al. 2000) is installed on the ESO 3.6m telescope at La Silla.

Asteroseismology requires very long time series of stellar photometry or velocimetry/spectrometry, ideally up to several months. On Earth this is a complicated task with only one telescope except at the poles. In Earth's polar regions, the Sun is observable with astronomical conditions during uninterrupted weeks. For other stars, international consortia have built networks of telescopes capable of observing stars without interruption during a very long time. Observers take advantage of the powerful and large optics only possible in ground telescopes. However, they need to cope with atmospheric distortion, wind turbulence,

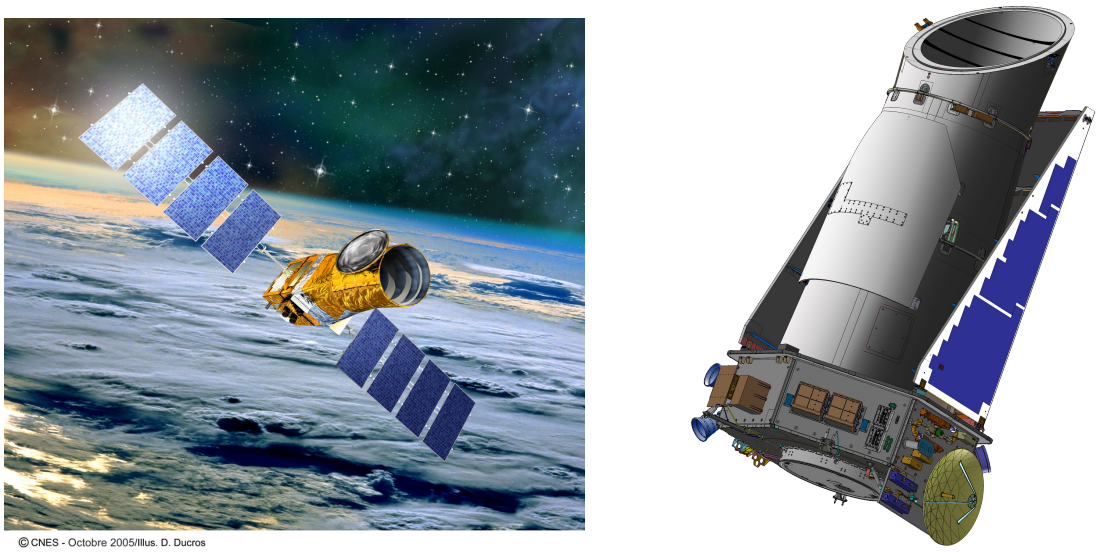

Figure 4.1: Artistic view of CoRoT (*left*) and *Kepler* (*right*)

filtering effect of the atmosphere, etc. Among those networks one can cite the Global Oscillation Network Group (GONG; Harvey et al. 1996) that counts 6 telescopes around the globe and its younger brother GONG++ that incorporates continuous magnetogram measurements (Hill et al., 2003); the Birmingham Solar Oscillation Network (BISON; Chaplin et al. 1996), also composed of 6 telescopes. These three networks are devoted only to the Sun, in complement of space-based operations. Finally the Stellar Oscillation Network Group (SONG; Grundahl et al. 2011) aims at observing stars other than the Sun, which is still under construction and have 3 telescopes at the moment.

4.1.3 Space-based observations

The availability of detailed constraints on stellar internal structure and rotation have made a big step forward with the advent of space-borne missions. The first mission launched into space, dedicated to the study of internal structure of the Sun using asteroseismology was SoHO (Solar and Heliospheric Observatory) launched in 1995 and still in activity today. SOHO takes on board two spectrometers, GOLF (Global Oscillations at Low Frequencies; Gabriel et al. 1995) and SOI-MDI (The Solar Oscillations Investigation - Michelson Doppler Imager; Scherrer et al. 1995) to measure small variations of velocity due to pressure modes in the outer envelope of the Sun. Velocity-measurement time series more than 24 years long are available for both these instruments and allow solar physicists to reach unprecedented precision on frequencies and on the solar internal structure inverted from them. In addition to helioseismic data, SOHO was also able to study the solar photosphere, chromosphere, corona and solar wind from different points of view: temperature, chemical composition, magnetic topology and intensity, density, etc. After SOHO, other satellites joined the armada, studying the Sun. The STEREO (Solar Terrestrial Relations Observatory; 2006) spacecrafts for stereoscopic imaging of, *i.e.* coronal mass ejection; SDO (Solar Dynamics Observatory; 2010) which studies the Sun's atmosphere and internal structure through imaging and helioseismology (velocity measurements). More recently launched, the Parker Solar Probe (2018) and Solar Orbiter (2020) will approach the Sun closely. They are mainly devoted to the study of the mechanisms of acceleration of the solar wind and its dynamics. Solar Orbiter will, in addition increase the inclination of its orbit in order to have a better view on the poles, regions of emanation of the fast solar wind.

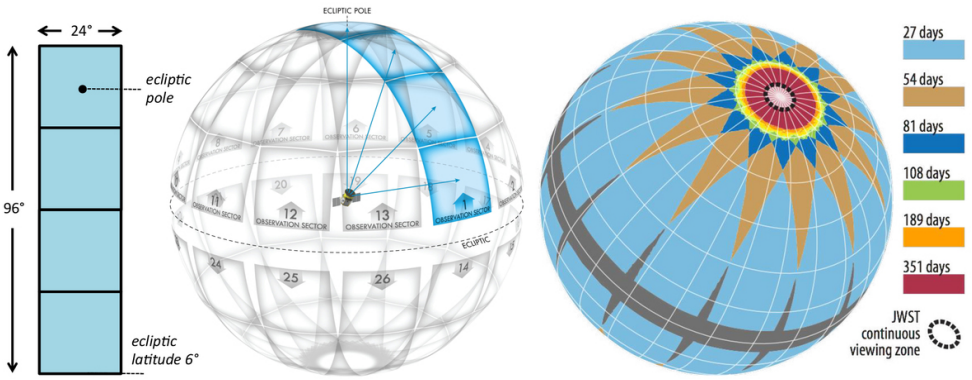

Figure 4.2: TESS field of view. Graph shows superimposition of each 26 sectors along the two years of TESS mission.

Vast and precise studies of the internal structure of other stars began with the space telescope CoRoT (Convection Rotation and Transits) originally devoted to the detection of stellar oscillations using photometry (Catala et al., 1995; Baglin et al., 2006; Michel et al., 2008) and secondarily extended to the exo-planetologists community during the development phase (Deleuil et al., 1997). The detection surface is paved with 4 CCD: two devoted to asteroseismology with an exposure time of 1 s, and two dedicated to finding exoplanets, with an exposure time of 32 s (faint stars are favoured in order to get a large number of targets for exoplanet hunting). These last two CCDs actually appeared to be well designed for detecting oscillations in RGB stars which oscillate much slower than MS stars. CoRoT observed fix regions of the sky during continuous periods of around 150 days (long runs) for detailed study of oscillating stars and for the detection of planets; and during periods of around 10 to 20 days (short runs) for exploratory programs. CoRoT measured its first light early in 2007 and was retired mid-2013, after twice the nominal duration.

Two years after CoRoT's first light, on march 2009, NASA's space telescope *Kepler* started operating. *Kepler* (Borucki et al., 2010) is equipped with 42 CCDs, read every 6.5 s and added-up to 59 s for short cadence targets and to 29.4 min for long cadence targets. During 4 years, from may 2009 to may 2013, *Kepler* stared at a 105 square degree region in Cygnus-Lyra. The mission was then further extended in degraded mode following the brake-down of two reaction wheels. The secondary mission, called *K2* takes advantage of the radiation pressure of solar photons to keep its orientation, but is forced to stare at regions near the ecliptic plane in order to maintain a symmetric pressure, and to change the region of interest every 83.5 days. The regions observed by *Kepler* are displayed in Fig. 4.4, right panel. As CoRoT, *Kepler*'s goal was to find exoplanets and measure stellar oscillation spectra. During its nominal mission, it observed around 200 000 stars with magnitudes ranging from 9 to 16. As I write these lines, *Kepler* found 2341 confirmed exoplanets and *K2* found 409 (among the 4274 exoplanets reported by the Encyclopédie des Planètes Extrasolaires[2]).

The last space-borne mission is TESS (Transiting Exoplanet Survey Satellite; Ricker et al. 2014). It was launched in April 2018 with the primary goal of measuring stellar oscillation spectra and detecting smaller exoplanets than *Kepler* did. In practice it needs to observe brighter stars. Contrary to *Kepler*, TESS has four on-board wide-angle camera which span a band of 24° in azimuth from pole to equator (actually the equator is not mapped, the field of view stops 6° above it) and stare at it for 27.4 days (two orbits around Earth). The field of view is represented in Fig. 4.2, on the left, on a sphere aligned with the ecliptic pole. After 27.4

[2] http://exoplanet.eu/

days of observations, the satellite rotates 28° and repeats the observations. After 13 periods of observation, TESS will have done a complete revolution around itself and mapped a whole hemisphere. It flips over and then maps the other hemisphere with 13 new sectors. Apart from scarce regions around the ecliptic plane, TESS will gather photometric data on all the celestial sphere for at least 27.4 days. Furthermore, after each rotation, some regions mapped by TESS superimpose (see Fig. 4.2, right part). The duration of observation will add-up for those regions, increasing the signal-to-noise ratio and the number of exoplanets discoverable. The mission has recently been extended for 2 years for a second full map if the sky. Up to now, 51 new exoplanets observed by TESS (at mid 2020[3]) have been confirmed, but more than 2 000 objects are suspected to host one or more exoplanets and are waiting for confirmation.

Apart from broad surveys, the advent of nanosatellites makes it possible to focus on a very limited number of stars. For instance, the constellation of nanosatellites BRITE (Bright-star Target Explorer; Weiss et al. 2014) is composed of 6 nanosatellites (actually one of them is not responding). They carry a 3 cm aperture telescope, with a blue filter for three of them and a red filter for other the three. Each telescope can see approximately 15 stars at the same time. As we will see later, multi-band photometry is crucial for mode identification. Although CoRoT supported three-band photometry, the BRITE constellation provides two-band photometry at a much cheaper cost. Furthermore, as BRITE is a constellation with redundant instruments, it allows continuous observations of targeted stars.

4.1.4 What for the future?

Concerning long photometric measurements, an ESA mission is being prepared for launch in 2026: PLATO (PLAnetary Transits and Oscillations of stars; Rauer et al. 2014). PLATO is constituted of 26 cameras: 2 fast cadence (2.5 s) cameras meant primarily to observe bright stars and 24 slow cadence cameras (25 s) for other stars. The slow cadence cameras are divided into 4 groups, each group pointing towards a slightly different direction. Fig. 4.4, left panel, represents these four fields of view. Due to overlapping, regions are seen not only by 6 cameras but by 12, 18 or 24. It is designed for a 6 years primary mission decomposed into two phases. First, PLATO will look at two regions for 2 years each. These regions have been chosen because they present a high density of solar-like stars. The duration of two years would allow astronomers to observe two transits of an exoplanet with an Earth-like orbit period. The next phase is called *step-and-stare*. PLATO will cover around half of the whole sky by staring at regions for up to 5 months.

Despite many claims of detection, there is no community consensus on the discovery of g-modes in Sun and even less in solar-like stars. The only detectable oscillations that can propagate in the radiative zone of these stars are from mixed-modes. The amplitude of perturbations generated by purely g-modes at the surface of the Sun is currently below the sensitivity of our instruments. However, with the recent detection of gravitational waves[4], old ideas have re-emerged. Gravity modes propagating inside the radiative zone of the Sun induce perturbations in the gravitational field. With space-borne interferometer LISA (Laser Interferometer Space Antenna; Amaro-Seoane et al. 2017; Baker et al. 2019) dedicated to the detection of very small amplitude gravitational waves, such tiny perturbations in the gravitational field could become measurable. Previous works have shown that, with the specifications of LISA known at the turn of the new millennium, amplitude of the order of $1 - 10$ mm s^{-1}

[3] https://tess.mit.edu/publications/

[4] Not to be confused with gravity waves. Gravity waves are waves for which the restoring force is the gravity. Gravitational waves are the propagation of a disturbance of the space-time. Their restoring force can be seen as the elasticity of space-time (Tenev & Horstemeyer, 2018)

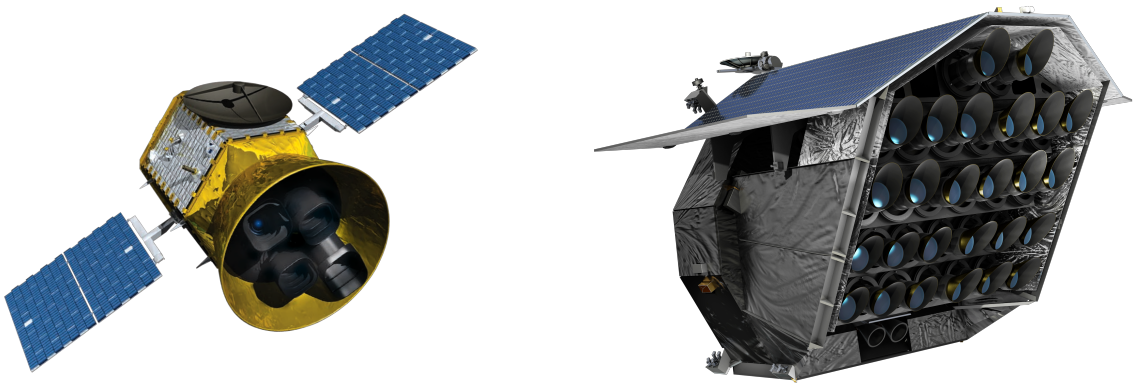

Figure 4.3: Artistic view of TESS (*left*) and PLATO (*right*)

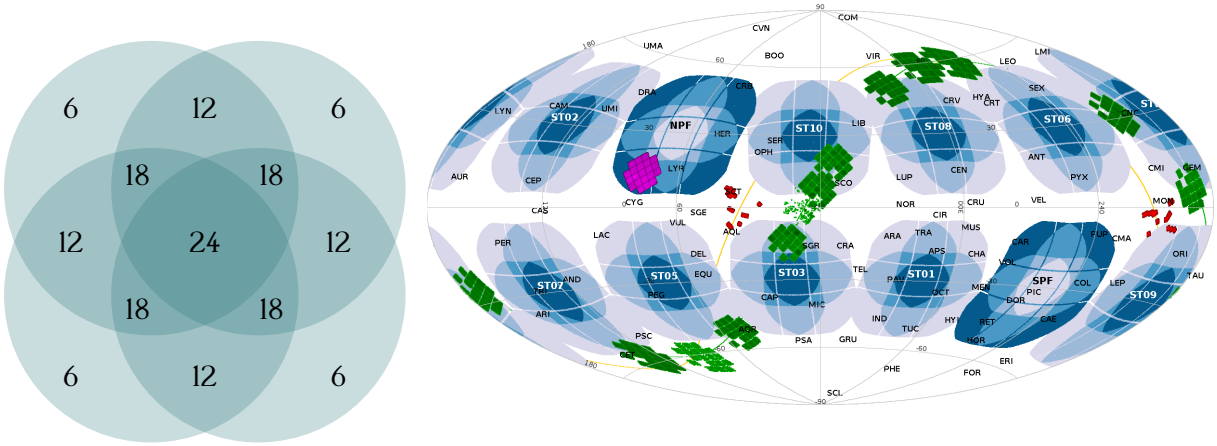

Figure 4.4: *left*: Field of view of the 4 groups of slow-cadence cameras. Each group points in a different direction separated by an angle of 9.2° with the telescope vertical axis. Numbers refer to the number cameras seeing the filled zones. *right*: PLATO fields of view are represented in dark blue for the first phase of the mission and light blue for the step-and-stare phase. For comparison, *Kepler*'s nominal mission field of view is shown in purple and K2 fields of view are represented in green. The difference in the shapes of those fields is due to the two dead CCDs. Finally, red rectangles show CoRoT's fields of view.

at the surface of the Sun would be detectable (Giampieri et al., 1998; Roxburgh et al., 2001). The studying of GOLF data has shown that the amplitude of velocity variations generated by g-modes at the surface of the Sun should be less than 10 mm s^{-1} which is not incompatible with LISA' sensitivity.

In the following I will first detail the observational constraints that we have on the Sun's rotation profile and in the next section I will focus on other stars.

4.2 Constraints on the Sun's rotation profile

4.2.1 From the surface to $0.4R_\odot$

The first evidence that the Sun was rotating came from the observation of sunspots drifting at its surface. Johannes Fabricius was the first in 1611 to systematically study the motions of those spots for few months and to propose that their apparent motion was due to rotation of

the Sun. Later, in 1630, Christoph Scheiner measured the equatorial surface rotation period to be of 27 days and noticed that the rotation speed was lower as he came nearer to the poles. This is the first evidence of a surface differential rotation. Nowadays, the surface solar rotation rate Ω_s is expressed in the following form (*e.g.* Schröter, 1985):

$$\Omega_\mathrm{s}(\theta) = A + B\sin^2\theta + C\sin^4\theta, \tag{4.20}$$

with θ the latitude and $A \simeq 14.1$ deg d^{-1}, $B \simeq -1.7$ deg d^{-1} and $C \simeq -2.3$ deg d^{-1}, which gives a period of rotation at the equator of $\simeq 25.5$ days and $\Omega_\mathrm{s} \simeq 14.1\ \mathrm{deg\,d^{-1}} = 1.64 \times 10^{-4}\ \mathrm{deg\,s^{-1}} = 0.248\ \mathrm{rad\,d^{-1}} = 2.868 \times 10^{-6}\ \mathrm{rad\,s^{-1}} \simeq 456$ nHz. In velocity, it gives $\simeq 1.98$ km s^{-1}. I give this value in various units because in the rest of this thesis, it will facilitate the comparison with stellar rotation rates that can be expressed in different physical units. At a latitude of $60°$, the rotation rate is $\Omega_\mathrm{s} \simeq 11.5\ \mathrm{deg\,d^{-1}} \simeq 370$ nHz, thus corresponding to a period of 31.2 days.

Using 15 days of discontinuous Doppler measurements of the surface of the Sun, Brown & Morrow (1987) were the first to determine a two-dimensional rotation profile of the Sun. They found that Ω varies in latitude and radii in the convective zone and then stays constant in the radiative zone, at least down to $0.4\ R_\odot$. This result was later refined with the continuous 144 days time series from the early measurements of MDI on board SOHO. Kosovichev & Schou (1997) detected latitudinal differential rotation below the surface of the Sun for the first time. In order to do that, they used the rotational splitting of the fundamental mode (f-mode: $n = 0$) for degrees ℓ in the range 120 to 250[5]. Fig. 4.5, left panel, taken from Kosovichev & Schou (1997) represents the measured rotation rate as a function of latitude at the surface and at a depth of $2 - 9$ Mm ($0.29 - 1.29\ \%R_\odot$) below the surface. This figure shows that the latitudinal differential rotation stays almost the same as we go just below the surface. Using the same data, the rotation rate profile at different latitudes are shown in Fig. 4.5, right panel, for the whole star (Schou & SOE Internal Rotation Team, 1998). At the very right of this graph, we recognize the same variation of the rotation rate with latitude near the surface as measured by Kosovichev & Schou (1997). Following the solid lines from right to left, we notice a distinct increase of the rotation rate at high latitudes and an decrease at low latitudes. For the rotation rate at 75°, we see between 0.9 and $0.95R_\odot$ a brusque increase. This was coined a "jet" of fast rotation by Schou & SOE Internal Rotation Team (1998). However, the jet was absent in the more recent inversions made, for instance, with GONG data (Howe et al., 2000) and it is now considered as an artefact induced by the MDI data analysis. As long as we go deeper, the $1-\sigma$ uncertainties increase but the inverted rotation rate at different latitudes do not overlap, until all measured rotation rates converges around $\simeq 0.7R_\odot$. This is the location of the tachocline, a region of transition between the convective and radiative region. From 0.7 and $0.3R_\odot$, the rotation rates at any latitude converge to a mean value around 440 nHz. More recent inversions reduced the dispersion on the inverted values and confirmed a solid rotation in this region (no r or θ gradients). From $0.3R_\odot$ to the centre, the 1σ uncertainties diverge and nothing can be said about this region. The modes propagating in this region are radial *p*-modes and *g*-modes. The former are not affected by rotation and measuring the rotational splitting of the latter would require at least detecting them, which we do not.

Stellar models did not always compare favourably with these rotation profiles. In his seminal paper, Zahn (1992) produces solar-like stellar models with shear-induced turbulence and wind-driven meridional circulation. However, these models end up with differential rotation in their radiative zones. By adding an additional AM transport mechanism, internal gravity waves (IGW; see Chapter 5), Talon & Zahn (1998) managed to obtain a nearly flat rotation profile for a solar

[5]The detection of such high degree oscillations is only possible with the Sun. For other stars, oscillations are usually detected with degrees ℓ up to 3 in the best cases.

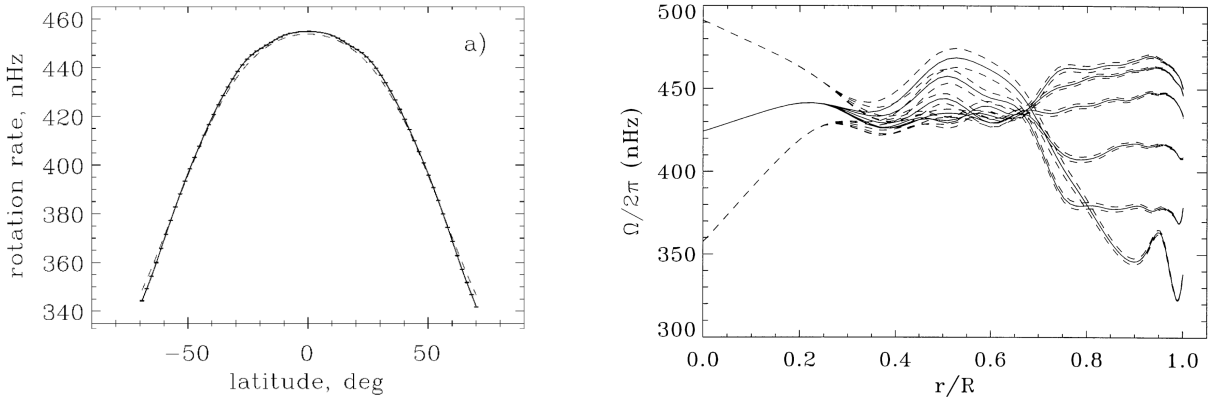

Figure 4.5: *left*: Rotation of the Sun as a function of latitude at a depth of $2-9$ Mm (solid line) and at the surface (dashed line). Credits to Kosovichev & Schou (1997). *right*: Rotation rates inverted for different latitudes against radius. On the right side of the graph, from top to bottom, the rotation rate are at 0°, 15°, 30°, 45°, 60° and 75°. The dashed lines represent the $1-\sigma$ uncertainty. Credits to Schou & SOE Internal Rotation Team (1998).

model after 2.8 gigayr. However they used a prescription for the IGW angular momentum luminosity that overestimates their efficiency, they say. A more recent work has confirm this result (Charbonnel & Talon, 2005) but starting from the ZAMS, with an initially flat rotation profile. However, such a model requires *non-standard* mechanisms of transport of AM. There are a lot of candidates and their possible interactions when put together in a stellar evolution have never been tested (see Chapter 5). Turck-Chièze et al. (2010) tested the impact of initial conditions on the rotation evolution of a solar model. They used two different stellar evolution codes, no additional transport mechanism (and no magnetic braking) and three different initial conditions: ~ 2 km s^{-1}, ~ 20 km s^{-1} and ~ 53 km s^{-1}. The first corresponds to a very low (unrealistic) initial rotation velocity while the last two are more realistic. They found that only the first initial condition produces, at the age of the Sun, a rotation profile not too far from the current solar rotation profile. The last two end up with rotation rates around four time larger than the one presumed in the radiative zone of the Sun.

4.2.2 From $0.4R_\odot$ to the centre

In order to obtain information on the very core of the Sun through asteroseismology, one must detect the modes in which the core oscillates: *g*-modes. However, *g*-modes are evanescent in the convective zones and their detection is hindered by their very small residual amplitude at the surface of the Sun. Their discovery has been the object of many claims in the history of helioseismology. Nonetheless, all claims have been intensely debated and no consensus is emerging in the community regarding their detection. García et al. (2007) were the first to claim the detection of solar *g*-modes. They studied the power spectrum density (PSD) obtained from almost 10 years of GOLF measurements. They found a large bump in the period domain of asymptotic *g*-modes[6], between 25 µHz and 140 µHz. The likelihood that this bump is not produced by noise is at least 99.85 %. Furthermore, its location is close to the one predicted with theoretical models. However, this detection has not been reproduced by other methods or in MDI data (Appourchaux & Pallé, 2013). Recently, Fossat et al. (2017); Fossat & Schmider (2018) argued for a new detection of solar *g*-modes based on a different method. They were not searching directly for *g*-modes but for modulation of *p*-mode frequencies due to small changes

[6]Where the period separation between *g*-modes of successive order n is nearly constant (see Sect. 3.2.2).

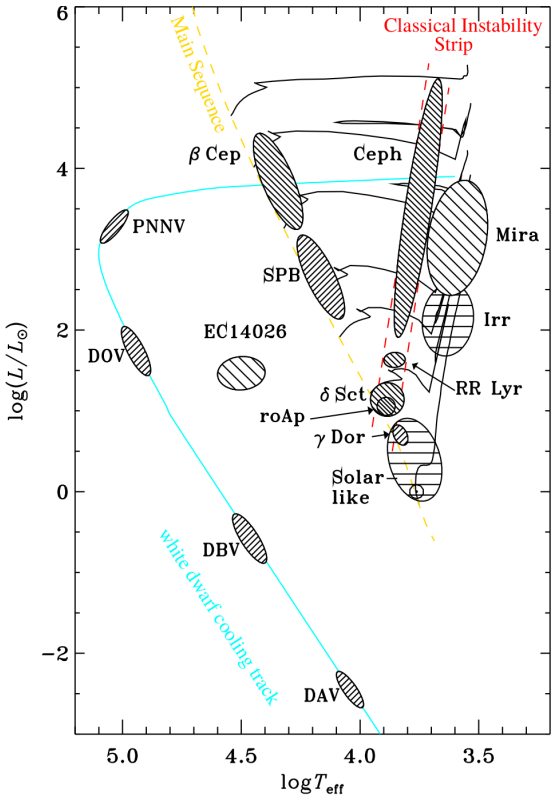

Figure 4.6: Hertzsprung-Russel diagram in which the location of some of the most important classes of pulsators (and rotators) are highlighted. Credits: Kim et al. (2006).

in the deep solar structure induced by g-modes. Their results have rapidly been rejected (Schunker et al., 2018; Appourchaux et al., 2018; Appourchaux & Corbard, 2019; Scherrer & Gough, 2019).

4.3 Constraints on the stellar rotation profiles across the Hertzsprung-Russell diagram

In this section, I present the observational constraints we have on the rotation of stars other than the Sun. This section is organized according to the stellar evolutionary status. The Universe counts many varieties of stars (see Fig. 4.6) with different rotation characteristics. Therefore I will not describe what we know about rotation in all categories of stars but I will go through the ones that are the most important for this manuscript. In PMS stars, rotation is very much dependent on the characteristics of the disk and has many links to magnetic activity. Concerning MS stars, I describe the usual solar-like stars and I focus on two categories of rapid rotators: δ Sct and γ Dor stars. I close this section with evolved stars, and concentrate on Red Giant Branch (RGB) stars, the aged counterparts of MS solar-like stars.

4.3.1 Rotation in pre-main-sequence stars

The surface rotation velocity of PMS stars is fairly well reproduced by models. Low mass stars ($M \lesssim 1.5 M_{\odot}$) arrive fully convective on the PMS. They have their convective zone locked with the disk due to the magnetic field lines connecting them, and co-rotate with it during its lifetime (Bouvier et al., 1997). After their disk disappears, they lose AM at the surface through

magnetized winds. The same process must occur for more massive stars ($\gtrsim 1.5M_{\odot}$). These stars quickly develop a central radiative zone and it rapidly becomes the dominant zone, in mass and in extent. The remaining convective zone is forced to co-rotate with the possibly present disk. However, it is not clear if the radiative zone is also coupled to the disk or if it can evolve freely.

Large surveys of young stellar cluster (YSC) have provided data to test this scenario. A YSC offers many advantages. As it is formed from one molecular cloud, all stars in it have the same age and the same chemical composition. They offer a homogeneous sample where only the mass and the initial rotation vary. Fig. 4.7, left panel, displays the rotation period of stars with a mass $0.1M_{\odot} < M < 1.0M_{\odot}$ in various stellar clusters with different ages. Stars with $1M_{\odot}$ reach the main sequence at ~ 40 Myr and stars with mass below $0.5M_{\odot}$ reach it after ~ 150 Myr. Therefore, only a small fraction of the stars represented on this graph are not on the PMS. As long as the age increases, the proportion of fast rotators also increases, which is coherent with the above model. Irwin et al. (2008) tested it in more detail. They first used stellar models calibrated to reproduce global quantities of the Orion Nebula Cluster (ONC) (Fig. 4.7, left panel, top graph) computed with solid body rotation and AM losses by magnetized winds but no disk locking. After an evolution from 1 Myr to 5 Myr, the periods of rotation of their synthetic cluster are significantly faster than the one of a cluster of equivalent age (NGC 2362), strongly suggesting that a process of AM loss is missing. It is worth noting that the hypothesis of solid rotation is to be ruled out as a cause of these high rotation rates because such young and low mass stars are fully convective and the AM should be well mixed at this stage. The authors point out that the age of the ONC cluster is subject to a controversy and that it is sometimes estimated around 2 Myr. However, even by assuming this initial age, the stars in the modelled cluster still rotate too fast. Starting with another synthetic 2 Myr cluster (NGC 2264) evolved to 5 Myr again gave too rapid rotators.

However, while Irwin et al. (2008)'s work clearly shows the need for an additional AM loss mechanism, the disk-locking-model does not produce unanimity among astrophysicists. More recent studies have shown that the rotation periods of disk-less and disk-bearing stars overlap (Cody & Hillenbrand, 2010). Concerns have also been raised on the interpretation given to the measured rotation period. It is usually assumed that the rotation-induced brightness modulation observed in stars is due to spots on the surface. Artemenko et al. (2012) suggested that it could also be due to accretion disk and the measured rotation period would not only be the one of the star. Moreover, the disk-locking-model supposes that the magnetic field lines are closed and that they connect almost to the whole disk. A work by Matt et al. (2015) have shown that if a high enough differential rotation sets-in between the star and the disk, the field lines tend to open, reducing the extent of the disk coupled to the star and the amount of torque felt by the star from the disk. The authors encouraged the use of more detailed models of star-disk interaction when considering the PMS evolution of angular momentum.

4.3.2 Rotation in main-sequence stars

Solar-like stars

Solar-type stars are stars with a significant convective envelope [7]. The study of such stars allows us to gather information about the past and future of the Sun. The exploitation of CoRoT, *Kepler* and TESS data have allowed astronomers to retrieve surface rotation periods and internal rotation profiles of dozens of thousands of solar-type main sequence stars. Leão et al. (2015) extracted from the CoRoT and *Kepler* input catalogues three samples of stars. In

[7] The principal solar parameters are given in Appendix A.

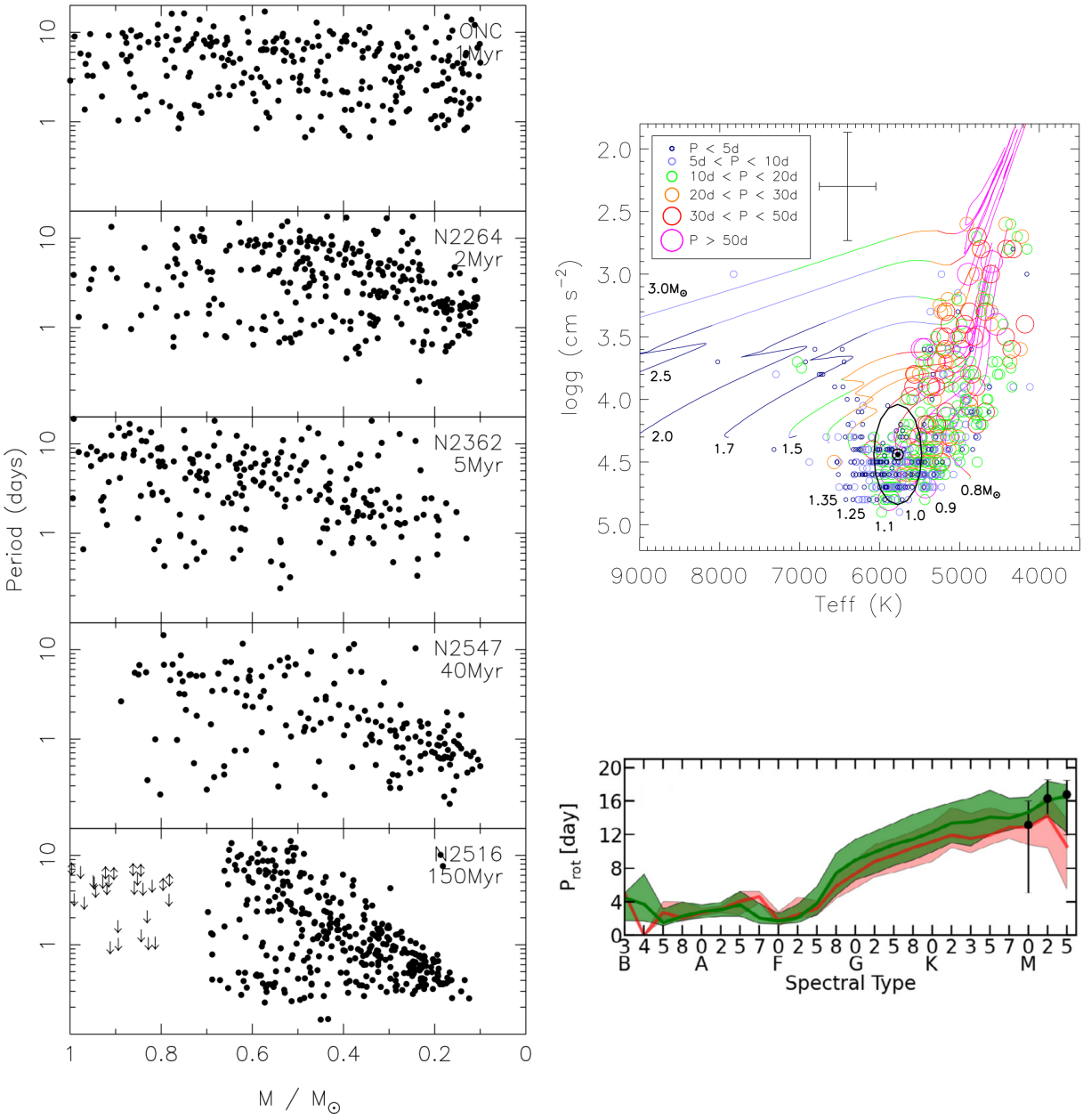

Figure 4.7: *Left:* Rotation periods against mass for several young stellar clusters. From top to bottom, the stellar clusters are ONC, NGC 2264, NGC 2362, NGC 2547 and NGC 2516. Credits: Irwin et al. (2008). *Top right:* HR diagram of the CoRoT sample described in 4.3.2. The rotation period is colour- and shape-coded. Credits: Leão et al. (2015). *Bottom right:* Average period with associated uncertainties for each spectral types in a sample of $\sim$ 12000 stars (in green). The Sun is a G2 type star. Red shaded area corresponds to an earlier determination. Credits: Nielsen et al. (2013).

order to select solar-like stars, they start with global parameters close to the solar values, within the range allowed by CoRoT or *Kepler* uncertainties on the measurement. Hence, the stars in the CoRoT sample have $T_{\rm eff} = T_{\rm eff,\odot} \pm 300$ K and $\log g = \log g_\odot \pm 0.4$ dex, for a total of 175 stars; and two samples from *Kepler* with $T_{\rm eff} = T_{\rm eff,\odot} \pm 170$ K, $\log g = \log g_\odot \pm 0.2$ dex and $[{\rm Fe/H}] = [{\rm Fe/H}]_\odot \pm 0.2$ dex, for a total of 1836 and 2525 stars. These ranges correspond to CoRoT and *Kepler* typical uncertainties. All three samples actually contains PMS, MS and more evolved stars. Leão et al. (2015) divided them into two groups: below 1 Gyr old and above. The surface rotation rates of stars in the CoRoT sample are represented in Fig. 4.7, top right panel. We immediately see that as stars age, their rotation periods increase, as predicted by the Skumanich law. This is confirmed by the period distribution of the two groups defined above: the peak in the period distribution of the young *Kepler* group is of ~ 12 days and ~ 18 days for the old one. Another study on ~ 12000 *Kepler* main-sequence stars (not only solar-type) show that B- or A-type stars are significantly faster rotators than later types (see Fig. 4.7, bottom right panel; Nielsen et al. 2013). The Sun is a G2-type star but rotates almost twice slower than the average rotation period found in this work. However, their sample is biased toward shorter period, as mentioned by the authors.

More detailed measurements have been made possible using asteroseismology. Benomar et al. (2015) have compared the surface rotation rates measured using $v \sin i$ and the average internal rotation rate (excluding the core convective zone, if present) measured using rotational splittings. They found a maximum factor 2 between surface and internal rotation rates for 21 of their 22 stars. Such a nearly flat rotation profile could be reproduced with the standard transport of angular momentum described in Chapter 2. Benomar et al. (2018) later managed to extract from the rotational splittings evidence of latitudinal differential rotation in 13 solar-type main sequence stars. Fig. 4.8, left panel shows the latitudinal differential rotation between the equator and a latitude of 45° as a function of the average rotation rate measured using rotational splittings. Surface rotation profiles where the equator rotates faster than higher latitudes are called solar rotation, otherwise they are called anti-solar rotation. Half of the stars in this sample have their equatorial rotation rates 64% higher than their rotation rate at 45°. It must be noted that the uncertainty on the differential rotation increases when the average rotation rate decreases. This explains the large error bars for the slow rotators. The authors also found stars showing anti-solar rotation but the uncertainty was so important that the detection was not reliable. In comparison, Sun's 45° latitude rotates at 90% of its equator angular velocity. Some of the stars present in the sample have a significantly higher differential rotation. Such high latitudinal differential rotation was not reproduced by models, suggesting that a mechanism counteracts the turbulence reductive effect on shear.

γ Doradus (γ Dor) and δ Scuti (δ Sct) stars

The classes of γ Dor and δ Sct stars are intermediate mass stars with $1.2 M_\odot \lesssim M \lesssim 2.5 M_\odot$. On the MS, their nuclear energy generation process is mainly the CNO cycle which can reduce to ${}^{12}{\rm C} + 4\,{}^{1}{\rm H} \rightarrow {}^{12}{\rm C} + {}^{4}{\rm He} + 2e^+ + 2\nu_e$, by going through the production of nitrogen and oxygen. As this cycle produces an enormous amount of energy, their core is convective, inducing chemical transport by penetrative convection inside the radiative region. These stars are also rapid rotators and we might expect important transport of chemicals and AM by shear-induced turbulence and meridional circulation. They are of interest for us because the effects of rotation are easily visible and they can be used to test our models (see Sect. 8.2.2).

The categories of γ Dor and δ Sct are very close to one another in the HR diagram (see Fig. 4.6). What differentiates them is the properties of their oscillation modes: the former oscillate in *g*-modes while the latter oscillate in *p*-modes. In δ Sct stars, the modes are excited by the

κ mechanism enhanced in the H and He ionization regions. In the case of γ Dor stars, there are two driving mechanisms, depending on whether the γ Dor is warm or cold. For cold γ Dor, the driving mechanism is the so-called *convective blocking* mechanism (Pesnell, 1987; Guzik et al., 2000). At the base of convective envelope, if the characteristic convective time-scale is smaller than the pulsation period, then the convection will not be fast enough to adapt to a small excess of luminosity caused by the energy brought by the wave. This energy is blocked, the pressure increases and drives a pulsation. For that to be true, the convective envelope needs to have a precise extent. For warm γ Dor, the convective envelope is too shallow and convective blocking is not efficient. Pulsations in these stars are excited by κ mechanism due to second ionization of helium (Xiong et al., 2016).

Exploiting the information contained in the oscillation spectra of γ Dor and δ Sct is a thorny issue because rapid rotation of high or intermediate mass causes the creation of complicated oscillation patterns (Lignières & Georgeot, 2009; Reese et al., 2017). In order to extract information on their interior, astronomers must combine multiple techniques. The detailed study of δ Sct such as HD 174966 (García Hernández et al., 2013), HD 50870 (Mantegazza et al., 2012) or massive study of CoRoT or *Kepler* δ Sct targets (Michel et al., 2017; Balona & Dziembowski, 2011) have revealed regular patterns in their oscillation spectra which could provide the same kind of information as $\Delta\nu$ or $\nu_{\max}$ of solar-like and red giant stars.

Let us take the example of HD 174966 (García Hernández et al., 2013). The authors used the CoRoT light curve and extracted from it 185 mode frequencies between 0 µHz to 900 µHz with the highest amplitude modes grouped around 300 µHz. These data where complemented by 53 nights of spectroscopic observations using the spectrographs SOPHIE, FOCES and HARPS. It allowed them to obtain a first estimate of global parameters: $T_{\rm eff} = 7555 \pm 50$ K, $\log g = 4.21 \pm 0.05$, $[{\rm Fe/H}] = -0.08 \pm 0.1$, $M = 1.70 \pm 0.20\ M_\odot$ and $R = 1.70 \pm 0.20 R_\odot$. In the spectroscopic time series, they also isolated 18 mode frequencies, 12 shared with CoRoT frequencies. Furthermore, the rotational surface velocity was estimated to be 142 km s^{-1} or equivalently have a period of 0.64 days. It is actually estimated to be $\simeq 33\%$ of its break-up velocity (424 km s^{-1}), much faster than the Sun. In order to identify the different modes, the authors used multi-band photometry technique. Pulsations introduce amplitude variations and phase shifts between the light curves measured in different photometric bands that depends on the order ℓ of the mode (Garrido et al., 1990). As this method does not make possible the determination of the azimuthal number m in a unique way, multi-band photometry can lead to degenerate mode identification. The degeneracy should be lift by using modelling methods. However, the models used in (García Hernández et al., 2013) neglect the influence of rotation on mode propagation which could lead to mis-identification. Nonetheless, they looked for periodicities in the oscillation spectra and found a period pattern with a frequency spacing of 64 µHz that they related to the large separation. Knowing the large separation is important because it provides a very precise measurement of the stellar mean density (see Eq. (3.53)).

In order to explore the internal rotation profile, new asteroseismic diagnostics must be developed. In the case of a non-rotating star, the period spacing of g-modes is almost constant as the period of the mode varies. In the case of γ Dor stars however, the period spacings $\Delta\Pi$ do not stay constant any more but follow a linear relation as a function of the period. Ouazzani et al. (2017) define this relation as:

$$\Delta\Pi_{n\ell m} = \Sigma_{\ell m}\Pi_{n\ell m} + r_{n\ell m}, \tag{4.21}$$

where $\sigma_{\ell m}$ is the slope and $r_{n\ell m}$ is the value of $\Delta\Pi_{n\ell m}$ extrapolated at the origin. They show that $\sigma_{\ell m}$ does not depend on the internal structure but only on ℓ, m and on the rotation rate. They applied this method on 4 *Kepler* stars and found internal periods of rotation ranging from 2.31 days to 0.68 days. Guo et al. (2017) found for a hybrid γ Dor/δ Sct KIC 9592855

an internal period of 0.8 days. Furthermore, this star is part of a binary system with orbital frequency also of 0.8 days, suggesting that the star is synchronized and is in a nearly-uniform rotation. Further studies managed to determine near-core rotation rates for dozens of γ Dor stars (Van Reeth et al., 2016; Christophe et al., 2018; Ouazzani et al., 2019) and confirmed previous individual results: rotation periods are comprised between ~ 0.4 d and ~ 2 d.

The significant number of measurements of near-core rotation rates allows stellar physicists to perform comparisons with rotation evolution models. Ouazzani et al. (2019) compared the core rotation rate of 37 γ Dor stars observed with *Kepler* to "standard" rotation models with meridional circulation and shear-induced turbulence. The set of models is composed of three different masses (1.4, 1.6 and $1.8 M_\odot$) with fast initial conditions ($P_{\rm disk} = 2.4$ d, and $\tau_{\rm disk} = 3$ Myr) or slow initial conditions ($P_{\rm disk} = 7.2$ d). Those initial conditions were determined based on surface rotation in young stellar clusters. The results are represented as solid blue line in Fig. 4.9, left panel. It displays observed or computed near-core rotation rates as a function of the buoyancy radius P_0

$$P_0 = 2\pi^2 \left(\int_{\rm g\ cav.} \frac{N(r)}{r} {\rm d}r \right)^{-1}, \tag{4.22}$$

which decreases with age. Standard models fail to reproduce the near-core rotation of the slowest rotators. Moreover, it tends to predict young fast rotators that are not observed. Ouazzani et al. (2019) also tried to include overshooting (Fig. 4.9, purple lines) which increases the size of the inner convective zone and therefore increases the buoyancy radius and decreases the apparent age of the star. As a matter of fact, purple lines are basically blue lines shifted to the young side in Fig. 4.9. It reduces discrepancies concerning the number of fast young rotators but does not explain the slow ones. A better agreement is found for models with solid rotation which is not physically motivated but it suggests that an efficient AM transport mechanism that would enforce solid body rotation is lacking. They also tried to mimic such an additional mechanism by increasing the horizontal or the vertical viscosities, keeping the standard framework. This gives quite similar results to solid body rotation. It is another peace of evidence for a missing process transporting AM.

All these observations of γ Dor and δ Sct stars show that they are fast rotators with rotation periods of the order of a day. An average internal rotation frequency can be found for γ Dor by exploiting their period spacing if enough of them are measured. Obtaining a detailed rotation profile is still a challenging task. Even in the domain of fast rotation, the study of γ Dor and δ Sct stars show that, once again, the standard modelling of angular momentum transport is strikingly deficient.

The lithium depletion problem

A nagging problem in stellar physics is the so-called lithium depletion problem. It has now been known for more than sixty years that the Li abundance measured at the surface decreases with stellar age. Fig. 4.8, right panel, shows measured Li abundances for cool stars in Hyades cluster (625 Myr). The hottest stars in this sample have an abundance close to the initial Li abundance, measured in younger stellar clusters. The initial abundance can decrease in several ways. Li is consumed through proton capture at a temperature of $T_{\rm Li} \sim 2.5 \times 10^6$ K. If this temperature is reached inside the convective zone, convection mixes up the material and Li abundance decreases. This is the case at the very right of the graph. Otherwise, if this temperature is reached below the surface convective zone, Li abundance should only decrease through diffusion. However, Fig. 4.8, right panel, clearly shows a gap around $T_{\rm eff} \simeq 6700$ K called the Li dip (Boesgaard, 1991). The Li dip is not only observed in the Hyades cluster but in all clusters

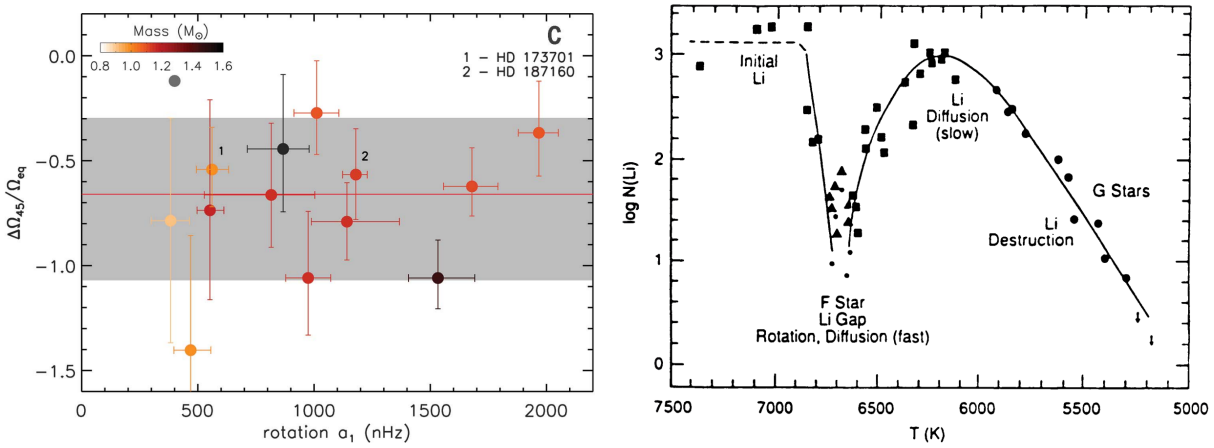

Figure 4.8: *left*: Relative differences between rotation rates at the equator and at 45° as a function of of the average rotation rates for 13 main sequence solar-like stars. The red horizontal line is the median of the sample. Credits: Benomar et al. (2018). *Right:* Measured lithium abundances for F and G stars of Hyades cluster as a function of effective temperature. Different symbols corresponds to measurements by different teams. Credits: Boesgaard (1991).

with age $\gtrsim 300$ Myr. Understanding this dip has been a challenge since its discovery because the location where the proton capture occurs is located well below the convective zone. The usual explanation is to invoke convective overshoot coupled with rotational effects. Overshoot causes exchanges of material between the radiative and the convective zones, which explains the decrease in Li abundance between the diffusion dominated region at $T_{\rm eff} \simeq 6200$ K to the region where $T_{\rm Li}$ is reached inside the convective zone. In a non-rotating star, the radiative zone is not mixed, except by diffusion, and if overshoot cannot reach the location where $T_{\rm Li}$ is reached, no lithium poor material is brought inside the convective zone. If on the contrary the star is rotating, meridional circulations participate to the mixing of the radiative zone.

This mechanism has been tested and works for the hot side of the Li dip (Palacios et al., 2003), but fails for the cool side. Indeed, as we pass to the cool side of the dip, the convective zone deepens which increases the magnetic torque applied to the star. We should then see still a decrease of the Li abundance, and it is obviously not the case. This observation pleads for the existence of another mechanism that transports AM and therefore reduces the radial differential rotation, but at the same time do *not* transport chemicals. Concomitantly, such additional mechanisms, namely Internal Gravity Waves (IGW), have been tested (Talon & Charbonnel, 2003; Charbonnel & Talon, 2005). IGW are better excited as the convection deepens and according to excitation models, they must have a non negligible impact on the transport of angular momentum around the temperature of the cool side. Including IGW has been found to reproduce the cool side of dip in the Hyades (Talon & Charbonnel, 2003; Charbonnel & Talon, 2005).

While the IGW model reproduces the observations, these works rely on modelling of IGW excitation that are not unique and have not been fully validated. They also computed IGW angular momentum fluxes with 1D rotation profile, while they should be strongly impacted by 2D effects. Furthermore, other transport mechanisms have been proposed such as mechanisms relying on magneto-hydrodynamic processes (see Sect. 5.2) that should also be investigated.

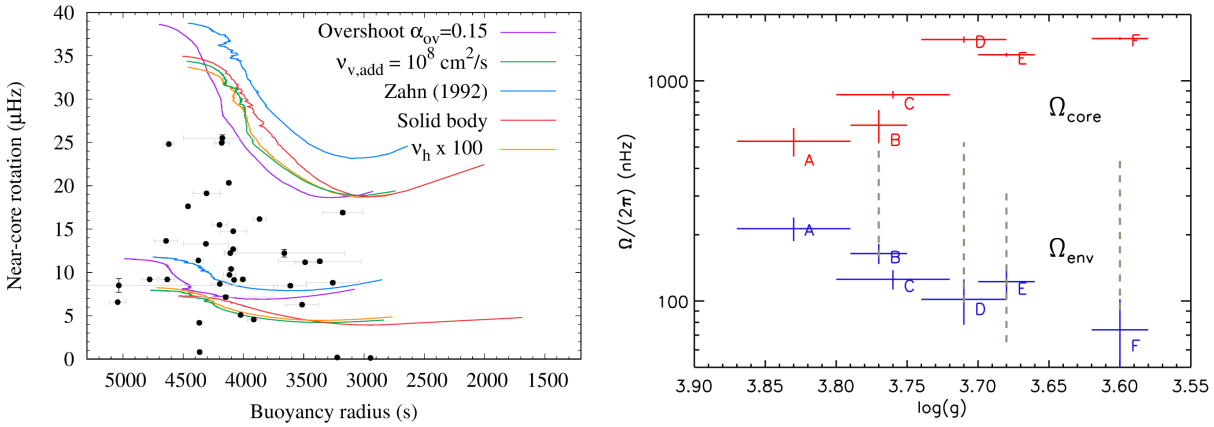

Figure 4.9: *left*: Near-core rotation frequency as a function of the buoyancy radius. Observations are depicted as black dots. Solid lines represent near-core rotation frequency obtained with a $1.6M_{\odot}$ CESTAM models with various physical prescriptions and initial conditions. Top lines correspond to fast initial conditions ($P_{\rm disk}$ = 2.4 d, and $\tau_{\rm disk}$ = 3 Myr) and bottom lines to slow initial conditions ($P_{\rm disk}$ = 7.2 d, and $\tau_{\rm disk}$ = 5 Myr). Credits: Ouazzani et al. (2019). *right*: Core (red) and envelope (blue) rotation rates for 6 *Kepler* stars, as a function of logarithmic surface gravity. Credits: Deheuvels et al. (2014).

4.3.3 Rotation in red giant stars (RGB stars)

Red giant stars have been extensively studied since the launch of CoRoT and *Kepler*. In particular, thanks to its very long time series, *Kepler* gave the opportunity to detect mixed modes that propagate as *g*-modes in the radiative region of RGB stars and as *p*-modes into the convective region. Mosser et al. (2011) showed that their detection and the measurement of their rotational splittings makes possible to access the rotation profile of those stars. Yet, For RGB stars with $\Delta\nu > 10$ μHz, it is difficult not to mistake rotational multiplets and mixed-modes. Mosser et al. (2012) demonstrated that gravity-dominated mixed-modes (which are more numerous than pressure-dominated ones) have characteristics very similar to pure *g*-modes. In particular, their distribution in period is close to that of asymptotic pure *g*-modes.

It was first done by Beck et al. (2012) and Deheuvels et al. (2012) in two different stars of the *Kepler* catalogue. They measured rotational splittings of the order 0.1 μHz and revealed that the core was rotating at least 5 times faster than the envelope. This result was among the first confirmations of the predicted strong radial differential rotation of RGB stars. Indeed, as a star evolves and leaves the main sequence, its envelope expands and slows down and its core contracts and speeds up, due to AM conservation. Deheuvels et al. (2014) repeated the same process on 6 *Kepler* RGB low-mass stars. They used inversion technique on the measured rotational splittings (again of order 0.1 μHz) and found 6 rotation profile, showing again similar core-to-envelope rotation rate ratios. There results are represented in Fig. 4.9, right panel.

These observational constraints have rapidly been confronted with stellar rotation evolution models. Marques et al. (2013) used an earlier version of CESTAM to compute 1D stellar model with standard physics as well as standard transport of AM including shear-induced turbulence and meridional circulation as well as a magnetic breaking for some of the models. The initial rotation velocity was chosen to be 20 km s^{-1}. They calibrated a solar model with and without braking in order to match solar luminosity, radius and metallicity. They also computed similar models but with a mass of $1.3M_{\odot}$, which is a typical mass of RGB stars. Stars with a mass of $M \simeq 1.3M_{\odot}$ also have a central convective zone which allow them to test the influence of an overshoot: the penetration of the central cz into the RZ brings hydrogen rich material in the region where the nuclear reactions are the most efficient, thus increasing the stellar lifetime.

The modelled internal structure have been given as input to an oscillation code: ADIPLS (Christensen-Dalsgaard, 2008), that produces an oscillation spectrum from which oscillation characteristics such as rotational splittings can be extracted.

These models, evolved up to the RGB phase, have an important radial differential rotation in the radiative region. However, the core rotation rate is much larger than the one observed. Indeed, the computed rotational splitting are of the order of 10 to 100 µHz, compared with ~ 0.1 µHz observed. The authors suggest that uncertainty on the physics used in the standard modelling could explain such a high rotation velocity. First, the impact of initial rotation condition can be ruled-out as the surface rotation of such an evolved star does not depend on initial conditions. A different prescription for the magnetic breaking law changes the core rotation rate of only $\sim 2\%$. Second, a $1.3 M_{\odot}$ star has convective overshoot during the MS phase. The presence of overshoot mimics a higher mass. Therefore, for a star to reach a given radius on the RGB, a star with overshoot would have less time to speed up and the rotation rate would be reduced (of $\sim 30\%$ in this case). Third, other hydrodynamic instabilities may occur, such as the GSF instability (see Chapter 5). They found that it changes the central rotation rate of only $\sim 3\%$. Finally, the turbulent diffusion coefficient can be underestimated. In order to increase the extraction of angular of angular momentum from the radiative zone to the convective zone, the velocity of the meridional circulation and the vertical diffusion coefficient of the shear-induced turbulent should be increased. To that end, Marques et al. (2013) increased by two orders of magnitude the value of $D_{\rm h}$ and set the critical Richardson number to 1. The change in the value of $D_{\rm h}$ is motivated by the fact that an enhanced horizontal diffusion reduces the inhibiting effect of the μ-gradient on the meridional circulation velocity. We have seen in Sect. 2.3 that there is no consensus on the prescription of $D_{\rm h}$ and increasing it by a factor 100 represents a limit value. The change in the critical Richardson number $\mathrm{Ri}_{\rm c}$ has an impact on the value of the vertical diffusion coefficient $D_{\rm v}$. All prescriptions express $D_{\rm v}$ in quite a similar form, the value of the critical Richardson number that they assume changes. A value of $\mathrm{Ri}_{\rm c} = 1$ is recommended by Woods (1969); Canuto (2002). They argue that the original value of $\mathrm{Ri}_{\rm c} = \frac{1}{4}$ proposed by Taylor (1931) was derived by looking at the critical Richardson number that characterizes the passage from a laminar to a turbulent flow. However, Woods (1969); Canuto (2002) looked at the situation where the flow is already turbulent and what should be the threshold value of Ri for the flow to become laminar. They found it to be $\mathrm{Ri}_{\rm c} = 1$. This enhancement of extraction of angular momentum, produces a reduction by a factor 10 of the core rotation velocity, still ten times higher than the observed one, thus providing another argument in favour of a missing mechanism of transport of angular momentum.

Conclusion of Part I

This first part was devoted to the basic concepts required to understand the stellar rotation evolution. Classically, a star is assumed to be a sphere of gas in which the pressure gradient counterbalances gravity. The mean flow is assumed to be steady, and static and the physics is kept rather simple. Therefore there is no diffusion, the convection is reduced to its essence, *i.e.* a single vertical eddy, magnetic fields and rotation are neglected. This modelling may seem simplistic but has known many achievement. It reproduces with a remarkable precision the majority of the stellar parameters accessible to observation, it has succeeded in obliging the particle physicists to include two new types of neutrinos.

In-depth study of stellar interior is made possible by asteroseismology which allows astronomers to collect information about the zones of propagation of waves observed at the surface. We describe the main principles of asteroseismology in the case of rotation and no rotation and we made a detour on a tiny blip in the well-oiled machinery of standard models. Indeed, the high-frequency oscillation modes of the upper zone of stars are observed with slightly different frequencies than the ones predicted. While this discrepancy is around 1% of the mode frequency, it is around 100 times larger than the observation resolution, and therefore, highly significant. This gap between models and reality is caused by an oversimplified modelling of convection at the surface of the star. Here, the hypotheses that made possible the approximation of convection by a single eddy breaks down. The turbulence that is normally forgotten in the computation of the stellar-structure becomes non-negligible and the frequencies are modified. This problem called the surface effect has for long been tackled by trying to correct *a posteriori* the discrepancies. Correction laws are given depending on main stellar parameters: $T_{\rm eff}$ and $\log g$. However, these works forgot the influence of other parameters such as the chemical composition and above all, rarely study the physical motivations of such a correction law. These two drawbacks have been the focus of a work and a first author article realized during the first year of my PhD (Manchon et al., 2018).

The standard model of stellar physics allows modellers to incorporate non-standard processes, in a very approximate way. Indeed, the impact of these processes are often studied *a posteriori*, *i.e.* after the evolution of a model is done. Therefore, they have no impact on the physics of the star: they depend on the stellar-structure but the stellar-structure does not depend on them. Therefore, the standard modelling of rotation evolution neglects almost all the effects of rotation on the structure equation. Rotation intervenes only through an additional term of approximated centrifugal acceleration in the hydrostatic equation. Then in the star, the transport of angular momentum is described in the following way. Convective zones (CZ) are assumed to have a uniform angular velocity or a uniform angular momentum distribution. The surface CZ can lose AM through magnetized wind or because it is forced to co-rotate with an accretion disk, and all CZs can exchange AM with the radiative zone through the meridional circulation. In the radiative zone (RZ), AM can be advected by meridional circulation and angular velocity can be diffused by shear-induced turbulence.

Another major contribution of asteroseismology has been to provide the proof that this

modelling of rotation evolution is deficient. Indeed, the Sun is observed to have latitudinal differential rotation profile in its cz and a nearly flat rotation profile in the rz, while models predict radial differential rotation in the rz and flat rotation profile in the cz. In other stars, young stars with effective temperatures around 6500 K are observed to lack Lithium in their photosphere which argues for the presence of a mechanism transporting chemicals (linked to the transport of am). Main sequence fast rotators (γ Dor and δ Sct) have an almost rigid rotation profile in their interior while standard models predict strong radial differential rotation. Finally, the asteroseismic study of red giant branch stars has revealed that they do have a radial differential rotation in their core, as expected by models, but with a core rotation velocity 100 times smaller than the one anticipated. All these strong disagreements support the need for a better modelling of the transport of angular momentum and for the inclusion of additional transport processes.

Chapters 1 and 2 presented how to properly model the transport of angular momentum in 2D and how structure equations should be modified to correctly take into account the influence of a rotating flow. As said before, the standard modelling of rotation, implements simplistic versions of these equations. It is now time to describe in detail the main work I have done during my PhD, *i.e.* the implementation in the stellar evolution code cestam of the modelling of transport of angular momentum in 2D. This work is the base upon which additional transport mechanisms modelling will be built.

Part II

Non-standard modelling and numerical aspects in CESTAM

Chapter 5

Additional transport mechanisms

Contents

We have shown in Chapter 2 that the variation of angular momentum (AM) per unit time in the radiative zone amounts, on one side of the equation, to the AM extracted from or injected into it and results, on the other side, in an advection of AM by meridional circulation in addition to a diffusion of angular velocity induced by shear instability, which is thought to be the most dominant instability. However, as we have argued in Chapter 4, this modelling is far from being complete, which suggests that, either mechanisms of extraction/injection of AM are missing on the left hand side, or sources of diffusion have been missed on the right hand side.

I gathered those additional mechanisms into four categories. First, the instabilities that may occur without the intervention of a magnetic field. They may be qualified as baroclinic instabilities in the sense that they stem from displacement of fluid particles along misaligned isobars, isopycnals, isentropics, etc. Then, we have the magneto-hydrodynamic (MHD) instabilities. Since they involve a magnetic field that we excluded from our modelling, their inclusion in a stellar evolution code must be regarded with much care. Some caveats may be raised. All those instabilities are usually modelled as diffusive processes and their contribution is included in the equations for the transport of AM by adding their diffusion coefficients and completely ignoring correlations between them. Furthermore, prescriptions often assume a linear growth

of the instabilities. The possibility of a saturation is rarely evoked. These restrictions are addressed in Sect 5.3. Once we are finished, we will move to another kind of AM carriers: waves. Two types of waves have been envisaged to transport AM outside/inside radiative zones. Mixed-modes have recently been suggested (Belkacem et al., 2015b,a) and are described in Sect 5.4. Then, a long time candidate are internal gravity waves. I describe them in more detail.

5.1 Hydrodynamic (non-magnetic) instabilities

5.1.1 Rayleigh-Taylor instability

As for now we have only seen the shear instabilities that are described by the Richardson criterion. However, there exist many more instabilities. The first in the list is the Rayleigh-Taylor instability (Rayleigh, 1916). The criterion for this instability has already been derived in Chapter 1, with the equation of motion (1.92). In an axisymmetric fluid, we consider two infinitely close fluid particles at a distance ϖ and $\varpi_2 = \varpi + \delta\varpi$ from the rotation axis and with a specific AM of $j = \varpi^2\Omega$ and $j_2 = \varpi_2^2\Omega_2$. At each of these locations, the fluid is at an equilibrium state, *i.e.* forces balance each other. Now, let us imagine that the inner particle, rotating with an angular velocity Ω is moved to location ϖ_2. The equation of motion of this particle is the same as Eq. (1.92), assuming no change in the density:

$$\frac{\mathrm{d}^2 r}{\mathrm{d}t^2} = \varpi_2 \left(\Omega^2 - \Omega_2^2\right). \tag{5.1}$$

From this, we see that, if $\Omega = \Omega_2$, the equilibrium is maintained. If $\Omega < \Omega_2$ then the acceleration is negative, the particle is pushed back to its initial position and the situation is stable. Finally, if $\Omega > \Omega_2$, the acceleration is positive and the displaced particle is moved further away, leading to an unstable flow. This condition can be formalized in another way by a first order approximation of the right hand side:

$$\varpi_2 \left(\Omega^2 - \Omega_2^2\right) \simeq \frac{1}{\varpi^3}\left(j^2 - j_2^2\right) = -\frac{1}{\varpi^3}\frac{\mathrm{d}\left(\varpi^2\Omega\right)^2}{\mathrm{d}\varpi}(\varpi - \varpi_2) = -N_\Omega^2 \delta\varpi, \tag{5.2}$$

where the epicyclic frequency has been introduced (see Eq. (1.94)). We see that the medium is stable to Rayleigh-Taylor instability if $N_\Omega^2 > 0$, *i.e.* if the AM $j = \varpi^2\Omega$ is increasing outward. Therefore, a necessary condition for a distribution of AM to be stable is to satisfy *everywhere* the criterion $N_\Omega^2 > 0$, while it suffices to have $N_\Omega^2 < 0$ somewhere for this distribution to be unstable. This instability acts on a time scale of $1/N_\Omega$, which is of the order of a rotation period Ω^{-1}.

5.1.2 Goldreich-Schubert-Fricke (GSF) instability

The Goldreich-Schubert-Fricke (GSF) instability was first theorized by Goldreich & Schubert (1967) in the case of a negligible ratio of viscosity to thermal diffusivity and then extended in the case of a non-negligible one by Fricke (1968); Acheson & Gibbons (1978). They showed that an instability occurs if one of these two conditions is met:

$$\frac{\nu}{K}N_T^2 + N_\Omega^2 < 0 \quad \text{or} \quad \left|\varpi\frac{\partial\Omega^2}{\partial z}\right| > \frac{\nu}{K}N_T^2, \tag{5.3}$$

where ν is the viscosity, K is the thermal diffusivity and z is the coordinate in a cylindrical frame, parallel to the rotation axis. I also recall that N_T is the thermal part of the Brunt-Väisälä frequency, defined in Eq. (1.26); and N_Ω is its rotation part or equivalently the epicyclic

frequency, defined in Eq. (1.95). The first condition is similar to the Solberg-Høiland with no compositional gradient and taking into account the thermal diffusion. Indeed, we have seen above that, if N^2_Ω is negative somewhere, the distribution of AM is unstable. This is not counting on the stabilizing effect of the buoyancy that raises the threshold on N^2_Ω. However, this argument assumes the displacement to be adiabatic, *i.e.* there is no exchange of heat between a slightly perturbed material and the surrounding. If one allows now for exchanges of heat, then the stabilizing effect of buoyancy is reduced and the fluid becomes more easily unstable. This inequality can also be modified to include the stabilizing effects of a μ-gradient:

$$\frac{\nu}{K}N^2_T + \frac{\nu}{K_\mu}N^2_\mu + N^2_\Omega < 0, \tag{5.4}$$

where $K_\mu \simeq \nu$ is the particle diffusivity (Talon & Zahn, 1997; Hirschi & Maeder, 2010) and N_μ is the composition part of the Brunt-Väisälä frequency, already defined in Eq. (1.26).

In Eq. (5.3), the second inequality shows that for the fluid to be stable, in the absence of any other force (e.g. a magnetic field), the rotation velocity profile must not deviate too much from cylindrical rotation. With the assumption of shellular rotation, this condition is met almost nowhere, except near the equator where a shellular rotation profile can be approximated by a cylindrical profile. Therefore, the region near the equator is the least prone to develop the GSF instability (e.g. Barker et al., 2019). This point makes it clear that a 2D description of Ω is needed to properly model the transport of angular momentum by the GSF instability.

This instability is somewhat similar to the thermohaline (or double-diffusive) instability that we have seen at the end of Sect. 2.5. The thermohaline instability occurs for instance in the ocean when hot salty water sits on cooler and less salty water. Since salt diffuses more slowly than heat, when a small perturbation brings a salty water parcel downward, the temperature rapidly equals the surrounding temperature and the saltier (and denser) parcel keeps descending. This instability has the shape of radially elongated eddies called "fingers". The same situation appears in stars when angular momentum and temperature[1] decrease upward. The GSF instability creates elongated vortices that carry angular momentum upwards (Knobloch & Spruit, 1982; Korycansky, 1991). However, due to rotation, AM fingers do not exactly look like salt fingers but are sheared in the azimuthal direction. This shear again creates instabilities which limits the growth of GSF instability.

The implementation of GSF in stellar evolution code suffers inconsistencies. It is modelled through a coefficient of diffusion and it is assumed that GSF takes place in a inviscid medium. However, we have shown that viscosity has a stabilizing effect on GSF instability and indeed, when molecular viscosity and kinematic viscosity coming from shear-induced turbulence are taken into account, GSF instability is be suppressed, especially in the tachocline where shear becomes very important (Caleo et al., 2016).

5.1.3 Axisymmetric BaroClinic Diffusive (ABCD) instability

ABCD instability (Knobloch & Spruit, 1983) is not very different from the GSF instability when also taking into account μ-gradients, except that this time it is the thermal diffusion and not the particle diffusivity that reduces the stabilizing effect of the chemical stratification.

$$\frac{\nu}{K}\left(N^2_T + N^2_\mu\right) + N^2_\Omega < 0. \tag{5.5}$$

As the GSF instability, ABCD instability acts on the thermal time-scale.

[1]Note that this is always the case for temperature to decrease upward in a star.

5.2 Magneto-hydrodynamic instabilities

In radiative zones, a magnetic field can also be sustained by induction generated by the motion of electrically charged particles due to rotation and to meridional circulation (Mathis & Zahn, 2005). The torque and the divergence of the Lorentz force are included into, respectively, the equation of the transport of AM and of the velocity of the meridional circulation (see Eq. (2.105)). However, the implementation of this kind of model in a stellar evolution code is a formidable task and would only account for axisymmetric fields and would skip all its dynamical effects[2], especially instabilities. Nonetheless, some of the effects of the magnetic field can readily be implemented into codes following prescriptions derived from more complex simulations. We have already seen that the interaction of rotation and convection can create or sustain an already existing magnetic field thanks to the dynamo effect. This magnetic field has an important impact on the rotation evolution through stellar wind that carries away angular momentum or through magnetic field lines frozen into the star and into the disk that forces them to rotate as a solid body.

When a differentially rotating star is plunged into a magnetic field, instabilities may occur. These instabilities have been the subject of a lot of study for more than half of a century and have been brought to the field of stellar physics by Spruit (1999). In this seminal paper, he identifies at least 5 instabilities, including the magnetorotational instability (MRI) and the Tayler instability (also known as Tayler-Spruit instability). I describe both of them in the following.

5.2.1 Magnetorotational instability

This instability is also called the *magnetic shear instability* (Velikhov, 1959; Chandrasekhar, 1960; Balbus & Hawley, 1991). Let us consider a differentially rotating star with angular velocity decreasing outward. This star is immersed into a vertical axisymmetric magnetic field for which the axis of symmetry is the rotation axis. We imagine that a small parcel of fluid is displaced outward. Due to the conservation of angular momentum, the angular velocity of this parcel should decrease. However, magnetic field lines tend to maintain rigid rotation. Therefore, the parcel has an excess of centrifugal force compared to its surrounding, which chases it away. This is of course a destabilizing effect. On the other hand, because of the frozen flux theorem, magnetic field lines acts as a restoring force for any perturbation that would move material away from them. It provides a stabilizing effects, in addition to the effect of the stable stratification. A sufficient and necessary condition for instability is that

$$q = -\frac{\mathrm{d}\ln\Omega}{\mathrm{d}\ln r} > \frac{N_T^2}{2\Omega^2}\frac{\eta}{K}, \tag{5.6}$$

where η is the magnetic diffusivity. It should be noticed that the field strength does not appear in the instability criterion. The reason is that the magnetic field is responsible for both stabilizing and destabilizing effects. This expression is somewhat very similar to the GSF or Solberg-Høiland criterion in which N_Ω^2 has been replaced by $2\Omega^2\mathrm{d}\ln\Omega/\mathrm{d}\ln r$. The angular momentum transported by MRI is often modelled as a diffusive phenomena with diffusion coefficient $\eta \simeq 2\Omega^2 qK/N_T^2$. MRI is thought to be important only in stars with a strong radial differential rotation.

5.2.2 Tayler-Spruit instability

This instability was originally found by Tayler (1973), this time considering a weak toroidal magnetic field $\mathbf{B}$, *i.e.* with field loops wrapped-up around the rotation axis. This configuration

[2]Processes occurring on characteristic time-scales much shorter than the nuclear or contraction time-scales.

is thought to occur in rotating stars thanks to the winding-up mechanism. Indeed, with a poloidal field as initial condition, the rotating material will stretch the frozen-in field lines (magnetic diffusivity is very weak) around the rotation axis. The wound up line increases the magnetic field strength at each turn. The magnetic field creates a magnetic pressure perpendicular to the field lines, which compresses the loops. In more simple words, one can imagine the magnetic field loops wrapped-up around the rotation axis as a high stack of plates. The loops are compressed by magnetic pressure as the plates are compressed by gravity. Therefore, it is easy to imagine that a little pinch in the stack sends all the plates to the floor. This instability may occur even if the field is weak, which makes it very interesting as a way of transporting angular momentum. In this case, an instability could not gain a lot of energy from the field to fight against the gas pressure or the buoyancy force. Therefore, the instability that would develop from this field would tend to minimize its work against pressure and buoyancy, meaning that the displacement will be *almost* parallel to isobars and equipotentials (Spruit, 2002). In order to find condition for the stability of this magnetic field, we shall study its response to a wave-like perturbation of the form

$$\exp\left[i\left(l\varpi + m\varphi + nz - \sigma t\right)\right], \tag{5.7}$$

where we have adopted a cylindrical frame (ϖ, φ, z), and l, m, n and σ are constant integers with $\sigma = \sigma_{\rm R} + i\sigma_{\rm I}$ the complex frequency (Acheson & Gibbons, 1978; Zahn et al., 2007). Because horizontal modes are more unstable, we assume $n \to 0$ and by neglecting thermal and magnetic diffusion, it can be shown that the conditions for instabilities are (Tayler, 1957; Spruit, 1999)

$$\begin{aligned} p \equiv \frac{\mathrm{d}\ln B}{\mathrm{d}\ln\varpi} > \frac{m^2}{2} - 1 \quad &\text{for} \quad m \neq 0 \\ p > 1 \quad &\text{for} \quad m = 0. \end{aligned} \tag{5.8}$$

For the moment, we did not included the effect of rotation on the instability, it was just invoked to provide a justification for the geometry of the assumed magnetic field. In the equations governing the dynamic of the perturbation, rotation appears only in the equation of motion through the centrifugal acceleration $\mathbf{\Omega} \times (\mathbf{\Omega} \times \mathbf{r})$ and the Coriolis acceleration $2\mathbf{\Omega} \times \mathbf{v}$, where $\mathbf{v}$ is the velocity of the perturbation. With Pitts & Tayler (1985) we assume that $\mathbf{\Omega}$ is small enough so that the effects on the shape of the star due to centrifugal acceleration are negligible. Then we are left with only the influence of the Coriolis term. It shall be recalled that, in a radiative zone, the restoring force is buoyancy. Therefore, we see that the impact of rotation on Tayler-Spruit instability will depend on the orientation of $\mathbf{\Omega}$ with respect to $\mathbf{g}$. Near the pole, close to the rotation axis, $\mathbf{\Omega} \parallel \mathbf{g}$ and $\mathbf{\Omega} \times \mathbf{v} \perp \mathbf{g}$. Here, the Coriolis force has no impact on the evolution of the instability. On the contrary, near the equator, $\mathbf{\Omega} \perp \mathbf{g}$ and $\mathbf{\Omega} \times \mathbf{v}$ is not perpendicular to $\mathbf{g}$ and the last two vectors have opposite directions. In this region, the Coriolis force will have a stabilizing effect on the growth of the instability. With no rotation, the characteristic growth rate of the instability is of the order of the Alfvén frequency $\omega_{\rm A} = B/(r\sqrt{4\pi\rho}) \ll \Omega$ (Spruit, 1999; Pitts & Tayler, 1985). When the Coriolis force intervenes, the characteristic growth rate is modified by a factor $\omega_{\rm A}/\Omega \ll 1$.

As usual, the AM transported by the Tayler-Spruit instability is modelled as a diffusive process. A general expression for this additional viscosity is proposed by (Maeder & Meynet, 2004) without making the approximation of no thermal and magnetic diffusion:

$$\nu = \frac{\Omega r^2}{q}\left(\frac{\omega_{\rm A}}{\Omega}\right)^3 \left(\frac{\Omega}{N_{\rm B}}\right) \quad \text{with} \quad q = -\frac{\mathrm{d}\ln\Omega}{\mathrm{d}\ln r}, \tag{5.9}$$

and N is a slightly different Brunt-Väisälä frequency:

$$N_{\rm B}^2 = \frac{\eta/K}{\eta/K + 2} N_T^2 + N_\mu^2. \tag{5.10}$$

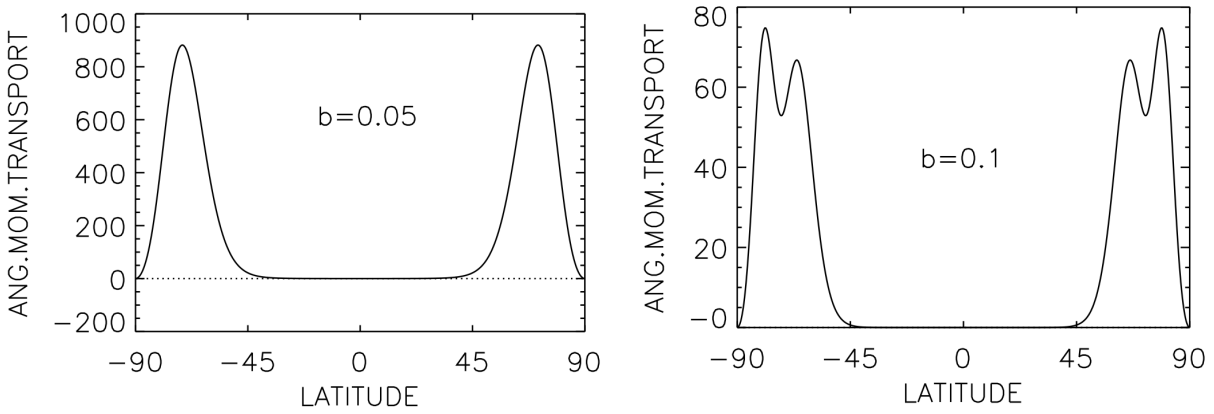

Figure 5.1: Latitudinal angular momentum transport near the solar tachocline for $b \simeq 10\sqrt{b^{(0)}}$ the normalized intensity of the toroidal field, with $b^{(0)}$ the intensity of the fossil poloidal field. *Left:* $b = 0.05$. *Right:* $b = 0.1$. Credits: Rüdiger et al. (2014).

This expression is consistent with the previous expressions found by Spruit (2002).

As a side remark, Tayler-Spruit instability has been proposed by Spruit (2002) to be the engine of a dynamo in a radiative zone. We have seen that, starting from a purely poloidal field, rotation wind-up the magnetic field lines to create a toroidal field. Then this configuration is destabilized by the Tayler-Spruit instability and recreates a poloidal field and so on. This is a similar mechanism as the one invoked for the dynamo into convective zones, however differential rotation is much stronger inside the convective than radiative zone. As we have seen in Chapter 4, the core rotation of the Sun is almost uniform while in its envelope, there is a difference of rotation rate between pole and equator of about 40%. This difference vanishes when going from the convective region to the tachocline (Spiegel & Zahn, 1992) which is about $0.05R_\odot$ thick. In the tachocline, Spruit (2002) showed that the conditions for the instability to occur are gathered and operates on a characteristic time-scale of the order of 100 years. With such a short time-scale, any speed-up of rotation would immediately be flattened by the Tayler-Spruit instability. This hypothesis was tested in the case of RGB stars (Cantiello et al., 2014) including hydrodynamic rotational instabilities (Sect. 5.1) as well as the Tayler-Spruit dynamo. They modelled two red giants for which rotational splittings are available. Their different models were started with an initial rotation period and then left to evolve. For their models with only the hydrodynamic instabilities, even with an extremely low initial rotation period, their modelled rotational splittings are still one order of magnitude too high. With more realistic initial rotation period and all the instabilities taken into account, they could not do better than one order of magnitude too high, even by artificially increasing the Tayler-Spruit viscosity by a factor 100. It shall be stressed that the remaining gap of a factor 10 between actual and modelled rotation rate of RGB stars is still far better than the factor 10^3 that exists when implementing the standard transport of AM. While the physics of Tayler-Spruit instability is well understood, the fact that Tayler-Spruit dynamo actually occurs in stars is still largely debated.

The efficiency of these instabilities in transporting angular momentum has been tested in magneto-hydrodynamic (MHD) codes (e.g Rüdiger et al., 2015; Jouve et al., 2015). Rüdiger et al. (2015) tested the impact on the rotation profile on turbulent viscosity ν_T associated with the azimuthal magneto-rotational instability. They imposed two types of cylindrical rotation profile: $\Omega \propto 1/s$ or $\Omega \propto 1/s^2$. They found that ν_T scales as the rotation profile, *i.e.* the stronger the angular velocity, the stronger the turbulent viscosity. In MHD simulation, a useful way

to characterize the medium is to give is magnetic Prandtl number, which is the ratio of the molecular viscosity ν to the magnetic one η: $\mathrm{Pm} = \nu/\eta$. For a model of red giant with $\mathrm{Pm} = 1$, they found that the decay time of the differential rotation to be around 200 times the period of rotation, making MRI a very efficient mechanism of transport. The study of the angular momentum transport near the tachocline show a strong latitudinal dependence (Rüdiger et al., 2014). These results are reproduced in Fig. 5.1 for two intensities of the toroidal magnetic field. The latitudinal dependence of the MRI-induced angular momentum transport is, of course, a new justification for the 2D description of the stellar interior and angular velocity profile. Because of this anisotropy, and of the effect of the toroidal field, Rüdiger et al. (2014) propose to define an effective magnetic Prandtl number $\mathrm{Pm}_{\mathrm{eff}}$ which incorporate an additional molecular and magnetic viscosity. Rüdiger et al. (2016) showed that the MRI-induced transport of angular momentum could explain the small radial differential rotation profile in the core of red giant at the condition that the differential rotation decreases faster than the intensity of the magnetic field. This condition is fulfilled when $\mathrm{Pm}_{\mathrm{eff}} \gg 1$. In the core of the Sun, $\mathrm{Pm} \simeq 5 \times 10^{-3}$ (not $\mathrm{Pm}_{\mathrm{eff}}$) while in the core of red giants, it is between 0.1 and 10. However, the effective magnetic Prandtl is estimated to be of order 10^3 at the top of the solar convection zone which suggest an efficient MRI in this region.

5.3 Correlation between instabilities

In the two previous sections, I gave an overview of the principal instabilities that may occur in rotating, possibly magnetized, stars and the criteria necessary for them to occur. I have also tried to make apparent the entanglements between many instabilities. When non-standard AM transport mechanisms are added into the modelling they are often treated as diffusive processes and the total diffusion coefficient is the sum of the independent diffusion coefficients. Such a summation supposes that the occurrence of an instability is not impacted by the presence of another one in the medium, which seems clearly wrong. For instance, if shear turbulence develops somewhere in the star, the μ-gradient is changed, therefore, all the criterion that depends on N_μ^2 must take into account that its value is also affected by shear (Maeder et al., 2013). A similar idea could be applied to Rayleigh-Taylor instability. In the Rayleigh-Taylor instability, it is the difference of centrifugal acceleration acquired by a displaced element of fluid that can destabilized the fluid if this acceleration is sufficiently important to overcome stable stratification. However, if this condition is almost satisfied in a region where shear-turbulence occur,, the small additional velocity of the turbulence can provide the missing kinetic energy needed to overcome stable stratification. In other words, Rayleigh-Taylor instability could occur in a region where $N_\Omega^2 > 0$. As a last example, a single look at the criterion for GSF and ABCD instabilities look like the same instability in two different regimes.

Maeder et al. (2013) aimed at taking into account all the couplings between instabilities to provide a proper modelling for them. Let us take a look at their criterion for Rayleigh-Taylor instabilities:

$$\frac{\Gamma}{\Gamma+1}N_T^2 + \frac{\Gamma_\mu}{\Gamma_\mu+1}N_\mu^2 + N_\Omega^2 \sin\theta < \mathrm{Ri_c}\left(\frac{\mathrm{d}v}{\mathrm{d}r}\right)^2, \tag{5.11}$$

with Γ being the ratio of the energy transported by an element of fluid to the energy lost during this motion by thermal diffusion, and Γ_μ is the same but with the energy being lost by particle diffusion, and $\mathrm{Ri_c}$ is the critical Richardson number that controls shear turbulence. The first term represents the stabilizing effect of buoyancy, but also takes into account the thermal diffusivity that may reduce it. Next we have the stabilizing effect of the chemical stratification

with the same limitation as before but this time due to the particle diffusion induced by the shear turbulence (through D_h). Finally we have the epicyclic frequency for the stabilizing effect of the distribution of angular momentum and the Richardson criterion. What is needed here is a way of finding a diffusion coefficient that takes into consideration all the above. We recall that the coefficient of diffusion can be written $D_\mathrm{tot} = v\ell/3$ (see Eq. (2.15)), with v and ℓ the characteristic velocity and mean free path of the fluid motion. To introduce v and ℓ into Eq. (5.11), one must find an expression for Γ and Γ_μ. Such expressions are provided by Maeder (1995); Talon & Zahn (1997). It is based on the same idea as the one underlying the mixing length theory for convection. A turbulent eddy of dimension ℓ is approximated by a sphere of volume V, surface A and $V/A = \ell/6$. The eddy is further assumed optically thick and therefore within the mixing length frame work, (Kippenhahn et al., 2012), the amount of energy carried $\mathcal{E}_\mathrm{c}$ by the eddy and lost $\mathcal{E}_\mathrm{l}$ during its motion are:

$$\mathcal{E}_\mathrm{c} = 2c_p\rho\Delta T V \quad \text{and} \quad \mathcal{E}_\mathrm{l} = \frac{4ac}{3\kappa\rho}\frac{\Delta T}{2\ell}\frac{\ell}{v}A, \tag{5.12}$$

where ΔT is the difference of temperature between the eddy and the surroundings, ℓ/v is the motion duration and all other quantities have their usual meanings. From this, it follows that

$$\Gamma = \frac{v\ell}{6K} \quad \text{and} \quad \Gamma_\mu = \frac{v\ell}{6D_\mathrm{h}}, \tag{5.13}$$

where the expression for Γ_μ was derived by replacing ΔT by $\Delta\mu$ and K by D_h (Talon & Zahn, 1997).

Finally, by injecting Eq. (5.13) into Eq. (5.11) and replacing $v\ell$ by x, one obtains a polynomial inequality, easy to solve for $D_\mathrm{tot} = 2x$:

$$\frac{x}{x + K + D_\mathrm{h}}N_T^2 + \frac{x}{x + D_\mathrm{h}}N_\mu^2 + N_{\Omega+\delta v}^2 < 0, \tag{5.14}$$

where $N_{\Omega+\delta v}^2$ is the slightly modified epicyclic frequency which introduces the little difference of velocity brought by shear turbulence:

$$N_{\Omega+\delta v}^2 = \frac{1}{\varpi^3}\frac{\mathrm{d}\varpi^4\Omega^2}{\mathrm{d}\varpi}\sin\theta + \mathrm{Ri}_\mathrm{c}\left(\frac{\mathrm{d}v}{\mathrm{d}r}\right)^2. \tag{5.15}$$

5.4 Mixed modes

We now turn to another kind of physical processes transporting angular momentum: waves. Waves and modes can exchange angular momentum and energy with the mean flow. In stellar radiative zones, two kinds of modes have been studied: mixed-modes and internal gravity waves (IGW). Section 5.4 is devoted to mixed-modes and Section 5.5 to IGW.

Mixed-modes as a mechanism of transport of AM have been suggested very recently by Belkacem et al. (2015b,a). Their modelling couples the action of non-radial mixed-modes on the angular momentum transport equation and, a fact that is often neglected, on the equation of the transport of energy. This transport mechanism is thought to have non-negligible effects in subgiants and red giants stars. In these stars, mixed-modes are excited by turbulent convection. Furthermore, their amplitudes have been measured by missions CoRoT, *Kepler* and TESS (e.g. Mosser et al., 2011) and have been theoretically studied (Belkacem & Samadi, 2013). I present here the main ideas leading to the expression of the mixed-modes-induced transport of angular momentum.

We start from the system of equations stated at the beginning of Chapter 3: Eqs. (3.1) to (3.3). In these equations, for clarity and to stick to Belkacem et al. (2015b)'s notations, we gathered the non-conservative forces $\mathbf{X}$ and all the heating and cooling terms Q as

$$\mathbf{X} = \rho\mathbf{f} + \boldsymbol{\nabla}\cdot\boldsymbol{\tau}, \tag{5.16}$$

$$Q = \rho(\varepsilon_{\rm nuc} + \varepsilon_{\rm visc}) - \boldsymbol{\nabla}\cdot\mathbf{F}. \tag{5.17}$$

By denoting $h = \varpi u_\varphi = \varpi^2\Omega$ the specific angular momentum, Eq. (3.2), once projected on the azimuthal component, becomes:

$$\frac{\partial\rho h}{\partial t} + \boldsymbol{\nabla}\cdot(\rho h\mathbf{u}) = \frac{\partial p}{\partial\varphi} - \rho\frac{\partial\phi}{\partial\varphi} + \varpi X_\varphi. \tag{5.18}$$

Each of the fields A above can be decomposed as a sum of a mean field $\overline{A}$ and a non-radial wave perturbation A', with $\overline{A} = \frac{1}{2\pi}\int_0^{2\pi} A\mathrm{d}\varphi$. In addition we make the following assumptions. First, for low frequency waves (frequency much lower than the Brunt-Väisälä frequency), the anelastic approximation applies and the terms in factor of ρ' can be neglected. Secondly, the Cowling approximation allows us to neglect the terms ϕ'. Hence, by injecting the field decomposition in our system, by averaging along the azimuth and by doing the above-mentioned approximations, our equations become:

$$\frac{\partial\overline{\rho}}{\partial t} + \boldsymbol{\nabla}_{\rm m}\cdot(\overline{\rho}\,\overline{\mathbf{u}}_{\rm m}) = 0, \tag{5.19}$$

$$\overline{\rho}\frac{\partial\overline{h}}{\partial t} + \overline{\rho}\,(\overline{\mathbf{u}}_{\rm m}\cdot\boldsymbol{\nabla}_{\rm m})\,\overline{h} = -\boldsymbol{\nabla}_{\rm m}\cdot\left(\varpi\overline{\rho}\overline{\mathbf{u}'_\varphi\mathbf{u}'_{\rm m}}\right) + \varpi\overline{X}_\varphi, \tag{5.20}$$

$$\overline{\rho}\frac{\partial\overline{s}}{\partial t} + \overline{\rho}\,(\overline{\mathbf{u}}_{\rm m}\cdot\boldsymbol{\nabla}_{\rm m})\,\overline{s} = -\boldsymbol{\nabla}_{\rm m}\cdot\left(\varpi\overline{\rho}\overline{s'\mathbf{u}'_{\rm m}}\right) + \overline{Q}, \tag{5.21}$$

where $\boldsymbol{\nabla}_{\rm m} = (\partial/\partial r, \frac{1}{r}\partial/\partial\theta, 0)$ is the gradient in the meridional plane, and $\mathbf{u}_{\rm m} = (u_r, u_\theta, 0)$ is the meridional component of the velocity. This system is supplemented by an equation of state giving $\overline{s}(\overline{p},\overline{\rho})$ and a fourth equation: the baroclinic equation, in order to link $\overline{h}$ and $\overline{s}$:

$$\overline{\rho}^2\boldsymbol{\nabla}_{\rm m}\left(\frac{\overline{h}}{\varpi^2}u_\varphi\right)\times\boldsymbol{\nabla}_{\rm m}\varpi = -\boldsymbol{\nabla}_{\rm m}\overline{\rho}\times\boldsymbol{\nabla}_{\rm m}\overline{p}. \tag{5.22}$$

The flux of mean specific angular momentum (resp. mean specific entropy) carried by the waves is: $\varpi\overline{\rho}\overline{\mathbf{u}'_\varphi\mathbf{u}'_{\rm m}}$ (resp. $\varpi\overline{\rho}\overline{s'\mathbf{u}'_{\rm m}}$). Since $\overline{h}$ and $\overline{s}$ are coupled by the baroclinic equation, the waves can induce a meridional circulation and therefore they have an impact on the mean flow. In order to separate the changes on the mean flow due to the waves and the part that is truly a perturbation, Belkacem et al. (2015b) make use of the so-called *transformed Eulerian mean* (TEM) formalism. The wave heat flux $\mathbf{R} = \overline{s'\mathbf{u}'_{\rm m}}$ is written as the sum of a vector perpendicular to isentropics and of one parallel to them, called the skew flux:

$$\mathbf{R} = \underbrace{(\mathbf{n}\times\mathbf{R})\times\mathbf{n}}_{\text{skew flux}} + (\mathbf{n}\cdot\mathbf{R})\mathbf{n} \quad\text{with}\quad \mathbf{n} = \frac{\boldsymbol{\nabla}_{\rm m}\overline{s}}{|\boldsymbol{\nabla}_{\rm m}\overline{s}|}, \tag{5.23}$$

where $\mathbf{n}$ is the normal vector to isentropics. In Eq. (5.20), $\mathbf{R}$ appears on the right hand side, the meridional gradient acting on it. After few steps, one obtains

$$\boldsymbol{\nabla}_{\rm m}\cdot[(\mathbf{n}\times\mathbf{R})\times\mathbf{n}] = \widetilde{\mathbf{u}}\cdot\boldsymbol{\nabla}_{\rm m}\overline{s} \quad\text{with}\quad \widetilde{\mathbf{u}} = \boldsymbol{\nabla}_{\rm m}\times\frac{\boldsymbol{\nabla}_{\rm m}\overline{s}\times\mathbf{R}}{|\boldsymbol{\nabla}_{\rm m}\overline{s}|^2} = \boldsymbol{\nabla}_{\rm m}\times(\overline{\psi}\mathbf{e}_\varphi), \tag{5.24}$$

where $\overline{\psi}$ is a stream function. Therefore, we see that the meridional gradient of the skew flux behaves like an advection of the mean entropy gradient by an additional meridional circulation $\tilde{\mathbf{u}}$. This is the contribution of the wave heat flux to the mean flow. This additional meridional circulation is added to the mean flow which can be written as

$$\overline{\rho}\overline{\mathbf{u}^\dagger} = \overline{\rho}\overline{\mathbf{u}} + \boldsymbol{\nabla}_\mathrm{m} \times (\overline{\rho}\overline{\psi}\mathbf{e}_\varphi). \tag{5.25}$$

We define the flux of specific angular momentum $\mathbf{F} = (F_r, F_\theta)$ and the flux of specific heat $\mathbf{G} = (G_r, G_\theta)$ carried by the waves as

$$F_r = \varpi\overline{u'_\varphi u'_r} + \frac{\overline{\psi}}{r}\frac{\partial\overline{h}}{\partial\theta}, \qquad F_\theta = \varpi\overline{u'_\varphi u'_\theta} + \frac{\overline{\psi}}{r}\frac{\partial\overline{h}}{\partial r}, \tag{5.26}$$

$$G_r = \overline{s'u'_r} + \frac{\overline{\psi}}{r}\frac{\partial\overline{s}}{\partial\theta}, \qquad G_\theta = \varpi\overline{s'u'_\theta} + \frac{\overline{\psi}}{r}\frac{\partial\overline{s}}{\partial r}. \tag{5.27}$$

$$\tag{5.28}$$

And by injecting Eqs. (5.24) and (5.25) into Eqs. (5.19)-(5.21), the system finally reads

$$\frac{\partial\overline{\rho}}{\partial t} + \boldsymbol{\nabla}_\mathrm{m} \cdot \left(\overline{\rho}\,\overline{\mathbf{u}}^\dagger\right) = 0, \tag{5.29}$$

$$\overline{\rho}\frac{\partial\overline{h}}{\partial t} + \overline{\rho}\left(\overline{\mathbf{u}}^\dagger \cdot \boldsymbol{\nabla}_\mathrm{m}\right)\overline{h} = -\boldsymbol{\nabla}_\mathrm{m} \cdot (\overline{\rho}\mathbf{F}) + \varpi\overline{X}_\varphi, \tag{5.30}$$

$$\overline{\rho}\frac{\partial\overline{s}}{\partial t} + \overline{\rho}\left(\overline{\mathbf{u}}^\dagger \cdot \boldsymbol{\nabla}_\mathrm{m}\right)\overline{s} = -\boldsymbol{\nabla}_\mathrm{m} \cdot (\overline{\rho}\mathbf{G}) + \overline{Q}. \tag{5.31}$$

For the moment, no assumptions have been made as to the nature of the mode (except low frequency). Assuming that the rotation profile is shellular and that isentropics nearly superimpose with isobars, the vertical equation for the transport of angular momentum can be written as

$$\rho\frac{\mathrm{d}r^2\overline{\Omega}}{\mathrm{d}t} = \frac{1}{r^2}\frac{\partial}{\partial r}\left(r^2\left(F_U + F_\nu + F_\mathrm{waves}\right)\right). \tag{5.32}$$

I recall that here, $\rho = \langle\rho\rangle$ is the density averaged over isobars, where $\langle\cdot\rangle$ is the average over an isobar defined in Eq. (1.69). The expression of F_U and F_ν are derived easily from Eq. (2.118), and Belkacem et al. (2015b) derive F_waves as:

$$F_\mathrm{waves} = \rho\left\langle\varpi\left[\overline{u'_\varphi u'_r} + 2\cos\theta\Omega_0\overline{u'_\theta s'}\left(\frac{\mathrm{d}\langle s\rangle}{\mathrm{d}r}\right)^{-1}\right]\right\rangle, \tag{5.33}$$

where $\Omega_0(r)$ temporarily denotes $\overline{\Omega}(r)$ defined in Eq. (1.44), so as not to mistake it with the mean flow notation. Belkacem et al. (2015b) provide a more detailed expression for F_waves carried by waves with degree ℓ and azimuthal number m. I do not reproduce either the relation or the long calculation necessary to its computation. It depends on equilibrium quantities as well as on the rotation profile and on the amplitudes of the displacement $\xi_{r,\theta}^{\ell m}$ or, equivalently, on the amplitudes of velocity $u_{r,\theta}^{\ell m}$ of the waves.

As said at the beginning of this section, mixed-modes have been the subject of a lot of observations which allowed the development of scaling relations providing, in case of low rotation rates and in the asymptotic limit, the surface velocity of radial ($\ell = 0$) and non-radial ($\ell > 0$) modes (Belkacem & Samadi, 2013; Belkacem et al., 2015a). The amplitude of the velocity of radial modes at ν_max is given as a power law of global quantities: $T_\mathrm{eff}, \nu_\mathrm{max}$ and $\Delta\nu$. For a radial mode with any frequency ν, the amplitude is found assuming a Gaussian envelope of

the amplitudes. For non-radial modes, Belkacem et al. (2015a) found a relation between the non-radial amplitude, the radial one and the ratio of the radial to non-radial mode inertia. In order to implement this mechanism of transport of AM in a stellar evolution code, one needs the frequencies of each mixed-mode. Of course, the frequency spectrum could be provided by an oscillation code, but it would lengthen the computations a lot and it would not be portable at all. The mixed-mode frequency spectrum, at each time step, is computed using asymptotic relations. References are provided at the end of Sect. 3.2.2.

Belkacem et al. (2015a) estimated the efficiency of the mixed-modes-induced transport by comparing two time-scales. The first one is the contraction time-scale T_c that characterizes the time-scale on which the rotation of the star increases/decreases due to contraction/dilation. The second one, T_L, is the ratio of the angular momentum contained in the same spherical shell in solid body rotation $\Omega_0(r)$ to the flux of angular momentum extracted from a spherical shell of radius r per unit time. Those time-scales were computed using three stellar models of subgiant, start of RGB and RGB, on which they supposed a rotation profile of the form of an erf function. The frequency spectrum was computed using ADIPLS (Christensen-Dalsgaard, 2008). It must be noted that the two time-scales were computed a posteriori, *i.e.* assuming no coupling between the rotation profile and the transport of AM by mixed-modes. They found that for the subgiant and young RGB models, $T_\mathrm{L} \gg T_\mathrm{c}$ meaning that mixed-modes are very inefficient to transport AM. In the evolved RGB model, $T_\mathrm{L} \ll T_\mathrm{c}$ in the hydrogen-burning shell. However, in the upper and deepest layers of the radiative region, mixed-modes become inefficient again. Mixed-modes are therefore an important extractor of angular momentum in very evolved stars. Furthermore, the authors did not take into account the feedback of the mixed-modes transport on the structure and on the mean flow. Indeed, T_L and T_c are computed *a posteriori* after the complete evolution of the model. In the regions of the RGB model where AM is efficiently extracted, the gradient of angular velocity should appear and induce shear induced turbulence as well as meridional circulation which should couple the regions of the radiative zone where mixed-modes are efficient and inefficient.

5.5 Internal gravity waves

5.5.1 Internal gravity waves in fluid: a simple approach

Internal gravity waves (IGW) are waves which have gravity as a restoring force. These waves are found in stars but also in the Earth's oceans[3] and atmosphere. Their study in geophysics has preceded their study in stellar interiors. Since, in the Earth, IGW have a small extent, which usually is below the spatial resolution of meteorological simulations, their interactions with the mean flow cannot be simulated from first principles and must be treated as a prescription. The study of such phenomena has motivated the development of wave-mean flow interaction theories (e.g. Bühler, 2014). Here, I want to describe the main and most interesting features of IGW.

One of the simplest models in which IGW can be found is a Boussinesq system. The model that will be developed here captures quite well the dynamics of IGW in the Earth's oceans. It is very far from what happens in the Earth's atmosphere or in stars but it is sufficient to reveal the main properties of IGW. In the following, we assume that the density gradients are small[4]

[3]Sea waves are surface gravity waves.

[4]This is why this model is adapted to oceans and not to the atmosphere. In Earth's atmosphere, it would be a better choice to assume that the entropy gradients are small. In the first case, it amounts to assuming that isobars and isopycnals are equal, while in the second case, that isobars equal to isentropics. In reality, the Earth, as well as rotating stars, is baroclinic and therefore, neither isopycnals nor isentropics equal isobars.

and that no sound waves can propagate: $\boldsymbol{\nabla}\cdot\mathbf{u}=0$. Furthermore, we write the equilibrium quantities, constant in time, with a 0 subscript. We place ourselves in a Cartesian coordinate system with a basis $(\mathbf{e}_x,\mathbf{e}_y,\mathbf{e}_z)$, z being the vertical coordinate. Within this framework, the Euler equation reads

$$\frac{\rho}{\rho_0}\frac{\mathrm{d}\mathbf{u}}{\mathrm{d}t}+\boldsymbol{\nabla}\left(\frac{p}{\rho_0}\right)=\frac{\rho}{\rho_0}g_0\mathbf{e}_z, \tag{5.34}$$

where all the quantities have their usual meanings and I recall that $\mathrm{d}/\mathrm{d}t$ is the material derivative $\partial/\partial t+\mathbf{u}\cdot\boldsymbol{\nabla}$. Since the density gradients are small, ρ/ρ_0 is close to unity, except in factor of gravity. We define $\widetilde{p}=p/\rho_0$ and $S=\rho g_0/\rho_0$, and this equation may be written as

$$\frac{\mathrm{d}\mathbf{u}}{\mathrm{d}t}+\boldsymbol{\nabla}\widetilde{p}=S\mathbf{e}_z. \tag{5.35}$$

Furthermore, the continuity equation together with the hypothesis of $\boldsymbol{\nabla}\cdot\mathbf{u}=0$ gives $\mathrm{d}S/\mathrm{d}t=0$. The quantity S is called the stratification and, in this case, surfaces of iso-S are isopycnals. Assuming that the background stratification $S_0(z)$ is known, new quantities can be introduced: $p=\widetilde{p}-\widetilde{P}_0$ and $S=b+S_0(z)$, where b is denoted the buoyancy. The buoyancy b is the perturbation of that equilibrium stratification S_0 and a $b\neq 0$ induces a change in the vertical velocity. Indeed, by using those new quantities and $\mathbf{u}=u\mathbf{e}_x+v\mathbf{e}_y+w\mathbf{e}_z$, above equation becomes

$$\frac{\mathrm{d}\mathbf{u}}{\mathrm{d}t}+\boldsymbol{\nabla}p=b\mathbf{e}_z \quad\text{and}\quad \frac{\mathrm{d}b}{\mathrm{d}t}+N^2w=0, \tag{5.36}$$

where N^2 is the Brunt-Väisälä frequency, or to stick to the denominations, usual in this kind of models, the buoyancy frequency. The vertical motion induced by a change in the buoyancy b is evident from last equation. The stratification S can also be written in an integral form:

$$S=b+\int N^2\mathrm{d}z. \tag{5.37}$$

Assuming that N^2 does not depend on z, $S_0(z)=N^2z$.

Eqs. (5.36) form the Boussinesq equations but for the moment, we did not see any waves. To make them emerge, Eqs. (5.36) is linearised by writing all quantities as the sum of a constant field and of a perturbation: $x=X+x'$, with $x'\ll X$. Then

$$\frac{\mathrm{d}u'}{\mathrm{d}t}+\frac{\partial p}{\partial x}=0, \qquad \frac{\mathrm{d}v'}{\mathrm{d}t}+\frac{\partial p}{\partial y}=0, \tag{5.38}$$

$$\frac{\mathrm{d}w'}{\mathrm{d}t}+\frac{\partial p}{\partial z}-b'=0, \qquad \frac{\mathrm{d}b'}{\mathrm{d}t}+N^2w'=0, \tag{5.39}$$

and the incompressibility constraint still holds: $\boldsymbol{\nabla}\cdot\mathbf{u}'=0$. Alternatively, the first three equations could be written as $\frac{\mathrm{d}\mathbf{u}}{\mathrm{d}t}+\boldsymbol{\nabla}p+\mathbf{b}'=0$, with $\mathbf{b}'=(0,0,b')$. Recalling that the vorticity is defined as $\boldsymbol{\omega}=\boldsymbol{\nabla}\times\mathbf{u}$ (see Eq. (2.5)) we take the curl of this equation and it leads to

$$\frac{\mathrm{d}}{\mathrm{d}t}\left(\frac{\partial u'}{\partial y}-\frac{\partial v'}{\partial x}\right)=0, \tag{5.40}$$

$$\frac{\mathrm{d}}{\mathrm{d}t}\left(\frac{\partial v'}{\partial z}-\frac{\partial w'}{\partial y}\right)=\frac{\partial b'}{\partial z}, \tag{5.41}$$

$$\frac{\mathrm{d}}{\mathrm{d}t}\left(\frac{\partial w'}{\partial x}-\frac{\partial u'}{\partial z}\right)=\frac{\partial b'}{\partial x}. \tag{5.42}$$

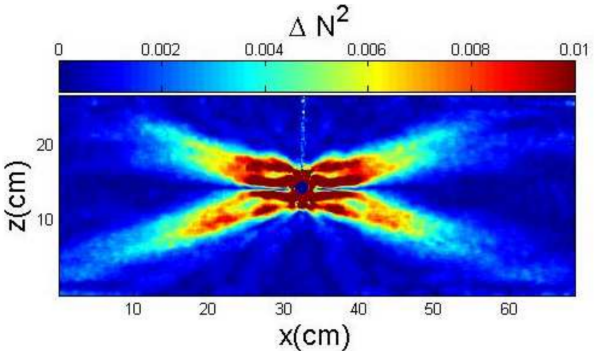

Figure 5.2: *Left:* Saint Andrew's cross obtained by making vertically oscillate a cylinder in a stratified fluid. The cylinder is viewed from above in the centre of this image. Credits: Mercier et al. (2008)

Finally, introducing the displacements $\boldsymbol{\xi}' = (\xi', \eta', \zeta')$ linked to the perturbation velocity by $\mathrm{d}\boldsymbol{\xi}'/\mathrm{d}t = \mathbf{u}'$ yields $\zeta' = N^2 w'$ and

$$\begin{aligned} \frac{\mathrm{d}\boldsymbol{\omega}'}{\mathrm{d}t} &= N^2 \mathbf{e}_z \times \boldsymbol{\nabla}_\perp \zeta' \\ \frac{\mathrm{d}^2\boldsymbol{\omega}'}{\mathrm{d}t^2} &= N^2 \mathbf{e}_z \times \boldsymbol{\nabla}_\perp w' \\ \frac{\mathrm{d}^2 \nabla^2 w'}{\mathrm{d}t^2} &= -N^2 \boldsymbol{\nabla}_\perp^2 w', \end{aligned} \qquad \begin{array}{l} \big) \ \frac{\mathrm{d}}{\mathrm{d}t} \\ \big) \ \boldsymbol{\nabla}\times \text{ and projection on } \mathbf{e}_z \end{array} \tag{5.43}$$

where $\boldsymbol{\nabla}_\perp = (\partial/\partial x, 0, \partial/\partial z)$ has been defined (Davidson, 2013) and where we used the identity $\boldsymbol{\nabla} \times (\boldsymbol{\nabla} \times \mathbf{u}) = \boldsymbol{\nabla}(\boldsymbol{\nabla} \cdot \mathbf{u}) - \nabla^2 \mathbf{u}$.

We assume a plane wave shape for $\mathbf{u}'$ with a wave number $\mathbf{k} = (n, \ell, m)$, and a frequency σ. In Chapter 3, we use ω to denote the frequency. We change notations locally so as not to confuse the frequency and the vorticity $\boldsymbol{\omega}$. With these notations, the dispersion relation is given by

$$\sigma \left(\sigma^2 - N^2 \frac{n^2 + \ell^2}{n^2 + \ell^2 + m^2} \right) = 0. \tag{5.44}$$

One of the solutions for this equation is, of course, $\sigma = 0$. For this to be true, one must have $w' = 0$, $\boldsymbol{\nabla} p' = b' \mathbf{e}_z$ and $\partial u'/\partial x + \partial v'/\partial y = 0$. Such mode conserves the so-called *potential vorticity* q (Vallis, 2006). The potential vorticity is the part of the vorticity that is frozen into the fluid, perpendicular to the stratification. In our case $q = \frac{(\boldsymbol{\nabla}\times\mathbf{u})\cdot\boldsymbol{\nabla} S}{\rho}$. Such modes are called *vortical modes*. On the contrary, waves with $\sigma \neq 0$, called *planar internal gravity waves* have a zero potential vorticity. Due the approximation that $\boldsymbol{\nabla} \cdot \mathbf{u}' = 0$, it follows that the velocity $\mathbf{u}'$ of the fluid is always perpendicular to the wave number $\mathbf{k}$, making them *transverse waves*. Two solutions remain valid for the dispersion relation (5.44):

$$\sigma = \pm N \sqrt{\frac{n^2 + \ell^2}{n^2 + \ell^2 + m^2}}. \tag{5.45}$$

These two solutions are actually a prograde and a retrograde wave. They propagate in two directions separated by an angle close to $\pi/2$ and form the famous shape of a *Saint Andrew's cross* (see Fig. 5.2). Furthermore, by adopting Einstein's notations,

$$k_i \frac{\partial \sigma}{\partial k_i} = k_i \mathbf{c}_\mathrm{g}^i = 0, \quad \text{with} \quad \{k_i\} = (n, \ell, m) \text{ and } \mathbf{c}_\mathrm{g} = \left(\frac{\partial \sigma}{\partial k_i} \right), \tag{5.46}$$

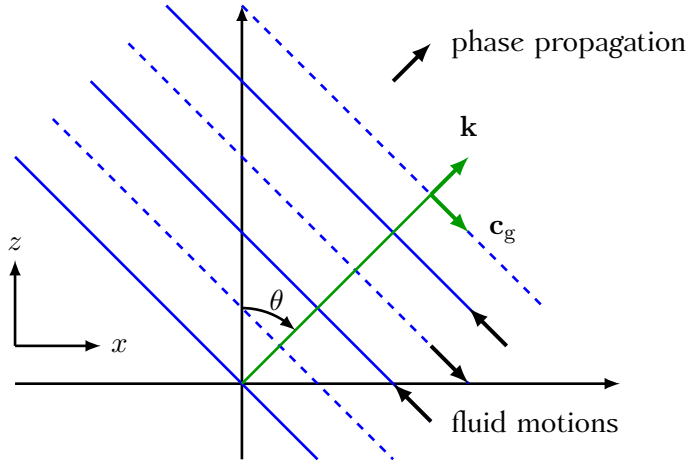

Figure 5.3: Drawing of an internal gravity wave with phase propagating in the direction $\mathbf{k}$ and phase velocity $\mathbf{c}_p \parallel \mathbf{k}$, and energy propagating with group velocity $\mathbf{c}_g \perp \mathbf{k}$. Solid blue lines represent surfaces of higher density and the dashed lines represent the the surfaces of lower density.

where $\mathbf{c}_g$ is the group velocity while $\mathbf{c}_\varphi = \mathbf{k}\sigma/|\mathbf{k}|^2$ is the phase velocity. Interestingly, we have $\mathbf{c}_g \perp \mathbf{c}_\varphi$, $\mathbf{c}_g \perp \mathbf{k}$ and $\mathbf{c}_\varphi \parallel \mathbf{k}$. This situation is illustrated Fig. 5.3 in which a IGW propagates with a wave number making an angle $\sin\theta = \sqrt{(n^2+\ell^2)\,/\,(n^2+\ell^2+m^2)}$ with the vertical. Following the $\mathbf{k}$ direction, we go from crest of high density with fluid motion perpendicular to $\mathbf{k}$ in a given direction, to a crest of low density with fluid motion in the opposite direction.

Those are some striking properties of IGW. Of course the Boussinesq models capture only the essence of IGW and almost nothing more. Specific models should be designed to fit specific situations.

5.5.2 Internal gravity waves excitation models

In order to account for the effects of IGW in the transport of angular momentum, a model describing their excitation should be provided. Many authors have work on this problem and developed a myriad of IGW excitation models. All of them agree on the fact that IGW are excited by convective motions at the transition between convective and radiative zones. I will describe in this section two models that assume very different excitation mechanism: excitation by Reynolds stresses (Press, 1981; Garcia Lopez & Spruit, 1991; Kumar & Quataert, 1997; Kumar et al., 1999) and excitation by convective plumes (Pinçon et al., 2016). These two models must not be seen as competitors because both Reynolds stress and plumes do excite IGW in stellar interiors. They are rather complementary since Reynolds stress models seems to miss part of the contribution of low frequency waves while the plume model does not excite high frequency IGW. I will not provide a full derivation of the wave fluxes and of all of the terms they include but I will present the main ideas and originalities of the models developed by Kumar et al. (1999) (hereafter K99) and Pinçon et al. (2016) (hereafter P16).

First of all, one needs to define the angular momentum flux of an IGW of intrinsic frequency ω and quantum numbers ℓ and m., *i.e.* the amount of angular momentum crossing through a unit surface. This flux can be expressed as a function of the wave energy flux F_E per unit frequency, and with same quantum numbers:

$$F_A(\ell, m, \omega; r) = \frac{m F_E(\ell, m, \omega; r)}{\omega}. \tag{5.47}$$

It is also very common to define the angular momentum luminosity of a wave with ℓ, m and ω and the flux $F_{\rm A}$ integrated over a spherical surface of radius r:

$$L_{\rm A}(\ell, m, \omega; r) = 4\pi r^2 F_{\rm A}(\ell, m, \omega; r). \tag{5.48}$$

Similarly, a wave energy luminosity $L_{\rm E}$ can be associated the flux $F_{\rm E}$ and the angular momentum luminosity can be written:

$$L_{\rm A}(\ell, m, \omega; r) = \frac{m L_{\rm E}(\ell, m, \omega; r)}{\omega}. \tag{5.49}$$

If the star is adiabatic, the total angular momentum flux (resp. luminosity) is the sum over ℓ and m and integral over frequency of $F_{\rm A}(\ell, m, \omega; r)$ (resp. $L_{\rm A}(\ell, m, \omega; r)$). It amounts to considering that the waves do not impact the mean flow. However, these waves experience damping as they propagate inside the star and their total effect is modulated by a damping term:

$$F_{\rm A}(r) = \sum_{\ell,m} \int_0^{+\infty} F_{\rm A}(\ell, m, \omega; r_{\rm C}) \exp\left[-\tau(\omega, \ell, m; r)\right] {\rm d}\omega, \tag{5.50}$$

or

$$L_{\rm A}(r) = \sum_{\ell,m} \int_0^{+\infty} L_{\rm A}(\ell, m, \omega; r_{\rm C}) \exp\left[-\tau(\omega, \ell, m; r)\right] {\rm d}\omega, \tag{5.51}$$

where $\tau(\omega, \ell, m; r)$ can be seen as a "optical" damping depth and $r_{\rm C}$ is the radius of excitation of internal gravity waves, or the radius from which IGW can propagate without any energy being added to it. This location can be located just below the convective zone (Kumar et al., 1999; Pinçon et al., 2016), in the overshoot region Press (1981); Lecoanet & Quataert (2013).

The excitation models presented below provide an expression for $F_{\rm E}(\ell, m, \omega; r)$ and $\tau(\omega, \ell, m; r)$.

Reynold stress excitation model (Kumar et al., 1999)

The model of excitation developed by K99 is an evolution of the model designed by Press (1981). The excitation mechanism is the same but the region in which the waves are excited is not. In both models, IGW are excited by the turbulent pressure. While in K99's model, IGW are excited in all the convective zone and then tunneled into the radiative one, the Press (1981) model assumes that the waves are only excited inside the overshoot region. This idea is also developed by Lecoanet & Quataert (2013). I will only describe K99 because it is one of the most used.

This model is based on an expression for the energy flux $F_{\rm E}^{\rm C}(\ell, m, \omega)$ per unit frequency at the base of the convection zone derived by Goldreich et al. (1994):

$$F_{\rm E}^{\rm C}(\ell, m, \omega) = \frac{\omega^2}{4\pi} \int_{r_{\rm b}^{\rm C}}^{r_{\rm t}^{\rm C}} \frac{\rho^2}{r^2} \left[\left(\frac{\partial \xi_r}{\partial r} \right)^2 + \ell(\ell+1) \left(\frac{\partial \xi_{\rm h}}{\partial r} \right)^2 \right] \exp\left[-\frac{h_\omega^2 \ell(\ell+1)}{2r^2} \right] \frac{v^3 L^4}{1 + (\omega \tau_{\rm L})^{15/2}} {\rm d}r. \tag{5.52}$$

This expression was derived under the hypothesis that turbulence follows a Kolmogorov spectrum and ignoring the excitation of waves in the overshoot regions. The limits $r_{\rm b}^{\rm C}$ and $r_{\rm t}^{\rm C}$ stand for the bottom and top boundary radii of the convection zone. The eigenfunctions ξ_r and $\xi_{\rm h}$ are the radial and horizontal displacements normalized by unit of IGW energy right

below the convective zone. The displacements can be expressed using the JWKB approximation (Jeffreys-Wentzel-Kramers-Brillouin). This approximation is valid when the wavelength of the wave is much shorter than the characteristic spatial scale of variation of the equilibrium quantities, or else that the phase should vary much faster that the amplitude of the wave (for more detail, see Aerts et al., 2010). The quantity v is the convective velocity and L the characteristic size of the eddies transporting energy. The duration $\tau_{\rm L} \simeq L/v$ is called the convective turnover time. Finally, $h_\omega(r)$ is the radial characteristic size of the largest eddy with frequency ω at radius r. This model assumes that the eddies providing energy to IGW follow a Gaussian distribution with standard deviation $\sqrt{2}/(h_\omega\sqrt{\ell(\ell+1)})$. The length h_ω is defined by $h_\omega = L\min\left[1,(2\omega\tau_{\rm L})^{-3/2}\right]$.

Those waves are assumed to be damped by radiation. K99 provide an expression for the damping depth $\tau(\omega,\ell,m;r)$:

$$\tau(\omega,\ell,m;r) = \int_r^{r_{\rm b}^{\rm C}} \frac{\gamma(\omega_\star,\ell;r')}{v_{\rm gr}(\omega_\star,\ell;r')}{\rm d}r' \quad \text{with} \quad \omega_\star(r) = \omega + m\left[\Omega_{\rm C} - \Omega(r)\right] = \omega + m\delta\Omega, \tag{5.53}$$

where γ is the damping rate (already mentioned in Eq. (3.68)), $v_{\rm gr} \simeq \omega^2/(k_{\rm h}N)$ is the group velocity of the wave, and $\omega_\star$ is the well-known intrinsic frequency, but with the angular velocity measured with respect to the angular velocity at the base of the convective zone $\Omega_{\rm C}$. The damping rate is expressed by

$$\gamma(\omega,\ell,m;r) \simeq Kk_r^2 \quad \text{with} \quad K = \frac{16\sigma T^3}{3\rho^2\kappa c_p} \simeq \frac{2F_{\rm r}H_{\rm T}}{5p}, \tag{5.54}$$

where K is the thermal diffusivity, already defined and used in Eq. (1.16), $k_r \simeq k_{\rm h}N/\omega$ is the radial wave number, $F_{\rm r}$ is the radiative flux and $H_{\rm T}$ the temperature scale height, also defined in Eq. (2.99).

Convective plume excitation model (Pinçon et al., 2016)

As stressed by K99, the two dominant processes of IGW excitation in stellar interiors are the Reynold stresses and the convective plumes, with the last one thought by the authors to be the most important. However, because of the poor models of plumes available (at that time), they focused only on excitation by Reynolds stresses. The study of convective penetration has been the subject of numerical (e.g. Dintrans et al., 2005; Rogers & Glatzmaier, 2006; Alvan et al., 2014) and theoretical studies, especially models of plumes (Rieutord & Zahn, 1995).

The model of Pinçon et al. (2016) assumes that, $\mathcal{N}$ plumes per unit time penetrate into the radiative zone, exciting waves. Each plume is located at latitude and azimuth (θ_i,φ_i) (see Fig. 5.4, left panel), and, assuming that $\mathcal{N}$ is sufficiently large, the mean radial wave energy flux is given by:

$$F_{\rm E}(\omega,\ell,m;r) = \mathcal{N}\widetilde{\mathcal{E}}_{\ell m}(\omega;r)v_{\rm gr}(\omega,\ell;r), \tag{5.55}$$

with

$$\widetilde{\mathcal{E}}_{\ell m}(\omega;r) = \frac{\nu_{\rm P}}{8\pi^2}\rho\int_{\Omega_0}\left\{|\hat{v}_{r,\ell m}|^2 + \ell(\ell+1)|\hat{v}_{{\rm h},\ell m}|^2\right\}\frac{{\rm d}\Omega_0}{4\pi}, \tag{5.56}$$

where $\widetilde{\mathcal{E}}_{\ell m}(\omega;r)$ is the average energy injected by a plume into the component of a wave with quantum numbers ℓ and m and frequency ω. The functions $\hat{v}_{r,\ell m}$ and $\hat{v}_{{\rm h},\ell m}$ are the radial and horizontal components of the Fourier transform of the wave velocity field. The quantity Ω_0 is the solid angle. The term $\nu_{\rm P} = 1/\tau_{\rm P}$ is the inverse of the characteristic plume lifetime

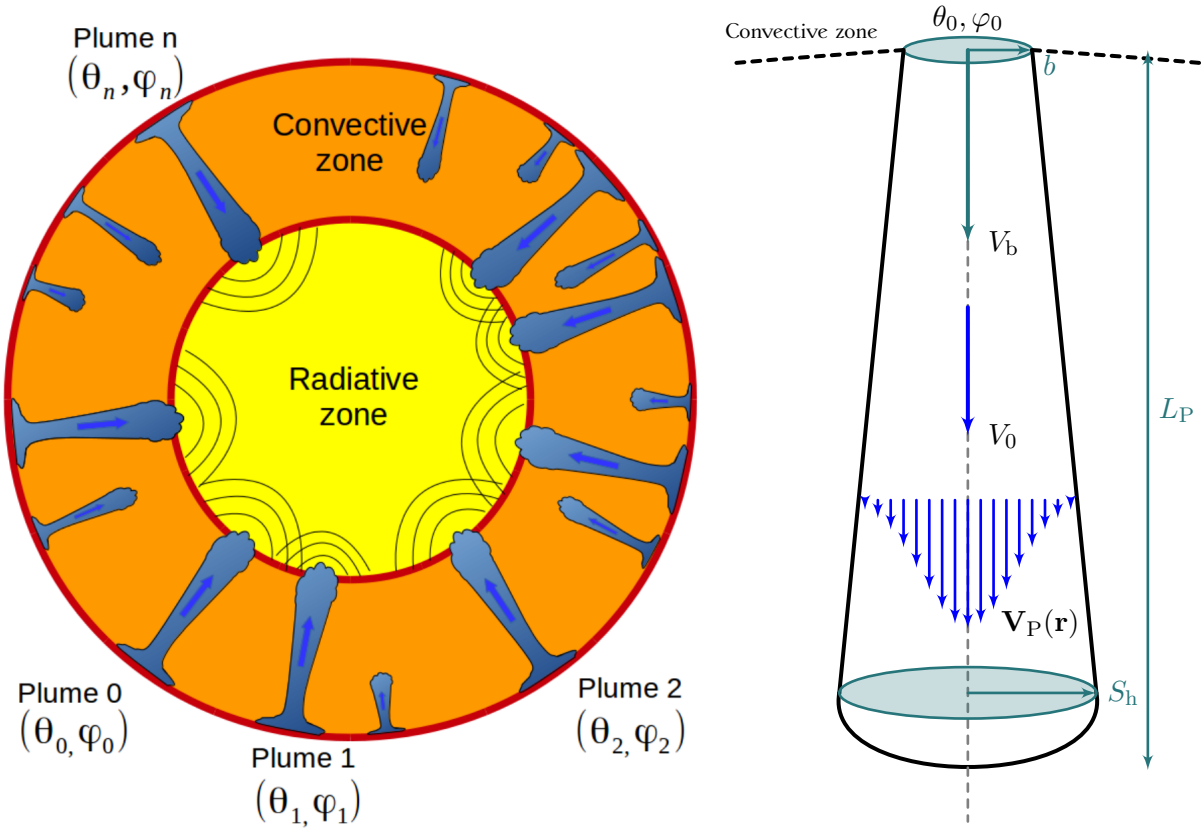

Figure 5.4: *Left:* Drawing of plumes inside stars. Each plumes is characterized by its latitude and azimuth of emission (θ_i, φ_i). Credits: Pinçon et al. (2016). *Right:* Schematic view of a plume at angular location (θ_0, φ_0), central velocity V_0, plume velocity field $\mathbf{V}_P(r) = V_0 e^{-S_h^2/2b^2} e^{-t^2/\tau_P^2} \mathbf{e}_r$, characteristic radius b, the penetration length L_P and initial vertical velocity V_b. The dashed line is the axis of symmetry of the plume.

τ_P. Finally, $v_{gr}(\omega, \ell; r)$ is the radial component of the group velocity which has the following expression (P16):

$$v_{gr}(\omega, \ell; r) = \frac{\omega^2}{N^2} \frac{(N^2 - \omega^2)^{1/2}}{k_h} \quad \text{with} \quad k_h = \frac{\sqrt{\ell(\ell+1)}}{r}. \tag{5.57}$$

In order to be able to compute the various unknowns introduced above, this model needs to be supplemented by a geometrical description of a plume (Rieutord & Zahn, 1995). Fig. 5.4, right panel, represents a schematic view of a plume. Inside a plume located at angles θ_0 and φ_0, the velocity field is assumed to have a Gaussian shape in the horizontal direction and in time:

$$\mathbf{V}_P(\mathbf{r}) = V_0(r) e^{-S_h^2/2b^2} e^{-t^2/\tau_P^2} \mathbf{e}_r, \tag{5.58}$$

where

- S_h is the distance on a sphere of radius r to the axis of symmetry of the plume:

$$S_h(\mathbf{r}; \theta_0, \varphi_0) = r \arccos\left[\sin\theta_0 \sin\theta \cos(\varphi - \varphi_0) + \cos\theta \cos\theta_0\right]. \tag{5.59}$$

- V_0 is the vertical convective plume velocity:

$$V_0(z) = V_\mathrm{b}\left[1 - \left(\frac{z}{L_\mathrm{P}}\right)^2\right]^{1/3} \quad \text{with} \quad V_\mathrm{b} = \left(\frac{8F_{1,\mathrm{P}}}{\pi\rho_\mathrm{b}b^2}\right)^{1/3}, \tag{5.60}$$

  where $z = r_\mathrm{b} - r$ the distance between the base of the convective zone r_b and the radius r, V_b is the initial velocity of the plume at the base of the convective zone, L_P is the penetration distance of the plume (P16 estimated it to be around $0.1H_\mathrm{p}$, given the lack of consensus on its value), $F_{1,\mathrm{P}}$ is the sum of the kinetic and enthalpic luminosities carried by the plume and ρ_b its density. The authors propose to write $\mathcal{N}F_{1,\mathrm{P}} \simeq L\mathcal{A}$, where L is the star luminosity and $\mathcal{A} = \mathcal{N}b^2/4r_\mathrm{b}^2$ is the filling factor, *i.e.* fraction occupied by plumes at the base of the convective zone. Using this expression, V_b simplifies to

$$V_\mathrm{b} = \left(\frac{2L}{\pi\rho_\mathrm{b}r_\mathrm{b}^2}\right)^{1/3}. \tag{5.61}$$

- b is the plume radius at the bottom of the convective zone:

$$b = \frac{z_0}{\sqrt{2}}\frac{3\alpha_\mathrm{E}(\Gamma_1 - 1)}{2\Gamma_1 - 1}, \tag{5.62}$$

  with z_0 the thickness of the convective zone and α_E is the entrainment coefficient[5]. The entrainment coefficient $\alpha_\mathrm{E}\rho_\mathrm{b}bV_\mathrm{b}$ can be seen as the amount of matter that is swept away by the plume (Rieutord & Zahn, 1995).

- τ_P is the lifetime of the plume. In order to estimate it, one must find a damping mechanism for the plume (not to be mistaken with the damping mechanism of the excited waves). P16 suggest three mechanisms:

  - Radiative thermalization: it is the destruction of the plume due to the radiative thermal diffusion. They find it to be highly inefficient because it operates on time-scales much longer than the dynamical time-scale $L\mathrm{P}/V_\mathrm{b} \simeq 10^4$ s of the propagation of the plume;
  - Turbulence inside the plume: in the description of the plume, it is assumed that the flow is laminar, while in reality it is turbulent. The turbulence destroys the plume in a few turnovers, *i.e.* on a turbulence time-scale $t_\mathrm{turb} \simeq b/V_\mathrm{b}$. This time-scale is one order of magnitude higher than the dynamical time-scale scale but much shorter than the radiative thermalization time-scale.
  - The last mechanism suggested by P16 is the restratification by lateral baroclinic eddies that was first suggested in oceanic physics. When the convective plume penetrates into the radiative region, the density gradient between them drives baroclinic instabilities taking the form of lateral eddies mixing the material of both regions. The restratification time-scale is hard to evaluate but can be estimated around two or three orders of magnitude higher than the dynamical time-scale.

  Without any better prescription, the author took $\tau_\mathrm{P} \in [10^5 - -10^7]$ s in case of the Sun.

[5]The word "entrainment" used in Rieutord & Zahn (1995) seems not to be part of any English dictionary. It is the direct translation of the same French word which, for the English reader, could be translated as "driving coefficient".

The plumes are supposed to penetrate on a distance $L_{\rm P}$ where the Brunt-Väisälä frequency is nearly zero. Then the plume stops and IGW are excited. They first propagate in a transition region of size d in which the Brunt-Väisälä frequency goes from nearly 0 to a nearly constant value N_0^2, and then in the radiative zone. The bottom radius of the transition region (therefore the radius at which we enter the radiative region) is $r_{\rm d} = r_{\rm b} - L_{\rm P} - d$. In the transition region, the velocity of the plume is much lower than $V_{\rm b}$. After some mathematical manipulations, P16 arrive at an expression of the energy flux of the form:

$$F_{\rm E}(\omega, \ell, m; r) = f(\gamma_{\rm d}) \frac{\mathcal{N}}{4} \frac{\sqrt{\ell(\ell+1)}}{4\pi r^2} \frac{(N_0^2 - \omega^2)^{1/2}}{N_0^2} \frac{e^{-\omega^2/4\nu_{\rm P}^2}}{\nu_{\rm P}} \mathcal{B}_\ell \mathcal{H}_\ell^2. \tag{5.63}$$

The new terms have the following signification:

- $f(\gamma_{\rm d})$ is a transmission function that characterizes the smoothness of the transition ($\gamma_{\rm d} \ll 1$: very sharp; $\gamma_{\rm d} \gg 1$: very smooth). The function f is given by

$$f(x) = \begin{cases} 1 & \text{if} \quad x < 1 \\ D\sqrt{x}\left(1 - \frac{\omega^2}{N_0^2}\right) & \text{if} \quad x > 1 \quad (D \simeq 3.7) \end{cases}. \tag{5.64}$$

  and $\gamma_{\rm d}$ by

$$\gamma_{\rm d} = \left(\frac{k_{\rm h} d N_0}{\omega}\right)^{2/3} \frac{N_0^2 - \omega^2}{N_0^2} \simeq (k_r d)^{2/3}. \tag{5.65}$$

- $e^{-\omega^2/4\nu_{\rm P}^2}/\nu_{\rm P}$ is the temporal correlation term. A longer plume lifetime causes the energy to be transferred to higher frequency waves.

- The horizontal spatial wave/plume correlation is expressed as

$$\beta_\ell^m(\theta_0, \varphi_0) = \int_\Omega \exp\left(-\frac{S_{\rm h}^2}{b^2}\right) \overline{Y_\ell^m} {\rm d}\Omega, \tag{5.66}$$

  with $\overline{Y_\ell^m}$ the Fourier transform of the spherical harmonics. The function $\mathcal{B}_\ell$ is the average of β_ℓ^m over angular position (θ_0, φ_0) of a plume:

$$\mathcal{B}_\ell = \frac{1}{4\pi} \int_{\Omega_0} |\beta_\ell^m|^2 {\rm d}\Omega_0. \tag{5.67}$$

- Finally, $\mathcal{H}_\ell$ is coined the *wave driving term* and is expressed by

$$\mathcal{H}_\ell = \int_{r_{\rm b} - L_{\rm P}}^{r_{\rm b}} \frac{{\rm d}\rho V_0^2}{{\rm d}r} \rho^{-1/2} r^{1/2} \left(\frac{r_{\rm b} - L_{\rm P}}{r}\right)^{\sqrt{\ell(\ell+1)}} {\rm d}r. \tag{5.68}$$

  The quantity $\mathcal{H}_\ell$ is the power injected into a wave per unit time.

The expression for the energy flux $F_{\rm E}$ can be further simplified as explained in P16. It remains to provide an expression for the damping depth and the author follow the work done by Press (1981) and use

$$\tau(\omega_\star, \ell; r) = [\ell(\ell+1)]^{3/2} \int_r^{r_{\rm d}} K \frac{N^3}{\omega_\star^4} \left(\frac{N^2}{N^2 - \omega_\star^2}\right)^{1/2} \frac{{\rm d}r}{r^3}, \tag{5.69}$$

where $\omega_\star$ has the same definition as in Eq. (5.53).

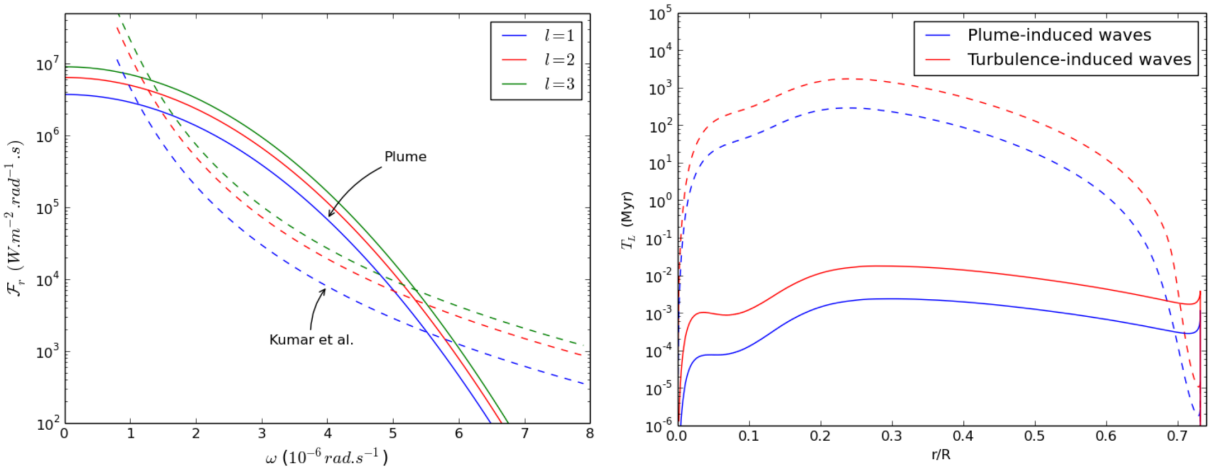

Figure 5.5: *Left:* Mean radial energy per unit frequency at r_d as function of the wave frequency in a solar model, for three different order ℓ for K99's model (dashed lines) and P16's model (solid lines). Credits: Pinçon et al. (2016). *Right:* IGW spin-down characteristic time-scale as a function of the normalized radius for a low differential rotation $\delta\Omega = 0.15 \times 10^{-6}$ rad s^{-1} (dashed lines) and a stronger one $\delta\Omega = 10^{-6}$ rad s^{-1} (solid lines). Credits: Pinçon et al. (2016).

Efficiency of internal gravity waves excitation and associated transport

Pinçon et al. (2016) performed an extensive testing of their model and the impact of the various parameters, especially the impact of different profiles for the transition region. They compared the efficiency of their model of IGW excitation in transporting angular momentum against the one K99, but also compared it to the one developed by Press (1981) and Lecoanet & Quataert (2013). Press (1981); Kumar et al. (1999); Lecoanet & Quataert (2013) produce quite similar mean radial energy fluxes, therefore I will only describe the differences for K99 and P16. In Fig. 5.5 is represented the mean radial energy per unit frequency computed for K99 and P16 in a solar model. K99 predicts a higher energy flux in waves with $\omega < 10^{-6}$ rad s^{-1} than P16, then P16 predicts that plume are much more efficient in exciting waves in the range 1.5×10^{-6} rad s$^{-1}\omega < 5.5 \times 10^{-6}$ rad s^{-1}, and then the Reynolds stress becomes more efficient again. Of course, this result depends on the values of the chosen parameters, especially the value of L_P that changes the wave amplitude and τ_P that changes the frequency range of excited waves. This figure also supports the fact that these two models are complementary because they do not excite preferentially the same range of frequency.

P16 also studied the efficiency of the transport of angular momentum by IGW by comparing the spin-down time-scale already defined in Sect. 5.4. Their results for a present-day solar model are shown in Fig. 5.5, right panel, for K99 and P16 models and for two differential rotations. This time, it accounts for the energy flux integrated on all the frequency range and summed for all degree ℓ (in this case the development is stopped at $\ell = 50$) and azimuthal number m. This figure shows that the turbulent-related spin-down time-scale T_L^{K99} is always almost 10 time higher than the plume-related one T_L^{P16}. It suggest that the plume excitation mechanism is more efficient than the turbulent one, as already expected by Kumar et al. (1999). However, some caveats must be raised. First of all, plumes are not present in all stellar convective zones, but only in the one with large Péclet numbers, *i.e.* where radiative thermalization is inefficient. In such regions, the turbulent excitation must be more important. Furthermore, in the case of the Sun, $T_L^{P16} \simeq 0.1 T_L^{K99}$ meaning that the turbulent excitation mechanism is less efficient than the plume, but still it contributes to around 10% of it, which

makes it non negligible. The results presented in Fig. 5.5, right panel, show that the stronger the rotation gradient, the more efficient the IGW are in extracting angular momentum. The spin-down time is of the order of 100 Myr for plumes in case of small differential rotation and of 10000 yr in the case of a strong one.

The interactions between the two excitation mechanisms should also be studied. Indeed, the plumes are supposed to stay coherent before vanishing into the radiative medium. In reality they are turbulent and the effect of the turbulence of the plumes on the excitation of IGW may also be included into the Reynolds stresses description. One must also point one of the limits of the testing presented above. The angular momentum flux is computed *a posteriori* on the model, *i.e.* IGW had no feedback on the stellar-structure and on the rotation profile. IGW are known to produce the so-called shear layer oscillations (SLO; equivalent to the quasi-biennal oscillation on Earth), which are caused by the local depositing of AM by IGW. It produces a strong and very localized gradient of angular velocity which oscillates on a small extent with a period of a few years. This SLO has the main effect of filtering out IGW and therefore reducing the amount of AM deposited below or above the location of the SLO. This effect is very complicated to implement in stellar evolution codes because it acts on a very small time-scale, much shorter that the nuclear or contraction time-scales (e.g. Talon & Charbonnel, 2003). Finally, the effect of the Coriolis force on the propagation of the plume must also be taken into account as the Coriolis force deforms the trajectory of the plumes. This work is already ongoing.

Chapter 6

Implementation of the 2D rotation modelling in CESTAM

> Il ne faut pas courir. Il faut marcher sans impatience en comptant le nombre de ses pas. Si on ne se trompe pas, si on tourne à gauche au moment voulu, on ne touchera pas de ses bras étendus l'arbre à miel et collant. Il faut à se stade de la marche interrompre les calculs et repartir à zéro. Si on ne se trompe pas dans les calculs, si on saute à pieds joints au moment voulu, on ne tombera pas dans la fosse aux serpents. A ce stade de la marche, il faut interrompre les calculs et repartir à zéro. Si on ne se trompe pas dans les calculs, si on se baisse au moment voulu, on ne sera pas happé par le piège à mâchoires. A ce stade de la marche, il faut interrompre les calculs et repartir à zéro. Si on ne se trompe pas dans les calculs et si on crie Sara Magre au moment voulu, on tombera dans les bras de l'incomparable, de la gigantesque, de la savante Sara.
>
> Monique Wittig, *Les guérillères*

Contents

The stellar evolution code CESAM (Code d'Evolution Stellaire Adaptatif et Modulaire) has been developed first by Berthomieu et al. (1993); Morel (1997) based on earlier codes with the aim of modelling the evolution of the Sun, from its arrival on the main sequence[1] to its present age. CESAM was first written in FORTRAN77 and aggregated many other codes to perform the interpolation of the Equation of State tables, opacity, etc. At the turn of the millennium, the code was modernized and rewritten in Fortran95 and renamed CESAM2K (Morel & Lebreton, 2008). Later it was also redesigned by Marques et al. (2013) to include a description of rotation in 1D and renamed CESTAM (Code d'Evolution Stellaire, avec Transport, Adaptatif et Modulaire). During its almost three decades of life, CESTAM has been a framework to test many models on various aspects of stellar evolution. The user can choose between many models of convection, prescriptions of angular momentum loss by winds, atmospheric models, coefficients of shear-induced turbulence, etc, as well as more curious models, for instance falls of planetoids. In the following, I will always use CESTAM, either to speak about the 1D version or the 2D one.

I explain in a first section how CESTAM works, numerically speaking: in what order computations are executed, what numerical methods are used, etc. Then I enter into the details of the work of code development that I have done during my PhD. The 2$^{\text{nd}}$ section is devoted to the algorithm performing the deformation of a rotating-model (Roxburgh, 2004, 2006) and then I describe the computation of the meridional circulation and of the angular velocity profile. All along this chapter, I am going to focus on some points of details that are never addressed in the literature, while they require some care.

6.1 How CESTAM works

6.1.1 Main numerical methods used in CESTAM

The vast majority of stellar evolution codes rely on finite element schemes to solve the stellar-structure equations. With these schemes, the star is divided into layers and k-th order derivatives are approximated using the values of each quantities at the faces of the nearest layers. Those methods are very fast, very well tested and simple. However, they provide solutions only at the faces of each layer and not between them. Furthermore, during stellar evolution, the mesh frequently needs to be adapted in order to resolve regions with strong gradients. The re-meshing is complicated by the fact that the solutions are only known at a few discrete points. CESTAM follows a different path. In CESTAM, solutions are represented by a linear combination of B-Splines (Schumaker, 2007). The B-Splines form an orthogonal basis of piecewise continuous polynomials. Representing the solution of an equation as a linear combination of B-Splines provides an (approximate) knowledge of this quantity *everywhere*, by only knowing the exact solution at the collocation points. Another advantage is that a different mesh for different systems of equations can be used. For instance, the masses at which the structure equations are solved are not the same as the ones on which the equations for the transport of chemical are solved. It can also be the case for the transport of angular momentum.

[1] ZAMS: Zero Age Main Sequence

Grid point allocation

As said in Chapter 1, the mass enclosed in a spherical shell of radius r plays the role of our independent variable. Each spherical shell is then labelled by a mass m_k. Hence, how should we choose them? We want to increase the resolution where the gradients of the significant quantities are strong. Therefore, the masses should be chosen so that these gradients are minimized, or at least so that they stay below a certain threshold. To that end, we introduce a quantity Q called the *spacing function*. It is a quantity that must been defined so that, at a given time step, the variation of Q between two consecutive masses m_k of layers k is constant:

$$Q(m_{k+1},t) - Q(m_k) = \left.\frac{\mathrm{d}Q}{\mathrm{d}q}\right|_t \equiv \psi(t) = \mathrm{cst} \quad \text{and} \quad \left.\frac{\mathrm{d}^2Q}{\mathrm{d}q^2}\right|_t = 0, \tag{6.1}$$

where q is called the *index function* and takes integer values at each layer, from 1 to n, if n is the total number of layers. These integers also nicely correspond to the indices of Fortran's arrays. The quantity ψ becomes a sixth independent quantity added to the five others: p, T, L, r and m, dependent on the variable q. The definition of ψ can be written as a function of the mass:

$$\left.\frac{\mathrm{d}Q}{\mathrm{d}q}\right|_t = \left.\frac{\mathrm{d}Q}{\mathrm{d}m}\right|_t \left.\frac{\mathrm{d}m}{\mathrm{d}q}\right|_t = \theta(t) \left.\frac{\mathrm{d}m}{\mathrm{d}q}\right|_t = \psi(t). \tag{6.2}$$

It must be noted that, of course, $\theta(t)$ and $\psi(t)$ have, nothing to do with, respectively, the colatitude and the gravito-centrifugal quasi-potential defined in Chapter 1. We now find ourselves with two more differential equations that are to be added to the four structure equations.

$$\frac{\mathrm{d}m}{\mathrm{d}q} = \frac{\psi}{\theta} \quad \text{and} \quad \frac{\mathrm{d}\psi}{\mathrm{d}q} = 0. \tag{6.3}$$

Equations (6.3) are complemented by boundary conditions: at $q = 1$, $m = 0$ and at $q = n$, $m = M_\star$.

We still need a definition for the spacing function Q. Strictly speaking, Q is defined as follow:

$$Q(m,t) = \frac{p}{\Delta p} + \frac{T}{\Delta T} + \frac{L}{\Delta L} + \frac{r}{\Delta r} + \frac{m}{\Delta m}, \tag{6.4}$$

where the operator Δ is defined as $\Delta f \equiv f(n) - f(1)$. The terms Δf are called *repartition factors* and are weighting the importance of each quantity. With this choice, we see that $Q(m_{k+1},t) - Q(m_k)$ is the sum of the normalized gradients of each independent variables. If no quantity is to be favoured over the others, Eq. (6.4) can be used. However, years of use of CESTAM have shown that a simpler expression of Q may be used: $Q = ap + bm$, with $a \simeq -1$ and $b \simeq 15$. They can be tweaked to meet more rigorous resolution requirements.

6.1.2 Dimensionless quantities

In CESTAM, the physical quantities are expressed in terms of dimensionless variables, of order 1, in order to improve floating-point precision. These dimensionless variables are $\xi = \ln p$, $\eta = \ln T$, $\lambda = (L/L_\odot)^a$, $\zeta = (r/R_\odot)^2$ and $\nu = (m/M_\odot)^{2/3}$. The power a on the luminosity is either $2/3$ or 1. Powers $2/3$ have been chosen in order to avoid problems of derivability near the centre, but we now use $a = 1$. In terms of these dimensionless variables, the structure equation system reads (accounting for the 2D modifications):

$$\frac{\partial \xi}{\partial q} = \frac{-3\mathcal{G}}{8\pi}\left(\frac{M_\odot}{R_\odot^2}\right)^2 \left(\frac{\nu}{\zeta}\right)^2 \exp(-\xi) f_p \frac{\psi}{\theta},$$

$$
\begin{aligned}
&\frac{\partial \eta}{\partial q} = \frac{\partial \xi}{\partial q} \min\left(\nabla_{\rm ad}, \nabla_{\rm rad} \frac{f_T}{f_p}\right), \\
&\frac{\partial \zeta}{\partial q} = \frac{3}{4\pi}\frac{M_\odot}{R_\odot^3}\left(\frac{\nu}{\zeta}\right)^{1/2}\frac{1}{\rho}\frac{\psi}{\theta}, \\
(a=1)\quad &\frac{\partial \lambda}{\partial q} = \frac{M_\odot \nu^{1/2}}{L_\odot \lambda^{1/2}}\left(\varepsilon - \frac{\partial U}{\partial t} + \frac{\exp\xi}{\rho^2}\frac{\partial \rho}{\partial t}\right)\frac{\psi}{\theta} = \frac{M_\odot \nu^{1/2}}{L_\odot \lambda^{1/2}}\Lambda\frac{\psi}{\theta}, \\
(a=2/3)\quad &\frac{\partial \lambda}{\partial q} = \frac{3}{2}\frac{M_\odot \nu^{1/2}}{L_\odot}\left(\varepsilon - \frac{\partial U}{\partial t} + \frac{\exp\xi}{\rho^2}\frac{\partial \rho}{\partial t}\right)\frac{\psi}{\theta} = \frac{3}{2}\frac{M_\odot \nu^{1/2}}{L_\odot}\Lambda\frac{\psi}{\theta}, \\
&\frac{\partial \nu}{\partial q} = \frac{\psi}{\theta}, \\
&\frac{\partial \psi}{\partial q} = 0.
\end{aligned}
\tag{6.5}
$$

I gave here the system incorporating the rotation-induced modifications, highlighted in **blue**. Removing the blue parts allows us to retrieve the "standard" system.

6.1.3 Collocation method

Let us rewrite the above system of first order ordinary differential equations in a more compact way. By denoting $\mathbf{y} = (y_1, y_2, y_3, y_4, y_5, y_6) = (\xi, \eta, \zeta, \lambda, \nu, \psi)$ our unknowns, system (6.5) may be written on the form:

$$
\mathbf{E}(q; \mathbf{y}, \mathbf{y}') = \frac{\mathrm{d}\mathbf{y}}{\mathrm{d}q} - \mathbf{g}(q, \mathbf{y}) = \mathbf{0} \quad \text{with} \quad q \in [q_1, q_n], \tag{6.6}
$$

with $\mathbf{g}$ a suitable vector of functions representing the differential system.

The quantities to be minimized are therefore (keeping only $a = 1$ for simplicity):

$$
\begin{aligned}
E_1 &= \frac{\partial y_1}{\partial q} - \frac{-3\mathcal{G}}{8\pi}\left(\frac{M_\odot}{R_\odot^2}\right)^2\left(\frac{y_5}{y_3}\right)^2 \exp(-y_1) f_p \frac{y_6}{\theta} = 0, \\
E_2 &= \frac{\partial y_2}{\partial q} - \frac{\partial y_1}{\partial q}\min\left(\nabla_{\rm ad}, \nabla_{\rm rad}\frac{f_T}{f_p}\right) = 0, \\
E_3 &= \frac{\partial y_3}{\partial q} - \frac{3}{4\pi}\frac{M_\odot}{R_\odot^3}\left(\frac{y_5}{y_3}\right)^{1/2}\frac{1}{\rho}\frac{y_6}{\theta} = 0, \\
E_4 &= \frac{\partial y_4}{\partial q} - \frac{M_\odot y_5^{1/2}}{L_\odot y_4^{1/2}}\Lambda\frac{y_6}{\theta} = 0, \\
E_5 &= \frac{\partial y_5}{\partial q} - \frac{y_6}{\theta} = 0, \\
E_6 &= \frac{\partial y_6}{\partial q} = 0.
\end{aligned}
\tag{6.7}
$$

And we look for $E_i = 0, \forall i \in [\![1; 6]\!]$. This system is also supplemented with a set of bottom and top boundary conditions $\mathbf{E}^{\rm b}(q_1, \mathbf{y})$ and $\mathbf{E}^{\rm t}(q_n, \mathbf{y})$.

This system can be solve using a pseudo-spectral method called the collocation method (e.g De Boor, 2001). Unknowns $\{y_i\}_{i=1}^{n_{\rm e}}$, with $n_{\rm e}$ the number of unknowns ($n_{\rm e} = 6$ in the

above system) will be decomposed as a linear combination of B-Splines. Let $\{q_i\}_{i=0}^{n}$ be a set of abscissa that verify the condition $a = q_0 < q_1 \cdots < q_n = b$ with a and b the limits of the interval on which system (6.6) is to be solved. We denote $\{N_i^m\}_{i=1}^{M}$ the basis of B-Splines of the vector space of dimension M of all the piecewise polynomials of order[2] m that match at $\{q_i\}_{i=1}^{n-1}$. Important properties of B-Splines are:

- B-Splines have a closed support;
- They are always positive or zero;
- At each point, there exists at most m non-zero B-Splines;
- The derivative of the B-Splines of order m is a linear combination of B-Splines of order $m-1$.

Any unknown y_i of system (6.6) can be decomposed as:

$$y_i(q) = \sum_{j=1}^{M} y_{ij} N_j^m(q) \quad \text{and} \quad y_i'(q) = \frac{\mathrm{d}y_i}{\mathrm{d}q} = \sum_{j=1}^{M} y_{ij} \frac{\mathrm{d}N_j^m}{\mathrm{d}q}. \tag{6.8}$$

Finally, let us define $\mathcal{J} = [\![1; n_\mathrm{e}]\!]$, and $\mathcal{B} \subseteq \mathcal{J}$ (resp. $\mathcal{T} = C_\mathcal{J}\mathcal{B}$, with $C_\mathcal{J}\mathcal{B}$ the complementary of $\mathcal{B}$ in $\mathcal{J}$) is the set of indices of the unknowns for which a bottom (resp. top) boundary condition is provided.

We found ourselves with a set of equations of the form:

- At the bottom: E_i^b, with $i \in \mathcal{B}$ is

$$E_i^\mathrm{b}\left(\sum_{j=1}^{M} y_{1,j} N_j^m(q_1); \ldots; \sum_{j=1}^{M} y_{n_\mathrm{e},j} N_j^m(q_1)\right) = 0; \tag{6.9}$$

- At the top: E_i^t, with $i \in \mathcal{T}$ is

$$E_i^\mathrm{t}\left(\sum_{j=1}^{M} y_{1,j} N_j^m(q_n); \ldots; \sum_{j=1}^{M} y_{n_\mathrm{e},j} N_j^m(q_n)\right) = 0; \tag{6.10}$$

- Elsewhere ($q \in [q_1; q_n]$), for $i \in \mathcal{J}$,

$$E_i\left(q; \sum_{j=1}^{M} y_{1,j} N_j^m; \ldots; \sum_{j=1}^{M} y_{n_\mathrm{e},j} N_j^m; \sum_{j=1}^{M} y_{1,j} \frac{\mathrm{d}N_j^m}{\mathrm{d}q}; \ldots; \sum_{j=1}^{M} y_{n_\mathrm{e},j} \frac{\mathrm{d}N_j^m}{\mathrm{d}q}\right) = 0. \tag{6.11}$$

This time, we are looking for the coefficients $y_{i,j}$.

On $M-1$ well chosen collocation points (using Gauss-Legendre quadrature) $c_k \in]q_1, q_n[$ (see De Boor, 2001, for details), the coefficients $y_{i,j}$ are found using an iterative method: the Newton-Raphson method. The solution, at a given iteration $p \geq 0$, is estimated by :

- At the bottom: $\forall i \in \mathcal{B}$,

$$E_i^\mathrm{b}\left(\sum_{j=1}^{M} y_{1,j}^p N_j^m(q_1); \ldots; \sum_{j=1}^{M} y_{n_\mathrm{e},j}^p N_j^m(q_1)\right) = \sum_{l=1}^{n_\mathrm{e}} \sum_{j=1}^{M} \frac{\partial E_i^\mathrm{b}}{\partial y_l} N_j^m(q_1) \mathrm{d}y_{lj}^p; \tag{6.12}$$

[2] We recall that the order of a polynomial is its degree minus unity.

- At the top: $\forall i \in \mathcal{T}$,

$$E_i^{\mathrm{t}}\left(\sum_{j=1}^{M} y_{1,j}^p N_j^m(q_n);\ldots;\sum_{j=1}^{M} y_{n_{\mathrm{e}},j}^p N_j^m(q_n)\right) = \sum_{l=1}^{n_{\mathrm{e}}}\sum_{j=1}^{M}\frac{\partial E_i^{\mathrm{t}}}{\partial y_l} N_j^m(q_n)\mathrm{d}y_{lj}^p; \tag{6.13}$$

- Elsewhere, $\forall j \in \mathcal{J}$, $\forall k \in [\![1; M-1]\!]$,

$$\begin{aligned} & E_i\left(c_k;\sum_{j=1}^{M} y_{1,j}^p N_j^m(c_k);\ldots;\sum_{j=1}^{M} y_{n_{\mathrm{e}},j}^p N_j^m(c_k);\sum_{j=1}^{M} y_{1,j}^p \frac{\mathrm{d}N_j^m}{\mathrm{d}q}(c_k);\ldots;\sum_{j=1}^{M} y_{n_{\mathrm{e}},j}^p \frac{\mathrm{d}N_j^m}{\mathrm{d}q}(c_k)\right) \\ = & \sum_{l=1}^{n_{\mathrm{e}}}\sum_{j=1}^{M}\left(\frac{\partial E_i}{\partial y_l} N_j^m(c_k) + \frac{\partial E_i}{\partial y_l'}\frac{\mathrm{d}N_j^m}{\mathrm{d}q}(c_k)\right)\mathrm{d}y_{lj}^p. \end{aligned} \tag{6.14}$$

The quantities $\mathrm{d}y_{lj}^p$ are small corrections to the coefficients y_{lj}^p and they are our unknowns. With the value of $\mathrm{d}y_{lj}^p$, we can determine the value of y_{lj} at next iteration:

$$y_{lj}^{p+1} = y_{lj}^p - \mathrm{d}y_{lj}^p; \quad \forall l \in [\![1; n_{\mathrm{e}}]\!], \forall j \in [\![1; M]\!]. \tag{6.15}$$

The collocation method offer the advantage of *superconvergence*. Indeed, instead of reaching a precision of order m, the collocation method, by choosing the point in a judicious way, reaches a precision of order $2m$.

6.1.4 The General flowchart of CESTAM

The general path followed by CESTAM to compute the evolution during one time step is summarized in Fig. 6.1. At the end of the computation at a given time t, a new time step Δt is estimated. During the computation of the next time step $t + \Delta t$, CESTAM will use some quantities that have been computed using the previous structure. Such quantities are the factors f_p, f_T and f_{d} (defined in Eq. (1.75)), the radii of isobars, the meridional circulation profile, etc. Concerning factors f_p, f_T and f_{d}, this approximation is justified because their values are close to one, even for a high rotation rate, and they do not change much between two consecutive time steps. Concerning the radii $r(p, \theta)$ of an isobar, it can be written:

$$r(p,\theta) = \overline{r}(p) + \sum_{\ell} \tilde{r}_\ell(p) P_\ell(\cos\theta). \tag{6.16}$$

The value of $\overline{r}(p)$ depends a lot on the new quasi-static structure, and indeed, it is an unknown of the system of structure equations. Therefore, $\overline{r}(p)$ is not taken from previous time step. However, the terms $\tilde{r}_\ell(p)$ will not change much. Thus, until its new determination (at point 6. in Fig 6.1), $r^{t+\Delta t}(p,\theta) \simeq \overline{r}^{t+\Delta t}(p) + \sum_\ell \tilde{r}_\ell^t(p) P_\ell(\cos\theta)$. Finally, the most questionable approximation is the one on the meridional circulation profile. The profile of meridional circulation from the previous time step is used for computing the transport of chemicals. During the main sequence this simplification does not lead to large inconsistencies because the star's properties vary slowly. However, during the PMS or evolved phases, it could lead to rather important modifications of the stellar-structure. This last point should be studied in more detail in a future work.

Then CESTAM goes to the evolution of the chemical composition, that incorporates evolution due to nuclear reactions, convection and diffusion by shear-induced turbulence. In parallel of my work, Morgan Deal (e.g. Deal et al., 2020) is working on the implementation of microscopic and radiative diffusion in CESTAM. These non-standard processes can also be integrated into

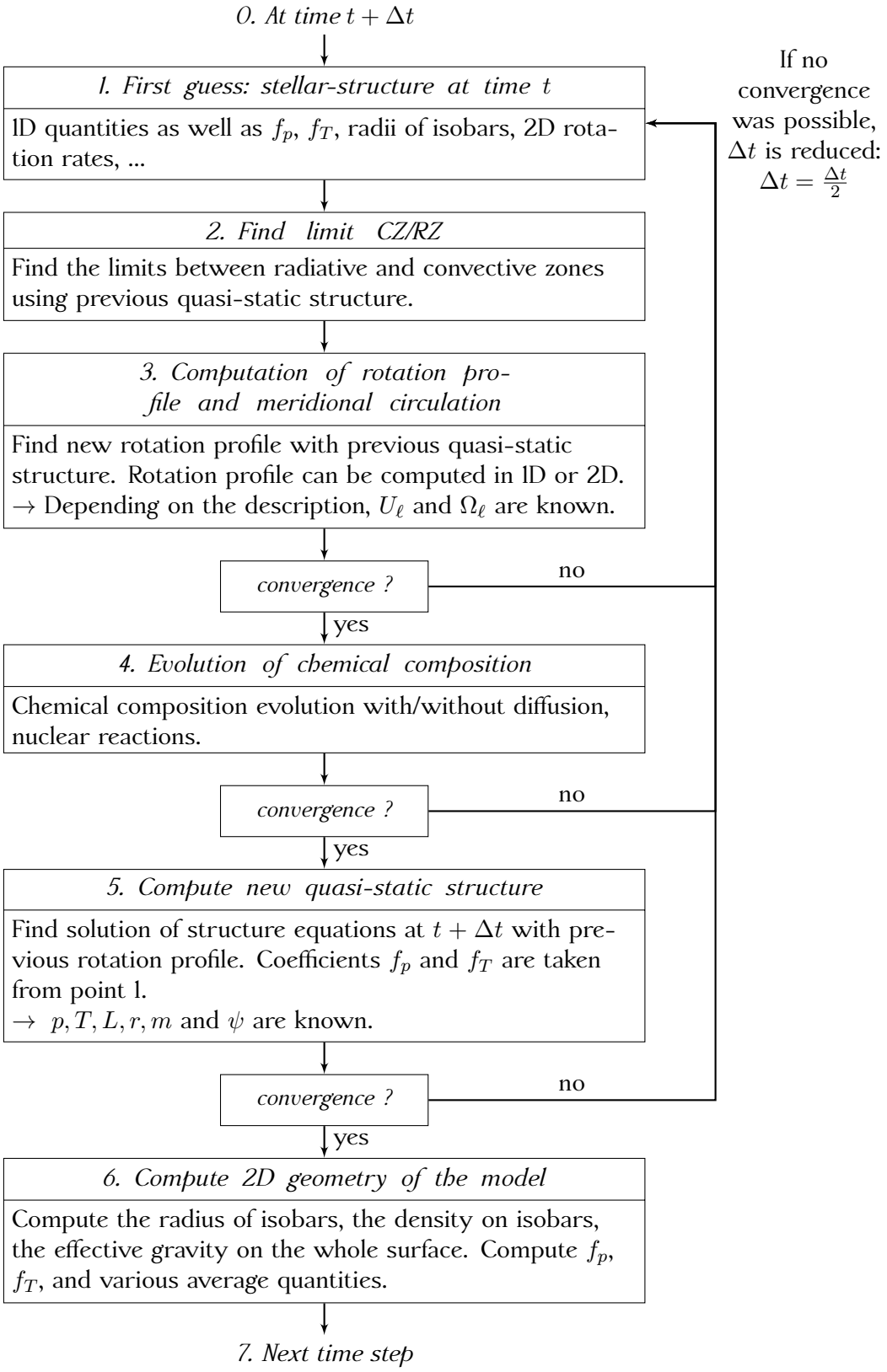

Figure 6.1: Schematic representation of the steps followed by CESTAM during the computation of a time step.

the modelling. If the computation of the chemical composition does not converge, the time step is divided by two and we restart from last time step. Otherwise, with the chemical composition known at time $t + \Delta t$, CESTAM looks to precisely determine the junctions between the radiative and convective zones by studying Schwarzschild's criterion (or Ledoux's) using dichotomy method[3]. If needed, more layers can be added or removed in order to preserve the desired resolution and so that the limits of the zones fall exactly on grid points. If the grid changes, so does the spacing function and hence the B-Splines basis on which quantities are interpolated. Sometimes, convective zones can be found near the centre or near the surface or somewhere in the star, but with too short an extent. Those spurious zones are eliminated.

With properly determined limits, structure equations (6.7) are solved using the collocation method described above. Again, if it does not converge (convergence is reached when the correction applied to the solutions goes below a certain threshold), the time step is divided by two, otherwise CESTAM goes to the next step. The non-convergence criterion is manifold: the number of iterations exceeds a predefined value, the correction between two consecutive time steps is too high, the break-up velocity was reached somewhere inside the star, etc. The next step is the solving of angular momentum transport equations and of meridional circulation. Section 6.3 describes how I implemented it for the 2D case. Upon convergence, we proceed the same as before. And we finally arrive at the point where the quasi-static structure and the rotation profile are known. The model can be deformed in order to compute f_p, f_T, etc. needed for the next time step. The deformation is described in Section 6.2.

6.1.5 ESTER: another code for the stellar rotation in 2D

ESTER (Evolution STEllaire en Rotation) is a 2D code that initially simulated the steady state of fully radiative stars (Espinosa Lara & Rieutord, 2007, 2013) and then was improved to provide a modelling of convection zones (Rieutord et al., 2016). It relies on spectral methods to solve 1st principle equations: Poisson equation, conservation of mass, momentum and energy, and an equation of state. The scalars and vectors are decomposed on spherical harmonics for the angular parts and on Tchebyshev polynomials for the radial one, using a multi-domain approach. Each of the equations to be solved are projected onto them. The convection zones are modelled assuming that the entropy is constant everywhere in them: $\boldsymbol{\nabla} s = \mathbf{0}$. The approximation is valid almost everywhere (it actually supports the MLT modelling), except at the surface (where we have seen that the modelling of convection needs refinement). Until recently, ESTER was not capable of simulating stellar evolution. Gagnier et al. (2019) recently implemented a simplified temporal evolution into ESTER that assumes small variations, *i.e.* evolution along the main sequence only. The chemical composition is evolved by computing the hydrogen mass fraction X change due to PP-chain between two time steps. This change is expressed as

$$\frac{\partial X}{\partial t} = -\frac{4 m_{\mathrm{p}}}{\mathcal{Q}} \frac{L_{\mathrm{core}}}{M_{\mathrm{core}}}, \tag{6.18}$$

[3]Gabriel et al. (2014) have shown that the only proper way to define the boundary of a convective zone (in the MLT framework) is that, at this location, the following conditions are met:

$$\begin{cases} \mathbf{F}_{\mathrm{rad}} &= \mathbf{F}, \\ v_{\mathrm{r}} &= 0, \\ \nabla_{\mathrm{rad}} &= \nabla_{\mathrm{ad}}, \end{cases} \tag{6.17}$$

where $\mathbf{F}_{\mathrm{rad}}$ is the radiative flux, $\mathbf{F}$ is the total flux and v_{r} is the radial component of the convective velocity. This condition is currently being implemented into CESTAM.

where $\mathcal{Q}$ is the energy released by the fusion of four protons into a helium nucleus, $m_{\rm p}$ is the mass of a proton, $L_{\rm core}$ is the Luminosity at the boundary of the core convection zone and $M_{\rm core}$ its mass. They proceed as follow: a steady model of the star is computed in 2D at a given time, the change of X after a given duration ΔT is computed, a new steady model with the new chemical composition is computed, etc. This approach is considered valid if the time-scales of dynamical processes (Eddington-Sweet and Kelvin-Helmholtz time-scales; see Eq. (2.12)) are small compare to the time scales of evolution (nuclear and mass-loss time-scales). Comparisons with non-rotating model of the time needed for hydrogen to entirely fuse in the core was performed with the Geneva 1D stellar evolution code (Eggenberger et al., 2008). ESTER overestimated this time by 20% (> 10 Gyr instead of 8 Gyr for the Geneva model), which is quite large.

6.2 The deformation of a 1D CESTAM model

6.2.1 Isobaric mesh and initialization

The deformation of a 1D spherical model into a 2D spheroidal one necessitates adding an angular mesh to the radial one. The former is fixed, *i.e.* the number of angular sectors is and their locations do not change overtime (except for one, as we will see in Sect. 6.2.3). Let us define two systems of coordinates. The first system, hereafter referred to as the *spherical (coordinate) system*, is the union of an angular mesh in which each angular sector has colatitude θ_j and of a radial mesh in which each layer has a radius r_i. The radial mesh *may* not be evenly spaced, whereas the angular mesh is *never* evenly spaced, as we will see shortly. The second system, hereafter referred to as the *isobaric (coordinate) system*, is the union of the same angular mesh and of the radius $r_{p_i}(\theta_j)$ of isobars. The construction of this isobaric system will be described later. In the following, n_θ denotes the number of angles in the angular mesh and $N_r^{\rm 1D}$ (resp. $N_r^{\rm 2D}$) denotes the number of layers in the initial 1D model (resp. in the new 2D model).

How must we choose the angles? Remember that we want, at the end, to evaluate integrals over spheroidal surfaces. Indeed the deformation of a 1D model must provide averages of some quantities needed to compute f_p, f_T, etc., such as $\langle g_{\rm eff}\rangle$, $\left\langle g_{\rm eff}^{-1}\right\rangle$, etc. A naive approach would be to pick angles evenly. In this case, the integral of a function f between 0 and π can be expressed using the trapezoidal rule:

$$\int_0^\pi f(\theta)\mathrm{d}\theta = \frac{1}{2}\sum_{k=2}^{n_\theta}\Delta\theta_i(f_i + f_{i-1}) + E_{n_\theta}^{\rm trpz}. \tag{6.19}$$

The angles θ_i are evenly spaced angles between 0 and π, with $\theta_1 = 0$, $\theta_{n_\theta} = \pi$ and $\forall i \in [\![2; n_\theta]\!], \theta_i - \theta_{i-1} = \Delta\theta_i$. The values $f_i = f(\theta_i)$ and $E^{\rm trpz}(n_\theta) = \mathcal{O}(n_\theta^{-3})$ are the error committed on approximating the integral. It decreases linearly with n_θ as n_θ increases. Can the abscissa be chosen in a way that the error decreases faster ? Gauss found a way to do so (Gauss, 1814). If one assumes that f can be decomposed on Legendre polynomials, which is our case, the Gauss-Legendre quadrature provides a method to calculate a set of angles $\{\theta_i\}_1^{n_\theta}$ and of weights $\{w_i\}_1^{n_\theta}$ so that

$$\int_0^\pi f(\theta)\mathrm{d}\theta = \sum_{k=1}^{n_\theta} w_i f_i + E_{n_\theta}^{\rm GL}, \tag{6.20}$$

and $E_{n_\theta}^{\rm GL} = \mathcal{O}(f^{(2n_\theta)}(\xi)/(2n_\theta)!)$, with $\xi \in [0, \pi]$.

Our angular mesh is therefore composed of n_θ angles θ_j, each of them affected by a weight w_j given by Gauss-Legendre quadrature. Angles $\theta_j \in]0, \frac{\pi}{2}[$ because, for symmetry reasons, the

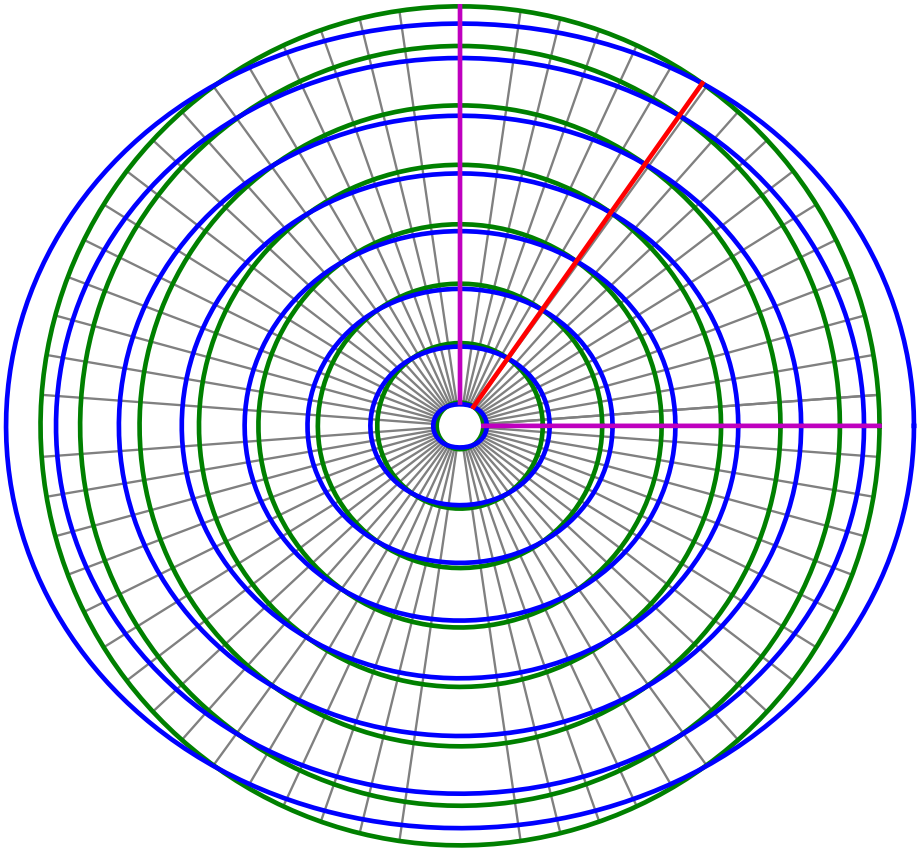

Figure 6.2: Representation of spherical mesh (green and grey) and spheroidal mesh (blue and grey), for an arbitrary deformation. The grey lines are plotted at angles determined by a Gauss-Legendre quadrature for 32 points. The red line corresponds to the characteristic angle $\theta_{\rm m}$ such that $P_2(\cos\theta_{\rm m}) = 0$. The purple lines correspond to the angles at $\theta = 0$ and $\theta = \pi/2$.

quarter of a meridional cross-section suffices to retrieve the whole solution in 2D. This set of angles does not contain:

- $\theta = \pi/2$ and $\theta = 0$. Knowing the value of any quantity at these points would ensure continuity of the solution between each quarter.

- $\theta_{\rm m}$ such that $P_2(\cos\theta_{\rm m}) = 0 \rightarrow \theta_{\rm m} = \arccos(1/\sqrt{3})$. This angle is the intersection angle between spherical and isobaric systems (when only P_0 and P_2 are taken into account). In the following, any quantity X along $\theta = \theta_{\rm m}$ is written $X(r, \theta_{\rm m}) = X_{\rm m}(r) = \overline{X}(r)$.

In CESTAM, these angles are added to the angular mesh with a null weight so that the value of the Gauss-Legendre quadrature is not affected. For this reason I call them *ghost angles*. The final mesh then includes $N_\theta = n_\theta + 3$ angles (see Fig. 6.2).

Let us denote $R_\star$ the radius of the 1D model. The new radial mesh has a radius of $R_{\rm max} = 2R_\star$. From 0 to $R_\star$, the layers are positioned at the same radii as for the 1D model. Above $R_\star$, the layers are evenly spaced, with a radial spacing of $\mathrm{d}r = R_\star/N_r^{\rm 1D}$. The new radial coordinates

go from 0 to $2R_{\max}$ with $N_r^{2\mathrm{D}} = 2N_r^{1\mathrm{D}} + 1$ layers. Adopting such a radial mesh amounts to plunging the star into a spherical void with twice the radius of the star. The initial guess for the deformation is obtained by interpolating all the 1D quantities obtained in point 4. of Fig. 6.1. For instance, the first guess of the density is

$$\begin{cases} \rho(r_i, \theta_j) = \rho(r_i)^{1\mathrm{D}}, & \text{for } r \in [0, R_\star] \\ \rho(r_i, \theta_j) = 0, & \text{for } r \in [R_\star, 2R_\star] \end{cases} . \tag{6.21}$$

The initialization of the angular mesh is done once and for all while the radial mesh and the first guesses are, of course, renewed at each time step.

6.2.2 Computation of the effective gravity and of averaged quantities

After having defined the first guesses (box 1. of Fig. 6.3), Eq. (2.39) for the gravitational potential is solved assuming $\rho^{2\mathrm{D}}(r, \theta)$ is known, and then the radius of isobars (characteristic radius; Eq. (2.47)) and the density on isobars (Eq. (2.48)) are computed. If the maximum change between $\phi(r, \theta)$ computed at current and previous iteration exceeds a certain maximum error, then ϕ is computed again. It usually necessitates four iterations to go below a 10^{-12} maximum variation. However, for fast and massive rotating stars ($M \gtrsim 2M\odot$), it can take forever and the process is usually forced to stop after 42 unsuccessful iterations.

Once the solutions for ϕ and ρ have converged, the r- and θ-components of $\mathbf{g}_{\mathrm{eff}}$ can be computed using Eq. (1.52) and (1.53). Then $p(r, \theta)$ is deduced from:

$$\frac{\partial p}{\partial r} = -\rho \left(\frac{\partial \phi}{\partial r} - \Omega^2 r_p \sin^2 \theta_{\mathrm{m}} \right). \tag{6.22}$$

This equation is complemented with the boundary condition: $p(R_\star, \theta_{\mathrm{m}}) = p^{1\mathrm{D}}(R_\star)$. It is needless to say that since we are computing solution over isobars, the pressure needs to be known at only one angle. The averages of g_{eff} follows from their definition in Eqs. (1.69), with the slight difference that we actually compute $S_p \langle g_{\mathrm{eff}} \rangle$, (resp. $S_p \langle 1/g_{\mathrm{eff}} \rangle$, etc.) instead of just $\langle g_{\mathrm{eff}} \rangle$, (resp. $\langle 1/g_{\mathrm{eff}} \rangle$, etc.), because the factor S_p is always present when averages of g_{eff} are used. Those averages are computed using Gauss-Legendre quadrature (Eq. (6.20)). The expression of the needed averages are:

$$S_p \langle g_{\mathrm{eff}} \rangle = 4\pi \int_{\psi_p} g_{\mathrm{eff}} \frac{r_p^2 \sin\theta \mathrm{d}\theta}{\cos\varepsilon}, \tag{6.23}$$

$$S_p \left\langle g_{\mathrm{eff}}^{-1} \right\rangle = 4\pi \int_{\psi_p} g_{\mathrm{eff}}^{-1} \frac{r_p^2 \sin\theta \mathrm{d}\theta}{\cos\varepsilon}, \tag{6.24}$$

$$S_p \left\langle g_{\mathrm{eff}}^{-1} \varpi^2 \right\rangle = 4\pi \int_{\psi_p} g_{\mathrm{eff}}^{-1} \frac{r_p^4 \sin^3\theta \mathrm{d}\theta}{\cos\varepsilon}. \tag{6.25}$$

The factor $\cos\varepsilon$ easily follow from Eq. (1.67), once $r_p(\theta)$ is known. The above averages enter in the composition of f_p, f_T and f_{d}, that I recall:

$$f_p = \frac{4\pi r_p^4}{\mathcal{G} m_p} \frac{1}{S_p \left\langle g_{\mathrm{eff}}^{-1} \right\rangle}, \tag{6.26}$$

$$f_T = \left(\frac{4\pi r_p^2}{S_p} \right)^2 \frac{1}{\langle g_{\mathrm{eff}} \rangle \left\langle g_{\mathrm{eff}}^{-1} \right\rangle}, \tag{6.27}$$

$$f_{\mathrm{d}} = \frac{(1 - \varpi^2 \Omega \alpha) \left\langle g_{\mathrm{eff}}^{-1} \right\rangle}{\left\langle g_{\mathrm{eff}}^{-1} \right\rangle - \left\langle g_{\mathrm{eff}}^{-1} \varpi^2 \right\rangle \Omega \alpha}. \tag{6.28}$$

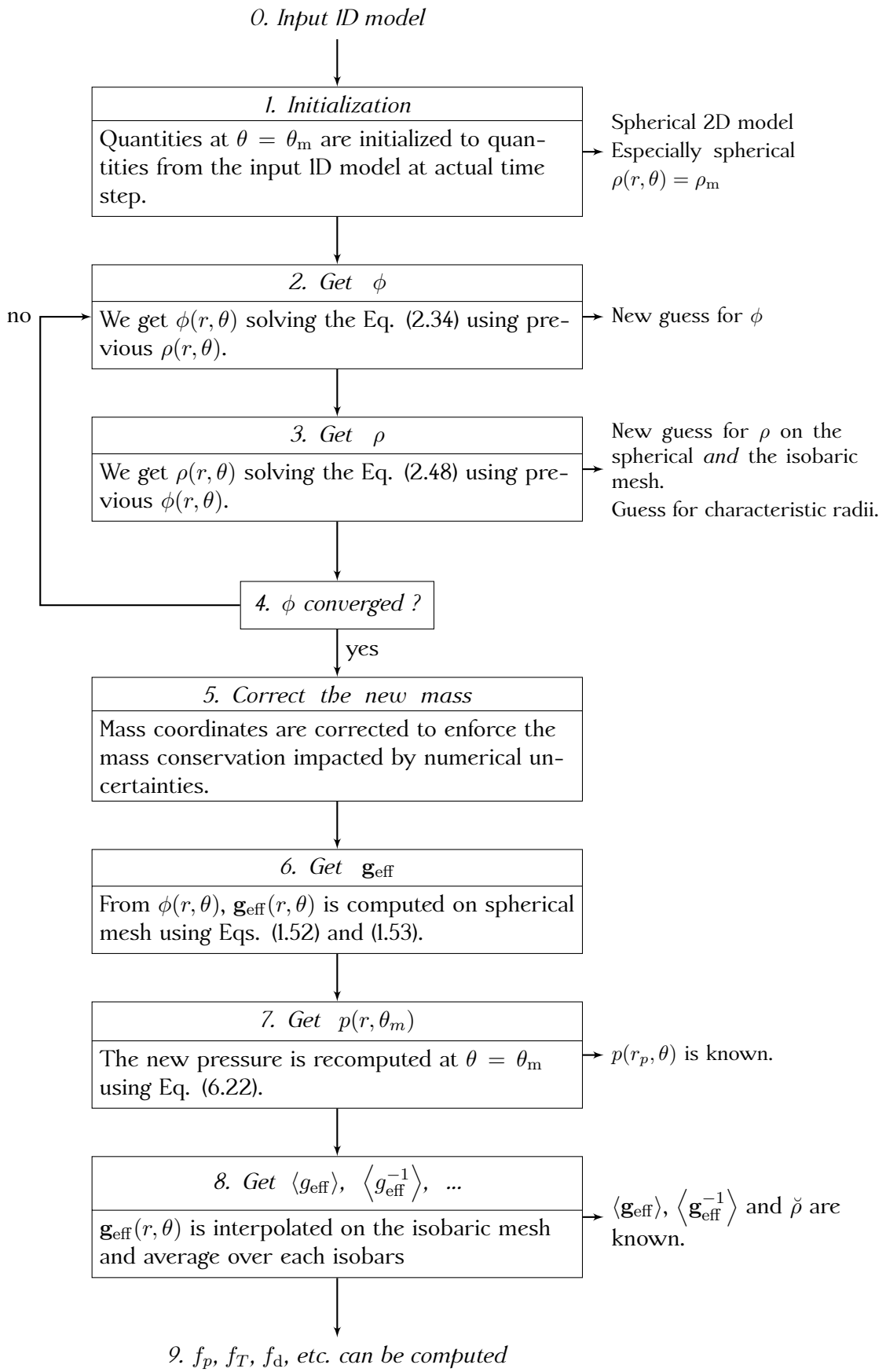

Figure 6.3: Schematic representation of the steps followed until the determination of $\mathbf{g}_{\rm eff}(r)$ averaged over each isobars.

6.2.3 Various points of interest

I will now give some details about issues or questions that the implementation has raised and which, in my opinion, will help someone whose project is to perform the same task in another stellar evolution code.

On the decomposition on Legendre polynomials above 2nd order

Above, I made profitable use of the critical angle $\theta_{\rm m}$. In the literature, it is often assumed that, for any quantity X, at $\theta_{\rm m} = \arccos(1/\sqrt{3})$,

$$\overline{X}(r) + \sum_{\ell=0}^{\infty} \tilde{X}_\ell P_\ell(\cos\theta_{\rm m}) = \overline{X}(r) = X(r,\theta). \tag{6.29}$$

However, this is, in general, not true. While $\arccos(1/\sqrt{3})$ is a root of P_2, it is not one of $P_{\ell>2}$. Therefore, except by accident,

$$X(r,\theta_{\rm m}) = \overline{X}(r) + \widetilde{X}_4 P_4(\cos\theta_{\rm m}) + \ldots \neq \overline{X}(r), \tag{6.30}$$

where $P_4(\cos\theta_{\rm m})$ does not vanish. In the following I denote $\theta_{{\rm m},2} = \arccos(1/\sqrt{3})$ the root of P_2 and $\theta_{\rm m}$ the hypothetical root for the polynomial $\sum_{\ell=2} \tilde{X}_\ell P_\ell(\cos\theta_{\rm m})$.

It is important to notice that the method developed in (Roxburgh, 2004, 2006), does *not* need a specific angle to work. Indeed, Roxburgh (2004) uses $\pi/2$ as reference angle and Roxburgh (2006) uses $\arccos(1/\sqrt{3})$. This specific angle is only needed afterward. In reality, the 1D solutions of the structure equation, at a given radius (or pressure), provide the average value over an isobar that the decomposition shall ensure:

$$\langle X \rangle_{\rm isobar}(r) = \overline{X}(r) = X_{\rm 1D} = X(r,\theta_{\rm m}), \tag{6.31}$$

The angle $\theta_{\rm m}$ does exist because of first mean value theorem[4]. Can we find $\theta_{\rm m}$?

The $\widetilde{\rho}_\ell$ components are known and $\rho_{\rm 1D}$ is found when computing the quasi-static structure. Let Q be the polynomial defined as

$$Q(x) = \sum_{k=0}^{N_\ell} \widetilde{\rho}_k P_k(x) - \rho_{\rm 1D} = \sum_{k=0}^{N_\ell} \gamma_k P_k(x), \tag{6.33}$$

where $\gamma_0 = \widetilde{\rho}_0 - \rho_{\rm 1D} = \overline{\rho} - \rho_{\rm 1D}$ and $\forall k > 0, \gamma_k = \widetilde{\rho}_k$. The integer N_ℓ is the maximum order of the Legendre polynomial on which ρ is decomposed.

The angle $\theta_{\rm m}$ is among Q's roots, especially, it is inside $[0, \pi/2]$. Finding roots of a polynomial is painful when the degree increases, but this is forgetting that Legendre polynomials are orthogonal. Day & Romero (2005) developed a very efficient method for finding all roots of such a polynomial. This method reduces to searching for the eigenvalues of an almost diagonal matrix.

Legendre polynomials being orthogonal, there exists a recursive relation of the form:

$$xP_{n-1}(x) = \sum_{k=0}^{n} h_{k,n-1} P_k(x) \quad \text{indeed} \quad (n+1)P_{n+1}(x) = (2n+1)xP_n(x) - nP_{n-1}(x). \tag{6.34}$$

[4]For a function f defined on $[a,b] \to \mathbb{R}$, $\exists c \in [a,b]$ such that

$$\int_a^b f(x){\rm d}x = f(c)(b-a). \tag{6.32}$$

Then

$$h_{i-1,i} = \frac{i}{2i+1}, \tag{6.35}$$

$$h_{i+1,i} = \frac{i+1}{2i+1}, \tag{6.36}$$

$$\text{and for } k \neq i \pm 1, \quad h_{k,i} = 0. \tag{6.37}$$

Those coefficients form a $N_\ell \times N_\ell$ matrix $\mathfrak{H}_{N_\ell} = (h_{i,j})_{0 \leq i,j \leq N_\ell - 1}$.

$$\mathfrak{H}_{N_\ell} = \begin{pmatrix} 0 & 1/3 & 0 & \cdots & & \cdots & 0 \\ 1 & 0 & 2/5 & \ddots & & & \vdots \\ 0 & 2/3 & 0 & & 0 & & \\ \vdots & 0 & 3/5 & \ddots & \frac{N_\ell-3}{2N_\ell-5} & 0 & \vdots \\ & & 0 & & 0 & \frac{N_\ell-2}{2N_\ell-3} & 0 \\ \vdots & & & \ddots & \frac{N_\ell-2}{2N_\ell-5} & 0 & \frac{N_\ell-1}{2N_\ell-1} \\ 0 & \cdots & & \cdots & 0 & \frac{N_\ell-1}{2N_\ell-3} & 0 \end{pmatrix}. \tag{6.38}$$

We also define three vectors:

$$\mathbf{f}_{N_\ell}(x) = \left(P_0(x), \ldots, P_{N_\ell-1}(x)\right)^{\mathrm{T}}, \tag{6.39}$$

$$\mathbf{c}_{N_\ell}^{\mathrm{T}} = \left(\gamma_0, \ldots, \gamma_{N_\ell-1}\right), \tag{6.40}$$

$$\mathbf{e}_{N_\ell-1} = (0, \ldots, 0, 1)^{\mathrm{T}}. \tag{6.41}$$

Therefore our polynomial P can now be written

$$Q(x) = \mathbf{f}_{N_\ell}^{\mathrm{T}}(x)\mathbf{c}_{N_\ell} + \gamma_{N_\ell} P_{N_\ell}(x), \tag{6.42}$$

whose roots are the eigenvalues of the matrix

$$\mathfrak{B}_{N_\ell} = \mathfrak{H}_{N_\ell} - h_{N_\ell,N_\ell-1} \frac{\mathbf{c}_{N_\ell}}{\gamma_{N_\ell}} \mathbf{e}_{N_\ell-1}^{\mathrm{T}} = \tag{6.43}$$

$$\begin{pmatrix}
0 & h_{0,1} & 0 & \cdots & & \cdots & -h_{N_\ell,N_\ell-1}\frac{\gamma_0}{\gamma_{N_\ell}} \\
h_{1,0} & 0 & h_{1,2} & \ddots & & & \vdots \\
0 & h_{2,1} & 0 & & 0 & & \\
\vdots & 0 & h_{3,2} & \ddots & h_{N_\ell-4,N_\ell-3} & 0 & \vdots \\
 & & 0 & & 0 & h_{N_\ell-3,N_\ell-2} & -h_{N_\ell,N_\ell-1}\frac{\gamma_{N_\ell-3}}{\gamma_{N_\ell}} \\
\vdots & & & \ddots & h_{N_\ell-2,N_\ell-3} & 0 & h_{N_\ell-2,N_\ell-1} - \\
 & & & & & & h_{N_\ell,N_\ell-1}\frac{\gamma_{N_\ell-2}}{\gamma_{N_\ell}} \\
0 & \cdots & & \cdots & 0 & h_{N_\ell-1,N_\ell-2} & -h_{N_\ell,N_\ell-1}\frac{\gamma_{N_\ell-1}}{\gamma_{N_\ell}}
\end{pmatrix}$$

$\mathfrak{B}_n$ is upper-Hessenberger, meaning that $\forall i,j \in [0,n-1]$, if $i > j+1$, then $\mathfrak{B}_{n,i,j} = 0$. The library Lapack (Anderson et al., 1999) provides Fortran routines built to find eigenvalues of such a matrix. A special case of upper-Hessenberger matrices are the reduced upper-Hessenberger matrices. However, in general, $\mathfrak{B}_n$ is un-reduced because $\forall i \in [0,n-2], \mathfrak{B}_{n,i+1,i} \neq 0$. Two strategies have been adopted in CESTAM:

- either one extracts the eigenvalues of $\mathfrak{B}_n$ at a given point of the radial mesh and selects $\theta_{\rm m}$ as the closest to $\arccos(1/\sqrt{3})$;
- or one extracts them at few points of the radial mesh and keeps the one common to all the sets of eigenvalues;
- or one extracts them at all points of the radial mesh and averages eigenvalues that are close to one another and in the right interval;
- or one extracts $\theta_{\rm m}$ at all points of the radial mesh. Then, the representation of $\theta_{\rm m}$ as a function of r makes it possible to have a varying $\theta_{\rm m}$ at different layers.

It is still not clear what is the good choice and they shall be tested thoroughly. However, the penultimate option should probably be ruled out because, at the centre, $\theta_{\rm m}$ becomes undefined. These variations certainly affect the mean value. The one I usually choose in CESTAM is the fourth.

Should we deform the atmosphere ?

Roxburgh (2004, 2006)'s method is developed to deform the internal structure. The atmosphere is just here to provide some boundary conditions. In our first implementation of the deformation CESTAM, the equations of the atmosphere structure were modified to include the factor $f_{p,T,{\rm d}}$, computed at the surface. The atmosphere computed in 1D was then "patched" on

the deformed surface. However, if a certain rotation threshold was to be reached, the deformed isobars could cross the small extent of the atmosphere. It was then decided to include the atmosphere in the deformation process. The atmosphere is supposed to rotate uniformly with the same angular velocity as the surface. Of course, more sophisticated models of rotating atmospheres should be developed, but this is less of a priority than a rotating convection model.

Numerical mass loss

Roxburgh (2006) pointed out that when deforming a model, the total mass suffered from a slight decrease. This loss of mass is purely numerical and is due to the readjustment of density in 2D. As an example, they showed that when deforming a $2M_\odot$ model, the final mass after the deformation was $1.9995M_\odot$. It may seem small but a change of $10^{-4}M_\odot$ is of the same order as the total mass loss that the Sun has experienced through stellar winds during its whole MS lifetime. In addition, the total numerical mass loss a model would suffer along its evolution is not a function of time but of the number of time steps needed to reach the desired age. If a star loses $10^{-5}M_\odot$ at each time step due to deformation, after an evolution counting around 1000 time steps, the change of mass would be of order 1%, which is far from being negligible ! Our implementation of the deformation method in CESTAM produces a rather better conservation of mass. The mass difference goes from $10^{-12}M_\odot$ to $10^{-8}M_\odot$. Roxburgh (2006) used 2400 radial grid points and 240 angular grid points, which is rather similar to us. We do not have much details on how the radial points were located, but the angles are evenly spaced. Our better mass loss could come from better located radial points and angles chosen with a Gauss-Legendre quadrature. As a workaround, the final mass of the deformed model is corrected with a multiplicative factor that ensures $M^{1\mathrm{D}} = M^{2\mathrm{D}}$.

6.3 The transport of angular momentum in 2D

Before the adoption of the numerical scheme that will be presented in this section, we hesitated and tested several of them. They all presented stability problem, however it may be interesting in the future to re-investigate the causes of this instabilities and try and make them work. The method that finally worked is based on a relaxation method developed in Press et al. (1992). By expressing the Jacobian of the system of equation, the successive guesses for the solutions are guided toward the true solution.

6.3.1 Relaxation method

In order to solve our system of equations, we will use a numerical method, called the *relaxation method* (Press et al., 1992), that shares common points with the collocation. This method works on systems of first order ordinary differential equations, of the same form as in Eq. (6.6). We denote $\mathbf{E} = \{E_i\}_{i=1}^{n_\mathrm{e}}$ the vector containing our n_e differential equations. These equations depend on a quantity x and on the n_e unknowns $\mathbf{y} = \{y_i\}_{i=1}^{n_\mathrm{e}}$ and their x-derivatives. With these notations, the system is written

$$\mathbf{E}(x; \mathbf{y}, \mathbf{y}') = \frac{\mathrm{d}\mathbf{y}}{\mathrm{d}x} - \mathbf{g}(x, \mathbf{y}) = \mathbf{0}, \tag{6.44}$$

with $\mathbf{g}$ a suitable vector of functions representing the differential system.

For a domain divided into N layers, and by labelling independent variables at each layers with a superscript k, this problem has $\{\mathbf{y}^k\}^{k=1,N} = \{y_i^k\}_{i=1,n_\mathrm{e}}^{k=1,N}$ as independent variables, *i.e.*

$n_e N$ unknowns. We denote $\mathbf{E} = \{\mathbf{E}_i^k\}^{k=1,N} = \{E_i^k\}_{i=1,n_e}^{k=1,N}$, the equations linking the variables y_i^k. They are of the form:

$$\forall k \in [\![2; N]\!], \quad \mathbf{E}^k = \mathbf{y}^k - \mathbf{y}^{k-1} - (x^k - x^{k-1})\mathbf{g}^k(x^k, x^{k-1}, \mathbf{y}^k, \mathbf{y}^{k-1}) = \mathbf{0}. \tag{6.45}$$

Contrarily to the collocation method, the solutions $\mathbf{y}$ are not decomposed on a basis of B-Splines, therefore, we do not have to express the differential system for all coefficients of the B-Splines, at all mesh points. These mesh points are the one located at the faces of each layer already determined by CESTAM. We do not introduce new points between them using a Gauss-Legendre quadrature and therefore we do not seek to obtain superconvergence.

Equation (6.45) provides $n_e(N-1)$ equations while we have $n_e N$ unknowns. We need n_e more equations, $\mathbf{E}^1(x^1, \mathbf{y}^1)$ and $\mathbf{E}^{N+1}(x^N, \mathbf{y}^N)$, that come from boundary conditions, so that the system is complete. There is no need to have the same number of boundary conditions at top and bottom, the n_e can be at the same location. Once we have our set of differential equations, the idea is to start from a first guess for $\mathbf{y}$, for instance their solutions at previous time step. Then, iteratively, to tweak their values in order to minimize $\mathbf{E}_i^k$. In order to guide the adjustment of $\mathbf{y}$ to the right solution, equations $\mathbf{E}_i^k$ are developed to 1st-order in Taylor series:

$$\begin{aligned}\mathbf{E}^k(\mathbf{y}^k + \Delta\mathbf{y}^k, \mathbf{y}^{k-1} + \Delta\mathbf{y}^{k-1}) &\simeq \mathbf{E}^k(\mathbf{y}^k, \mathbf{y}^{k-1}) + \sum_{i=1}^{n_e} \frac{\partial \mathbf{E}^k}{\partial y_{i,k-1}} \Delta y_i^{k-1} + \sum_{i=1}^{n_e} \frac{\partial \mathbf{E}^k}{\partial y_{i,k}} \Delta y_i^k \\ &\simeq \mathbf{E}^k(\mathbf{y}^k, \mathbf{y}^{k-1}) + \mathbf{S}^i_{k,k-1}\Delta y_i^{k-1} + \mathbf{S}^i_{k,k}\Delta y_i^k.\end{aligned} \tag{6.46}$$

Einstein notation

We want $\mathbf{E}^k(\mathbf{y}^k + \Delta\mathbf{y}^k, \mathbf{y}^{k-1} + \Delta\mathbf{y}^{k-1})$ to be as small as possible. The errors $\mathbf{E}^k(\mathbf{y}^k, \mathbf{y}^{k-1})$ are known from previous iteration step, $\mathbf{S}^i_{k,j} = \partial \mathbf{E}_i^k / \partial y_j$ is the Jacobian of the system (6.7). It gives the slopes that lead to the solutions. We look for the small modifications Δy_i^{k-1} and Δy_i^k that solve the system:

$$\mathbf{E}^k(\mathbf{y}^k, \mathbf{y}^{k-1}) + \sum_{i=1}^{n_e} \frac{\partial \mathbf{E}_i^k}{\partial y^{k-1}} \Delta y_i^{k-1} + \sum_{i=1}^{n_e} \frac{\partial \mathbf{E}_i^k}{\partial y^k} \Delta y_i^k = \mathbf{0}. \tag{6.47}$$

6.3.2 First order differential system

I recall that the system of equations we are trying to solve is:

$$\left\{\begin{array}{rcl} \dfrac{L_p}{m_p}\mathcal{T}_\ell & = & \overline{T} c_p \left[\dfrac{\mathrm{d}\Psi_\ell}{\mathrm{d}t} + \Phi \dfrac{\mathrm{d}\ln\overline{\mu}}{\mathrm{d}t}\Lambda_\ell + \dfrac{U_\ell}{H_\mathrm{p}}\left(\nabla_\mathrm{ad} - \nabla\right)\right] \\ \rho \dfrac{\mathrm{d}r^2\overline{\Omega}}{\mathrm{d}t} & = & \dfrac{1}{5r^2}\dfrac{\partial}{\partial r}\left(\rho r^4 \overline{\Omega} U_2\right) + \dfrac{1}{r^2}\dfrac{\partial}{\partial r}\left(\rho \nu_\mathrm{v} r^4 \dfrac{\partial \overline{\Omega}}{\partial r}\right) \end{array}\right. , \tag{6.48}$$

with

$$\begin{aligned}\mathcal{T}_\ell &= 2\left(1 - \frac{\overline{f}_\mathrm{C}}{4\pi\mathcal{G}\overline{\rho}} - \frac{\overline{\varepsilon} + \overline{\varepsilon}_\mathrm{g}}{\varepsilon_\mathrm{m}}\right)\frac{\widetilde{g}_\ell}{\overline{g}} + \frac{\widetilde{f}_{\mathrm{C},\ell}}{4\pi\mathcal{G}\overline{\rho}} - \frac{\overline{f}_\mathrm{C}}{4\pi\mathcal{G}\overline{\rho}}\Theta_\ell \\ &+ \frac{\rho_\mathrm{m}}{\overline{\rho}}\left[\frac{r}{3}\frac{\mathrm{d}}{\mathrm{d}r}\left(H_\mathrm{T}\frac{\partial\Psi_\ell}{\partial r} - (1 - \delta + \chi_T)\Psi_\ell - (\varphi + \chi_\mu)\Lambda_\ell\right) - \frac{\ell(\ell+1)H_\mathrm{T}}{3r}\left(1 + \frac{D_\mathrm{h}}{K}\right)\Psi_\ell\right] \\ &+ \frac{\overline{\varepsilon} + \overline{\varepsilon}_\mathrm{g}}{\varepsilon_\mathrm{m}}\left[\left(H_\mathrm{T}\frac{\partial\Psi_\ell}{\partial r} - (1 - \delta + \chi_T)\Psi_\ell - (\varphi + \chi_\mu)\Lambda_\ell\right) + (f_\varepsilon\varepsilon_T - f_\varepsilon\delta + \delta)\Psi_\ell\right. \\ &+ \left.(f_\varepsilon\varepsilon_\mu + f_\varepsilon\varphi - \varphi)\Lambda_\ell\right].\end{aligned} \tag{6.49}$$

The first equation of system (6.48) actually is one equation for each term ℓ of the meridional circulation. This system can also be supplemented by the equation for the horizontal transport of angular momentum (or even higher orders):

$$\rho\frac{\mathrm{d}r^2\Omega_2}{\mathrm{d}t}+\frac{1}{r^2}\frac{\partial}{\partial r}\left(\rho r^4\overline{\Omega}U_2\right)-\frac{10}{6}\frac{\mathrm{d}\rho r^2U_2}{\mathrm{d}r}\overline{\Omega}=\frac{1}{r^2}\frac{\partial}{\partial r}\left[\rho\nu_{\mathrm{v}}r^4\frac{\partial\Omega_2}{\partial r}\right]-10\rho\nu_{\mathrm{h}}\Omega_2. \tag{6.50}$$

I will treat the systems (6.48) and (6.48)+(6.50) separately.

Our goal is to make use of the relaxation method presented in Sect. 6.3.1 to solve those systems. The relaxation method works on first order differential systems, which is the case for neither (6.48) nor (6.50). To transform them into 1st-order ODES, we introduce more independent variables. The first one has been defined in Eq. (2.107):

$$\Upsilon_\ell=H_{\mathrm{T}}\frac{\partial\Psi_\ell}{\partial r}-(1-\delta+\chi_T)\,\Psi_\ell-(\varphi+\chi_\mu)\,\Lambda_\ell. \tag{6.51}$$

The two others are the first order radial derivatives of $\overline{\Omega}$ and Ω_2:

$$F_{\nu,0}=\frac{\partial\overline{\Omega}}{\partial r}\quad\text{and}\quad F_{\nu,2}=\frac{\partial\Omega_2}{\partial r}. \tag{6.52}$$

Those new variables having been defined, our equations reads:

$$\begin{aligned}\frac{\nabla_{\mathrm{ad}}-\nabla}{H_{\mathrm{p}}}U_\ell=\frac{L_p}{c_p\overline{T}m_p}\Bigg\{&2\left(1-\frac{\overline{f}_{\mathrm{C}}}{4\pi\mathcal{G}\overline{\rho}}-\frac{\overline{\varepsilon}+\overline{\varepsilon}_{\mathrm{grav}}}{\varepsilon_{\mathrm{m}}}\right)\frac{\widetilde{g}_\ell}{\overline{g}}+\frac{\widetilde{f}_{\mathrm{C}\ell}}{4\pi\mathcal{G}\overline{\rho}}-\frac{\overline{f}_{\mathrm{C}}}{4\pi\mathcal{G}\overline{\rho}}\Theta_\ell\\&+\frac{\rho_{\mathrm{m}}}{\overline{\rho}}\left[\frac{r_p}{3}\frac{\partial\Upsilon_\ell}{\partial r}-\frac{\ell(\ell+1)H_{\mathrm{T}}}{3r_p}\left(1+\frac{D_{\mathrm{h}}}{K}\right)\Psi_\ell\right]\\&+\frac{\overline{\varepsilon}+\overline{\varepsilon}_{\mathrm{grav}}}{\varepsilon_{\mathrm{m}}}\left[\Upsilon_\ell+(f_\varepsilon\varepsilon_T-f_\varepsilon\delta+\delta)\,\Psi_\ell+(f_\varepsilon\varepsilon_\mu-f_\varepsilon\varphi+\varphi)\,\Lambda_\ell\right]\Bigg\}\\&-\frac{\mathrm{d}\Psi_\ell}{\mathrm{d}t}-\Phi\frac{\mathrm{d}\ln\overline{\mu}}{\mathrm{d}t}\Lambda_\ell,\end{aligned} \tag{6.53}$$

$$\Upsilon_\ell=H_{\mathrm{T}}\frac{\partial\Psi_\ell}{\partial r}-(1-\delta+\chi_T)\,\Psi_\ell-(\varphi+\chi_\mu)\,\Lambda_\ell, \tag{6.54}$$

$$\rho\frac{\mathrm{d}r^2\overline{\Omega}}{\mathrm{d}t}=\frac{1}{5r^2}\frac{\partial}{\partial r}\left(\rho r^4\overline{\Omega}U_2\right)+\frac{1}{r^2}\frac{\partial}{\partial r}\left(\rho\nu_{\mathrm{v}}r^4F_{\nu,0}\right), \tag{6.55}$$

$$\rho\frac{\mathrm{d}r^2\Omega_2}{\mathrm{d}t}=\frac{10}{6}\frac{\mathrm{d}\rho r^2U_2}{\mathrm{d}r}\overline{\Omega}+\frac{1}{r^2}\frac{\partial}{\partial r}\left[\rho\nu_{\mathrm{v}}r^4F_{\nu,2}\right]-\frac{1}{r^2}\frac{\partial}{\partial r}\left(\rho r^4\overline{\Omega}U_2\right)-10\rho\nu_{\mathrm{h}}\Omega_2. \tag{6.56}$$

Just as a side remark, the term $(\nabla_{\mathrm{ad}}-\nabla)/H_{\mathrm{p}}$ is kept on the left side of the equation because, near the tachocline, the term $\nabla_{\mathrm{ad}}-\nabla$ goes to zero. If it is in the denominator, the term $H_{\mathrm{p}}/(\nabla_{\mathrm{ad}}-\nabla)$ would explode and introduce spurious results in the solution of U_ℓ.

6.3.3 Dimensionless system for U_2 and $\overline{\Omega}$

For CESTAM to be able to solve Eqs. (6.53) to (6.55), we need to do more work. First of all, we shall introduce dimensionless variables. While they have the same name as the one defined in 6.1.2, their definition is slightly different:

$$\begin{aligned}\zeta=\frac{r}{R_\odot}\quad&\rightarrow\quad r=\zeta R_\odot=\zeta R_\odot,&\qquad\lambda=\frac{L_p}{L_\odot}\quad&\rightarrow\quad L_p=\lambda L_\odot,\\ m=\frac{m_p}{M_\odot}\quad&\rightarrow\quad m_p=mM_\odot,&\qquad\nu=\left(\frac{m_p}{M_\odot}\right)^{2/3}\quad&\rightarrow\quad m_p=\nu^{3/2}M_\odot,\\ \frac{\partial}{\partial r}\quad&\rightarrow\quad\frac{\partial}{\partial r}=\frac{8\pi R_\odot^2}{3M_\odot}\frac{\breve{\rho}\zeta^2}{\sqrt{\nu}}\frac{\partial}{\partial\nu},&\qquad\frac{\partial}{\partial r}\quad&\rightarrow\quad\frac{\partial}{\partial r}=\frac{4\pi R_\odot^2}{M_\odot}\breve{\rho}\zeta^2\frac{\partial}{\partial m}.\end{aligned} \tag{6.57}$$

The radial derivatives in equation for U_ℓ and Υ_ℓ will be replaced by $\partial/\partial\nu$, while the one in the vertical angular momentum transport equation will be replaced by $\partial/\partial m$. Doing so allows us to clearly see the fact that our numerical scheme conserves angular momentum by construction and mixing m and ν is not a problem for the relaxation method. With those dimensionless quantities, our system reads

$$\begin{aligned}
\Upsilon_\ell &= H_{\rm T}\frac{8\pi R_\odot^2}{3M_\odot}\frac{\breve{\rho}\zeta^2}{\sqrt{\nu}}\frac{\partial\Psi_\ell}{\partial\nu} - (1-\delta+\chi_T)\,\Psi_\ell - (\varphi+\chi_\mu)\,\Lambda_\ell,\\
\frac{\nabla_{\rm ad}-\nabla}{H_{\rm p}}U_\ell &= \frac{L_\odot}{M_\odot}\frac{\lambda}{c_p\overline{T}\nu^{3/2}}\left\{2\left(1-\frac{\overline{f}_{\rm C}}{4\pi\mathcal{G}\overline{\rho}}-\frac{\overline{\varepsilon}+\overline{\varepsilon}_{\rm grav}}{\varepsilon_{\rm m}}\right)\frac{\widetilde{g}_\ell}{\overline{g}}+\frac{\widetilde{f}_{{\rm C}\ell}}{4\pi\mathcal{G}\overline{\rho}}-\frac{\overline{f}_{\rm C}}{4\pi\mathcal{G}\overline{\rho}}\Theta_\ell\right.\\
&\quad+\frac{\rho_{\rm m}}{\overline{\rho}}\left[\frac{8\pi R_\odot^3}{9M_\odot}\frac{\zeta^3\breve{\rho}}{\sqrt{\nu}}\frac{\partial\Upsilon_\ell}{\partial\nu}-\frac{\ell(\ell+1)H_{\rm T}}{3R_\odot\zeta}\left(1+\frac{D_{\rm h}}{K}\right)\Psi_\ell\right]\\
&\quad\left.+\frac{\overline{\varepsilon}+\overline{\varepsilon}_{\rm grav}}{\varepsilon_{\rm m}}\left[\Upsilon_\ell+(f_\varepsilon\varepsilon_T-f_\varepsilon\delta+\delta)\,\Psi_\ell+(f_\varepsilon\varepsilon_\mu-f_\varepsilon\varphi+\varphi)\,\Lambda_\ell\right]\right\}\\
&\quad-\frac{{\rm d}\Psi_\ell}{{\rm d}t}-\Phi\frac{{\rm d}\ln\overline{\mu}}{{\rm d}t}\Lambda_\ell,\\
\frac{\rm d}{{\rm d}t}\left(\zeta^2\overline{\Omega}\right) &= \frac{R_\odot^2}{M_\odot}\frac{\partial}{\partial m}\left(\frac{4\pi}{5}\rho\zeta^4\overline{\Omega}U_2\right)+\left(\frac{R_\odot^2}{M_\odot}\right)^2\frac{\partial}{\partial m}\left(16\pi^2\rho^2\zeta^6\nu_{\rm v}\frac{\partial\overline{\Omega}}{\partial m}\right).
\end{aligned}\tag{6.58}$$

Furthermore, the following quantities may be simplified:

$$\begin{aligned}
H_{\rm p} &= -\frac{1}{p}\frac{{\rm d}p}{{\rm d}r}=\frac{p}{\rho g_{\rm eff}}, & H_{\rm T} &= -\frac{1}{T}\frac{{\rm d}T}{{\rm d}r}=\frac{H_{\rm p}}{\nabla}=\frac{p}{\rho g_{\rm eff}\nabla},\\
\frac{\overline{\varepsilon}+\overline{\varepsilon}_{\rm grav}}{\varepsilon_{\rm m}} &= \frac{M_p}{L_p}\frac{\partial L_p}{\partial M_p}=\frac{\partial\ln\lambda}{\partial\ln\nu}, & \mathcal{Z} &= \frac{8\pi R_\odot^2}{3M_\odot},\\
f_\varepsilon &= \frac{\overline{\varepsilon}}{\overline{\varepsilon}+\overline{\varepsilon}_{\rm grav}}, & f_\varepsilon\frac{\overline{\varepsilon}+\overline{\varepsilon}_{\rm grav}}{\varepsilon_{\rm m}} &= \frac{\overline{\varepsilon}}{\varepsilon_{\rm m}}=\frac{M_\odot}{L_\odot}\frac{\varepsilon_{\rm nuc}}{\lambda}\nu^{3/2}.
\end{aligned}\tag{6.59}$$

Injecting those quantities in system (6.57) gives:

$$\begin{aligned}
\Upsilon_\ell &= \frac{8\pi R_\odot^2}{3M_\odot}\frac{\breve{\rho}\zeta^2}{\sqrt{\nu}}\frac{H_{\rm p}}{\nabla}\frac{\partial\Psi_\ell}{\partial\nu} - (1-\delta+\chi_T)\,\Psi_\ell - (\varphi+\chi_\mu)\,\Lambda_\ell,\\
\frac{\nabla_{\rm ad}-\nabla}{H_{\rm p}}U_\ell &= \frac{L_\odot}{M_\odot}\frac{\lambda}{c_p\overline{T}\nu^{3/2}}\left\{2\left(1-\frac{\overline{f}_{\rm C}}{4\pi\mathcal{G}\overline{\rho}}-\frac{\partial\ln\lambda}{\partial\ln\nu}\right)\frac{\widetilde{g}_\ell}{\overline{g}}+\frac{\widetilde{f}_{{\rm C}\ell}}{4\pi\mathcal{G}\overline{\rho}}-\frac{\overline{f}_{\rm C}}{4\pi\mathcal{G}\overline{\rho}}\Theta_\ell\right.\\
&\quad+\frac{\rho_{\rm m}}{\overline{\rho}}\left[\frac{8\pi R_\odot^3}{9M_\odot}\frac{\zeta^3\breve{\rho}}{\sqrt{\nu}}\frac{\partial\Upsilon_\ell}{\partial\nu}-\frac{\ell(\ell+1)}{3R_\odot\zeta}\frac{H_{\rm p}}{\nabla}\left(1+\frac{D_{\rm h}}{K}\right)\Psi_\ell\right]+\frac{\partial\ln\lambda}{\partial\ln\nu}\left(\Upsilon_\ell+\delta\Psi_\ell+\varphi\Lambda_\ell\right)\\
&\quad\left.+\frac{M_\odot}{L_\odot}\frac{\varepsilon_{\rm nuc}}{\lambda}\nu^{3/2}\left[(\varepsilon_T-\delta)\,\Psi_\ell+(\varepsilon_\mu-\varphi)\,\Lambda_\ell\right]\right\}-\frac{{\rm d}\Psi_\ell}{{\rm d}t}-\Phi\frac{{\rm d}\ln\overline{\mu}}{{\rm d}t}\Lambda_\ell,\\
\frac{\rm d}{{\rm d}t}\left(\zeta^2\overline{\Omega}\right) &= \frac{R_\odot^2}{M_\odot}\frac{\partial}{\partial m}\left(\frac{4\pi}{5}\rho\zeta^4\overline{\Omega}U_2\right)+\left(\frac{R_\odot^2}{M_\odot}\right)^2\frac{\partial}{\partial m}\left(16\pi^2\rho^2\zeta^6\nu_{\rm v}\frac{\partial\overline{\Omega}}{\partial m}\right).
\end{aligned}\tag{6.60}$$

From now on, I only restrict myself to the $\ell=2$ component. We introduce the notation $y_1=U_2$, $y_2=\Upsilon_2$, $y_{3,0}=\overline{\Omega}$ and $y_{4,0}=\frac{\partial\overline{\Omega}}{\partial m}$. The variable Ψ_2, Λ_2 are linked to Θ_2 and U_2. The $2^{\rm nd}$-order term Θ_2 is precisely computed by Roxburgh (2006)'s method. However, this method is applied at the end of the computation of a time step (see Fig. 6.1). Therefore, the Θ_2 that has been computed using the deformation module, was computed at the previous time step and it

may have changed significantly. I said earlier that Mathis & Zahn (2004) provide an expression for Θ_ℓ. We did not used this expression to compute the final value of Θ_2, however such a relation can be used to provide an approximate Θ_2 in order to compute U_2 and $\overline{\Omega}$. When the horizontal transport of angular momentum is neglected,

$$\Theta_2 = \frac{r^2}{3\bar{g}_{\rm eff}}\frac{\partial\bar{\Omega}^2}{\partial r} = \mathcal{Z}R_\odot^2\breve{\rho}\frac{\zeta^4}{\bar{g}_{\rm eff}}y_{3,0}y_{4,0}. \tag{6.61}$$

When this expression is injected into the one of U_2, it explicitly introduces a dependence of U_2 on Ω_2, which is good for the stability of our algorithm. The fluctuations of mean molecular weight are expressed through a time derivative in Eq. (2.83). This time derivative is discretized and reduced as follow:

$$\frac{{\rm d}\Lambda_\ell}{{\rm d}t}(m) = \frac{\Lambda_\ell(m)-\Lambda_\ell^t(m)}{\Delta t} = -\left(\frac{\ell(\ell+1)}{R_\odot^2\zeta^2}D_{\rm h} - \frac{{\rm d}\ln\overline{\mu}}{{\rm d}t}\right)\Lambda_\ell + \frac{U_\ell}{H_{\rm p}}\nabla_\mu, \tag{6.62}$$

$$\Lambda_\ell = \frac{\Lambda_\ell^t/\Delta t + \frac{U_\ell}{H_{\rm p}}\nabla_\mu}{\frac{1}{\Delta t}+\frac{\ell(\ell+1)}{R_\odot^2\zeta^2}D_{\rm h} - \frac{{\rm d}\ln\overline{\mu}}{{\rm d}t}} = \mathcal{A}_0 + \mathcal{A}_1 U_\ell, \tag{6.63}$$

where $\Lambda_\ell^t(m)$ is the mean molecular weight fluctuation at the previous time step and mass m, and $\mathcal{A}_0$ and $\mathcal{A}_1$ are defined as

$$\mathcal{A}_0 = \frac{\Lambda^t}{1+\Delta t\left(\frac{\ell(\ell+1)}{R_\odot^2\zeta^2}D_{\rm h} - \frac{{\rm d}\ln\bar{\mu}}{{\rm d}t}\right)} \quad \text{and} \quad \mathcal{A}_1 = \frac{\nabla_\mu}{H_{\rm p}\left(1/\Delta t + \frac{\ell(\ell+1)}{R_\odot^2\zeta^2}D_{\rm h} - \frac{{\rm d}\ln\bar{\mu}}{{\rm d}t}\right)}. \tag{6.64}$$

With Θ_2 and Λ_2 known, Ψ_2 is simply expressed as:

$$\Psi_2 = \frac{\varphi\Lambda_2-\Theta_2}{\delta} = \frac{\varphi\mathcal{A}_0+\varphi\mathcal{A}_1 y_1 - \mathcal{Z}R_\odot^2\breve{\rho}\frac{\zeta^4}{\bar{g}_{\rm eff}}y_{3,0}y_{4,0}}{\delta} = \mathcal{C}_0+\mathcal{C}_1 y_1+\mathcal{C}_2 y_{3,0}y_{4,0}, \tag{6.65}$$

where we defined $\mathcal{C}_0$, $\mathcal{C}_1$ and $\mathcal{C}_2$ as

$$\mathcal{C}_0 = \frac{\varphi\mathcal{A}_0}{\delta}, \qquad \mathcal{C}_1 = \frac{\varphi}{\delta}\mathcal{A}_1 \quad \text{and} \quad \mathcal{C}_2 = -\mathcal{Z}R_\odot^2\breve{\rho}\frac{\zeta^4}{\bar{g}_{\rm eff}\delta}. \tag{6.66}$$

And we also need the ν-derivative of Ψ_2:

$$\begin{aligned}\frac{\partial\Psi_2}{\partial\nu} &= \frac{\partial\mathcal{C}_0}{\partial\nu}+\frac{\partial\mathcal{C}_1}{\partial\nu}y_1+\mathcal{C}_1\frac{\partial y_1}{\partial\nu}+\frac{\partial\mathcal{C}_2}{\partial\nu}y_{3,0}y_{4,0}+\mathcal{C}_2\frac{\partial y_{3,0}}{\partial\nu}y_{4,0}+\mathcal{C}_2 y_{3,0}\frac{\partial y_{4,0}}{\partial\nu}\\ &= \mathcal{D}_0+\mathcal{D}_1 y_1+\mathcal{C}_1\frac{\partial y_1}{\partial\nu}+\mathcal{D}_2 y_{3,0}y_{4,0}+\mathcal{C}_2\left(\frac{\partial y_{3,0}}{\partial\nu}y_{4,0}+y_{3,0}\frac{\partial y_{4,0}}{\partial\nu}\right),\end{aligned} \tag{6.67}$$

where $\mathcal{D}_i = \partial\mathcal{C}_i/\partial\nu$.

The expressions for Θ_2, Λ_2, Ψ_2 and $\partial\Psi_2/\partial\nu$ as a function of y_1, y_2, $y_{3,0}$ and $y_{4,0}$ can be injected into system (6.60) and we obtain:

$$\begin{aligned}y_2 = &\left[\mathcal{Z}\frac{\breve{\rho}\zeta^2}{\sqrt{\nu}}\frac{H_{\rm p}}{\nabla}\mathcal{D}_0-(1-\delta+\chi_T)\mathcal{C}_0-(\varphi+\chi_\mu)\mathcal{A}_0\right]\\ &+y_1\left[\mathcal{Z}\frac{\breve{\rho}\zeta^2}{\sqrt{\nu}}\frac{H_{\rm p}}{\nabla}\mathcal{D}_1-(1-\delta+\chi_T)\mathcal{C}_1-(\varphi+\chi_\mu)\mathcal{A}_1\right]+\frac{\partial y_1}{\partial\nu}\left[\mathcal{Z}\frac{\breve{\rho}\zeta^2}{\sqrt{\nu}}\frac{H_{\rm p}}{\nabla}\mathcal{C}_1\right]\\ &+y_{3,0}y_{4,0}\left[\mathcal{Z}\frac{\breve{\rho}\zeta^2}{\sqrt{\nu}}\frac{H_{\rm p}}{\nabla}\mathcal{D}_2-(1-\delta+\chi_T)\mathcal{C}_2\right]+\left(\frac{\partial y_{3,0}}{\partial\nu}y_{4,0}+y_{3,0}\frac{\partial y_{4,0}}{\partial\nu}\right)\left[\mathcal{Z}\frac{\breve{\rho}\zeta^2}{\sqrt{\nu}}\frac{H_{\rm p}}{\nabla}\mathcal{C}_2\right],\end{aligned} \tag{6.68}$$

$$
\begin{aligned}
\frac{\nabla_{\rm ad}-\nabla}{H_{\rm p}}y_1 &= \left\{\frac{L_\odot}{M_\odot}\frac{\lambda}{c_p\overline{T}\nu^{3/2}}\left(2\left[1-\frac{\overline{f}_{\rm C}}{4\pi\mathcal{G}\overline{\rho}}-\frac{\partial\ln\lambda}{\partial\ln\nu}\right]\frac{\widetilde{g}_\ell}{\overline{g}}+\frac{\widetilde{f}_{{\rm C}\ell}}{4\pi\mathcal{G}\overline{\rho}}+\frac{\partial\ln\lambda}{\partial\ln\nu}\varphi\mathcal{A}_0\right.\right.\\
&\quad\left.+\left[\frac{\partial\ln\lambda}{\partial\ln\nu}\delta-\frac{\rho_{\rm m}}{\overline{\rho}}\frac{H_{\rm p}}{\nabla}\frac{\ell(\ell+1)}{3R_\odot\zeta}\left(1+\frac{D_{\rm h}}{K}\right)\right]\mathcal{C}_0+\frac{\varepsilon_{\rm nuc}}{c_p\overline{T}}\left[\left(\varepsilon_T-\delta\right)\mathcal{C}_0+\left(\varepsilon_\mu-\varphi\right)A_0\right]\right)\\
&\quad\left.+\frac{\Psi_\ell^t-\mathcal{C}_0}{\Delta t}-\Phi\frac{{\rm d}\ln\overline{\mu}}{{\rm d}t}\mathcal{A}_0\right\}\\
&\quad+y_2\left\{\frac{L_\odot}{M_\odot}\frac{\lambda}{c_p\overline{T}\nu^{3/2}}\frac{\partial\ln\lambda}{\partial\ln\nu}\right\}+\frac{\partial y_2}{\partial\nu}\left\{\frac{L_\odot}{M_\odot}\frac{\lambda}{c_p\overline{T}\nu^{3/2}}\frac{\rho_{\rm m}}{\overline{\rho}}\mathcal{Z}\frac{R_\odot}{3}\frac{\zeta^3\breve{\rho}}{\sqrt{\nu}}\right\}\\
&\quad+y_1\left\{\frac{L_\odot}{M_\odot}\frac{\lambda}{c_p\overline{T}\nu^{3/2}}\left(\left[\frac{\partial\ln\lambda}{\partial\ln\nu}\delta-\frac{\rho_{\rm m}}{\overline{\rho}}\frac{H_{\rm p}}{\nabla}\frac{\ell(\ell+1)}{3R_\odot\zeta}\left(1+\frac{D_{\rm h}}{K}\right)\right]\mathcal{C}_1+\frac{\partial\ln\lambda}{\partial\ln\nu}\varphi\mathcal{A}_1\right)\right.\\
&\quad\left.+\frac{\varepsilon_{\rm nuc}}{c_p\overline{T}}\left[\left(\varepsilon_T-\delta\right)\mathcal{C}_1+\left(\varepsilon_\mu-\varphi\right)\mathcal{A}_1\right]-\frac{\mathcal{C}_1}{\Delta t}-\Phi\frac{{\rm d}\ln\overline{\mu}}{{\rm d}t}\mathcal{A}_1\right\}\\
&\quad+y_{3,0}y_{4,0}\left\{\frac{L_\odot}{M_\odot}\frac{\lambda}{c_p\overline{T}\nu^{3/2}}\left[\frac{\partial\ln\lambda}{\partial\ln\nu}\delta\mathcal{C}_2-\mathcal{Z}R_\odot^2\breve{\rho}\frac{\zeta^4}{\overline{g}_{\rm eff}}\frac{\overline{f}_{\rm C}}{4\pi\mathcal{G}\overline{\rho}}-\frac{\rho_{\rm m}}{\overline{\rho}}\frac{H_{\rm p}}{\nabla}\frac{\ell(\ell+1)}{3R_\odot\zeta}\left(1+\frac{D_{\rm h}}{K}\right)\mathcal{C}_2\right.\right.\\
&\quad\left.\left.+\frac{\varepsilon_{\rm nuc}}{c_p\overline{T}}\left[\left(\varepsilon_T-\delta\right)\mathcal{C}_2\right]\right]-\frac{\mathcal{C}_2}{\Delta t}\right\}. \qquad (6.69)
\end{aligned}
$$

The last equation of system (6.60) needs a little more work. We integrate it over a spheroidal shell located in between two masses m_{k-1} and m_k, as follow

$$
\begin{aligned}
\int_{m_{k-1}}^{m_k}\frac{\rm d}{{\rm d}t}\left(\zeta^2\overline{\Omega}\right){\rm d}m &= \int_{m_{k-1}}^{m_k}\frac{R_\odot^2}{M_\odot}\frac{\partial}{\partial m}\left(\frac{4\pi}{5}\rho\zeta^4\overline{\Omega}U_2\right){\rm d}m+\int_{m_{k-1}}^{m_k}\left(\frac{R_\odot^2}{M_\odot}\right)^2\frac{\partial}{\partial m}\left(16\pi^2\rho^2\zeta^6\nu_{\rm v}\frac{\partial\overline{\Omega}}{\partial m}\right){\rm d}m\\
\int_{m_{k-1}}^{m_k}\left(\zeta^2\overline{\Omega}\right){\rm d}m &= \int_{m_{k-1}}^{m_k}\left(\zeta^2\overline{\Omega}\right)^t{\rm d}m+\Delta t\frac{R_\odot^2}{M_\odot}\frac{4\pi}{5}\left[\left(\rho\zeta^4\overline{\Omega}U_2\right)_k-\left(\rho\zeta^4\overline{\Omega}U_2\right)_{k-1}\right]\\
&\quad+\Delta t\left(\frac{R_\odot^2}{M_\odot}\right)^2\left[\left(16\pi^2\rho^2\zeta^6\nu_{\rm v}\frac{\partial\overline{\Omega}}{\partial m}\right)_k-\left(16\pi^2\rho^2\zeta^6\nu_{\rm v}\frac{\partial\overline{\Omega}}{\partial m}\right)_{k-1}\right], \qquad (6.70)
\end{aligned}
$$

with $\left(\zeta^2\overline{\Omega}\right)^t$ the value of $\left(\zeta^2\overline{\Omega}\right)$ at previous time step. Finally:

$$
\begin{aligned}
&\frac{1}{2}\left[\left(\zeta^2y_{3,0}\right)_k+\left(\zeta^2y_{3,0}\right)_{k-1}\right](m_k-m_{k-1})\\
=\;&\frac{1}{2}\left[\left(\zeta^2\overline{\Omega}\right)_k^t+\left(\zeta^2\overline{\Omega}\right)_{k-1}^t\right](m_k-m_{k-1})+\Delta t\frac{R_\odot^2}{M_\odot}\frac{4\pi}{5}\left[\left(\rho\zeta^4y_{3,0}y_1\right)_k-\left(\rho\zeta^4y_{3,0}y_1\right)_{i+1}\right]\\
&+16\pi^2\Delta t\left(\frac{R_\odot^2}{M_\odot}\right)^2\left[\left(\rho^2\zeta^6\nu_{\rm v}y_{4,0}\right)_k-\left(\rho^2\zeta^6\nu_{\rm v}y_{4,0}\right)_{k-1}\right]. \qquad (6.71)
\end{aligned}
$$

Equations (6.68), (6.69) and (6.71) form our new system. The final way to write it, *i.e.* the way as it is written in CESTAM, is to pack and rename all the factors after the independent variables:

$$
\left\{
\begin{array}{rcl}
E_1^k &=& \left(\overline{K_{1,1}} - \overline{K_{1,5}}\right)\overline{y_1} - \overline{K_{1,2}} - \overline{K_{1,3}}\overline{y_2} - \overline{K_{1,4}}\dfrac{\partial y_2}{\partial \nu} - \overline{K_{1,6}}\overline{y_{3,0}y_{4,0}} = 0,\\
E_2^k &=& \overline{y_2} - \overline{K_{2,1}} - \overline{K_{2,2}}\overline{y_1} - \overline{K_{2,3}}\dfrac{\partial y_1}{\partial \nu} - \overline{K_{2,4}}\overline{y_{3,0}y_{4,0}} - \overline{K_{2,5}}\left(\dfrac{\partial y_{3,0}}{\partial \nu}\overline{y_{4,0}} + \overline{y_{3,0}}\dfrac{\partial y_{4,0}}{\partial \nu}\right) = 0,\\
E_3^k &=& \dfrac{1}{2}\left(K_{3,3}^{k-1}y_{3,0}^{k-1} + K_{3,3}^k y_{3,0}^k\right)\Delta m - \dfrac{1}{2}\left(K_{3,4}^{k-1} + K_{3,4}^k\right)\Delta m\\
&& -\dfrac{R_\odot^2 \Delta t}{M_\odot}\left[\dfrac{R_\odot^2}{M_\odot}\left[K_{3,1}^k K_{3,2}^k y_{4,0}^k - K_{3,1}^{k-1}K_{3,2}^{k-1}y_{4,0}^{k-1}\right] + \dfrac{1}{5}\left(K_{3,1}^k y_{3,0}^k y_1^k - K_{3,1}^{k-1}y_{3,0}^{k-1}y_1^{k-1}\right)\right]\\
&=& 0,\\
E_4^k &=& \overline{y_{4,0}} - \dfrac{\partial y_{3,0}}{\partial m} = 0.
\end{array}
\right. \tag{6.72}
$$

We introduced several notations and defined several quantities. The notations first. For variables f defined on a grid with values $\{f_k\}_1^N$, $\overline{f}$ is defined as:

$$\overline{f} = \frac{f_k + f_{k-1}}{2}. \tag{6.73}$$

Also,

$$
\begin{array}{ll}
\dfrac{\partial f}{\partial \nu} = \dfrac{f_k - f_{k-1}}{\nu_k - \nu_{k-1}}, & \dfrac{\partial f}{\partial m} = \dfrac{f_k - f_{k-1}}{m_k - m_{k-1}},\\
\Delta\nu = \nu_k - \nu_{k-1}, & \Delta m = m_k - m_{k-1}.
\end{array} \tag{6.74}
$$

Then the new variables:

$$
\begin{aligned}
K_{1,1} &= \frac{\nabla_{\rm ad} - \nabla}{H_{\rm p}},\\
K_{1,2} &= \frac{L_\odot}{M_\odot}\frac{\lambda}{c_p\overline{T}\nu^{3/2}}\left(2\left[1 - \frac{\overline{f}_{\rm C}}{4\pi\mathcal{G}\overline{\rho}} - \frac{\partial \ln\lambda}{\partial\ln\nu}\right]\frac{\widetilde{g}_\ell}{\overline{g}} + \frac{\widetilde{f}_{{\rm C}\ell}}{4\pi\mathcal{G}\overline{\rho}} - \frac{\overline{f}_{\rm C}}{4\pi\mathcal{G}\overline{\rho}}\Theta_\ell + \frac{\partial\ln\lambda}{\partial\ln\nu}\varphi\mathcal{A}_0\right.\\
&\quad \left. + \left[\frac{\partial\ln\lambda}{\partial\ln\nu}\delta - \frac{\rho_{\rm m}}{\overline{\rho}}\frac{H_{\rm p}}{\nabla}\frac{\ell(\ell+1)}{3R_\odot\zeta}\left(1 + \frac{D_{\rm h}}{K}\right)\right]\mathcal{C}_0 + \frac{\varepsilon_{\rm nuc}}{c_p\overline{T}}\left[\left(\varepsilon_T - \delta\right)\mathcal{C}_0 + \left(\varepsilon_\mu - \varphi\right)A_0\right]\right)\\
&\quad + \frac{\Psi_\ell^t - \mathcal{C}_0}{\Delta t} - \Phi\frac{{\rm d}\ln\overline{\mu}}{{\rm d}t}\mathcal{A}_0,\\
K_{1,3} &= \frac{L_\odot}{M_\odot}\frac{\lambda}{c_p\overline{T}\nu^{3/2}}\frac{\partial\ln\lambda}{\partial\ln\nu},\\
K_{1,4} &= \frac{L_\odot}{M_\odot}\frac{\lambda}{c_p\overline{T}\nu^{3/2}}\frac{\rho_{\rm m}}{\overline{\rho}}\mathcal{Z}\frac{R_\odot}{3}\frac{\zeta^3\breve{\rho}}{\sqrt{\nu}},\\
K_{1,5} &= \frac{L_\odot}{M_\odot}\frac{\lambda}{c_p\overline{T}\nu^{3/2}}\left(\left[\frac{\partial\ln\lambda}{\partial\ln\nu}\delta - \frac{\rho_{\rm m}}{\overline{\rho}}\frac{H_{\rm p}}{\nabla}\frac{\ell(\ell+1)}{3R_\odot\zeta}\left(1 + \frac{D_{\rm h}}{K}\right)\right]\mathcal{C}_1 + \frac{\partial\ln\lambda}{\partial\ln\nu}\varphi\mathcal{A}_1\right)\\
&\quad + \frac{\varepsilon_{\rm nuc}}{c_p\overline{T}}\left[\left(\varepsilon_T - \delta\right)\mathcal{C}_1 + \left(\varepsilon_\mu - \varphi\right)\mathcal{A}_1\right] - \frac{\mathcal{C}_1}{\Delta t} - \Phi\frac{{\rm d}\ln\overline{\mu}}{{\rm d}t}\mathcal{A}_1,
\end{aligned}
$$

$$K_{1,6} = \frac{L_\odot}{M_\odot}\frac{\lambda}{c_p\overline{T}\nu^{3/2}}\left[\frac{\partial \ln\lambda}{\partial\ln\nu}\delta\mathcal{C}_2 - \mathcal{Z}R_\odot^2\breve{\rho}\frac{\zeta^4}{\overline{g}_{\rm eff}}\frac{\overline{f}_{\rm C}}{4\pi\mathcal{G}\overline{\rho}} - \frac{\rho_{\rm m}}{\overline{\rho}}\frac{H_{\rm p}}{\nabla}\frac{\ell(\ell+1)}{3R_\odot\zeta}\left(1+\frac{D_{\rm h}}{K}\right)\mathcal{C}_2 + \frac{\varepsilon_{\rm nuc}}{c_p\overline{T}}\left[\left(\varepsilon_T-\delta\right)\mathcal{C}_2\right]\right] - \frac{\mathcal{C}_2}{\Delta t}, \tag{6.75}$$

and

$$\begin{aligned}
K_{2,1} &= \mathcal{Z}\frac{\breve{\rho}\zeta^2}{\sqrt{\nu}}\frac{H_{\rm p}}{\nabla}\mathcal{D}_0 - \left(1-\delta+\chi_T\right)\mathcal{C}_0 - \left(\varphi+\chi_\mu\right)\mathcal{A}_0, & K_{3,1} &= 4\pi\zeta^4\breve{\rho},\\
K_{2,2} &= \mathcal{Z}\frac{\breve{\rho}\zeta^2}{\sqrt{\nu}}\frac{H_{\rm p}}{\nabla}\mathcal{D}_1 - \left(1-\delta+\chi_T\right)\mathcal{C}_1 - \left(\varphi+\chi_\mu\right)\mathcal{A}_1, & K_{3,2} &= 4\pi\breve{\rho}\zeta^2\nu_{{\rm v},k},\\
K_{2,3} &= \mathcal{Z}\frac{\breve{\rho}\zeta^2}{\sqrt{\nu}}\frac{H_{\rm p}}{\nabla}\mathcal{C}_1, & K_{3,3} &= \zeta^2,\\
K_{2,4} &= \mathcal{Z}\frac{\breve{\rho}\zeta^2}{\sqrt{\nu}}\frac{H_{\rm p}}{\nabla}\mathcal{D}_2 - \left(1-\delta+\chi_T\right)\mathcal{C}_2, & K_{3,4} &= \zeta_t^2\overline{\Omega}_t,\\
K_{2,5} &= \mathcal{Z}\frac{\breve{\rho}\zeta^2}{\sqrt{\nu}}\frac{H_{\rm p}}{\nabla}\mathcal{C}_2.
\end{aligned} \tag{6.76}$$

The final quantity we need to express is the Jacobian of this system defined in Eq. (6.46):

$$\begin{aligned}
S_{1,1} &= \frac{\partial E_1}{\partial y_1^{k-1}} = \frac{\overline{K}_{1,1}-\overline{K}_{1,5}}{2}, & S_{2,1} &= \frac{\partial E_2}{\partial y_1^{k-1}} = -\frac{\overline{K}_{2,2}}{2}+\frac{\overline{K}_{2,3}}{\Delta\nu},\\
S_{1,2} &= \frac{\partial E_1}{\partial y_2^{k-1}} = -\frac{\overline{K}_{1,3}}{2}+\frac{\overline{K}_{1,4}}{\Delta\nu}, & S_{2,2} &= \frac{\partial E_2}{\partial y_2^{k-1}} = \frac{1}{2},\\
S_{1,3} &= \frac{\partial E_1}{\partial y_{3,0}^{k-1}} = -\frac{\overline{K}_{1,6}}{2}\overline{y}_{4,0}, & S_{2,3} &= \frac{\partial E_2}{\partial y_{3,0}^{k-1}} = \overline{y}_{4,0}\left(\frac{\overline{K}_{2,5}}{\Delta\nu}-\frac{\overline{K}_{2,4}}{2}\right)-\frac{\overline{K}_{2,5}}{2}\frac{\partial y_{4,0}}{\partial\nu},\\
S_{1,4} &= \frac{\partial E_1}{\partial y_{4,0}^{k-1}} = -\frac{\overline{K}_{1,6}}{2}\overline{y}_{3,0}, & S_{2,4} &= \frac{\partial E_2}{\partial y_{4,0}^{k-1}} = \overline{y}_{3,0}\left(\frac{\overline{K}_{2,5}}{\Delta\nu}-\frac{\overline{K}_{2,4}}{2}\right)-\frac{\overline{K}_{2,5}}{2}\frac{\partial y_{3,0}}{\partial\nu}\\
S_{1,5} &= \frac{\partial E_1}{\partial y_1^{k}} = S_{1,1}, & S_{2,5} &= \frac{\partial E_2}{\partial y_1^{k}} = -\frac{\overline{K}_{2,2}}{2}-\frac{\overline{K}_{2,3}}{\Delta\nu},\\
S_{1,6} &= \frac{\partial E_1}{\partial y_2^{k}} = -\frac{\overline{K}_{1,3}}{2}-\frac{\overline{K}_{1,4}}{\Delta\nu}, & S_{2,6} &= \frac{\partial E_2}{\partial y_2^{k}} = S_{2,2},\\
S_{1,7} &= \frac{\partial E_1}{\partial y_{3,0}^{k}} = S_{1,3}, & S_{2,7} &= \frac{\partial E_2}{\partial y_{3,0}^{k}} = -\overline{y}_{4,0}\left(\frac{\overline{K}_{2,5}}{\Delta\nu}+\frac{\overline{K}_{2,4}}{2}\right)-\frac{\overline{K}_{2,5}}{2}\frac{\partial y_{4,0}}{\partial\nu},\\
S_{1,8} &= \frac{\partial E_1}{\partial y_{4,0}^{k}} = S_{1,4}, & S_{2,8} &= \frac{\partial E_2}{\partial y_{4,0}^{k}} = -\overline{y}_{3,0}\left(\frac{\overline{K}_{2,5}}{\Delta\nu}+\frac{\overline{K}_{2,4}}{2}\right)-\frac{\overline{K}_{2,5}}{2}\frac{\partial y_{3,0}}{\partial\nu},
\end{aligned} \tag{6.77}$$

and

$$
\begin{aligned}
S_{3,1} &= \frac{\partial E_3}{\partial y_1^{k-1}} = \frac{R_\odot^2 \Delta t}{5M_\odot} K_{3,1}^{k-1} y_{3,0}^{k-1}, & S_{4,1} &= \frac{\partial E_4}{\partial y_1^{k-1}} = 0,\\
S_{3,2} &= \frac{\partial E_3}{\partial y_2^{k-1}} = 0, & S_{4,2} &= \frac{\partial E_4}{\partial y_2^{k-1}} = 0,\\
S_{3,3} &= \frac{\partial E_3}{\partial y_{3,0}^{k-1}} = \frac{K_{3,3}^{k-1}}{2} + \frac{R_\odot^2 \Delta t}{5M_\odot} K_{3,1}^{k-1} y_1^{k-1}, & S_{4,3} &= \frac{\partial E_4}{\partial y_{3,0}^{k-1}} = \frac{1}{\Delta m},\\
S_{3,4} &= \frac{\partial E_3}{\partial y_{4,0}^{k-1}} = \frac{R_\odot^4 \Delta t}{M_\odot^2} K_{3,1}^{k-1} K_{3,2}^{k-1}, & S_{4,4} &= \frac{\partial E_4}{\partial y_{4,0}^{k-1}} = \frac{1}{2},\\
S_{3,5} &= \frac{\partial E_3}{\partial y_1^{k}} = -\frac{R_\odot^2 \Delta t}{5M_\odot} K_{3,1}^{k} y_{3,0}^{k}, & S_{4,5} &= \frac{\partial E_4}{\partial y_1^{k}} = 0,\\
S_{3,6} &= \frac{\partial E_3}{\partial y_2^{k}} = 0, & S_{4,6} &= \frac{\partial E_4}{\partial y_2^{k}} = 0,\\
S_{3,7} &= \frac{\partial E_3}{\partial y_{3,0}^{k}} = \frac{K_{3,3}^{k}}{2} - \frac{R_\odot^2 \Delta t}{5M_\odot} K_{3,1}^{k} y_1^{k}, & S_{4,7} &= \frac{\partial E_4}{\partial y_{3,0}^{k}} = -\frac{1}{\Delta m},\\
S_{3,8} &= \frac{\partial E_3}{\partial y_{4,0}^{k}} = -\frac{R_\odot^4 \Delta t}{M_\odot^2} K_{3,1}^{k} K_{3,2}^{k}, & S_{4,8} &= \frac{\partial E_4}{\partial y_{4,0}^{k}} = \frac{1}{2}.
\end{aligned}
\tag{6.78}
$$

Before going to the next subsection, let us show that equation E_3 in the system (6.72) conserves AM by construction if the mesh is evenly spaced in mass. This equation is nothing more than the time variation of AM in a shell between mass m_{k-1} and m_k. Let us sum all the terms between m_1 and m_N, the masses of the boundaries of the radiative zone. This sum is zero by definition:

$$
\begin{aligned}
\sum_{k=2}^{N} E_3^k &= \sum_{k=2}^{N} \left\{ \frac{1}{2}\left(K_{3,3}^{k-1} y_{3,0}^{k-1} + K_{3,3}^{k} y_{3,0}^{k}\right)\Delta m - \frac{1}{2}\left(K_{3,4}^{k-1} + K_{3,4}^{k}\right)\Delta m \right. \qquad (6.79)\\
&\quad \left. - \frac{R_\odot^2 \Delta t}{M_\odot}\left[\frac{R_\odot^2}{M_\odot}\left[K_{3,1}^{k} K_{3,2}^{k} y_{4,0}^{k} - K_{3,1}^{k-1} K_{3,2}^{k-1} y_{4,0}^{k-1}\right] + \frac{1}{5}\left(K_{3,1}^{k} y_{3,0}^{k} y_1^{k} - K_{3,1}^{k-1} y_{3,0}^{k-1} y_1^{k-1}\right)\right]\right\}\\
&= 0. \qquad (6.80)
\end{aligned}
$$

It is easy to see that consecutive terms cancel each other and we are only left with

$$
\begin{aligned}
\sum_{k=2}^{N} E_3^k &= \Delta m \left[\frac{1}{2}\left(K_{3,3}^{1} y_{3,0}^{1} + K_{3,3}^{N} y_{3,0}^{N} - K_{3,4}^{1} - K_{3,4}^{N}\right) + \sum_{k=2}^{N-1}\left(K_{3,3}^{k} y_{3,0}^{k} - K_{3,4}^{k}\right)\right] \qquad (6.81)\\
&\quad - \frac{R_\odot^2 \Delta t}{M_\odot}\left[\frac{R_\odot^2}{M_\odot}\left[K_{3,1}^{N} K_{3,2}^{N} y_{4,0}^{N} - K_{3,1}^{1} K_{3,2}^{1} y_{4,0}^{1}\right] + \frac{1}{5}\left(K_{3,1}^{N} y_{3,0}^{N} y_1^{N} - K_{3,1}^{1} y_{3,0}^{1} y_1^{1}\right)\right]\\
&= 0. \qquad (6.82)
\end{aligned}
$$

If there is a central CZ or not, $y_{4,0}^{1,N} = 0$. The above equation simplifies to:

$$
\sum_{k=2}^{N} E_3^k = \Delta m \left[\frac{1}{2}\left(K_{3,3}^{1} y_{3,0}^{1} + K_{3,3}^{N} y_{3,0}^{N} - K_{3,4}^{1} - K_{3,4}^{N}\right) + \sum_{k=2}^{N-1}\left(K_{3,3}^{k} y_{3,0}^{k} - K_{3,4}^{k}\right)\right] \qquad (6.83)
$$

$$= \frac{1}{5}\frac{R_\odot^2\Delta t}{M_\odot}\left(K_{3,1}^N y_{3,0}^N y_1^N - K_{3,1}^1 y_{3,0}^1 y_1^1\right). \tag{6.84}$$

The left hand side formally expresses the variation of the amount of angular momentum in the radiative zone during a time step Δt. The right hand side expresses this exchange at the boundaries of the radiative zone: it is the angular momentum advected from/to by the meridional circulation. The quantity $(-2R_\odot^2\Delta t)/(5M_\odot)K_{3,1}^1 y_{3,0}^1 y_1^1$ (resp. $(2R_\odot^2\Delta t)/(5M_\odot)K_{3,1}^N y_{3,0}^N y_1^N$) represents the angular momentum given to or received by the bottom (resp. top) convective zone. Integrated over the whole star, the net variation of angular momentum between two time steps is zero (if no losses by stellar winds or by disk-coupling are included).

6.3.4 Dimensionless system for U_2, $\overline{\Omega}$ and Ω_2

Once we have done that, adding the equation for the horizontal transport of angular momentum is easy. Eq. (6.56) expressed with the dimensionless quantities reads

$$\frac{\mathrm{d}\zeta^2\Omega_2}{\mathrm{d}t}+\frac{R_\odot^2}{M_\odot}\frac{\partial}{\partial m}\left(4\pi\rho\zeta^4\overline{\Omega}U_2\right)-\frac{5}{3}\frac{R_\odot^2}{M_\odot}\zeta^2\frac{\partial}{\partial m}\left(4\pi\rho\zeta^2U_2\right)\overline{\Omega}=\frac{R_\odot^4}{M_\odot^2}\frac{\partial}{\partial m}\left[16\pi^2\rho^2\nu_{\mathrm{v}}\zeta^6\frac{\partial\Omega_2}{\partial m}\right]-10\frac{\nu_{\mathrm{h}}}{R_\odot^2}\Omega_2. \tag{6.85}$$

By defining $y_{3,2}=\Omega_2$ and $y_{4,2}=\partial\Omega_2/\partial m$, and by integrating over a spheroidal shell located by two masses m_{k-1} and m_k, we obtain

$$\begin{aligned}
&\frac{1}{2}\left[\left(\zeta^2+10\frac{\Delta t}{R_\odot^2}\nu_{\mathrm{h}}\right)_k y_{3,2}^k+\left(\zeta^2+10\frac{\Delta t}{R_\odot^2}\nu_{\mathrm{h}}\right)_{k-1} y_{3,2}^{k-1}\right]\Delta m\\
=\;&\frac{1}{2}\left[\left(\zeta^2\overline{\Omega}_2\right)_k^t+\left(\zeta^2\overline{\Omega}_2\right)_{k-1}^t\right]\Delta m-\Delta t\Bigg[4\pi\frac{R_\odot^2}{M_\odot}\left(\rho\zeta_k^4 y_{3,0,k}y_{1,k}-\rho\zeta_{k-1}^4 y_{3,0,k-1}y_{1,k-1}\right)\\
&+\frac{20\pi}{6}\frac{R_\odot^2}{M_\odot}\Delta m\left\{\frac{\partial y_1}{\partial m}\left[\left(\rho\zeta^4 y_{3,0}\right)_k+\left(\rho\zeta^4 y_{3,0}\right)_{k-1}\right]+\left(\zeta^2\frac{\partial\rho\zeta^2}{\partial m}y_1y_{3,0}\right)_k+\left(\zeta^2\frac{\partial\rho\zeta^2}{\partial m}y_1y_{3,0}\right)_{k-1}\right\}\\
&+16\pi^2\frac{R_\odot^4}{M_\odot^2}\left(\rho_k^2\nu_{\mathrm{v}}^k\zeta_k^6y_{4,2,k}-\rho_{k-1}^2\nu_{\mathrm{v}}^{k-1}\zeta_{k-1}^6y_{4,2,k-1}\right)\Bigg].
\end{aligned} \tag{6.86}$$

And the new independent relations are:

$$\begin{cases}
E_5 &= \overline{K_{4,1}y_{3,2}}\Delta m-\overline{K_{4,2}}\Delta m+\Delta t\dfrac{R_\odot^2}{M_\odot}\Bigg[\left(K_{4,3}^kK_{4,4}^ky_{3,0}^ky_1^k-K_{4,3}^{k-1}K_{4,4}^{k-1}y_{3,0}^{k-1}y_1^{k-1}\right)\\
&\quad-\dfrac{5\Delta m}{3}\left(\dfrac{\partial y_1}{\partial m}\overline{K_{4,3}K_{4,4}y_{3,0}}+\overline{K_{4,4}K_{4,6}y_{3,0}y_1}\right)-\dfrac{R_\odot^2}{M_\odot}\left(K_{4,5}^kK_{4,3}^ky_{4,2}^k-K_{4,5}^{k-1}K_{4,3}^{k-1}y_{4,2}^{k-1}\right)\Bigg],\\
E_6 &= \overline{y_{4,2}}-\frac{\partial y_{3,2}}{\partial m}
\end{cases} \tag{6.87}$$

with

$$\begin{aligned}
K_{4,1}&=\zeta^2+10\frac{\Delta t}{R_\odot^2}\nu_{\mathrm{h}}, & K_{4,2}&=\zeta_t^2\overline{y_{4,2}}_t,\\
K_{4,3}&=4\pi\rho_k\zeta_k^2, & K_{4,4}&=\zeta_k^2,\\
K_{4,5}&=4\pi\rho_k\nu_{\mathrm{v}}\zeta_k^4, & K_{4,6}&=\frac{\partial K_{4,3}}{\partial m}.
\end{aligned} \tag{6.88}$$

The Jacobian is supplemented by these terms:

$$
\begin{aligned}
S_{5,1} &= \frac{\partial E_5}{\partial y_1^{k-1}} = \Delta t \frac{R_\odot^2}{M_\odot}\left[\frac{5}{3}\left(\overline{K_{4,3}K_{4,4}y_{3,0}} - \frac{\Delta m}{2}K_{4,4}^{k-1}K_{4,6}^{k-1}y_{3,0}^{k-1}\right) - K_{4,3}^{k-1}K_{4,4}^{k-1}y_{3,0}^{k-1}\right],\\
S_{5,2} &= \frac{\partial E_5}{\partial y_2^{k-1}} = 0,\\
S_{5,3} &= \frac{\partial E_5}{\partial y_{3,0}^{k-1}} = -\Delta t \frac{R_\odot^2}{M_\odot}\left[K_{4,3}^{k-1}K_{4,4}^{k-1}y_1^{k-1} + \frac{5\Delta m}{6}\left(\frac{\partial y_1}{\partial m}K_{4,3}^{k-1}K_{4,4}^{k-1} + K_{4,4}^{k-1}K_{4,6}^{k-1}y_1^{k-1}\right)\right],\\
S_{5,4} &= \frac{\partial E_5}{\partial y_{4,0}^{k-1}} = 0,\\
S_{5,5} &= \frac{\partial E_5}{\partial y_{3,2}^{k}} = K_{4,1}^{k-1}\frac{\Delta m}{2},\\
S_{5,6} &= \frac{\partial E_5}{\partial y_{4,2}^{k}} = \Delta t \frac{R_\odot^4}{M_\odot^2}K_{4,5}^{k-1}K_{4,3}^{k-1},\\
S_{5,7} &= \frac{\partial E_5}{\partial y_1^{k}} = \Delta t \frac{R_\odot^2}{M_\odot}\left[-\frac{5}{3}\left(\overline{K_{4,3}K_{4,4}y_{3,0}} + \frac{\Delta m}{2}K_{4,4}^{k}K_{4,6}^{k}y_{3,0}^{k}\right) + K_{4,3}^{k}K_{4,4}^{k}y_{3,0}^{k}\right],\\
S_{5,8} &= \frac{\partial E_5}{\partial y_2^{k}} = 0,\\
S_{5,9} &= \frac{\partial E_5}{\partial y_{3,0}^{k}} = \Delta t \frac{R_\odot^2}{M_\odot}\left[K_{4,3}^{k}K_{4,4}^{k}y_1^{k} - \frac{5\Delta m}{6}\left(\frac{\partial y_1}{\partial m}K_{4,3}^{k}K_{4,4}^{k} + K_{4,4}^{k}K_{4,6}^{k}y_1^{k}\right)\right],\\
S_{5,10} &= \frac{\partial E_5}{\partial y_{4,0}^{k}} = 0,\\
S_{5,11} &= \frac{\partial E_5}{\partial y_{3,2}^{k}} = K_{4,1}^{k}\frac{\Delta m}{2},\\
S_{5,12} &= \frac{\partial E_5}{\partial y_{4,2}^{k}} = -\Delta t \frac{R_\odot^4}{M_\odot^2}K_{4,5}^{k}K_{4,3}^{k},
\end{aligned}
\tag{6.89}
$$

and

$$
\begin{aligned}
S_{6,1} &= \frac{\partial E_6}{\partial y_1^{k-1}} = 0, & S_{6,7} &= \frac{\partial E_6}{\partial y_1^{k}} = 0,\\
S_{6,2} &= \frac{\partial E_6}{\partial y_2^{k-1}} = 0, & S_{6,8} &= \frac{\partial E_6}{\partial y_2^{k}} = 0,\\
S_{6,3} &= \frac{\partial E_6}{\partial y_{3,0}^{k-1}} = 0, & S_{6,9} &= \frac{\partial E_6}{\partial y_{3,0}^{k}} = 0,\\
S_{6,4} &= \frac{\partial E_6}{\partial y_{4,0}^{k-1}} = 0, & S_{6,10} &= \frac{\partial E_6}{\partial y_{4,0}^{k}} = 0,\\
S_{6,5} &= \frac{\partial E_6}{\partial y_{3,2}^{k}} = \frac{1}{\Delta m}, & S_{6,11} &= \frac{\partial E_6}{\partial y_{3,2}^{k}} = -\frac{1}{\Delta m},\\
S_{6,6} &= \frac{\partial E_6}{\partial y_{4,2}^{k}} = \frac{1}{2}, & S_{6,12} &= \frac{\partial E_6}{\partial y_{4,2}^{k}} = \frac{1}{2}.
\end{aligned}
\tag{6.90}
$$

If one takes into account the term Ω_2, the expression giving us an approximation for the fluctuation of the density Θ_2 should be modified accordingly. The expression given by Mathis

& Zahn (2004) is

$$\begin{aligned}\Theta_2 &= \frac{r}{\bar{g}_{\rm eff}}\left(\frac{r}{3}\frac{\partial\bar{\Omega}^2}{\partial r}+\frac{8r}{35}\frac{\partial\bar{\Omega}\Omega_2}{\partial r}+\frac{8}{7}\bar{\Omega}\Omega_2\right)\\ &= \frac{R_\odot^2}{M_\odot}\frac{\zeta}{\bar{g}_{\rm eff}}\left\{4\pi R_\odot^2\breve{\rho}\zeta^3\left[\frac{2}{3}\bar{\Omega}\frac{\partial\bar{\Omega}}{\partial m}+\frac{8}{35}\left(\Omega_2\frac{\partial\bar{\Omega}}{\partial m}+\bar{\Omega}\frac{\partial\Omega_2}{\partial m}\right)\right]+\frac{8M_\odot}{7R_\odot}\bar{\Omega}\Omega_2\right\}\\ &= \frac{4\pi R_\odot^4}{M_\odot}\frac{\breve{\rho}\zeta^4}{\bar{g}_{\rm eff}}\left[\frac{2}{3}y_{3,0}y_{4,0}+\frac{8}{35}\left(y_{3,2}y_{4,0}+y_{3,0}y_{4,2}\right)\right]+R_\odot\frac{\zeta}{\bar{g}_{\rm eff}}\frac{8}{7}y_{3,0}y_{3,2}.\end{aligned} \tag{6.91}$$

This modification impacts the expression of Ψ_2 which in turn makes the expression of U_2 and Υ_2 more complicated. Errors E_1 and E_2 as well as the respective Jacobian must take those changes into account. Nonetheless I will not write them in order not to over complicate the text. The relations needed to compute U_4, Ω_4 can also be formalized to be added to CESTAM and we may need to do so in a near future. However, the careful reader may have notice that such a task is painful.

Chapter 7

Validation, results and performances

[...]
LE DOCTEUR PARPALAID

Juste! Juste! *(On entend une explosion.)* Écoutez, mon cher confrère, comme le moteur part bien. A peine quelques tours de manivelle pour appeler les gaz, et tenez... une explosion... une autre... voilà! voilà!... Nous marchons.

[...]
JEAN, *à l'oreille du docteur Parpalaid.*

Monsieur, monsieur. Il y a quelque chose qui ne marche pas. Il faut que je démonte le tuyau d'essence.

Jules Romain, *Knock*

Contents

This chapter is devoted to the physical and numerical tests of the codes developed during my PhD. As seen in the previous chapter, the implementation is separated into two parts: the deformation module and the new prescription for the resolution of the transport of angular momentum. The advantage is that the deformation module can be used without describing the transport in two dimensions (however the contrary is not possible). This is why this chapter is separated into a test of the deformation module alone, then a test of the transport of angular momentum in the 2D geometry. The chapter is concluded by an evaluation of the additional computational cost that the 2D computations induce.

7.1 Validation of the deformation module

7.1.1 Conservation of mass and of angular momentum

The first thing we need to check is that the deformation does not introduce any change in the total mass or in the total angular momentum (AM) of the star. It must be recalled that, while the 2D treatment of AM transport only concerns the radiative zone, the deformation is applied to the entire star, even to the reconstructed atmosphere. In order to look at the conservation, we build a small grid of stellar models computed with various initial disk rotation conditions and with and without deformation for each model. The transport of AM and the computation of the meridional circulation are computed using the formalism of Talon et al. (1997)[1]. This formalism shared many similarities with the one of Mathis & Zahn (2004), however, the fluctuation of the gravitational acceleration are computed in a different way and radial derivatives of both Θ_2 and Λ_2 are present, instead of only Ψ_ℓ in the expression derived in Mathis & Zahn (2004) (see Sect. 7.2 for a more detailed description). This grid is described in more detail in Table 7.1.

Global effects of the deformation on evolution

The global parameters ($T_{\rm eff}$, $R_{\rm surf}(\theta_{\rm m})$, $\log L/L_\odot$, etc.) of the non-rotating 1D and 2D models are the same. This is of course a necessary condition for our code to be validated because we do not want the deformation module to introduce any deviation on the star's history if it is not deformed. On the contrary, global parameters of rotating stars slightly change between 1D/2D simulations. The differences are small, except on effective temperature. These higher variations are due to the fact that rotating stars cannot be in local radiative equilibrium over an isobar. This induces a change in the average effective temperature. The non-local radiative equilibrium of course does not impact the total luminosity that depends mainly on opacity. This rate is not affected much by the deformation, because of the small centrifugal force in the core.

[1] in the literature, this formalism is also often referred to as the formalism of Maeder & Zahn (1998)

Table 7.1: Small grid containing 24 models. Half of them are computed as usual in 1D and the other half are computed with deformation (even the ones without rotation). In both cases, the transport of angular momentum is computed using the formalism of Talon et al. (1997). The initial disk lifetime is 5 Myr for all models and there are no wind-induced loss of angular momentum. The 2D models use 240 angular sectors (without counting the ghost angles). The maximum degree $\ell_{\max}$ taken into account in the Legendre decomposition is $\ell_{\max} = 2$. The quantity X_c is the central hydrogen abundance. Angle θ_m is the critical colatitude. The $1M_\odot$ are stopped at Sun's age, however, these models have also been pushed slightly further, in the early stages of the sub-giant branch.

Model	M	$P_{\rm disk}$	Geom-	$t_{\rm final}$	$\Omega(t_{\rm final})$	X_c	$T_{\rm eff}$	$R_\star(\theta_m)$	$\log \frac{L}{L_\odot}$
	$[M_\odot]$	[d]	etry	[Gyr]	[% $\Omega_{\rm K,surf}$]	[%]	K	$[R_\odot]$	
M08P00G1D	0.8	∞	1D	15	0	0.233	5159	0.83	−0.36
M08P00G2D	0.8	∞	2D	15	0	0.233	5159	0.83	−0.36
M08P10G1D	0.8	10	1D	15	3.91	0.231	5161	0.83	−0.36
M08P10G2D	0.8	10	2D	15	3.91	0.231	5156	0.83	−0.36
M08P03G1D	0.8	3	1D	15	13.16	0.235	5139	0.83	−0.37
M08P03G2D	0.8	3	2D	15	13.90	0.239	5078	0.84	−0.37
M10P00G1D	1.0	∞	1D	4.57	0.00	0.384	5778	1.00	0.00
M10P00G2D	1.0	∞	2D	4.57	0.00	0.384	5778	1.00	0.00
M10P10G1D	1.0	10	1D	4.57	5.82	0.382	5777	1.00	0.00
M10P10G2D	1.0	10	2D	4.57	5.46	0.382	5771	1.00	0.00
M10P03G1D	1.0	3	1D	4.57	21.77	0.386	5746	1.00	−0.01
M10P03G2D	1.0	3	2D	4.57	19.59	0.388	5664	1.03	−0.01
M15P00G1D	1.5	∞	1D	1	0	0.483	7192	1.58	0.78
M15P00G2D	1.5	∞	2D	1	0	0.483	7192	1.58	0.78
M15P10G1D	1.5	10	1D	1	14.49	0.487	7179	1.58	0.77
M15P10G2D	1.5	10	2D	1	14.47	0.483	7168	1.58	0.77
M15P03G1D	1.5	3	1D	1	46.71	0.491	7027	1.64	0.77
M15P03G2D	1.5	3	2D	1	46.62	0.491	6980	1.65	0.76
M20P00G1D	2.0	∞	1D	0.5	0	0.449	8775	1.91	1.29
M20P00G2D	2.0	∞	2D	0.5	0	0.449	8775	1.91	1.29
M20P10G1D	2.0	10	1D	0.5	26.93	0.452	8723	1.93	1.29
M20P10G2D	2.0	10	2D	0.5	26.83	0.454	8705	1.94	1.29
M20P03G1D	2.0	3	1D	0.5	69.79	0.462	8437	2.04	1.28
M20P03G2D	2.0	3	2D	0.5	69.96	0.474	8328	2.05	1.26

Evolutionary tracks in an HR diagram are displayed for both 1D and 2D models in Fig. 7.1, top left panel. Non-rotating models and models rotating with an initial period of 10 days follow barely indistinguishable paths. At their final age, they reach an effective temperature separated by a few tens of Kelvins. This difference is almost not measurable (at least without Gaia, Perryman et al. 2001; Turon et al. 2005; Lindegren et al. 2008). On the other side, the models with an initial period of 3 days reach a surface rotation at their final age around 3 to 4 times faster than the ones with $P_{\rm disk} = 10$ days. Compared with the non rotating models, their effective temperature is shifted by ~ 80 K for the $0.8M_\odot$ models to ~ 350 K for the $2M_\odot$ models. Between 1D and 2D models, this difference goes from ~ 60 K for the $0.8M_\odot$ models to ~ 110 K for the $2M_\odot$ models. Those differences are measurable, even without Gaia, and they could change further if more complex physics (like overshoot) were to be taken into account.

Figure 7.2 shows a meridional cut of the 2D models of Table 7.1. The first column gathers the non-rotating 2D models. The colour scale represents the density profile inside the star. In

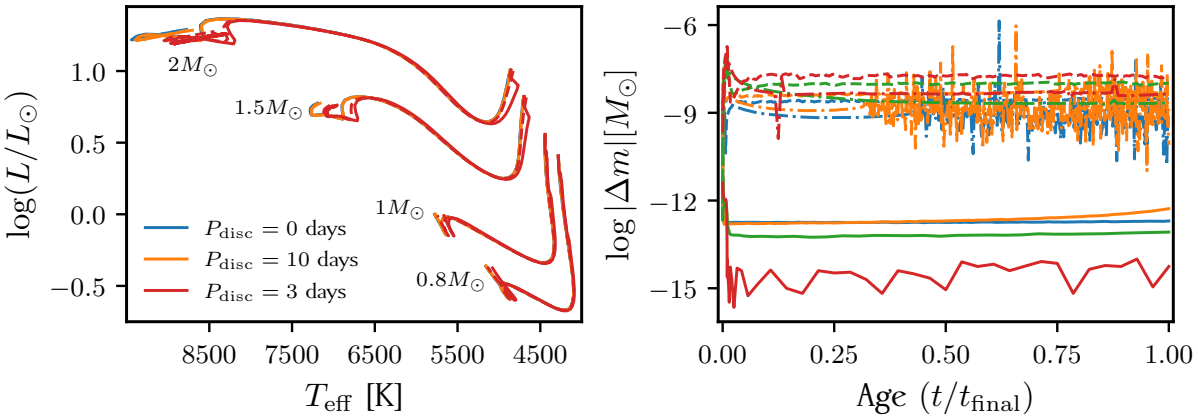

Figure 7.1: The models are the ones presented in Table 7.1. *Left:* HR diagram of all models. *Right:* Numerical mass loss at the end of each deformation and before correction as a function of the stellar age normalized to final age. Non rotating models ($P_{\rm disk} = \infty$ days) are represented with solid lines,$P_{\rm disk} = 10$ with dotted-dashed lines and $P_{\rm disk} = 3$ days with dashed lines. $0.8M_\odot$ are in blue, $1M_\odot$ in orange, $1.5M_\odot$ in green and $2M_\odot$ in red.

the two other columns, the colour scale codes for $\rho(p,\theta)/\overline{\rho} - 1$ on the left side and for $\overline{\Omega}$ in percent of $\Omega_{\rm K,surf}$ on the right side. We see, by looking at the first column, that the stars mean density decreases with increasing stellar mass. Indeed, higher mass stars are more efficient in producing nuclear energy. The hotter material induces a stronger pressure gradient opposed to the gravity and the radius of the star is larger.

In Fig. 7.2, the axes limits go from -1 to 1, in unit of the equatorial radius. The axes aspect ratio is the same, therefore, the deformation that we see in the plots is due to the true deformation, not a graphical artefact. The deformation is barely noticeable for the 2nd column models ($P_{\rm disk} = 10$ days) but is striking for the last one ($P_{\rm disk} = 3$ days). The convective zones are modelled with a uniform rotation profile and no wind-braking is included. Since $\overline{\Omega}$ is uniform in convective zones, the density is constant over isobars, as stated by Eqs. (2.43) and (2.48). The limits of the convective/radiative zones are therefore visible in the profile of the fluctuations of density and produce a large circle at around $0.7R_{\rm eq}$. An other circle is visible is the $\rho(p,\theta)/\overline{\rho} - 1$ profiles of the low mass models. This circle is not due to a central convection zone because those models do not have one, but to a region of steeper $\overline{\Omega}$ gradient. The angular velocity profile retrieved by the 1D computation of the AM profile produces a quite noisy pattern in the $\overline{\Omega}$ radial derivative. This induces large and very localized variations of density fluctuation.

Finally, we see that, for almost all the rotating models, density is higher near the equator than near the pole. The latitudinal variations of ρ are described by Eq. (2.48):

$$\frac{\mathrm{d}\rho}{\mathrm{d}\theta} = -\rho \frac{\frac{\partial}{\partial r}\left(\Omega^2 r^2 \sin\theta\cos\theta\right) - \frac{\partial}{\partial\theta}\left(\Omega^2 r \sin^2\theta\right)}{\frac{\partial\phi}{\partial r} - \Omega^2 r \sin^2\theta}. \tag{7.1}$$

Since the angular velocity profile, in general, decreases with radius, the first derivative in the numerator is negative. We have assumed a shellular rotation profile, therefore the θ-derivative is zero, and the whole numerator is negative. The denominator is a local break-up velocity criterion. It is also positive, otherwise we would have reached the breakup velocity and stopped the evolution. Hence, generally, $\mathrm{d}\rho/\mathrm{d}\theta$ is positive and ρ increases from pole to equator. However, we remark that the last two models of the 3rd column ($P_{\rm disk} = 3$ days and $1.5M_\odot$ or

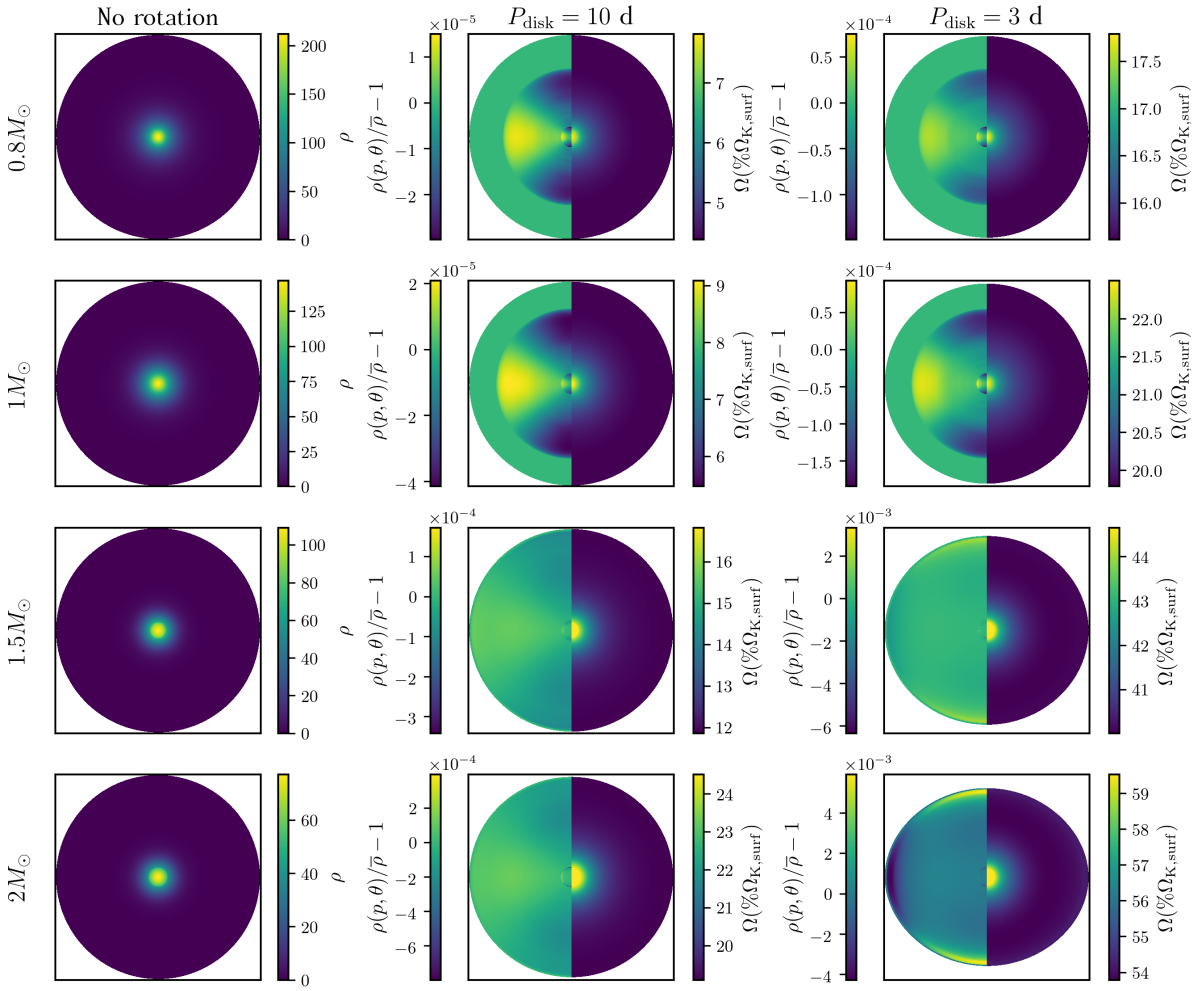

Figure 7.2: Meridional cut of the 2D models of Table 7.1. Aspect ratio between the two is the axes is the same. Each row corresponds to a given mass: $0.8M_\odot$ (1$^{\rm st}$), $1M_\odot$ (2$^{\rm nd}$), $1.5M_\odot$ (3$^{\rm rd}$) and $2M_\odot$ (4$^{\rm th}$). Each column corresponds to an initial rotation period: non-rotting ($P_{\rm disk}=\infty$ days; 1$^{\rm st}$), $P_{\rm disk}=10$ days (2$^{\rm nd}$) $P_{\rm disk}=3$ days (3$^{\rm rd}$). On the 1$^{\rm st}$ column, only the density profile is represented because the angular velocity is null. For the two other columns, the left part of the 2D map represents $\rho(p,\theta)/\overline{\rho}-1$ and the other half represents the angular velocity profile (Ω depending only on p) in units of $\Omega_{\rm K,surf}$.

$2M_\odot$), the density is higher near the poles. It indicates that, in the region close to the surface, the angular velocity profile is an increasing function of the radius.

Mass conservation

Let us focus now on mass conservation. Concern has been raised in Chapter 2 that the deformation method could lead to a non-negligible numerical mass loss along the evolution. In the following, we denote $\Delta m_{\rm num}$ the numerical mass loss induced by the deformation. Roxburgh (2006) reported a $\Delta m_{\rm num}$ of order $10^{-5}M_\star$ which is quite high. Indeed, an evolution consisting of a thousand time steps would lead to a change of 1% of the total mass. Fig. 7.1, top right panel shows $\Delta m_{\rm num}$ in units of solar mass that the models of Table 7.1 experienced after each deformation. The abscissa is the stellar age normalized to the final age of the model. Our code displays much better results than what Roxburgh (2006) obtained. The non-rotating models have a $\Delta m_{\rm num}$ of order $10^{-13}-10^{-16}M_\odot$ while the rotating ones have losses of order

$10^{-8} - 10^{-11} M_{\odot}$. Quite interestingly for us, this rate does not vary much with rotation speed. The noisy pattern is due to the $\Delta m_{\rm num}$ changing sign. The logarithmic of the absolute value of $\Delta m_{\rm num}$ introduces the noisy pattern. It is not very clear what are the cause of such better performances for our code. Our number of grid point in the radial and latitudinal directions are similar to what Roxburgh (2006) used. Although they may be located at different positions. Another possible explanation would be that we used higher floating point precision.

In his work, Roxburgh (2006) proposed to correct $\Delta m_{\rm num}$ by a multiplicative factor on the density. It implicitly assumes that numerical artefacts introduced in the density distribution should be corrected by the same factor everywhere in the star. This solution raises some questions. The centrifugal acceleration is, in general, stronger at the surface than at the centre. Thus, the unphysical changes to the density distribution induced by the deformation should be stronger at the surface than at the centre. Moreover, the density is higher by several orders of magnitude in the centre than at the surface. Therefore, correcting the density by the same factor everywhere would lead to a numerical concentration of mass at the centre. At each time step, the deformation module implemented by Roxburgh (2006) redistributes $10^{-5} M_{\star}$ in the star, preferentially in the inner regions. In CESTAM, we use the same method of correction, however, our $\Delta m_{\rm num}$ is at most $10^{-7} - 10^{-8} M_{\odot}$ which significantly diminishes the issue. A last point that we must address in the future would be to verify that the new density profile still satisfy the EOS.

Angular momentum conservation

The first row of plots in Fig. 7.3, displays the relative variations of AM with respect to the AM at final time step. These variations are shown on the left column for 2D models and on the right for 1D models. We did not include in Fig. 7.3 the initial phase where the models are coupled to a disk (first 5 Myr). The disk induces a loss of AM that is physically motivated, contrary to possible numerical losses of AM that we are trying to find. In both panels, we see that the maximum variation of AM over a complete evolution is at most 10^{-3} for the fastest rotating, and lowest mass models, which is very good. The variations of AM are noisier in the 1D models (right) than in the 2D ones (left). This may be a side effect of a better description of the effect of rotation on the structure: it stabilizes the numerical schemes and smooths the evolution of the solutions in time. The second row displays the relative variations of AM between two consecutive time steps. The relative variation is at most 10^{-5} and goes to 10^{-9}. We find again a noisier pattern in the 1D models. As a whole, either for the total or the "instantaneous" relative variations, 1D and 2D models show very similar results. It supports the fact that the deformation module does not introduce significant numerical artefacts in the conservation of AM.

7.1.2 Seismic comparison

The comparison we performed above could have revealed the most important problems of the deformation module. But for a deeper study, one needs to perform a seismic comparison of deformed and non-deformed models. In order to do so, I used the non-perturbative two-dimensional oscillation code ACOR for which I developed an interface with the 2D version of CESTAM. In order to understand this section, I need to give some general insight on 2D non-perturbative oscillation codes and explain the pre-processing that ACOR performs on input files generated by CESTAM.

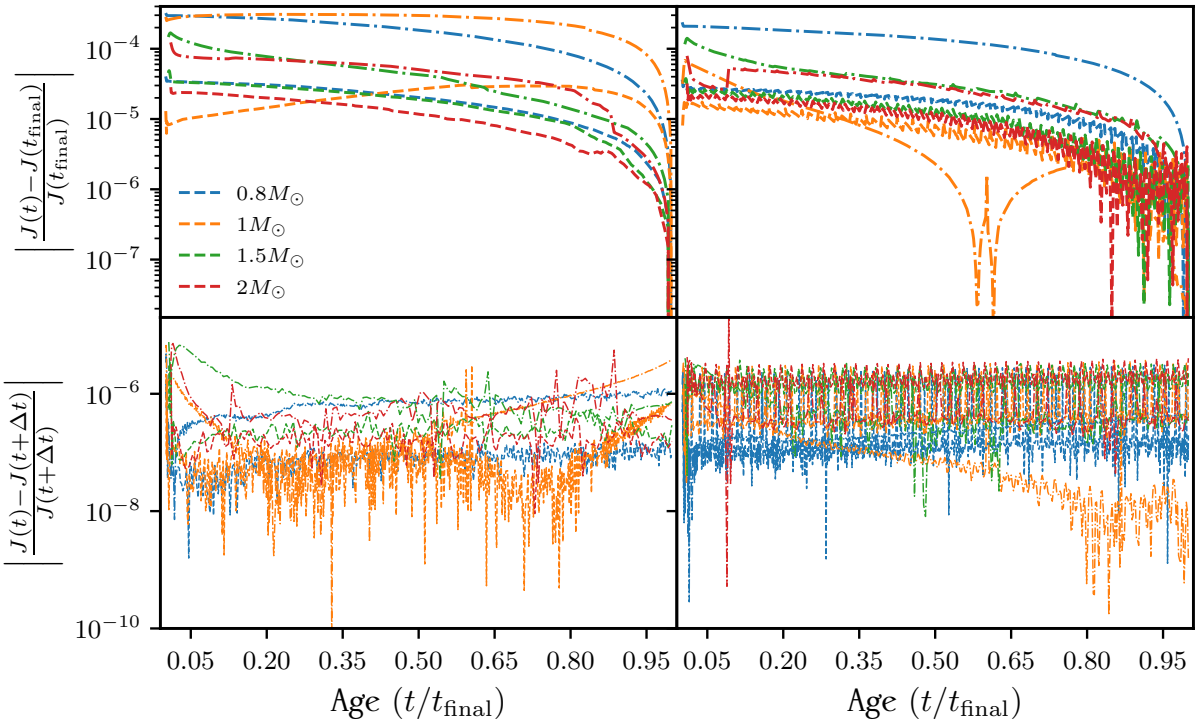

Figure 7.3: The models are the ones presented in Table 7.1. For all panels, the quantities are plotted as a function of the stellar age normalized to final age. The colours code for the mass of the models. Models with $P_{\rm disk} = 10$ with dotted-dashed lines and $P_{\rm disk} = 3$ days with dashed lines. The total angular momentum of the star is $J = \int_0^{R_\star} r^2 \Omega {\rm d}m$. Refer to Table 7.1 for more detail on the initial conditions. *Top left:* Absolute value of the relative variations between angular momentum at time t to angular momentum at $t_{\rm final}$, in 2D models. *Top right:* Same as in top left panel but with 1D models. *Bottom left:* Absolute value of the relative variations between angular momentum at time t to angular momentum at $t + \Delta t$, in 2D models. *Bottom right:* Same as in bottom left panel but with 1D models.

2D non-perturbative oscillation codes

Rotation can act in two ways on the oscillations of rotating stars. The Coriolis force modifies the motions of the waves while the centrifugal force deforms the star and therefore distorts the propagation cavity. Numerical 2D oscillation codes have been created to account for these effects without having to resort to perturbative methods. Basically, they can be considered as solvers of oscillation Eqs. (3.13) to (3.16). The main 2D oscillation codes are TOP (Two-dimensional Oscillation Program; Reese et al. 2006) and ACOR (Adiabatic Code of Oscillation including Rotation; Ouazzani et al. 2012). They work on a similar coordinate system and with the same surface conditions. However, the central boundary conditions differ and they implement different numerical schemes to solve their equations. ACOR relies on finite different schemes while TOP was originally developed to use a spectral method by decomposing the radial coefficients on Tchebyshev polynomials. It now also implement finite different schemes. This last approach is particularly adapted to polytropic models[2] where the structural quan-

[2]Polytropic models are models in which the pressure is described by a law of the form

$$p = K\rho^\gamma, \tag{7.2}$$

with K called the polytropic constant, $\gamma = 1 + 1/\mu$ is the polytropic exponent and μ (an integer) is the polytropic index.

tities vary smoothly. It may be less appropriate when strong gradients, not captured by the polytropic model, are present. However, to my knowledge, no deep comparisons of TOP and ACOR have been performed on such models.

Those codes have allowed asteroseismologists to distinguish several classes of modes, largely based on the graphical representation of their amplitudes and on ray dynamics. It shall be stressed that, while those distinctions suggest that the different classes of modes form strictly separate entities, the transition between two classes may not be as sharp as it seems. Some modes could display features from two different classes.

Classification of rotating stars' modes of oscillation

Modes can be classified using ray tracing methods. A ray is defined as the trajectory tangent to the group velocity $\mathbf{c}_\mathrm{g}$. It applies in the asymptotic limit, *i.e.* high frequencies, and is very similar to the study of geometrical paths in a medium of varying optical index. The study of orbits in a Poincaré section helps to differentiate the modes.

Pressure modes Let us start by p-modes. Three classes have been identified.

- Island modes (see Fig. 7.4, left panel). The modes of this class can be identified using modified quantum numbers. This feature is very important because mode identification is primordial if we want to use the individual frequencies in order to constrain models. The modified quantum numbers $(\widetilde{n}, \widetilde{\ell})$ are defined as follow

$$\widetilde{n} = 2n + \varepsilon \qquad \text{and} \qquad \widetilde{\ell} = \frac{\ell - |m| - \varepsilon}{2} \qquad \text{with} \qquad \varepsilon = (l + m)(\mathrm{mod}\ 2). \tag{7.3}$$

  They correspond to the number of nodes along the lines drawn in the left panel of Fig. 7.4. The modified quantum numbers allowed Lignières et al. (2006) to re-express the asymptotic relation of p-modes in the case of slow-rotating stars. By defining $\Delta_n = \omega_{n+1,\ell m} - \omega_{n\ell m}$, $\Delta_\ell = \omega_{n,\ell+1,m} - \omega_{n\ell m}$ and $\Delta_m = \omega_{n,\ell,m+1} - \omega_{n\ell m}$, Eq. (3.50) becomes

$$\omega_{n\ell m} = n\Delta_n + \ell\Delta_\ell + |m|\Delta_m + \alpha^\pm, \tag{7.4}$$

  with $\alpha^\pm$ an additional constant that depends on the stellar-structure. The term α^+ is used for modes symmetric with respect to the equatorial plane ($\ell + m$ even) and α^- is used for modes antisymmetric with respect to it ($\ell + m$ odd). Studying the ray dynamics, Lignières & Georgeot (2009) found physically-grounded expressions of those quantities. For island modes in fast rotating stars, this formulation of the asymptotic relation keeps its form, provided some modifications are made:

$$\omega_{n\ell m} = \widetilde{n}\widetilde{\Delta}_n + \widetilde{\ell}\widetilde{\Delta}_\ell + |\widetilde{m}|\widetilde{\Delta}_m + \widetilde{\alpha}^\pm, \tag{7.5}$$

  where $\widetilde{\Delta}_n = \Delta_n/2$, $\widetilde{\Delta}_\ell = 2\Delta_\ell$, $\widetilde{\Delta}_m = \Delta_\ell + \Delta_m$, $\widetilde{\alpha}^+ = \alpha^+$ and $\widetilde{\alpha}^- = \alpha^- + \Delta_\ell - \Delta_n/2$. In the the Poincaré section, Island modes are form periodic orbits, as the one shown in Fig. 7.5, left panel. All the reflections of a ray are together in a limited region and periodically overlap.

- Chaotic modes (see Fig. 7.4, middle panel). Chaotic modes may occupy a very large fraction of the Poincaré section, depending on the rotation rate. The ray tracing in Fig. 7.5, middle panel, show trajectories that never overlap. It does not mean that the kinetic energy distribution of the mode is homogeneous: the rays are more concentrated in some regions which translates into regions of more concentrated kinetic energy. It is also important to notice that these modes can propagate to the centre of the star, as opposed to p-modes in non-rotating stars.

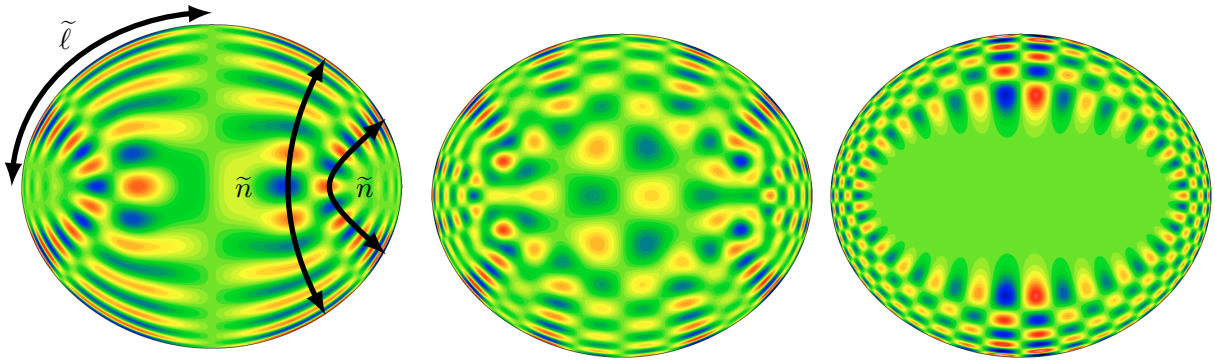

Figure 7.4: Spatial distributions in the meridional plane of the kinetic energy of p-modes in a $25M_\odot$ polytropic stellar model ($\mu = 3$), rotating at $0.6\Omega_\mathrm{K}$. *Left:* Island mode. *middle:* Chaotic mode. *Right:* Whispering gallery mode. Credits: Reese et al. (2009).

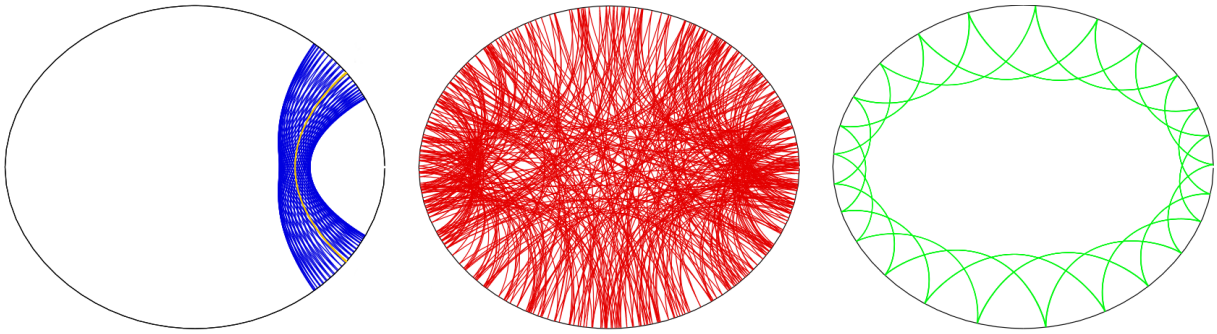

Figure 7.5: Ray dynamics in the meridional plane of p-modes in a polytropic stellar model, rotating at $0.59\Omega_\mathrm{K}$. *Left:* Island mode. *middle:* Chaotic mode. *Right:* Whispering gallery mode. Credits: Lignières & Georgeot (2008).

- Whispering gallery modes (see Fig. 7.4, right panel). Finally, whispering gallery modes are the ones that resemble the most the p-modes in non-rotating stars. We see in the figure that the kinetic energy stays in the envelope and does not propagate toward the centre. Their corresponding ray trajectories revolve around the centre, in a limited surface region. Whispering gallery modes also display regular patterns. These modes can also be described using quantum numbers, probably the same as in the non-rotating case.

As the angular velocity, and therefore the distortion, increases, the amplitudes of whispering gallery and island modes may become less and less important. When observed as a point, the surface averaging effect make them difficult to detect and therefore the oscillation spectra are very complicated to interpret.

Gravito-inertial modes In rotating stars, the Coriolis force must be taken into account in the case of g-modes. To be precise, these modes should not rigorously be called gravity modes any more but *gravito-inertial modes*[3] (GI modes). This denomination stresses the fact that, not only the buoyancy is a restoring force, but also the Coriolis force. Let us consider a mode with displacement of the form $\boldsymbol{\xi} \propto \exp(i(\mathbf{k}\cdot\mathbf{r} - \omega t))$, with a short wavelength and low frequency. Unno et al. (1989) give the dispersion relation

$$\omega^2 \simeq \frac{N^2 k_\mathrm{h}^2 - (2\boldsymbol{\Omega}\cdot\mathbf{k})^2}{\mathbf{k}^2}. \tag{7.6}$$

[3]Not to be confuse with internal gravity waves.

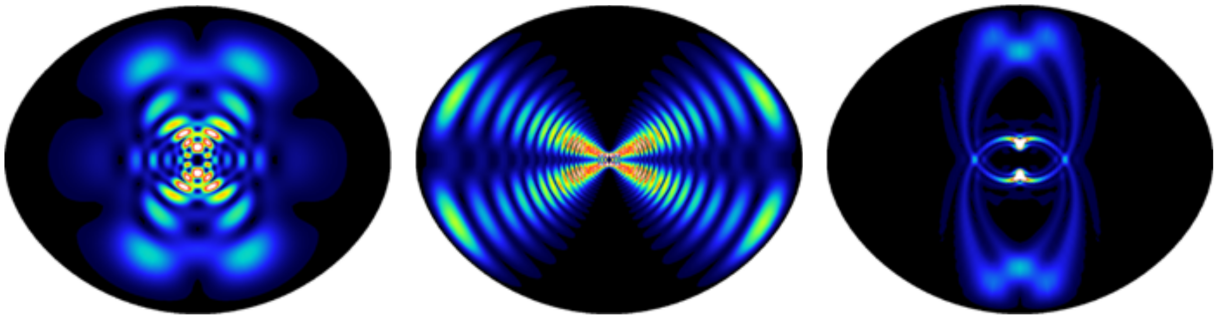

Figure 7.6: Spatial distribution in a meridional plane of the kinetic energy of g-modes in a $25M_\odot$ polytropic stellar model ($\mu = 3$), rotating at $0.7\Omega_\mathrm{K}$. *Left:* Mode in the super-inertial domain ($\omega > 2\overline{\Omega}$). *middle:* Mode in the sub-inertial domain ($\omega < 2\overline{\Omega}$). *Right:* Special case of super-inertial mode called rosette mode. Credits: Ballot et al. (2013).

If in addition $\omega, \overline{\Omega} \ll N$, the above equation needs $k_\mathrm{h} \ll |\mathbf{k}|$ to be valid. If we furthermore assume that the medium is nearly incompressible, then $\boldsymbol{\nabla} \cdot \mathbf{u} \simeq 0$, with $\mathbf{u} = \partial\boldsymbol{\xi}/\partial t$ the wave velocity field. It follows from this condition that $\mathbf{k}\cdot\boldsymbol{\xi} = k_r\xi_r + k_\mathrm{h}\xi_\mathrm{h} \simeq 0$, yielding $\xi_r/\xi_\mathrm{h} \simeq -k_\mathrm{h}/k_r$. Since $k_\mathrm{h} \ll k_r$, we have $\xi_r \ll \xi_\mathrm{h}$. We see that GI modes propagate almost horizontally, *i.e.* perpendicular to $\mathbf{k}$. These trajectories are spirals converging toward the centre. GI modes can be separated into categories.

- The sub-inertial modes with $\omega < 2\overline{\Omega}$ (see Fig. 7.6, middle panel). These modes do not change a lot compared with their equivalent in non-rotating stars. The most striking difference is the appearance of a forbidden region in which the modes do not propagate. The condition of propagation is formalized as (Dintrans & Rieutord, 2000)

$$\omega^2 N^2 r^2 \sin^2\theta + (f^2 - \omega^2)(\omega^2 r^2 - N^2 r^2 \cos^2\theta) \geq 0, \tag{7.7}$$

  with θ the colatitude and $f = 2\overline{\Omega}$. With the approximation that $N \gg \omega, f$, the criterion on the limiting angle is $|\cos\theta| \leq \omega/f$.

- The super-inertial modes with $\omega > 2\overline{\Omega}$ (see Fig. 7.6, left and right panels). The mode on the left panel has almost the same characteristics as the mode with same quantum numbers in a similar non-rotating star. On the contrary, some super-inertial modes (right panel) experience dramatic changes in the shape of their eigenfunctions compared with the non-rotating case. These modes are called *rosette modes*. These modes have been discovered in numerical simulations by (Ballot et al., 2012) and they appear even at low rotation rates. The physical nature of rosette modes have been thoroughly studied by Takata & Saio (2013); Saio & Takata (2014); Takata (2014). These authors have shown that rosette modes are formed from the combination of modes that have quasi-degenerate frequency in a non-rotating star and provided some conditions on their order n and degree ℓ are met. In such cases, the Coriolis acceleration can overcome the frequency gaps between the modes and makes the interactions sufficiently strong to build rosette modes.

ACOR pre-processing

In order to be able to perform a seismic study of my 2D models, I had to interface ACOR with CESTAM. ACOR was already able to read outputs from various stellar evolution codes, especially 1D outputs of CESTAM. To use it on 2D models, I had to create a new output format specially designed for ACOR's needs. The two kinds of output that CESTAM can write are the following:

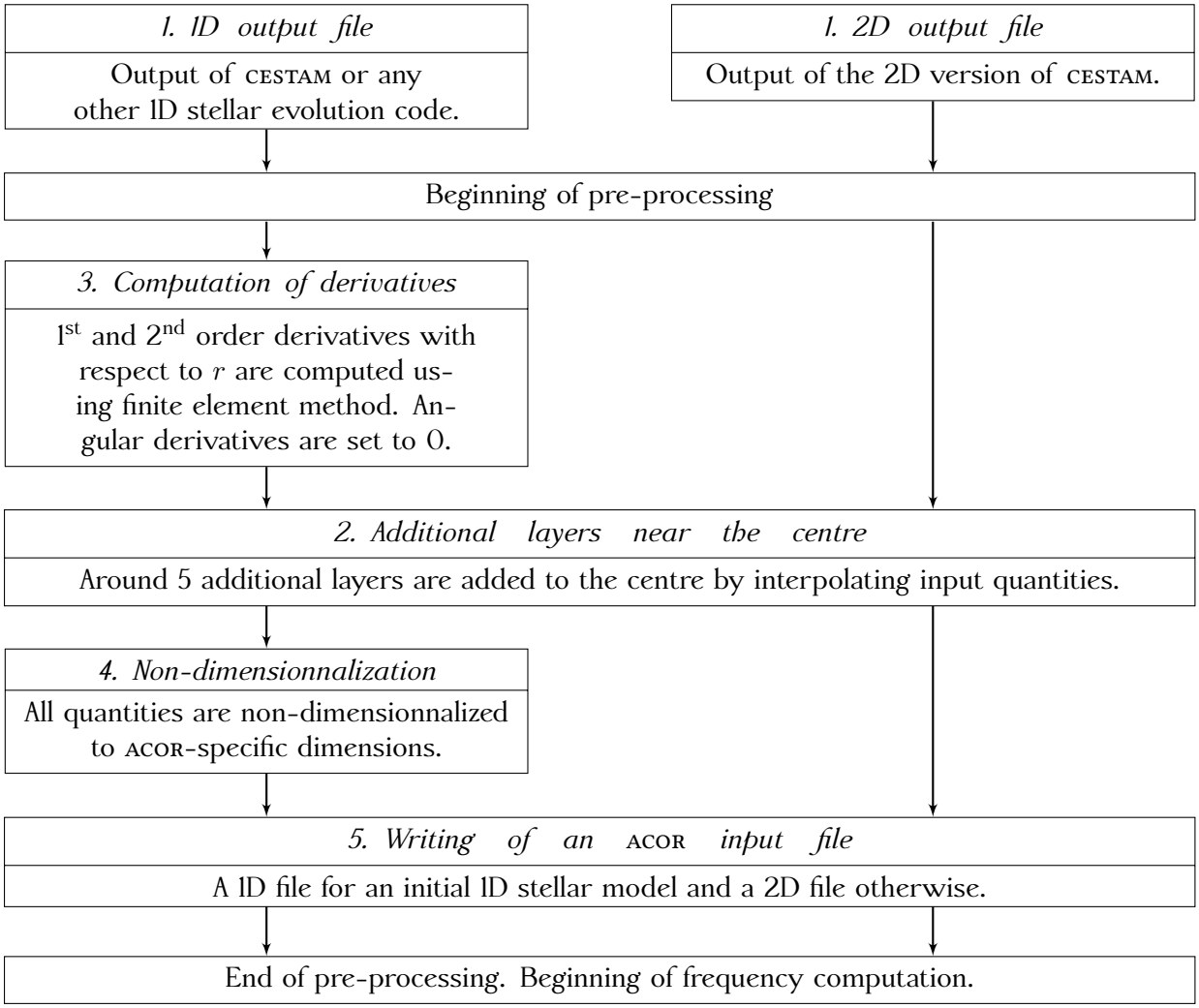

Figure 7.7: Schematic pre-processing performed by ACOR.

- `.osc` files: These files are written for 1D computation of oscillations. It contains a lot of different quantities: the radius, the pressure, the temperature, the density, the angular velocity, as well as thermodynamics quantities and derivatives. Not all data are used by ACOR. In particular, it does not contain their radial derivatives. Therefore, they must be computed internally by ACOR using finite difference schemes.

- `.osc2d` files: These files are designed to fit ACOR's needs for 2D computations. Therefore, it does not contains the same variables as the `.osc` files but only the following fields: the radii of isobars, pressure, density, Γ_1, $\overline{\Omega}$; their respective 1st and 2nd radial derivatives. One also have the derivative of some quantities with respect to $\zeta = r(\theta_{\rm m})$, and the 1st and 2nd order derivatives with respect to $\cos\theta$. The radial derivatives are computed thanks to the B-Spline representation provided by CESTAM. The only special case is for the first radial derivative of the pressure which is computed using Eq. (6.22). This last point is important because it may introduce discrepancies in the comparison of 1D and 2D frequencies. The computation of the $\cos\theta$-derivatives are made easier by the decomposition in Legendre polynomials. The derivatives of P_ℓ are analytical and we do not need to use a numerical approximation. All the quantities written in `.osc2d` files

are actually normalized to ACOR normalization coefficients that will be described later.

When a 2D CESTAM model is computed, we can choose to output, in addition to the `.osc2d` file, the 1D structure written in a `.osc` file. This structure is exactly the same as the one before the deformation, and along $\theta_{\rm m}$. If the input file given to ACOR is not specially designed for it (it is generally the case for 1D inputs), ACOR needs to perform some pre-processing. The pre-processing steps are summarized in Fig. 7.7. First, the various derivatives need to be computed. They are approximated using a $2^{\rm nd}$ order finite difference method. This point is important because it can introduce differences between the derivatives computed internally to CESTAM (with B-Splines) or internally to ACOR (with a finite difference method). Computing derivatives with B-Spline is more complex, computationally speaking, but gives a more precise estimation of the derivatives. This difference of method can be a source of discrepancies between the frequencies computed using a 1D or 2D model as input. We will come back to it later.

The next step of the pre-processing is to improve the quality of the boundary conditions. To do so, in the centre, ACOR adds a few layers (usually 5). The values of the various fields are interpolated at those points using parabolas. This treatment applies for 1D *and* 2D inputs. The last step is the normalization of the various quantities. The quantities r, p, ρ and $\overline{\Omega}$ are replaced by

$$\widetilde{r} = \frac{r}{R_{\rm eq}} \qquad \widetilde{p} = p \times p_\dagger \qquad \widetilde{\rho} = \rho \times \rho_\dagger \qquad \Omega = \frac{\overline{\Omega}}{\Omega_{\rm K}} \tag{7.8}$$

where $R_{\rm eq}$ is the equatorial radius, including the atmosphere, $\Omega_{\rm K}$ is the Keplerian break-up velocity and

$$p_\dagger = \frac{4\pi R_{\rm eq}^4}{\mathcal{G} M_\star^2} \qquad \rho_\dagger = \frac{4\pi R_{\rm eq}^3}{M_\star} \tag{7.9}$$

One of the goals of the normalization is to reduce the value of the floats that will be represented in memory, which increases the precision. After the normalization, a new file is created. This file is called an ACOR *input file* and contains data ready to be digested by ACOR. Before starting the seismic studies of the 2D version of CESTAM, it must be noted that this study may also reveal some imperfections of ACOR itself.

To be certain that we are only investigating the numerical effects of the deformation module on the frequencies, we only studied non-rotating models. In this case, frequencies are, of course, not affected by differences in the angular velocity. We ensure that, in the ACOR input files, Ω, $\partial\Omega/\partial r$, $\partial\Omega/\partial\cos\theta$ were indeed exactly 0. ACOR input files are basic ASCII files. Therefore, they are easy to modify after ACOR's preprocessing if one wants to check the influence or a certain quantity or of certain numerical treatment used to produce these quantities. In particular, we have already seen that the method used to computed the derivatives is not the same for 2D and 1D computations. It can be seen as a post-pre-processing. Therefore, we studied frequencies obtained with four kinds of ACOR input files.

- A 1D ACOR input file (hereafter called input 1) generated from an `.osc` file, following the procedure detailed above (normal pre-processing);
- A 2D ACOR input file (hereafter called input 2) generated from an `.osc2d` file, following the procedure detailed above (normal pre-processing);
- A synthetic 1D ACOR input file (hereafter called input 3) build using the data at $\theta_{\rm m}$ in an `.osc2d` file. Such files allow us to test if the structure in the `.osc2d` file is truly spherical;

- A synthetic 1D ACOR input file (hereafter called input 4) build using an input 1 file in which we replaced the derivatives computed using the finite element method by the one taken from the `.osc2d` file, computed using B-Splines. Such a file allows us to test the influence of the method used to compute derivatives.

Results of the seismic comparison

We performed a seismic comparison of the frequencies computed for the four kinds of input described above, for non-rotating models with four different masses: $0.8M_\odot$, $1M_\odot$, $1.5M_\odot$ and $2M_\odot$. These models are the non-rotating models described in Table. 7.1. The results are displayed in Figs. 7.8, 7.9 and 7.10. The top panel of each figure displays the frequency differences $\delta\nu$ obtained between the different inputs. The radial order n goes from $n = 1$ to $n \simeq 20 - 30$. We focused only on radial modes ($\ell = 0$) the advantage is that they propagate in the entire star. Therefore, their frequency is sensitive to changes in the structure anywhere in the star. The middle panel displays a quantity A with variations similar to the Brunt-Väisälä frequency $N^2 = \mathbf{g}_{\rm eff} \cdot \mathbf{A}$ (although it has the dimensions of an inverse distance). In the middle panel, only the profile of A extracted from inputs 1 and 2 are represented. The bottom panel represents the relative differences between these two profiles.

In the top panel, the differences $\delta\nu^{1,2}$ between inputs 1 and 2 are represented as blue dots. Figures 7.8 and 7.9 show the better results: $\delta\nu^{1,2} \simeq 0.4$ µHz, which is around 4 times above the frequency resolution of CoRoT and *Kepler*. PLATO's requirement is to reach a resolution of 0.2 µHz. This is good without being excellent. Indeed, observed rotational splittings are of order 0.1 µHz (Deheuvels et al., 2012). For all other models, the frequency differences are higher. Do these differences comes from the deformation module or from the pre-processing of ACOR? The first possible explanation is that, the deformation module, even when the model is not rotating, introduces some very small asphericities, of the order of the numerical precision. This hypothesis can be tested by comparing input 2 with input 3. Input 3 is created to mimic a perfect sphere, even after the pre-processing. The frequency differences $\delta\nu^{3,2}$ are exactly 0 for all masses, at all frequencies, which rules out this first possibility. A second explanation would be that the derivatives computed using finite difference method are too far from the one computed from B-Splines. To test this idea, we compare input 4 and input 2. Input 4 is exactly the same as input 1, except that all the finite difference derivatives have been replaced by the one computed using B-Splines. The differences $\delta\nu^{4,2}$ is represented as green points and are strongly improved compared with $\delta\nu^{1,2}$. For models with $0.8M_\odot$, $1M_\odot$ and $1.5M_\odot$, the $\delta\nu^{4,2}$ is well below the space mission's frequency resolution. The one computed for the $2M_\odot$ model, which was not that bad, have been slightly improved by few tens of nHz. However, in this last case, $\delta\nu^{4,2}$ remains too high. One could think that this has something to do with the mass of the model. Yet, we performed the same analysis on an other $1M_\odot$ model but with an age of 11 Gyr (the one in Fig. 7.9 has an age of 4570 Myr). This model is at the beginning of the sub-giant phase. We see that near the centre, $|A|$ presents a sharper peak than in the $1M_\odot$ MS model of Fig. 7.9. This peak (or glitch) is not as sharp as in the $1.5M_\odot$ or $2M_\odot$ model but is still significant. It betrays the presence of a large gradient of mean molecular weight due to the exhaustion of hydrogen in the core. This model has $\delta\nu^{1,2} \simeq 0.8$ µHz and this bad result is not improved for $\delta\nu^{4,2}$. The presence of a peak in the profile of a certain quantity often leads to into errors in the numerical computation of the derivatives. This aspect should be studied in more detail in order to find the cause of such high frequency differences.

To that end, we compared in more detail the structural profiles written in inputs 1 and 2. Figure 7.11 displays on the first row the relative differences $\eta(p)$ and $\eta(\rho)$ of the pressure and density between the profiles written in inputs 1 and 2, for all four models. The relative

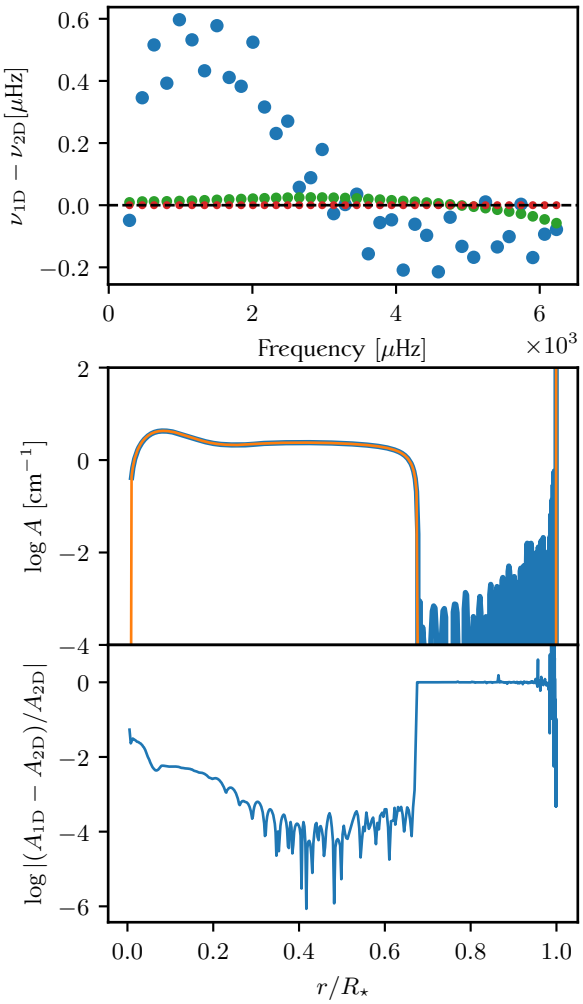

Figure 7.8: Seismic comparison of non-rotating $0.8M_\odot$ models. *Top:* Differences between the frequencies computed with one of the 1D input model and with the 2D model as a function of the associated mode frequency. Four non-rotating input models are used: the 1D model (blue, input 1) and the 2D model (orange, input 2), the 1D model extracted from the 2D model along θ_m (red, input 3; see text for a description) and a mixed 1D/2D model (green, input 4; see text for a description). The colour codes the couples of models being compared: (input1/2; blue), (input3/2; red), (input4/2; green). The dashed black line represents the 0 frequency difference. *Middle:* value of $|\mathbf{A}|$ (see Eq. (3.18)) as a function of $r/R_\star$ for model 1 (blue thick line) and input 2 (orange line). *Bottom:* Relative differences between $|\mathbf{A}|$ from input 1 and 2 as a function of $r/R_\star$. It must be noted that the value of $|\mathbf{A}|$ input 1 in the convective zone have been artificially set to 10^{-30} (only when plotting this figure), which explain the large, relative differences in those regions.

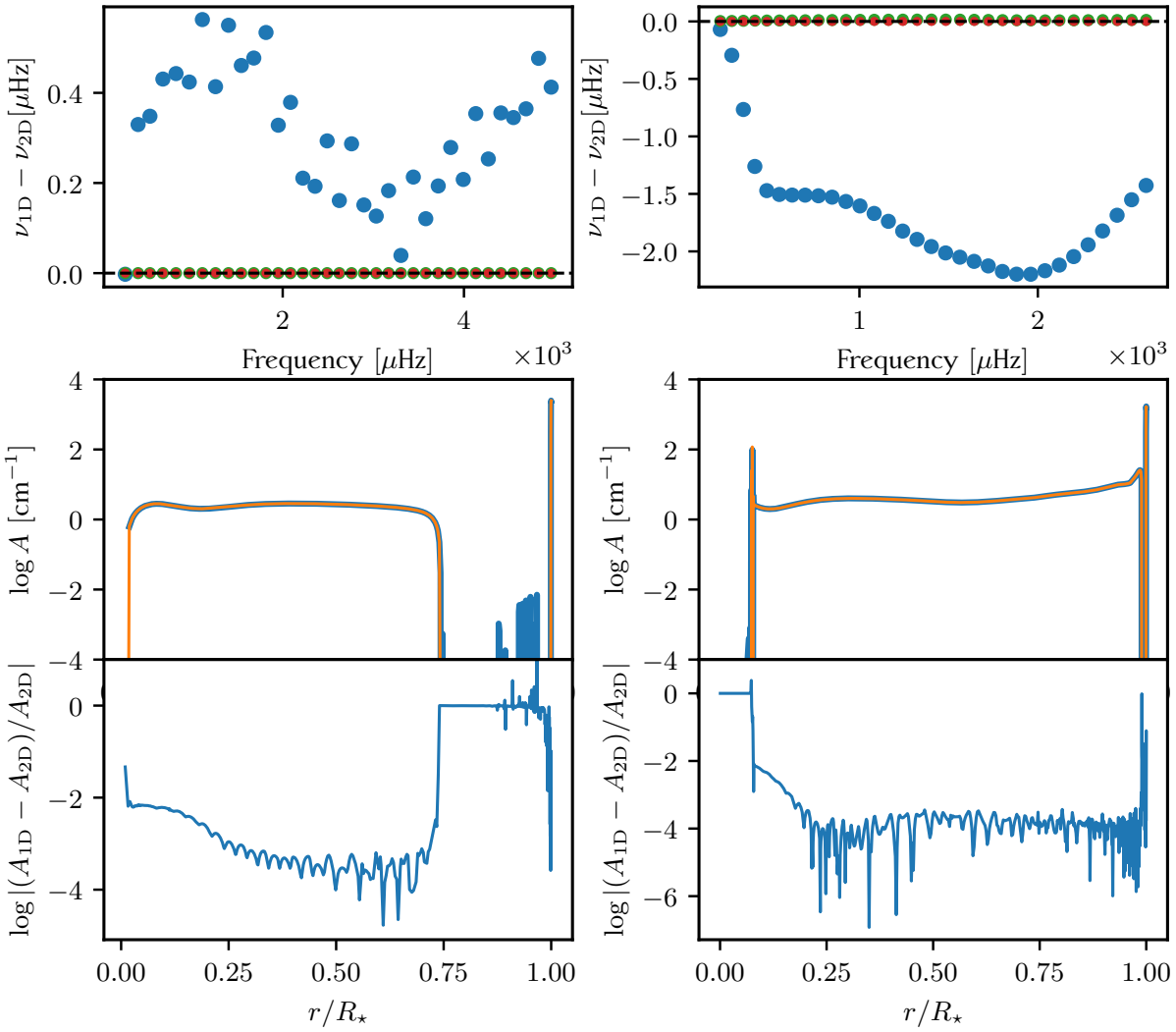

Figure 7.9: Same as in Fig. 7.8 for $1M_\odot$ models (left) and $1.5M_\odot$ models (right).

difference η of a quantity x is defined as

$$\eta(x) = \left| \frac{x_{2D}(\theta_m) - x_{1D}}{x_{1D}} \right|, \tag{7.10}$$

where x_{1D} (resp. $x_{2D}(\theta_m)$) is read from input 1 (rep. input 2). The second row displays the relative differences of their radial derivatives. Pressure profiles are quite in a good agreement, except at the surface where, in a very small region, a gap of around 10% is found between the 1D and the 2D inputs. It can seem unimportant, however the frequency of a star's modes of oscillations strongly depend on boundary conditions. Such a gap at the surface could lead to frequency differences exceeding the space mission frequency resolution. Moreover, we notice that models with $1M_\odot$ and $2M_\odot$ have the largest $\eta(p)$ in the rest of star: around 10^{-3} for the $1M_\odot$ model and 10^{-4} for the $2M_\odot$ model. On the contrary, the density profiles have, in the worst cases, a relative difference of 10^{-6}, which is far better. In addition, they present no peaks at the surface. The only noticeable ripple is very close to the centre, *i.e.* in the zone in which extra layers were added. Nonetheless, the amplitude of this ripple is very small and probably does not affect frequencies.

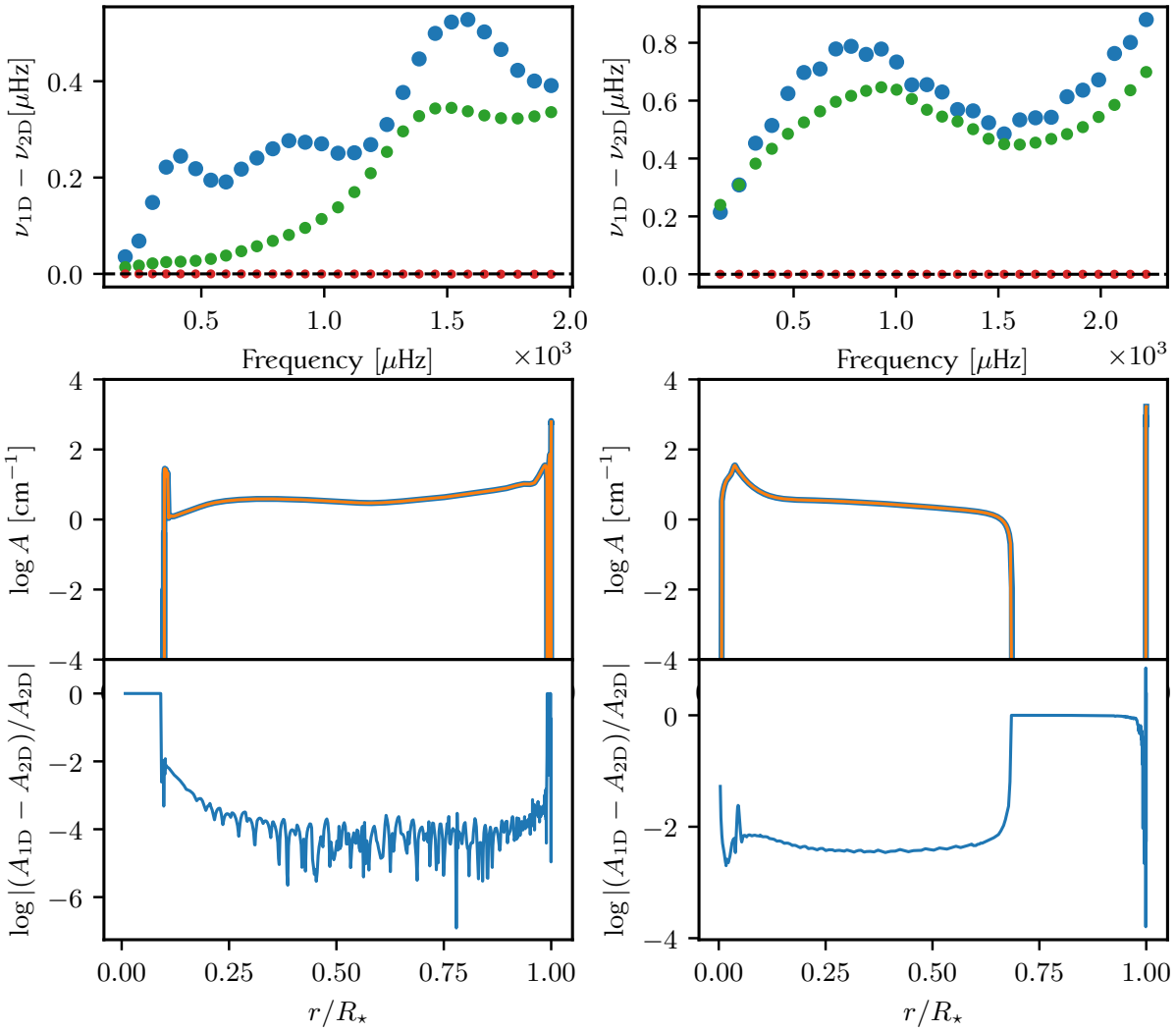

Figure 7.10: Same as in Fig. 7.8 for $2M_\odot$ models (left) and for a 11 Gyr old $1M_\odot$ models (right). This model is a subgiant.

How do we explain that the density profiles present better agreement than the pressure between 1D and 2D? When the model is deformed, the density along colatitude θ_m is set to be equal to the one from the resolution of the 1D structural equations. At the end of the deformation, the density profile is corrected so that the total mass of the deformed model matches the one of the initial 1D model. As we have seen in previous section, this correction is small. Furthermore, in order to produce this figure, *i.e.* to compare densities from 1D and 2D models, at the same mass coordinates, I had to re-interpolate the density profiles using a cubic spline which may have introduced small numerical errors. On the other side, the pressure profiles of the 2D models are computed in a different way. Once $\widetilde{\phi}_\ell$, $\widetilde{\rho}_\ell$, $\widetilde{r}_{p,\ell}$ and g_eff are known, the new pressure profile is integrated using Eq. (6.22).

$$\frac{\partial p}{\partial r} = -\rho \left(\frac{\partial \phi}{\partial r} - \Omega^2 r_p \sin^2 \theta_\mathrm{m} \right). \tag{7.11}$$

In order to integrate this equation, we assumed that the pressure at the upper atmosphere limit is zero, which physically is not exactly true. This assumption has almost no impact on

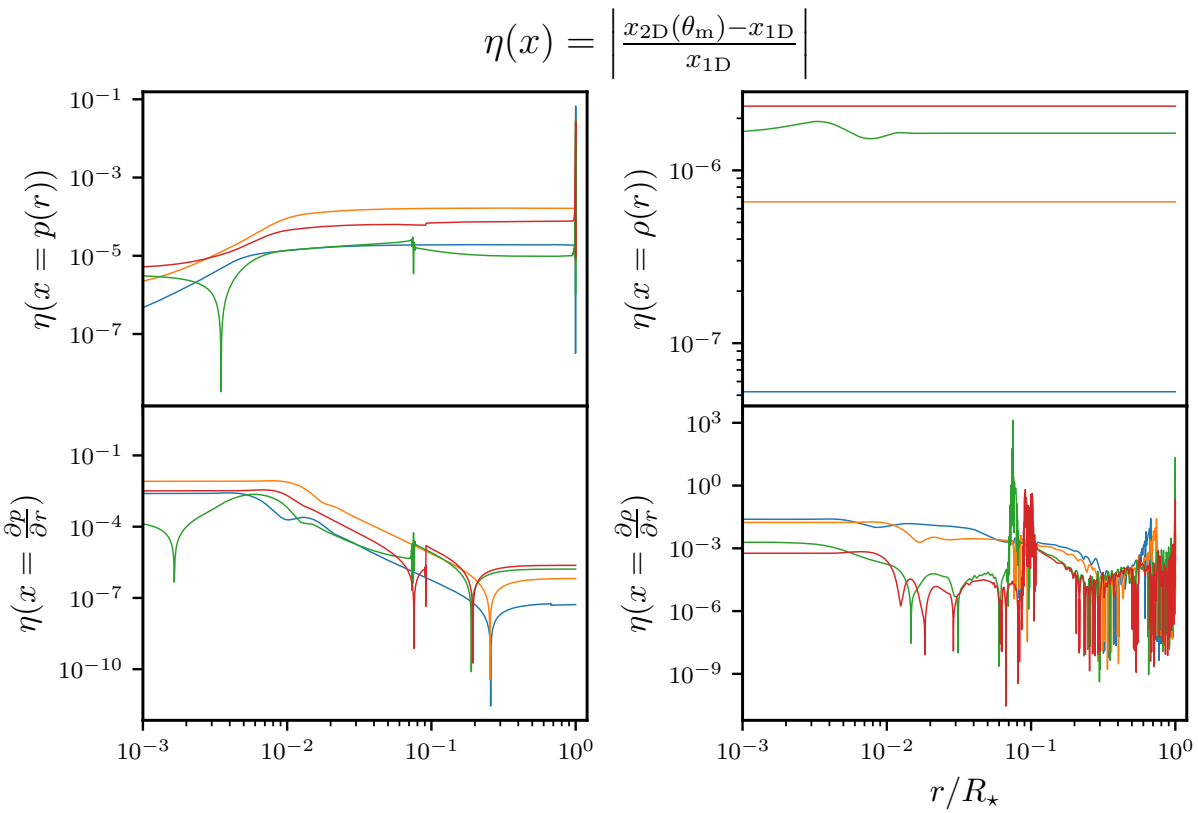

Figure 7.11: In this figure x_{1D} is understood as the quantities written in the 1D ACOR input file and $x_{2D}(\theta_m)$ is understood as the quantities written in the 2D ACOR input file. Those ACOR input files are the result of the pre-processing by ACOR of a CESTAM 1D or 2D output file. The colour code for the mass of the non-rotating models: $0.8M_\odot$ (blue), $1M_\odot$ (orange), $1.5M_\odot$ (green) and $2M_\odot$ (red) *Top left:* Relative differences of the pressures $p(r)$ as a function of $r/R_\star$. *Top right:* Relative differences of the densities as a function of $r/R_\star$. *Bottom left:* Relative differences of $\partial p/\partial r$ as a function of $r/R_\star$. *Bottom right:* Relative differences of $\partial \rho/\partial r$ as a function of $r/R_\star$.

the final pressure at the centre. However, the pressure in the upper regions of the star may be significantly impacted, which explains the disagreement of order 10% in the upper atmosphere.

Let us now take a look at the second row of Figure 7.11 where the relative differences $\eta(\partial p/\partial r)$ and $\eta(\partial \rho/\partial r)$ are presented. The derivative of the pressure shows much better agreement than the pressure itself in the upper 99% of the star. This is consistent with the fact that the discrepancies in the pressure profiles come from the integration constant, not from the computation of Eq. (7.11). The only notable difference is near the centre where the relative differences are of order 1%. This could be explained by the extra layers added by ACOR, but also by the interpolation that we used to produce the figure, which, near the limit of the interpolation interval may be less reliable. On the contrary, the radial derivatives of the densities display a lot of glitches. We found one located around $r/R_\star = 0.1$, one around $r/R_\star = 0.7$ and at the surface. The peaks around $r/R_\star = 0.1$ are present in the $1.5M_\odot$ and $2M_\odot$ models, while the ones around $r/R_\star = 0.7$ are present in the $0.8M_\odot$ and $1M_\odot$ models. They translate the transition from a convective to a radiative zone in the first case and the reverse in the other one. In the first case, the relative error increases by around 5 orders of magnitude, and 2 orders of magnitude in the second case. Despite being localized in a very thin region, these errors impact the boundary conditions and may cause a shift in the frequencies. We

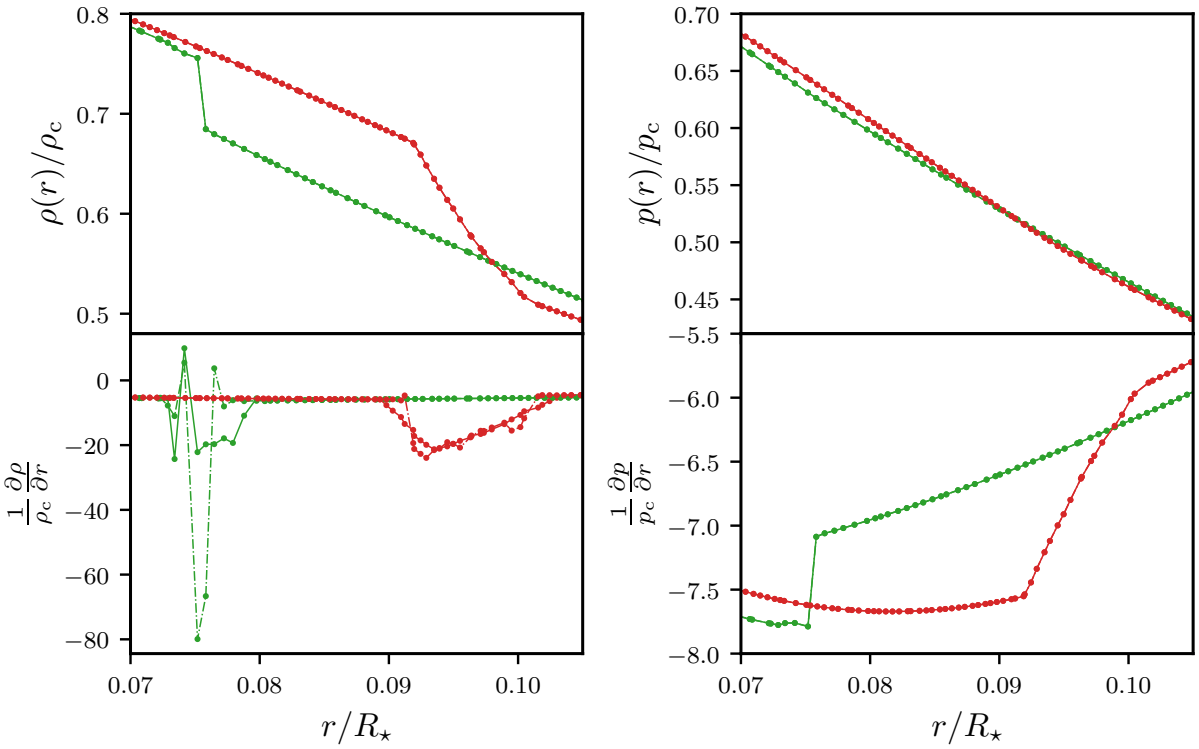

Figure 7.12: Zoom in on the pressure and density profiles and their respective radial derivatives. The colour code for the mass of the non-rotating models: $1.5M_\odot$ (green) and $2M_\odot$ (red). Quantities from the 1D models are represented as solid lines, and from the 2D models as dotted-dashed lines. The quantities p_c and ρ_c are the central pressure and density.

see that the model with the smallest $\delta\nu^{1,2}$ was the $0.8M_\odot$ model and it also has the smallest increase of $\eta(\partial\rho/\partial r)$. The model with the largest $\delta\nu^{1,2}$ was the $1.5M_\odot$ model and it also has the highest increase of $\eta(\partial\rho/\partial r)$. The rise of relative errors at the surface may also cause a shift of frequency, for similar reasons.

However, it does not explain everything: if the problem was only an issue in the computation of the derivatives, $\delta\nu^{4,2}$ should be always much smaller than $\delta\nu^{1,2}$. It is not the case for the $2M_\odot$ model (see Fig. 7.10). In this case, the important $\delta\nu^{4,2}$ may be only caused by the high $\eta(p)$ at the surface displayed in top left panel of Fig. 7.11.

For the moment, we only looked at how do the data stored in the input files compare. We looked at the reliability of two different numerical methods in approaching a derivative: either using the B-Spline representation or a 2$^{\text{nd}}$ order finite difference scheme. However, we did not look at the physics. From the Brunt-Väisälä frequency profiles in the middle right panel of Fig. 7.9 and the middle left panel of Fig. 7.10, we see a sharp peak around $r/R_\star \simeq 0.1$ this peak is not there in the lower mass models (except in the old $1M_\odot$ model). The peaks observed in the plots of Fig. 7.11 are caused by numerical approximation, but they also reveal a physical fact of interest. The gap in the frequencies computed from input 1 and input 2 are therefore partly linked to a bad reproduction of the physics of the model at the peak locations. Figure 7.12 represents a zoom on the profiles of ρ, $\frac{\partial\rho}{\partial r}$, p and $\frac{\partial p}{\partial r}$, where the glitches occur, for the two higher mass models. The glitch in the $1.5M_\odot$ is extremely localized: it occurs in one layer, while the one in the $2M_\odot$ occupies more than 10 layers. The glitches mark the discontinuity between the convective and radiative zones. This difference significantly impact the quality of

the derivative, especially for the one computed with the B-Splines (see Fig. 7.12). B-Splines are known not to reproduce rapid variations well. However, one could set up the B-Splines basis to handle such discontinuities. The routines that would allow us to do that have already been implemented in CESTAM for other purposes and will soon be used for the generation of 2D outputs.

On the contrary, the glitches in the pressure profiles are very small and the derivatives are well reproduced. In particular, the one of the 2D model is not interpolated but computed physically from Eq. (7.11). The handling of glitches in mode frequency computations is one of the current most important problem in asteroseismology (e.g. Verma et al., 2014; Pinçon, 2019).

7.1.3 Impact of various numerical parameters

The method used to deform the star depends on several numerical parameters. Its precision is mainly impacted by the number of Legendre polynomial that enter the decomposition of each fields and of the number of angular sectors in the angular mesh. We study the influence of those parameters in the following sections.

Maximal order $\ell_{\max}$ in the Legendre decomposition

As we have already seen, in the 2D version of CESTAM, any scalar f is decomposed on Legendre polynomials:

$$f(p,\theta) = \sum_{\ell}^{\ell_{\max}} \widetilde{f}_\ell(p) P_\ell(\cos\theta). \tag{7.12}$$

All odd degree $\widetilde{f}_\ell$ with ℓ odd are zero, due to the symmetry with respect to the equator. The degree $\ell_{\max}$ is decided by the user at the beginning of a simulation. The current implementation supports $\ell_{\max} \leq 8$, but adding more Legendre polynomial would be simple.

In order to test how an increase of $\ell_{\max}$ impacts the evolution of a stellar model, we computed four models with $\ell_{\max} = 2, 4, 6$ and 8, with mass $1.6 M_\odot$, initial disk period of 3.5 days and disk lifetime of 5 Myr. The evolution was pushed until 200 Myr. It must be noted that the model with $\ell_{\max} = 8$ crashed at a few Myr old. This suggest that adding $P_8(\cos\theta)$ destabilized the computation and the term $\widetilde{f}_8$ was physically insignificant. Including the term $P_8(\cos\theta)$ for a faster rotating model could be interesting, but not in this case. The model with $\ell_{\max} = 6$, crashed several times during its evolution, however, I was able to resume the computation until reaching the desired age. The models with, $\ell_{\max} = 2$, $\ell_{\max} = 4$ and $\ell_{\max} = 6$ will be called model P_2, model P_4 and model P_6. I will come back to it later but I must stress that we neglected the variation of $\theta_{\rm m}$ caused by the inclusion of $P_{\ell>2}$. It must be recalled that the the deformation module does not need the knowledge of this angle, but it is needed afterwards because the 1D structure is supposed to match the 2D structure at $\theta_{\rm m}$.

Figure 7.13, top left panel, displays a meridional cut of the angular velocity in the model. We see that Ω is of the order of 37% $\Omega_{\rm K}$, which makes the star significantly deformed. Nonetheless, much strongly deformed models can be computed (see Figure 7.2). The polar radius is around 94% of the equatorial radius. The top right panel is a Kippenhahn diagram. A vertical slice represents the convective zones (grey) and the radiative zone (white) at a given age. At the final age (200 Myr), the model has a small convective core that concentrates around 18% of the mass and a very thin convective envelope. The bottom left panel represents the rotation profiles of models P_2, P_4 and P_6. While the rotation profiles are comparable, small differences have appeared. Increasing the value of $\ell_{\max}$ has changed the values of f_p and f_t and in turn has affected the structure. The HR diagram of the bottom right panel show no discrepancies

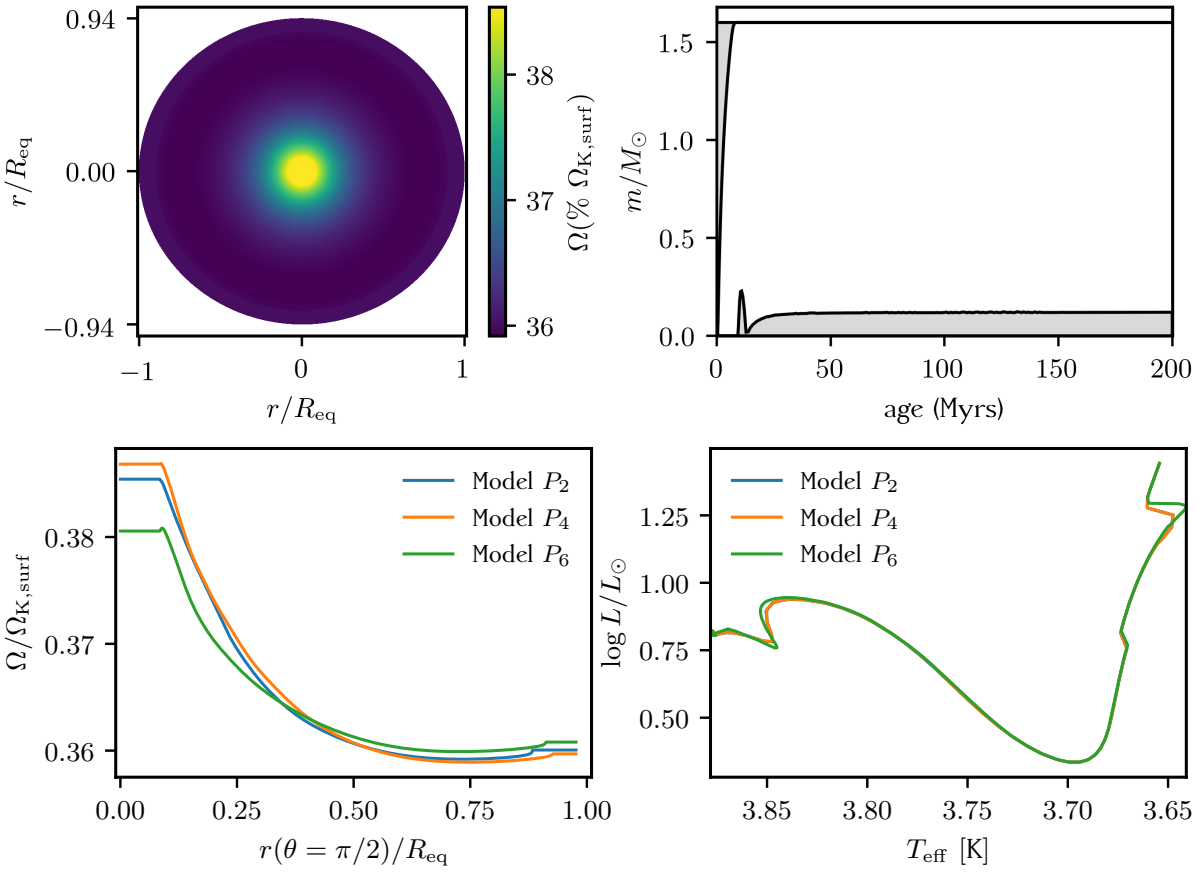

Figure 7.13: Various internal quantities from three models with $1.6 M_\odot$, an initial disk period of 3.5 days and disk lifetime of 5 Myr, but with the deformation computed with $\ell_{\rm max} = 2$ (blue curves), $\ell_{\rm max} = 4$ (orange) and $\ell_{\rm max} = 6$ (green), thereafter labelled as the P_2, P_4 and P_6 models. These four models have an age of 200 Myr and a core mass fraction of hydrogen of 68%. *Top left:* Meridional cut showing rotation profile in the P_2 model. The angular velocity is normalized by the Keplerian break-up velocity $\Omega_{\rm K,surf}$ computed at the surface. The radius is normalized by the equatorial radius. *Top right:* Kippenhahn diagram of the P_2 model, representing the evolution of the mass locations of the convective zones (grey areas) and of the radiative zone (white area), as a function of time. *Bottom left:* Angular velocity normalized to $\Omega_{\rm K,surf}$ as a function of the normalized equatorial radius for the three models. *Bottom right:* Hertzsprung-Russell diagram of the three models.

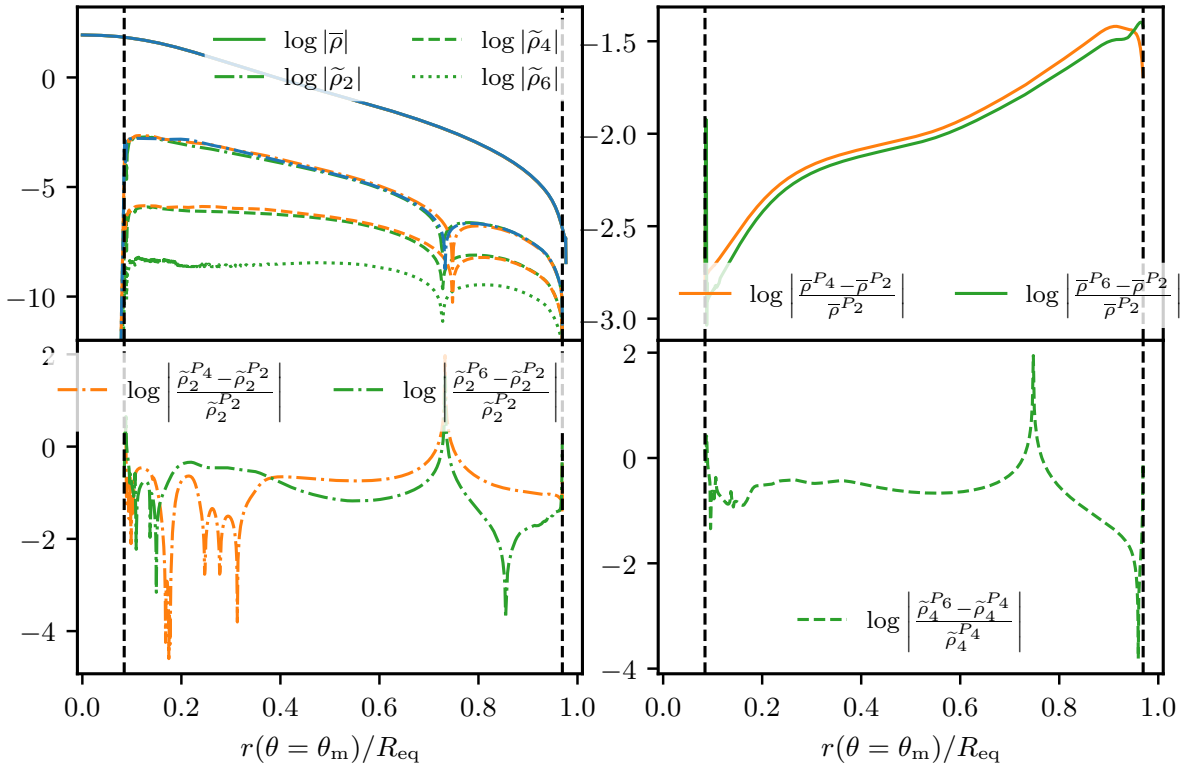

Figure 7.14: Same models and colour codes as in Fig. 7.13. The superscript refers to the model from which the quantities are computed. *Top left:* Logarithm of the density profile and of the fluctuations $\widetilde{\rho}_\ell/\overline{\rho}$, as a function of the normalized equatorial radius. The limits of the convective zones are represented by the vertical dashed black lines. *Top right:* Relative differences of $\overline{\rho}$ with respect to $\overline{\rho}^{P_2}$ computed in model P_2 as a function of the normalized equatorial radius. *Bottom left:* Relative differences of $\widetilde{\rho}_2$ with respect to $\widetilde{\rho}_2^{P_2}$ as a function of the normalized equatorial radius. *Bottom right:* Relative differences of $\widetilde{\rho}_4$ with respect to $\widetilde{\rho}_4^{P_4}$ as a function of the normalized equatorial radius.

in the evolutionary tracks. All these changes are certainly not measurable, at least for a star which such parameters, but they must be kept mind because they could have lead to larger differences if the evolution was to be pushed further.

One last point: in the HR diagram, we notice that, at the beginning of the evolution in the top right corner, models make a hook to the cool side of the diagram. This is the result of a small numerical trick that I had to implement in order to avoid rotational break-up at the start of an evolution. As I said in Chapter 1, a stellar evolution is started with a cloud that already has the desired mass and that is self gravitating but it also has a very large radius. Of course, if we impose a small initial rotation period (therefore large Ω), the break-up velocity is immediately reached and the model can not collapse. It may be a consequence of the simplified modelling of the star formation. In order to be able to evolve fast rotating star and to pass this difficult period, I impose for several time steps (in this case 3) an initial period 10 times higher than the one asked by the user. After those time steps, the real initial period is set-up and the model continues its evolution. The number of initial time steps that are computed in a reduced rotation rate regime must be adjusted manually. At a given initial rotation period, it also depend on the mass: the heavier the model, the larger the initial radius. However, in order to simplify the comparisons, the same number of slow rotating time steps have been set for all the models. In the Hayashi track, soon after the desired period of rotation has been

set, a second hook is observe, still going to cool side of the HR diagram. This hook signals the appearance of a central radiative zone which will rapidly extends almost to the top layers. The entropy of radiative zone is an increasing function of the radius while it is constant in a convective zone (except in the superadiabatic zone). Therefore, when an initially convective region becomes radiative, the central entropy must decrease so that that the entropy can increase with the radius. The entropy reduction translates in a loss of heat and and the core contracts. The contraction reduces the stellar surface and the luminosity decreases.

In Fig. 7.14, top left panel, we displayed the values of $\log \overline{\rho}$ and $\log |\widetilde{\rho_\ell}|$ for all three models, whenever it was possible. The other panels display the relative differences between model $P_{\ell_{\max}}$ and the reference model P_2 (an arbitrary choice) of $\overline{\rho}$ (top right), $\widetilde{\rho}_2$ (bottom left) and $\widetilde{\rho}_4$ (bottom right). All those quantities are in very good agreement. Was it expected ? If one had extended the Legendre decomposition to an unnecessary order $\ell_{\max}$, the coefficient $\widetilde{\rho_{\ell_{\max}}}$ would not reflect a physical meaning. Then, if one pushes the decomposition further to $\ell_{\max}+1$, coefficient $\widetilde{\rho_{\ell_{\max}}}$ would not have the same value because its value is the result of numerical artefacts. It does not contain physical information. The fact that all coefficients keep a very similar value when $\ell_{\max}$ is increased is a good indication regarding its physical significance.

In our case, the highest discrepancies between the $\widetilde{\rho_\ell}$ are found near $r/R_{\rm eq} \simeq 0.1$, at the location of the limit of the core convective zone. Here, gradients of angular velocity are stronger and may perturb the estimation of $\widetilde{\rho_\ell}$. Furthermore, a small change in $\overline{\rho}$ and $\widetilde{\rho_\ell}$ induces small shift of the location of the limit and therefore increases the disparities between the different models. Overall, even in this region, the agreement between the $\widetilde{\rho_\ell}$ stays very good. We also see that, around $r/R_{\rm eq} \simeq 0.7$ a sharp peak occurs in the profiles of $\log |\widetilde{\rho_\ell}|$. These peaks mark the location where $\widetilde{\rho_\ell}$ change sign. The change of sign corresponds to the change of a region with decreasing Ω as a function of the radius to a region of increasing Ω. Since rotation profiles are not the same from one model to another, the location of the peaks varies and leads to important discrepancies in each profiles of ρ_ℓ.

We performed the same comparison on models with the same initial parameters (mass and rotation of the disk) but much older (1.78 Gyr), on the sub-giant branch (see Fig. 7.15). This time, the model with $\ell_{\max} = 6$ is not shown. Despite I manage to compute the evolution until the desired age, the rotation profile became, at some point of the evolution, completely flat. It suggests a computational problem somewhere. This point left aside, we see on the meridional cut representing the angular rotation profile (7.15, top left panel) that the ratio of the polar to equatorial radii has not evolved much. In contrast, the radial gradient of Ω has significantly sharpened, with a difference of rotation rate of around 40% between the core and the surface while it was around 6% for the younger models. This phenomenon is of course due to the contraction of the core and the dilation of the envelope. With an additional mechanism of transport of AM, the gradient would certainly be reduced. The changes in the evolutionary track are not visible, nonetheless, we see that the core rotation of the model P_2 is a little lower than the one of P_4. Model P_2 has a core hydrogen abundance of 5.8% while model P_4 have respectively 7.3%. Its seems that model P_2 evolved slightly faster than the other two and it could explain the higher increase of the core rotation rate. The good agreement between the $\overline{\rho}$ and $\widetilde{\rho_\ell}$ for all models is still good. The ordering $\overline{\rho} \gg \widetilde{\rho}_2 \gg \widetilde{\rho}_4$ is also preserved is the whole radiative zone.

As a final test, we applied the same treatment on two models with $2M_\odot$ and 800 Myr ($X_{\rm c} \simeq 27\%$). This grid contains only two models because models P_6 and P_8 crashed during the pre-main sequence. The initial rotation conditions were the same as before: $\tau_{\rm disk} = 5$ Myr and $P_{\rm disk} = 3$ days. The star is significantly more distorted than before with $R_{\rm p}/R_{\rm eq} \simeq 82\%$. Conclusions similar to what we found before can be drawn. The rotation profiles are quite similar between Model P_2 and P_4 and the evolutionary tracks are almost identical. The

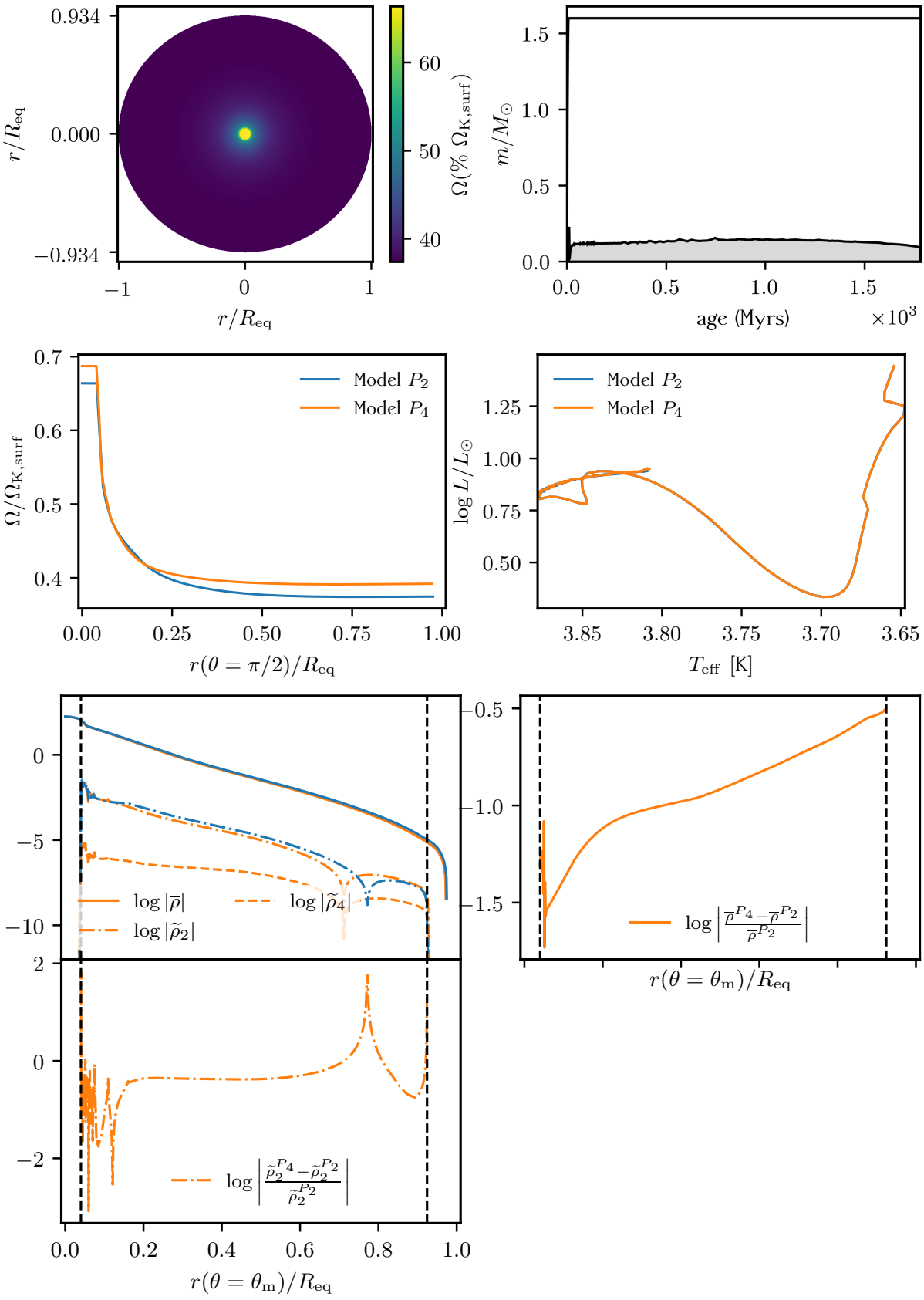

Figure 7.15: Same as in Figs. 7.13 and 7.14, but at 1.78 Gyr, *i.e.* at the beginning of the sub-giant phase.

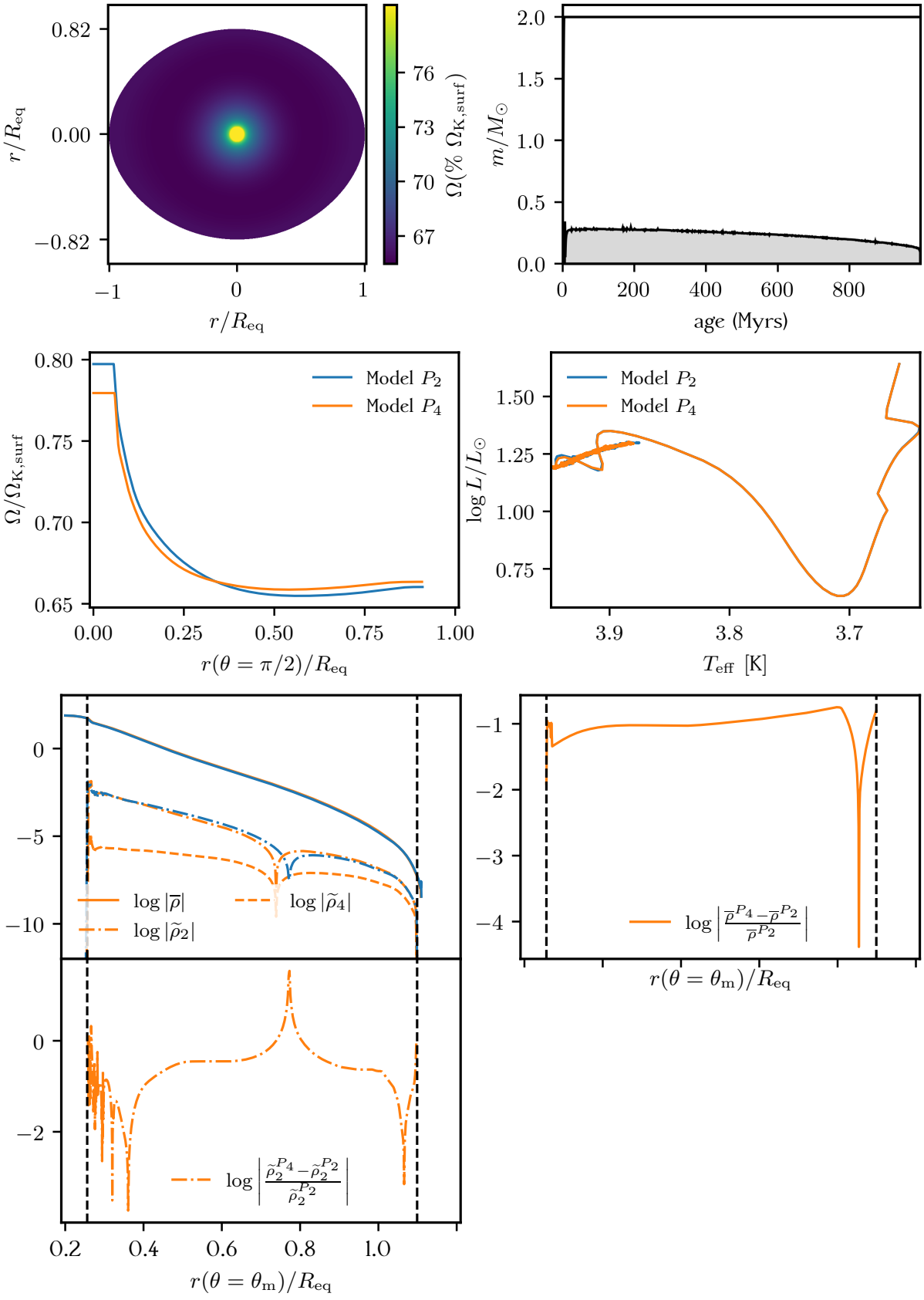

Figure 7.16: Same as in Figs. 7.13 and 7.14, but with a $2M_\odot$ model at 800 Myr. The core hydrogen abundance is $\sim 27\%$.

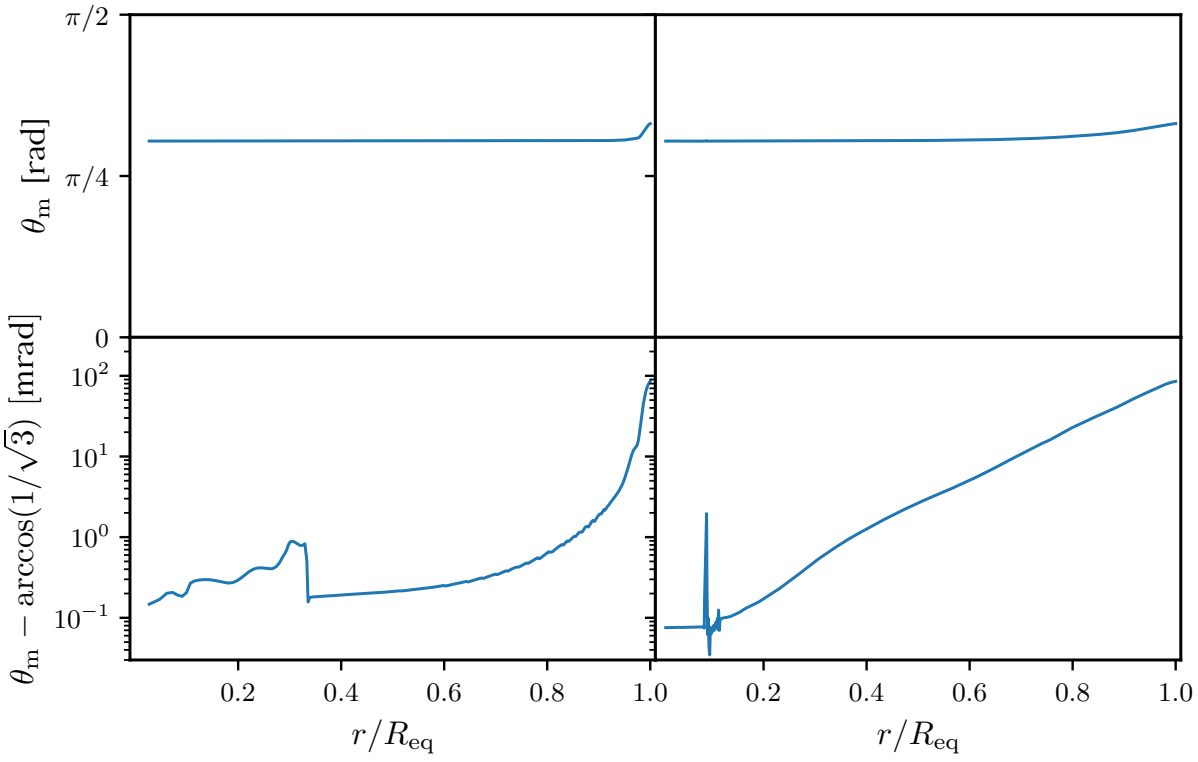

Figure 7.17: Variation of angle θ_m as a function of r/R_{eq} for a $1.6M_\odot$ model with $\tau_{disk} = 5$ Myr and $P_{disk} = 3$ days, and at an age of 1Myr (left) and of 200Myr (right).

quantities $\overline{\rho}$ and $\widetilde{\rho}_\ell$ compare as before in a large portion of the star, *i.e.* $\widetilde{\rho}_4 \ll \widetilde{\rho}_2 \ll \overline{\rho}$.

It is unfortunate that the model with $\ell_{max} = 6, 8$ crashed during the PMS. Indeed, since the star is much more deformed, they should be needed. It may be that the inclusion of these higher order prevents the good convergence of the deformation module during the PMS but would help it after, once the contraction is finished. In the future, it would be interesting to implement a method to adapt ℓ_{max} to the situation and make it possible to vary during evolution.

Variation of θ_m

The question of how to take variations of θ_m into account is yet to be solved. In Fig 7.17, I present the values of the angle θ_m as a function of the radius determined with the method described in 6.2.3, for the model P_4, with $1.6M_\odot$ at 1 Myr old (left panels) and 200 Myr old (right). In the young model, differences of order 100 mrad are limited to the surface region. In the evolved model, θ_m increases in almost all the star (while the maximal difference compared with $\arccos(1/\sqrt{3}$ is still of order 100 mrad). It must be noted that θ_m was computed a posteriori and for the whole simulation we assumed $\theta_m = \arccos(1/\sqrt{3})$. The deformation module is able to account for a non constant θ_m. However, in the early phase of this model, aberrant values of θ_m have been found in the atmospheric regions: θ_m increases by ~ 0.1 rad in a single layer or even no solutions at all in the $[0, \frac{\pi}{2}]$ interval. These "glitches" led CESTAM to crash at a very early age while the computations would probably go well once this complicated phase is passed. It is worth noting that the peak we see on the bottom right panel of Fig 7.17 cannot be qualified as a glitches because, here, the variation is of the order of 1 mrad between two

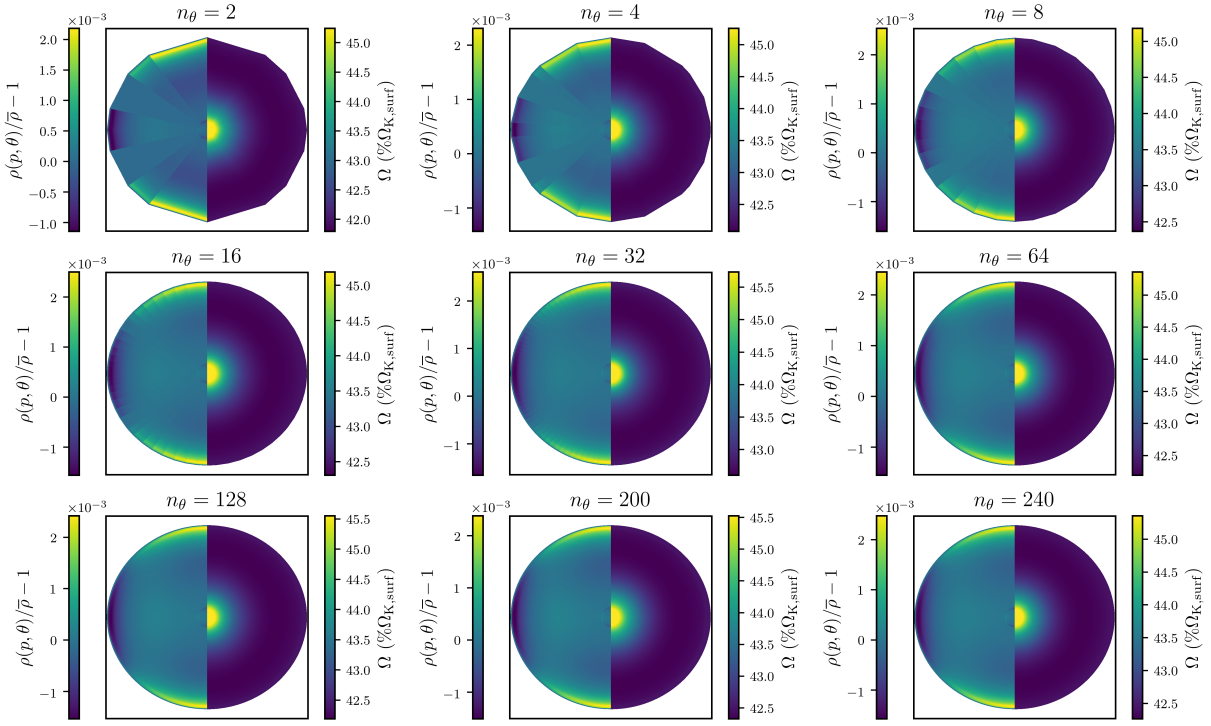

Figure 7.18: Meridional cut of of $1.6 M_\odot$ models with varying n_θ and $\ell_{\max} = 2$. Models are described in Table 7.1. Axes represent the $r(p,\theta)/R_{\mathrm{eq}}$ and the aspect ratio between the two is the axes is the same. The number of angular sectors in each models is indicated in the title of each plots. The left part of the meridional cut represents $\rho(p,\theta)/\overline{\rho} - 1$ and the other half represents the angular velocity profile (Ω depending only on p) in percents of $\Omega_{\mathrm{K,surf}}$.

layers while the glitches that make CESTAM crash are of order $100 - 1000$ mrad.

In Sect. 6.2.3, I proposed several solutions on how to account for the variation of θ_{m} in the deformation module. It seems, in the view of Fig. 7.17, that the only good proposition is the last one, *i.e.* evaluate θ_{m} at every layers of the model and represent it as a function of the radius. It remains to find a way to avoid the problems of the glitches. It would certainly be a way of improvement for the future.

Number of angular sectors

The last point that needs to be investigated is the influence of the number of angular sectors on the quality of the models. Let us recall that n_θ is the number of angles used in the Gauss-Legendre quadrature. These angles lie in the interval $]0;\pi/2[$. To these n_θ angles, 3 ghost angles are added: $0, \pi/2$ and θ_{m}. The first two are added so that the solutions are known at the poles and at the equator, allowing us to plot continuous 2D functions. They do not improve the quality of the solutions of the various equations that are solved by the deformation module. Indeed, these solution are determined only by using the n_θ angles. We already talked in details about the last ghost angle θ_{m}. It is kept in the angular mesh because at this precise colatitude, the 2D quantities match the 1D structure. One last point: the ACOR code only uses the quantities defined at the n_θ angles and does not use the ghost ones.

In order to test the influence of n_θ on the quality of the models, we computed a grid of models (see Table 7.2) with three different masses and a varying number of n_θ. They are evolved up to 200 Myr. In all models, the decomposition in Legendre polynomials is stopped

at $\ell_{\max} = 2$. Because the models with $1.6M_\odot$ are the most deformed, we also computed three models with a mass of $1.6M_\odot$ and $\ell_{\max} = 4$. They will be described in more detail later.

Figure 7.18 represents the meridional cut of the $1.6M_\odot$ models (with $\ell_{\max} = 2$) for different values of n_θ. Lower mass models are less deformed and therefore we do not represent their 2D shape. The left side of each meridional cut represents the density fluctuations with respect to the 0^{th}-order component of the density in the Legendre decomposition: $\Theta_2 - 1$. The right side is the angular velocity in unit of Ω_{K}. It is quite easy to see in the first 2D map (first column, first row) that there are 5 angles in each interval $[(i-1)\pi/2; (i-1)\pi/2]_{i=1,2,3,4}$: the 2 from the Gauss-Legendre quadrature and the 3 ghost angles. We already see, for instance, by looking at the maximum value of Ω in the colour bar, that the rotation profiles are not found identical when n_θ varies.

We computed the radial mode frequencies using ACOR for each of these models. At each mass, we took as reference model the one computed with 240 quadrature angles. For all sets of models with same mass, we computed the frequency differences between a model with any n_θ and the reference model. We denote these frequency differences as $\delta\nu_{n_\theta} = \nu^{n_\theta} - \nu^{n_\theta=240}$. The frequency differences are displayed in Fig. 7.19. It must be noted that at all masses, $\delta\nu_n^{n_\theta=2}$ is so high that it almost never fits in the frames. The frequency resolution specification of PLATO is 0.2 µHz, therefore, we would want the frequency differences to converge below this threshold as n_θ increases.

The results plotted in Fig. 7.19 do not match these requirements. First of all, we would expect the frequency differences to decrease as n_θ increases, *i.e.* $|\delta\nu_n^2| > |\delta\nu_n^4| > \ldots > |\delta\nu_n^{200}|$. However, in all panels, the better agreement with the reference model is never reached for the models with the highest n_θ. The models with $1M_\odot$ are the one that show the better agreement. Models with any $n_\theta \geq 8$ have frequency differences falling bellow the threshold of 0.2 µHz. We also notice that in the top panel of Fig. 7.19, all $\delta\nu_n^{n_\theta}$ follows a linear trend. This is the result of a small variation in the value of the large separation $\Delta\nu$, which is proportional to the mean stellar density. The mass of the model is the same but the radius is not. The equatorial and polar radius are nearly the same for all $1M_\odot$ models (see Table 7.2), at least up to 3 digits, but the small difference can produce a difference of $\Delta\nu \simeq 0.01$ µHz which adds up to a $\delta\nu_n^{n_\theta} \simeq 0.2$ µHz for the radial modes with $n \simeq 20$.

In the second set of models with $1.2M_\odot$, $\delta\nu_n^{n_\theta}$ is again of order 0.1 µHz but many models have their $\delta\nu_n^{n_\theta}$ rising above the PLATO resolution threshold. Surprisingly, models with poor angular resolution, $n_\theta = 8$ and $n_\theta = 32$ display significantly better results than the high resolution ones. These good performances may be accidental. The majority of the models have there $\delta\nu_n^{n_\theta}$ varying linearly, due to changes in the large separation. Looking at Table 7.2, we see that the changes of R_{eq} and R_{p} from one model to another are more significant. Although, in some models, especially the one with $n_\theta = 8$, $\delta\nu_n^{n_\theta}$ do not follow a linear trend. Such variations probably signal more serious changes in the structure of the star than a simple tiny change in the mean stellar density.

Finally, let us study the frequency differences in the last set of models with $1.6M_\odot$ (with $\ell_{\max} = 2$). Here, the $\delta\nu_n^{n_\theta}$ are enormous, of order 1 µHz if not more. The frequency differences $\delta\nu_n^{n_\theta}$ still varies almost linearly but this time we can see small wavelets superimposed to the linear trend. We actually already saw similar wavelets, although much more pronounced, in the frequency differences induced by the surface effects (for instance bottom panel of Fig. 2 in Manchon et al. 2018). These wavelets were caused by glitches due to discrepancies in the locations of the HI and HeII ionization regions. The wavelets observed in the bottom panel of Fig. 7.19 are probably not caused by a shift of the location of these ionization regions because, these would affect high frequency modes. However they could be caused by other small changes in the structure, deeper in the star, for instance the location of the the boundaries of

Table 7.2: Grid of models with varying number of points n_θ in the angular mesh used for the Gauss-Legendre quadrature. The models have three different masses, different initial rotation conditions and an age of 200 Myr. All models are computed with $\ell_{\max} = 2$, except the last three for which $\ell_{\max} = 4$. The angular velocity Ω is given as a percentage of $\Omega_{\rm K}$ at the surface and at the final age of the models. The quantity $X_{\rm c}$ is the abundance of hydrogen at the centre. The radii $R_{\rm eq}$ and $R_{\rm p}$ are the equatorial and polar radii. The quantities $p_\dagger$ and $\rho_\dagger$ have been defined in Eq. (7.9) and have the dimension of the inverse of a pressure and of a density.

Model	n_θ	Ω [% $\Omega_{\rm K}$]	$X_{\rm c}$ [%]	$T_{\rm eff}$ [K]	$R_{\rm eq}$ [$R_\odot$]	$R_{\rm p}$ [$R_\odot$]	$p_\dagger$ [cgs]	$\rho_\dagger$ [cgs]	$\Omega_{\rm K}$ [mrad s^{-1}]
$1M_\odot$, $P_{\rm disk} = 3$ days, $\tau_{\rm disk} = 5$ Myr									
M10N2	2	13.42	58.58	5647	0.952	0.944	$9.162 \cdot 10^{-16}$	1.836	0.6758
M10N4	4	13.39	58.58	5648	0.952	0.943	$9.158 \cdot 10^{-16}$	1.835	0.6759
M10N8	8	13.41	58.58	5647	0.952	0.943	$9.162 \cdot 10^{-16}$	1.836	0.6758
M10N16	16	13.40	58.58	5647	0.952	0.943	$9.164 \cdot 10^{-16}$	1.836	0.6757
M10N32	32	13.40	58.58	5647	0.952	0.943	$9.165 \cdot 10^{-16}$	1.836	0.6757
M10N64	64	13.41	58.58	5647	0.952	0.943	$9.166 \cdot 10^{-16}$	1.836	0.6757
M10N128	128	13.40	58.58	5647	0.952	0.943	$9.165 \cdot 10^{-16}$	1.836	0.6757
M10N200	200	13.40	58.58	5647	0.952	0.943	$9.164 \cdot 10^{-16}$	1.836	0.6757
M10N240	240	13.41	58.58	5647	0.952	0.943	$9.166 \cdot 10^{-16}$	1.836	0.6757
$1.2M_\odot$, $P_{\rm disk} = 4$ days, $\tau_{\rm disk} = 5$ Myr									
M12N2	2	18.70	62.04	6212	1.198	1.179	$1.599 \cdot 10^{-15}$	3.053	0.5240
M12N4	4	18.72	61.74	6213	1.199	1.180	$1.605 \cdot 10^{-15}$	3.062	0.5233
M12N8	8	18.70	61.76	6212	1.200	1.179	$1.606 \cdot 10^{-15}$	3.063	0.5232
M12N16	16	18.69	62.03	6211	1.198	1.178	$1.600 \cdot 10^{-15}$	3.055	0.5238
M12N32	32	18.69	62.03	6212	1.198	1.178	$1.600 \cdot 10^{-15}$	3.054	0.5239
M12N64	64	18.72	62.03	6212	1.198	1.178	$1.600 \cdot 10^{-15}$	3.055	0.5238
M12N128	128	18.72	62.05	6211	1.199	1.178	$1.601 \cdot 10^{-15}$	3.056	0.5238
M12N200	200	18.68	62.02	6212	1.198	1.178	$1.600 \cdot 10^{-15}$	3.055	0.5239
M12N240	240	18.65	62.03	6212	1.198	1.178	$1.600 \cdot 10^{-15}$	3.054	0.5239
$1.6M_\odot$, $P_{\rm disk} = 3$ days, $\tau_{\rm disk} = 5$ Myr									
M16N2	2	41.94	68.14	7489	1.576	1.454	$2.688 \cdot 10^{-15}$	5.206	0.4013
M16N4	4	42.24	68.25	7487	1.578	1.453	$2.707 \cdot 10^{-15}$	5.233	0.4003
M16N8	8	42.55	68.14	7483	1.582	1.452	$2.733 \cdot 10^{-15}$	5.270	0.3989
M16N16	16	42.45	68.15	7482	1.582	1.451	$2.729 \cdot 10^{-15}$	5.265	0.3990
M16N32	32	42.79	68.12	7466	1.588	1.455	$2.775 \cdot 10^{-15}$	5.331	0.3966
M16N64	64	42.33	68.21	7475	1.582	1.451	$2.731 \cdot 10^{-15}$	5.267	0.3990
M16N128	128	42.35	68.11	7485	1.581	1.451	$2.727 \cdot 10^{-15}$	5.262	0.3992
M16N200	200	42.48	68.10	7473	1.587	1.455	$2.764 \cdot 10^{-15}$	5.316	0.3971
M16N240	240	42.41	68.14	7478	1.583	1.452	$2.737 \cdot 10^{-15}$	5.276	0.3986
$1.6M_\odot$, $P_{\rm disk} = 3$ days, $\tau_{\rm disk} = 5$ Myr, $\ell_{\max} = 4$									
M16N128L4	128	42.31	68.11	7485	1.581	1.451	$2.727 \cdot 10^{-15}$	5.262	0.3992
M16N200L4	200	42.22	68.11	7479	1.582	1.452	$2.731 \cdot 10^{-15}$	5.268	0.3989
M16N240L4	240	42.35	68.11	7482	1.582	1.452	$2.734 \cdot 10^{-15}$	5.272	0.3988

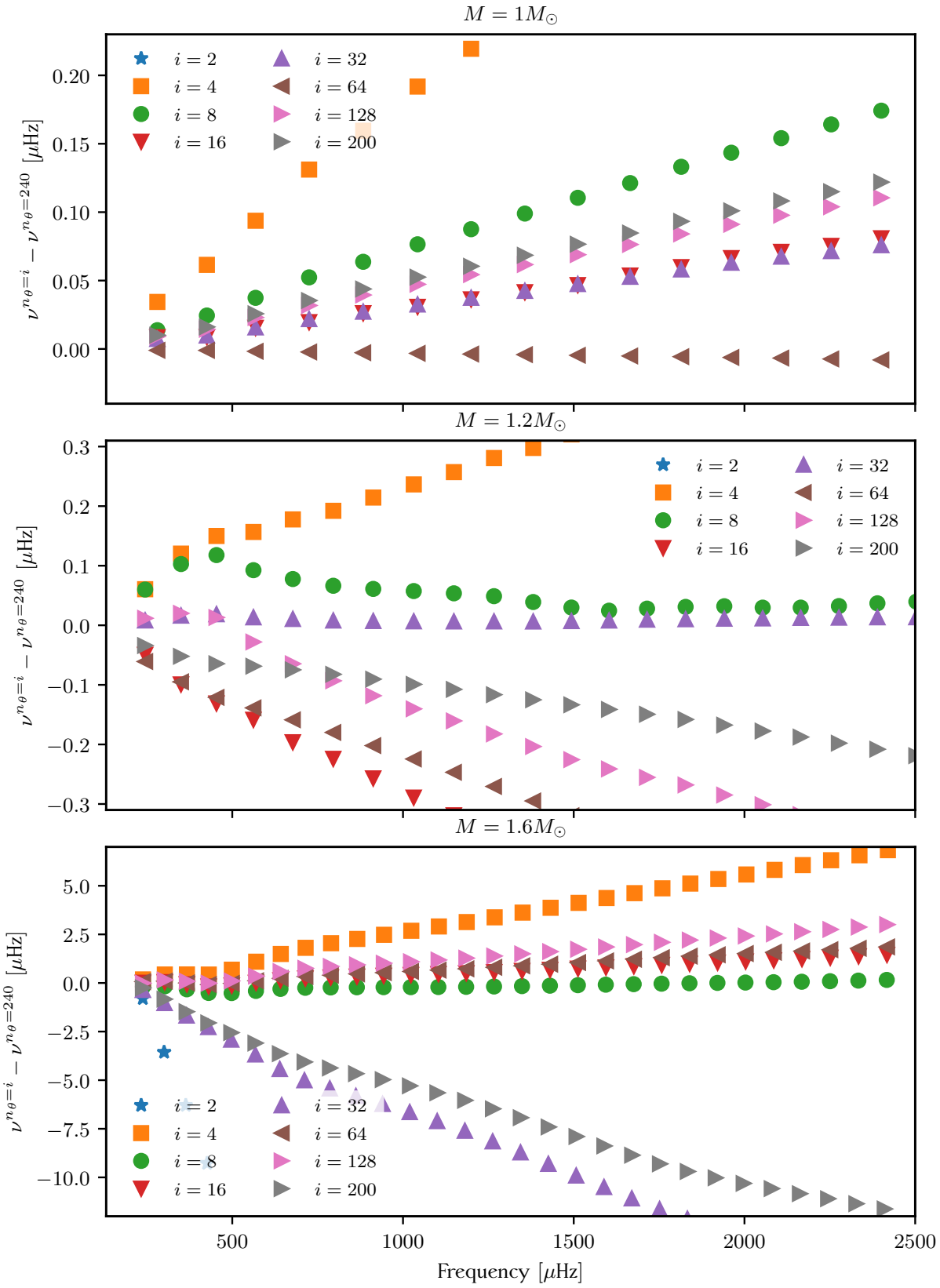

Figure 7.19: Seismic comparison of the models described in Table 7.2. Frequency differences between the mode frequencies of models with the same mass but different n_θ, compared with a reference model with $n_\theta = 240$. *Top:* Models with $1M_\odot$. *Middle:* Models with $1.2M_\odot$. *Bottom:* Models with $1.6M_\odot$ and Legendre decomposition stopped at $\ell_{\max} = 2$.

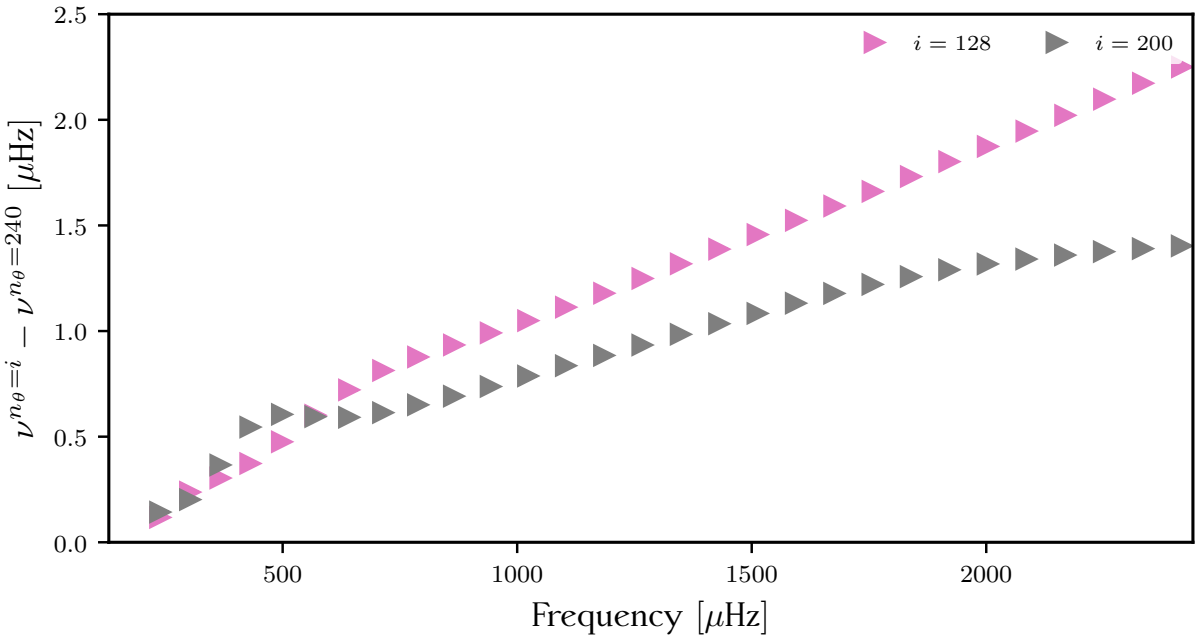

Figure 7.20: Same as in Fig. 7.19 but with the $1.6M_\odot$ models computed with the Legendre decomposition extended to $\ell_{\max} = 4$.

the convection zones.

How can we explain these bad results? Models with $1.6M_\odot$ are rotating significantly faster that the ones above. There rotation rates are around $42\%\ \Omega_{\rm K}$ while they were $\sim 13.4\%\ \Omega_{\rm K}$ for the $1M_\odot$ models and $\sim 18.7\%\ \Omega_{\rm K}$ for the $1.2M_\odot$. Because of the fast rotation, the error made when computing the values of parameters f_p, f_T and $f_{\rm d}$, etc. from one model to another is much more important than for slow rotators. As these coefficients directly impact the structure and the evolution, it may be possible that during the evolution, the structures of these models slowly diverge from each other. Therefore, the models on which we computed frequencies are significantly different. This is the reason why we compared models that are only 200 Myr old: it reduces the structural differences due to evolution. However, we would have expected a better agreement with the reference model as long as n_θ increases, which is not the case. Another source of error comes from ACOR itself. Indeed, the θ derivatives that are calculated using finite difference methods are of course strongly influenced by the resolution of the angular mesh. A last explanation comes from the fact that we limited ourselves to a decomposition up to $\ell_{\max} = 2$. In fact, it is likely that at such rotation rates, this simple decomposition "misses" a large fraction of the fluctuations of the various fields over isobars, which in the end lead to large differences between the models with $1.6M_\odot$. In order to check if the inclusion of a higher order Legendre polynomial in the decomposition would improve the agreement between models with different n_θ, we computed another set of models with $1.6M_\odot$ and $\ell_{\max} = 4$. Unfortunately, we were not able to keep CESTAM running with $n_\theta < 128$ and $\ell_{\max} = 4$. All defective models stopped at the same age, around 2 Myr, when the surface rotation rate reaches a maximum due to contraction. The use of a higher order Legendre decomposition seems to require a high resolution angular mesh in order to be stable.

Nonetheless, we managed to carry out the evolution up to 200 Myr for models with $n_\theta = 128, 200$ and 240. The frequency differences between their spectrum and the reference spectrum of the $n_\theta = 240$ model are displayed in Fig. 7.20. The frequency differences $\delta\nu_n^{128}$ are not

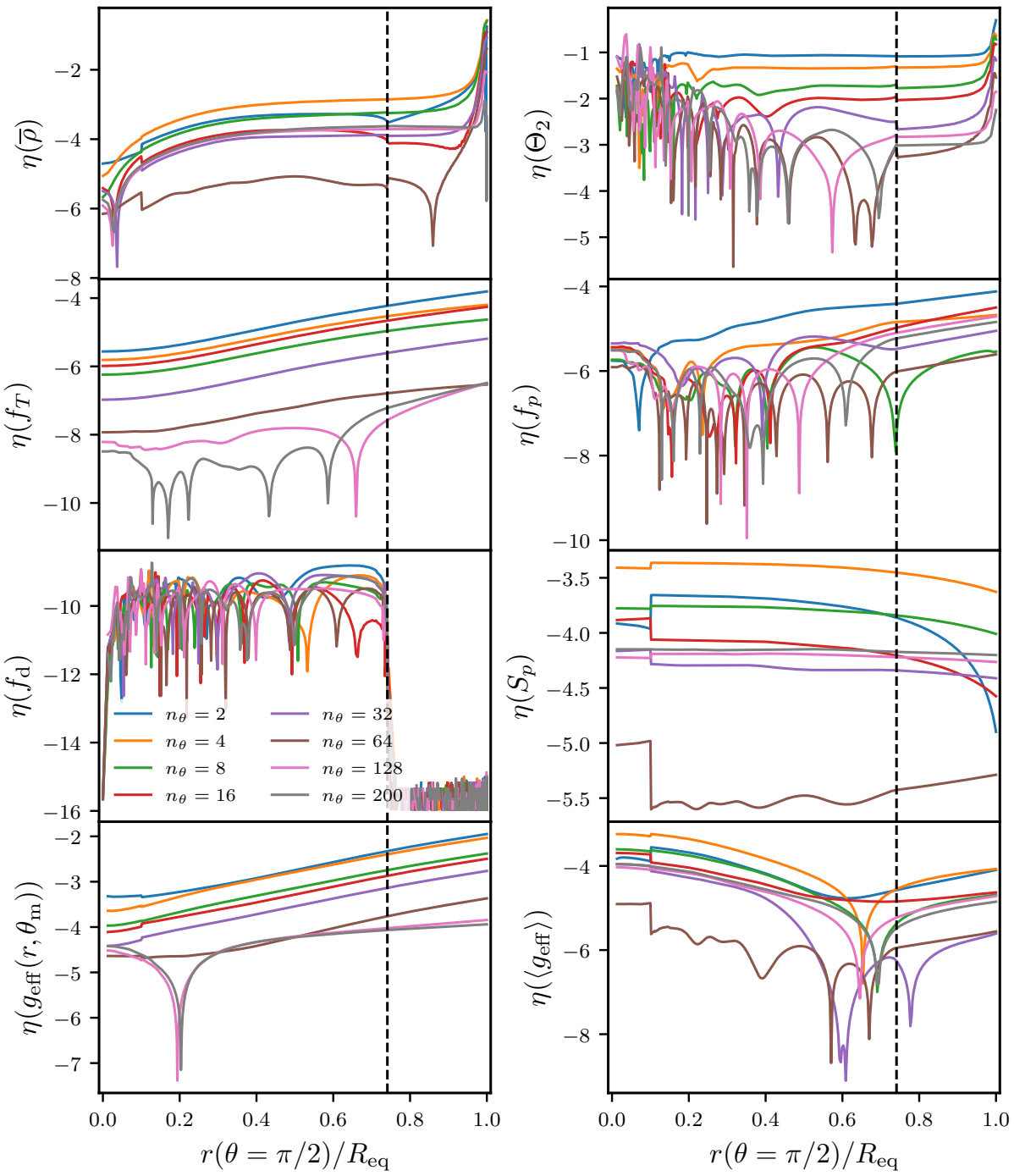

Figure 7.21: Comparison of quantities related to the 2D geometry computed with a varying n_θ. The colours code for n_θ and their meaning is given in the legend of left panel in the 3$^{\rm rd}$ row. In all the subplots, η defines the relative variation of a quantity x as $\eta(x) = \left|(x^{n_\theta} - x^{n_\theta=240})/x^{n_\theta=240}\right|$. In the top right panel, $\eta(\Theta_2)$ is not significant outside the convective zone boundaries because in the present case of shellular rotation, $\widetilde{\rho_2} = 0$ in the convective zones.

changed much, however, $\delta\nu_n^{200}$ are almost divided by a factor ten. This is encouraging and shows the importance of stopping the decomposition at the right order $\ell_{\max}$. Nevertheless, the $\delta\nu_n^{n_\theta}$ stay very high and are still not satisfying. They can be explained by the conjugated effects of remaining discrepancies and error in the determination of $\theta_{\rm m}$. Concerning the first effect, the global parameters presented in Table 7.2 show significantly reduced discrepancies from one model to the other compared with what we had when P_4 was not included, but they remain quite large. Figure 7.17 shows the variation of $\theta_{\rm m}$ in model `M16N240L4` (see Table 7.2). I recall that the computation of $\theta_{\rm m}$is performed *a posteriori* because the implementation of a varying $\theta_{\rm m}$ into CESTAM is too unstable for the moment. The gap between $\theta_{\rm m}$ and $\arccos(1/\sqrt{3})$ are stronger close to the surface. The impact should be rather similar as the surface effect induced by the omission of the turbulent pressure in the structure and mode equations. Indeed, in Fig. 7.20 $\delta\nu_n^{200}$ do not follow a linear trend symptomatic of a variation of $\Delta\nu$, but more a power of a shifted frequency, similar to surface-induced frequency differences.

Let us now take a closer look at the structure differences of all these models. For clarity, we only took a look at structure variations in the $1M_\odot$ set of models, that showed very good frequency agreements, and at structure variations in the $1.6M_\odot$ set of models (with $\ell_{\max} = 2$), that showed very bad frequency agreements. Figure 7.21 is devoted to the $1M_\odot$ models and Fig. 7.22 to the $1.6M_\odot$ ones. In these plots we display the relative variations of various quantities between a model with $n_\theta = i$ and a reference model with $n_\theta = 240$. The relative variation for any quantity X is denoted:

$$\eta(X) \equiv \left| \frac{X^{n_\theta} - X^{n_\theta=240}}{X^{n_\theta=240}} \right|. \tag{7.13}$$

It is interesting to notice that the gap between the model's structure and reference's structure reduces when n_θ increases. This feature was not observed when studying the frequencies. Its not true for all the quantities represented (e.g. f_p second row and column or $f_{\rm d}$ third row, first column), but the agreement is already very good. Surprisingly, we see that the model with $n_\theta = 64$ for the set of $1M_\odot$ and $n_\theta = 8$ agree significantly better with the reference model than the other ones. The reason why this happens is not clear yet but these two models also have the smallest frequency differences in Fig. 7.19, top and bottom panel. In Fig. 7.21, first panel, the density profile agrees at least to 10^{-3} with the reference model, except near the surface where the relative differences reach values of order 10%. Fortunately, these large errors are restricted to very few layers at the surface. However, we see in the plot in Fig. 7.22 that these large discrepancies exist in a much wider region, probably causing the large frequency differences displayed in the bottom panel of Fig. 7.19. As we said in the previous section of this Chapter, these errors at the surface may, in part, be from a numerical origin and some hope exists that they could be reduced with no need to increase n_θ or the maximum order of the Legendre decomposition. More generally, if we compare each corresponding plot in both figures, we see that the relative errors are almost 100 times higher for the $1.6M_\odot$ models than the $1M_\odot$ ones. In addition, in Fig. 7.21 we see that, very often, the structure of models with $n_\theta = 128$ and 200 agree significantly better with the reference model than models with lower n_θ. In Fig. 7.22, the relative errors associated with models with $n_\theta = 128$ and 200 are always almost of the same order as the models with lower n_θ.

What are the take away from this last section? First, the 2D version of CESTAM seems to give pretty reliable deformed structures and frequency spectra provided that the modelled star is a slow rotators ($\Omega \lesssim 10\%\ \Omega_{\rm K}$) and that $n_\theta > 50$. Second great care should be taken when modelling fast rotators. Choosing to decompose quantities up to $\ell_{\max} = 2$ implicitly amounts to saying that higher order components are very small compared with the lower ones. This

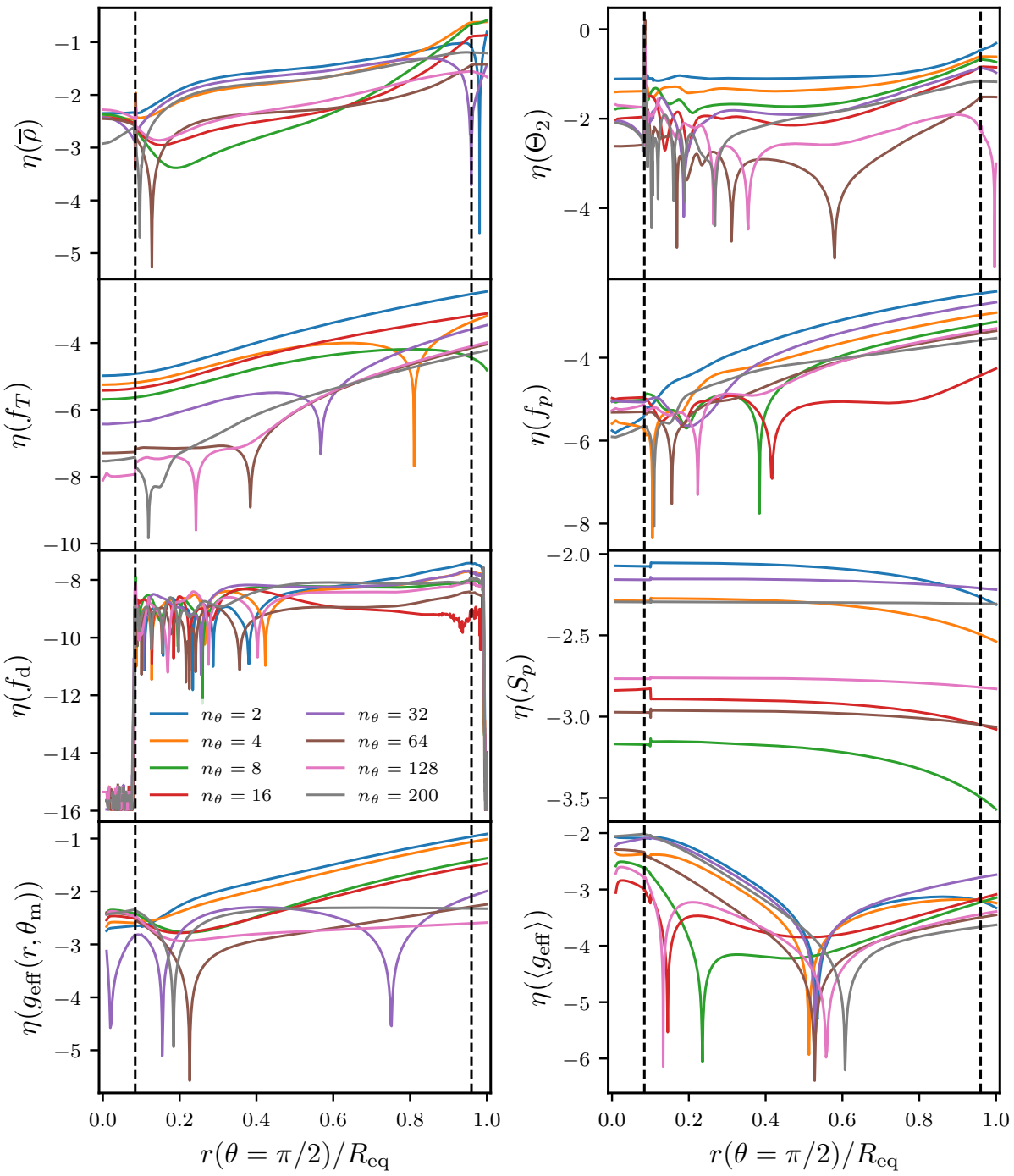

Figure 7.22: Comparison of quantities related to the 2D geometry computed with a varying n_θ. The colours code for n_θ and their meaning is given in the legend of left panel in the 3$^{\rm rd}$ row. In all the subplots, η defines the relative variation of a quantity x as $\eta(x) = \left|(x^{n_\theta} - x^{n_\theta=240})/x^{n_\theta=240}\right|$. In the top right panel, $\eta(\Theta_2)$ is not significant outside the convective zone boundaries because in the present case of shellular rotation, $\widetilde{\rho_2} = 0$ in the convective zones.

hypothesis should be tested and the precision of the modelling adapted to specific situations. However, CESTAM now allows great refinements of the description of the geometry.

7.2 Validation of the new transport of angular momentum prescription

Now that the deformation module has been thoroughly tested, we can move to the second part of CESTAM's new skills: the new prescription for the transport of angular momentum (AM) supported by some insight in the 2D geometry obtained with the deformation method. This new prescription cannot be used without the deformation module. Moreover, the computation of degrees $\ell > 2$ for U_ℓ and Ω_ℓ cannot rely on crude approximations but must take advantage of the fine description of the 2D geometry allowed by the Roxburgh (2006)'s method. Therefore, the models computed with the old transport of AM prescription and without deformation will be often referred to as 1D models and the ones with the new transport of AM and the deformation will be called 2D models. We start by checking that the AM is well conserved and then we present some results and a comparison with the models computed with the old version of CESTAM.

7.2.1 Conservation of angular momentum

Similarly to the previous section, one needs to verify that our method for the resolution of the equations for the meridional circulation velocity and transport of AM does conserve AM. This time, there is no need to check that mass is conserved because this method does not modify internal structure. Again, we computed a grid of models computed with the old and with the new prescription of transport of angular momentum. Each pairs of 1D and 2D models have the same initial conditions, except for the treatment of the rotation. Models computed with old version of CESTAM use the formalism of Talon et al. (1997) (hereafter T97) and of course, no deformation. The models computed with the new version incorporate the deformation and the model of transport of AM developed by Mathis & Zahn (2004) (hereafter M04) which will allow us to compute terms with $\ell > 2$. The main global parameters of this grid are summarized in Table 7.3.

The differences between the formalism of T97 and M04 are the following. M04 developed an expression for the coefficients U_ℓ, Ω_ℓ, etc., for any $\ell \geq 2$, while T97 stopped at $\ell = 2$. M04 also tried to make the resolution of there expressions less sensitive to sharp composition gradients, numerically speaking. Therefore, the expressions found in M04 only depend on derivatives of Ψ_ℓ, while the one in T97 depends on both $\partial\Theta_\ell/\partial r$ and $\partial\Lambda_\ell/\partial r$. In addition, in M04, only the Schwarzschild criterion appears ($\nabla_{\rm ad} - \nabla$), while T97 introduce Ledoux's criterion ($\nabla_{\rm ad} - \nabla + \varphi\nabla_\mu/\delta$). Last but not least, T97 uses an approximation for the fluctuations of the gravity:

$$\frac{\widetilde{g}_\ell}{\overline{g}} \simeq \frac{4}{3}\left(\frac{\Omega^2 r^3}{\mathcal{G}M}\right) \tag{7.14}$$

While M04 provide a full expression, for any $\ell \geq 2$ in the case of shellular profile. In our case we use the value provided by the deformation module and in the near future, we will add the possibility to compute higher order terms ($\ell > 2$.

It must be noted that we did not solve the equations for Ω_2 and $\partial\Omega_2/\partial r$ because our algorithm is not stable enough for the moment. It suffers from the so-called $2\Delta x$ *oscillations*.

Table 7.3: Small grid containing 20 models. Half of them are computed with the old approach, using Talon et al. (1997) formalism of transport of angular momentum and the other half is computed with deformation and Mathis & Zahn (2004) formalism. The initial disk lifetime is 5 Myr for all models and there are no wind-induced loss of angular momentum. The 2D models use 240 angular sectors (without counting the ghost angles) and $\ell_{\max} = 2$. The quantity X_c is the abundance of hydrogen at the centre. The radius $R_\star$ is the radius of th star taken at the characteristic angle θ_m.

Model	M $M_\odot$	$P_{\rm disk}$ days	Geom-etry	$t_{\rm final}$ Gyr	$\Omega(t_{\rm final})$ % $\Omega_{\rm K,surf}$	X_c	$T_{\rm eff}$ K	$R_\star$ $R_\odot$	$\log \frac{L}{L_\odot}$
M08P03G1D	0.8	3	1D	14	11.82	0.267	5120	0.82	−0.3
M08P03G2D	0.8	3	2D	14	13.66	0.274	5053	0.83	−0.4
M08P10G1D	0.8	10	1D	14	3.86	0.264	5137	0.82	−0.38
M08P10G2D	0.8	10	2D	14	3.87	0.267	5128	0.82	−0.38
M10P03G1D	1.0	3	1D	4.57	18.89	0.386	5746	1.00	−0.01
M10P03G2D	1.0	3	2D	4.57	19.74	0.390	5660	1.03	−0.01
M10P10G1D	1.0	10	1D	4.57	5.50	0.382	5777	1.00	0.00
M10P10G2D	1.0	10	2D	4.57	5.49	0.385	5768	1.00	−0.00
M15P05G1D	1.5	5	1D	2.5	21.84	0.0	5929	2.94	0.98
M15P05G2D	1.5	5	2D	2.5	24.54	0.0	5885	2.98	0.98
M15P10G1D	1.5	10	1D	2.5	9.60	0.0	5875	2.96	0.97
M15P10G2D	1.5	10	2D	2.5	6.58	0.0	5544	3.03	0.89
M20P06G1D	2.0	6	1D	1.026	5.68	0.0	4796	7.75	1.46
M20P06G2D	2.0	6	2D	1.026	8.08	0.0	5034	4.88	1.14
M20P10G1D	2.0	10	1D	0.546	26.93	0.418	8636	1.99	1.29
M20P10G2D	2.0	10	2D	0.545	27.66	0.425	8631	1.99	1.29
M25P04G1D	2.5	4	1D	0.539	6.29	0.0	4757	11.16	1.76
M25P04G2D	2.5	4	2D	0.539	67.52	$2.5 \cdot 10^{-04}$	9306	3.23	1.85
M25P13G1D	2.5	13	1D	0.508	38.09	$1.0 \cdot 10^{-05}$	9463	3.10	1.84
M25P13G2D	2.5	13	2D	0.508	40.52	$1.9 \cdot 10^{-02}$	8657	3.36	1.76

The equation for the radial derivative of Ω_2 is (see Eq. (6.87))

$$E_{6,k} = \frac{1}{2}(\Omega_{2,k} + \Omega_{2,k-1}) - \frac{\Omega_{2,k} - \Omega_{2,k-1}}{m_k - m_{k-1}} = \overline{\Omega_{2k}} - \frac{\partial \Omega_2}{\partial m} = 0, \tag{7.15}$$

supplemented by the boundary conditions $\partial\Omega_2/\partial m|_{\rm top/bottom} = 0$. Generally $\overline{\Omega_{2k}} \simeq 0$ because the shellular approximation seems well verified. Therefore, we have $\Omega_{2,k} - \Omega_{2,k-1} \simeq 0$. A simple solution to this equation is $\Omega_{2,k} = (-1)^k a$ and $\Omega_{2,k-1} = (-1)^{k-1} a$, with a, *any* real. Therefore, consecutive values of Ω_2 oscillates between a and $-a$, from one grid point to the other. A wavy pattern in the variable $\partial\Omega_2/\partial m$ translates into a wavy pattern in the solution of Ω_2. If $\overline{\Omega_2}$ is not almost 0, the equation $\Omega_{2,k} - \Omega_{2,k-1} \simeq \overline{\Omega_2} \neq 0$ would also accept an oscillation solution, but the boundary condition prevents this solution from being accepted. Nonetheless, during the main-sequence we have seen that an approximate (algebraic) equation is verified by Ω_2:

$$\nu_{\rm h}\Omega_2 = \frac{1}{5} r \left[2V_2 - \alpha U_2\right] \overline{\Omega}, \tag{7.16}$$

which allows us to retrieve a value for Ω_2 a posteriori. We will show some results for Ω_2 at the end of this section.

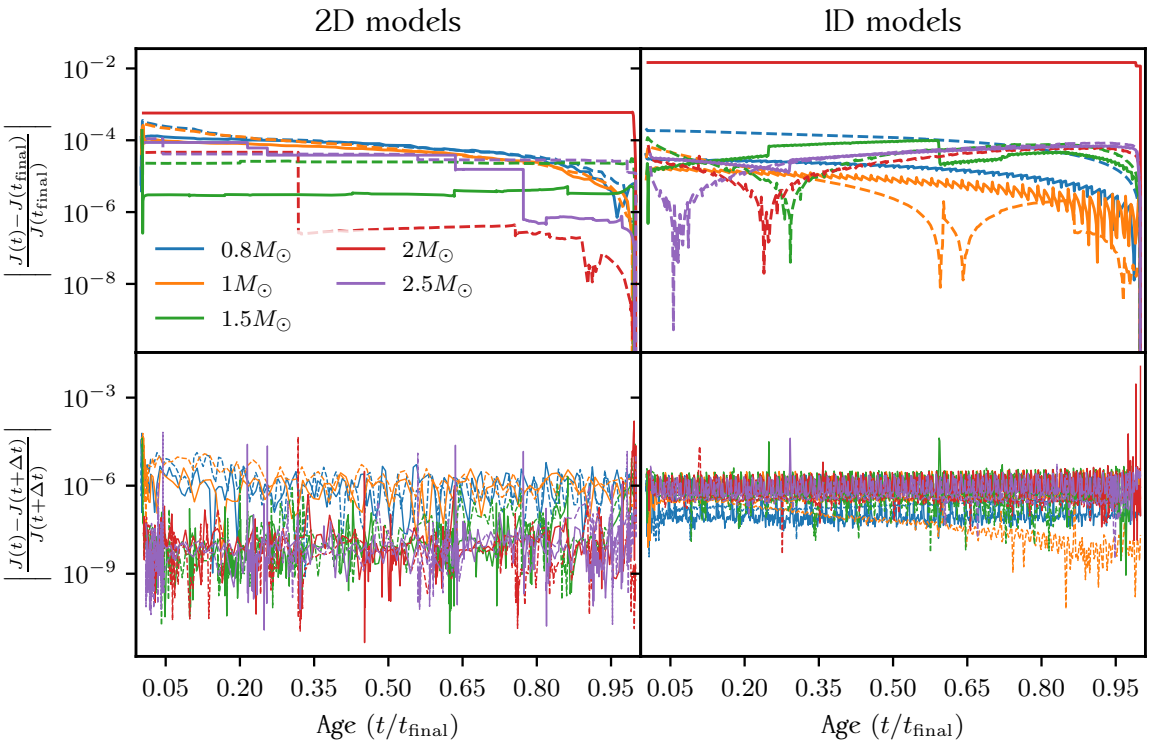

Figure 7.23: Angular momentum conservation with the new transport of angular momentum prescription. The models are the ones presented in Table 7.3. For all panels, the plotted quantities are function of the stellar age normalized to final age. The colours code for the mass of the models. Models with $P_{\rm disk} = 10$ with dotted-dashed lines and $P_{\rm disk} = 3$ days with dashed lines. The total angular momentum of the star is $J = \int_0^{R_\star} r^2 \Omega {\rm d}m$. Refer to Table 7.3 for more detail on the initial conditions. *Top left:* Absolute value of the relative variations between angular momentum at time t to angular momentum at $t_{\rm final}$, in 2D models. *Top right:* Same as in top left panel but with 1D models. *Bottom left:* Absolute value of the relative variations between angular momentum at time t to angular momentum at $t + \Delta t$, in 2D models. *Bottom right:* Same as in bottom left panel but with 1D models.

7.2.2 Comparison with the old version of CESTAM

The goal with this section is to present the main differences obtained when computing models with identical initial parameters but different treatment of the rotation. To begin, we can just take a look at the global parameters gathered in Table 7.3. Models have been computed for five different masses and different initial rotation conditions. The final age is not necessarily the same for all models with the same mass.

Central hydrogen abundance

Let us first focus on core hydrogen abundance $X_{\rm c}$. Table 7.3 shows that 2D models have always a larger $X_{\rm c}$ that 1D models. The gap is also more pronounced with initially fast rotators. We recall that rotation modifies structure equations, especially by the inclusion of a factor f_T/f_p (see Eqs. (1.72) and (1.85)) in the expression $\partial T/\partial m$ in radiative zones. In models computed with old approach of transport of AM, CESTAM is not able to compute f_T and f_P precisely and the pressure gradient is modified by the addition of an approximated centrifugal force:

$$\frac{\partial p}{\partial m} = -\frac{\mathcal{G}m}{4\pi r^4} + \frac{\Omega^2}{6\pi r}, \tag{7.17}$$

which also acts in the temperature gradient: $\partial T/\partial m = \partial p/\partial m(T\nabla/p)$. The temperature profiles resulting from the old and new approaches of the transport of angular momentum are very similar but differs by around 1% at the same age, 1D models being hotter. Since the nuclear generation rates heavily depends on the temperature, a difference of core temperature of 1% can produce noticeable changes in the core chemical composition after few Gyr of evolution. The 2D models being slightly cooler, nuclear reactions in their core are slightly less efficient leading to a higher $X_{\rm c}$ than in the 1D model of same age.

One could have argued that this difference of $X_{\rm c}$ comes from a different meridional circulation velocity obtained with the old and new transport of AM. Indeed, in addition to advecting angular momentum, meridional circulation is also responsible for an advection of chemicals (see Eq. (2.56)). During the main sequence, the advection can be treated as a diffusion process. Its influence appears through the expression (2.57) of the effective diffusion coefficient $D_{\rm eff}$:

$$D_{\rm eff} = \sum_{\ell>0} \frac{r^2 U_\ell^2}{\ell(\ell+1)(2\ell+1))D_{\rm h}} \overset{\ell=2}{=} \frac{r^2 U_2^2}{30 D_{\rm h}}. \tag{7.18}$$

In the equation for the transport of chemicals, the term of diffusion by shears and effective diffusion by meridional circulation is of the form:

$$\frac{1}{r^2}\frac{\partial}{\partial r}\left[r^2\rho(D_{\rm v}+D_{\rm eff})\frac{\partial \overline{c_i}}{\partial r}\right], \tag{7.19}$$

(see Eq. (2.56)). What is the dominant term ? Our simulations show that $D_{\rm eff}$ is actually 3 to 4 orders of magnitude lower than $D_{\rm v}$ in main-sequence stars. Moreover, $|U_\ell|$ and $D_{\rm eff}$ is often found higher with the old than with the new approach (see Figs. 7.24 and 7.27), which is incompatible with the idea that the meridional circulation would be responsible for the large $X_{\rm c}$ in 2D models.

Is this idea also ruled out in more evolved stars? Equation (2.56) has been derived assuming the star is slowly evolving and the characteristic time-scale of horizontal diffusion $r^2/D_{\rm h}$ is much shorter than the evolution time-scale. When this approximation is not valid, the time derivative in Eq. (2.54) must not be neglected and the equation of transport of the mean chemical abundances per unit mass becomes:

$$\rho\frac{{\rm d}\overline{c_i}}{{\rm d}t} + \frac{1}{r^2}\frac{\partial}{\partial r}\left(r^2\rho\sum_{\ell>0}\frac{\widetilde{c}_{i\ell}U_\ell}{2\ell+1}\right) + \frac{1}{r^2}\frac{\partial}{\partial r}\left(r^2\rho\overline{c_i}U_i^{\rm diff}\right) = \frac{1}{r^2}\frac{\partial}{\partial r}\left(r^2\rho D_{\rm v}\frac{\partial\overline{c_i}}{\partial r}\right). \tag{7.20}$$

The first row of Fig. 7.25 do not show striking differences in the magnitude of the meridional circulation velocities obtained with old and new approaches of the transport of AM. It is more probable that the difference of $X_{\rm c}$ is the result of the gap in hydrogen abundance dug during the main-sequence.

Density fluctuations over isobars

Regarding the 2nd order fluctuations of the density, the computations with the new and old prescriptions for the transport of AM produce different results. They are displayed in the 2nd row of Fig. 7.24 and 7.25. We denote by $\Theta_2^{\rm new}$ (resp. $\Theta_2^{\rm old}$) the value of Θ_2 computed with the new (resp. old) approach. Going from the bottom of the radiative zone to its top (from left to right), $\Theta_2^{\rm new}$ and $\Theta_2^{\rm old}$ start with quite noisy patterns that are very comparable in terms of magnitude and extent. $\Theta_2^{\rm new}$ then remains almost constant until a sharp peak that marks the change of sign due to the change of sign of ${\rm d}\overline{\Omega}/{\rm d}r$. Right above this region, $\Theta_2^{\rm new}$ keeps increasing by one or two orders of magnitude until the top boundary of the radiative zone. On

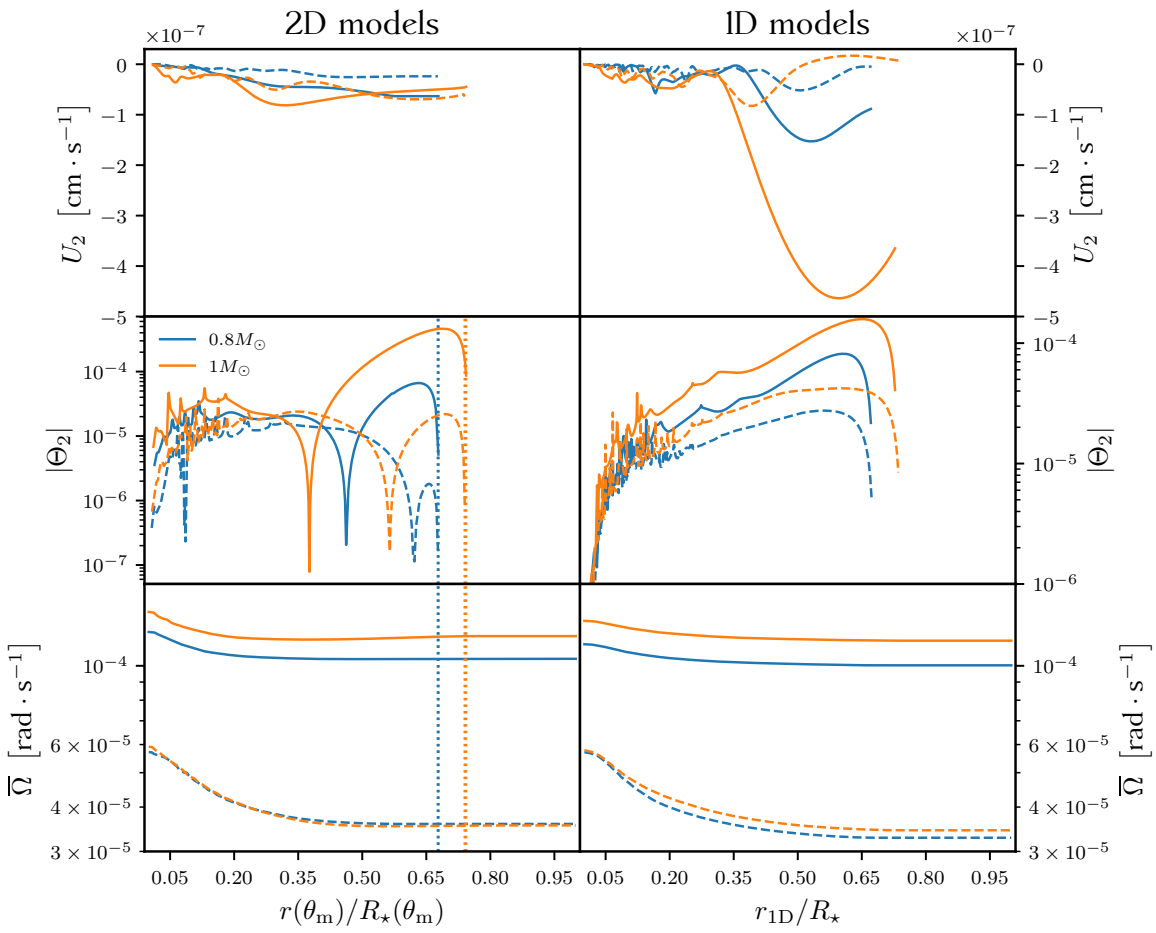

Figure 7.24: The models used in this figure are the $0.8M_\odot$ (blue) and $1M_\odot$ (orange) models presented in Table 7.1. 1st and 2nd column are respectively devoted to quantities in models computed with old and new versions of CESTAM. All quantities are represented as a function of the normalized radius (along θ_m in the case of the 2D models). The 1st row displays the radial velocity of the meridional circulation in the radiative zone. The 2nd row displays the the fluctuations of density $\Theta_2 = \widetilde{\rho}_2/\overline{\rho}$ (only in the radiative zone for the 1D models). The 3rd row is the angular velocity. For each stellar mass, we have computed an initially fast (solid lines) and slow rotator (dashed lines). Refer to Table 7.3 for more detail on the initial conditions. Vertical dashed lines mark the location of the tachocline.

the contrary, $\Theta_2^{\rm old}$ keeps increasing at a regular rate from the bottom to the top of the radiative zone. Both $\Theta_2^{\rm new}$ and $\Theta_2^{\rm old}$ drop to 0 at the very top. After the tachocline, $\Theta_2^{\rm new}$ and $\Theta_2^{\rm old}$ are 0 because of the hypothesis of shellular rotation.

The reason for these differences is that we are not solving the same equations. The coefficient $\Theta_2^{\rm old}$ is computed using the approximation

$$\Theta_2 = \frac{1}{3}\frac{r^2}{\overline{g}}\frac{\partial \Omega^2}{\partial r}, \tag{7.21}$$

proposed by Zahn (1992). This expression is actually the first order term of a more complex expression proposed by Mathis & Zahn (2004) and reproduced in Eq. (6.91). It includes higher order terms such as $\overline{\Omega}\,\Omega_2$ and $\partial(\overline{\Omega}\,\Omega_2)/\partial r$. This description is derived assuming a shellular rotation profile. And Θ_2 may not have the same functional form if rotation is not shellular. Furthermore, the solution for $\Theta_2^{\rm old}$ is strongly affected by the boundary condition at the top of

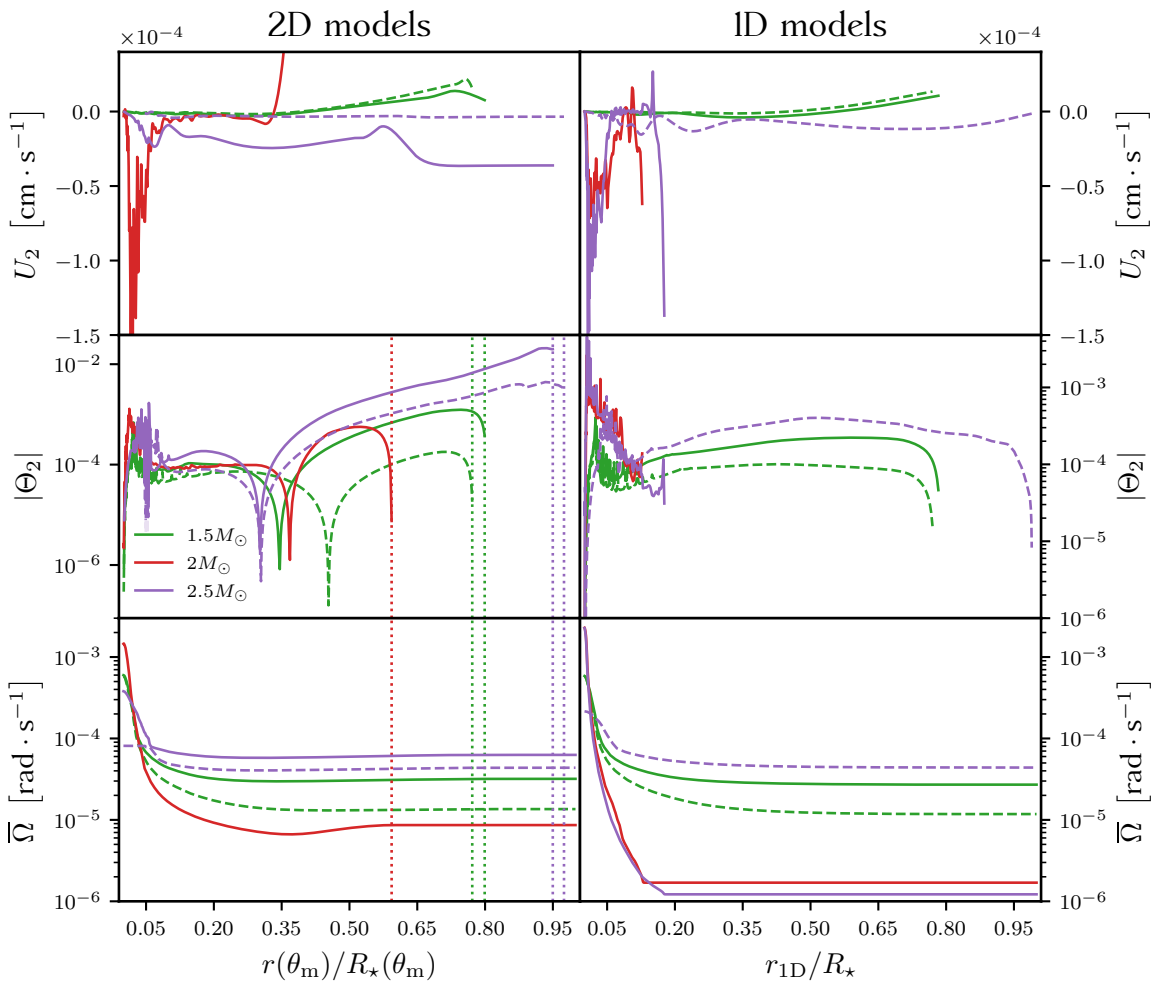

Figure 7.25: The models used in this figure are the $1.5M_\odot$, $2M_\odot$ and $2.5M_\odot$ models presented in Table 7.1. See caption of Fig. 7.24 for a description of this figure..

the radiative zone: $\Theta_2^{\rm old} = 0$. This is neither confirmed by the results from Roxburgh (2006)'s method nor justified physically. It is a suitable choice.

Our approach is different. Let me remind you how we proceed. Our treatment of rotation in the new version of CESTAM is separated into two parts.

- *(i)*: in the first part we solve the structure equations, then we solve our system of equations (with unknowns U_2, Υ_2, $\overline{\Omega}$ and $\partial\overline{\Omega}/\partial m$) and we iterate until convergence.
- *(ii)*: the second part starts at this point and we deform the 1D model by finding $\widetilde{\rho}_\ell$, $\widetilde{\phi}_\ell$, $\widetilde{g}_{{\rm eff},\ell}$, etc.

For the computations of the first part, $\Theta_2 = \widetilde{\rho}_2/\overline{\rho}$ is needed and its value is known at the previous time step. The assumption that Θ_2 does not vary much from one time step to the next is a good approximation, and we may use it. With such a choice, the differential equations that provide U_2 and Υ_2 do not depend on $\overline{\Omega}$ and are decoupled from the system of equations for $\overline{\Omega}$ and $\partial\overline{\Omega}/\partial m$ (see discussion in Sect. 6.3.4). Therefore we choose to approximate Θ_2 by Eq. (7.21), only in the computations of the first part *(i)*. Despite being very different from the "unapproximated" value of Θ_2, it has little impact on the value of U_2 because it is not in factor

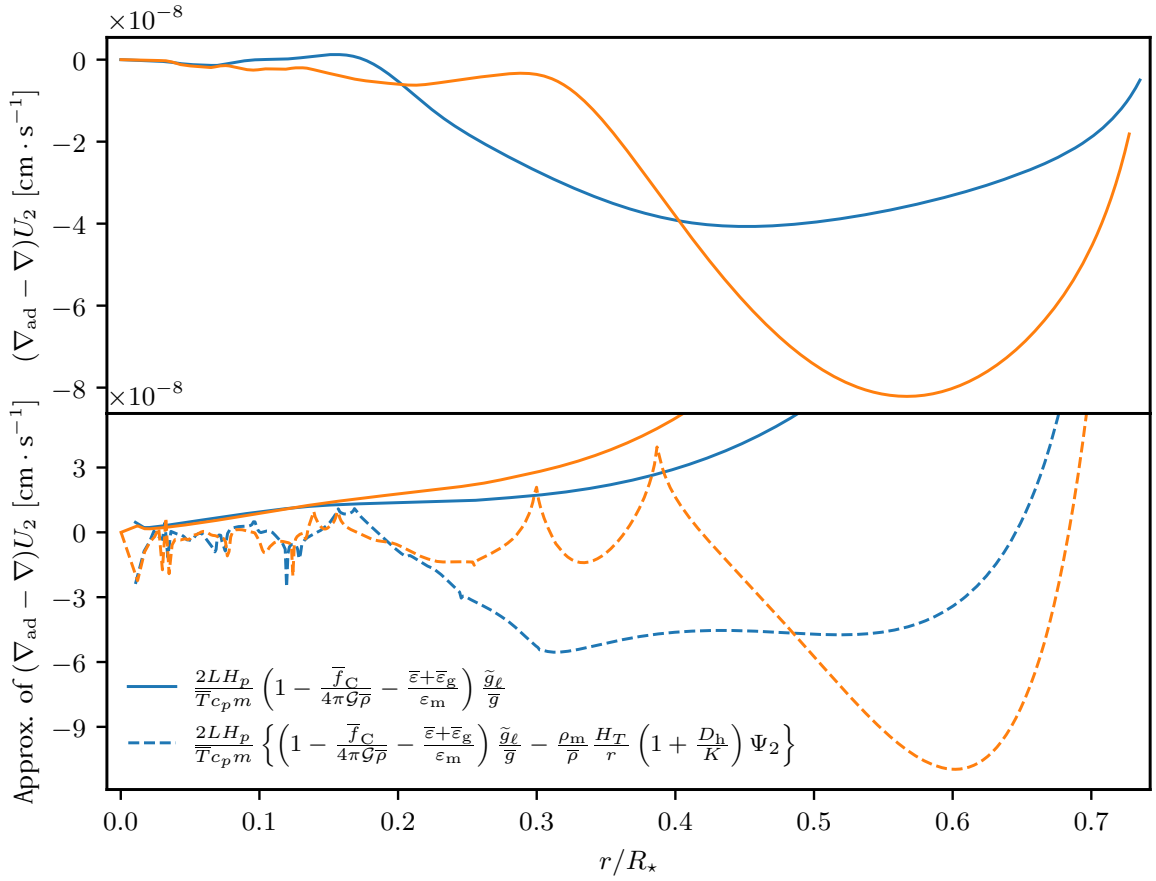

Figure 7.26: Approximation of the radial velocity of the meridional circulation. The models used to produce this Figure are models `M10P03G1D` (blue lines) and `M10P03G2D` (orange lines) of Table 7.1. All quantities are function of the radius normalized to the surface radius and represented only in the radiative zone. *Top*: Velocity $(\nabla_{\rm ad}-\nabla)U_2$ (the term in parenthesis is dimensionless) in the radiative zone as a function of normalized radius. *Bottom*: Approximation of $(\nabla_{\rm ad}-\nabla)U_2$ by the expressions written in the labels.

of the first order term. The values of $\Theta_2^{\rm new}$ presented in Figs. 7.24, 7.25 and 7.27 are the one computed with the method developed by Roxburgh (2006).

Radial velocity of the meridional circulation

It appears from the meridional velocity profiles presented in Fig. 7.24 and 7.25 that the magnitude of U_2, especially close to the tachocline are often computed smaller with the new than with the old approach of the transport of angular momentum. To get a clearer picture, we focus on the $1M_\odot$, initially fast rotating, models (`M10P03G1D` and `M10P03G2D`; see Table 7.1). The value of $(\nabla_{\rm ad}-\nabla)\,U_2$ are displayed in Fig. 7.26, as well as two approximations for this quantity. Various quantities relevant to the understanding of the variations of the meridional circulation velocity in these models are displayed in Fig. 7.27. Let us recall the expressions of the meridional circulation velocity given in Eqs. (2.105) and (2.106):

$$U_\ell \;=\; \frac{LH_{\rm p}}{\overline{T}c_pm\,(\nabla_{\rm ad}-\nabla)}\left\{2\left(1-\frac{\overline{f}_{\rm C}}{4\pi\mathcal{G}\overline{\rho}}-\frac{\overline{\varepsilon}+\overline{\varepsilon}_{\rm g}}{\varepsilon_{\rm m}}\right)\frac{\widetilde{g}_\ell}{\overline{g}}+\frac{\widetilde{f}_{{\rm C},\ell}}{4\pi\mathcal{G}\overline{\rho}}-\frac{\overline{f}_{\rm C}}{4\pi\mathcal{G}\overline{\rho}}\Theta_\ell\right.$$

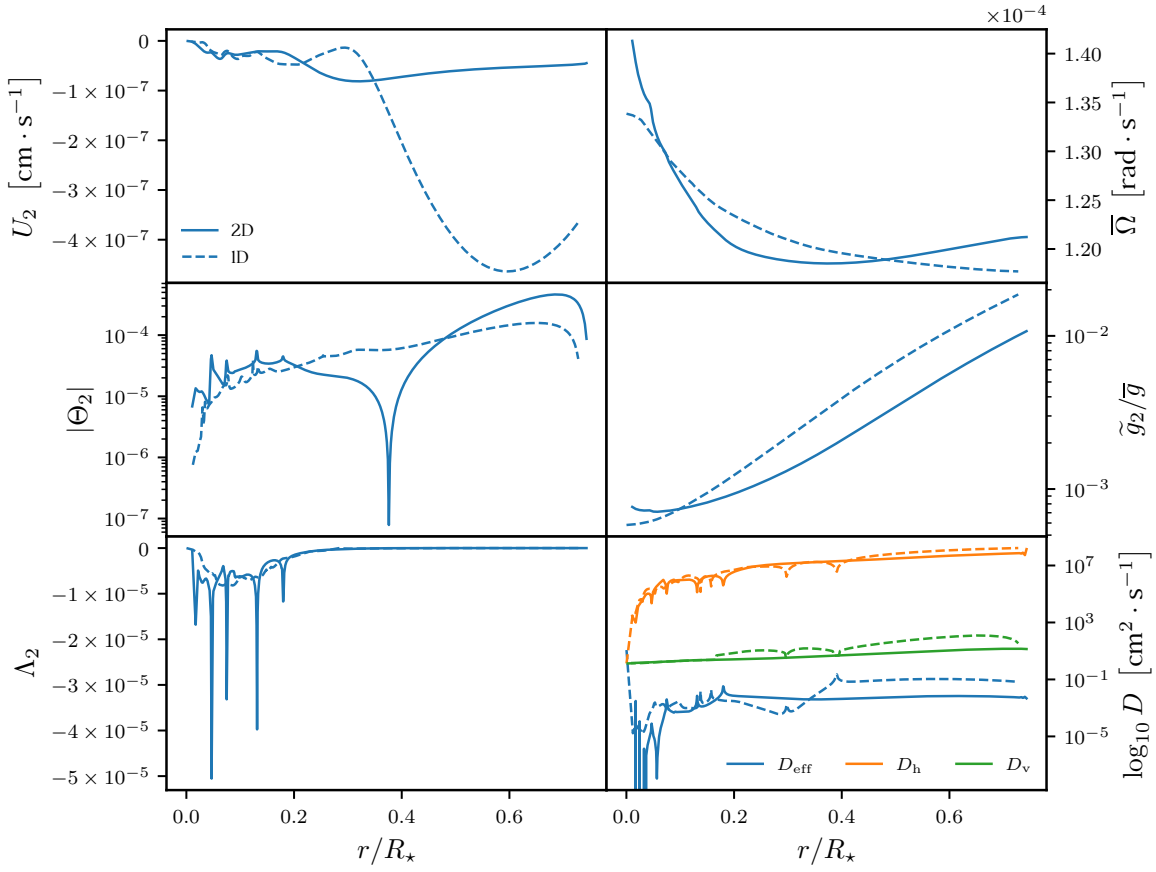

Figure 7.27: Quantities relevant to understanding the profile of meridional circulation during the MS. The models used to produce this Figure are models `M10P03G1D` and `M10P03G2D` of Table 7.1. All quantities are function of the radius normalized to the surface radius and represented only in the radiative zone, even if some of them are also known outside. Solid and dashed lines correspond respectively to quantities from the models computed with the new and old versions of CESTAM. *Top left*: 2$^{\rm nd}$ order component of the meridional circulation U_2. *Top right*: Angular velocity $\overline{\Omega}$. *Middle left*: 2$^{\rm nd}$ order component of the density fluctuation Θ_2. *Middle right*: 2$^{\rm nd}$ order component of the gravitational acceleration fluctuation $\widetilde{g}_2/\overline{g}$. *Bottom left*: 2$^{\rm nd}$ order component of the mean molecular weight fluctuation Λ_2. *Bottom right*: Diffusion coefficients $D_{\rm eff}$ (blue), $D_{\rm h}$ (orange) and $D_{\rm v}$ (green).

$$
\begin{aligned}
&+ \quad \frac{\rho_{\rm m}}{\overline{\rho}}\left[\frac{r}{3}\frac{\mathrm{d}}{\mathrm{d}r}\left(H_{\rm T}\frac{\partial\Psi_\ell}{\partial r}-(1-\delta+\chi_T)\,\Psi_\ell-(\varphi+\chi_\mu)\,\Lambda_\ell\right)-\frac{\ell(\ell+1)H_{\rm T}}{3r}\left(1+\frac{D_{\rm h}}{K}\right)\Psi_\ell\right]\\
&+ \quad \frac{\overline{\varepsilon}+\overline{\varepsilon}_{\rm g}}{\varepsilon_{\rm m}}\left[\left(H_{\rm T}\frac{\partial\Psi_\ell}{\partial r}-(1-\delta+\chi_T)\,\Psi_\ell-(\varphi+\chi_\mu)\,\Lambda_\ell\right)+(f_\varepsilon\varepsilon_T-f_\varepsilon\delta+\delta)\,\Psi_\ell\right.\\
&+ \quad \left.(f_\varepsilon\varepsilon_\mu+f_\varepsilon\varphi-\varphi)\,\Lambda_\ell\right]-\overline{T}c_p\left[\frac{\mathrm{d}\Psi_\ell}{\mathrm{d}t}+\Phi\frac{\mathrm{d}\ln\overline{\mu}}{\mathrm{d}t}\Lambda_\ell\right]\Bigg\}. \qquad (7.22)
\end{aligned}
$$

for simplicity, we dropped the p-subscripts on m and L.

The behaviour of the radial velocity of the meridional circulation is well approximated by

the sum of two terms:

$$\underbrace{\left(\nabla_{\rm ad}-\nabla\right)}_{(i)}U_2 \simeq \underbrace{\frac{2LH_{\rm p}}{\overline{T}c_p m}}_{(ii)}\left\{\underbrace{\left(1-\frac{\overline{f}_{\rm C}}{4\pi\mathcal{G}\overline{\rho}}-\frac{\overline{\varepsilon}+\overline{\varepsilon}_{\rm g}}{\varepsilon_{\rm m}}\right)\overbrace{\frac{\widetilde{g}_\ell}{\overline{g}}}^{(iv)}}_{(iii)}-\underbrace{\frac{\rho_{\rm m}}{\overline{\rho}}\frac{H_{\rm T}}{r}\left(1+\frac{D_{\rm h}}{K}\right)\Psi_\ell}_{(v)}\right\}. \tag{7.23}$$

We moved the difference of gradients $(\nabla_{\rm ad}-\nabla)$ to the other side because otherwise it would reach zero in the denominator at the transition between the radiative and the convective zones. The quantities $\nabla_{\rm ad}$ and ∇ are dimensionless therefore the left hand side of Eq. (7.23) is still a radial velocity. In addition, the multiplication by $(\nabla_{\rm ad}-\nabla)$ do not change the general variations of U_2 (at least in our particular case. Term $(ii)\times(iii)$ in Eq. (7.23) is sometimes called the *barotropic term* (Maeder, 2009) with the argument that it is the only term that exists in a barotropic star. However, this is not exact. In a barotropic star, Θ_ℓ are indeed zero[4], but $\Psi_\ell=\widetilde{T}_\ell/\overline{T}$ are zero if and only if $\Lambda_\ell=\widetilde{\mu}_\ell/\overline{\mu}$ is zero too. Moreover, even if this last condition is met, there remains the time derivative $\mathrm{d}\Psi_\ell/\mathrm{d}t$ which *cannot* be zero in a rotation star, as shown by the Von Zeipel paradox (see 2.2 and von Zeipel 1924). For simplicity, we keep the denomination of barotropic term.

In Eq. (7.23), term (i) is positive because we are in a radiative zone and $\nabla<\nabla_{\rm ad}$. Term (ii) is also positive and $\overline{g}$ and $\widetilde{g}_\ell$ are both negative therefore term (iv) is positive. During the main sequence, the quantity $\overline{\varepsilon}+\overline{\varepsilon}_{\rm g}$ is dominated the nuclear energy generation rate $\overline{\varepsilon}$ in the core. The denominator, $\varepsilon_{\rm m}$ is the average power per unit mass in a sphere. In the inner core, $\left(\overline{\varepsilon}+\overline{\varepsilon}_{\rm g}\right)/\varepsilon_{\rm m}\simeq 1$ (for $r<1\%R_\odot$ in our case). In this region, the Gratton-Öpik term $\overline{f}_{\rm C}/\left(4\pi\mathcal{G}\overline{\rho}\right)$ reaches a finite value. In the case of shellular rotation, the coefficient $\overline{f_{\rm C}}$ is[5]

$$\overline{f_{\rm C}}=\frac{2}{3r^2}\frac{\partial r^3\overline{\Omega}^2}{\partial r}=\frac{2}{3}\left(3\overline{\Omega}^2+2r\overline{\Omega}\frac{\partial\overline{\Omega}}{\partial r}\right). \tag{7.24}$$

Thus, the Gratton-Öpik term and therefore term $(ii)\times(iii)$ have a finite, very small value at the centre. It can be seen as a problem because it means a non-zero value of U_2 at this location, *i.e.*, matter flows out of the centre. Yet, this value is very small and $U_2=0$ at the centre can be imposed as a boundary condition. Approximation of $\left(\nabla_{\rm ad}-\nabla\right)U_2$ by only the first part of Eq. (7.23), *i.e.* $(ii)\times(iii)$. We see that for $r<0.15R_\star$, this approximation follows $\left(\nabla_{\rm ad}-\nabla\right)U_2$ pretty close but quickly diverges. This is caused by the fact that $\left(\overline{\varepsilon}+\overline{\varepsilon}_{\rm g}\right)/\varepsilon_{\rm m}$ decreases and reaches a value close to zero at $r\simeq 0.7R_\star$. On the other hand, the Gratton-Öpik term is still small in this region.

Toward the surface, when $\overline{\rho}$ become small, the Gratton-Öpik term becomes dominant. In this case, it can form an surface meridional cell rotating in the inverse direction as the inner cell. This situation is illustrated in Fig. 7.28 This figure represents stream plots of the meridional circulation velocity field in a $2.5M_\odot$ model at two different ages. On the left panel, the model is on the main sequence. We distinguish two cells, the inner one rotates from the poles to the equator which is the sign of a positive value of U_2. The outer one is rotating in the opposite direction, because of the negative Gratton-Öpik sign. On the right panel, the model in on the subgiant branch. its density is small in a large fraction of the star therefore the meridional circulation is negative on more extended region.

In Eq. (7.23), as long as we move toward the top of the radiative zone, the term (v) becomes dominant. It is part of a bigger term called the driving term, constituted of all the terms in

[4]Because isobars and isopycnals coincide.

[5]The divergence of centrifugal acceleration, decomposed in Legendre polynomials is $\overline{f_{\rm C}}+\sum_{\ell>0}\widetilde{f_{\rm C}}_\ell P_\ell(\cos\theta)$.

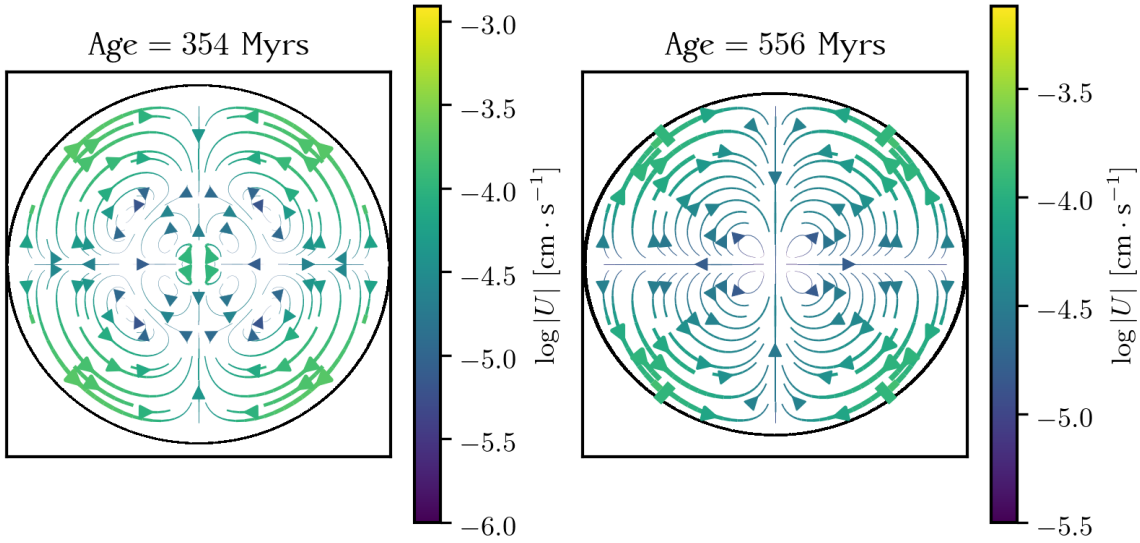

Figure 7.28: Stream plots of the meridional circulation velocity field in a $2.5M_\odot$ model (model `M25P04G2D` of grid presented in Table 7.3), at two different time steps. Stellar surface is represented with a solid black curve.

factor of Ψ_ℓ in Eq. (7.22). The approximation of $(\nabla_{\rm ad} - \nabla)\, U_2$ suggested in Eq. (7.23) is plotted for 1D and 2D models in bottom panel of Fig. 7.26. This approximation reproduce pretty well the variations of $(\nabla_{\rm ad} - \nabla)\, U_2$ showed in top panel of Fig. 7.26. In the variations of our approximation, we recognize the bumpy profile of the horizontal diffusion coefficient $D_{\rm h}$, also displayed in bottom right panel of Fig. 7.27. Of course, the other terms that we neglected smooth these variations and gives the profile of $(\nabla_{\rm ad} - \nabla)\, U_2$ presented in the top panel. The difference of magnitude in the profiles of meridional circulation at the top of the radiative zone is thus explained by the difference in the value of $D_{\rm h}$ between the models obtained with the old and new versions. We see in Fig. 7.27, that $D_{\rm h}^{\rm old}$ is higher by almost one order of magnitude compared to $D_{\rm h}^{\rm new}$.

Estimates of Ω_2

As mentioned above, our code is not stable enough for the moment when solving the equation of transport of angular momentum including Ω_2. However, we computed an estimate of Ω_2 *a posteriori* for the main sequence models with $M = 0.8M_\odot$ and $1M_\odot$ and the results are displayed in Fig. 7.29. The estimates are computed using the relation $\nu_{\rm h}\Omega_2 = \frac{1}{5} r\,[2V_2 - \alpha U_2]\,\overline{\Omega}$. The fluctuations Ω_2 of the angular velocity are around 10^{-8} rad s^{-1} and can peak at $\sim 5 \times 10^{-8}$ rad s^{-1}, while the angular velocity $\overline{\Omega}$ is of order $10^4 - 10^5$ rad s^{-1}. These values are compatible with the hypothesis of shellular rotation profile: $\Omega_2 \ll \overline{\Omega}$. Of course, this approximation should be tested in more detail with a full calculation of Ω_2.

Computation of higher orders $\ell > 2$

As explained in Chapter 6, the new method we implemented for the transport of angular momentum is currently able to compute only 2$^{\rm nd}$-order terms U_2, Υ_2 (see Eq. (2.107)), and $\overline{\Omega}$. However, the structure of the algorithm has been designed to be easily modified if one wants to compute higher order terms U_4, Υ_4, Ω_2, etc. Higher order of Θ_ℓ are of course made available by the deformation module and, assuming that the fluctuations of mean molecular weight Λ_ℓ

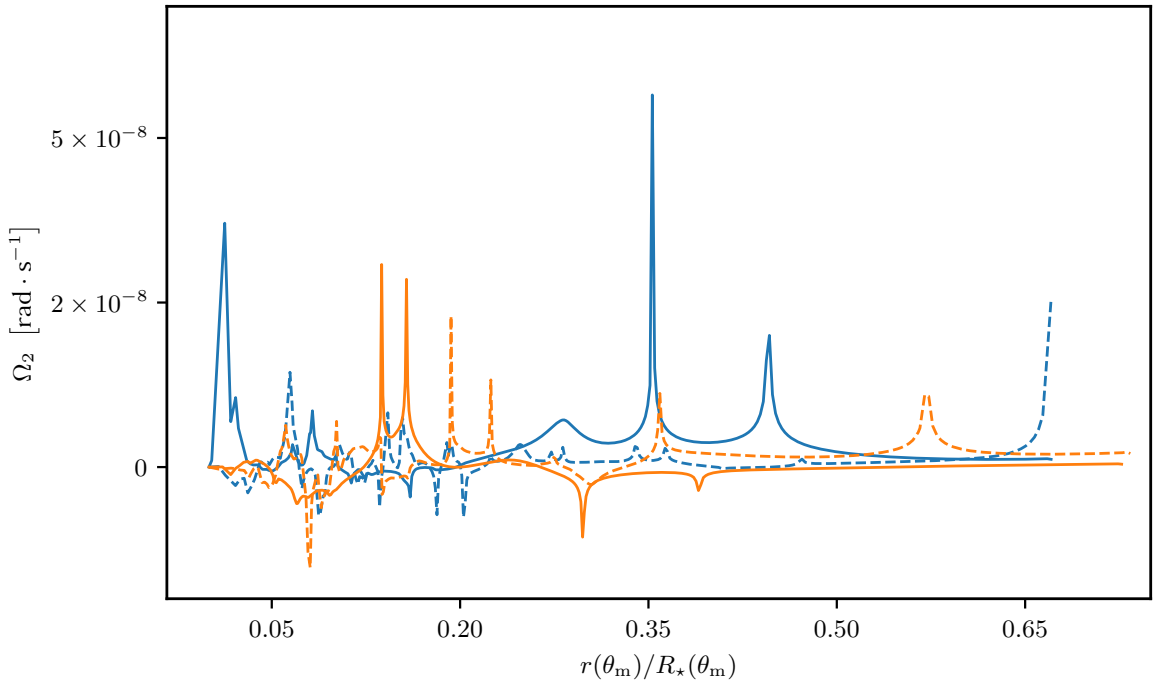

Figure 7.29: Estimates of Ω_2 with the new version of CESTAM in MS models in the radiative zone as a function of the normalized radius. The colours code for the mass of the models: $0.8M_\odot$ (blue), $1M_\odot$ (orange). Vertical dashed lines mark the location of the transition between radiative and convective envelopes. For each stellar mass, we have computed an initially fast (solid lines) and slow rotator (dashed lines). Refer to Table 7.3 for more detail on the initial conditions.

Table 7.4: Time consumption required by the deformation module on a $1.6M_\odot$ model. The integer N_θ is the number of angular sector (without counting the three ghost angles), the operator $\langle\cdot\rangle$ stand for the average along all the evolution, $\langle N_{\rm it}\rangle$ is the average number of iteration needed by the deformation module to converge to the deformed structure, τ is the time needed to perform a single iteration and $\tau_{\text{all its}}$ is the time needed to perform all iteration until convergence (usually 3 or 4). Finally $\tau_{\rm deform}$ is the total time spent in the deformation module at a given time step. It includes the time needed to iterate towards the solution of $\widetilde{\rho}_\ell$, $\widetilde{\phi}_\ell$ but also the time needed to compute $\mathbf{g}_{\rm eff}$, f_p, f_T, etc.

Model	N_θ	$\langle N_{\rm it}\rangle$	$\langle\tau_{\rm it}\rangle$ [s]	$\langle\tau_{\text{all its}}\rangle$ [s]	$\langle\tau_{\rm deform}\rangle$ [s]
NT2	2	2.75	0.03	0.19	0.34
NT4	4	3.87	0.08	0.40	0.71
NT8	8	3.90	0.09	0.42	0.75
NT16	16	3.80	0.11	0.49	0.86
NT32	32	3.85	0.15	0.63	1.06
NT64	64	3.81	0.22	0.87	1.43
NT128	128	3.81	0.38	1.41	2.27
NT240	240	3.81	0.63	2.20	3.51

are negligible compared with Θ_ℓ, higher order of the fluctuations of temperature can readily be computed. In order to do so, we need to derive the Jacobian of the new system that needs to be solved. This task is currently ongoing and presents no particular mathematical difficulty. The new results will require some testing (the implementation of the version in which only Ω_2 is added to the unknowns is pretty well advanced). CESTAM will be the first stellar evolution code to be able to compute these terms.

7.3 Additional computational time and memory usage

7.3.1 Use of numerical resources by the deformation module

What usually hinders the use of higher dimensional simulations is the additional time consumption they induce. Stellar evolution models need to be computed rapidly so that they provide the main feature of the stellar-structure, stellar rotation profile, etc. for thousands of stars observed by space missions. We cannot afford spending days or weeks calculating models for each of them. One of the great advantages of our method is that it does not lead to a significant increase of the time consumption. We measure the average time needed to deform a $1.6M_\odot$ model as a function of the number of angular sectors used in the angular mesh and with the Legendre decomposition stopped at P_2. Our results are reproduced in Table 7.4. The average number of iterations needed to converge to the correct deformed structure rapidly converge toward 3.81 while the number of angular sector increases. Noteworthy, the number of iterations can increase for old models. The evolution is stopped if $N_{\rm it}$ exceeds 42. Fortunately, such cases are really rare. These models were evolved until 200 Myr so that the model NT2 took around 14 min to compute and 31 min for NT240. As a comparison, the same model but with no rotation needs around 4 min 30 s to compute and around 14 min also for a model with rotation but in 1D. It may seem important but for $N_\theta = 240$ it only double the computation time, while a full 2D computation of evolution (which anyway does not exist) would take a time orders of magnitude higher.

On the side of memory usage, the change to two dimensions increases by around one or two order of magnitudes the size of output files. If the number of angular sectors needed is

Table 7.5: Time needed to compute a $1M_\odot$ with old or new treatment of the transport of angular momentum. The computation time is measured for two age: 4570 Myr and 12 000 Myr.

Age	Time (old)	Time (new)
4570 Myr	28 min	11 min
12 000 Myr	2 h 15 min	23 min

100, the size of all working arrays is multiplied by 100. 1D and 2D output files (`*.osc` and `*.osc2d`) output roughly the same number of quantities. Therefore, the size of the output should be 100 times larger. The size of these file has been reduced by a factor ~ 2 by switching from an ASCII output for `osc` to a binary output for `osc2d`. It also saves a large amount of time reading those files. But in any case the new size of the files is very important and it must be taken into account if the goal is to compute large stellar model grids in 2D.

7.3.2 Use of numerical resources for the transport of angular momentum

Concerning the time consumption needed for the resolution of the transport of angular momentum, it is surprisingly much faster with the new than with the old approach for the transport of AM. We measured the time needed to compute an $1M_\odot$ evolutionary model to an age of 4570 Myr (Sun's age) and 12 000 Myr. The resulting computation time are gathered in Table 7.5. How do we explain these results ? It is actually not very clear, however two explanations can be suggested. First of all, the system of equations in 1D has 5 unknowns ($\overline{\Omega}$, U_2, Υ_2, Θ_2 and Λ_2), while the new approach has 4 (U_ℓ, Υ_ℓ, $\overline{\Omega}$ and $\partial\overline{\Omega}/\partial r$). One equation less does not make a significant difference for the time to compute one iteration. However, 4 equations instead of 5 can reduce the number of iterations until convergence and speed up calculations. The second idea is that because our computation of $\widetilde{\rho}_\ell$, $\widetilde{g}_\ell$, etc. is more realistic because of the module dedicated to the model deformation, it may also improve the stability of the code and again, reduce the number of iterations

Chapter 8

Ongoing work and conclusions

Contents

8.1 Summary

8.1.1 On the transport of angular momentum

In this PhD I focused on the modelling of the transport of angular momentum in the radiative zone of low and intermediate mass stars, across their whole evolution. In addition we choose to include two-dimensional aspects in a modelling that has always been done only in 1D. These choices were motivated by several factors.

- First of all, rotation has always been set aside or simplified a lot in stellar modelling. The main reason for that is because rotation results in a deformation of the star, hence breaking the spherical symmetry upon which the standard model of stellar physics rests. Stars are central for two reasons in astrophysics. *(i)*: they provide energy to their hosted planets and strongly interact with them. *(ii):* They are used as proxies to estimate the age of their host and hosted structures (clusters, galaxies, exoplanets, etc.). Taking rotation into account in stellar modelling is of crucial importance because, through its implication in the stellar dynamo, an increase of angular velocity, in the end induces an increase of the UV and X ray flux received by the planets orbiting around them and hinders the development of life. Rotation also induces mixing of chemical which alter the element abundances on which age estimates are based. This effect is very far from being negligible and can lead to mis-estimates of several Gyr.

- Layers in stars can be differentiated according to the dominant energy transport process inside them. In convective zones, the energy is mainly advected by large scale fluid motions due to the unstably stratified material. The modelling of these motions and their interaction with rotation is very complicated and would require dedicated models. However, these complicated motions are also an advantage because they lead to simplifications. For instance, the convection zone can be considered chemically homogeneous region. For this reason, we focus on the rotation modelling of the radiative zone.

- Stars with mass below $0.3M_\odot$ have no radiative zone. Stars with $0.3M_\odot < M < 1.25M_\odot$ have a central radiative region, surrounded by an convective envelope. These stars are quite similar in structure to our Sun, which makes them very interesting. Finally, stars with $M > 1.25M_\odot$ have a central convective zone and a very thin or no convective envelope. Furthermore, in these stars, other "non-standard" phenomena come into play such as radiative accelerations or mass loss. The higher the mass, the less negligible they are. The range of mass studied in this PhD spans almost the entire mass range of stars observed by CoRoT, *Kepler* and TESS.

- Some stellar models offer precise modelling of the stellar rotating interiors, especially ESTER (Espinosa Lara & Rieutord, 2007, 2013) which was designed for a fully 2D study of stellar rotation, or the ASH code (Brun & Toomre, 2002; Miesch et al., 2006, 2008) primarily designed for MHD computations of rotating convective zones. They are much more realistic in rendering the effect of rotation on the structure. However, these codes are computationally expensive and are not able to model the star rotation over evolution time-scales. The possibility to simulate evolution through a varying hydrogen abundance in the core has recently been introduced in ESTER, but this prescription is far from being accurate. What CESTAM can now do is to start from an initial rotation profile and evolve it to the desired evolutionary stage, in addition to taking into account two-dimensional effects of rotation.

- Treating part of the problem in two dimensions is motivated my many arguments.

  - In order to keep a 1D description of the rotating stellar-structure, we had to assume a shellular rotation profile, *i.e.* that the angular velocity is constant over (spheroidal) isobars. The approximation of shellular rotation in the radiative zone is valid if, due to the stable stratification, the horizontal shear-induced turbulence is much stronger than vertical one. The horizontal diffusion coefficient, as we have shown in Sect 2.2 is proportional to the gradient of angular velocity with respect to the distance to the rotation axis. Near this axis, the gradient becomes small and the shellular rotation approximation may no longer be valid. If it is not, it is not clear if one can find another way to keep structure equations one dimensional. The 2D version of CESTAM will allows us to test this hypothesis in the radiative zone.
  - The rotation profiles presented in Chapter 4 showed that, in convective zones, the angular velocity depends on the radius *and* on the latitude and then the latitudinal gradients vanish in a thin transition region and stay very small in the radiative one. Therefore, the boundary conditions that need to be applied at the transitions from radiative to convective zones *must* depend on the latitude, and a 2D approach is necessary for that.
  - 1D stellar evolution codes that can perform a modelling of rotation evolution reach angular velocity profiles that are orders of magnitude higher than the rotation rates measured in evolved stars (see Chapter 4). To overcome these disparities, many

additional mechanisms of transport of angular momentum have been suggested and they are summed up in Chapter 5. They can be sorted into two categories: transport by waves or by diffusion induced by hydrodynamic or magneto-hydrodynamic instabilities. For the first categories, the amount of angular momentum transported by a wave and its properties inside the radiative zone depend partly on the latitude of emission. For the second categories, several of the criteria that rule these instabilities depend also on the latitude, which can lead to instabilities occurring only above or below a certain latitude. Here again, the two dimension must be accounted for.

We established the numerical framework that will allow the future studies of stellar rotation evolution. This framework is decomposed into two parts. The first one is a deformation module that implements a method proposed by Roxburgh (2004, 2006). The main idea is to start from a 1D model and an angular rotation profile. The method assumes that any field can be decomposed on Legendre polynomials. By using this decomposition in the Poisson equation and in the force balance equation (hydrostatic equilibrium with centrifugal force), one obtains 1$^{\text{st}}$-order differential equations that can easily be solved with the method of characteristics. The characteristic surfaces turn out to be isobars. This method therefore provides us with the coordinates of the isobars, the fluctuations of density and gravitational potential over them and the effective gravity (the combined effect of the gravity acting radially and the centrifugal acceleration acting perpendicularly to the rotation axis) in 2D. Knowing those quantities allows us to compute the additional factors that enter the modified structure equations written on isobars, and to resume the evolution. After the deformation, the 1D structure taken as input is equal to the 2D one at a particular latitude denoted $\theta_{\rm m}$. This characteristics latitude is the one at which all the Legendre polynomials vanish but the 0$^{\text{th}}$-order one. In the literature, the angle is taken to be $\theta_{\rm m} = \arccos(1/\sqrt{3})$. Nonetheless, the implementation of Roxburgh (2006)'s method was the opportunity to notice that if Legendre polynomials with degree strictly higher than 2 are taken into accounted, this value of $\theta_{\rm m}$ is not exact. In particular, near the surface where the centrifugal acceleration is the strongest, it significantly diverges from $\arccos(1/\sqrt{3})$ which induces errors in the deformation. I propose a method to implement the Roxburgh (2006)'s method with a varying $\theta_{\rm m}$. This method works during the main sequence but experience some difficulties during the pre-main sequence and needs to be polished.

The mass and angular momentum are very well conserved after the deformation. We also performed a seismic study of our models using the 2D, non-perturbative, oscillation code ACOR (Ouazzani et al., 2012). All the fields along the characteristic latitude are almost not modified, except for the pressure field that is recomputed at the end of the deformation. This re-computation results in very small changes in the pressure of the uppermost layers, which induce small frequency changes, quite similar to the surface effect. This problem is not found in every star and at every evolutionary stage, and we should be able to suppress it after a deeper study. This "numerical surface effect" seems also to be the cause of the non convergence of the frequencies computed in models with tighter angular grids. As we have shown, those frequency differences seem to have two distinct causes. The first is due to a change in the mean density of the star, related to the large frequency separation $\Delta\nu$. The mean density can be affected by numerical errors in the computation of the density fluctuations but most certainly by changes in the value of the surface of isobars, which have a repercussion on the isobar-averaged quantities involved in the structure equation. This change in $\Delta\nu$ is easily seen by the fact that the frequency differences vary in a linear way, as expected by the asymptotic relation (3.50). The second cause is related to the maximum order $\ell_{\rm max}$ taken into account in the decomposition in Legendre polynomials. For rapidly rotating stars, stopping the development

at $\ell_{\max} = 2$ seems not to be sufficient and higher degrees must be added. It will be the work of the modeler to tune the numerical parameters in order to obtain an accurate model.

Regarding the new prescription for the transport of angular momentum, we also obtained very good results. The angular momentum is very well conserved along stellar evolution. Furthermore, the computation performed with the new prescription seems to be more stable than with the old one and significantly faster, to our surprise. The results are also very different. The central hydrogen abundance is always found higher in 2D than in 1D models, which is due to a slightly higher central temperature in 1D than in 2D models. It has a significant impact on the latter stages of stellar evolution. The radial component of the meridional circulation was often smaller in 2D than in 1D models, leading to sharper gradients in the angular velocity. Nonetheless, it must be noted that our tests have been conducted without loss of angular momentum by magnetized wind. The inclusion of such a process in the modelling induces a coupling between the meridional circulation U_2 near the tachocline and the angular momentum extracted at the surface. It could change the way U_2 compare in 1D and 2D models. Finally we computed the 2^{nd} order component of the angular velocity Ω_2 in the radiative zones of main sequence stars. The value obtained are consistent with the assumption of a shellular profile. However, this question should be investigate more thoroughly.

This work open the path to new studies of the transport of angular momentum. Some of these studies have already started and this is the topic Sect. 8.2 in which I summarize the collaborations started soon before the lockdown and the writing of this PhD. The third and final section 8.3 gather the future prospect for the works that could be carried out with CESTAM.

8.1.2 On the problem of surface effects

We have computed a grid of 29 patched models with effective temperature ranging in $T_{\text{eff}} = [5000; 6800]$ K, surface gravities ranging from $\log g = [3.5; 4.5]$ and iron to hydrogen ratio ranging from $[\text{Fe/H}] = [-1.0; +0.5]$. Our aim was to study and understand physically what impact a non-solar metallicities would have on the surface effect. We focused on the turbulent origin of the surface effect and left the non-adiabatic cause aside. In the region of the parameter space $((T_{\text{eff}}; \log g; [\text{Fe/H}]))$ we focused on, we showed that at fixed T_{eff} and $\log g$, the frequency differences computed at $\nu_{\max}$ could vary by up to a factor 3 with varying $[\text{Fe/H}]$ between the lowest and highest frequency difference. However, it appears that our first idea which consisted in studying the amplitude of the frequency differences as a function of the metallicity did not lead to a clear trend. On the contrary, the Rosseland mean opacity κ turned out to be the most adapted quantity for understanding the frequency differences. Based on simple physical arguments we derived a scaling relation between the frequency differences at $\nu_{\max}$ and the global parameters T_{eff} , $\log g$ and the opacity κ computed at the photosphere. In a second part, this scaling law was improved using the grid of patched models.

In this work, we also perform a comparison of the existing surface effects correction laws by comparing the residual frequency difference after correction given by all these laws. The corrections were also applied on non-radial mode frequency spectra when mixed-modes were present. We found that, for a vast majority of our models, the cubic correction relation proposed by Ball & Gizon (2014) is found to be the best performer and manages to reduce the frequency differences below the 0.1 µHz for the coldest models, which is of the order of the CoRoT or *Kepler* frequency resolution. The Lorentzian correction suggested by Sonoi et al. (2015) is the second best performer with corrected frequency differences slightly higher than the one corrected by Ball & Gizon (2014). Almost all the proposed correction leave frequency differences smaller than 1 µHz. The first ever proposed correction (Kjeldsen et al., 2008)

have pretty bad results for correcting high frequencies, however, on the low frequency range $0 < \nu/\nu_{\max} < 1.05$, it often provides results similar to the one of Ball & Gizon (2014). As for the correction of mixed modes only a modified version (see Manchon et al., 2018) of the corrections proposed by Ball & Gizon (2014) manages to satisfyingly correct the frequency differences.

This review of the correction relation allowed us to provide a scaling relation between the different adjustable parameters involved in these laws and the same global parameters as before ($T_{\rm eff}$, $\log g$ and κ). The advantage of such scaling relations is that they could easily be implemented in a 1D stellar evolution code. Furthermore, there is no need to adjust these parameter so that the modelled spectrum fits the observed one. We have seen that this method poses a problem of uniqueness of the solution. With scaling relations that constraint the values of the adjustable parameters, the values of the adjustable parameters depend only on the values of $T_{\rm eff}$, $\log g$ and κ.

8.2 Ongoing work

8.2.1 Implementation and testing of the prescription for the transport of angular moment with $\ell > 2$

Mathis & Zahn (2004) developed the equations for the transport of angular momentum and for the meridional circulation for any degree $\ell \geq 2$. The resolution of these equations for $\ell > 2$ is currently being added into CESTAM. The usual tests for the conservation of angular momentum will soon be performed. This new version will allow us to compute coefficients U_4, Λ_4, Ψ_4. Furthermore, we will be able to compute Ω_2 not only during the main sequence but also during fast evolution phases. Estimates of Ψ_4 can already be derived with the value of Θ_4 provided by the deformation module if we assume that Λ_4 is very small compared to Θ_4. In a near future, we will be able to compute even higher orders. However, it has been shown in this PhD that situations where coefficients of order $\ell \geq 8$ are physically significant seem to be very rare.

8.2.2 Seismology of δ Sct

As I said earlier in this manuscript, δ Sct and γ Dor offer very good test case for the new 2D abilities of CESTAM. Indeed, δ Sct and γ Dor are stars with mass $\sim 2 - 3M_{\odot}$, well in our mass range of interest. They are also fast rotators which translates into very important deformations, with the equatorial radius being more than 10% higher than the polar one. In these stars, the CNO cycle is the dominant source of energy and they have a convective core. Convective overshoot causes injection of hydrogen-rich material in the region where nuclear reactions occur, thus extending the star lifetime. Due to the fast rotation, meridional circulation and shear-induced turbulence inside radiative zones must be important and so is the associated chemical mixing. The questions raised by these stars are therefore, what are their profile of chemical composition and rotation ? What transport mechanisms do they reveal ?

The seismology of these stars is complicated by the strong distortion that impedes mode identification. γ Dor stars oscillate in gravity modes while δ Sct oscillate in pressure modes. I am starting a collaboration that focuses on the latter and associate researchers from the LESIA and the GEPI in Meudon, France, and from the IAA in Granada, Spain. The general idea is to combine photometric measurements with spectroscopic ones to derive seismic constrains on δ Sct using new 2D evolutionary models computed with CESTAM and 2D non perturbative oscillation codes ACOR (Ouazzani et al., 2012) and TOP (Reese et al., 2006).

The ultra-precise photometry will be obtained using the BRITE satellites constellation presented in Sect. 4.1, that allows for multi-wavelength measurements. Modes of oscillation do not

have the same amplitude and the same phase in all photometric bands. The amplitude ratios and phase differences depend on the numbers (n, ℓ, m). The theoretical prediction of their values have been the focus of many works in the past decades (Balona & Evers, 1999; Breger et al., 1999; Reese et al., 2009; Handler et al., 2017; Reese et al., 2018). The multi-band technique mainly works for modes with $\ell \leq 2$ (Daszynska-Daszkiewicz, 2008). In order to obtain information in higher degree mode, we must add radial velocity measurements obtained through high-resolution spectroscopic observations. These observations will be mainly collected using the SOPHIE spectrometer. The aim is to measure the variations in time of an absorption line profile (line profile variations; LPV). The LPV are due to the Doppler effect induced by the mode velocity. Spectroscopy must also provide us with estimates of the inclination angle and of the equatorial velocity. To that end, effects of the gravity darkening must be estimated and 2D models of CESTAM will be of great help for that.

On the modelling side, the interfacing of CESTAM with ACOR will allow us to find and study new seismic constraints. We have seen in Chapter 3 that the large separation $\Delta\nu$ is proportional to the mean stellar density $\sqrt{\langle\rho\rangle}$. In moderate and fast rotating stars, regular patterns in the frequency spectra can also be found. In such stars, an equivalent of the $\Delta\nu$ has been theorized (Ouazzani et al., 2015; Suárez et al., 2014). Suárez et al. (2014), found the following relation $\Delta\nu \propto \langle\rho\rangle^{0.46}$, pretty close to the one in the non-rotating case. To do so, they used 1D stellar models rotating at most at 40% $\Omega_{\rm K}$, from which they computed the mean densities and a 1D oscillation code for calculating the frequency spectrum and extract the $\Delta\nu$. In a very recent work, Rodríguez-Martín et al. (2020) performed the same analysis on a grid of fast rotating 1D CESTAM models, of which they calculated the frequency spectra using a 1D oscillation code with a 2$^{\rm nd}$ order perturbative method accounting for centrifugal deformation. The CESTAM models were computed in 1D, therefore the mean density had to be corrected. To that end, they assumed that the models had their shape given by the Roche model (isobars equals equipotentials) and in this case, the mean density is given by:

$$\langle\rho\rangle = \frac{3}{4\pi}\frac{M_\star}{R_{\rm eq}^2 R_{\rm p}}, \tag{8.1}$$

where $R_{\rm eq}$ and $R_{\rm p}$ are the equatorial and polar radii. They are given by the Roche model as:

$$R_{\rm p} = \frac{R_{\rm 1D}}{1 + \frac{\Omega^2 R_{\rm 1D}^3}{3\mathcal{G}M_\star}} \quad \text{and} \quad R_{\rm eq} = 1 + \frac{\Omega^2}{2\Omega_{\rm C}^2}, \tag{8.2}$$

where $R_{\rm 1D}$ is the radius of the star provided by the 1D CESTAM models and $\Omega_{\rm C}$ is a critical velocity in the Roche model, very similar to the Keplerian break-up velocity. When $\Omega_{\rm C}$ is reached, the centrifugal acceleration counterbalances the gravitational one and $R_{\rm p} = 2/3R_{\rm eq}$:

$$\Omega_{\rm C}^2 = \frac{8\mathcal{G}M_\star}{27R_{\rm p}}. \tag{8.3}$$

This quantities comes from the definition of $\Omega_{\rm K} \equiv \sqrt{\mathcal{G}M/R_{\rm eq}^3}$ given in Eq. (1.55), in which the equatorial radius $R_{\rm eq}$ has been replaced by $3/2R_{\rm p}$. They finally found the scaling between $\langle\rho\rangle$ and $\Delta\nu$ to be: $\langle\rho\rangle \propto \Delta\nu^{2.02\pm0.10}$. In the conclusion of there article, Rodríguez-Martín et al. (2020) propose that this study should be carried again with more precise 2D models. They suggest using ESTER models initialized with a 1D seed coming from a 1D CESTAM model. This would allow to have a more accurate stellar evolution and a more accurate 2D stellar-structure. The new 2D version of CESTAM can actually do this without the need of interfacing two stellar codes.

Table 8.1: Parameters of the grid of 2D CESTAM models for the study of δ Sct stars. Models are computed without overshoot.

Parameter	Value or range	step	Unit
Mass	$[1.5; 2.5]$	0.05	$M_\odot$
[Fe/H]	$[-0.4; 0.2]$	0.2	dex
$\alpha_{\rm MLT}$	$[1.5; 1.8]$	0.3	
$P_{\rm disk}$	0, 3, 4, 5, 6, 7		days
$\tau_{\rm disk}$	5		Myr

And this is what we started to with the computation of grid of evolutionary tracks of 2D CESTAM models. The characteristics of the models in this grid are summarized in Table 8.1. In total, it represents 960 models: 20 different masses, 4 different metallicities, 2 different values of $\alpha_{\rm MLT}$ and 6 different initial disk periods. As for now, around 40% of the models have been computed. The computation was slightly delayed by the pandemic and because of insufficient storage on the cluster at the IAS. The grid parameters of Table 8.1 are quite similar to the one of the grid used in Rodríguez-Martín et al. (2020). It appeared that it was impossible to evolve some models past the PMS because they reached the break-up velocity. Interestingly, the break-up velocity can be reached outside the characteristic latitude $\theta_{\rm m}$, which would not have been detected by the 1D version of CESTAM. This new 2D grid of stellar evolution models will then be exploited with ACOR.

Concerning ACOR and the problem of mode identification in fast rotating stars, R.-M. Ouazzani recently proposed (private comm.) to use artificial intelligence (AI) to identify modes. This method has already been used (e.g. Mirouh et al., 2019): AI should be able to identify, for instance using the 2D spatial distribution of the kinetic energy of a mode (see 7.4), what kind of mode it is (island mode, super-inertial mode, etc.) and its quantum numbers when it is possible. First, the AI must be trained on a subset of modes that a human already identified. As of today, AI must be trained on very large subset in order to be accurate enough and it complicates their use. The idea here would be to create a project of citizen science. The AI would be trained by a single human but by, let say smart-phone users, who would identify series of mode and quickly train the AI.

8.2.3 TAR accounting for centrifugal acceleration

In rotating star, the Coriolis force must be taken into account in the case of g-modes. As we said, to be more rigorous, these modes should not be called gravity modes any more but *gravito-inertial modes*. This denomination stresses the fact that, not only the gravity is a restoring force, but also the Coriolis force. We focus here on low frequency modes satisfying the conditions $2\Omega \ll N$ and $\sigma \ll N$. In this case, the problem can become separable in an angular and a radial part by making the so-called *Traditional Approximation of Rotation* (TAR) (Eckart, 1960; Gerkema et al., 2008), originally developed in geophysics. The TAR consists in neglecting the latitudinal component of the Coriolis force (Lee & Saio, 1997). This approximation relies on the same argument developed in the small calculation performed around the dispersion relation (7.6). For waves with $\omega, \Omega \ll N$, we have seen that $k_{\rm h}/|\mathbf{k}| \simeq 0$. From Eq. (7.6), it yields $\mathbf{\Omega} \cdot \mathbf{k} \simeq \Omega_r k_r$, meaning that the horizontal component of $\mathbf{\Omega}$ has almost no influence on the frequency of the mode and can be neglected. This approximation was first considered together with other approximations such as sphericity (non centrifugal acceleration) and uniform rotation. It has since be generalized for the case of differential rotation (Ogilvie & Lin, 2004; Mathis, 2009) and recently the formalism has been developed to allow small deformation of the star (Mathis &

Prat, 2019). The frequency spectrum found using the TAR has been compared (Ballot et al., 2012) with the one obtained with the full computation made by the TOP code. The authors compared the frequency spectrum computed with TAR with the one computed with TOP on a deformed and on a spherical fast rotating-models, all other things being equal. Their results show very good accordance between TAR and full computations for $m = 0$ and $m = +\ell$ modes. In the case of $m = -\ell$, a significant discrepancy can be observed when full computations are made on the deformed model but the gap decreases when TOP is applied to the spherical model, suggesting that the error made by the TAR comes from centrifugal acceleration, as expected. The work performed by Mathis & Prat (2019) proposes to adapt the TAR formalism to small centrifugal deformation. In a collaboration involving V. Prat and S. Mathis (CEA) and R.-M. Ouazzani (LESIA), we want to test the prediction of the model developed in Mathis & Prat (2019) by comparing with the oscillation spectrum computed with ACOR on deformed CESTAM models.

8.2.4 Study of two solar analogues

Solar analogues are stars with masses very close to $1M_{\odot}$, and possibly different age. Their study is very promising to better understand Sun's past and future. Such a study is currently ongoing, focusing on two stars observed by CoRoT: HD42618 (slightly less massive than the Sun) and HD43587 (slightly more massive). modelling and accurate determination of the global parameters of these stars has been conducted using CESTAM, for the moment without rotation. The new rotation and two-dimensional abilities of CESTAM will be applied to this model, in order to gain insight on the efficiency of internal mixing and transport of angular momentum.

8.3 Future work

First of all, several points must be addressed in the modelling of CESTAM:

- I will shortly implement in CESTAM the transport of angular momentum by internal gravity waves (IGW). This work will be done with C. Pinçon who developed the IGW excitation model by plumes (Pinçon et al., 2016). It would also be interesting to implement a Reynold stresses excitation model (e.g. Kumar et al., 1999), so that both models can be compared.

- We have seen that the modelling of rotation inside convective zone have been left aside. For the moment it is only modelled assuming a constant angular velocity or a constant angular momentum distribution which do not correspond to what is observed, especially with these approximations, the rotation profile is constant in latitude. The most consistent way to tackle the problem would be to have a model of rotating-convection. Many have been proposed (Rogachevskii & Kleeorin, 2018; Augustson & Mathis, 2019; Augustson et al., 2020; Jermyn et al., 2020a,b). Choosing one among them will require additional work but in the meantime we shall use prescriptions of angular velocity profiles derived from 3D simulations of convective zones (Brun et al., 2017).

What studies are now feasible with the new 2D version of CESTAM? Apart from the three ongoing collaborations described above, some works are already possible or will be soon with the implementation of the transport of angular momentum by IGW.

- Even without the improvements listed above, the hypothesis of shellular rotation can readily be tested. Indeed, CESTAM is already able to provide the coordinates of isobars and the velocity field of the meridional circulation. Assuming a shellular rotation profile, we can study how turbulent viscosity coefficients vary with latitude. In particular, it

may be possible that the shear instability cannot develop near the rotation axis because the rotation velocity (not the angular velocity) is zero on this axis. Of course, if shear instabilities are not found near the rotation axis, it does not mean that the shellular rotation is not verified here. If the zone in which the shear disappears is small, the angular velocity profile could stay close to a shellular one, for continuity reasons. In this case, it would be interesting to have access to the 2nd order component Ω_2 to see if it becomes non negligible. This study will also be improved by using the new prescriptions of turbulent diffusion coefficients (Prat et al., 2016; Mathis et al., 2018).

- Transport of angular momentum by IGW is suggested to be a very efficient mechanism of transport. For the moment, it has only been tested in 1D stellar evolution codes (e.g. Talon & Charbonnel, 2003; Fuller et al., 2014) and those studies show that IGW cannot reproduce the core rotation of RGB stars. However, as we have explained in this manuscript, the flux of AM transported by the IGW depend on the latitude of emission and CESTAM2D will allow a deeper study of this mechanism of transport.

- In addition to trying to reproduce the core rotation of RGB stars, it will be interesting to see if, when IGW are included, we find a flat rotation profile in the radiative zone of the Sun. It could be used also to confirm the good results of IGW on the understanding of the cold side of the Li dip (see Sect. 4.3.2).

- M. Deal has recently included a 2D prescription (Barker et al., 2019) for the GSF instability in CESTAM and the transport by mixed-modes (Belkacem et al., 2015b,a) has already been implemented for a few years. Being able to study all these process of transport with the same stellar evolution code will be a good opportunity to study the interplays between them, similarly to what was done theoretically by Maeder et al. (2013).

Concerning the future of our work on the surface effects, we could focus on several points

- First of all, the method of model patching may be improved. Until now, the stratification extracted from the 3D simulations that are patched onto the 1D stellar models are constructed by averaging horizontally the modelled box. Our patching technique is designed to ensure the matching of the effective temperature, the surface gravity and of the temperature at the bottom of the 3D simulated box. The 1D model and the horizontally averaged stratification extracted from the 3D one are in hydrostatic equilibrium (HSE, however the patching technique *per se* does not preserve the HSE at the junction point. A quick check on two models of our grid showed that they were indeed in HSE but this verification should be conducted on all our models. Furthermore, we could think of a way to enforce HSE during the patching process, so that no verification would be needed. Of course, one could add a fourth constraint and impose that the quantity $\boldsymbol{\nabla} p$ is continuous from the 1D model to the horizontally averaged 3D stratification, but including a fourth constraint implies that we also include a fourth tunable parameter which increases the complexity of the patching. We could also change our way of obtaining the 3D stratification. The horizontal average is the most simple way of averaging one could think of but we could also average the stratification at constant pressure scale height $H_{\rm p}$. With this method, the radial derivative of the pressure would be continuous at the matching point, thus, here, the HSE would be preserved *by default* after the patching process.

- Our study of the impact of a different chemical composition on the surface-induced frequency differences have focused on the effects caused by the turbulence and non-adiabatic effects were left aside. This aspect was already studied by Houdek et al. (2017)

who showed that, on a solar model, when the surface-effect was corrected only for the turbulent pressure part, non-negligible frequency differences remained. This residual disappears when non-adiabatic effects were accounted for. Such study should be carried out on non-solar models and especially with non-solar metallicities.

- Finally, we have see in the last section of Manchon et al. (2018) that mixed-modes can also be surface-affected. Correcting their modelled frequency is of crucial importance because in many cases, mixed-modes are the only observable waves that probe the radiative region. Only the correction prescriptions proposed by Ball & Gizon (2014) were adapted to mixed-modes. This point should be investigated further.

Appendices

A. Constants and global solar parameters

A.1 Universal constants

Light speed	c	299 792 498 $\mathrm{m\,s^{-1}}$
Stefan-Boltzmann constant	σ	5.670373×10^{-8} $\mathrm{W\,m^{-2}\,K^{-4}}$
Gravitational constant	$\mathcal{G}$	$6.674 \times 10^{-11} \mathrm{m^3\,kg^{-1}\,s^{-2}}$

A.2 Main present-day solar parameters

Age		4570 Myr
Mass	$M_\odot$	1.9891×10^{30} kg
Luminosity	$L_\odot$	3.828×10^{26} W
Radius	$R_\odot$	6.957×10^{8} m
Mean density	$\langle\rho\rangle_\odot$	1 408 $\mathrm{kg\,m^{-3}}$
Effective temperature	$T_{\mathrm{eff},\odot}$	5 777 K
Surface gravity	$\log g_\odot$	4.44
Surface gravity	$g_\odot$	27 540 $\mathrm{cm\,s^{-2}}$
Large separation	$\Delta\nu_\odot$	134.9 µHz
	$\nu_{\max}$	3 090 µHz

A.3 Main determinations of present-day solar mass photospheric-abundances

	Grevesse & Sauval (1998)	Asplund et al. (2005)	Asplund et al. (2009)
$X_\odot$	0.735	0.7392	0.7381
$Y_\odot$	0.248	0.2486	0.2485
$Z_\odot$	0.017	0.0122	0.0134
$Z_\odot/X_\odot$	0.023	0.0165	0.0181

A.4 Main determinations of solar initial mass abundances

	Grevesse & Sauval (1998)	Asplund et al. (2005)	Asplund et al. (2009)
$X_\odot$	0.7120	0.7166	0.7154
$Y_\odot$	0.2701	0.2704	0.2703
$Z_\odot$	0.0180	0.0130	0.0142
$Z_\odot/X_\odot$	0.0253	0.0181	0.0199

B. Legendre polynomials

Legendre polynomials are the solutions of the following differential equation for $x \in [-1;1]$

$$\frac{\mathrm{d}}{\mathrm{d}x}\left[\left(1-x^2\right)\frac{\mathrm{d}P_\ell(x)}{\mathrm{d}x}\right] + \ell(\ell+1)P_\ell(x) = 0, \tag{B.1}$$

with $\ell \in \mathbb{N}$ (Abramowitz & Stegun, 1972). One can find the solutions for any $\ell \in \mathbb{N}$ using the Rodrigues formula

$$P_\ell(x) = \frac{1}{2^\ell \ell!}\frac{\mathrm{d}^\ell}{\mathrm{d}x^\ell}\left[\left(x^2-1\right)^\ell\right], \tag{B.2}$$

which gives, for the 6 first Legendre polynomials:

$$\begin{aligned} P_0(x) &= 1, & P_1(x) &= x, \\ P_2(x) &= \frac{1}{2}\left(3x^2-1\right), & P_3(x) &= \frac{1}{2}\left(5x^3-3x\right), \\ P_4(x) &= \frac{1}{8}\left(35x^4-30x^2+3\right), & P_5(x) &= \frac{1}{8}\left(63x^5-70x^3+15x\right). \end{aligned} \tag{B.3}$$

B.1 Scalar product

We can define a scalar product $\langle\cdot,\cdot\rangle$ such that $\forall n, m \in \mathbb{N}$,

$$\langle P_m, P_n\rangle = \int_{-1}^{1} P_m(x)P_n(x)\mathrm{d}x = \frac{2}{2n+1}\delta_{m,n}, \tag{B.4}$$

where $\delta_{m,n}$ is the Kronecker symbol.

B.2 Integral of triple product

We define the integral of the triple product as, $\forall i, j, k \in \mathbb{N}$,

$$\mathcal{T}(i;j;k) = \int_{-1}^{1} P_i(x)P_j(x)P_k(x)\mathrm{d}x. \tag{B.5}$$

Following Gupta & Narasimhan (2007), $\mathcal{T}(i;j;k) = 0$ if either one of these two conditions is met:

- The triplet (i,j,k) does not satisfy to the triangle inequality, *i.e.* either $i+j<k$, or $i+k<j$, or $j+k<i$.
- $(i+j+k) \mod 2 \neq 0$

In any other case,

$$\mathcal{T}(i;j;k) = 2\begin{pmatrix} i & j & k \\ 0 & 0 & 0 \end{pmatrix}^2, \tag{B.6}$$

where the matrix is a Wigner 3-jm symbol. For instance, $\mathcal{T}(2;2;2) = \int_{-1}^{1}(P_2(x))^3\mathrm{d}x = 4/35$.

B.3 Useful relations

Any vector field of the form $\mathbf{F} = F_r(r)P_\ell(\cos\theta)\mathbf{e}_r + F_\theta(r)\frac{\mathrm{d}P_\ell(\cos\theta)}{\mathrm{d}\theta}\mathbf{e}_\theta$ will have its divergence in spherical coordinate written as

$$\begin{aligned}\boldsymbol{\nabla}\cdot\mathbf{F} &= \frac{1}{r^2}\frac{\partial r^2 F_r}{\partial r}P_\ell(\cos\theta) + F_\theta\frac{1}{r\sin\theta}\frac{\mathrm{d}}{\mathrm{d}\theta}\left[\sin\theta\frac{\mathrm{d}P_\ell(\cos\theta)}{\mathrm{d}\theta}\right] \\ &= \frac{1}{r^2}\frac{\partial r^2 F_r}{\partial r}P_\ell(\cos\theta) + F_\theta\frac{\ell(\ell+1)}{r}P_\ell(\cos\theta). \end{aligned} \tag{B.7}$$

B.4 Associated Legendre polynomial

Equation (B.1) is actually the simplified version of a more complex differential equation:

$$\frac{\mathrm{d}}{\mathrm{d}x}\left[\left(1-x^2\right)\frac{\mathrm{d}P_\ell^m(x)}{\mathrm{d}x}\right] + \left[\ell(\ell+1) - \frac{m^2}{1-x^2}\right]P_\ell^m(x) = 0, \tag{B.8}$$

and the solutions become of the form

$$P_\ell^m(x) = (-1)^m(1-x^2)^{m/2}\frac{\mathrm{d}^m P_\ell}{\mathrm{d}x^m}. \tag{B.9}$$

This form of the Legendre differential equation appears for instance when studying propagation of waves in a rotating frame.

B.5 Interesting integrals

With $x = \cos\theta$ and taking into account above relations,

$$\int_0^\pi P_\ell^m(\cos\theta)\frac{\mathrm{d}P_\ell^m}{\mathrm{d}\theta}\frac{\cos\theta}{\sin\theta}\sin\theta\mathrm{d}\theta = \frac{1}{2}\int_{-1}^1 P_\ell^m(x)^2\mathrm{d}x \tag{B.10}$$

$$\int_0^\pi \left[\left(\frac{\mathrm{d}P_\ell^m}{\mathrm{d}\theta}\right)^2 + \frac{m^2}{\sin^2\theta}P_\ell^m(\cos\theta)\right]\sin\theta\mathrm{d}\theta = \ell(\ell+1)\int_{-1}^1 P_\ell^m(x)^2\mathrm{d}x \tag{B.11}$$

And the scalar product of two associated Legendre polynomials with same m and different degree ℓ now reads

$$\langle P_\ell^m, P_k^m\rangle = \int_{-1}^1 P_\ell^m(x)P_k^m(x)\mathrm{d}x = \frac{2(\ell+|m|)!}{(2\ell+1)(\ell-|m|)!}\delta_{\ell,k} \tag{B.12}$$

The following integral is found in various expression:

$$\begin{aligned} I_\ell = \frac{\int_0^\pi P_\ell(\cos\theta)\sin^3\theta\mathrm{d}\theta}{\int_0^\pi \sin^3\theta\mathrm{d}\theta} &= \frac{1}{2}\int_0^\pi (P_0(\cos\theta)P_\ell(\cos\theta) - P_2(\cos\theta)P_\ell(\cos\theta))\sin\theta\mathrm{d}\theta \\ &= \delta_{0,\ell} - \frac{1}{5}\delta_{2,\ell} \neq 0 \end{aligned} \tag{B.13}$$

where $\delta_{i,j}$ is the Kronecker symbol and we have used the results $\sin^2\theta = \frac{2}{3}(1 - P_2(\cos\theta))$ and $\int_0^\pi \sin^3\theta\mathrm{d}\theta = 4/3$.

B.6 Useful relations: spherical harmonics

Spherical harmonics have been defined in Eq. (3.28) as

$$Y_\ell^m(\theta,\varphi) = (-1)^m c_{\ell,m} P_\ell^m(\cos\theta) e^{im\varphi} \quad \text{with} \quad c_{\ell,m} = \sqrt{\frac{2\ell+1}{4\pi}\frac{(\ell-m)!}{(\ell+m)!}} \tag{B.14}$$

Noting $Y_\ell^m|^*$ the complex conjugate of Y_ℓ^m, it easily follows

$$\begin{aligned}
Y_\ell^m|^*\, Y_\ell^m &= c_{\ell m}^2 P_\ell^m(\cos\theta)^2 \\
\frac{\partial Y_\ell^m}{\partial\theta} &= (-1)^{m+1} c_{\ell,m} \frac{\partial P_\ell^m}{\partial\theta} e^{im\varphi} \qquad \frac{\partial\, Y_\ell^m|^*}{\partial\theta} = (-1)^{m+1} c_{\ell,m} \frac{\partial P_\ell^m}{\partial\theta} e^{-im\varphi} \\
\frac{\partial Y_\ell^m}{\partial\varphi} &= imY_\ell^m \qquad\qquad\qquad\qquad \frac{\partial\, Y_\ell^m|^*}{\partial\varphi} = -imY_\ell^m
\end{aligned} \tag{B.15}$$

B.7 Spherical harmonics addition theorem

$$P_\ell(\cos\alpha) = \frac{4\pi}{2\ell+1} \sum_{m=-\ell}^{\ell} (-1)^m Y_\ell^{-m}(\theta_1,\varphi_1) Y_\ell^m(\theta_2,\varphi_2) \tag{B.16}$$

with

$$\cos(\alpha) = \cos\theta_1\cos\theta_2 + \sin\theta_1\sin\theta_2\cos(\varphi_1-\varphi_2) \tag{B.17}$$

C. Some details on the derivation of the meridional circulation velocity

C.1 Finding an expression for Φ

Maeder & Zahn (1998) provided a simplified expression for it and we follow their reasoning to find a more general expression. The entropy of a mixture can be written:

$$S_{\rm mix} = -N\mathcal{R}\sum_i (x_i \ln x_i) + x_e \ln x_{\rm e}, \tag{C.1}$$

where N is the number of moles, $\mathcal{R}$ is the perfect gas constant, x_i the abundance of i$^{\rm th}$ chemical species and x_e the abundance of electrons. Furthermore, $x_i = \mu X_i/A_i$ and $x_{\rm e} = \mu\sum_i X_i Z_i/A_i$, with X_i the mass fraction of element i, A_i its atomic mass and Z_i its number of electrons. For the abundances of hydrogen X, helium Y and metals Z, we can write:

$$x_{\rm H} = \mu X \qquad x_{\rm He} = \frac{\mu Y}{4} \qquad x_{\rm Z} \simeq \frac{\mu Z}{16}, \tag{C.2}$$

where $\mathrm{d}S_{\rm mix}$ corresponds to the third term in Eq. (2.75). It can be shorten by $\mathrm{d}S_{\rm mix} = -N\mathcal{R}\mathcal{B}\mathrm{d}\mu/\mu$ with $\mathcal{B}$ being expressed using Eqs. (C.1) and (C.2) and provide an expression for Φ:

$$\begin{aligned}\mathcal{B} = \Phi c_p &= \mu\Big[X\left(1+\ln\mu X\right) + \frac{Y}{4}\left(1+\ln\frac{\mu Y}{4}\right) + \frac{Z}{16}\left(1+\ln\frac{\mu Z}{16}\right) &\text{(C.3)}\\ &+ \left(X+\frac{Y}{2}+\frac{\mu Z}{64}\right)\left(1+\ln\left(X+\frac{Y}{2}+\frac{\mu Z}{128}\right)\right)\Big]. &\text{(C.4)}\end{aligned}$$

C.2 First simplification of the right hand side

Our goal is to provide an expression for the following term:

$$\boldsymbol{\nabla}\cdot(\chi\boldsymbol{\nabla}T) + \rho\varepsilon + \overline{\rho\varepsilon}_{\rm g} - \boldsymbol{\nabla}\cdot\mathbf{F}_{\rm h} = \text{RHS}. \tag{C.5}$$

Gathering Eqs. (2.88) to (2.93) yields:

$$\begin{aligned}\text{RHS} &= \rho\chi\left(\frac{\mathrm{d}\overline{T}}{\mathrm{d}p} + \sum_{\ell>0}^{\infty}\frac{\mathrm{d}\widetilde{T}_\ell}{\mathrm{d}p}P_\ell(\cos\theta)\right)\boldsymbol{\nabla}\cdot\left(\frac{\boldsymbol{\nabla}p}{\rho}\right) + \boldsymbol{\nabla}\left[\rho\chi\left(\frac{\mathrm{d}\overline{T}}{\mathrm{d}p} + \sum_{\ell>0}^{\infty}\frac{\mathrm{d}\widetilde{T}_\ell}{\mathrm{d}p}P_\ell(\cos\theta)\right)\right]\cdot\frac{\boldsymbol{\nabla}p}{\rho}\\ &+ \sum_{\ell>0}^{\infty}\boldsymbol{\nabla}(\chi\widetilde{T}_\ell)\cdot\boldsymbol{\nabla}P_\ell(\cos\theta) + \sum_{\ell>0}^{\infty}\chi\widetilde{T}_\ell\boldsymbol{\nabla}^2P_\ell(\cos\theta) + \overline{\rho\varepsilon} + \sum_{\ell>0}\widetilde{\rho\varepsilon}_\ell P_\ell(\cos\theta) + \overline{\rho\varepsilon}_{\rm g}\\ &- \sum_{\ell>0}\frac{\ell(\ell+1)}{r^2}\overline{\rho}\overline{T}D_{\rm h}c_p\left(\Psi_\ell + \Phi\Lambda_\ell\right)P_\ell(\cos\theta).\end{aligned} \tag{C.6}$$

In this equation, $\boldsymbol{\nabla}(\chi\widetilde{T}_\ell)$ and $\boldsymbol{\nabla}P_\ell(\cos\theta)$ are orthogonal, therefore their scalar product is zero.

$$\begin{aligned}\text{RHS} &= \left(\overline{\rho\chi} + \sum_{\ell>0}\widetilde{\rho\chi}_\ell P_\ell(\cos\theta)\right)\left(\frac{\mathrm{d}\overline{T}}{\mathrm{d}p} + \sum_{\ell>0}^{\infty}\frac{\mathrm{d}\widetilde{T}_\ell}{\mathrm{d}p}P_\ell(\cos\theta)\right)\\ &\times\left(-4\pi\mathcal{G}\overline{\rho} - 4\pi\mathcal{G}\sum_{\ell>0}\widetilde{\rho}_\ell P_\ell(\cos\theta) + \overline{f}_{\rm C} + \sum_{\ell>0}\widetilde{f}_{{\rm C},\ell}\right)\\ &+\frac{\mathrm{d}}{\mathrm{d}r}\left[\left(\overline{\rho\chi} + \sum_{\ell>0}\widetilde{\rho\chi}_\ell P_\ell(\cos\theta)\right)\left(\frac{\mathrm{d}\overline{T}}{\mathrm{d}p} + \sum_{\ell>0}^{\infty}\frac{\mathrm{d}\widetilde{T}_\ell}{\mathrm{d}p}P_\ell(\cos\theta)\right)\right]\left(\overline{g} + \sum_{\ell>0}\widetilde{g}_\ell P_\ell(\cos\theta)\right)\end{aligned}$$

$$
\begin{aligned}
&-\sum_{\ell>0}^{\infty}\frac{\ell(\ell+1)}{r^2}\chi\widetilde{T}_\ell P_\ell(\cos\theta)+\overline{\rho\varepsilon}+\sum_{\ell>0}\widetilde{\rho\varepsilon}_\ell P_\ell(\cos\theta)+\overline{\rho\varepsilon}_{\mathrm{g}}\\
&-\sum_{\ell>0}\frac{\ell(\ell+1)}{r^2}\overline{\rho}\overline{T}D_{\mathrm{h}}c_p\left(\Psi_\ell+\Phi\Lambda_\ell\right)P_\ell(\cos\theta)\\
=\;&\overline{\rho}\left(\overline{\varepsilon}+\overline{\varepsilon}_{\mathrm{g}}\right)+\sum_{\ell>0}\widetilde{\rho\varepsilon}_\ell P_\ell(\cos\theta)-\left(\overline{\rho\chi}+\sum_{\ell>0}\widetilde{\rho\chi}_\ell P_\ell(\cos\theta)\right)\left(\frac{\mathrm{d}\overline{T}}{\mathrm{d}p}+\sum_{\ell>0}^{\infty}\frac{\mathrm{d}\widetilde{T}_\ell}{\mathrm{d}p}P_\ell(\cos\theta)\right)\\
&\times\left(4\pi\mathcal{G}\overline{\rho}+4\pi\mathcal{G}\sum_{\ell>0}\widetilde{\rho}_\ell P_\ell(\cos\theta)-\overline{f}_{\mathrm{C}}-\sum_{\ell>0}\widetilde{f}_{\mathrm{C},\ell}\right)+\left(\overline{\rho}+\sum_{\ell>0}\widetilde{\rho}_\ell P_\ell(\cos\theta)\right)\\
&\times\left(\overline{g}+\sum_{\ell>0}\widetilde{g}_\ell P_\ell(\cos\theta)\right)^2\frac{\mathrm{d}}{\mathrm{d}p}\left[\left(\overline{\rho\chi}+\sum_{\ell>0}\widetilde{\rho\chi}_\ell P_\ell(\cos\theta)\right)\left(\frac{\mathrm{d}\overline{T}}{\mathrm{d}p}+\sum_{\ell>0}^{\infty}\frac{\mathrm{d}\widetilde{T}_\ell}{\mathrm{d}p}P_\ell(\cos\theta)\right)\right]\\
&-\sum_{\ell>0}^{\infty}\frac{\ell(\ell+1)}{r^2}\left(\overline{\chi}\widetilde{T}_\ell+\overline{\rho}\overline{T}D_{\mathrm{h}}c_p\left(\Psi_\ell+\Phi\Lambda_\ell\right)\right)P_\ell(\cos\theta). \qquad \text{(C.7)}
\end{aligned}
$$

Now we average RHS over an isobar. The horizontal averaging is denoted by $\langle\cdot\rangle$:

$$
\begin{aligned}
\text{RHS}\;=\;&\left\langle\overline{\rho\chi}\frac{\mathrm{d}\overline{T}}{\mathrm{d}p}\left(\overline{f}_{\mathrm{C}}-4\pi\mathcal{G}\overline{\rho}\right)+\overline{\rho}\frac{\mathrm{d}}{\mathrm{d}p}\left(\overline{\rho\chi}\frac{\mathrm{d}\overline{T}}{\mathrm{d}p}\right)\overline{g}^2+\overline{\rho}(\overline{\varepsilon}+\overline{\varepsilon}_{\mathrm{g}})\right\rangle\\
&+\sum_{\ell>0}^{\infty}\left\{\left(\overline{\rho\chi}\frac{\mathrm{d}\widetilde{T}_\ell}{\mathrm{d}p}+\widetilde{\rho\chi}_\ell\frac{\mathrm{d}\overline{T}}{\mathrm{d}p}\right)\left(\overline{f}_{\mathrm{C}}-4\pi\mathcal{G}\overline{\rho}\right)+\overline{\rho\chi}\frac{\mathrm{d}\overline{T}}{\mathrm{d}p}\left(\widetilde{f}_{\mathrm{C},\ell}-4\pi\mathcal{G}\widetilde{\rho}_\ell\right)\right.\\
&+2\overline{\rho}\frac{\mathrm{d}}{\mathrm{d}p}\left(\overline{\rho\chi}\frac{\mathrm{d}\overline{T}}{\mathrm{d}p}\right)\overline{g}\widetilde{g}_\ell+\widetilde{\rho}\frac{\mathrm{d}}{\mathrm{d}p}\left(\overline{\rho\chi}\frac{\mathrm{d}\overline{T}}{\mathrm{d}p}\right)\overline{g}^2+\overline{\rho}\frac{\mathrm{d}}{\mathrm{d}p}\left(\overline{\rho\chi}\frac{\mathrm{d}\widetilde{T}_\ell}{\mathrm{d}p}\right)\overline{g}^2+\overline{\rho}\frac{\mathrm{d}}{\mathrm{d}p}\left(\widetilde{\rho\chi}_\ell\frac{\mathrm{d}\overline{T}}{\mathrm{d}p}\right)\overline{g}^2\\
&\left.-\frac{\ell(\ell+1)}{r^2}\left(\overline{\chi}\widetilde{T}_\ell+\overline{\rho}\overline{T}D_{\mathrm{h}}c_p\left(\Psi_\ell+\Phi\Lambda_\ell\right)\right)+\widetilde{\rho\varepsilon}_\ell\right\}P_\ell(\cos\theta). \qquad \text{(C.8)}
\end{aligned}
$$

C.3 Second simplification of the right hand side

In Eq. (C.8), all terms will be simplified one by one. Assuming that $\overline{\rho\chi}=\overline{\rho}\overline{\chi}$, $\widetilde{\rho\chi}=\tilde{\rho}\tilde{\chi}$ and that

$$
\overline{\rho\chi}\frac{\mathrm{d}\overline{T}}{\mathrm{d}p}=\frac{L(r)}{4\pi\mathcal{G}M(r)}, \qquad \text{(C.9)}
$$

the summed term reads

$$
\begin{aligned}
\left(\overline{\rho\chi}\frac{\mathrm{d}\widetilde{T}_\ell}{\mathrm{d}p}+\widetilde{\rho\chi}_\ell\frac{\mathrm{d}\overline{T}}{\mathrm{d}p}\right)\left(\overline{f}_{\mathrm{C}}-4\pi\mathcal{G}\overline{\rho}\right)&=\overline{\rho\chi}\frac{\mathrm{d}\overline{T}}{\mathrm{d}p}\left(\frac{\mathrm{d}\widetilde{T}_\ell}{\mathrm{d}\overline{T}}+\frac{\widetilde{\rho\chi}_\ell}{\overline{\rho\chi}}\right)\left(\overline{f}_{\mathrm{C}}-4\pi\mathcal{G}\overline{\rho}\right)\\
&=\frac{L(r)\overline{\rho}}{M(r)}\left(\frac{\mathrm{d}\widetilde{T}_\ell}{\mathrm{d}\overline{T}}+\frac{\widetilde{\rho\chi}_\ell}{\overline{\rho\chi}}\right)\left(\frac{\overline{f}_{\mathrm{C}}}{4\pi\mathcal{G}\overline{\rho}}-1\right). \qquad \text{(C.10)}
\end{aligned}
$$

Next, in Eq. (2.95), the terms in factor of gravity are

$$
\overline{\rho}\,\overline{g}^2\left[2\frac{\mathrm{d}}{\mathrm{d}p}\left(\overline{\rho\chi}\frac{\mathrm{d}\overline{T}}{\mathrm{d}p}\right)\frac{\widetilde{g}_\ell}{\overline{g}}+\frac{\widetilde{\rho}_\ell}{\overline{\rho}}\frac{\mathrm{d}}{\mathrm{d}p}\left(\overline{\rho\chi}\frac{\mathrm{d}\overline{T}}{\mathrm{d}p}\right)+\frac{\mathrm{d}}{\mathrm{d}p}\left(\overline{\rho\chi}\frac{\mathrm{d}\widetilde{T}_\ell}{\mathrm{d}p}\right)+\frac{\mathrm{d}}{\mathrm{d}p}\left(\widetilde{\rho\chi}_\ell\frac{\mathrm{d}\overline{T}}{\mathrm{d}p}\right)\right]. \qquad \text{(C.11)}
$$

Using the relation stating global radiative equilibrium

$$
\overline{\rho}\,\overline{g}^2\frac{\mathrm{d}}{\mathrm{d}p}\left(\overline{\rho\chi}\frac{\mathrm{d}\overline{T}}{\mathrm{d}p}\right)=-\overline{\rho\chi}\frac{\mathrm{d}\overline{T}}{\mathrm{d}p}\left(\overline{f}_{\mathrm{C}}-4\pi\mathcal{G}\overline{\rho}\right)-\overline{\rho}(\overline{\varepsilon}+\overline{\varepsilon}_{\mathrm{g}}), \qquad \text{(C.12)}
$$

we rewrite Eq. (C.11) as

$$\begin{aligned}
&\left[\frac{L(r)\overline{\rho}}{M(r)}\left(1-\frac{\overline{f}_{\rm C}}{4\pi\mathcal{G}\overline{\rho}}\right)-\overline{\rho}(\overline{\varepsilon}+\overline{\varepsilon}_{\rm g})\right]\left(2\frac{\widetilde{g}_\ell}{\overline{g}}+\Theta_\ell\right)+\overline{\rho}\,\overline{g}^2\frac{\mathrm{d}}{\mathrm{d}p}\left(\overline{\rho\chi}\frac{\mathrm{d}\widetilde{T}_\ell}{\mathrm{d}p}+\widetilde{\rho\chi}_\ell\frac{\mathrm{d}\overline{T}}{\mathrm{d}p}\right)\\
=\;&\frac{L\overline{\rho}}{M}\left(1-\frac{\overline{f}_{\rm C}}{4\pi\mathcal{G}\overline{\rho}}-\frac{M}{L}(\overline{\varepsilon}+\overline{\varepsilon}_{\rm g})\right)\left(2\frac{\widetilde{g}_\ell}{\overline{g}}+\Theta_\ell\right)+\overline{\rho}\,\overline{g}^2\frac{\mathrm{d}}{\mathrm{d}p}\left(\overline{\rho\chi}\frac{\mathrm{d}\overline{T}}{\mathrm{d}p}\left(\frac{\mathrm{d}\widetilde{T}_\ell}{\mathrm{d}\overline{T}}+\frac{\widetilde{\rho\chi}_\ell}{\overline{\rho\chi}}\right)\right)\\
=\;&\frac{L\overline{\rho}}{M}\left(1-\frac{\overline{f}_{\rm C}}{4\pi\mathcal{G}\overline{\rho}}-\frac{M}{L}(\overline{\varepsilon}+\overline{\varepsilon}_{\rm g})\right)\left(2\frac{\widetilde{g}_\ell}{\overline{g}}+\Theta_\ell\right)+\overline{\rho}\,\overline{g}^2\frac{L(r)}{4\pi\mathcal{G}M(r)}\frac{\mathrm{d}}{\mathrm{d}p}\left(\frac{\mathrm{d}\widetilde{T}_\ell}{\mathrm{d}\overline{T}}+\frac{\widetilde{\rho\chi}_\ell}{\overline{\rho\chi}}\right)\\
&+\frac{L\overline{\rho}}{M}\left(1-\frac{\overline{f}_{\rm C}}{4\pi\mathcal{G}\overline{\rho}}-\frac{M}{L}(\overline{\varepsilon}+\overline{\varepsilon}_{\rm g})\right)\left(\frac{\mathrm{d}\widetilde{T}_\ell}{\mathrm{d}\overline{T}}+\frac{\widetilde{\rho\chi}_\ell}{\overline{\rho\chi}}\right).
\end{aligned}\tag{C.13}$$

Equation (C.11) finally reads

$$\frac{L\overline{\rho}}{M}\Bigg\{\left[1-\frac{\overline{f}_{\rm C}}{4\pi\mathcal{G}\overline{\rho}}-\frac{M}{L}(\overline{\varepsilon}+\overline{\varepsilon}_{\rm g})\right]\left(2\frac{\widetilde{g}_\ell}{\overline{g}}+\frac{\mathrm{d}\widetilde{T}_\ell}{\mathrm{d}\overline{T}}+\frac{\widetilde{\rho\chi}_\ell}{\overline{\rho\chi}}+\Theta_\ell\right)+\frac{\overline{g}^2}{4\pi\mathcal{G}}\frac{\mathrm{d}}{\mathrm{d}p}\left(\frac{\mathrm{d}\widetilde{T}_\ell}{\mathrm{d}\overline{T}}+\frac{\widetilde{\rho\chi}_\ell}{\overline{\rho\chi}}\right)\Bigg\}.\tag{C.14}$$

We are almost there. Injecting Eqs. (C.9), (C.10) and (C.14) into the ℓ-component of Eq. (2.95) gives:

$$\begin{aligned}
\text{RHS}\;=\;&\frac{L\overline{\rho}}{M}\left(\frac{\mathrm{d}\widetilde{T}_\ell}{\mathrm{d}\overline{T}}+\frac{\widetilde{\rho\chi}_\ell}{\overline{\rho\chi}}\right)\left(\frac{\overline{f}_{\rm C}}{4\pi\mathcal{G}\overline{\rho}}-1\right)+\frac{L}{4\pi\mathcal{G}M}\left(\widetilde{f}_{{\rm C},\ell}-4\pi\mathcal{G}\widetilde{\rho}_\ell\right)\\
&+\frac{L\overline{\rho}}{M}\Bigg\{\left[1-\frac{\overline{f}_{\rm C}}{4\pi\mathcal{G}\overline{\rho}}-\frac{M}{L}(\overline{\varepsilon}+\overline{\varepsilon}_{\rm g})\right]\left(2\frac{\widetilde{g}_\ell}{\overline{g}}+\frac{\mathrm{d}\widetilde{T}_\ell}{\mathrm{d}\overline{T}}+\frac{\widetilde{\rho\chi}_\ell}{\overline{\rho\chi}}+\Theta_\ell\right)+\frac{\overline{g}^2}{4\pi\mathcal{G}}\frac{\mathrm{d}}{\mathrm{d}p}\left(\frac{\mathrm{d}\widetilde{T}_\ell}{\mathrm{d}\overline{T}}+\frac{\widetilde{\rho\chi}_\ell}{\overline{\rho\chi}}\right)\Bigg\}\\
&-\frac{\ell(\ell+1)}{r^2}\left(\overline{\chi}\widetilde{T}_\ell+\overline{\rho}\overline{T}D_{\rm h}c_p\left(\Psi_\ell+\Phi\Lambda_\ell\right)\right)+\widetilde{\rho\varepsilon}_\ell.
\end{aligned}\tag{C.15}$$

The first term cancels part of the term in curl brackets. Furthermore, pressure derivatives replaced by $-\frac{1}{\overline{\rho}\overline{g}}\mathrm{d}/\mathrm{d}r$

$$\begin{aligned}
\text{RHS}\;=\;&-\overline{\rho}\left(\frac{\mathrm{d}\widetilde{T}_\ell}{\mathrm{d}\overline{T}}+\frac{\widetilde{\rho\chi}_\ell}{\overline{\rho\chi}}\right)(\overline{\varepsilon}+\overline{\varepsilon}_{\rm g})+\frac{L}{4\pi\mathcal{G}M}\left(\widetilde{f}_{{\rm C},\ell}-4\pi\mathcal{G}\widetilde{\rho}_\ell\right)\\
&+\frac{L\overline{\rho}}{M}\Bigg\{\left(1-\frac{\overline{f}_{\rm C}}{4\pi\mathcal{G}\overline{\rho}}-\frac{M}{L}(\overline{\varepsilon}+\overline{\varepsilon}_{\rm g})\right)\left(2\frac{\widetilde{g}_\ell}{\overline{g}}+\Theta_\ell\right)-\frac{\overline{g}}{4\pi\mathcal{G}\overline{\rho}}\frac{\mathrm{d}}{\mathrm{d}r}\left(\frac{\mathrm{d}\widetilde{T}_\ell}{\mathrm{d}\overline{T}}+\frac{\widetilde{\rho\chi}_\ell}{\overline{\rho\chi}}\right)\Bigg\}\\
&-\frac{\ell(\ell+1)}{r^2}\left(\overline{\chi}\widetilde{T}_\ell+\overline{\rho}\overline{T}D_{\rm h}c_p\left(\Psi_\ell+\Phi\Lambda_\ell\right)\right)+\widetilde{\rho\varepsilon}_\ell.
\end{aligned}\tag{C.16}$$

C.4 Final expression of the meridional circulation velocity

Eventually we will use Eq. (2.79) and we denote $\mathcal{T}_\ell$ the term between curl brackets:

$$\begin{aligned}
\mathcal{T}_\ell\;=\;&2\left(1-\frac{\overline{f}_{\rm C}}{4\pi\mathcal{G}\overline{\rho}}-\frac{\overline{\varepsilon}+\overline{\varepsilon}_{\rm g}}{\varepsilon_{\rm m}}\right)\frac{\widetilde{g}_\ell}{\overline{g}}+\frac{\widetilde{f}_{{\rm C},\ell}}{4\pi\mathcal{G}\overline{\rho}}-\frac{\overline{f}_{\rm C}}{4\pi\mathcal{G}\overline{\rho}}\Theta_\ell-\frac{\overline{\varepsilon}+\overline{\varepsilon}_{\rm g}}{\varepsilon_{\rm m}}\Theta_\ell\\
&+\frac{\overline{\varepsilon}}{\varepsilon_{\rm m}}\left[\left(\varepsilon_T-\delta\right)\Psi_\ell+\left(\varphi+\varepsilon_\mu\right)\Lambda_\ell\right]+\left(H_{\rm T}\frac{\partial\Psi_\ell}{\partial r}-\left(1-\delta+\chi_T\right)\Psi_\ell-\left(\varphi+\chi_\mu\right)\Lambda_\ell\right)\frac{\overline{\varepsilon}+\overline{\varepsilon}_{\rm g}}{\varepsilon_{\rm m}}\\
&-\frac{\ell(\ell+1)}{r^2}c_p\overline{T}\frac{K}{\varepsilon_{\rm m}}\left(1+\frac{D_{\rm h}}{K}\right)\Psi_\ell+\frac{\overline{g}}{4\pi\mathcal{G}\overline{\rho}}\frac{\mathrm{d}}{\mathrm{d}r}\left(H_{\rm T}\frac{\partial\Psi_\ell}{\partial r}-\left(1-\delta+\chi_T\right)\Psi_\ell-\left(\varphi+\chi_\mu\right)\Lambda_\ell\right)\\
=\;&2\left(1-\frac{\overline{f}_{\rm C}}{4\pi\mathcal{G}\overline{\rho}}-\frac{\overline{\varepsilon}+\overline{\varepsilon}_{\rm g}}{\varepsilon_{\rm m}}\right)\frac{\widetilde{g}_\ell}{\overline{g}}+\frac{\widetilde{f}_{{\rm C},\ell}}{4\pi\mathcal{G}\overline{\rho}}-\frac{\overline{f}_{\rm C}}{4\pi\mathcal{G}\overline{\rho}}\Theta_\ell+\frac{\overline{\varepsilon}+\overline{\varepsilon}_{\rm g}}{\varepsilon_{\rm m}}\Bigg[\left(H_{\rm T}\frac{\partial\Psi_\ell}{\partial r}-\left(1-\delta+\chi_T\right)\Psi_\ell\right.
\end{aligned}$$

$$- (\varphi + \chi_\mu)\,\Lambda_\ell\Big) - \Theta_\ell + \left(f_\varepsilon\,(\varepsilon_T - \delta)\,\Psi_\ell + f_\varepsilon\,(\varphi + \varepsilon_\mu)\,\Lambda_\ell\right)\Big] \tag{C.17}$$
$$+\frac{\overline{g}}{4\pi\mathcal{G}\overline{\rho}}\frac{\mathrm{d}}{\mathrm{d}r}\left(H_\mathrm{T}\frac{\partial\Psi_\ell}{\partial r} - (1-\delta+\chi_T)\,\Psi_\ell - (\varphi+\chi_\mu)\,\Lambda_\ell\right) - \frac{\ell(\ell+1)}{r^2}c_p\overline{T}\frac{K}{\varepsilon_\mathrm{m}}\left(1+\frac{D_\mathrm{h}}{K}\right)\Psi_\ell.$$

The last line of this equation needs some cleaning. With $\rho_\mathrm{m} = \frac{M(r)}{\frac{4}{3}\pi r^3}$ and $\overline{g} \simeq \frac{\mathcal{G}M}{r^2}$, and by setting

$$\Upsilon_\ell = H_\mathrm{T}\frac{\partial\Psi_\ell}{\partial r} - (1-\delta+\chi_T)\,\Psi_\ell - (\varphi+\chi_\mu)\,\Lambda_\ell, \tag{C.18}$$

(which will be useful in Chapter 6), we obtain:

$$\begin{aligned}
\frac{\overline{g}}{4\pi\mathcal{G}\overline{\rho}}\frac{\mathrm{d}\Upsilon_\ell}{\mathrm{d}r} - \frac{\ell(\ell+1)}{r^2}c_p\overline{T}\frac{K}{\varepsilon_\mathrm{m}}\left(1+\frac{D_\mathrm{h}}{K}\right)\Psi_\ell &= \frac{M}{4\pi r^2\overline{\rho}}\frac{\mathrm{d}\Upsilon_\ell}{\mathrm{d}r} + \frac{\ell(\ell+1)}{r^2}\frac{H_\mathrm{T}M}{L}\frac{\mathrm{d}T}{\mathrm{d}r}\frac{\overline{\chi}}{\overline{\rho}}\left(1+\frac{D_\mathrm{h}}{K}\right)\Psi_\ell \\
&= \frac{\rho_\mathrm{m}}{\overline{\rho}}\frac{r}{3}\frac{\mathrm{d}\Upsilon_\ell}{\mathrm{d}r} - \frac{\ell(\ell+1)}{r^2}H_\mathrm{T}\frac{\overline{g}}{4\pi\mathcal{G}\overline{\rho}}\left(1+\frac{D_\mathrm{h}}{K}\right)\Psi_\ell \\
&= \frac{\rho_\mathrm{m}}{\overline{\rho}}\left(\frac{r}{3}\frac{\mathrm{d}\Upsilon_\ell}{\mathrm{d}r} - \frac{\ell(\ell+1)H_\mathrm{T}}{3r}\left(1+\frac{D_\mathrm{h}}{K}\right)\Psi_\ell\right),
\end{aligned} \tag{C.19}$$

where we have used Eq. (C.9) between first and second line. Finally, we write $\mathcal{T}_\ell$ in the same way as Mathis & Zahn (2004):

$$\begin{aligned}
\mathcal{T}_\ell &= 2\left(1 - \frac{\overline{f}_\mathrm{C}}{4\pi\mathcal{G}\overline{\rho}} - \frac{\overline{\varepsilon}+\overline{\varepsilon}_\mathrm{g}}{\varepsilon_\mathrm{m}}\right)\frac{\widetilde{g}_\ell}{\overline{g}} + \frac{\widetilde{f}_{\mathrm{C},\ell}}{4\pi\mathcal{G}\overline{\rho}} - \frac{\overline{f}_\mathrm{C}}{4\pi\mathcal{G}\overline{\rho}}\Theta_\ell \\
&+ \frac{\rho_\mathrm{m}}{\overline{\rho}}\left[\frac{r}{3}\frac{\mathrm{d}}{\mathrm{d}r}\left(H_\mathrm{T}\frac{\partial\Psi_\ell}{\partial r} - (1-\delta+\chi_T)\,\Psi_\ell - (\varphi+\chi_\mu)\,\Lambda_\ell\right) - \frac{\ell(\ell+1)H_\mathrm{T}}{3r}\left(1+\frac{D_\mathrm{h}}{K}\right)\Psi_\ell\right] \\
&+ \frac{\overline{\varepsilon}+\overline{\varepsilon}_\mathrm{g}}{\varepsilon_\mathrm{m}}\Big[\left(H_\mathrm{T}\frac{\partial\Psi_\ell}{\partial r} - (1-\delta+\chi_T)\,\Psi_\ell - (\varphi+\chi_\mu)\,\Lambda_\ell\right) + (f_\varepsilon\varepsilon_T - f_\varepsilon\delta + \delta)\,\Psi_\ell \\
&+ (f_\varepsilon\varepsilon_\mu + f_\varepsilon\varphi - \varphi)\,\Lambda_\ell\Big].
\end{aligned} \tag{C.20}$$

And the equation expressing the term of degree ℓ of the meridional circulation is

$$\overline{T}c_p\left[\frac{\mathrm{d}\Psi_\ell}{\mathrm{d}t} + \Phi\frac{\mathrm{d}\ln\overline{\mu}}{\mathrm{d}t}\Lambda_\ell + \frac{U_\ell}{H_\mathrm{p}}\left(\nabla_\mathrm{ad} - \nabla\right)\right] = \frac{L_p}{M_p}\mathcal{T}_\ell. \tag{C.21}$$

D. Some details on the derivation of the transport of angular momentum equations

D.1 Vertical transport of angular momentum

In order to recover the equation for the vertical transport of AM, we integrate Eq. (2.117) times $\sin\theta \mathrm{d}\theta$ between 0 and π:

$$\begin{aligned}&\int_0^\pi \frac{\partial}{\partial t}\left(\rho r^2 \sin^2\theta \Omega\right)\sin\theta \mathrm{d}\theta + \int_0^\pi \boldsymbol{\nabla}\cdot\left(\rho r^2 \sin^2\theta \Omega \boldsymbol{\mathcal{U}}\right)\sin\theta \mathrm{d}\theta \\ = &\int_0^\pi \frac{\sin^2\theta}{r^2}\frac{\partial}{\partial r}\left(\rho \nu_\mathrm{v} r^4 \frac{\partial \Omega}{\partial r}\right)\sin\theta \mathrm{d}\theta + \int_0^\pi \frac{1}{\sin\theta}\frac{\partial}{\partial \theta}\left(\rho \nu_\mathrm{h} \sin^3\theta \frac{\partial \Omega}{\partial \theta}\right)\sin\theta \mathrm{d}\theta. \end{aligned} \tag{D.1}$$

- The first term leads to

$$\int_0^\pi \frac{\partial}{\partial t}\left(\rho r^2 \sin^2\theta \Omega\right)\sin\theta \mathrm{d}\theta = \frac{\partial}{\partial t}\left(\rho r^2 \int_0^\pi \sin^3\theta \Omega(r,\theta)\mathrm{d}\theta\right). \tag{D.2}$$

  Until now, we have defined our horizontal averages of a quantity X as $\int X \sin\theta \mathrm{d}\theta / \int \sin\theta \mathrm{d}\theta$. With the above equation, it seems that a better choice of averaging in the particular case Ω is to define

$$\overline{\Omega}(r) = \frac{\int_0^\pi \Omega(r,\theta)\sin^3\theta \mathrm{d}\theta}{\int_0^\pi \sin^3\theta \mathrm{d}\theta}. \tag{D.3}$$

  With this choice, the first term can be rewritten $\partial_t\left(\rho r^2 \overline{\Omega}\right)\int_0^\pi \sin^3\theta \mathrm{d}\theta$.

  We shall do a small break on the decomposition of Ω on Legendre polynomials. Usually, Ω would have been decomposed as any other quantity on Legendre polynomials, with the 0^{th}-order term following the averaging defined in Eq. (1.49). But with this new definition, there is a little subtlety. Indeed, if we keep the usual definition $\Omega(r,\theta) = \sum_\ell \widetilde{\Omega}_\ell(r) P_\ell(\cos\theta)$ we should have the following:

$$\overline{\Omega}(r) = \frac{\int_0^\pi \Omega(r,\theta)\sin^3\theta \mathrm{d}\theta}{\int_0^\pi \sin^3\theta \mathrm{d}\theta} = \overline{\Omega}(r) + \sum_{\ell>0} \widetilde{\Omega}_\ell(r)\frac{\int_0^\pi P_\ell(\cos\theta)\sin^3\theta \mathrm{d}\theta}{\int_0^\pi \sin^3\theta \mathrm{d}\theta}. \tag{D.4}$$

  Then for this to be true, we should have $\forall \ell \in \mathbb{N}, \int_0^\pi P_\ell(\cos\theta)\sin^3\theta \mathrm{d}\theta = 0$. Yet, the integral in the right hand side is not 0 but $\delta_{0,\ell} - \frac{1}{5}\delta_{2,\ell}$ (see Eq. (B.13)). Therefore Ω is not decomposed in a linear combination of Legendre polynomials but on a slightly different basis of polynomials $Q_\ell(\cos\theta) = P_\ell(\cos\theta) - I_\ell$

$$\Omega(r,\theta) = \sum_\ell \widetilde{\Omega}_\ell(r) Q_\ell(\cos\theta) = \overline{\Omega}(r) + \widetilde{\Omega}_2(r)\left[P_2(\cos\theta) + \frac{1}{5}\right] + \widetilde{\Omega}_4 P_4(\cos\theta) + \dots. \tag{D.5}$$

- The second term reads

$$\begin{aligned}\int_0^\pi \boldsymbol{\nabla}\cdot\left(\rho r^2 \sin^2\theta \Omega \boldsymbol{\mathcal{U}}\right)\sin\theta \mathrm{d}\theta &= \int_0^\pi \frac{1}{r^2}\frac{\partial}{\partial r}\left(\rho r^4 \sin^3\theta \Omega (U_r + \dot{r})\right)\mathrm{d}\theta \\ &+ \int_0^\pi \frac{1}{r\sin\theta}\frac{\partial}{\partial\theta}\left(\rho r^2 \sin^3\theta \Omega U_\theta\right)\sin\theta \mathrm{d}\theta, \end{aligned} \tag{D.6}$$

  where we used the definition of $\boldsymbol{\mathcal{U}}$ in Eq. (2.73) by denoting U_r (resp. U_θ) the radial (resp. latitudinal) part.

Let us first express $\int_0^\pi \frac{1}{r^2}\frac{\partial}{\partial r}\left(\rho r^4 \sin^3\theta \Omega U_r\right)\mathrm{d}\theta$. When Ω and U_r are replaced by their Legendre decomposition, this equation involves integrals such as, $m, n \in \mathbb{N}$

$$\int_0^\pi \sin^3\theta P_m(\cos\theta)Q_n(\cos\theta)\mathrm{d}\theta = \int_0^\pi (1-P_2(\cos\theta))P_m(x)Q_n(x)\mathrm{d}x, \tag{D.7}$$

which, in general are not 0 (see Sect. B.2). Therefore, contrary to what many authors said (Mathis & Zahn, 2004), all orders of the vertical meridional circulation are able to advect AM. However, since $\forall \ell, \widetilde{\Omega}_\ell \ll \widetilde{\Omega}_{\ell+1}$ and $U_\ell \ll U_{\ell+1}$, one can neglect all terms but the $\overline{\Omega}U_2$ term (remember that $U_0 = 0$), leading to

$$\begin{aligned}
& \frac{1}{r^2}\frac{\partial}{\partial r}\left(\rho r^4 \int_0^\pi \sin^3\theta \sum_\ell \widetilde{\Omega}_\ell Q_\ell(\cos\theta)\sum_\ell U_\ell P_\ell(\cos\theta)\mathrm{d}\theta\right) \\
= & \frac{1}{r^2}\frac{\partial}{\partial r}\left(\rho r^4 \overline{\Omega} U_2 \int_0^\pi \sin^3\theta P_2(\cos\theta)\mathrm{d}\theta\right) \\
= & -\frac{1}{5r^2}\frac{\partial}{\partial r}\left(\rho r^4 \overline{\Omega} U_2\right)\int_0^\pi \sin^3\theta \mathrm{d}\theta,
\end{aligned} \tag{D.8}$$

where the last line was obtained using (B.13).

In a Lagrangian description, the term $\dot{r}$ conveniently vanishes and we are left with the momentum advected vertically by the horizontal velocity which of course is 0. Indeed, by removing all the terms depending only on r, above integral reads

$$\int_0^\pi \frac{1}{\sin\theta}\frac{\partial}{\partial\theta}\left(\sin^3\theta\Omega U_\theta\right)\sin\theta\mathrm{d}\theta \tag{D.9}$$

$$\begin{aligned}
= & \int_0^\pi \frac{\partial}{\partial\theta}\left(\sin^3\theta\sum_\ell \widetilde{\Omega}_\ell Q_\ell(\cos\theta)\sum_\ell V_\ell \frac{\partial P_\ell(\cos\theta)}{\partial\theta}\mathrm{d}\theta\right)\mathrm{d}\theta \\
= & \sin^3\theta\sum_\ell \widetilde{\Omega}_\ell Q_\ell(\cos\theta)\sum_\ell V_\ell \frac{\partial P_\ell(\cos\theta)}{\partial\theta}\Bigg|_0^\pi \\
= & 0.
\end{aligned} \tag{D.10}$$

- Third term is again very simple:

$$\int_0^\pi \frac{\sin^2\theta}{r^2}\frac{\partial}{\partial r}\left(\rho\nu_{\mathrm{v}} r^4\frac{\partial\Omega}{\partial r}\right)\sin\theta\mathrm{d}\theta = \frac{1}{r^2}\frac{\partial}{\partial r}\left(\rho\nu_{\mathrm{v}} r^4\frac{\partial\overline{\Omega}}{\partial r}\right)\int_0^\pi \sin^3\theta\mathrm{d}\theta. \tag{D.11}$$

- and last term is zero for the same reason as for the horizontal advection term.

Wrapping up everything and dividing by $\int_0^\pi \sin^3\theta\mathrm{d}\theta$ yields the average equation for the vertical transport of angular momentum:

$$\rho\frac{\mathrm{d}r^2\overline{\Omega}}{\mathrm{d}t} = \frac{1}{5r^2}\frac{\partial}{\partial r}\left(\rho r^4\overline{\Omega}U_2\right) + \frac{1}{r^2}\frac{\partial}{\partial r}\left(\rho\nu_{\mathrm{v}} r^4\frac{\partial\overline{\Omega}}{\partial r}\right). \tag{D.12}$$

D.2 Horizontal transport of angular momentum

Coming back to Eq. (2.117), we replace Ω by $\bar{\Omega} + \Omega_2 Q_2(\cos\theta)$, $\boldsymbol{\mathcal{U}}$ by Ω by $U_2 P_2(\cos\theta) + V_2 \mathrm{d}P_2(\cos\theta)/\mathrm{d}\theta$. Hence,

$$\rho\frac{\mathrm{d}}{\mathrm{d}t}\left[r^2\sin^2\theta\left(\bar{\Omega}+\Omega_2 Q_2(\cos\theta)\right)\right] + \frac{1}{r^2}\partial_r\left[\rho r^4\sin^2\theta\left(\bar{\Omega}+\Omega_2 Q_2(\cos\theta)\right)U_2 P_2(\cos\theta)\right]$$

$$+\frac{1}{r\sin\theta}\partial_\theta\left[\rho r^2\sin^3\theta\left(\bar{\Omega}+\Omega_2 Q_2(\cos\theta)\right)V_2\frac{\mathrm{d}P_2(\cos\theta)}{\mathrm{d}\theta}\right] \tag{D.13}$$
$$= \frac{\sin^2\theta}{r^2}\partial_r\left[\rho\nu_\mathrm{v} r^4\partial_r\left(\bar{\Omega}+\Omega_2 Q_2(\cos\theta)\right)\right]+\frac{1}{\sin\theta}\partial_\theta\left[\rho\nu_\mathrm{h}\sin^3\theta\partial_\theta\left(\bar{\Omega}+\Omega_2 Q_2(\cos\theta)\right)\right].$$

And by neglecting 4$^{\text{th}}$ order terms, one obtains

$$\begin{aligned}
&\rho\frac{\mathrm{d}}{\mathrm{d}t}\left(r^2\sin^2\theta\left(\bar{\Omega}+\Omega_2 Q_2(\cos\theta)\right)\right)+\frac{1}{r^2}\frac{\partial}{\partial r}\left(\rho r^4\sin^2\theta\bar{\Omega}U_2\right)P_2(\cos\theta)\\
&+\frac{1}{r\sin\theta}\rho r^2 V_2\bar{\Omega}\frac{\partial}{\partial\theta}\left(\sin^3\theta\frac{\mathrm{d}P_2(\cos\theta)}{\mathrm{d}\theta}\right)\\
=\;&\frac{\sin^2\theta}{r^2}\left[\frac{\partial}{\partial r}\left(\rho\nu_\mathrm{v} r^4\frac{\partial\bar{\Omega}}{\partial r}\right)+\frac{\partial}{\partial r}\left(\rho\nu_\mathrm{v} r^4\frac{\partial\Omega_2}{\partial r}Q_2(\cos\theta)\right)\right]\\
&+\frac{1}{\sin\theta}\frac{\partial}{\partial\theta}\left(\rho\nu_\mathrm{h}\sin^3\theta\Omega_2\frac{\mathrm{d}Q_2(\cos\theta)}{\mathrm{d}\theta}\right).
\end{aligned} \tag{D.14}$$

Then we multiply Eq. (2.118) by $\sin^2\theta$ and subtract it to Eq. (D.14), which gives

$$\begin{aligned}
&\rho\frac{\mathrm{d}}{\mathrm{d}t}\left(r^2\sin^2\theta\Omega_2 Q_2(\cos\theta)\right)+\frac{1}{r^2}\frac{\partial}{\partial r}\left(\rho r^4\sin^2\theta\bar{\Omega}U_2\right)P_2(\cos\theta)+\frac{\sin^2\theta}{5r^2}\frac{\partial}{\partial r}\left(\rho r^4\bar{\Omega}U_2\right)\\
+\;&\frac{1}{r\sin\theta}\rho r^2 V_2\bar{\Omega}\frac{\partial}{\partial\theta}\left[\sin^3\theta\frac{\mathrm{d}P_2(\cos\theta)}{\mathrm{d}\theta}\right]=\frac{\sin^2\theta}{r^2}\frac{\partial}{\partial r}\left[\rho\nu_\mathrm{v} r^4\frac{\partial\Omega_2}{\partial r}Q_2(\cos\theta)\right]\\
+\;&\frac{1}{\sin\theta}\frac{\partial}{\partial\theta}\left[\rho\nu_\mathrm{h}\sin^3\theta\Omega_2\frac{\mathrm{d}Q_2(\cos\theta)}{\mathrm{d}\theta}\right].
\end{aligned} \tag{D.15}$$

We neglect the variations of $\rho\nu_\mathrm{h}$ over an isobar and we note that $\frac{1}{\sin\theta}\frac{\mathrm{d}}{\mathrm{d}\theta}\left(\sin^3\theta\frac{\mathrm{d}P_2(\cos\theta)}{\mathrm{d}\theta}\right)$ simplifies to $-10\sin^2\theta Q_2(\cos\theta)$. Therefore,

$$\begin{aligned}
&\rho\frac{\mathrm{d}}{\mathrm{d}t}\left(r^2\sin^2\theta\Omega_2 Q_2(\cos\theta)\right)+\frac{1}{r^2}\underbrace{\left(P_2(\cos\theta)+\frac{1}{5}\right)}_{Q_2(\cos\theta)}\frac{\partial}{\partial r}\left(\rho r^4\sin^2\theta\bar{\Omega}U_2\right)-10\rho r V_2\bar{\Omega}\sin^2\theta Q_2(\cos\theta)\\
&=\frac{\sin^2\theta}{r^2}\frac{\partial}{\partial r}\left[\rho\nu_\mathrm{v} r^4\frac{\partial\Omega_2}{\partial r}Q_2(\cos\theta)\right]-10\rho\nu_\mathrm{h}\Omega_2\sin^2\theta Q_2(\cos\theta).
\end{aligned} \tag{D.16}$$

Finally simplifying by $Q_2(\cos\theta)$ and making use of Eq. (2.74) yields the equation for the horizontal transport of angular momentum:

$$\rho\frac{\mathrm{d}}{\mathrm{d}t}\left(r^2\Omega_2\right)+\frac{1}{r^2}\frac{\partial}{\partial r}\left(\rho r^4\bar{\Omega}U_2\right)-\frac{10}{6}\frac{\mathrm{d}\rho r^2 U_2}{\mathrm{d}r}\bar{\Omega}=\frac{1}{r^2}\frac{\partial}{\partial r}\left[\rho\nu_\mathrm{v} r^4\frac{\partial\Omega_2}{\partial r}\right]-10\rho\nu_\mathrm{h}\Omega_2. \tag{D.17}$$

E. Synthèse en français: Du transport de moment cinétique dans les zones radiatives stellaires, en 2D

Henyey et al. (1955, 1959a,b, 1964) ont été les premiers à calculer des modèles stellaires en utilisant des ordinateurs et ces modèles ont par la suite été étendus par Iben (1965a,b, 1966a,b). Ces travaux ont abouti au modèle standard de la physique stellaire. Les étoiles sont considérées comme des sphères de plasma en équilibre hydrostatique et thermique local. L'énergie produite par les réactions de fusion nucléaire, ou perdue par les neutrinos à l'intérieur des étoiles, peut être rayonnée ou convertie en énergie thermique. Tous les autres phénomènes susceptibles de compliquer la physique des étoiles ont été longtemps négligés. Parmi eux, on peut citer les champs magnétiques, les processus de diffusion, les forces de marée, la rotation, etc. Avec ces hypothèses, un système physique aussi complexe qu'une étoile peut être simplifié en un système unidimensionnel, c'est-à-dire où toutes les quantités ne dépendent que de la coordonnée radiale.

Cependant, la modélisation de la rotation stellaire et de son évolution est importante, et ce pour plusieurs raisons. D'abord, la rotation est intimement liée à l'activité magnétique stellaire par son interaction avec la convection. Une activité magnétique accrue peut avoir un impact déterminant sur l'atmosphère des planètes et peut entraver le développement de la vie sur celles-ci. Une deuxième raison d'étudier la rotation est liée à l'estimation de l'âge des étoiles. Les étoiles sont très souvent utilisées comme des indicateurs pour estimer l'âge de leur structure hôte ou de celles qu'elles hébergent (amas, galaxies, exoplanètes, etc.). Les erreurs dans l'estimation de l'âge sont principalement due au mélange chimique induit par l'interaction de la rotation et de l'overshoot convectif. Cet overshoot injecte du matériau riche en hydrogène dans les régions où se produit la combustion nucléaire. Comme il y a plus d'hydrogène à brûler, la durée de vie stellaire est prolongée.

Jusqu'à la fin des années 80, la plupart des modèles de rotation stellaire supposaient que les étoiles étaient barotropes, c'est-à-dire que la vitesse angulaire est constante dans des cylindres. La mesure du profil de rotation interne du soleil obtenue par Brown & Morrow (1987) a fait apparaître que l'approximation barotrope n'était pas vérifiée. Peu après, Spiegel & Zahn (1992) et Zahn (1992) ont proposé un modèle pour expliquer la forme du profil de rotation dans la zone radiative et son évolution. Ce modèle repose sur trois idées principales. Premièrement, dans la zone radiative, le moment cinétique est advecté par la circulation méridienne. Deuxièmement, les gradients de vitesse angulaire créent du cisaillement, sujets à des instabilités. La turbulence induite par ce cisaillement etraîne la diffusion de la vitesse angulaire. Cette turbulence est supposée être beaucoup plus forte horizontalement que radialement, en raison de la stratification stable. Il en résulte un profil de rotation constant en latitude, appelé profil de rotation shellulaire. Cette hypothèse permet de conserver une description unidimensionnelle de la structure stellaire, même si celle-ci est en rotation.

Le développement de l'astéroséismologie pour d'autres étoiles que le Soleil et surtout les données de haute qualité mises à disposition par les missions spatiales CoRoT (Catala et al., 1995; Baglin et al., 2006; Michel et al., 2008) et *Kepler* (Borucki et al., 2010) ont fait apparaître des décalages importants entre les prédictions des modèles et le profil de rotation observés. Le modèle de Zahn (1992) et ses améliorations ultérieurs (Maeder, 1995; Meynet & Maeder, 1997; Talon et al., 1997; Maeder, 2003) prévoient une rotation différentielle radiale dans la zone radiative du Soleil, en contradiction avec le profil de rotation observé qui est presque constant. De plus, le taux de rotation du cœur des étoiles géantes rouges s'est avéré être environ deux ordres de grandeur plus élevé que celui prédit par les modèles (Beck et al., 2012; Deheuvels et al., 2012; Marques et al., 2013). Ces observations ont montré clairement que des mécanismes supplémentaires de transport du moment angulaire doivent être inclus dans la modélisation. Beaucoup d'entre eux ont été suggérés : instabilités hydrodynamiques, instabilités magnéto-

hydrodynamiques, modes mixtes, ondes internes de gravité (IGW), etc. Actuellement, aucun de ces mécanismes n'est modélisé correctement et de manière cohérente. Pour permettre une modélisation correcte de ces mécanismes supplémentaires de transport du moment angulaire, il faut apporter quelques modifications au modèle standard de la physique stellaire.

Dans cette thèse, nous avons choisi de sortir de la description unidimensionnelle. Différents arguments peuvent être avancés pour motiver ce changement dans la modélisation. Tout d'abord, dans la zone convective, la vitesse angulaire dépend de la latitude. Par conséquent, à la transition entre la zone convective et la zone radiative, les conditions aux bords doivent dépendre de la latitude. Une autre raison est que l'accélération centrifuge brise la symétrie sphérique. De plus, l'approximation shellulaire n'est peut être plus valide près de l'axe de rotation car à cet endroit, la vitesse de rotation devient nulle et il ne devrait donc plus y avoir de cisaillement. Or, c'est l'hypothèse d'un profil de rotation shellulaire qui permet de conserver une description 1D. Enfin, une description 2D est fondamentale pour une modélisation correcte des mécanismes de transport supplémentaires.

J'ai établi le cadre numérique en améliorant un code d'évolution stellaire, CESTAM, qui permettra les futures études de l'évolution de la rotation stellaire. Ces améliorations peuvent être séparées en deux parties. La première est un module de déformation qui met en œuvre une méthode proposée par Roxburgh (2004, 2006). L'idée principale est de partir d'un modèle 1D et d'un profil de rotation angulaire. On résout ensuite l'équation de Poisson et l'équilibre des forces en supposant que toutes les quantités peuvent être décomposées sur des polynômes de Legendre. Cette méthode nous fournit donc les coordonnées des isobares, les fluctuations sur ces idobares de la densité et du potentiel gravitationnel sur celles-ci et la gravité effective (l'effet combiné de la gravité agissant radialement et de l'accélération centrifuge agissant perpendiculairement à l'axe de rotation). La connaissance de ces quantités nous permet de calculer des facteurs supplémentaires qui entrent dans les équations de la structure modifiée et améliore considérablement la description de l'impact de la rotation sur la structure.

La deuxième partie de ce travail est l'implémentation d'une nouvelle prescription pour le transport du moment cinétique, qui tire parti de la description en 2D de l'étoile. Ce nouveau modèle permettra prochainement d'étudier très finement le champ de vitesse de la circulation méridienne et les éventuelles variations latitudinales de la vitesse angulaire. Ce nouevau code conserve très bien la masse et le moment cinétique. Nous avons également effectué une étude sismique de nos modèles en utilisant le code d'oscillation 2D, non perturbatif, ACOR (Ouazzani et al., 2012). Pour cela, j'ai dû bâtir une interface entre ACOR et CESTAM. Les calculs effectués avec la nouvelle prescription sont plus stables qu'avec l'ancienne et significativement plus rapides.

Ce travail ouvre la voie à de nouvelles études sur le transport de moment cinétique. Certaines de ces études ont déjà commencé. Ce nouveau modèle est, par exemple, utilisé pour améliorer la compréhension de rotateurs rapides tels que les étoiles δ Sct et γ Dor, ou la caractérisation d'analogues solaires. Elle est également utilisée pour tester un nouveau modèle de l'approximation traditionnelle de la rotation, utilisé pour estimer la fréquence des ondes de basse fréquence dans les étoiles en rotation (Mathis & Prat, 2019).

References

Aarnio, A. N., Matt, S. P., & Stassun, K. G. 2012, The Astrophysical Journal, 760

Aarnio, A. N., Matt, S. P., & Stassun, K. G. 2013, Astronomische Nachrichten, 334

Abramowitz, M. & Stegun, I. A. 1972, Handbook of Mathematical Functions with Formulas, Graphs, and Mathematical Tables, ninth dover printing edn. (Dover)

Acheson, D. J. & Gibbons, M. P. 1978, Philosophical Transactions of the Royal Society of London Series A, 289, 459

Aerts, C., Christensen-Dalsgaard, J., & Kurtz, D. W. 2010, Asteroseismology

Aikawa, M., Arai, K., Arnould, M., Takahashi, K., & Utsunomiya, H. 2006, in American Institute of Physics Conference Series, Vol. 831, Frontiers in Nuclear Structure, Astrophysics, and Reactions, ed. S. V. Harissopulos, P. Demetriou, & R. Julin, 26–30

Alvan, L., Brun, A. S., & Mathis, S. 2014, Astronomy & Astrophysics, 565, A42

Amaro-Seoane, P., Audley, H., Babak, S., et al. 2017, arXiv e-prints, arXiv:1702.00786

Anderson, E., Bai, Z., Bischof, C., et al. 1999, LAPACK Users' Guide, 3rd edn. (Philadelphia, PA: Society for Industrial and Applied Mathematics)

André, P. 2002, in EAS Publications Series, Vol. 3, EAS Publications Series, ed. J. Bouvier & J.-P. Zahn, 1–38

Appourchaux, T., Boumier, P., Leibacher, J. W., & Corbard, T. 2018, Astronomy & Astrophysics, 617, A108

Appourchaux, T. & Corbard, T. 2019, Astronomy & Astrophysics, 624, A106

Appourchaux, T. & Pallé, P. L. 2013, in Astronomical Society of the Pacific Conference Series, Vol. 478, Fifty Years of Seismology of the Sun and Stars, ed. K. Jain, S. C. Tripathy, F. Hill, J. W. Leibacher, & A. A. Pevtsov, 125

Artemenko, S. A., Grankin, K. N., & Petrov, P. P. 2012, Astronomy Letters, 38, 783

Artigau, É., Kouach, D., Donati, J.-F., et al. 2014, Society of Photo-Optical Instrumentation Engineers (SPIE) Conference Series, Vol. 9147, SPIRou: the near-infrared spectropolarimeter/high-precision velocimeter for the Canada-France-Hawaii telescope, 914715

Asplund, M., Grevesse, N., & Sauval, A. J. 2005, Astronomical Society of the Pacific Conference Series, Vol. 336, The Solar Chemical Composition, ed. I. Barnes, Thomas G. & F. N. Bash, 25

Asplund, M., Grevesse, N., Sauval, A. J., & Scott, P. 2009, Annual Review of Astronomy & Astrophysics, 47, 481

Augustson, K. C. & Mathis, S. 2019, Astrophysical Journal, 874, 83

Augustson, K. C., Mathis, S., & Astoul, A. 2020, arXiv e-prints, arXiv:2009.10473

Aurière, M. 2003, in EAS Publications Series, Vol. 9, EAS Publications Series, ed. J. Arnaud & N. Meunier, 105

Babcock, H. W. 1947, Astrophysical Journal, 105, 105

Bachmann, K. T., Duvall, Jr., T. L., Harvey, J. W., et al. 1995, ApJ, 443, 837

Badnell, N. R., Bautista, M. A., Butler, K., et al. 2005, Monthly Notices of the Royal Astronomical Society, 360, 458

Baglin, A., Auvergne, M., Barge, P., et al. 2006, in ESA Special Publication, Vol. 1306, The CoRoT Mission Pre-Launch Status - Stellar Seismology and Planet Finding, ed. M. Fridlund, A. Baglin, J. Lochard, & L. Conroy, 33

Baker, J., Bellovary, J., Bender, P. L., et al. 2019, arXiv e-prints, arXiv:1907.06482

Balbus, S. A. & Hawley, J. F. 1991, Astrophysical Journal, 376, 214

Ball, W. H., Beeck, B., Cameron, R. H., & Gizon, L. 2016, Astronomy & Astrophysics, 592, A159

Ball, W. H. & Gizon, L. 2014, A&A, 568

Ballot, J., Lignières, F., Prat, V., Reese, D. R., & Rieutord, M. 2012, in Astronomical Society of the Pacific Conference Series, Vol. 462, Progress in Solar/Stellar Physics with Helio- and Asteroseismology, ed. H. Shibahashi, M. Takata, & A. E. Lynas-Gray, 389

Ballot, J., Lignières, F., & Reese, D. R. 2013, Numerical Exploration of Oscillation Modes in Rapidly Rotating Stars, ed. M. Goupil, K. Belkacem, C. Neiner, F. Lignières, & J. J. Green, Vol. 865, 91

Balmforth, N. J. 1992, MNRAS, 255, 603

Balona, L. A. & Dziembowski, W. A. 2011, Monthly Notices of the Royal Astronomical Society, 417, 591

Balona, L. A. & Evers, E. A. 1999, Monthly Notices of the Royal Astronomical Society, 302, 349

Barker, A. J., Jones, C. A., & Tobias, S. M. 2019, Monthly Notices of the Royal Astronomical Society, 487, 1777

Beck, P. G., Montalban, J., Kallinger, T., et al. 2012, Nature, 481, 55
Becquerel, H. 1896, Comptes-rendus de l'Académie des sciences
Belkacem, K., Goupil, M. J., Dupret, M. A., et al. 2011, A&A, 530, A142
Belkacem, K., Marques, J. P., Goupil, M. J., et al. 2015a, Astronomy & Astrophysics, 579, A31
Belkacem, K., Marques, J. P., Goupil, M. J., et al. 2015b, Astronomy & Astrophysics, 579, A30
Belkacem, K. & Samadi, R. 2013, Connections Between Stellar Oscillations and Turbulent Convection, ed. M. Goupil, K. Belkacem, C. Neiner, F. Lignières, & J. J. Green, Vol. 865, 179
Belkacem, K., Samadi, R., Goupil, M. J., & Kupka, F. 2006a, Astronomy & Astrophysics, 460, 173
Belkacem, K., Samadi, R., Goupil, M. J., Kupka, F., & Baudin, F. 2006b, Astronomy & Astrophysics, 460, 183
Benomar, O., Bazot, M., Nielsen, M. B., et al. 2018, Science, 361, 1231
Benomar, O., Takata, M., Shibahashi, H., Ceillier, T., & García, R. A. 2015, Monthly Notices of the Royal Astronomical Society, 452, 2654
Berthomieu, G., Provost, J., Morel, P., & Lebreton, Y. 1993, Astronomy & Astrophysics, 268, 775
Boesgaard, A. M. 1991, Astrophysical Journal Letters, 370, L95
Böhm-Vitense, E. 1958, Zeitschrift für Astrophysik, 46, 108
Böhm-Vitense, E. 1992, Introduction to Stellar Astrophysics. Vol.3: stellar-structure and evolution (Cambridge University Press)
Borucki, W. J., Koch, D., Basri, G., et al. 2010, Science, 327, 977
Bouchaud, K., Domiciano de Souza, A., Rieutord, M., Reese, D. R., & Kervella, P. 2020, Astronomy & Astrophysics, 633, A78
Bouvier, J., Forestini, M., & Allain, S. 1997, Astronomy & Astrophysics, 326, 1023
Brandenburg, A. 2020, Magnetic field evolution in solar-type stars
Breger, M., Pamyatnykh, A. A., Pikall, H., & Garrido, R. 1999, Astronomy & Astrophysics, 341, 151
Broggini, C., Bemmerer, D., Caciolli, A., & Trezzi, D. 2018, Progress in Particle and Nuclear Physics, 98, 55
Brown, T. M. 1984, Science, 226, 687
Brown, T. M. & Morrow, C. A. 1987, Astrophysical Journal Letters, 314, L21
Brüggen, M. & Hillebrandt, W. 2001, Monthly Notices of the Royal Astronomical Society, 320, 73
Brun, A. S., Strugarek, A., Varela, J., et al. 2017, Astrophysical Journal, 836, 192
Brun, A. S. & Toomre, J. 2002, Astrophysical Journal, 570, 865
Busse, F. H. 1981, Geophysical and Astrophysical Fluid Dynamics, 17, 215
Busse, F. H. 1982, Astrophysical Journal, 259, 759
Bühler, O. 2014, Waves and Mean Flows, 2nd edn. (Cambridge University Press)
Caleo, A., Balbus, S. A., & Tognelli, E. 2016, Monthly Notices of the Royal Astronomical Society, 460, 338
Cantiello, M., Mankovich, C., Bildsten, L., Christensen-Dalsgaard, J., & Paxton, B. 2014, Astrophysical Journal, 788, 93
Canuto, V. M. 2002, Astronomy & Astrophysics, 384, 1119
Canuto, V. M., Goldman, I., & Mazzitelli, I. 1996, ApJ, 473, 550
Canuto, V. M. & Mazzitelli, I. 1991, ApJ, 370, 295
Canuto, V. M. & Mazzitelli, I. 1992, ApJ, 389, 724
Catala, C., Mangeney, A., Gautier, D., et al. 1995, Astronomical Society of the Pacific Conference Series, Vol. 76, COROT: A Proposal to Study Stellar Convection and Internal Rotation, ed. R. K. Ulrich, J. Rhodes, E. J., & W. Dappen, 426
Chandrasekhar, S. 1957, An introduction to the study of stellar-structure.
Chandrasekhar, S. 1960, Proceedings of the National Academy of Science, 46, 253
Chaplin, W. J., Elsworth, Y., Isaak, G. R., et al. 1996, in American Astronomical Society Meeting Abstracts, Vol. 188, American Astronomical Society Meeting Abstracts #188, 69.04
Chapman, S. & Cowling, T. G. 1970, The mathematical theory of non-uniform gases (Cambridge University Press)
Charbonnel, C. & Talon, S. 2005, Science, 309, 2189
Christensen-Dalsgaard, J. 2008, Astrophysics and Space Science, 316, 113
Christensen-Dalsgaard, J., Dappen, W., Ajukov, S. V., et al. 1996, Science, 272, 1286
Christensen-Dalsgaard, J. & Thompson, M. J. 1997, MNRAS, 284, 527
Christophe, S., Ballot, J., Ouazzani, R. M., Antoci, V., & Salmon, S. J. A. J. 2018, Astronomy & Astrophysics, 618, A47
Cody, A. M. & Hillenbrand, L. A. 2010, Astrophysical Journal, Supplement Series, 191, 389
Cowling, T. G. 1941, Monthly Notices of the Royal Astronomical Society, 101, 367
Cox, J. P. & Giuli, R. T. 1968, Principles of stellar-structure
Czekala, I., Chiang, E., Andrews, S. M., et al. 2019, Astrophysical Journal, 883, 22
Darwin, C. 1859, On the Origin of Species by Means of Natural Selection, or the Preservation of

Favoured Races in the Struggle for Life (London: Murray)
Daszynska-Daszkiewicz, J. 2008, Communications in Asteroseismology, 152, 140
Davidson, P. A. 2013, Turbulence in Rotating, Stratified and Electrically Conducting Fluids (Cambridge University Press)
Day, D. M. & Romero, L. A. 2005, SIAM J. Numerical Analysis, 43, 1969
De Boor, C. 2001, A practical guide to splines; rev. ed., Applied mathematical sciences (Berlin: Springer)
Deal, M., Goupil, M. J., Marques, J. P., Reese, D. R., & Lebreton, Y. 2020, Astronomy & Astrophysics, 633, A23
Deheuvels, S., Dogan, G., Goupil, M. J., et al. 2014, Astronomy & Astrophysics, 564, A27
Deheuvels, S., García, R. A., Chaplin, W. J., et al. 2012, Astrophysical Journal, 756, 19
Deleuil, M., Barge, P., Leger, A., & Schneider, J. 1997, Astronomical Society of the Pacific Conference Series, Vol. 119, Detection of Earth-Sized Planets with the COROT Space Mission, ed. D. Soderblom, 259
Dintrans, B., Brandenburg, A., Nordlund, Å., & Stein, R. F. 2005, Astronomy & Astrophysics, 438, 365
Dintrans, B. & Rieutord, M. 2000, Astronomy & Astrophysics, 354, 86
Domiciano de Souza, A., Kervella, P., Jankov, S., et al. 2005, Astronomy & Astrophysics, 442, 567
Donati, J. F., Catala, C., Landstreet, J. D., & Petit, P. 2006, Astronomical Society of the Pacific Conference Series, Vol. 358, ESPaDOnS: The New Generation Stellar Spectro-Polarimeter. Performances and First Results, ed. R. Casini & B. W. Lites, 362
Donati, J. F. & Landstreet, J. D. 2009, Annual Review of Astronomy & Astrophysics, 47, 333
Dziembowski, W. A., Paterno, L., & Ventura, R. 1988, A&A, 200, 213
Eckart, C., ed. 1960 (Pergamon)
Eddington, A. S. 1925, The Observatory, 48, 73
Eddington, A. S. 1926, Nature, 117, 25
Eggenberger, P., Meynet, G., Maeder, A., et al. 2008, Astrophysics and Space Science, 316, 43
Einstein, A. 1905, Annalen der Physik, 323, 639
Emden, R. 1902, Astrophysical Journal, 15, 38
Endal, A. S. & Sofia, S. 1976, Astrophysical Journal, 210, 184
Endal, A. S. & Sofia, S. 1978, Astrophysical Journal, 220, 279
Endal, A. S. & Sofia, S. 1979, Astrophysical Journal, 232, 531
Espinosa Lara, F. & Rieutord, M. 2007, Astronomy & Astrophysics, 470, 1013
Espinosa Lara, F. & Rieutord, M. 2011, Astronomy & Astrophysics, 533, A43
Espinosa Lara, F. & Rieutord, M. 2013, Astronomy & Astrophysics, 552, A35
Evans, J. W. & Michard, R. 1962, ApJ, 136, 493
Feireisl, E., Karper, T. G., & Pokorný, M. 2016, Mathematical Theory of Compressible Viscous Fluids - Analysis and Numerics
Ferguson, J. W., Alexander, D. R., Allard, F., et al. 2005, Astrophysical Journal, 623, 585
Fossat, E., Boumier, P., Corbard, T., et al. 2017, Astronomy & Astrophysics, 604, A40
Fossat, E. & Schmider, F. X. 2018, Astronomy & Astrophysics, 612, L1
Freytag, B., Steffen, M., & Dorch, B. 2002, Astronomische Nachrichten, 323, 213
Freytag, B., Steffen, M., Ludwig, et al. 2012, Journal of Computational Physics, 231, 919
Fricke, K. 1968, Zeitschrift für Astrophysik, 68, 317
Fuller, J., Lecoanet, D., Cantiello, M., & Brown, B. 2014, Astrophysical Journal, 796, 17
Gabriel, A. H., Grec, G., Charra, J., et al. 1995, Solar Physics, 162, 61
Gabriel, M. 1989, Astronomy & Astrophysics, 226, 278
Gabriel, M. & Belkacem, K. 2018, Astronomy & Astrophysics, 612, A21
Gabriel, M., Noels, A., Montalbán, J., & Miglio, A. 2014, Astronomy & Astrophysics, 569, A63
Gagnier, D. & Garaud, P. 2018, Astrophysical Journal, 862, 36
Gagnier, D., Rieutord, M., Charbonnel, C., Putigny, B., & Espinosa Lara, F. 2019, Astronomy & Astrophysics, 625, A89
Gallet, F., Charbonnel, C., Amard, L., et al. 2017, Astronomy & Astrophysics, 597, A14
Garaud, P., Gagnier, D., & Verhoeven, J. 2017, Astrophysical Journal, 837, 133
Garaud, P. & Kulenthirarajah, L. 2016, Astrophysical Journal, 821, 49
García, R. A., Turck-Chièze, S., Jiménez-Reyes, S. J., et al. 2007, Science, 316, 1591
García Hernández, A., Moya, A., Michel, E., et al. 2013, Astronomy & Astrophysics, 559, A63
Garcia Lopez, R. J. & Spruit, H. C. 1991, Astrophysical Journal, 377, 268
Garrido, R., Garcia-Lobo, E., & Rodriguez, E. 1990, Astronomy & Astrophysics, 234, 262
Gauss, C. F. 1814, Commentationes Societatis Regiae Scientiarum Gottingensis Recentiores
Gerkema, T., Zimmerman, J. T. F., Maas, L. R. M., & van Haren, H. 2008, Reviews of Geophysics, 46, RG2004
Giampieri, G., Polnarev, A., Roxburgh, I., & Vorontsov, S. 1998, Astrophysics and Space Sci-

ence, 261, 35
Goldreich, P., Murray, N., & Kumar, P. 1994, Astrophysical Journal, 424, 466
Goldreich, P. & Schubert, G. 1967, Astrophysical Journal, 150, 571
Gough, D. O. 1977, Astrophysical Journal, 214, 196
Goupil, M. 2011, Seismic Diagnostics for Rotating Massive Main Sequence Stars, ed. J.-P. Rozelot & C. Neiner, Vol. 832, 223
Gratton, L. 1945, Memorie della Società Astronomica Italiana, 17, 5
Grevesse, N. & Noels, A. 1993, Physica Scripta Volume T, 47, 133
Grevesse, N. & Sauval, A. J. 1998, Space Science Reviews, 85, 161
Grevesse, N., Scott, P., Asplund, M., & Sauval, A. J. 2015, Astronomy & Astrophysics, 573, A27
Grigahcène, A., Dupret, M. A., Gabriel, M., Garrido, R., & Scuflaire, R. 2005, Astronomy & Astrophysics, 434, 1055
Grundahl, F., Christensen-Dalsgaard, J., Gråke Jørgensen, U., et al. 2011, in Journal of Physics Conference Series, Vol. 271, GONG-SoHO 24: A New Era of Seismology of the Sun and Solar-Like Stars, 012083
Guo, Z., Gies, D. R., & Matson, R. A. 2017, Astrophysical Journal, 851, 39
Gupta, M. & Narasimhan, S. G. 2007, Legendre polynomials Triple Product Integral and lower-degree approximation of polynomials using
Guzik, J. A., Kaye, A. B., Bradley, P. A., Cox, A. N., & Neuforge, C. 2000, Astrophysical Journal Letters, 542, L57
Haemmerlé, L., Eggenberger, P., Ekström, S., et al. 2019, Astronomy & Astrophysics, 624, A137
Handler, G., Rybicka, M., Popowicz, A., et al. 2017, Monthly Notices of the Royal Astronomical Society, 464, 2249
Hansen, C. J. & Kawaler, S. D. 1994, Stellar Interiors. Physical Principles, Structure, and Evolution, A&A Library (Springer)
Harvey, J. W., Hill, F., Hubbard, R. P., et al. 1996, Science, 272, 1284
Haxton, W. C. 1995, Annual Review of Astronomy & Astrophysics, 33, 459
Hayashi, C. 1961, Publications of the Astronomical Society of Japan, 13, 450
Henyey, L. G., Forbes, J. E., & Gould, N. L. 1964, Astrophysical Journal, 139, 306
Henyey, L. G., Lelevier, R., & Levée, R. D. 1955, Publications of the Astronomical Society of the Pacific, 67, 154
Henyey, L. G., Lelevier, R., & Levee, R. D. 1959a, Astrophysical Journal, 129, 2
Henyey, L. G., Wilets, L., Böhm, K. H., Lelevier, R., & Levee, R. D. 1959b, Astrophysical Journal, 129, 628
Hill, F., Bolding, J., Toner, C., et al. 2003, in ESA Special Publication, Vol. 517, GONG+ 2002. Local and Global Helioseismology: the Present and Future, ed. H. Sawaya-Lacoste, 295–298
Hill, G. M. 1995, Astronomy & Astrophysics, 294, 536
Hirschi, R. & Maeder, A. 2010, Astronomy & Astrophysics, 519, A16
Houdebine, E. R., Mullan, D. J., Paletou, F., & Gebran, M. 2016, Astrophysical Journal, 822, 97
Houdek, G., Trampedach, R., Aarslev, M. J., et al. 2017, MNRAS, 464
Howe, R., Christensen-Dalsgaard, J., Hill, F., et al. 2000, Science, 287, 2456
Hubeny, I. & Mihalas, D. 2014, Theory of stellar atmospheres: An introduction to astrophysical non-equilibrium quantitative spectroscopic analysis (Princeton University Press)
Hummer, D. G. & Mihalas, D. 1988, Astrophysical Journal, 331, 794
Iben, I. J. 1965a, Astrophysical Journal, 141, 993
Iben, I. J. 1965b, Astrophysical Journal, 142, 1447
Iben, I. J. 1966a, Astrophysical Journal, 143, 483
Iben, I. J. 1966b, Astrophysical Journal, 143, 505
Iglesias, C. A. & Rogers, F. J. 1996, Astrophysical Journal, 464, 943
Irwin, J., Hodgkin, S., Aigrain, S., et al. 2008, Monthly Notices of the Royal Astronomical Society, 384, 675
Jermyn, A. S., Chitre, S. M., Lesaffre, P., & Tout, C. A. 2020a, Monthly Notices of the Royal Astronomical Society, 498, 3758
Jermyn, A. S., Chitre, S. M., Lesaffre, P., & Tout, C. A. 2020b, Monthly Notices of the Royal Astronomical Society, 498, 3782
Jørgensen, A. C. S., Mosumgaard, J. R., Weiss, A., Silva Aguirre, V., & Christensen-Dalsgaard, J. 2018, Monthly Notices of the Royal Astronomical Society, 481, L35
Jørgensen, A. C. S. & Weiss, A. 2019, Monthly Notices of the Royal Astronomical Society, 488, 3463
Jørgensen, A. C. S., Weiss, A., Angelou, G., & Silva Aguirre, V. 2019, Monthly Notices of the Royal Astronomical Society, 484, 5551
Jouve, L., Gastine, T., & Lignières, F. 2015, Astronomy & Astrophysics, 575, A106
Kawaler, S. D. 1988, Astrophysical Journal, 333, 236
Kim, A., Winget, D. E., Montgomery, M. H., & Kepler, S. O. 2006, Memorie della Società Astronomica Italiana, 77, 376
Kippenhahn, R., Weigert, A., & Weiss, A. 2012, stellar-structure and Evolution, A&A Library (Springer)
Kitchatinov, L. L. & Brandenburg, A. 2012, As-

tronomische Nachrichten, 333, 230
Kjeldsen, H., Bedding, T. R., & Christensen-Dalsgaard, J. 2008, ApJ, 683
Knobloch, E. & Spruit, H. C. 1982, Astronomy & Astrophysics, 113, 261
Knobloch, E. & Spruit, H. C. 1983, Astronomy & Astrophysics, 125, 59
Kochukhov, O. 2016, Doppler and Zeeman Doppler Imaging of Stars, ed. J.-P. Rozelot & C. Neiner, Vol. 914, 177
Korycansky, D. G. 1991, Astrophysical Journal, 381, 515
Kosovichev, A. G. & Schou, J. 1997, Astrophysical Journal Letters, 482, L207
Kuhi, L. V. 1964, Astrophysical Journal, 140, 1409
Kuhi, L. V. 1966, Astrophysical Journal, 143, 991
Kulenthirarajah, L. & Garaud, P. 2018, Astrophysical Journal, 864, 107
Kumar, P. & Quataert, E. J. 1997, Astrophysical Journal Letters, 475, L143
Kumar, P., Talon, S., & Zahn, J.-P. 1999, Astrophysical Journal, 520, 859
Kupka, F. & Muthsam, H. J. 2017, Living Reviews in Computational Astrophysics, 3, 1
Lamb, H. 1881, Proceedings of the London Mathematical Society, s1-13, 189
Lane, H. J. 1870, On the theoretical temperature of the Sun, under the hypothesis of a gaseous mass maintaining its volume by its internal heat, and depending on the laws of gases as known to terrestrial experiment
Leão, I. C., Pasquini, L., Ferreira Lopes, C. E., et al. 2015, Astronomy & Astrophysics, 582, A85
Lebreton, Y. & Goupil, M. J. 2014, A&A, 569
Lecoanet, D. & Quataert, E. 2013, Monthly Notices of the Royal Astronomical Society, 430, 2363
Ledoux, P. 1947, Astrophysical Journal, 105, 305
Lee, U. & Saio, H. 1997, Astrophysical Journal, 491, 839
Leibacher, J. W. & Stein, R. F. 1971, Astrophysical Letters, 7, 191
Leighton, R. B. 1960, in Aerodynamic Phenomena in Stellar Atmospheres, ed. R. N. Thomas, Vol. 12, 321–325
Leighton, R. B., Noyes, R. W., & Simon, G. W. 1962, ApJ, 135, 474
Lignières, F. & Georgeot, B. 2008, Physical Review E, 78, 016215
Lignières, F. & Georgeot, B. 2009, Astronomy & Astrophysics, 500, 1173
Lignières, F., Rieutord, M., & Reese, D. 2006, Astronomy & Astrophysics, 455, 607
Lindegren, L., Babusiaux, C., Bailer-Jones, C., et al. 2008, in IAU Symposium, Vol. 248, A Giant Step: from Milli- to Micro-arcsecond Astrometry, ed. W. J. Jin, I. Platais, & M. A. C. Perryman, 217–223
Lovekin, C. C., Deupree, R. G., & Short, C. I. 2006, Astrophysical Journal, 643, 460
Lucy, L. B. 1967, Zeitschrift für Astrophysik, 65, 89
Ludwig, H.-G., Freytag, B., & Steffen, M. 1999, Astronomy & Astrophysics, 346, 111
Lyell, C. 1863 (Philadelphia, G.W. Childs)
Maeder, A. 1995, Astronomy & Astrophysics, 299, 84
Maeder, A. 2003, Astronomy & Astrophysics, 399, 263
Maeder, A. 2009, Physics, Formation and Evolution of Rotating Stars
Maeder, A. & Meynet, G. 2004, Astronomy & Astrophysics, 422, 225
Maeder, A., Meynet, G., Lagarde, N., & Charbonnel, C. 2013, Astronomy & Astrophysics, 553, A1
Maeder, A. & Zahn, J.-P. 1998, Astronomy & Astrophysics, 334, 1000
Magic, Z. & Weiss, A. 2016, Astronomy & Astrophysics, 592, A24
Manchon, L., Belkacem, K., Samadi, R., et al. 2018, Astronomy & Astrophysics, 620, A107, reproduced with permission © ESO
Mantegazza, L., Poretti, E., Michel, E., et al. 2012, Astronomy & Astrophysics, 542, A24
Marques, J. P., Goupil, M. J., Lebreton, Y., et al. 2013, Astronomy & Astrophysics, 549, A74
Mathis, S. 2009, Astronomy & Astrophysics, 506, 811
Mathis, S., Palacios, A., & Zahn, J. P. 2004, Astronomy & Astrophysics, 425, 243
Mathis, S. & Prat, V. 2019, Astronomy & Astrophysics, 631, A26
Mathis, S., Prat, V., Amard, L., et al. 2018, Astronomy & Astrophysics, 620, A22
Mathis, S. & Zahn, J.-P. 2004, Astronomy & Astrophysics, 425, 229
Mathis, S. & Zahn, J. P. 2005, Astronomy & Astrophysics, 440, 653
Matt, S. P., Brun, A. S., Baraffe, I., Bouvier, J., & Chabrier, G. 2015, Astrophysical Journal Letters, 799, L23
McAlister, H. A., ten Brummelaar, T. A., Gies, D. R., et al. 2005, Astrophysical Journal, 628, 439
Mercier, M. J., Garnier, N. B., & Dauxois, T. 2008, Physics of Fluids, 20, 086601
Mestel, L. 1953, Monthly Notices of the Royal Astronomical Society, 113, 716
Meynet, G. & Maeder, A. 1997, Astronomy & Astrophysics, 321, 465
Meynet, G. & Maeder, A. 2002, Astronomy & Astrophysics, 390, 561
Michel, E., Baglin, A., Auvergne, M., et al. 2008, Sci-

ence, 322, 558
Michel, E., Dupret, M.-A., Reese, D., et al. 2017, in European Physical Journal Web of Conferences, Vol. 160, European Physical Journal Web of Conferences, 03001
Miesch, M. S., Brun, A. S., DeRosa, M. L., & Toomre, J. 2008, Astrophysical Journal, 673, 557
Miesch, M. S., Brun, A. S., & Toomre, J. 2006, Astrophysical Journal, 641, 618
Miller, S. L. 1953, Science, 117, 528
Mirouh, G. M., Angelou, G. C., Reese, D. R., & Costa, G. 2019, Monthly Notices of the Royal Astronomical Society, 483, L28
Morel, P. 1997, Astronomy and Astrophysics Supplement Series, 124, 597
Morel, P. & Lebreton, Y. 2008, Astrophysics and Space Science, 316, 61
Mosser, B., Barban, C., Montalbán, J., et al. 2011, Astronomy & Astrophysics, 532, A86
Mosser, B., Benomar, O., Belkacem, K., et al. 2014, A&A, 572
Mosser, B., Gehan, C., Belkacem, K., et al. 2018, Astronomy & Astrophysics, 618, A109
Mosser, B., Goupil, M. J., Belkacem, K., et al. 2012, Astronomy & Astrophysics, 540, A143
Mosser, B., Pinçon, C., Belkacem, K., Takata, M., & Vrard, M. 2017, Astronomy & Astrophysics, 600, A1
Mosser, B., Vrard, M., Belkacem, K., Deheuvels, S., & Goupil, M. J. 2015, Astronomy & Astrophysics, 584, A50
Mosumgaard, J. R., Jørgensen, A. C. S., Weiss, A., Silva Aguirre, V., & Christensen-Dalsgaard, J. 2019, arXiv e-prints, arXiv:1910.10163
Nielsen, M. B., Gizon, L., Schunker, H., & Karoff, C. 2013, Astronomy & Astrophysics, 557, L10
Nordlund, A. & Galsgaard, K. 1995, 1
Núñez, A., Agüeros, M. A., Covey, K. R., et al. 2015, Astrophysical Journal, 809, 161
Odert, P., Leitzinger, M., Guenther, E. W., & Heinzel, P. 2020, Stellar coronal mass ejections II. Constraints from spectroscopic observations
Odert, P., Leitzinger, M., Hanslmeier, A., & Lammer, H. 2017, Monthly Notices of the Royal Astronomical Society, 472, 876
Ogilvie, G. I. & Lin, D. N. C. 2004, Astrophysical Journal, 610, 477
Ohishi, N., Nordgren, T. E., & Hutter, D. J. 2004, Astrophysical Journal, 612, 463
Öpik, E. J. 1951, Monthly Notices of the Royal Astronomical Society, 111, 278
Ouazzani, R.-M. 2011, PhD: La rotation et son interaction avec les oscillations dans les étoiles
Ouazzani, R.-M., Dupret, M.-A., Goupil, M.-J., & Reese, D. R. 2010, Astronomische Nachrichten, 999, 1
Ouazzani, R. M., Dupret, M. A., & Reese, D. R. 2012, Astronomy & Astrophysics, 547, A75
Ouazzani, R. M., Marques, J. P., Goupil, M. J., et al. 2019, Astronomy & Astrophysics, 626, A121
Ouazzani, R. M., Roxburgh, I. W., & Dupret, M. A. 2015, Astronomy & Astrophysics, 579, A116
Ouazzani, R.-M., Salmon, S. J. A. J., Antoci, V., et al. 2017, Monthly Notices of the Royal Astronomical Society, 465, 2294
Palacios, A. 2013, in EAS Publications Series, Vol. 62, EAS Publications Series, ed. P. Hennebelle & C. Charbonnel, 227–287
Palacios, A., Talon, S., Charbonnel, C., & Forestini, M. 2003, Astronomy & Astrophysics, 399, 603
Parker, E. N. 1958, Astrophysical Journal, 128, 664
Paxton, B., Smolec, R., Schwab, J., et al. 2019, Astrophysical Journal, Supplement Series, 243, 10
Pepe, F., Mayor, M., Benz, W., et al. 2000, in From Extrasolar Planets to Cosmology: The VLT Opening Symposium, ed. J. Bergeron & A. Renzini, 572
Perryman, M. A. C., de Boer, K. S., Gilmore, G., et al. 2001, Astronomy & Astrophysics, 369, 339
Pesnell, W. D. 1987, Astrophysical Journal, 314, 598
Piau, L., Collet, R., Stein, R. F., et al. 2014, Monthly Notices of the Royal Astronomical Society, 437, 164
Pinçon, C. 2019, arXiv e-prints, arXiv:1907.00201
Pinçon, C., Belkacem, K., & Goupil, M. J. 2016, Astronomy & Astrophysics, 588, A122
Pinçon, C., Goupil, M. J., & Belkacem, K. 2020, Astronomy & Astrophysics, 634, A68
Pinsonneault, M. H., Elsworth, Y., Epstein, C., et al. 2014, Astrophysical Journal, Supplement Series, 215, 19
Pitts, E. & Tayler, R. J. 1985, Monthly Notices of the Royal Astronomical Society, 216, 139
Prat, V., Guilet, J., Viallet, M., & Müller, E. 2016, Astronomy & Astrophysics, 592, A59
Prat, V. & Lignières, F. 2013, Astronomy & Astrophysics, 551, L3
Prat, V. & Lignières, F. 2014, Astronomy & Astrophysics, 566, A110
Press, W. H. 1981, Astrophysical Journal, 245, 286
Press, W. H., Teukolsky, S. A., Vetterling, W. T., et al. 1992, Numerical Recipes in FORTRAN, The Art of Scientific Computing, 2nd edn. (Cambridge University Press)
Rauer, H., Catala, C., Aerts, C., et al. 2014, Experimental Astronomy, 38, 249
Rayleigh, L. 1916, Proceedings of the Royal Society of London, Philosophical Transactions of the Royal Society, 93
Reese, D. R., Dupret, M.-A., & Rieutord, M. 2018, in

3rd BRITE Science Conference, ed. G. A. Wade, D. Baade, J. A. Guzik, & R. Smolec, Vol. 8, 80–87
Reese, D. R., Lignières, F., Ballot, J., et al. 2017, Astronomy & Astrophysics, 601, A130
Reese, D. R., Lignières, F., & Rieutord, M. 2006, Astronomy & Astrophysics, 455, 621
Reese, D. R., MacGregor, K. B., Jackson, S., Skumanich, A., & Metcalfe, T. S. 2009, Astronomy & Astrophysics, 506, 189
Regev, O., Umurhan, O. M., & Yecko, P. A. 2016, Modern Fluid Dynamics for Physics and Astrophysics
Richard, D. & Zahn, J.-P. 1999, Astronomy & Astrophysics, 347, 734
Ricker, G. R., Winn, J. N., Vanderspek, R., et al. 2014, Society of Photo-Optical Instrumentation Engineers (SPIE) Conference Series, Vol. 9143, Transiting Exoplanet Survey Satellite (TESS), 914320
Rieutord, M. 1987, Geophysical and Astrophysical Fluid Dynamics, 39, 163
Rieutord, M. 2015, Fluid Dynamics: An Introduction
Rieutord, M., Espinosa Lara, F., & Putigny, B. 2016, Journal of Computational Physics, 318, 277
Rieutord, M. & Zahn, J. P. 1995, Astronomy & Astrophysics, 296, 127
Rodríguez-Martín, J. E., García Hernández, A., Suárez, J. C., & Rodón, J. R. 2020, Monthly Notices of the Royal Astronomical Society, 498, 1700
Rogachevskii, I. & Kleeorin, N. 2018, Journal of Plasma Physics, 84, 735840201
Rogers, F. J. & Iglesias, C. A. 1992, Astrophysical Journal, 401, 361
Rogers, F. J. & Nayfonov, A. 2002, ApJ, 576, 1064
Rogers, T. M. & Glatzmaier, G. A. 2006, Astrophysical Journal, 653, 756
Rosenthal, C. S., Christensen-Dalsgaard, J., Houdek, G., et al. 1995, in ESA Special Publication, Vol. 376, Helioseismology, 459–464
Rosenthal, C. S., Christensen-Dalsgaard, J., et al. 1999, A&A, 351, 689
Rosing, M. T., Bird, D. K., Sleep, N. H., Glassley, W., & Albarède, F. 2006, Palaeogeography, Palaeoclimatology, Palaeoecology, 232, 99
Roxburgh, I. W. 2004, Astronomy & Astrophysics, 428, 171
Roxburgh, I. W. 2006, Astronomy & Astrophysics, 454, 883
Roxburgh, I. W., Polnarev, A. G., Giampieri, G., & Vorontsov, S. V. 2001, arXiv e-prints, astro
Roxburgh, I. W. & Vorontsov, S. V. 1994, Monthly Notices of the Royal Astronomical Society, 268, 143
Roxburgh, I. W. & Vorontsov, S. V. 2003, A&A, 411, 215
Royer, F., Gerbaldi, M., Faraggiana, R., & Gómez, A. E. 2002, Astronomy & Astrophysics, 381, 105
Rüdiger, G., Gellert, M., Spada, F., & Tereshin, I. 2015, Astronomy & Astrophysics, 573, A80
Rüdiger, G., Schultz, M., & Kitchatinov, L. L. 2014, arXiv e-prints, arXiv:1404.3562
Rüdiger, G., Schultz, M., & Kitchatinov, L. L. 2016, Monthly Notices of the Royal Astronomical Society, 456, 3004
Saio, H. & Takata, M. 2014, Publications of the Astronomical Society of Japan, 66, 58
Samadi, R., Belkacem, K., Ludwig, H.-G., et al. 2013, Astronomy & Astrophysics, 559, A40
Samadi, R., Belkacem, K., & Sonoi, T. 2015, in EAS Publications Series, Vol. 73-74, EAS Publications Series, 111–191
Samadi, R. & Goupil, M. J. 2001, Astronomy & Astrophysics, 370, 136
Scherrer, P. H., Bogart, R. S., Bush, R. I., et al. 1995, Solar Physics, 162, 129
Scherrer, P. H. & Gough, D. O. 2019, Astrophysical Journal, 877, 42
Schou, J., Christensen-Dalsgaard, J., & Thompson, M. J. 1994, Astrophysical Journal, 433, 389
Schou, J. & SOE Internal Rotation Team. 1998, in IAU Symposium, Vol. 185, New Eyes to See Inside the Sun and Stars, ed. F.-L. Deubner, J. Christensen-Dalsgaard, & D. Kurtz, 141
Schröter, E. H. 1985, Solar Physics, 100, 141
Schumaker, L. 2007, Spline Functions: Basic Theory, 3rd edn., Cambridge Mathematical Library (Cambridge University Press)
Schunker, H., Schou, J., Gaulme, P., & Gizon, L. 2018, Solar Physics, 293, 95
Schwarzschild, M. & Härm, R. 1958, Astrophysical Journal, 128, 348
Scott, P., Asplund, M., Grevesse, N., Bergemann, M., & Sauval, A. J. 2015a, Astronomy & Astrophysics, 573, A26
Scott, P., Grevesse, N., Asplund, M., et al. 2015b, Astronomy & Astrophysics, 573, A25
Scuflaire, R. 1974, Astronomy & Astrophysics, 36, 107
Seaton, M. J. 2005, Monthly Notices of the Royal Astronomical Society, 362, L1
Seaton, M. J. 2007, Monthly Notices of the Royal Astronomical Society, 382, 245
Seaton, M. J., Yan, Y., Mihalas, D., & Pradhan, A. K. 1994, Monthly Notices of the Royal Astronomical Society, 266, 805
Semel, M. 1989, Astronomy & Astrophysics, 225, 456
Serenelli, A. 2016, European Physical Journal A, 52, 78
Shibahashi, H. 1979, Publications of the Astronomical Society of Japan, 31, 87

Silva Aguirre, V., Lund, M. N., Antia, H. M., et al. 2017, Astrophysical Journal, 835, 173
Skumanich, A. 1972, Astrophysical Journal, 171, 565
Sonoi, T., Belkacem, K., Dupret, M.-A., et al. 2017, ArXiv e-prints
Sonoi, T., Samadi, R., Belkacem, K., et al. 2015, A&A, 583
Spiegel, E. A. & Zahn, J. P. 1992, Astronomy & Astrophysics, 265, 106
Spruit, H. C. 1999, Astronomy & Astrophysics, 349, 189
Spruit, H. C. 2002, Astronomy & Astrophysics, 381, 923
Spruit, H. C. 2013, ArXiv e-prints
Stacey, F. D. 2000, Journal of Geophysical Research, 105, 13155
Stein, R. F. & Nordlund, A. 1991, Convection and its influence on oscillations (Springer Berlin Heidelberg), 195–212
Struve, O. & Elvey, C. T. 1931, Monthly Notices of the Royal Astronomical Society, 91, 663
Suárez, J. C., García Hernández, A., Moya, A., et al. 2014, Astronomy & Astrophysics, 563, A7
Sweet, P. A. 1950, Monthly Notices of the Royal Astronomical Society, 110, 548
Takata, M. 2014, Publications of the Astronomical Society of Japan, 66, 80
Takata, M. & Saio, H. 2013, Publications of the Astronomical Society of Japan, 65, 68
Talon, S. & Charbonnel, C. 2003, å, 450
Talon, S. & Zahn, J. P. 1997, Astronomy & Astrophysics, 317, 749
Talon, S. & Zahn, J.-P. 1998, Astronomy & Astrophysics, 329, 315
Talon, S., Zahn, J. P., Maeder, A., & Meynet, G. 1997, Astronomy & Astrophysics, 322, 209
Tassoul, M. 1980, Astrophysical Journal, Supplement Series, 43, 469
Tassoul, M. 1990, Astrophysical Journal, 358, 313
Tayler, R. J. 1957, Proceedings of the Physical Society B, 70, 31
Tayler, R. J. 1973, Monthly Notices of the Royal Astronomical Society, 161, 365
Taylor, G. I. 1923, Philosophical Transactions of the Royal Society of London Series A, 223, 289
Taylor, G. I. 1931, Proceedings of the Royal Society of London Series A, 132, 499
Tenev, T. G. & Horstemeyer, M. F. 2018, International Journal of Modern Physics D, 27, 1850083
Théado, S., Vauclair, S., Alecian, G., & LeBlanc, F. 2009, Astrophysical Journal, 704, 1262
Thomson, W. 1862, Transactions of the Royal Society of Edinburgh, 23, 157–169
Tomczyk, S., Streander, K., Card, G., et al. 1995, Solar Physics, 159, 1
Townsend, A. A. 1958, Journal of Fluid Mechanics, 4, 361
Trampedach, R. 2010, Astrophysics and Space Science, 328, 213
Trampedach, R., Aarslev, M. J., Houdek, G., et al. 2017, MNRAS, 466
Trampedach, R. & Stein, R. F. 2011, ApJ, 731, 78
Turck-Chièze, S., Palacios, A., Marques, J. P., & Nghiem, P. A. P. 2010, Astrophysical Journal, 715, 1539
Turon, C., O'Flaherty, K. S., & Perryman, M. A. C. 2005, in ESA Special Publication, Vol. 576, The Three-Dimensional Universe with Gaia
Ulrich, R. K. 1970, Astrophysical Journal, 162, 993
Ulrich, R. K. 1986, ApJ - Letters to the Editor, 306, L37
Unno, W., Osaki, Y., Ando, H., Saio, H., & Shibahashi, H. 1989, Nonradial oscillations of stars
Vallis, G. K. 2006, Atmospheric and Oceanic Fluid Dynamics (Cambridge, U.K.: Cambridge University Press), 745
Van Reeth, T., Tkachenko, A., & Aerts, C. 2016, Astronomy & Astrophysics, 593, A120
Velikhov, E. P. 1959, Zhur. Eksptl'. i Teoret. Fiz., 36
Verma, K., Antia, H. M., Basu, S., & Mazumdar, A. 2014, Astrophysical Journal, 794, 114
Vögler, A. 2003, Three-dimensional simulations of magneto-convection in the solar photosphere
Vogt, H. 1925, Astronomische Nachrichten, 223, 229
von Zeipel, H. 1924, Monthly Notices of the Royal Astronomical Society, 84, 665
Vorontsov, S. V. 1991, Soviet Astronomy, 35, 400
Vrard, M., Mosser, B., & Samadi, R. 2016, Astronomy & Astrophysics, 588, A87
Wasiutynski, J. 1946, Astrophysica Norvegica, 4, 1
Weber, E. J. & Davis, Leverett, J. 1967, Astrophysical Journal, 148, 217
Weiss, W. W., Rucinski, S. M., Moffat, A. F. J., et al. 2014, Publications of the Astronomical Society of the Pacific, 126, 573
White, T. R., Bedding, T. R., Stello, D., et al. 2011, Astrophysical Journal, 743, 161
Woods, J. D. 1969, Radio Science, 4, 1289
Wright, N. J., Drake, J. J., Mamajek, E. E., & Henry, G. W. 2011, Astrophysical Journal, 743, 48
Xiong, D. R., Deng, L., & Zhang, C. 2015, Monthly Notices of the Royal Astronomical Society, 451, 3354
Xiong, D. R., Deng, L., Zhang, C., & Wang, K. 2016, Monthly Notices of the Royal Astronomical Society, 457, 3163
Xu, Y., Takahashi, K., Goriely, S., et al. 2013, Nuclear Physics A, 918, 61
Yu, J., Huber, D., Bedding, T. R., et al. 2018, Astrophysical Journal, Supplement Series, 236, 42

Zahn, J. P. 1974, in Stellar Instability and Evolution, ed. P. Ledoux, A. Noels, & A. W. Rodgers, Vol. 59, 185
Zahn, J. P. 1992, Astronomy & Astrophysics, 265, 115
Zahn, J. P., Brun, A. S., & Mathis, S. 2007, Astronomy & Astrophysics, 474, 145
Zhao, M., Monnier, J. D., Pedretti, E., et al. 2009, Astrophysical Journal, 701, 209
Zorec, J., Frémat, Y., Domiciano de Souza, A., et al. 2017, Astronomy & Astrophysics, 602, A83

université PARIS-SACLAY

ÉCOLE DOCTORALE
Astronomie
et Astrophysique
d'Île-de-France (AAIF)

Titre: Du transport de moment cinétique dans les zones radiatives stellaires, en 2D

Mots clés: intérieurs stellaires; étoiles; rotation; turbulence; ondes; modélisation

Résumé: La rotation a d'importantes conséquences sur la structure interne des étoiles et leur évolution. La force centrifuge déforme l'étoile et s'oppose à la gravité, mimant une étoile de plus faible masse. Plus important encore, la circulation méridienne et la turbulence induites par la rotation mélangent les éléments chimiques, prolongeant la vie de l'étoile et altérant la détermination de son âge, un problème majeur en astrophysique. Enfin, l'interaction rotation-convection génère des champs magnétiques. L'activité associée a une influence décisive sur la survie des atmosphères planétaires.

Les données astérosismiques des missions spatiales CoRoT et *Kepler* ont montré que les modèles 1D actuels de transport du moment cinétique dans les zones radiatives (viscosité turbulente et circulation méridienne) ne sont pas satisfaisants. D'autres mécanismes doivent être actifs: les ondes internes de gravité, les champs magnétiques, etc. Tous les modèles les décrivant sont actuellement incomplets et doivent en particulier tenir compte des effets 2D.

La description 1D de la rotation est généralement justifiée par le fait que, dans les zones radiatives, la turbulence est beaucoup plus forte horizontalement que verticalement, supprimant les variation latitudinales de vitesse angulaire. Cette hypothèse pourrait être invalide près de l'axe de rotation. De plus, les ondes internes de gravité étant générées à la base des enveloppes convectives, le décalage Doppler qu'elles subissent en entrant dans la zone radiative dépend de la latitude. Elles sont ensuite filtrées dans la zone de transition entre les régions convective et radiative, présentant une forte rotation différentielle.

Cette thèse est dédiée à l'implémentation dans un code d'évolution stellaire d'un traitement simplifié du transport du moment cinétique en 2D. Ce traitement est basé sur une méthode de déformation permettant de calculer la structure 2D de l'étoile, ainsi que les perturbations des différents champs induites par la rotation. Le transport du moment cinétique est ensuite traité en 2D, et permettra d'étudier plus en détail d'autres mécanismes de transport.

Title: On the transport of angular momentum in stellar radiative zones in 2D

Keywords: stellar interiors; stars; rotation; turbulence; waves; modelling

Abstract: Rotation has important consequences for stellar internal structure and evolution. The centrifugal force deforms the star and balances gravity, mimicking a lower mass star. Most importantly, meridional circulations and rotation-induced turbulence mixes chemical elements, extending the stellar lifetime and affecting age determinations, one of the most important problems in astrophysics. Lastly, the rotation-convection interaction generates magnetic fields. The associated activity has a determining influence on the survival of planetary atmospheres.

Asteroseismic data from the space missions CoRoT and *Kepler* have shown that current 1D models of angular momentum transport in radiative zones (turbulent viscosity and meridional circulation) are not satisfactory. Other mechanisms must be active, such as internal gravity waves, magnetic fields, etc. All models proposed for these mechanisms are incomplete and must, in particular, account for 2D effects.

The 1D description of rotation is usually justified by the fact that turbulence is much stronger horizontally than vertically in radiative zones, suppressing variations of angular velocity. This assumption may not be verified at near the rotation axis. Moreover, because internal gravity waves are generated at the base of convective envelopes, the Doppler shift experienced by these waves when they enter the radiative zone should depend on latitude. These waves are further filtered in the transition zone between the convective and radiative zones, a zone that has a strong differential rotation.

This PhD is devoted to the implementation in a stellar evolution code of a simplified treatment of transport of angular momentum in 2D. This treatment is based on a deformation method that enables the computation of the 2D structure of the star, as well as the rotation-induced perturbations of the various fields. The transport of angular momentum is then treated in 2D, and will allow the further study of extra mechanisms of transport.

Université Paris-Saclay
Espace Technologique / Immeuble Discovery
Route de l'Orme aux Merisiers RD 128 / 91190 Saint-Aubin, France